

Proceedings

4th International Conference

Hybrid 2020

Materials and Structures

28 – 29 April 2020

Web-Conference, Germany

<https://hybrid2020.dgm.de>

DGM

The Scope

More than the sum of their parts!

Very often, innovative materials act as trailblazers for the introduction of new technologies and products. Hybrid materials and structures made or joined from several individual components are playing an increasingly important role in the industrial applications of mechanical engineering and construction.

„Hybrid Materials and Structures 2020“ covers the entire spectrum of topics, from basic materials to design, from production to application, and thus provides the basis for an in-depth understanding of application-specific material and component behavior. The only limitation is the focus on material combinations that perform structural tasks in some way.

The conference offers a diverse mix of short talks, poster presentations and poster forums. In addition, the interdisciplinary exchange between science and industry will enable extended networking among the participants.

Special Session: „Intrinsic Hybrid Composites“

In multi-material design, hybrid composites joined by downstream processes such as bonding or welding are already established, but often do not fully exploit the lightweight potential. An intrinsic hybrid composite, however, is an integral component in which the various materials are joined in the consolidation or forming process of the metal- or plastic-based component. Hybrid 2020 is dedicating a special session to these material systems.

Hosting a DFG priority programme on intrinsic hybrid composites and a German-Canadian graduate school on hybrid fibre composites, the Karlsruhe Institute of Technology (KIT) is home of two major research collaborations dedicated to this class of materials. This also applies to numerous industrial companies, especially from the automotive and supplier industries, and non-university research institutions in the Karlsruhe technology region.



Prof. Dr.-Ing. Joachim M. Hausmann

Institute for Composite Materials (IVW), Kaiserslautern



Prof. Dr.-Ing. Marc Siebert

PFH - Private University of Applied Sciences Göttingen



Dr.-Ing. Axel von Hehl

Leibniz Institute for Materials Engineering - IWT, Bremen



Prof. Dr.-Ing. Kay André Weidenmann

Institute for Materials Resource Management,
University of Augsburg

Table of Contents

Basics 7

INHYB – AN INTRINSIC HYBRID LAMINATE FOR CYCLICALLY LOADED COMPONENTS	8
<i>R. Brandt, A. Busch, S. Haller</i>	

RESIDUAL STRESS MEASUREMENTS IN GFRP/STEEL HYBRID COMPONENTS	14
<i>T. Wu, S. R. Tinkloh, T. Tröster, W. Zinn, T. Niendorf</i>	

STUDY ON HYGROTHERMAL AGEING BEHAVIOUR OF HYBRID CFRP/AL JOINTS: INFLUENCE OF PRE-TREATMENT, ADHESIVE COMPOSITION AND AGEING PROCESS	21
<i>J. Schanz, S. Kambach, D. Meinhard, A. De Silva, D. K. Harrison, H. Riegel, V. Knoblauch</i>	

Characterization 32

MECHANICAL CHARACTERIZATION OF AN INTERPENETRATING METAL-MATRIX- COMPOSITE BASED ON HIGHLY HOMOGENEOUS CERAMIC FOAMS	33
<i>J. Schukraft, C. Lohr, K. A. Weidenmann</i>	

CHARACTERIZATION AND MODELLING OF THE VIBRATION AND DAMPING BEHAVIOR OF CARBON FIBER-METAL-ELASTOMER LAMINATES BY USING MODAL ANALYSIS IN CANTILEVER SETUP	40
<i>V. Sessner, A. Jackstadt, W. Liebig, L. Kärger, K. Weidenmann</i>	

EVALUATION OF SURFACE MODIFIED ALUMINIUM/POLYAMIDE-6 FIBRE-METAL-LAMINATES	46
<i>F. Thum, A. Monden, M.G.R. Sause</i>	

MECHANICAL PROPERTIES ON IN-SITU POLYMERIZED FIBRE-METAL-LAMINATES	53
<i>H. O. Werner, W. Liebig, K. A. Weidenmann</i>	

INFLUENCE OF SURFACE TREATMENT ON INTERFACIAL STRENGTH AND TENSILE PROPERTIES OF THERMOPLASTIC BASED HYBRID LAMINATES	59
<i>M. Trautmann, S. Mrzljak, F. Walther, G. Wagner</i>	

INFLUENCE OF SURFACE TREATMENT ON FATIGUE PROPERTIES OF THERMOPLASTIC BASED HYBRID LAMINATES	65
<i>S. Mrzljak, M. Trautmann, G. Wagner, F. Walther</i>	

FATIGUE DAMAGE BEHAVIOR OF CONTINUOUS-DISCONTINUOUS FIBER REINFORCED SHEET MOLDING COMPOUNDS	71
<i>M. Bartkowiak, W. Liebig, K.A. Weidenmann</i>	

MICROSTRUCTURAL CHARACTERIZATION OF GLASS FIBER REINFORCED SMC BY NANOINDENTATION AND SINGLE-FIBER PUSH-OUT TEST <i>B. Rohrmüller, P. Gumbsch, J. Hohe</i>	78
SURFACE HYBRIDISATION OF SEMI-POROUS PARTICLE FOAMS <i>W. Koshukow, M. Stegelmann, M. Krahl, M. Gude, L. Enneking, C. Buske</i>	84
ON FIBER ORIENTATION STATISTICS FOR WOVEN FABRICS IN FIBER METAL LAMINATES <i>P. Pinter, H.O. Werner, K.A. Weidenmann, W. Liebig</i>	90
MICROSTRUCTURE CHARACTERIZATION OF DISCONTINUOUS FIBER REINFORCED POLYMERS BASED ON VOLUMETRIC IMAGES: FIBER BUNDLE TRACKING AND WELD LINE INVESTIGATION <i>L. Schöttl, W. V. Liebig, K. A. Weidenmann, K. Inal, P. Elsner</i>	97
DETECTION OF DAMAGE IN GLASS FIBRE-REINFORCED THERMOPLASTICS USING ACTIVE LOCK-IN THERMOGRAPHY <i>S. Poleschke, B. Engel</i>	102
COMPARISON OF ANOMALY CAPABILITIES OF PULSE PHASE THERMOGRAPHY IN TRANSMISSION AND REFLECTION SETUP ON SHEET MOLDING COMPOUND <i>L. Bretz, M. Wilke, B. Häfner, G. Lanza</i>	108
<h2>Design and Layout</h2>	117
SURROGATE MODELLING OF HYBRID MATERIAL PAIRINGS INCLUDING ORGANIC SHEETS <i>M. Richter, H. Gese, H. Dell, G. Oberhofer, F. Duddeck</i>	118
NUMERICAL INVESTIGATION OF THE HOLE-DRILLING METHOD APPLIED TO INTRINSIC MANUFACTURED METAL-CFRP HYBRIDS <i>S. Tinkloh, T. Wu, T. Tröster, T. Niendorf</i>	126
A HOLISTIC APPROACH TO OPTIMIZATION-BASED DESIGN OF HYBRID MATERIALS <i>M. Triebus, T. Tröster</i>	132
<h2>Intrinsic Hybrid Composites</h2>	137
HYBRID FIBRE REINFORCED THERMOPLASTIC HOLLOW STRUCTURES WITH A MULTI- SCALE STRUCTURED METAL LOAD INTRODUCTION ELEMENT <i>V. Würfel, R. Grützner, F. Hirsch, D. Barfuß, M. Gude, R. Müller, M. Kästner</i>	138
DESIGN & QUALITY ASSURANCE OF INTRINSIC HYBRID METAL-CFRP LIGHTWEIGHT STRUCTURES <i>L. Bretz, F. Günther, H. Jost, M. Schwarz, V. Kretzschmar, M. Pohl, L. Weiser, B. Häfner, J. Summa, H.-G. Herrmann, M. Stommel, G. Lanza</i>	144
QUANTITATIVE PASSIVE THERMOGRAPHY FOR EVALUATION OF FATIGUE DAMAGE IN AN INTRINSIC HYBRID COMPOSITE <i>J. Summa, F. Grossmann, H.-G. Herrmann</i>	160

Manufacturing 166

MANUFACTURING OF HYBRID COMPONENTS BY VARTM-PROCESS USING NEW SEALING TECHNIQUE DEVELOPED <i>Deviprasad C J, T. Stallmeister, Z. Wang and T. Tröster</i>	167
SCREENING TESTS OF AN ONE-SHOT FORMING PROCESS OF FIBRE-REINFORCED THERMOPLASTICS AND STEEL SHEETS TO DETERMINE THE GEOMETRICAL ACCURACY <i>P. Kabala, M. Demes, T. Ossowski, J. Beuscher, K. Dröder</i>	173
COMBINED DURING AND DEEP DRAWING OF FIBRE METAL LAMINATES TO SPHERICAL HYBRID COMPONENTS <i>H. Sapli, T. Heggemann, W. Homberg</i>	180
HYBRIDIZATION FOR SERIES PRODUCTION - CONTINUOUS PROFILE PRODUCTION BY PULTRUSION <i>D. Löpitz, M. Knobloch, D. Wagner, W.-G. Drossel, M. Gedan-Smolka, K. Schubert, A. Marschner</i>	186
PROCESS ANALYSIS OF THERMOPLASTIC-METAL COMPOSITE STRUCTURES IN 3D-HYBRID TECHNOLOGY - A COMBINED APPROACH TO QUALITY ASSURANCE FOR ROBUST MANUFACTURING PROCESSES <i>D. R. Haider, M. v. Unold, M. Krahl, M. Gude</i>	194
INFLUENCE OF THE MORPHOLOGY OF NANOPOROUS SILICON DIOXIDE BASED SURFACE COATINGS ON THE INTERFACIAL STRENGTH OF INJECTION-MOULDED POLYMER-METAL HYBRIDS <i>M. Laux, Y. Löhr, R. Dreher, R. Emmerich, F. Henning</i>	200
A HIGHLY ECONOMICAL INDUCTIVE JOINING TECHNOLOGY FOR FIBRE COMPOSITE CONNECTIONS <i>A. Fröhlich, M. Kroll, P. Rochala, V. Kräusel,</i>	206
INFLUENCE OF CONTINUOUS WAVE SURFACE STRUCTURING AND ZINC COATING ON BOND STRENGTH OF HYBRID JOINTS MADE OF STEEL AND TP-FRPC <i>S. Weidmann, P. Mitschang</i>	212
THERMAL JOINING OF METAL-POLYMER HYBRID STRUCTURES BY USING CONVENTIONAL WELDING PROCESSES <i>A. Haelsig, W. Georgi, E. Brueckner, P. Thieme, M. Gehde</i>	221
DETERMINATION OF THE MECHANICAL PROPERTIES OF A SINTERED CFRP CONNECTION MODULE JOINED BY A THREAD FORMING SCREW <i>A. Marx, T. Hutsch, P. Schiebel, D. Feltn, F. Hoffmeister, A. Babbel, A. Herrmann, T. Weißgärber</i>	227
JOINING OF ADDITIVELY MANUFACTURED TITANIUM WITH DIFFERENT SURFACE STRUCTURES WITH FIBER-REINFORCED PEEK FOR LIGHTWEIGHT DESIGN APPLICATIONS <i>J. Moritz, P. Götze, T. Schiefer, A. Klotzbach, J. Standfuß, E. López, F. Brückner, C. Leyens</i>	237

MULTI-COMPONENT HIGH PRESSURE DIE CASTING (M-HPDC): INFLUENCING FACTORS ON BOND QUALITY OF METAL-PLASTIC HYBRIDS AND ITS NECESSITY OF PROCESS DATA LOGGING <i>P. Messer, U. Vroomen, A. Bührig-Polaczek</i>	243
EXPERIMENTAL INVESTIGATION OF THE LOAD BEARING CAPACITY OF INSERTS EMBEDDED IN THERMOPLASTIC COMPOSITES <i>J. Troschitz, R. Kupfer, M. Gude</i>	249
INVESTIGATIONS ON POSSIBLE JOINING PROCESSES FOR LIGHTWEIGHT BODY STRUCTURES FOR COMMERCIAL VEHICLES IN MUNICIPAL SERVICE OPERATIONS <i>T. Schiefer, A. Mahlme, D. Theis, B. Ganbaatar, M. Sauer, F. Zimmermann, A. Klotzbach, J. Standfuß, M. Zimmermann</i>	255
INVESTIGATION OF AUTOMATED NIBBLING AS AN ALTERNATIVE CUTTING TECHNOLOGY FOR MACHINING OF FIBER-REINFORCED POLYMERS <i>J. Langer,, M. Gerstenmeyer, V. Schulze</i>	261
STUDY ON WATER JET CUTTING OF FIBRE-REINFORCED-PLASTICS-METAL-LAMINATES <i>V. Reichel, F. Rothe, F. Franke, D. Lattek, J. Beuscher, K. Dröder</i>	268
Oral Poster Presentation	275
CONTRIBUTION TO STRUCTURAL MECHANICS OF PATCH-BASED COMPOSITES <i>A. Baumer, A. Baeten</i>	276
PART AUTOMATED METHOD FOR REPAIRING COMPOSITE PARTS <i>B. Manin, A. Raina, T. Quadflieg, T. Gries</i>	282
MATERIAL SELECTION FOR TEMPERATURE SENSITIVE ACTUATORS MANUFACTURED FROM SHAPE MEMORY ALLOY WIRES EMBEDDED IN POLYMER STRUCTURES <i>P. Eyer, A. Trauth, K.A. Weidenmann</i>	288
PROCESSING RELATIONSHIPS OF HYBRID POLYMER-METAL COMPOSITES IN THE INJECTION MOULDING PROCESS <i>A. Schwarz, W. Liebig, K. Weidenmann, P. Elsner</i>	296

TOPIC

Basics



@DGM_eV

#Hybrid2020

InHyb – An Intrinsic Hybrid Laminate for Cyclically Loaded Components

R. Brandt¹, A. Busch², S. Haller¹

¹University of Siegen, 57076 Siegen, GERMANY

²MUBEA, 48340 Amorebieta-Etxano (Bizkaia), SPAIN

1 Introduction

Intrinsic hybrid¹ materials most frequently consist of a light metal, e.g. aluminum or titanium, and a fiber reinforced polymer like glass fiber reinforced plastic (GFRP) or carbon fiber reinforced plastic (CFRP). Only few approaches of an intrinsic hybrid laminate consisting of steel and CFRP are known from literature by Lauter, Both, and Monden [1–3]. In this study, a unidirectional (U-)GFRP and a high strength steel make the intrinsic hybrid laminate. The materials testing program sets the focus on the investigation of the strength of the interface between both constituents. Chemical as well as mechanical surface treatments have been benchmarked in order to find an appropriate strength of bonding. Two main load cases serve to characterize the bonding strength of the interface. A double cantilever beam (DCB) provides the data to evaluate the fracture toughness K_{Ic} by means of the energy release rate G_I . An Edge-Shear-Test (EST) according to Weidenmann et al. [4] as well as an interlaminar shear strength (ILSS)-test provide the static shear strength τ_s . Furthermore, the cyclical shear strength τ_c has been evaluated by means of a cyclical EST as well as an ILSS-test. Both testing methods deliver cyclical shear strength values τ_c^{EST} and τ_c^{ILSS} that are differing significantly among the methods. Therefore, residual stress assessments have been done in order to estimate the impact of residual stress on the fatigue strength. It becomes evident that residual stress within these hybrid laminates is relevant.

2 Specimens Preparation

Figure 1 shows an overview of the utilized test setups as well as the specimens of the mechanical testing, respectively. A detailed description of the dimensions of the DCB specimen is given in [5, 7]. In contrast to these former reports, however, the authors propose a reworked EST-specimen layout comprising a steel sandwich with a core made by U-GFRP and the outer dimensions of length $l_{EST} = 10 \text{ mm}$ and width $w_{EST} = 25 \text{ mm}$. The thickness t_{EST} of the specimen itself and the thickness of its constituents are chosen such that the blades of the EST tool only actuates the steel plates of the specimen. The ILSS-specimen is a U-GFRP sandwich with a steel core of length $l_{ILSS} = 30 \text{ mm}$ and width $w_{ILSS} = 25 \text{ mm}$. Its total layer thickness is $t_{ILSS} = 5 \text{ mm}$ with $t_{Steel} = 0,3 \text{ mm}$ and $t_{GFRP} = 2 \times 2,35 \text{ mm}$, respectively. The span of the support is $l_s = 20 \text{ mm}$.

The preparation of the specimens happens according to [5, 6]. It implies either a chemical surface treatment by primers, like silane and titanate, or a mechanical surface treatment, i. e. by means of sand blasting or laser structuring. The pressing process leads to a fiber volume content

¹ An intrinsic hybrid is an integral component that is compounded during primary forming or forming.

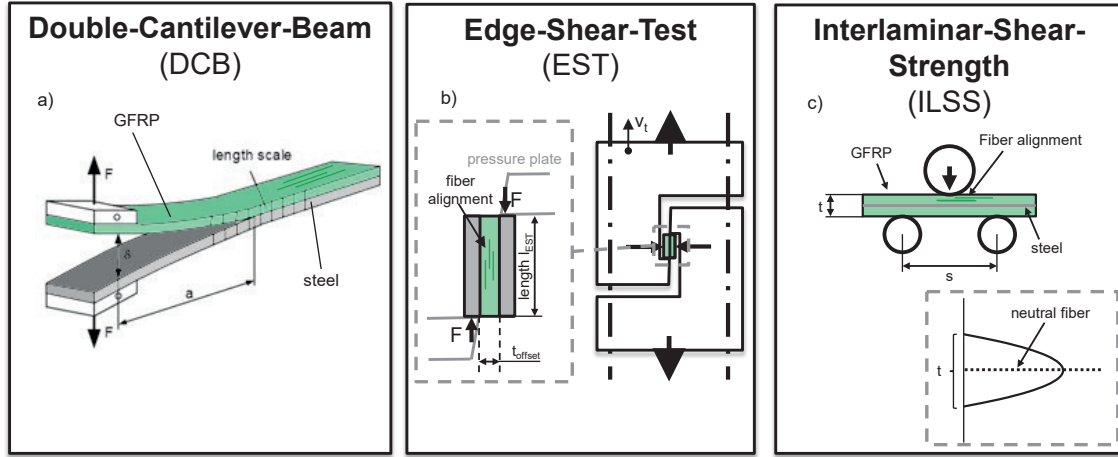


Figure 1: Specimen layout and set-ups for a) double cantilever beam (DCB) test b) edge shear test (EST) and c) interlaminar shear strength (ILSS) test

of approximately 60% within the GFRP constituents. Two variants of specimens are prepared for mechanical testing, namely (i) the as manufactured and (ii) the aged specimens. Aging of the specimens happens by depositing the as manufactured specimens into water at an elevated temperature of $T = 80^\circ C$ for one week. The term “aged” identifies this type of specimen.

3 Experimental Setup

Tensional and shear loads, respectively, are applied to the intrinsic hybrid laminate specimens by means of specific material tests. Testing generally happens in dry conditions at room temperature (RT) as well as at an elevated temperature $T = 80^\circ C$. A modified DCB test according to ASTM D 5528-01 serves to determine the energy release rate $G_{I, 50 mm}$ by the method of nonlinearity (NL) at the initial crack length $a = 50 mm$, which is proportional to the square of the fracture toughness K_{Ic} of the interface [5, 7]. An EST according to [4–6] delivers the shear strengths τ_s^{EST} at static and τ_c^{EST} at cyclical loading, respectively, by the shear stress definition

$$\tau^{EST} = \frac{F}{A_{EST}} = \frac{F}{l_{EST} \cdot w_{EST}} \quad (1)$$

where F denotes the force applied and A_{EST} the effective cross section area of the EST specimen. The static shear strength τ_s^{EST} is the shear stress that is achieved at the maximum force F_{max} right before failure of the specimen. Furthermore, the ILSS test according to DIN EN 2377 and DIN 53398 yields the shear strengths τ_s^{ILSS} at static and τ_c^{ILSS} at cyclical loading, respectively, by the shear stress definition

$$\tau^{ILSS} = \frac{3}{4} \cdot \frac{F}{w_{ILSS} \cdot t_{ILSS}} \quad (2)$$

which is a reasonable approximation since the steel layer of the ILSS sandwich type specimen is rather small. The static shear strength τ_s^{ILSS} is the shear stress at the maximum force F_{max} from the force-displacement-diagram according to DIN EN ISO 14130 (1998-02-00).

All cyclical tests are conducted with a swelling tension ratio of $R = 0.1$. At least three specimens have been tested at each load-level at a frequency $6 Hz < f < 8 Hz$. The EST maximum

loads for GFRP reference specimens are $F_{max} = 9.0\text{ kN}$, 7.0 kN , 5.3 kN and for the hybrid specimens 7.0 kN , 5.3 kN , 3.5 kN , respectively. The abort criterion of the cyclical EST is a failure due to disintegration similar to the static load case. The ILSS test maximum loads for GFRP reference specimens are $F_{max} = 11.25\text{ kN}$, 10 kN , 7.5 kN , 6.5 kN and for the hybrid specimens 10 kN , 9 kN , 8.5 kN , 8 kN , 7.5 kN , 6 kN , respectively. The failure of the specimens does not occur suddenly during the ILSS-test, but spreads out over many cycles. Hence, the abort criterium for the ILSS-Test is defined as a loss of stiffness that is caused by the progress of the continuous damage. An increase of the relative deflection by 15% represents the abort criterion for the cyclical ILSS-tests.

The residual stress measurements are performed at the example of two types of specimens, namely a) a steel-CFRP multilayer laminate (ML) made by five layers of steel and six layers of U-CFRP and b) a steel-GFRP sandwich (SW) made by a core of U-GFRP and two layers of steel. A heating device is mounted on the stage of the XRD so that a temperature dependent residual stress measurement is feasible. The details of the specimens as well as the procedures of the measurements have been outlined by the authors in [8].

4 Results

Compared to former reports [5, 6, 8] a reworked EST specimen layout has been applied so that **Table 1** shows the reworked shear strength values τ_s^{EST} for this new type of specimen.

Table 1: Mean values for static results for the sandwich specimen with 2 outer steel layers

	Static Shear Strength τ_s [MPa]			
	GFRP-reference	silane	titanate	Laser structuring
T = RT	55,1	58,1	47,4	53,1
T = 80°C	44,6	51,7	41,3	32,8
Aged, T = RT	46,5	40,5	17,6	30,0

Here, the focus is set on the cyclic shear strengths properties. The number N of load cycles until failure exhibit a Wöhler-type behavior (s. **Figure 2**) whereby the service-life curves are esti-

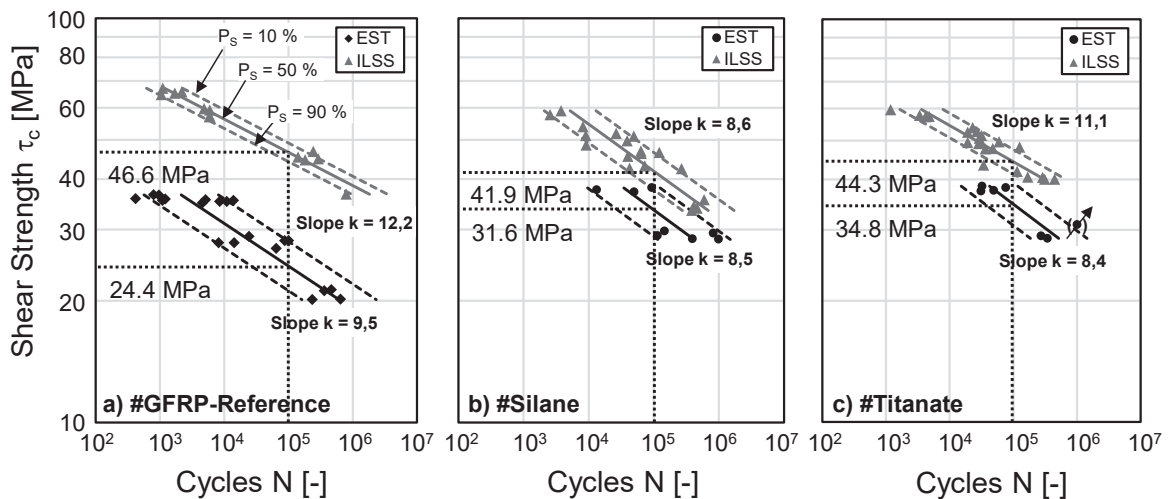


Figure 2: Wöhler-Type service-life curves assessed at room temperature. The survival probabilities for $P_s = 10\%$, $P_s = 50\%$ and $P_s = 90\%$ are determined according to DIN50100.

mated for survival probabilities of $P_S = 10\%$, $P_S = 50\%$, and $P_S = 90\%$. As a kind of reference, the cyclic shear strengths are assessed at $N = 10^5$ for $P_S = 50\%$, i. e. $\tau_{c,10^5}^{EST} = 24.4 \text{ MPa}$ and $\tau_{c,10^5}^{ILSS} = 46.6 \text{ MPa}$ for the GFRP-reference. For the hybrid specimens treated with silane they become $\tau_{c,10^5}^{EST} = 33.6 \text{ MPa}$, $\tau_{c,10^5}^{ILSS} = 41.9 \text{ MPa}$ and $\tau_{c,10^5}^{EST} = 34.8 \text{ MPa}$, $\tau_{c,10^5}^{ILSS} = 44.3 \text{ MPa}$ for those treated with titanate, respectively. Considering ILSS testing, the GFRP reference exhibits the highest cyclic shear strength followed by the titanate treated and the silane treated specimens. Surprisingly, the EST procedure delivers significantly smaller numbers, especially for the GFRP reference, and titanate and silane treated hybrid specimens are cyclically more robust by far. The sandwich specimens with GFRP core show a predominantly cohesive failure within the matrix next to the interface.

The magnitude of thermally induced residual stress and its assessment have been earlier discussed [8]. Here, the focus is set on the dependency of residual stress on the temperature T in order to validate the stress-free temperature T_0 , which is a key parameter for the numerical calculations. **Figure 3** shows a linearly growing, compressional residual stress component within the steel layer of a sandwich-type specimen (SW) transverse to the fiber direction of the U-GFRP with temperature T . The intersection at $\sigma_{ES} = 0$ occurs at the stress-free temperature $T_0 \approx 100^\circ\text{C}$. This is in line to the estimate by Schürmann [9] referring to the curing temperature $T_{g,onset}$, which is close to the glass transition temperature $T_g = 120^\circ\text{C}$ of the GFRP matrix polymer, that reads

$$T_0 = T_{g,onset} - 20^\circ\text{C}. \quad (3)$$

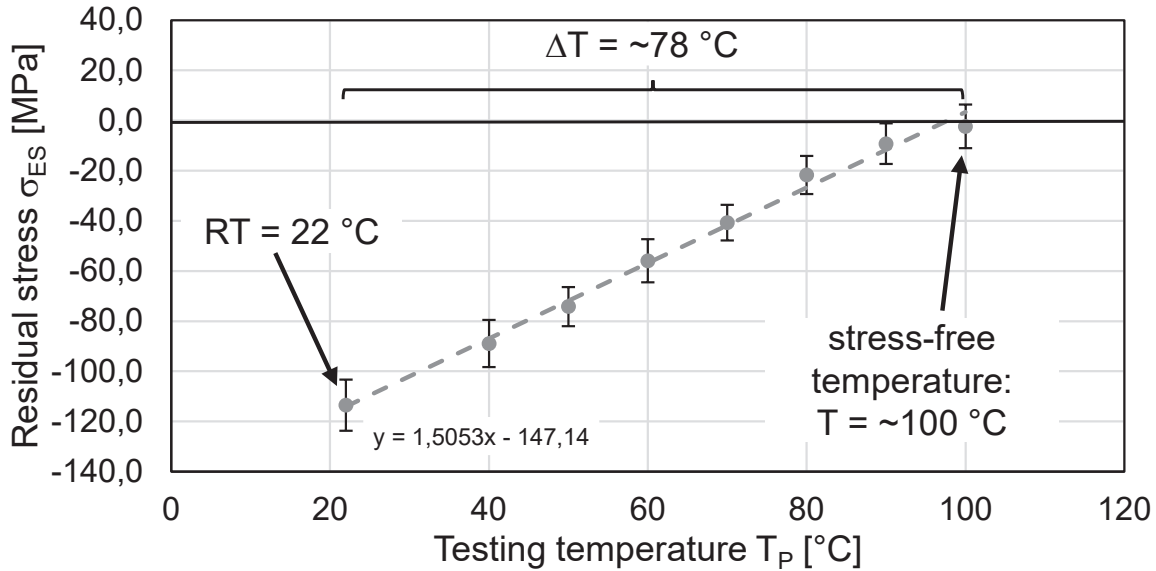


Figure 3: Temperature dependent residual stresses within the steel layer of a sandwich specimen (SW) transverse to the fiber direction of the U-GFRP

As a kind of summary, **Figure 4** shows the results of mechanical testing with respect to the GFRP reference that is set to be 100%. The results are listed in columns for the chemically and mechanically treated hybrid specimens, respectively. The here mentioned mechanical treatment of laser-structuring delivers very promising numbers for DCB-testing, e.g. 231 % of the reference value. Due to the penetration of the thin metal sheets, it is not considered in this study. As

a matter of this benchmark the authors choose a silane primer for their intrinsic hybrid laminate made by GFRP and steel.

Sample type:		Chemical surface treatment				Mechanical surface treatment			
		Silane		Titanate		Sand blasting		Laser structuring	
DCB	#RT	155 %	+	184 %	+	46 %	-	231 %	+
	#80°C	67 %	-	38 %	-	Evaluation not possible		146%	+
	#aged	58 %	-	29 %	-			80 %	○
EST	#RT	106 %	+	86 %	○	64 %	-	96 %	○
	#80°C	116 %	+	93 %	○	69 %	-	74 %	-
	#aged	87 %	○	38 %	-	51 %	-	65 %	-
	cycl. strength	138 %	+	142 %	+	Not analysed			
ILSS	#RT	99 %	○	93 %	○	Not applicable to sheets with a small thickness $t < 1$ mm			
	#80°C	101 %	+	95 %	○				
	#aged	92 %	○	86 %	○				
	cycl. strength	90 %	○	95 %	○				
Ranking:		1		2		Without rating		Without rating	

Figure 4: Summary of the mechanical properties assessment: The results are reported relative to the GFRP reference at 100%

5 Conclusions

An intrinsic hybrid composite consisting of GFRP and steel has been developed for its application as a cyclically stressed component. A comprehensive mechanical testing program yields that a chemical surface treatment with a silane primer provides the desired strength of the boundary layer under peel and shear stress. It has been shown in [8] that the numerical estimation and the experimental assessment of residual stress are showing a quite good correlation. Furthermore, the stress-free temperature, which has been experimentally assessed, correlates well with the figures known from literature [9]. Therefore, a numerical simulation by means of Finite Element Analysis (FEA) for the EST specimen has been utilized in order to discuss its experimentally gained cyclical shear strength τ_c^{EST} vs. τ_c^{ILSS} from ILSS testing. **Figure 5** shows the effective shear stress for the EST specimen that is made up by the load induced shear stress and the residual stress by means of the free edge effect in the interface between the different materials of the hybrid specimen. As a reference the nominal shear stress value $\tau_{c,10^5}^{EST} = 33.6$ MPa according to Eq. (1) is plotted here as a horizontal line. It becomes evident that the load induced shear stress shows a local maximum value of 40.7 MPa at $h = 1$ mm below the surface. At room temperature RT the maximum residual shear stress is $\tau_{||} = 8,3$ MPa at the surface $h = 0$ mm. Both stress components lead to an effective maximum shear stress of $\hat{\tau}_{c,10^5}^{EST} = 44,4$ MPa at $h = 0.8$ mm below the surface. For the ILSS specimens the nominal shear stress becomes $\tau_{c,10^5}^{ILSS} = 41.9$ MPa leading to an effective maximum

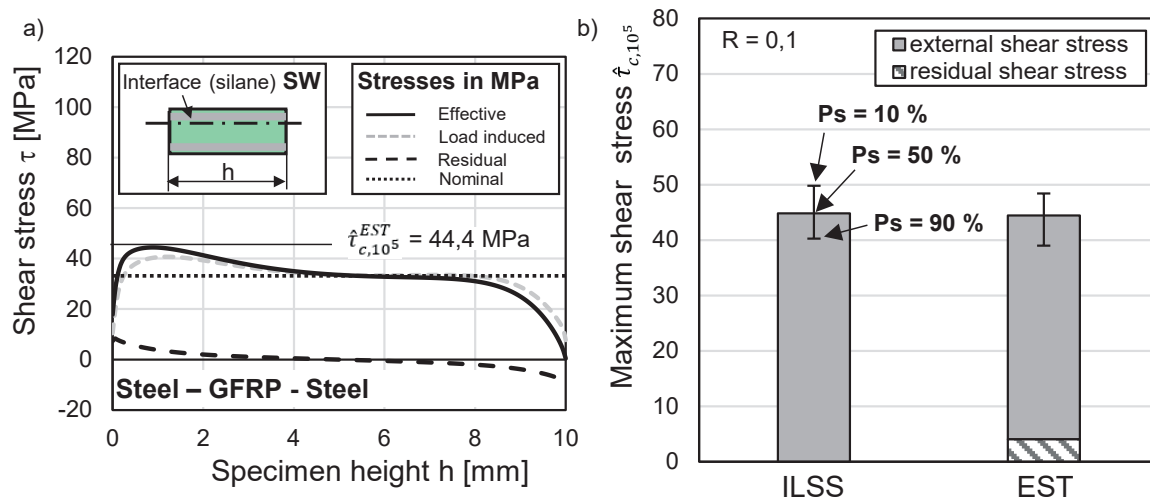


Figure 5: The impact of residual stress on the fatigue strength: a) Effective shear stress distribution at the interface of the constituent in the EST specimen. b) Comparison of the effective cyclical shear strengths values of EST compared to the values of ILSS

stress of $\hat{\tau}_{c,10^5}^{ILSS} = 44,8 \text{ MPa}$. Considering the maximum effective shear strength values, the results of fatiguing by means of EST and ILSS-testing, respectively, become almost identical (s. **Figure 5 b**).

Acknowledgement

This work has been funded by the European Union as a part of the competition “Neue Werkstoffe” EFRE.NRW. Further, the authors gratefully acknowledge the cooperation partner Mubea Fahrwerksfedern GmbH. Part of this work was performed at the Micro- and Nanoanalytics Facility (MNaF) of the University of Siegen.

6 References

- [1] C. Lauter, T. Tröster, B. Sköck-Hartmann, T. Gries, M. Linke, “Höchstfeste Multimaterialsysteme aus Stahl und Faserverbundkunststoffen,” *Konstruktion*, 11-12, pp. 8–9, 2010.
- [2] J. C. Both, “Tragfähigkeit von CFK-Metall-Laminaten unter mechanischer und thermischer Belastung,” Dissertation, Fakultät für Maschinenwesen, Lehrstuhl für Leichtbau, Technische Universität München, München, 2014.
- [3] A. Monden, M. G. R. Sause, A. Hartwig, C. Hammerl, H. Karl, S. Horn, “Evaluation of Surface Modified CFRP-Metal Hybrid Laminates,” in *Euro Hybrid Materials and Structures*, Stade, 2014, pp. 32–40.
- [4] K. A. Weidenmann, L. Baumgärtner, and B. Haspel, “The Edge Shear Test - An Alternative Testing Method for the Determination of the Interlaminar Shear Strength in Composite Materials,” *MSF*, 825-826, pp. 806–813, 2015, doi: 10.4028/www.scientific.net/MSF.825-826.806.
- [5] R. Brandt and A. Busch, “Fracture Toughness and Strength of the Interface of an Intrinsic Hybrid Laminate,” *Procedia Structural Integrity*, vol. 14, pp. 891–899, 2019, doi: 10.1016/j.prostr.2019.07.068.
- [6] R. Brandt and A. Busch, “Fracture Toughness and Strength of the Interface of a GFRP-Steel-Laminate,” in *Proceedings der 3. Internationalen Konferenz Hybrid*, Bremen, Apr. 2018, pp. 56–61.
- [7] *Standard Test Method for Mode I Interlaminar Fracture Toughness of Unidirectional Fiber-Reinforced Polymer Matrix Composites*, ASTM D 5528-01, 2010.
- [8] A. Busch, P. Brix, and R. Brandt, “Characterization of Residual Stresses in Fiber-Metal-Laminates by X-Ray Diffraction,” in *Proceedings der 3. Internationalen Konferenz Hybrid*, Bremen, Apr. 2018, pp. 34–39.
- [9] H. Schürmann, *Konstruieren mit Faser-Kunststoff-Verbunden*, 2nd ed. Berlin, Heidelberg, New York, NY: Springer, 2007.

Residual stress measurements in GFRP/steel hybrid components

T. Wu^{1*}, S. R. Tinkloh², T. Tröster², W. Zinn¹, T. Niendorf¹

1: University of Kassel, Institute of Materials Engineering, Germany

2: University of Paderborn, Institute of Automotive Lightweight Design, Germany

1 Introduction

Lightweight materials contribute to an efficient decrease of fuel consumption in automotive and aircraft industries. Due to their superior weight-specific mechanical properties, glass fiber-reinforced polymer (GFRP) composites are highly favorable in aerospace and automotive applications. However, their brittle failure behavior limits the structural integrity and damage tolerance in case of impact and crash events, respectively. Metallic materials are comparatively ductile but heavy. Hybrid materials allow to combine metals and GFRP in a manner to offset the drawbacks of every single material and reach an optimum of mechanical properties [1].

For cost and time effective processing of hybrid materials, new processes such as the prepreg-press-technology have been developed, in which the bonding between a metallic material and a fiber compound is exclusively realized by adhesive forces. However, upon processing of these hybrid structures at high temperature, the free or restricted warpage of the component induced by cooling mostly leads to the formation of residual stresses. These residual stresses can have detrimental effects on the mechanical properties of the structure and can cause defects such as delamination, part failure due to geometric distortion, built-in cracking or premature failure of parts subjected to alternating loading or corrosive environments [1].

Generally, the determination of residual stresses can be classified as non-destructive, semi-destructive and destructive. The most widely used non-destructive method is X-ray diffraction, which is capable of providing reliable near-surface residual stress measurements in crystalline materials. However, the technique fails to measure the residual stresses in fiber-reinforced polymer composites. In [2], fiber bragg grating (FBG) sensors were embedded in the materials for measuring in-plane strains during manufacturing of carbon fiber-reinforced plastic-steel laminates. The measured strains were then used to calculate residual stresses by using the classical laminate theory (CLT) approach. However, the adopted CLT approach relies on many assumptions, e.g., the thickness of the plate needs to be much smaller than any characteristic dimension. Often these assumptions clearly deteriorate the accuracy of residual stress results. A well-known semi-destructive approach is the hole drilling method (HDM), which has been standardized in ASTM E837-13a for isotropic materials [3]. The HDM is capable of providing reliable residual stress results within the range of 10 to 800 μm beneath the specimen surface of many materials [3-5]. In [4], the HDM was employed for measuring the residual stresses in unbalanced composite laminates [02/02]_s ($\theta = 0^\circ, 30^\circ, 45^\circ, 60^\circ, 90^\circ$) with the assumption that the relieved strain response has a simple trigonometric form. Clearly, this assumption does not work for orthotropic materials. Schajer et al. [5] developed a new model for orthotropic materials using a mathematical solution for the displacements around a hole in a stressed orthotropic plate, which was used for determining the relationship between the residual stresses and the hole-drilling relieved strains. Akbari et al. [6] extended the model proposed in [5] to allow for the incremental hole-drilling measurement of non-uniform residual stresses in laminated composites. However, only the plane

elastic constants ($E_x, E_y, \nu_{xy}, G_{xy}$) were used in the finite element analysis for calculating calibration coefficients to evaluate the residual stresses with a shell element.

The objective of this work is to employ the incremental hole drilling method for determining and analyzing the residual stresses in the hybrid material made of GFRP and steel. In this work, the developed evaluation formalism for orthotropic materials is adopted for measuring non-uniform residual stresses in hybrid materials. For calculating calibration parameters using finite element analysis, a solid element with nine elastic constants $E_x, E_y, E_z, \nu_{xy}, \nu_{xz}, \nu_{yz}, G_{xy}, G_{xz}, G_{yz}$, is adopted. Thereby, the present work tries to cover distribution of residual stresses across the thickness of the hybrid structure with focus on the transition zone between metal and GFRP.

1 Incremental hole drilling method

In the HDM, a small hole is drilled incrementally at the geometrical center of the rosettes of a strain gauge in a component. After the removal of each layer of the material, a new equilibrium is established around the hole. The relieved strains measured by the strain gauge are used for evaluating the residual stresses. A non-uniform residual stress state in orthotropic materials can be determined with the incremental integral formalism

$$(\varepsilon)_i = \begin{pmatrix} \varepsilon_1 \\ \varepsilon_2 \\ \varepsilon_3 \end{pmatrix}_i = \sum [C]_{ij} \cdot (\sigma)_j \quad 1 \leq j \leq i \quad (1)$$

Please note that the strain ε_i measured after drilling the j^{th} increments is not only function of the residual stresses σ_j present in the last drilled increment, but ε_i is also function of the residual stresses in all the previous increments. C_{kl} represent the influence of the residual stresses on the relieved strains after drilling through the material. For measuring the residual stress in GFRP, the strain gauge 1 is always parallel to the fiber direction X, while the strain gauge 3 is in the transverse direction Y.

Equation (1) can be iteratively solved with

$$\begin{pmatrix} \sigma_x \\ \sigma_y \\ \tau_{xy} \end{pmatrix}_i = \begin{bmatrix} C_{11} & C_{12} & C_{13} \\ C_{21} & C_{22} & C_{23} \\ C_{31} & C_{32} & C_{33} \end{bmatrix}_{ii}^{-1} \cdot \left(\begin{pmatrix} \varepsilon_1 \\ \varepsilon_2 \\ \varepsilon_3 \end{pmatrix}_i - \sum_{j=1}^{i-1} \begin{bmatrix} C_{11} & C_{12} & C_{13} \\ C_{21} & C_{22} & C_{23} \\ C_{31} & C_{32} & C_{33} \end{bmatrix}_{ij} \cdot \begin{pmatrix} \sigma_x \\ \sigma_y \\ \tau_{xy} \end{pmatrix}_j \right) \quad (2)$$

For calculating residual stresses, the measured strain at three fixed positions and the calibration coefficients for the specimen are required. The coefficients directly depend on the elastic constants of the material. The calibration coefficients can be calculated by finite element analysis.

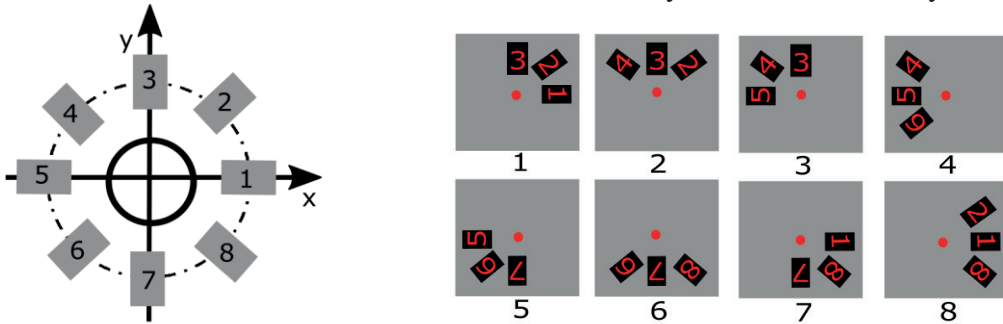


Figure 1: (Left) Strain gauge with 8 grids employed for the strain measurements in the hybrid material, (right) 8 different combinations of strain gauge grids.

The reliability of the results for the orthotropic material strongly depends on the orientation between the fiber and the strain gauge. Furthermore, the material may not be perfectly homogeneous, e.g. the repartition of the fibers could be an issue. Therefore, a customized strain gauge with eight grids is utilized in this work, see Figure 1. Practically, only three grids of the strain gauge are required for the evaluation of the residual stresses. By direct comparison of the results obtained with the different strain gauge combinations depicted in Figure 1, information with regard to possible inhomogeneity, damage, and most suitable strain gauge combinations can be deduced. Focusing on this special strain gauge rosette, equation (1) is adapted to consider the eight strain gauge grid

$$(\varepsilon) = \begin{pmatrix} \varepsilon_1 \\ \varepsilon_2 \\ \varepsilon_3 \\ \varepsilon_4 \\ \varepsilon_5 \\ \varepsilon_6 \\ \varepsilon_7 \\ \varepsilon_8 \end{pmatrix} = \Sigma \begin{bmatrix} C_{11} & C_{12} & C_{13} \\ C_{21} & C_{22} & C_{23} \\ C_{31} & C_{32} & C_{33} \\ C_{41} & C_{42} & C_{43} \\ C_{51} & C_{52} & C_{53} \\ C_{61} & C_{62} & C_{63} \\ C_{71} & C_{72} & C_{73} \\ C_{81} & C_{82} & C_{83} \end{bmatrix} \cdot \begin{pmatrix} \sigma_x \\ \sigma_y \\ \tau_{xy} \end{pmatrix} = \Sigma [C] \cdot (\sigma) \quad (3)$$

As mentioned before, only three strain gauge directions are required for residual stress evaluation $(\sigma)_j$ with the aid of coefficients $[C]_{ij}$. Each matrix $[C]_{ij}$ in equation (1) used for evaluating residual stresses is composed of 9 coefficients C_{kl} selected from the 24 coefficients shown in the matrix $[C]$ from equation (3). As detailed before, $[C]_{ij}$ represents the influence of the residual stress vector $(\sigma)_j$ placed on the j^{th} increment after drilling i increments. Similarly, the strain relieved after drilling i increments is not only due to the residual stress in the last increment, but also due to all the residual stresses being present on all previously drilled increments. Therefore, it is necessary to obtain separately all the matrices $[C]_{ij}$. In the finite element analysis, the first column of $[C]_{ij}$ (coefficient C_{k1ij}) can be determined by only using the stress σ_x , the second column with the stress σ_y , and the last column with the shear stress τ_{xy} .

2 Manufacturing samples

In this work, the prepreg-press technology was employed to manufacture hybrid components made of metal and GFRP. In this manufacturing process, an already formed steel sheet with the thickness of 1 mm is placed into a heated die. Two unidirectional GFRP prepregs with the thickness of 0.44 mm are placed onto and below the sheet metal, respectively, and then pressed by a heated punch with the pressure of 0.5 MPa at a temperature of 160 C°. As the epoxy resin acts as an adhesive, the joining and hybridization, respectively, of sheet metal and GFRP is realized during the curing of the GFRP. Figure 2 provides all information related to the dimensions and stacking configuration of the hybrid sample from cross-sectional and top views. As mentioned before, the HDM is capable of providing reliable results within the range of 10 to 800 μm beneath the specimen surface. Thus, the choice of the thickness of the GFRP allows to obtain residual stress within the transition zone between GFRP and metal. The general mechanical properties of the hybrid component are given in Table 1.

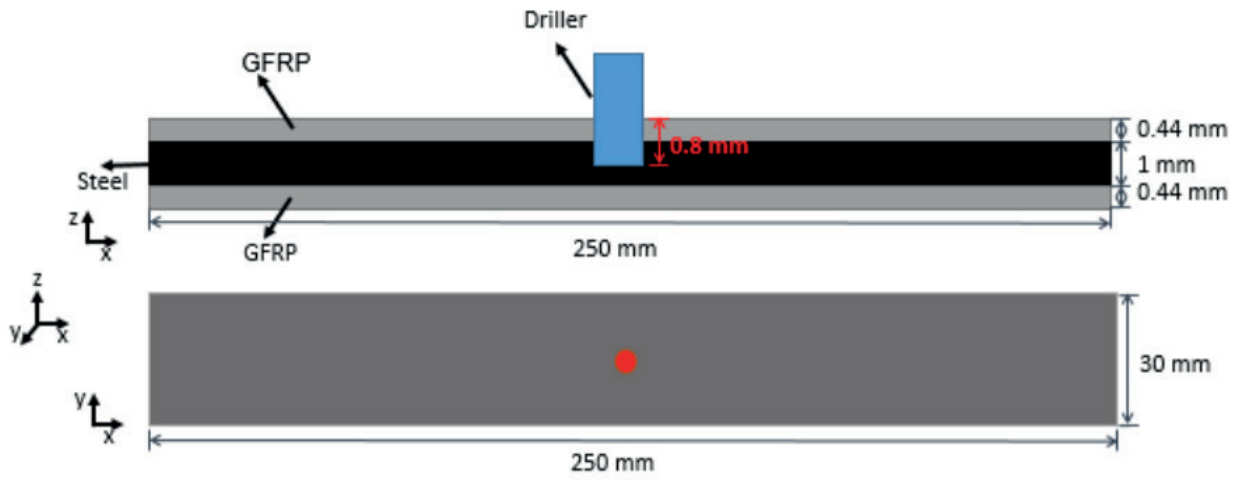


Figure 2: Geometry and dimensions of the hybrid component from (top) cross-sectional view and (bottom) top view.

	Young's modulus (GPa)			Poisson's ratio			Shear modulus (GPa)		
	E_x	E_y	E_z	ν_{xy}	ν_{xz}	ν_{yz}	G_{xy}	G_{xz}	G_{yz}
GFRP	33.98	8.78	8.78	0.33	0.33	0.37	5.23	5.23	3.2
Steel	190			0.29					

Table 1: Mechanical properties of the steel and the GFRP used.

3 Measurement results

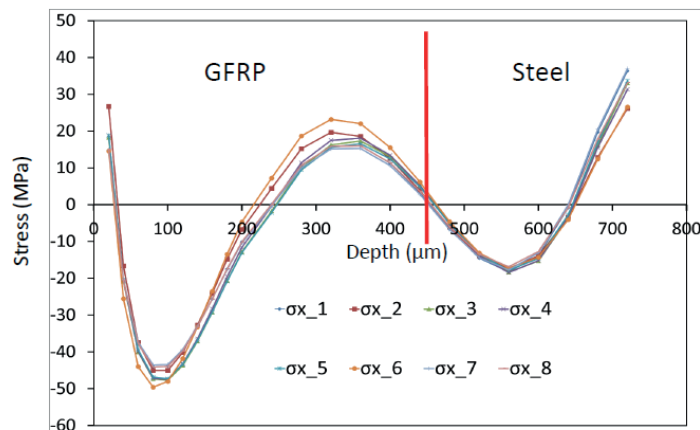


Figure 3: Residual stresses σ_x as determined by HDM in the hybrid component. See text for details.

This section discusses the results obtained through incremental HDM focusing on the in-depth stress distribution from the surface of one center point into the sample, cf. the red point in Figure 2. In order to improve the accuracy of the residual stress measurement, a small drilling increment of 20 μm was employed to follow the assumption considered in the model, i.e., the stress at each increment is uniform. In addition, the customized strain gauges with 8 grids were utilized. An air turbine is used to drill the holes at a drilling speed of about 300,000 rpm. The orbital technique applied enables the chips to freely move outside the hole eventually avoiding the induction of machining induced stresses in the material.

Figure 3 shows the residual stress distribution σ_x as a function of depth in the hybrid component with the dimension and stacking configuration given in Figure 2, where X is the fiber direction and 8 different strain gauge combinations are accounted for. It can be clearly seen that the residual stresses of most strain gauge combinations are in good agreement, however, the strain gauge combinations 2 and 6 show different trends, as they do not contain a strain gauge in the fiber direction X. As can be seen in Figure 3, the residual stresses close to the sample surface are tensile stresses with the value of about 20 MPa. As the depth increases, the residual stresses are reduced and then switch to compressive stresses at a depth of 30 μm . The stress values reach the maximum compressive stresses of about -45 MPa at the depth of 100 μm . After that point, residual stresses increase and switch to tensile stresses at the depth of 250 μm . Afterwards stresses increase to 15 MPa at a depth of 320 μm . The residual stresses at the transition zone between GFRP and steel are of highest interest, as they may lead to delamination. In the hybrid sample characterized the transition zone between GFRP and steel lies at the depth of around 440 μm . From Figure 3, the stresses at the transition zone are quite small, which can be rationalized based on the thermal expansion coefficients of GFRP and steel, which are very close. Furthermore, no obvious jump of residual stresses appears within the transition zone, which can be dedicated to two factors: (1) the reliable model for orthotropic materials prevents the jump from GFRP to steel; (2) the use of the small increment size for drilling ensures consistency.

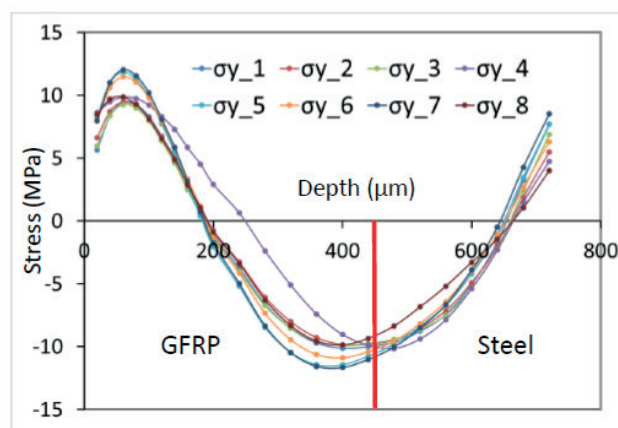


Figure 4: Residual stress σ_y as determined by HDM in the hybrid component. See text for details.

Figure 4 shows the residual stresses σ_y in the hybrid material. Close to the surface of the sample, the stresses are tensile stresses and have maximum values of 10 MPa at the depth of 80 μm . As the depth increases, the stresses are reduced and switch to compressive stresses at the depth of 200 μm . After

that, σ_y continues to be increased to the maximum values of -10 MPa at depth of 400 mm, which is in direct vicinity of the transition zone.

4 Conclusions and Outlooks

In this contribution, the incremental hole drilling method (HDM) is employed to determine the residual stress state in hybrid components made of glass fiber-reinforced polymer (GFRP) and steel. The developed evaluation formalism for orthotropic materials is adopted for measuring non-uniform residual stresses in the hybrid material. For calculating calibration parameters based on finite element analysis, a solid element with nine elastic constants $E_x, E_y, E_z, \nu_{xy}, \nu_{xz}, \nu_{yz}, G_{xy}, G_{xz}, G_{yz}$, is adopted, such that the orthotropic material behavior in each layer can be appropriately described. In addition, for improving the measurement accuracy, a customized strain gauge with 8 grids is employed for measuring the relieved strains. In present work, it is found that the residual stresses very close to the surface of the sample in X and Y directions are tensile stresses. Within the transition zone between GFRP and steel, the residual stresses in X direction along the fiber are pretty small, and the residual stresses in Y direction perpendicular to the fiber are compressive stresses with a value of -10 MPa. Prevailing stress can be explained based on the thermal expansion coefficients of GFRP and steel, which are very close.

In future work, the reliability of residual stress measurements in the hybrid component will be validated by mechanical bending. Furthermore, it is of highest importance to directly compare the results measured through HDM and through X-ray diffraction for in-depth evaluation of contributing factors on the overall residual stress state.

5 Acknowledgements

This research is supported by the Deutsche Forschungsgemeinschaft (DFG), project number 399304816. The authors gratefully acknowledge for the financial support.

6 Literature

- [1] S. Tinkloh, T. Wu, T. Tröster and T. Niendorf, A micromechanical-based finite element simulation of process-induced residual stresses in metal-CFRP-hybrid structures, *Composite Structures*, **2020**, (In Press).
- [2] R. Prussak, D. Stefaniak, C. Hühne and M. Sinapius, Evaluation of residual stress development in FRP-metal hybrids using fiber Bragg grating sensors, *Production Engineering*, **2018**, 12, 259-267.
- [3] ASTM: "Standard Test Method for Determining Residual Stresses by the Hole-Drilling Strain-Gage Method", *ASTM International*, **2013**, ASTM E837-13 (2013).
- [4] X.L. Gong, Z. Wen, Y. Su, Experimental determination of residual stresses in composite laminates [02/02]s. *Advanced Composite Materials*, **2014**, 1-15.
- [5] G. S. Schajer, L. Yang, Residual stress measurement in orthotropic materials using the hole drilling method. *Experimental Mechanics*, **1994**, 34, 324.

- [6] S. Akbari, F. Taheri-Behrooz, M. M. Shokrieh, Characterization of residual stresses in a thin-walled filament wound carbon/epoxy ring using incremental hole drilling method. *Composite Science Technology*, **2014**, 94, 8-15.

STUDY ON HYGROTHERMAL AGEING BEHAVIOUR OF HYBRID CFRP/AL JOINTS: INFLUENCE OF PRE-TREATMENT, ADHESIVE COMPOSITION AND AGEING PROCESS

Jochen Schanz^{1,2}, Sam Kambach¹, Dieter Meinhard¹, Anjali De Silva²,
David K. Harrison², Harald Riegel¹, Volker Knoblauch¹

¹ Aalen University, D-73430 Aalen, Deutschland

² Glasgow Caledonian University, Glasgow G4 0BA, Scotland, United Kingdom

ABSTRACT: Adhesively bonded hybrid joints based on carbon fibre reinforced polymers (CFRP) and aluminium enable cost efficient lightweight constructions. The pre-treatment of the surfaces is a very important step to achieve a high mechanical strength. In this work, different pre-treatment methods of CFRP and aluminium were investigated with respect to their long term stability in artificial hygrothermal ageing. Thereby, two laser systems with near-infrared (NIR) and ultraviolet (UV) wavelengths respectively with a variation of the laser energy densities were applied and compared to an acetone cleaning reference process. Different levels of matrix ablation and carbon fibre exposure were generated. Prior to ageing, all pre-treatment strategies achieved a high mechanical shear strength whereby a correlation between the laser energy density and the shear strength was detected. The artificial ageing was conducted according to the PV-1200 standard of the Volkswagen AG, which is based on ISO 9142:2003 D5. After different numbers of ageing cycles, the average shear strength decreased in the range of 12-25 % of the initial shear strength. A correlation between the strength decrease and the pre-treatment process or the level of matrix ablation was not detected.

KEYWORDS: adhesive bonding, hybrid joint, CFRP, aluminium, surface treatment, laser, hygrothermal ageing

1 INTRODUCTION

The efficiency improvement and reduction of material usage of a vehicle can be realised with lightweight constructions and suitable joining methods. Carbon fibre-reinforced polymers (CFRP) offer the highest lightweight potential [1] and will be used more frequently in the future [2]. Approx. 25 % weight savings compared to aluminium and 60 % compared to steel have already been proven [3]. However, in comparison to metals, CFRPs are more expensive. To reduce the costs, hybrid materials can be used and CFRP is applied locally in highly stressed structural sections [3].

A favourable joining method is adhesive bonding with its advantages of less stress concentration, no drilling of the materials and sealing shock absorption [4]. For a successful adhesive bonding, a surface pre-treatment of the materials is necessary since generally, surfaces are contaminated by inorganic and organic particles such as dust, fluids like oil, grease, separating and processing agents or moisture [5]. Those contaminations prevent a successful adhesion due to a reduced wetting behaviour of the adhesive on the substrate. In addition, the surface pre-treatments can improve the chemical attraction and enlarge the area of the surface by an increased roughness [5]. One flexible, highly automatable and ecological friendly method is the pre-treatment of the surface with laser sources. The laser wavelength definite the level of absorption in the epoxy of the CFRP. An ultraviolet (UV) wavelength of

$\lambda = 355 \text{ nm}$ is absorbed in the epoxy resin of more than 85 % [6] and a removal takes place by photochemical ablation [7]. This mechanism allows to expose the carbon fibres without breakage and damage or ablate the epoxy matrix partly without carbon fibre exposure [8,9]. The most used laser systems nowadays have a wavelength in near-infrared (NIR) of $\lambda = 1050\text{-}1070 \text{ nm}$. However, the absorption of this wavelength in epoxy is with approx. 4 % quite low [6]. Thus, most of the energy is absorbed by the carbon fibres and transferred to the epoxy layer which is consequently thermally decomposed. However, the carbon fibres might be damaged due to the heat input [9,10]. Beside the different ablation behaviour and the damage potential of the carbon fibres, different laser wavelengths and pre-treatment intensities lead to a variation of the surface topographies.

The mechanical and chemical properties of the CFRP and aluminium (Al) are fundamentally different and may lead to corrosion in the present of moisture and a degradation of the adhesive due to the different thermal expansion. To investigate aging due to moisture and temperature variations, accelerated artificial ageing tests with changing temperature and moisture content are commonly carried out and standards are published i.e. DIN EN ISO 9142:2003 or Volkswagen AG PV1200:2003. Since the epoxy of the CFRP and adhesive are polymers they are susceptible to chemical degradation under such conditions. Machado et al. found out that the shear strength of adhesively bonded hybrid CFRP/Al-joints is reduced after the CFRP was saturated with water. A drying procedure did not improve the shear strength on the level of the unaged specimens [11]. Mu et al. [12] and Qin et al. [13] revealed that the mechanical strength is reduced of up to 43 % respectively 40 % after different hygrothermal ageing procedures of hybrid joints.

In this work, adhesively bonded hybrid CFRK/Al-joints specimens that have been pre-treated by (a) acetone cleaning, (b) UV-laser and (c) NIR laser are artificial aged in a hygrothermal ageing cycle according the Volkswagen AG PV1200:2003 standard. Due to the different pre-treatment, various states of matrix ablation were realised. The influence of the surface topography of the CFRP and the present of exposed carbon fibres on the mechanical shear strength of single lap joint (SLJ) specimens after 25, 50 and 100 ageing cycles were investigated. The pre-treated surfaces and the post-mortem-analysis of the fracture pattern were done using microscopical methods.

2 EXPERIMENTAL

2.1 MATERIALS

The quasi-isotropic CFRP laminate is made of eight unidirectional plies lay-up of Hexcel HexPly® M21 and reinforced with 24k tow TORAYCA® fibres T800S. The fibre diameter is approx. 5 μm . The stacking sequence of $[0/45/90/-45]_{1s}$ is build up to the final thickness of 2.0 mm and cured for two hours in a hot press process at 180 °C and 7 bar. According DIN EN 1465:2009, the CFRP was cut from 200 x 300 mm plates to a dimensions of 100 x 25 mm² with a water cooled cutting machine. The second adherent was an aluminium alloy AlMg3 (EN AW-5754, H22, work hardened by rolling then annealed to quarter hard) with a thickness of 2.0 mm. The material was milled to the SLJ geometry of 100 x 25 mm². The hybrid joints were bonded with a two component epoxy-based TEROSON® EP 5065 from Henkel™. The technical specification of the adhesive is given in **Table 1**.

Table 1: Technical specifications of the applied adhesive TEROSON[®] EP 5065 [14]

Adhesive	Chemical base	Color of the mixture	Viscosity in Pa s	Pot life	Curing		σ_r in MPa	Adhesive film in mm
					t in min	T in °C		
EP 5065	2-C epoxides	black	23 (at 23 °C)	1h	30	80	25	0.2

2.2 SURFACE TREATMENT

Three different surface pre-treatments were applied to the CFRP and aluminium. Acetone cleaned specimens were used as a reference point. Thereby, the surfaces were only degreased and cleaned. Two different laser sources in near infrared (NIR) and ultraviolet (UV) wavelength were used to clean, activate and increase surface roughness. The CFRP and aluminium was pre-treated with a TRUMPF TruMark 5020 nanosecond short pulse laser system with a wavelength of 1062 nm (NIR) and an average laser power of 20 W. Two different types of focal optics were used. The first focal optic with an optical length of 254 mm was used for the CFRP pre-treatment. All aluminium substrates were laser structured with the TruMark 5020 and a focal optic length of 160 mm. The second laser system was a TRUMPF TruMark 6350 to pre-treat the CFRP. The emitting average power is 5 W with a wavelength of 355 nm (UV), **Table 2**.

Table 2: Technical specifications of the near-infrared and ultraviolet laser system

Characteristic	Unit	TRUMPF TruMark 5020	TRUMPF TruMark 6350
Wavelength	λ in nm	1062	355
Average power	P_{avg} in W	20	5
Beam quality	M^2	< 2	< 1.5
Pulse duration	t_L in ns	9 – 200	-
Pulse width	t_w in ns	-	1 – 50 at 20 kHz
Repetition rate	f_p in kHz	1 – 1000	1 – 120
Scanner head	-	Scanlab ScanCube 10	Scanlab intelliSCAN 10
Focal length	f in mm	160 / 254	160
Focal diameter	d_f in μ m	72 / 114	36

The applied pulsed laser sources emit different high pulse peak power and single pulse energy depending on the average laser pump power, the single pulse duration and the pulse frequency. To compare different laser parameters, an “applied-energy-per-area”-value called energy density ED_{Area} was used. A comparable calculation was presented by Genna et al. in 2017 [15].

$$ED_{Area} = \frac{P_{avg}}{v_{scan} \cdot d_{hatch}} \quad (1)$$

In preliminary investigations [16], different surface topographies and ablation depths were determined as a function of the applied energy density ED_{Area} . The chosen parameters for the hygrothermal investigations are given in **Table 3**.

Table 3: Near-infrared and ultraviolet laser parameters for CFRP and AlMg3 (5754)

Laser source		NIR 1062 nm			UV 355 nm			NIR 1062 nm
Material		CFRP						AlMg3 (5754)
Characteristics	Unit	NIR	NIR	NIR	UV	UV	UV	NIR
Average laser power	P_{avg} in W	12.0	11.7	20.0	16.0	40.0	80.0	273
Pulse repetition rate	f_{rep} in kHz	100.0	26.5	27.0	100.0	20.0		45.0
Pulse power	$P_{p,max}$ in kW	1.48	7.80	9.65	0.005	0.025		8.39
Pulse duration	t_L in ns	100	100	200	-	-	-	100
Pulse width	t_w in ns	-	-	-		10		-
Spot diameter	d_o in μm		114			36		72
Hatch distance	d_{hatch} in μm		104			25		62.5
Scanner velocity	v_{scan} in mm/s	5000	300	270	1250	500	250	117
Energy density	ED_{Area} in J/cm^2	2.31	37.37	71.22	16	40.0	80.0	273.50

The surface of the CFRP was pre-treated with hatching laser lines 90 degree to the top carbon fibre layer, which were orientated in the load direction of the SLJ-specimens. The laser beam was guided in a linear movement over the surface from one side. The aluminium substrate was also structured transverse to the load direction of the specimens.

2.3 SURFACE ANALYTICS

The surface of the untreated and processed areas as well as the fractographical analysis after mechanical testing was investigated with different methods. First, qualitative evaluation was done with a reflected light microscope Carl Zeiss AxioZoom.V16. More detailed analyses were carried out using a scanning electron microscope Carl Zeiss Sigma 300 VP.

2.4 SLJ-SPECIMEN MANUFACTURING, MECHANICAL TESTING AND ANALYSIS

The dimensions of the CFRP / aluminium adherents and the SLJ sample geometry were chosen according to DIN EN 1465:2009. After the cutting process, the overlap areas of 12.5 x 25 mm² were pre-treated as described above. For each batch, five specimens were manufactured. Directly after the pre-treatment, the adherents were placed in a joining holder. The curing of the joint was done according the technical data sheet of the adhesive, see **Table 1**. Prior to the mechanical testing, rectangular aluminium cap strips were applied to compensate the CFRP and aluminium thickness and prevent a deflection of the SLJ samples during mechanical testing. The quasi-static experiments were performed under normal temperature and pressure conditions in a universal materials testing machine Schenck RSA100. The samples were positioned in the clamping jaws and a pre-load of 100 N was applied. According to DIN EN 1465:2009 a traverse speed of 1.5 mm/min was applied. The test was stopped after a 90 % decrease of the maximum shear force that was detected. The fracture analysis was carried out according to DIN EN ISO 10365:1995 afterwards.

2.5 HYGROTHERMAL AGEING OF HYBRID JOINTS

The influence of different pre-treatment methods and surface topographies on the mechanical degradation of hybrid CFRP/Al-joints during a hygrothermal climate change test were investigated with the standard PV 1200:2004 of the Volkswagen AG. The pre and post conditioning of the substrate were considered according DIN EN ISO 9142:2003. The SLJ specimens were placed inside a climate change test chamber (Type Memmert CTC 256) in a pendant position, **Figure 1**. The distance between each other and to the housing of the chamber was considered according the standard ISO 9142.

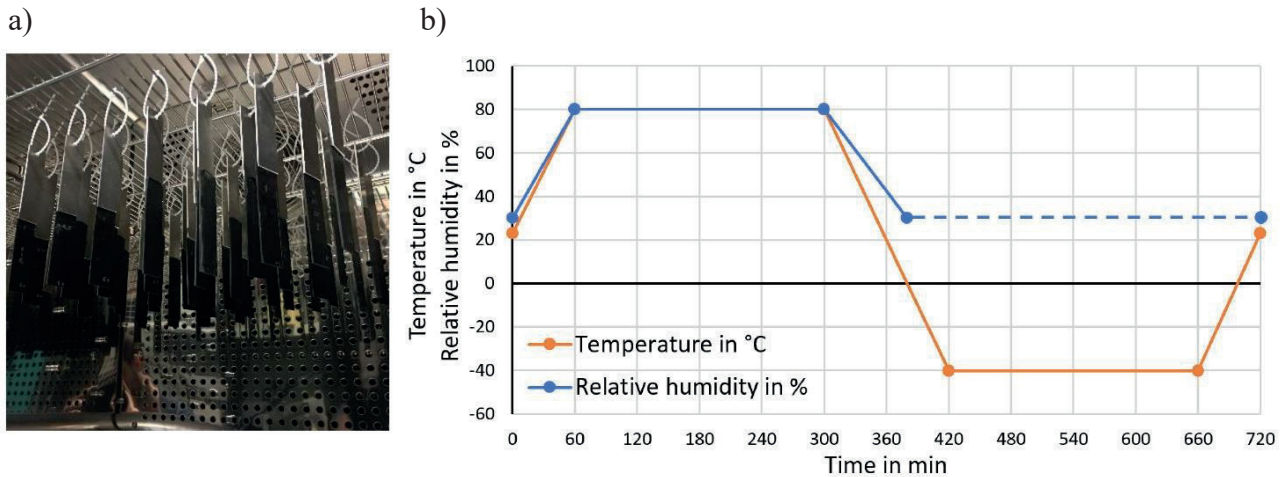


Figure 1: a) SLJ specimens placed in climate test chamber, b) temperature and relative humidity profile of standard PV 1200:2004

During the cycle duration of twelve hours, the maximum temperature of +80°C and 80 % relative humidity is reached within one hour. These conditions are maintained for four hours. Afterwards, the temperature is decreased to -40°C within 2 hours. During this step, the control of the humidity is stopped when the temperature undercuts 10°C. After four hours at -40°C, the temperature is raised back to the reference conditions (+23°C, 50 % relative humidity). The Acetone and all NIR pre-treatments were aged and mechanically tested after 25, 50 and 100 cycles. The UV pre-treatments were tested only after 50 cycles.

3 RESULTS

3.1 LASER SURFACE TREATMENT

In **Figure 2**, optical and scanning electron microscope (SEM) images of the initial, acetone cleaned and laser pre-treated surfaces are given. The initial surface prior and after acetone cleaning has a dark appearance with a slightly transparent matrix, **Figure 2 a)**. Applying a laser pre-treatment with a near infrared (NIR) areal energy density of $NIR = 2.3 \text{ J/cm}^2$, the matrix is getting brighter compared to the untreated surface. The matrix is removed and carbon fibres are exposed in a few sections. With an increased energy density of 37.3 J/cm^2 the matrix is fully removed and the carbon fibres are exposed completely. By doubling the energy density to NIR 71.2, the surface is getting even darker. However, by applying the UV laser source, other surfaces and grades of ablation can be realized. With an areal energy density of 16.0 J/cm^2 , no visible change can be observed using a light microscope. Applying

40.0 J/cm² one can observe a significant darkening in general, however, a few sections still expose a bright surface comparable to the initial area. Doubling the energy density (80.0 J/cm²) generates a dark surface with single bright lines which have the same direction as the carbon fibres.

The SEM image (Figure 2 b)) reveals no different surface appearance between the untreated surface and acetone cleaned area. The NIR pre-treatment with a density of 2.3 J/cm² can partially expose carbon fibres without damage in a few section, but most of the matrix is still covering the fibres and exhibits cracks. The NIR 37.3 laser parameter ablate several carbon fibre layers, the NIR 71.2 increase the level of carbon fibre ablation and damage. The UV 16.0 parameter does neither ablate the matrix nor expose any fibres. A change of the surface appearance is not visible in the SEM. An increase of the energy density to 40 J/cm² partly ablates the matrix and exposes the carbon fibres. Craters and residual matrix are also visible on the surface. The density of UV 80.0 fully ablates the matrix. It is also visible, that a few carbon fibres a broken or damaged.

The different pre-treatment methods and intensities generate different surface topographies. Acetone, NIR 02.3 and UV 16.0 do not expose the carbon fibres, UV 40.0 creates a rough matrix surface with section of exposed carbon fibres and NIR 37.3, NIR 71.2 and UV 80.0 fully expose the carbon fibres with different levels of carbon fibre damages.

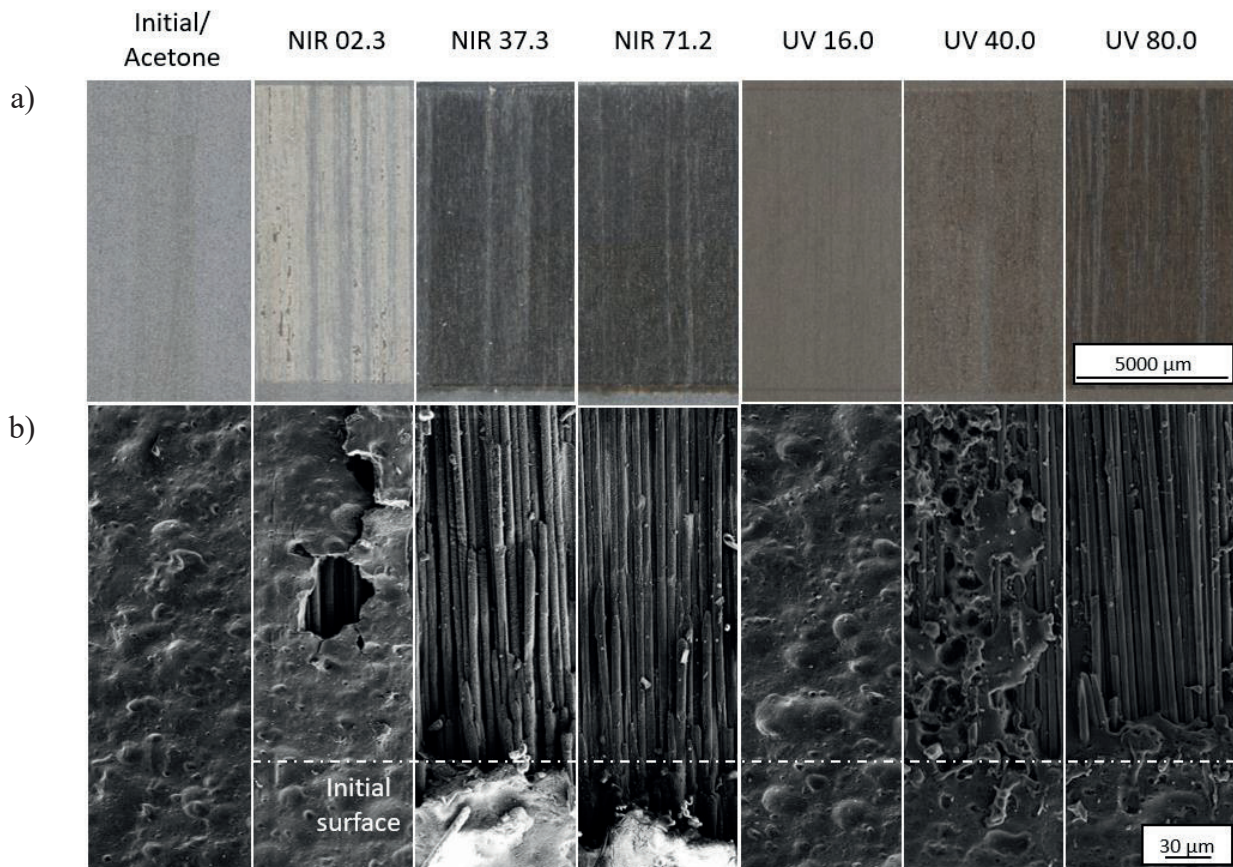


Figure 2: Top view images of untreated, acetone, NIR and UV pre-treated surfaces a) optical microscope b) SEM

3.2 MECHANICAL SHEAR STRENGTH OF UNAGED AND AGED CFRP/AL-JOINTS

Batches of the differently pre-treated hybrid CFRP/Al specimens were mechanically tested before and after aging. Figure 3 shows the average shear strength of the sample batches before and after 25,

50 and 100 cycles of PV-1200 ageing. The error bars indicate the lowest and highest value and therefore frame the whole range of the strength distribution. The green horizontal line shows the specified shear strength (25 MPa) of the applied adhesive taken from the technical data sheet provided by the supplier [14].

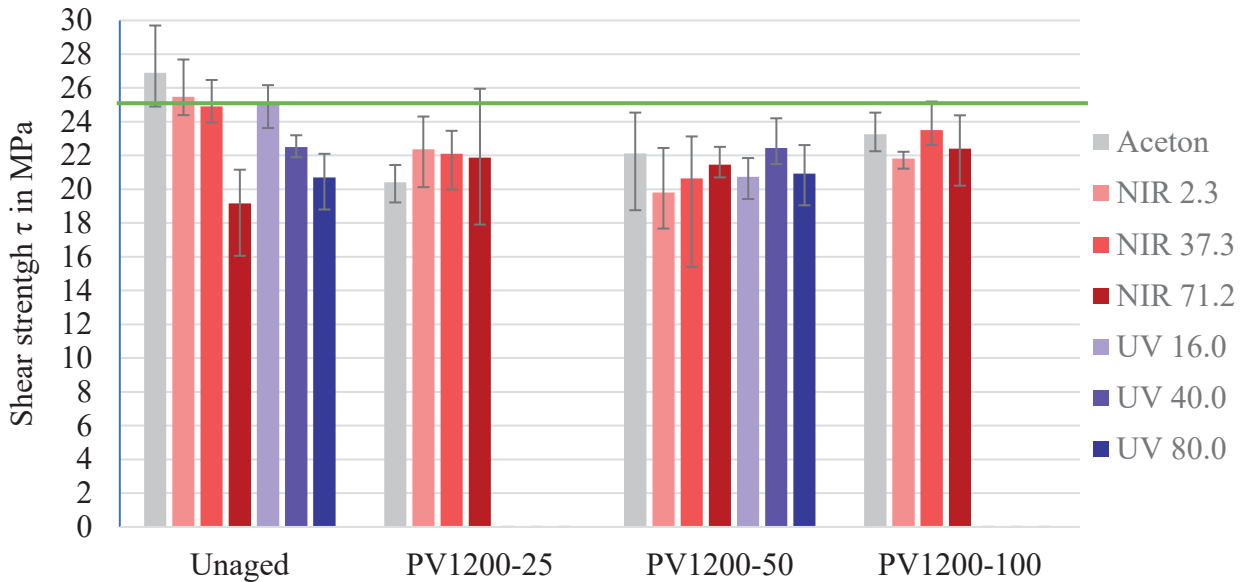


Figure 3: Average shear strength of different pre-treatment hybrid samples sorted by the number of ageing cycles (PV1200-x, where x represents the number of cycles). The green line indicates the shear strength 25 MPa of the adhesive according the technical data sheet.

In the unaged state, the acetone cleaned and two of the NIR laser pre-treated specimens that have been processed with low energy density (NIR 2.3 and NIR 37.3) achieve an average shear strength of 25 - 27 MPa. The strongest NIR parameter (NIR 71.2) exhibits a reduced strength of 19 MPa. The UV pre-treatments exhibit decreasing strength with increasing energy density starting from 25.1 MPa (UV 16.0) to 20.7 MPa (UV 80.0).

After 25 ageing cycles, all samples show a decrease of 2.8-6.5MPa of the shear strength, respectively 12 - 25 % without a clear correlation with the applied pre-treatment. Only the NIR 71.2-sample exhibits a slight increase compared to the unaged situation. The same holds true after 50 respectively 100 cycles. However, one might interpret even a slight increase after 100 cycles compared to 50 cycles. The samples processed with the UV laser were only tested after 50 cycles. The parameter with the lowest energy density (UV 16) shows a significant decrease of approx. 4.3 MPa respectively 18 %. In contrast, samples processed with higher energy densities (UV 40.0, UV 80.0) do not exhibit any strength decrease.

To sum it up: A significant decrease of the shear strength was observed for all samples that possessed high values in the range of shear strength of the adhesive before ageing. In contrast, samples that exhibited already lower values in the unaged state did not show a remarkable loss.

3.3 FRACTURE PATTERNS OF UNAGED AND AGED SPECIMENS

Unaged samples: The occurring failure behaviors are adhesion failure (AF), cohesion failure (CF), substrate near cohesion failure (SCF) and AF paired with cohesive substrate failure (CSF). In the unaged state, the fracture patterns show mainly a cohesive failure of the adhesive in the unaged state, **Figure 4 a)**. With NIR 2.3, sections of the epoxy were removed of the CFRP and remain on the

aluminium side. Only the acetone cleaned samples exhibit a partly adhesive failure (AF) on the aluminium side, **Figure 4 b**).

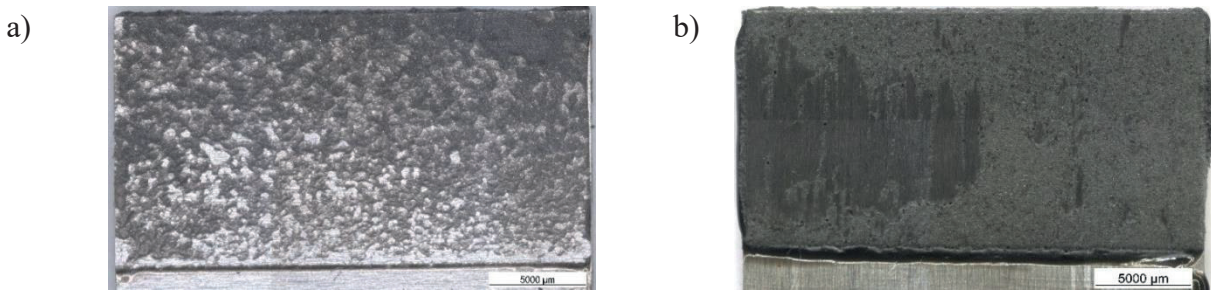


Figure 4: Breakage pattern of a) aluminium side of acetone cleaned unaged specimen, b) aluminium side of NIR 2.3 pre-treated unaged specimen

It is also visible, that an exposure of carbon fibres due to laser treatment with high energy input (NIR 37.3, NIR 71.2) leads to substrate near cohesion failure (SCF) on the CFRP side with carbon fibres remaining in the adhesive, which may indicate a cohesive substrate failure of the CFRP, **Figure 5 a**) and [9]. UV 40.0 and UV 80.0 exhibit a cohesive failure inside the adhesive, **Figure 5 b**).

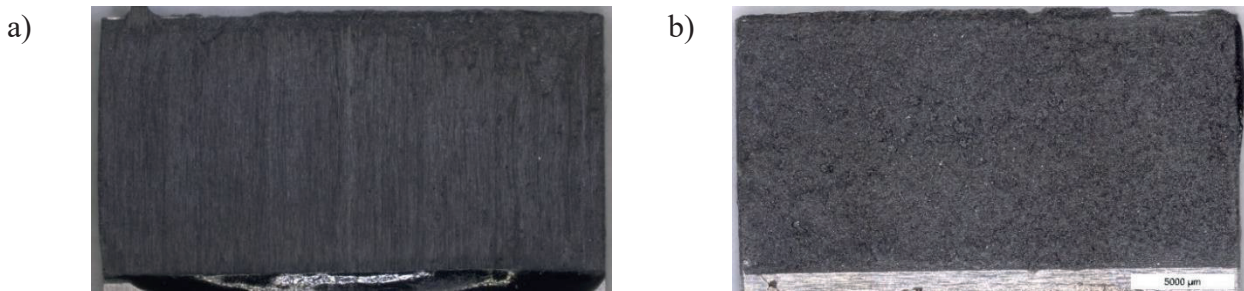


Figure 5: Breakage pattern of unaged specimens a) aluminium side of NIR 37.3 pre-treated specimen, b) aluminium side of UV 80.0 pre-treated specimen

Aged samples: Generally spoken, the fracture patterns do not change due to the hygrothermal ageing, independent of the cycle number and the pre-treatment process. Hygrothermal aged NIR 2.3 and NIR 37.3 breakage pattern are given in **Figure 6**

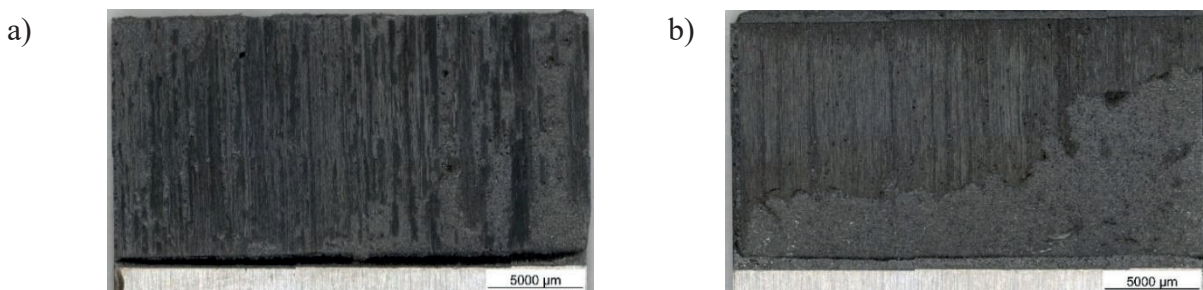


Figure 6: Breakage pattern after 50 cycles of a) aluminium side of NIR 2.3 pre-treated specimen, b) aluminium side of NIR 37.3 pre-treated specimen

However, after 50 cycles, the NIR 2.3 breakage pattern is in comparison to the unaged more unregularly and varies between a cohesive failure (CF) inside the adhesive and a cohesive substrate fail-

ure (CSF) inside the CFRP, **Figure 6 a**). In case of NIR 37.3, a section is broken cohesive in the adhesive and another section near the substrate (SCF) and inside the substrate (CSF) of the CFRP, **Figure 6 b**).

4 DISCUSSION

With the laser pre-treatment of CFRP, the level of matrix ablation and surface topography is effected by the applied laser parameters and energy density. The near-infrared wavelength enables a pre-treatment without an aerial ablation of matrix (NIR 2.3) or a fully carbon fibre exposure (NIR 37.3 & 71.2). However, a full ablation of the matrix without fibre damage is not possible. The mechanical strength of the hybrid CFRP/Al-joints revealed that an exposure of carbon fibres is not necessary. The specified shear strength of the adhesive was achieved with NIR 2.3 and Acetone. The fracture patterns confirm a high connection strength due to the mainly cohesive failure inside the adhesive. Higher NIR densities (NIR 37.3 & 71.2) lead to a reduced average shear strength and a breakage near the CFRP inside the adhesive with pulled out carbon fibres. This indicate that a damage inside the CFRP takes place. A similar result was determined by Reitz et al. [9].

The variation of the energy density with UV wavelength enables different states of ablation and surface topographies. A partly ablation of the matrix is possible. With UV 80.0, damaged and broken fibres were detected. The shear strength of UV specimens revealed a similar correlation to NIR pre-treatment whereby the lowest energy density achieved the highest shear strength. In contrast to several publication indicates this that an exposure of fibres is not necessary, on the contrary, it worsens the shear strength.

After different numbers of hygrothermal cycles, the mechanical strength is reduced in the range of 12-25 % to their unaged condition. With rising number of cycles, the mechanical strength stays constant in the range of approx. 20-22 MPa independent of the pre-treatment method and energy density. Except of NIR 2.3 and NIR 37.3, all breakage patterns are similar to their unaged reference. The constant mechanical strength after 25 cycles and more indicate, that an ageing of the adhesive within the first 25 cycles takes place. Further cycles do not have an additional influence on the strength of the adhesive. The different topographies of the surface and the exposed carbon fibres to not influence the ageing behaviour of the hybrid joint. This behaviour indicates that mainly a degradation of the adhesive itself takes place and the interaction zone between substrates and adhesive stays unaffected.

5 CONCLUSIONS

In this work, two laser systems with different wavelengths were applied to pre-treat the CFRP surface before bonding to aluminium. The aluminium substrate was laser structured with one parameter. The energy input with the NIR laser system was varied in between 2.3 and 71.2 J/cm², the UV system in the range of 16 and 80 J/cm². As a reference, acetone cleaned hybrid CFRP/Al specimens were used. After the adhesive joining, batches were hygrothermally aged according to PV1200:2003. The SLJ samples were tested mechanically in the pristine state as well as after 25, 50 and 100 cycles and fracture pattern were investigated. The following conclusions can be drawn:

- The energy density generates different levels of matrix ablation and surface topographies. With NIR wavelength, it is possible to laser process the samples with almost no exposure of the carbon

fibres applying a low energy density of 2.3 J/cm². Higher energy inputs lead to a full ablation of the matrix. However, the exposed carbon fibres are damaged to some extent.

- With the chosen parameters for the UV laser system, it is possible to pre-treat the CFRP-samples without (UV 16.0), with partial (UV 40.0) and full ablation (UV 80.0) of the matrix. However, fibre damage is observed as well when the matrix is fully ablated.
- The mechanical tests of the hybrid CFRP/Al-joints reveal that the highest shear strength is achieved when the matrix is not ablated. Acetone cleaned as well as NIR 2.3 and UV 16.0 samples exhibit values which are in the range of the specification of the adhesive.
- The ageing tests indicate that the adhesive bond degrades already within the first 25 cycles. A reduction of the shear strength in the range of 12-25 % is detected. Further cyclic ageing does not further decrease the shear strength.
- In addition, we conclude that when the matrix is ablated - which goes along with a lower shear strength in the unaged state - the different levels of ablation, surface topography and the exposed carbon fibres do not significantly affect the ageing behaviour of the hybrid joint.

6 ACKNOWLEDGEMENT

The authors acknowledge support by the German Federal Ministry of Education and Research within the program “FH-Impuls” (Project SmartPro, Subproject InDiMat, Grant no. 13FH4I03IA).

This research was supported by Dr. R. Kohlstrung from Henkel AG & Co. KGaA and Dr. B. Faißt from TRUMPF Laser- und Systemtechnik GmbH.

7 REFERENCES

- [1] Cambridge University, *Granta CES 2010 Edupack: Material and Process Selection Cart*, **2010**.
- [2] Witten E, Mathes V, Sauer M, Kuehnel M, *Composites Market Report 2018: Market developments, trends, outlooks and challenges*, **2018**.
- [3] Friedrich HE, *Leichtbau in der Fahrzeugtechnik, Springer Fachmedien Wiesbaden*. Wiesbaden, **2013**.
- [4] Teng JG, Yu T, Fernando D. *Journal of Constructional Steel Research*. **2012**, 78, p. 131–43 .
- [5] Rasche M, *Handbuch Klebtechnik, Hanser*. München, Wien, **2012**.
- [6] Blass D, Nyga S, Jungbluth B, Hoffmann H-D, Dilger K. *Materials (Basel)*. **2018**, 11(7).
- [7] Kawamura Y, Toyoda K, Namba S. *Appl. Phys. Lett.* **1982**, 40(5), p. 374–5 .
- [8] Fischer F, Kreling S, Dilger K. *Physics Procedia*. **2012**, 39, p. 154–60 .
- [9] Reitz V, Meinhard D, Ruck S, Riegel H, Knoblauch V. *Composites Part A: Applied Science and Manufacturing*. **2017**, 96, p. 18–27 .
- [10] Fischer F, Kreling S, Jäschke P, Fraunhofer M, Kracht D, Dilger K. *The Journal of Adhesion*. **2012**, 88(4-6), p. 350–63 .
- [11] Machado JJM, Marques EAS, Barbosa AQ, Silva LFM. *Fatigue Fract Eng Mater Struct*. **2019**, 42(10), p. 2325–39 .
- [12] Mu W, Qin G, Na J, Tan W, Liu H, Luan J. *Composites Part B: Engineering*. **2019**, 168, p. 87–97 .
- [13] Qin G, Na J, Mu W, Tan W, Yang J, Ren J. *Composites Part B: Engineering*. **2018**, 154, p. 43–55 .
- [14] Henkel AG & Co. KGaA, *Technical Data Sheet - TEROSON EP 5065*, **2014**.

- [15] Genna S, Leone C, Ucciardello N, Giuliani M. *Polym Eng Sci.* **2017**, 57(7), p. 685–92 .
- [16] Schanz J, Gooßen M, Meinhard D, Harrison D, Silva A de, Knoblauch V et al.,
SPIE Proceeding - **2020**.

TOPIC

Characterization



@DGM_eV

#Hybrid2020

Mechanical characterization of an interpenetrating metal-matrix-composite based on highly homogeneous ceramic foams

J. Schukraft¹, C. Lohr¹, K. A. Weidenmann¹

¹Institute for Materials Resource Management, Augsburg University

1 Abstract

In this study an interpenetrating metal-matrix-composite of a highly homogeneous alumina ceramic foam and an AlSi10Mg aluminum alloy, fabricated via gas pressure infiltration of the ceramic preform with the molten aluminum alloy is investigated mechanically. This composite shows promising mechanical properties compared to other interpenetrating aluminum-alumina composites due to its ceramic preform and manufacturing process. To get an understanding of the application potential and limits of this material, mechanical characterization is carried out in a compression test combined with an in-situ method of a digital microscope to analyze the failure mechanism and crack propagation during compression tests. The received results from this study are compared with other studies in this field to place this new material into the range of investigated interpenetrating phase composites (IPCs) based on aluminum-alumina composites.

2 Introduction

Light-weight materials for structural application play a key role in nowadays engineering success regarding the reduction of greenhouse gases and environmentally compatible implementations in mobility and transportation. The limits of light weight metals are reached mainly for mechanical load in an environment under elevated temperature. In this area of application, metal-matrix-composites (MMC) and especially interpenetrating phase composites show a great potential [1]. By combining ceramic structures with a metallic phase in an interpenetrating microstructure, each phase contributes to the macroscopic properties of the composite which gives the opportunity to tune the properties or also develop multifunctional materials [2]. Aluminum based MMCs are in special focus of research regarding their properties and potential. Therefore aluminum is the most utilized metallic alloy in the MMC development [3]. Infiltrating sintered ceramic preforms with a metallic phase is the most common used manufacturing method for interpenetrating composites [2, 4–7]. An overview of research on various manufactured IPCs based on aluminum-alumina, are given in **Table 1** with ceramic content, range of pore size in the ceramic phase, type of aluminum alloy used for the metallic phase, compressive strength, strain rate and elongation at compression strength as far as specified in the publications.

The mechanical properties as well as the microstructure of the composite is mainly based on the ceramic preform. For an isotropic mechanical behavior, a homogeneous pore distribution within the ceramic without a geometrically predominant direction, is required. Colombo and Bernardo [8] have shown the microstructural need of a small pore size for a mechanically durable ceramic foam. Previous microstructural investigations via X-ray computed tomography have shown a narrow pore-size distribution with open, homogeneous and spherical pores and dense ceramic struts in the ceramic foam investigated here [9].

Table 1. Overview of different interpenetrating ceramic metal composites of alumina and aluminum alloys from literature.

ceramic phase manufacturing method	ceramic content	pore size	type of metal	residual porosity	compression strength	strain rate	elongation at compression strength/break	publication
[-]	[%]	[μm]	[-]	[%]	[MPa]	[-]	[%]	[-]
freeze casting / pore former	35 - 40	NSF	AlSi12	NSF	500 – 900	NSF	0,01 - 10	[10]
freeze casting	43 \pm 2	NSF	AlSi12	NSF	270 - ca. 700**	10 ⁻³ 1/s	2,5 - 10	[11]
pyrolisable placeholder	24,3	NSF	AlSi12	NSF	277*	NSF	NSF	[12]
pyrolisable placeholder	29,5	NSF	AlSi12	NSF	301,5*	NSF	NSF	[12]
hollow alumina particle	NSF	NSF	AlSi7Mg0,3	NSF	up to 275	10 ⁻³ 1/s	NSF	[13]
replica technique	30,57	300 - 450	AlSi12CuMgNi	0,57	341	NSF	ca. 4	[14]
replica technique	28,52	450 - 550	AlSi12CuMgNi	1,6	317	NSF	ca. 4	[14]
replica technique	25,58	800 - 1000	AlSi12CuMgNi	1,44	294	NSF	ca. 4	[14]
gelcasting of foams	10	500	AlMg5	<1	320	NSF	0,09	[15]

NSF = Not specified

* Tensile, no compression values available

** lowest value for 34 ° angle to freeze direction, highest value in freezing direction tested

3 Experimental/ Materials and Methods

For the experiments, a macroscopic homogeneously and highly porous open-cell alumina ceramic foam, with an approximate relative density of 25 %, provided by Morgan Advanced Materials Haldenwanger GmbH, Waldkraiburg, Germany is used, who hold a patent on the low-cost manufacturing technique [16]. An interpenetrating metal ceramic composite is produced via gas pressure infiltration based on the ceramic foam and an AlSi10Mg aluminum alloy, as described by the authors [9]. The materials were cut into cubic samples of ca. 5 x 5 x 5 mm³ and the sample surface was grinded stepwise with silicon carbide paper up to grain size P800, with water as coolant. For in-situ microscopy one cube-surface also was polished with diamond suspensions (9, 3 and 1 μm) and OP-S-Suspension, each manufactured by Struers, Friedberg, Germany.

Compression tests were carried out with a universal testing machine of type 1464, with a load cell xforceK up to 50 kN, each of Zwick&Roell, Ulm, Germany. Interchangeable compression stamps with plane turned and then polished end faces (SiC grinding paper with grain size up to P4000 and water as coolant) were made of hardened machine screws of grade 12.9 with tensile strength of 1200 N/mm² and a yield strength of 1050 N/mm². Molybdenum sulfide (OKS Spezienschmierstoffe GmbH, Munich, Germany) was used as a solid lubricant between the sample and the stamps in accordance to DIN 50106 [17]. A preload of 20 N was applied onto the sample, before the data logging started. The strain rate during the compression tests was set to 10⁻³ 1/s. Abort criterions for the experiments were set for a minimum stamp distance of 3 mm and a drop in maximum force of 80 %. Three samples were tested with the in-situ testing. Therefore, load steps were integrated into the compression test procedure at stresses of 250, 300, 340, 360 and 380 MPa for the composite.

For optical elongation determination the ARAMIS Adjustable System with two 12 Megapixel cameras by GOM, Braunschweig, Germany was used. For the specific setup, lenses with a focal

length of 100 mm and one polar filter for each camera were used. The working distance between camera and sample was ca. 50 cm and two LED spotlights were used for the uniform illumination of the sample. A black and white speckle pattern was applied on the sample surface examined with the ARAMIS-System.

A digital microscope of type VHX-600 by Keyence, Neu-Isenburg, Germany was installed with a 50 to 500 x magnification (VH-Z50L, Keyence) on the opposite side of the sample, to investigate the damage behavior and the crack propagation during the compression test. The complete test setup of the in-situ compression tests is shown in **Figure 1**:

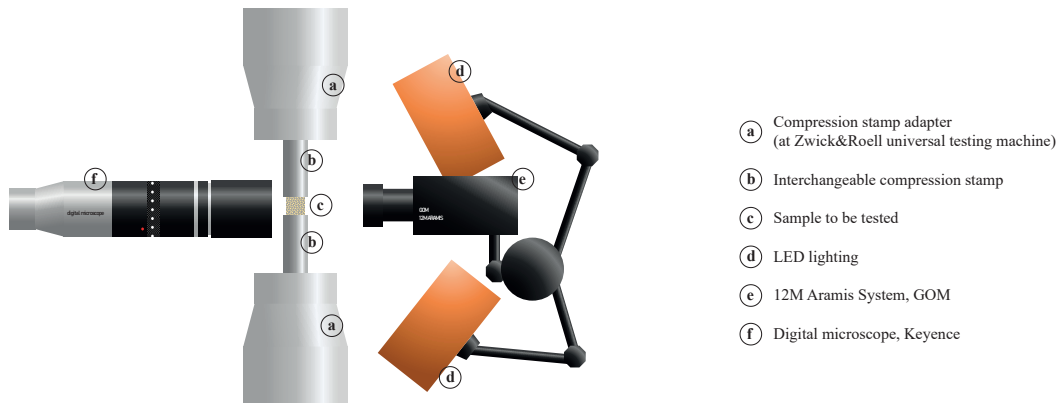


Figure 1. In-situ testing setup: Zwick&Roell universal testing machine, GOM ARAMIS Adjustable 12M System and Keyence digital microscopy.

4 Results and Discussion

The results of the compression tests for the ceramic preform are shown in **Figure 2**. The elongation has been tracked with the Aramis GOM-System, based on a speckle pattern. At the point of failure, the speckle pattern can spall from the brittle surface or because of spontaneous big displacements, the software is not able to calculate the elongation correctly anymore. Therefore, the values are just plotted until the point of failure. The curves were also smoothed with a Lowess algorithm.

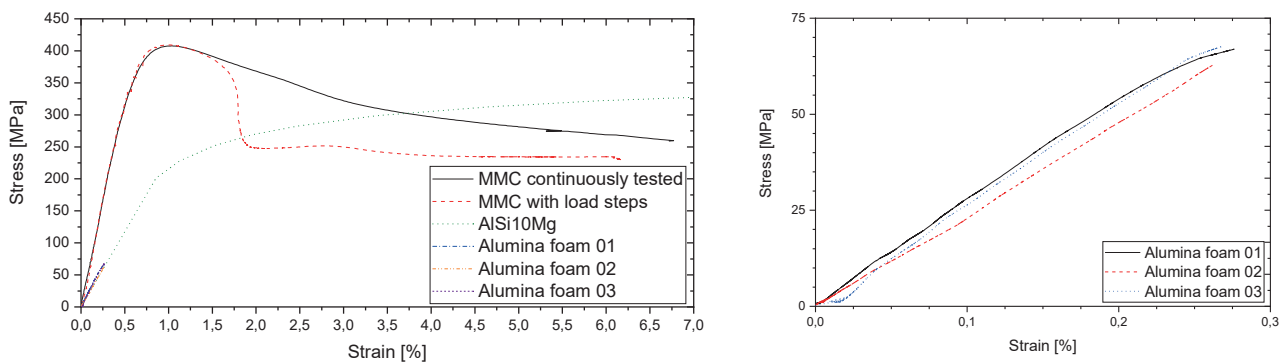


Figure 2. *Left:* Stress-strain diagram of the compression test with a strain rate of $\dot{\epsilon} = 10^{-3}$ 1/s for the alumina ceramic foam, the produced interpenetrating composite and an AlSi10Mg alloy (values taken from literature [20]).

Right: Enlarged visualization of the results for the ceramic foam.

The ceramic foam shows a linear behavior until failure and has an elongation at break higher than 0,25 %, which is more than twice the elongation at break of a dense alumina ceramic [18]. The compression strength of this ceramic foam lies between 60 and 65 MPa. Compared to some other studies on alumina based ceramic foams with a comparable porosity, produced in different ways, the

investigated ceramic foam has a higher compressive strength. Hadi et al. [19] produced a ceramic foam via replica technique with a porosity of 80 – 83 % and 14 pores per inch. The compressive strength of their foam reached 1,33 – 3,24 MPa. Prabhakaran et al. [20] used a pore-former process for their material with 67 – 76,7 % porosity and a bimodal pore size distribution in the range of 20 μm and 200 – 800 μm . They reached a compressive strength of 2,01 – 5,9 MPa for their material. Vijayan et al. [21] investigated a freeze gel-casting foam with 70 % porosity and an average pore size of 13,24 μm with a compressive strength of 39,6 MPa. Tallon et al. [22] investigated alumina foams produced via stabilized foams and gel casting process in a varying range of porosity between 65 – 93 %. They reached for small pore size between 100 and 150 μm a compressive strength of 57,8 MPa at a porosity of 63 %. For bigger pores around 300 μm they determined lower compressive strengths. Colombo et al. [8] showed a dependency of mechanical strength of the ceramic foams on the pore size. For small pores (8 μm) they determined a two to five times higher compressive strength than for bigger pores (100 – 600 μm). In the mentioned examples from literature, it becomes obvious, not only the pore size is responsible for the mechanical stability of ceramic foams. The microstructure resulting from the respective manufacturing process also plays a decisive role for the mechanical strength. For replica technique e.g., the ceramic struts often show pores inside, like it can be seen exemplarily in the following publications by Hadi et al. [19], Accher et al. [23], Boczkowska [24] and Dolata [25]. Studart et al. [26] give an overview of different ceramic foams, in which the compressive strength is shown as a function of porosity and the manufacturing process. The alumina foam of the present study can be placed in the upper area of the compressive strength of the open porous alumina foams within their diagram, which spans from 0,15 to 100 MPa (for relative densities from 0,04 to 0,54). The highly homogeneous pore distribution inside the ceramic and the dense ceramic struts as well as the narrow pore-size distribution with a low median pore diameter of approximately 20 μm [9] are microstructural reasons for the foam having such high load capacity. As an example, **Figure 2** shows two stress-strain curves of the composite in addition to the curves of the ceramic foam. One curve shows the course of the compression testing with constant strain rate (*MMC continuously tested*). The other curve shows the course where load steps were implemented for the in-situ investigations of the sample (*MMC with load steps*). For the *MMC with load steps* the test was terminated when a certain number of images was reached with the GOM-System. The experiment of the *MMC continuously tested* was terminated after a significant stress decrease from the maximum stress. The curves of the two compression tests correspond very well up to the maximum stress, where the ceramic phase fails with an audible cracking. The maximum compression strength is approximately 407 MPa. The further course of the *MMC with load steps* is different from the *MMC continuously tested* and shows a drop in stress. Reasons for that could be local failure of ceramic struts or microscopic crack growth in the ceramic phase during the load steps in combination with dislocation slip as well as dislocation creep in the metallic phase for high stresses, also occurring during the load steps, but this phenomenon is not finally investigated yet and the given reasons are just thesis which have to be proved. Also remarkable is the three times higher elongation in the composite at maximum compression stress in comparison with the ceramic foam (approximately 1 % compared with 0,25 % elongation at break), what can also be seen in other publications, like Boczkowska et al. [14] e.g. For the classification of the compressive strength of the composite, values from other publications were compiled in **Table 1**.

The compression stress-strain curve of a bulk AlSi10Mg alloy is shown in **Figure 2** for the same range of elongation. The data of the curve progression are cut off at the elongation of 7 % for a better overview and been obtained from Stanev et al. [27], who based their figure on Stanev et al. [28]. Due to the ceramic interpenetrating phase, the composite is significantly stiffened compared to the aluminum alloy and also gains in strength. The brittle material properties of the ceramic are

compensated largely by the metallic phase, as the course of the composite shows in **Figure 2** in comparison to the original materials of which the phases of the composite are made.

Representative micrographs of the sample, which is shown in the stress-strain diagram in **Figure 2** (*MMC with load steps*), are shown in **Figure 3** for the condition under preload and at the end of the compression test. The material contrast between metal and ceramic made a good differentiation of the phases. The local plastic deformation in the metallic phase as well as the crack growth in the ceramic phase, the metallic phase as well as at the phase boundaries up to macroscopically big cracks can be seen.

The experimental setup, introduced in **Figure 1**, makes additionally optical strain analysis accessible. The phenomenon of macroscopic cracks, tend to grow under $\pm 45^\circ$ in the material sample, can also be detected in the optical strain analysis like the results show in the middle of **Figure 3** in comparison to the micrograph in the right part. The strain orthogonal to the load direction shows also concentration along $\pm 45^\circ$ according to the load direction. This gives first indications to a shear driven failure mechanism in the section of decreasing stress after the maximum compression stress was reached and the main load-bearing structure of the ceramic phase has failed with an audible crack. But for consideration of the entire range of failure, the complex interpenetrating material structure shows a complex failure process with a multidirectional crack growing progress. Thereby a clear failing mechanism could not be determined yet. This shows that a two-dimensional investigation of crack growth and failure mechanism at the sample surface is not enough to get an understanding of the complete failure mechanism in this interpenetrating phase composite.

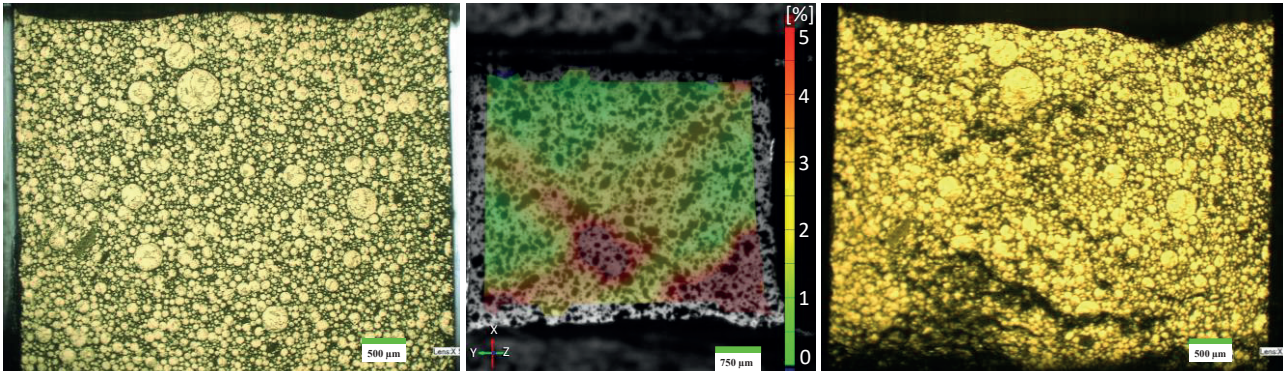


Figure 3. Micrographs of in-situ compression test. Overview of the sample “*MMC with load steps*” with preload (*left*) and at the end of the test (*right*), strain in Y-direction at one of the last images with full pattern identification of the software (*middle*). Strain scale is cut off at 5 % to illustrate the elongation course over the surface. Local maximum strains up to 15 % are reached in the lower right corner.

5 Conclusion/Summary and Outlook

Compression tests on an interpenetrating metal-ceramic composite and on a homogeneous ceramic foam, the composite is based on, were carried out successfully. The compression tests show a high load capacity of the ceramic foam (60 – 65 MPa) due to its well-developed microstructure for mechanical application. This property is also reflected in the composite, where high stiffness and high compression strength (407 MPa) can be seen. At the same time, the metallic phase compensates the brittle properties of the ceramic foam and the elongation at maximum compression stress of the MMC is three times higher than the elongation at break of the ceramic foam.

Furthermore, an in-situ setup was presented, to investigate two-dimensional crack growth and failure at the sample surface during compression testing. The method is especially suitable for composite materials with a good optical contrast.

This work also showed first results of crack growth at the surface of the interpenetrating aluminum-alumina composite. Because of the complex microstructure and load distribution inside the composite specimen, further investigations with three-dimensional in-situ methods (e.g. computed tomography) will be conducted to fully understand the failure mechanisms of interpenetrating composite structure.

6 Acknowledgements

The financial support for this work in the context of the DFG research project WE 4273/17 is gratefully acknowledged. We also want to thank Morgan Advanced Materials Haldenwanger GmbH for the friendly supply of material samples of the ceramic foam, used in this work.

7 References

- [1] Clarke, D. R., *J. Am. Ceram. Soc.* **1992**, 4, 739–758.
- [2] Peng, H. X., Fan, Z. und Evans, J.R.G., *Materials Science and Engineering: A* **2001**, 303, 37–45.
- [3] Bodunrin, M. O., Alaneme, K. K. und Chown, L. H., *Journal of Materials Research and Technology* **2015**, 4, 434–445.
- [4] Scherm, F., Völkl, R., Neubrand, A., Bosbach, F. und Glatzel, U., *Materials Science and Engineering: A* **2010**, 4-5, 1260–1265.
- [5] Roy, S. et al., *Materials Science and Engineering: A* **2011**, 28, 8226–8235.
- [6] Binner, J., Chang, H. und Higginson, R., *Journal of the European Ceramic Society* **2009**, 5, 837–842.
- [7] San Marchi, C., Kouzeli, M., Rao, R., Lewis, J. A. und Dunand, D. C., *Scripta Materialia* **2003**, 49, 861–866.
- [8] Colombo, P., *Composites Science and Technology* **2003**, 16, 2353–2359.
- [9] Horny, D., Schukraft, J., Weidenmann, K. A. und Schulz, K., Submitted to *Advanced Engineering Materials*, **December 2019**.
- [10] Roy, S., Gibmeier, J., Weidenmann, K. A., Nagel, A. und Wanner, A. in W. Udomkitchdecha, T. Böllinghaus, A. Manonukul und J. Lexow, Hg., Cham: Springer International Publishing, **2014**, 77–86.
- [11] Roy, S., Butz, B. und Wanner, A., *Acta Materialia* **2010**, 7, 2300–2312.

- [12] Dobrzanski, L. A., Kremzer, M., Nowak, A. J. und Nagel, A., *Archives of Materials Science and Engineering* **2009**, 1, 5–11.
- [13] Licitra, L., Luong, D. D., Strbik, O. M. und Gupta, N., *Materials & Design* **2015**, 504–515.
- [14] Boczkowska, A. et al., *SSP* **2012**, 57–66.
- [15] Potoczek, M. und Śliwa, R., *Archives of Metallurgy and Materials* **2011**, 4, 41.
- [16] Lavrentyeva, O. DE. Patent DE102015202277A, **2016**.
- [17] *Prüfung metallischer Werkstoffe - Druckversuche bei Raumtemperatur*, DIN 50106:2016-11, **2016**.
- [18] *CES EduPack*, GRANTA DESIGN, **2019**.
- [19] Hadi, A., Emadi, R., Baghshahi, S. und Naghavi, S. H., *Ceramics - Silikaty* **2015**, 90–95.
- [20] Prabhakaran, K., Melkeri, A., Gokhale, N. M. und Sharma, S. C., *Ceramics International* **2007**, 1, 77–81.
- [21] Vijayan, S., Narasimman, R. und Prabhakaran, K., *Journal of the European Ceramic Society* **2014**, 16, 4347–4354.
- [22] Tallon, C., Chuanuwatanakul, C., Dunstan, D. E. und Franks, G. V., *Ceramics International* **2016**, 7, 8478–8487.
- [23] Acchar, W. et al., *J Mater Sci* **2008**, 19, 6556–6561.
- [24] Boczkowska, A., Chabera, P., Dolata, A. J., Dyzia, M. und Oziębło, A., *Metalurgija* **2013**, 3, 345–348.
- [25] Dolata, A. J., *Journal of Materials Engineering and Performance* **2016**, 8, 3098–3106.
- [26] Studart, A. R., Gonzenbach, U. T., Tervoort, E. und Gauckler, L. J., *J. Am. Ceram. Soc.* **2006**, 6, 1771–1789.
- [27] Stanev, L., Kolev, M., Drenchev, B. und Drenchev, L., *Journal of Manufacturing Science and Engineering* **2017**, 5, 810.
- [28] Stanev, L., Drenchev, B., Yotov, A., and Lazarova, R., *Journal of Materials Science and Technology* **2014**, 1, 44–53.

Characterization and Modelling of the Vibration and Damping Behavior of Carbon Fiber-Metal-Elastomer Laminates by using Modal Analysis in Cantilever setup

V. Sessner¹, A. Jackstadt², W. Liebig¹, L. Kärger², K. Weidenmann³,

¹Karlsruhe Institute of Technologie, Institute for Applied Materials (IAM-WK), Karlsruhe;

²Karlsruhe Institute of Technologie, Institute of Vehicle System Technology (FAST), Karlsruhe;

³University of Augsburg, Insititute for Materials Resource Management (MRM), Augsburg

ABSTRACT: Common lightweight materials are often prone to vibrations, as loss factors of isotropic materials generally decrease with higher specific Young's moduli. This may reduce the comfort for the user but also increases the fatigue of the material due to unwanted vibrations.

Fiber-metal-elastomer laminates used in this study consist of alternating layers of carbon fibre reinforced plastics, elastomer layers and aluminium sheets. These laminates offer great potential in lightweight structures with adjustable damping properties, while also showing the benefits of conventional fiber metal laminates, with their damage tolerant behaviour. The material behavior is strongly influenced by the viscoelastic properties of the applied elastomer, which damp by the principle of constrained layer damping when the laminate is excited. Here, large shear strains are induced in the viscoelastic elastomer layers when the laminates are deformed under bending loads. The characterization in this study is done by modal analysis according to ASTM E756-05, with a cantilever beam under bending vibrations. Different laminate setups are investigated to show the influence of lay-up on the modal parameters. Therefore, frequency response functions are recorded and modal loss factors of the natural frequencies are extracted by using the half-power bandwidth method. The results are compared with an analytical model based on the so-called Ross-Kerwin-Ungar-equations (RKU) and numerical studies by using finite element simulations. The different models are compared and their limitations are discussed.

1. Introduction

Fiber metal laminates are well known for their good mechanical properties and damage tolerant behavior [1]. The usage of carbon fiber reinforced plastics (CFRP) in these laminates is often restricted due to degradation because of galvanic corrosion and thermal expansion coefficients. The integration of an elastomer layer has proven to overcome these drawbacks [2]. In addition, the elastomer layer also has strong influence on the damping behavior of such laminates. This principle is well known as constrained layer damping (CLD), where a compliant viscoelastic damping layer is constrained between two stiffer layers. This leads to high shear deformations in the damping layer under bending vibrations. The damping behavior depends on the viscoelastic layer and laminate lay-up. This principle was first described by Ross et al. [3], who also gave an analytical model for determining natural frequencies and damping factors for such laminates. The model and equations are known as the RKU-Model, which is used in wide variety of studies dealing with constrained layer damping [4–6]. Also more complicated analytical models were presented for more complex laminates [7]. However, hybrid materials consisting of fiber reinforced plastics, metal sheets and viscoelastic damping layers were rarely considered neither analytical nor experimental. Therefore, in this study the damping behavior of hybrid fiber metal elastomer laminates (FMEL) will be characterized by modal analysis. The experimental characterization of the FMEL will be done according to ASTM E756-05 [8]. Although this standard is primarily used to characterize the viscoelastic behavior of the

damping material, the procedure can also be used to characterize the entire laminate. The analytical model presented in this standard is also based on the RKU-Model and will be used in this investigation, as well as a numerical approach. The characterization of the neat materials is not part of this investigation, but can be found in previous studies [9].

2. Material

The FMEL were manufactured using a hot molding process at 150°C and 40 bar for 300 s. The hybrid material consists of aluminum sheets 2024 T3 ALCLAD AMS-QQA-250/5 with a thickness of 0.3 mm and CFRP layers in a biaxial $[0/90]_s$ lay-up of unidirectional HexPly M77/38%/UD150/CHS/12K/T700 with a single layer thickness of 0.15 mm according to the data sheet [10]. For the elastomer layers unvulcanized EPDM layers, provided by Gummiwerk KRAIBURG GmbH & Co. KG, were used. The mixture is called SAA9579-52 and was provided in a thicknesses of 0.5 mm. Beside the standard manufacturing process the elastomer was also applied in a dissolved condition described by Stoll et. al [11]. Thereby a 0.05 mm thick elastomer layer was manufactured. The laminates consist of alternating CFRP and aluminum layers, which are separated by an elastomer layer. In addition, a reference laminate was manufactured and tested which does not have an elastomeric layer as separating layer. The lay-ups of the laminates are summarized in Table 1. An abbreviated notation is also introduced for referring to the specific lay-up. Panels with quadratic dimensions of 400 mm x 400 mm were manufactured and specimens with dimensions of 250 mm x 15 mm were cut from these panels using water jet cutting. For each laminate lay-up three specimens were prepared for testing. The fiber orientation was chosen so that the outer fibre layer is oriented along the long side of the specimens.

3. Methods

3.1. Experimental modal analysis

The test set up for the modal analysis is shown in Figure 1 a).

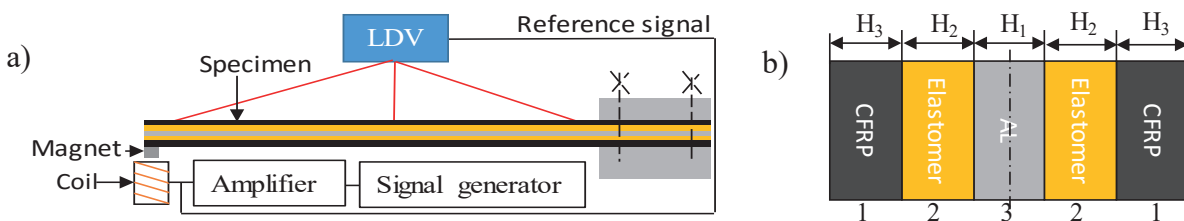


Figure 1: a) Test setup for experimental modal analysis on FMEL. b) Crosssection of an FMEL specimen with nomenclature for analytical model in section 3.2. H is the thickness of each layer.

The specimen is clamped at one side over a length of 40 mm, so that a free length of 210 mm can vibrate at the free end. The excitation is realized contactless via electromagnetic forces. Therefore, a small magnet is glued at the free end of each specimens. A coil is placed in front of the magnet, which is connected to an amplified signal generator. The signal is generated using the audio output of a PC and is used as a reference signal. Thereby a sweep signal with constant amplitude from 10 Hz to 6 kHz is generated. The vibration of the specimen is measured with a scanning laser-Doppler-vibrometer (Polytec PSV-500) at 57 evenly distributed points. Thus, the mode shapes are analyzed. Frequency response functions (FRFs) as the mean value of all 57 measurement points are determined

Table 1: Lay-up configurations and nomenclature according to Sessner et al. [9]: X_y^z : X: Material class (A: Aluminum, El: Elastomer, C: CFRP), y: thickness in mm, z: Additional information like orientation or different materials within the material class.

Nr.	Lay-up	Thickness / mm	Abbreviation
1.	$[(C_{0.15}^{0^\circ}/C_{0.15}^{90^\circ})_s/A_{0.3}/(C_{0.15}^{0^\circ}/C_{0.15}^{90^\circ})_s]$	1.5	C/A/C
2.	$[(C_{0.15}^{0^\circ}/C_{0.15}^{90^\circ})_s/El_{0.05}^{soft}/A_{0.3}/El_{0.05}^{soft}/(C_{0.15}^{0^\circ}/C_{0.15}^{90^\circ})_s]$	1.6	C/El _{0.05} ^s /A/El _{0.05} ^s /C
3.	$[(C_{0.15}^{0^\circ}/C_{0.15}^{90^\circ})_s/El_{0.5}^{soft}/A_{0.3}/El_{0.5}^{soft}/(C_{0.15}^{0^\circ}/C_{0.15}^{90^\circ})_s]$	2.5	C/El _{0.5} ^s /A/El _{0.5} ^s /C

by Fast Fourier Transformation (FFT) up to 6250 Hz with a minimum frequency resolution of 0.977 Hz. The modal loss factor is determined with the n dB method according to ASTM E756-05 [8]:

$$\eta = \left(\frac{1}{\sqrt{(x^2) - 1}} \right) \frac{\Delta f_n}{f_n} \quad (1)$$

With:
$$x = 10^{\left(\frac{n}{20}\right)}. \quad (2)$$

As a standard value $n=3$ dB is chosen for the modal damping, but lower values are picked for natural frequencies which are strongly damped. The standard also states that the first natural frequency should be considered with extra care, as it is very sensitive to higher damping due to the clamping. In addition, the frequency resolution of the FFT is not high enough to accurately measure the first natural frequency correctly. Therefore, the modal damping of the first natural frequency will not be evaluated.

3.2. Analytical model for FMEL modal parameters

According to ASTM E756-05 the n -th natural frequency f_n for an isotropic beam can be calculated with the following formula [8]:

$$E = \frac{12 \rho L^4 f_n^2}{H^2 c_n^2}. \quad (3)$$

L = Free length

ρ = Density

E = Young's modulus

$$c_n = \left(\frac{\pi}{2}\right)(n - 0.5)^2; \text{ for } n > 3; c_1 = 0.55959; c_2 = 3.5069; c_2 = 9.8194$$

For the hybrid FMEL lay-ups the modal parameters in cantilever setup shown in Figure 1 a) are modeled using the RKU equations and the model proposed by Nashif et al. [12]. Here, only the damping layers (see Figure 1 b) Elastomer) are modelled to be viscoelastic. The outer constraining layers and the center layer are seen as isotropic linear elastic. Although, this is not the case for the CFRP layer, a rule of mixture was applied to calculate the Young's modulus of the biaxial CFRP lay-up with results from tensile tests on unidirectional 0° and 90° CFRP. These modulus values and the DMA master curves of the elastomer materials can be found in Sessner et al. [9]. The aluminum layer is also modeled linear elastic with a Young's modulus of 70 GPa and a density of 2.7 g/cm^3 . Thus, the complex modulus of a five-layer structure for the n -th bending mode can be described with following formulas [12]:

$$EI(1 + i\eta) = E_1 I_1 + 2E_3 I_3 + 2E_3 H_3 H_{31}^2 \frac{g(1 + i\eta_2)}{1 + g(1 + i\eta_2)}. \quad (4)$$

With:
$$g = \frac{G_2 L^2}{E_3 H_3 H_2 a_n} \quad (5)$$

$$a_n = (2n - 1)^2 \pi^2 / 4 \quad \text{for } n \geq 2, \quad \text{and } a_n = 3.516 \quad \text{for } n = 1 \quad (6)$$

$$H_{31} = \frac{H_1 + H_3}{2} + H_2 \quad (7)$$

- I_1, I_3 = Second moment of inertia for layers 1 and 3
- η_2 = Loss factor (tan delta) of layer 2
- E_1, E_3 = Young's moduli for layers 1 and 3
- G_2 = Shear modulus of the elastomer layer.

Where $EI(1 + i\eta)$ represents the complex modulus of the FMEL. The storage and loss modulus can be derived by calculating the real and imaginary parts of it. The modal loss factor η is the ratio of loss and storage modulus and a_n is a constant factor depending on the mode number and boundary conditions of the specimen. For the present case, clamped-free boundary conditions are chosen. Note, this model can only depict bending mode shapes, hence it must be checked whether this applies to the experimental results. The storage modulus derived from equation (6) can be used in combination with equation (3) to calculate the natural frequencies of the hybrid FMEL or vice versa if the storage modulus is to be calculated from the natural frequency.

3.3. Numerical model for FMEL modal parameters

Additionally, finite element simulations using Abaqus/Standard are carried out in order to numerically determine the natural frequencies and modal loss factors of the laminates under investigation. The models consist of quadratic solid elements and each material layer is represented by three elements in thickness direction. The beams are modeled according to the lay-ups and dimensions in Sections 2 and 3.1. All translational degrees of freedom are restricted at the clamped face of the beam. The aluminum is modeled as linear elastic whereas the CFRP and elastomer layers have frequency dependent material properties. The eigenvalue extraction is followed by a complex eigenvalue analysis yielding each mode's effective damping ratio given by

$$d = -2 \frac{\text{Re}(\hat{u}_i)}{\text{Im}(\hat{u}_i)} \quad (8)$$

where \hat{u}_i is the eigenvalue of mode i . In order to comply with the results that are obtained experimentally, only bending modes are considered.

4. Results

Figure 2 shows the second to seventh mode shape of a C/El₅^S/A/El₅^S/C lay-up. For each specimen it was checked that only bending mode shapes are evaluated. The second to seventh natural frequencies for all lay-ups are shown in Figure 3 a) for the experimental numerical and analytical results with their corresponding loss factors. As stated before, for the evaluation, the first bending mode is not considered due to limited frequency resolution of the FFT and negative effects due to the clamping. The evaluated mode shapes of the natural frequencies correlate to the ones shown in Figure 2. For the specimens without elastomer a higher scatter range can be seen for the second bending mode compared to the remaining loss factors. This is still seen as a result of a limited frequency resolution, which is particularly noticeable at weakly damped low natural frequencies. It can be seen that for the lay-ups with elastomer the loss factor increases with increasing natural frequency. For the specimens without elastomer this trend can hardly be distinguished above the second bending mode.

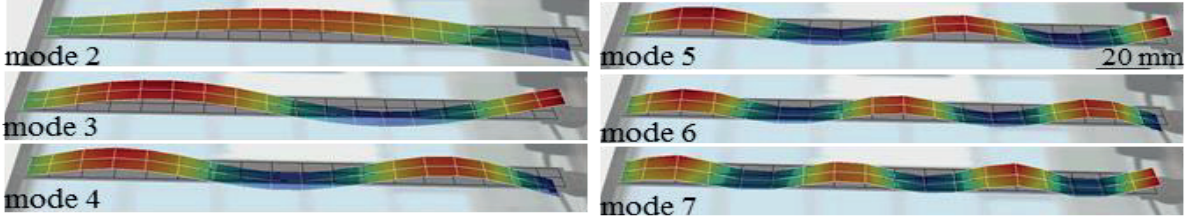


Figure 2: Second to seventh experimentally determined bending mode shapes of the $C/EI_5^s/A/EI_5^s/C$ lay-up.

The analytical and numerical loss factors show the same trend for the lay-ups with elastomer. In addition, the accordance with the experimental results is good with a slightly overestimation for the lay-up with the thicker elastomer. For the lay-up without elastomer, no analytical results were determined, as the RKU model is only valid for specimens with a low modulus interlayer. The numerical results for the $C/A/C$ lay-up also show the same trend, however the loss factor is underestimated by the model. The storage modulus of the lay-ups at their corresponding natural frequency can be seen in Figure 3 b). These storage moduli are calculated using equation (3). For the lay-up without elastomer ($C/A/C$) the storage modulus is constant for all natural frequencies. For the FMEL lay-ups the storage modulus decreases for higher bending mode shapes. The analytical model predicts the storage modulus well, with the biggest errors of 12.6 % at the lower frequencies for the 0.5 mm thick elastomer layer ($C/EI_5^s/A/EI_5^s/C$). The numerical model overestimates the storage modulus for all lay-ups, while with decreasing elastomer content the overestimation increases.

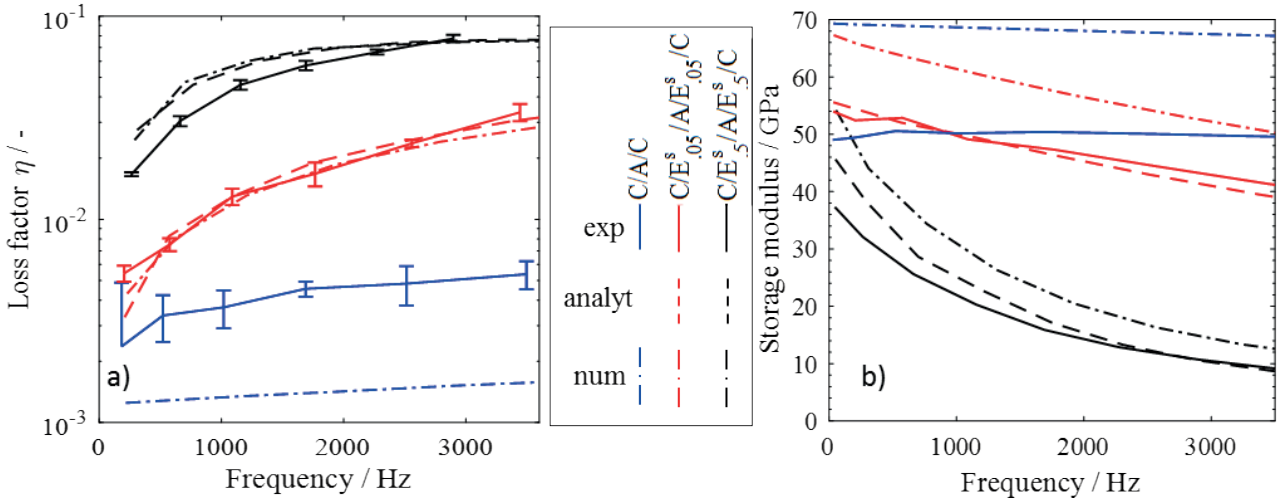


Figure 3 a): Experimental, analytical and numerical loss factors for all lay-ups starting from the second bending mode. For the experimental ones the mean values of three experiments is shown; **b):** Storage modulus of the lay-ups at the corresponding natural frequency starting from the second bending mode shape. For the experimental ones the mean values of three experiments are calculated.

5. Discussion

Two different types of behaviors have been examined for the specimens with and without an elastomer layer. With the additional elastomer layer, the specimens show a strong dependency on mode shape and frequency as it can be seen in Figure 3a. As stated by Nashif [12] the change of loss factor for CLD applications much more depends on the wave length of the corresponding mode shape as of the actual frequency. The characterization of storage and loss modulus of the neat elastomer can be found in Sessner et al., where a decrease of loss factor over the frequency range from 1 Hz to 10^4 Hz was shown [9]. Since the loss factors η of the modal analysis show an increasing behavior with frequency, the different mode shapes can be held responsible for that. The higher loss factor can be explained with higher shear strains in the elastomer layers for shorter wavelengths. For the lay-up

without elastomer this cannot be seen as the shorter wavelengths do not influence the damping mechanisms. Also the storage modulus in Figure 3 b) is not affected by the different mode shapes and stays constant over the frequency range for specimens without the low modulus interlayer. The difference in the storage modulus for the lay-up without elastomer (C/A/C) in Figure 3 b) for numerical and experimental results shows that the CFRP layers are modeled too stiff in the numerical approach. With increasing thickness of the elastomer layer the effect is less pronounced, however. Although in the analytical approach the CFRP layers are modeled linear elastic with no contribution to the damping behavior, the results of analytical and experimental approach show good agreement (see Figure 3a). This leads to the conclusion that the damping behavior is mostly affected by the elastomer and the CFRP layers only function as a constraining layer.

6. Summary

Modal analysis on hybrid fiber metal elastomer laminates have been performed to characterize the vibration and damping behavior. A cantilever setup was chosen where the specimens were excited contactless via electromagnetic forces at the free end. The vibration was measured contactless using a scanning laser-Doppler vibrometer. The experimental results were compared with an analytical and a numerical model. The experimental results showed that the damping of specimens containing the elastomer layers strongly depends on the mode shape, with increasing modal damping values for the investigated frequency range. This is caused by the higher shear deformations in the elastomer layers for shorter wavelengths of the mode shapes. Also the storage modulus decreases with decreasing wavelength of the mode shapes. This behaviour was much less pronounced for a reference specimen without elastomer layer. The analytical and numerical model could also depict the damping and vibration behavior well. However, the CFRP was assumed too stiff in the numerical approach, which results in a higher storage modulus especially when the elastomer layers are thin or not existing. As the damping of the fiber metal elastomer laminates is mostly influenced by the elastomer layers, the damping behavior of the lay-ups with elastomer can be modelled well with both models.

Acknowledgement

The research of this paper is kindly supported by the Deutsche Forschungsgesellschaft (DFG). It is part of project: „HyCEML - Hybride CFK/ Elastomer/ Metall-Laminate mit Elastomerschichten für die gezielte Einstellung des Dämpfungsverhaltens“ WE 4273/16-1 and KA 4224/3-1 under the priority program SPP 1897. The authors kindly acknowledge the Gummiwerk Kraiburg as part of the Kraiburg Holding GmbH & Co. KG for providing the elastomers.

References

- [1] R. Alderliesten, *Fatigue and fracture of fibre metal laminates*, Springer, Cham, **2017**.
- [2] M. Stoll, *Behavior of Fiber-Metal-Elastomer-Hybrid-Laminates*. Dissertation, Karlsruhe, **2018**.
- [3] D. Ross, E.E. Ungar, E.M. Kerwin, in *Structural Damping*, (Ed.: Ruzicka, Jerome, E.), New York, **1959**, pp. 49–87.
- [4] J. Fujimoto, T. Tamura, K. Todome, T. Tanimoto, *Journal of Reinforced Plastics and Composites* **1993**, *12*, 738–751.
- [5] F.-S. Liao, T.-C.J. Hsu, A.C. Su, *J. Appl. Polym. Sci.* **1993**, *48*, 1801–1809.
- [6] F.-S. Liao, A.-C. Su, T.-C.J. Hsu, *Journal of Composite Materials* **1994**, *28*, 1840–1854.
- [7] M.D. Rao, H. Shulin, *AIAA Journal* **1993**, *31*, 736–745.
- [8] ASTM, **2010** „E756-05, ASTM International, West Conshohocken, PA (2010).
- [9] V. Sessner, A. Jackstadt, W. Liebig, L. Kärger, K. Weidenmann, *J. Compos. Sci.* **2019**, *3*, 3.
- [10] Hexcel Corporation, *HexPly® M77/38%/UD150/CHS-12K T700 Datasheet*, **2014**.
- [11] M. Stoll, V. Sessner, M. Kramar, J. Technau, K.A. Weidenmann, *Composite Structures* **2019**, *219*, 90–96.
- [12] A.D. Nashif, D.I.G. Jones, J.P. Henderson, *Vibration damping*, Wiley, New York, **1985**.

Evaluation of surface modified aluminium/polyamide-6 fibre-metal laminates

F. Thum¹, A. Monden¹, M.G.R. Sause¹

¹ Institute of Materials Resource Management, University of Augsburg, Augsburg

Abstract:

The aim of this study was to investigate the bond strength between thermoplastic carbon fibre reinforced polymers (CFRP) and aluminium alloys with different surface modifications. The materials examined were sandwich laminates consisting of unidirectional carbon fibre reinforced polyamide-6 composites and two different types of aluminium alloys. The configuration chosen for studying the interfacial adhesion is symmetrical with one 0.3 mm thick aluminium foil at the neutral axis of the stack. Various surface modifications like laser structuring, diamond-like carbon (DLC) coating, corundum blasting and different chemical treatments were applied to the aluminium layer. In addition, polyamide-6 interlayers with and without glass-fibres were investigated as an electrochemically insulating layer between aluminium and carbon fibres. The specimens were evaluated using a short beam 3-point bending test to determine the apparent interlaminar shear strength (ILSS). For this purpose, three groups of specimens were stored under standard climate, in a vacuum oven and in hot/wet conditioning for one week, respectively. In addition, potentiodynamic corrosion measurements were performed on the aluminium alloys to evaluate the electrochemical barrier resulting from surface treatments and interlayers. It was observed that 1050 aluminium alloy performed better than 2014 alloy in this aspect. Compared to the configurations without an additional interlayer, interlayers with glass fibre insulation exhibited slightly lower ILSS values with mainly cohesive interfacial failure.

1 Introduction

Due to their specific mechanical properties, Fibre-Metal-Laminates (FML) are increasingly gaining importance with the growing demand for lightweight materials. Compared to conventional fibre reinforced polymers (FRP), the combination of metal and FRP leads to advantages like superior bearing strength, fatigue resistance, transverse fracture toughness and impact resistance [1]. There are different well-established examples for commercial FMLs, like GLARE® ([2], [3]) which is made of glass fibre/epoxy reinforced aluminium alloy or ARALL® [4] (aramid fibre/epoxy reinforced aluminium laminates). We replaced the glass/aramid-fibres with carbon-fibres, expecting to yield higher strength and stiffness. In addition, instead of a thermoset matrix, a thermoplastic polyamide-6 (PA6) matrix was used. This leads to advantages regarding production time and costs. Further, this offers the possibility of thermoforming semi-finished products. However, these modifications result in new challenges regarding the risk of contact corrosion as well as adhesion promotion between aluminium and PA6. Therefore, we studied surface treatments to increase adhesion, protective layers of a polymer (e.g. PA6) or glass-fibre reinforced polymers to prevent contact corrosion. To demonstrate the influence of the surface modifications used in this study, a short-beam shear (SBS) test was chosen to determine the apparent interlaminar shear strength (ILSS) following the conceptual work in [5]. For the evaluation of the electrochemical barrier, potentiodynamic corrosion measurements were conducted on a shortlist of material combinations after the SBS testing.

2 Experimental

2.1 Specimen design and preparation

For the experimental investigations, sandwich plates were produced using a symmetrical layup of eight layers of SIGRAPREG TP C U157-0/NF-T340/46% with a PA6 matrix on two sides of an aluminium foil with a thickness of 0.3 mm. The specimens for the SBS testing procedure of 20 x 10 mm were cut from plates of 100 x 100 mm using a wet cutting table saw. All samples were immediately dried to avoid any water absorption. Due to the different interlayer materials, the resulting thickness ranged from 2.8 – 3.3 mm as shown in Figure 1.

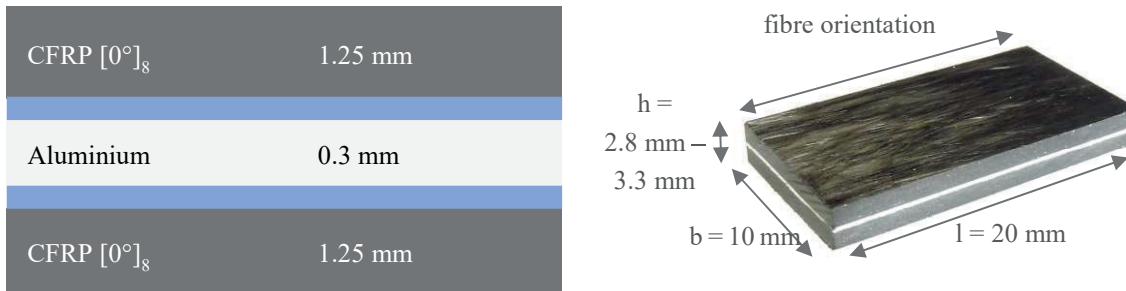


Figure 1: Stacking sequence of the FMLs (left) with schematic interlayers (blue) and specimen dimensions for SBS testing

In this paper, eight combinations of different alloys, surface treatments and interlayers are presented (cf. Table 1). As aluminium alloys, Al 1050A was chosen due to its electrical and mechanical properties and Al 2024 T3 as it is a widely used standard alloy in the aviation industry with good mechanical properties [3].

Laser treatment was used to prepare the metal surfaces for adhesive bonding as well as to clean potentially remaining impurities on the aluminium layer after the cleaning process. The increased surface area and modified topology leads to better mechanical interlocking and increases intermolecular bonding [6]. As a second surface treatment, a silane coupling agent was applied to the aluminium surfaces. On the oxide-surface of the aluminium, the silanes form a layer through covalent bonds [7]. The contact to the CFRP layer (or polymeric interlayer respectively) is improved via chemical bonds which connect to the thermoplastic matrix. The potential difference between aluminium and carbon fibres may lead to galvanic corrosion in case there is direct contact between these materials. To minimize the risk of corrosion, interlayers of PA6 and glass-fibres (GF) with PA6 matrix were added in some cases. As reference, two plates without any surface treatment or interlayers were produced.

Table 1: Configurations of tested FMLs

No.	1	2	3	4	5	6	7	8
Alloy			Al 1050				Al 2024	
Surface treatment	No treatment	Laser treatment	Silane treatment	Silane treatment	Silane treatment	No treatment	Laser treatment	Silane treatment
Inter-layer	-	-	-	PA6	PA6 + GF	-	-	-

Before testing the specimens in SBS, three different conditioning environments were chosen to compare their influence on the FMLs. One part of the samples was conditioned in standard climate for

160 hours, another part was dried in a vacuum oven ($T = 80\text{ }^{\circ}\text{C}$, 160 hours), the third part was stored in a hot-wet environment ($T = 80\text{ }^{\circ}\text{C}$, 95 % humidity, 160 hours). In 3.1, we present the results of standard climate and hot-wet conditioning, as the ILSS values from vacuum drying are similar to the standard climate results.

2.2 Methods

2.2.1 Screening via short-beam tests

After conditioning for one week, the FML specimens were investigated via SBS tests following the principles of DIN EN 2563. Load is applied at the centre of the specimen with a given length l_v between the support which depends on the thickness of the investigated specimen (Figure 2). To evaluate the testing process, the interlaminar shear strength (ILSS) τ is calculated from the force at delamination onset P_R :

$$\tau = \frac{3P_R}{4bh} \quad (1)$$

The maximum shear stress is induced at the specimen's centre plane, where the aluminium layer is located. For thin aluminium layers the ILSS formula gives a reasonable approximation for the actual shear stress at the interfaces between aluminium and CFRP [8]. However, for this study, the calculated values are solely used for comparison between the material configurations, not as actual interlaminar shear strength values. For each configuration, five samples were tested.

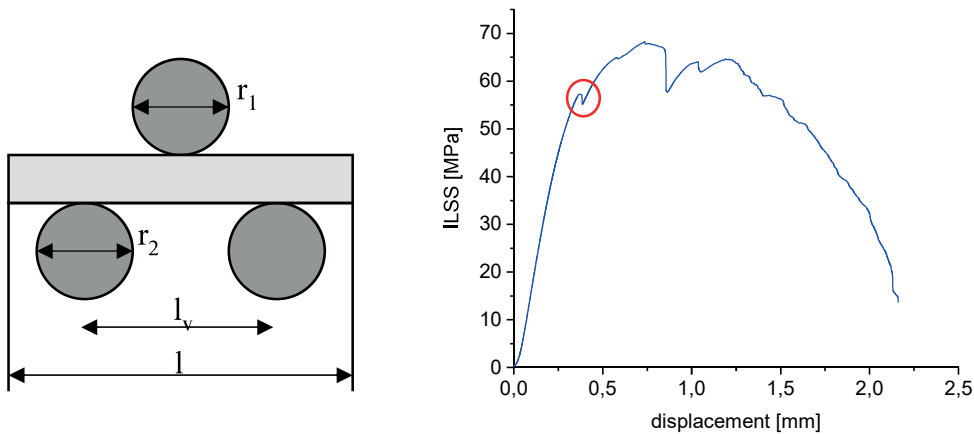


Figure 2: The short beam shear test is used for comparison of the ILSS values. The first signature within the stress-displacement curve (red circle) indicates the initial failure of the specimen and is used for further evaluation.

2.2.2 Corrosion measurements

The aluminium alloys and the surface modifications were investigated using potentiodynamic polarization. Samples were immersed in a sodium chloride solution ($c = 0.5\text{ mol/l}$) and a scan rate of 5 mV/s was chosen for the measurement using the *Interface 1000* by *Gamry Instruments*. As reference, a saturated Ag/AgCl electrode and as counter electrode a platinum wire was used. The aluminium samples were cut into $10 \times 10\text{ mm}$ pieces and cleaned before putting them into the

corrosion measuring setup (Figure 3). The electric current flows between the Platin counter electrode and the sample, which represents the working electrode. The polarization of the sample is varied in the range of -1.2 V to 0 V. For evaluation, the voltage is plotted against the logarithmic current as Evans diagram (Figure 5Figure 5).

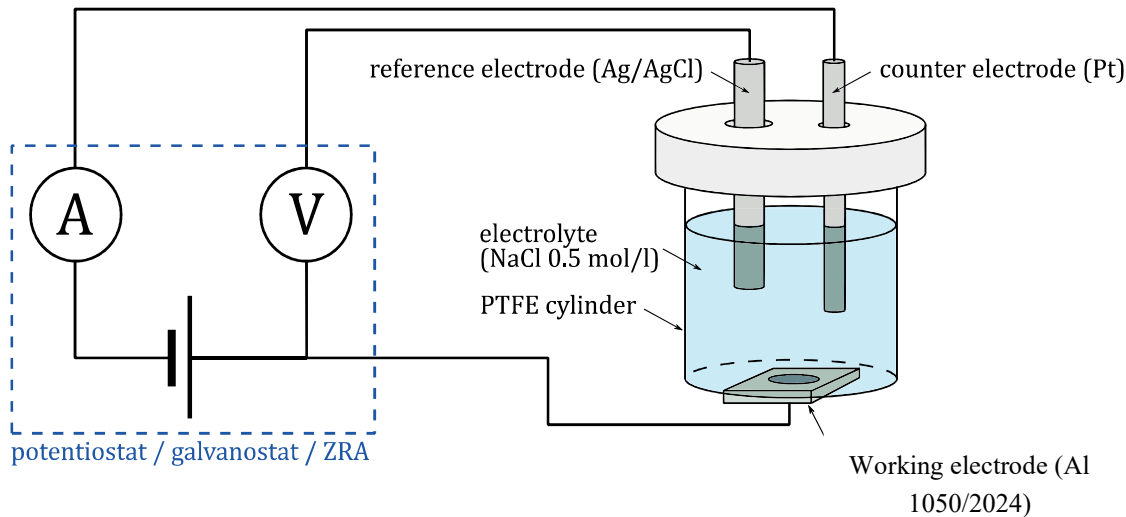


Figure 3: Schematic setup of the potentiodynamic corrosion measurement following [9]

3 Results

3.1 Short-beam shear test

After conditioning in a Hot/Wet climate chamber, the FML samples without any surface modification showed delamination at the interface to the aluminium layer and thus could not be tested. The SBS results presented in Figure 4 show the mean value of five samples for each configuration for the remaining six FMLs.

Two main failure mechanisms could be observed on the SBS samples after testing. For the configurations with silane and additional interlayers, the specimens showed mainly cohesive failure within the CFRP. The samples with laser treatment on the surface showed mainly adhesive failure. The laser treated samples show slightly lower ILSS values when compared to silane treated samples (without additional interlayers). This proves an increased delamination resistance for silane treatment which was also observed in earlier studies with steel/epoxy-based CFRP hybrid laminates [5], [8]. The ILSS values of Al 2024 based configurations consistently lie below the Al 1050 values, especially after Hot/Wet conditioning. This result is corresponding to the better galvanic corrosion resistance of Al 1050.

Despite the use of unreinforced PA6 and GF with lower mechanical properties compared to PA6 based CFRP, these samples in the SBS configuration performed almost as good as the FMLs without additional layers regarding their ILSS values and thus delamination resistance.

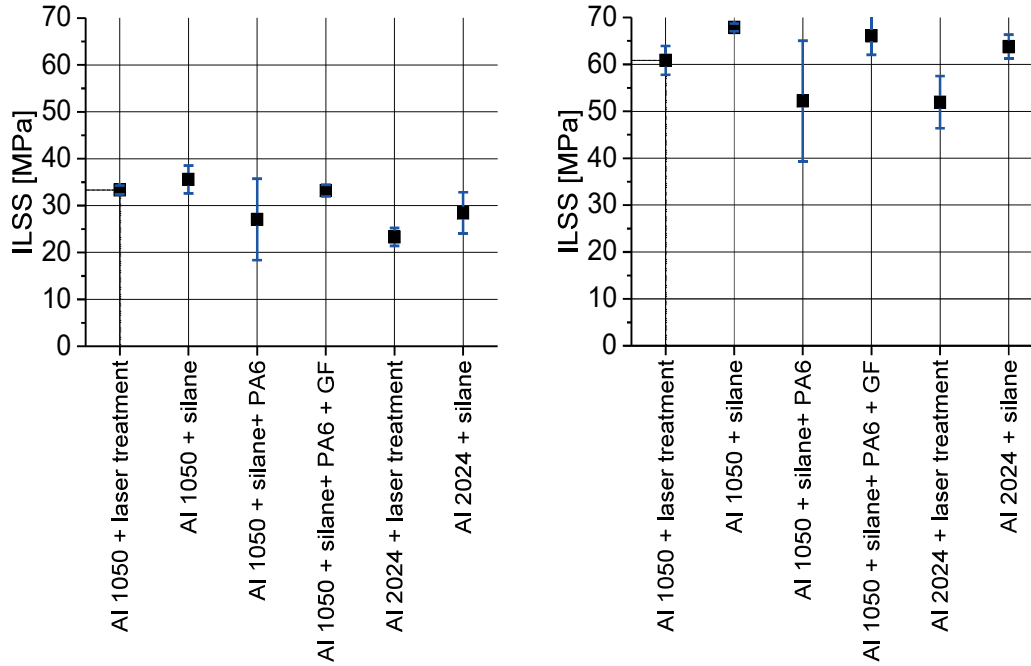


Figure 4: ILSS values obtained with SBS tests after standard climate conditioning (left) and after Hot/Wet conditioning (right). Five Samples were tested for each configuration.

3.2 Corrosion measurements

Based on the SBS test results, a subset of configurations was examined via potentiodynamic corrosion measurements. Al 2024 was solely used as a reference in two different configurations. The results of the potentiodynamic corrosion measurements of three surface configurations as well as the bare Al 1050 and Al 2024 samples are shown in an Evans diagram (Figure 5), showing the voltage plotted against the logarithmic current. The corrosion potential E_{corr} and corrosion current I_{corr} of all configurations are summarized in Table 2.

The polarization curves in Figure 5 show a slight decrease of electrical current for the silane treated Al 2024 specimen throughout the curve while the laser treated Al 1050 specimen stays at almost the same level. However, the E_{corr} values are in the same region for both alloys as well as the surface treatments. Only the specimen with PA6 interlayers show a clear indication for improved corrosion resistance. Here, the current decreases by several orders of magnitude and E_{corr} is significantly below the levels of non-treated aluminium samples as well as the ones with surface treatments only.

Table 2: Overview of the extracted corrosion parameters E_{corr} and I_{corr}

FML	Al 1050	Al 1050 + laser treatment	Al 1050 + silane treatment	Al 1050 + silane treatment + PA6	Al 1050 + silane treatment + PA6 + GF	Al 2024	Al 2024 + silane treatment
E_{corr}	-0.85	-0.86	-0.8	-0.53	-0.58	-0.79	-0.8
I_{corr}	1.36×10^{-8}	4.26×10^{-8}	8.17×10^{-9}	2.01×10^{-11}	1.35×10^{-11}	5.8×10^{-8}	2.26×10^{-8}

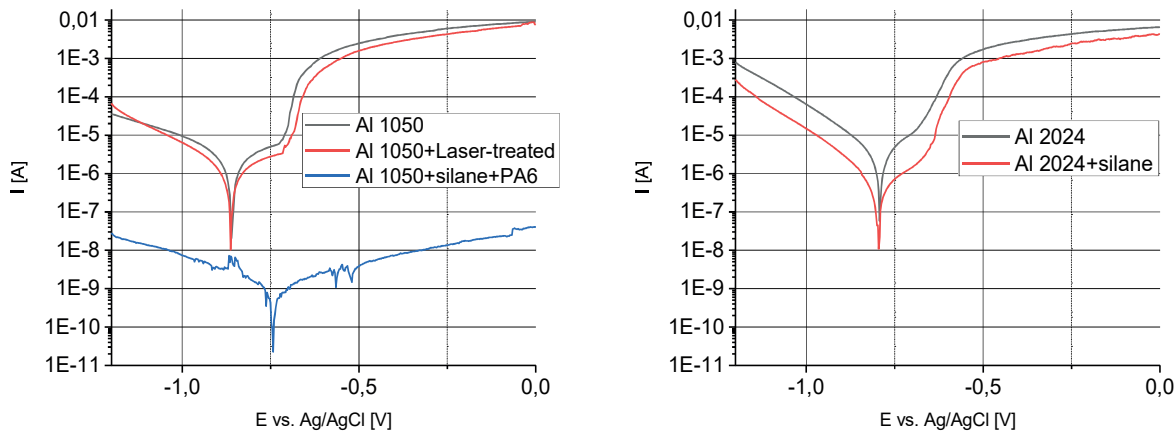


Figure 5: Evans diagrams showing the polarization curves for the differently pre-treated aluminium alloys

The E_{corr} values for Al 1050 with interlayers of PA6 and GFF are shifted to -0.53 V to -0.58 V compared to the samples without interlayers (surface treatment only), where E_{corr} is in the region of -0.8 V. In addition, the current rate is significantly below the other samples without interlayers. Therefore, the interlayers decrease the electrochemical potential difference between the carbon fibres and the metal core, which allows to expect a reduced corrosion rate.

4 Conclusions

Eight FML configurations were prepared and conditioned for SBS testing. Furthermore, promising combinations especially with Al 1050 were investigated with a potentiodynamic corrosion testing method.

The surface treatment of both Al 1050 and Al 2024 leads to significantly better performance regarding the interfacial adhesion, which was evaluated using SBS tests to determine ILSS values. In direct comparison, the Al 1050 FMLs show increased adhesion, especially after conditioning the samples in a Hot/Wet environment. FMLs with additional interlayers perform mechanically slightly worse than the ones without interlayers. However, the E_{corr} values for these samples show good corrosion resistance after potentiodynamic measurement. To investigate the corrosion resistance furthermore, a long term Hot/Wet ageing has been started.

5 Acknowledgement

The authors would like to thank Fabian Schubert from SGL Carbon for providing the Institute of Materials Resource Management with the Fibre Metal Laminates investigated in this study. The authors would like to thank the Bavarian State Ministry of Economic Affairs and Media, Energy and Technology (StMWi) for its financial support within the framework of Campus Carbon 4.0. Further thanks go to the project management organization Jülich (PtJ) and the MAI Carbon cluster management for their support in the project implementation of MAI CC4 Hybrid.

6 References

- [1] E.C. Botelho, R.A. Silva, L.C. Pardini, M.C. Rezende, A Review on the Development and Properties of Continuous Fiber/epoxy/aluminum Hybrid Composites for Aircraft Structures, *Mat. Res.* 9 (2006) 247– 256.
- [2] Vogelsang, L.B., Vlot, A. Development of fiber metal laminates for advanced aerospace structures. *Journal of Materials Processing Technology* 103 (2000) 1-5
- [3] Vlot, A.: Historical overview, In: Vlot, A. (Hrsg.), Gunnink, J. W. (Hrsg.): *Fibre metal laminates / an introduction*, Verlag Springer Netherlands, 2001, S. 3-21
- [4] Vermeeren, C. A. J. R., Beumler T., de Kanter, J. L. C. G., et al.: *Glare Design Aspects and Philosophies*, *Applied Composite Materials*, 10(4/5):257–276, 2003.
- [5] Monden A.: *Adhäsion zwischen epoxidharzbasiertem CFK und oberflächenmodifiziertem Stahl: Grenz-schichtversagen von Hybridlaminaten unter Mode I, Mode II und Mixed-Mode Belastung*. PhD thesis, University of Augsburg, 2016.
- [6] Peng Z., Nie X.: Galvanic corrosion property of contacts between carbon fiber cloth materials and typical metal alloys in an aggressive environment. *Surface and Coatings Technology*, 215(0):85–89, 2013.
- [7] Critchlow G. W., Yendall K. A., Bahrani D., Quinn A., Andrews F.: *Strategies for the re-placement of chromic acid anodizing for the structural bonding of aluminium alloys*. *International Journal of Adhesion and Adhesives* 26(6):419-453, 2006
- [8] Monden A., Sause M.G.R., Hartwig A., Hammerl C., Karl H., Horn S.: *Evaluation of Surface modified CFRP-Metal Hybrid Laminates*. In: *Proceedings of Euro Hybrid Materials and Structures 2014*, 2014.
- [9] Hartwig A.: *Titandioxid als Korrosionsschutz von X5CrNi18-10 Edelstahl und dessen Einsatz-möglichkeit in CFK-Metall Hybridstrukturen*. PhD thesis, University of Augsburg, 2015.

Mechanical Properties of In-Situ Polymerized Fiber-Metal-Laminates

H. O. Werner^{1,2}, W. Liebig¹, K. A. Weidenmann³

¹Karlsruhe Institute of Technology, Institute for Applied Materials, Karlsruhe, Germany

²Karlsruhe Institute of Technology, Institute of Vehicle System Technology, Karlsruhe, Germany

³University of Augsburg, Institute of Materials Resource Management, Augsburg, Germany

Abstract

This paper deals with a new manufacturing process for fiber-metal-laminates (FML). This is the wet-compression molding. Two fiber volume contents are manufactured and specimens are tested in tensile tests. The FML discussed here consists of 1 mm DC04 metal sheets and a varying number of E-glass fiber interlayers. It is found, that the Young's modulus and the yield strength are dominated by the metal sheet and the ultimate tensile strength by the fiber volume content of the glass fiber reinforced plastic (GFRP).

1 Introduction

New materials and lightweight construction strategies are needed in the course of electrifying the drive train of automobiles. Especially the crash safety of the accumulator box is a major challenge. Fiber-metal-laminates (FML) have high-energy absorption and shield sensitive components from electromagnetic radiation through their integrated metal layers in a very compact package. Traditional FML developed for the aviation industry are restricted in the forming process and thus in the producible geometries. The low elongation to fracture of fibers like E-glass or carbon fiber allow only small strains and thus big radii of curvature. Forming metal sheets into complex two-dimensional curved geometries requires high forming forces, which are not realizable in the traditional FML production process in an autoclave [1-3]. On the other hand, the recyclability of lightweight composites and FML is an increasingly important topic. Traditional FMLs are manufactured with a thermoset resin system.

For these reasons, an FML with a reactive thermoplastic matrix was developed, which can also be manufactured in complex shapes [4]. The here discussed FML consists of 1 mm DC04 metal sheets and a varying number of glass fiber interlayers. Mechanical properties of plates are tested by tensile tests and are used as references for the formed FML properties.

2 Experimental

2.1 Material and manufacturing process

The FML layup is a sandwich construction with metal sheets as face sheets and thermoplastic reinforced woven fabrics as intermediate layer. The DC04 metal sheet thickness is 1 mm. The amount of

Table 1. Overview of different interpenetrating ceramic metal composites of alumina and aluminum alloys from literature.

ceramic phase manufacturing method	ceramic content	pore size	type of metal	residual porosity	compression strength	strain rate	elongation at compression strength/break	publication
[-]	[%]	[μm]	[-]	[%]	[MPa]	[-]	[%]	[-]
freeze casting / pore former	35 - 40	NSF	AlSi12	NSF	500 – 900	NSF	0,01 - 10	[10]
freeze casting	43 \pm 2	NSF	AlSi12	NSF	270 - ca. 700**	10 ⁻³ 1/s	2,5 - 10	[11]
pyrolisable placeholder	24,3	NSF	AlSi12	NSF	277*	NSF	NSF	[12]
pyrolisable placeholder	29,5	NSF	AlSi12	NSF	301,5*	NSF	NSF	[12]
hollow alumina particle	NSF	NSF	AlSi7Mg0,3	NSF	up to 275	10 ⁻³ 1/s	NSF	[13]
replica technique	30,57	300 - 450	AlSi12CuMgNi	0,57	341	NSF	ca. 4	[14]
replica technique	28,52	450 - 550	AlSi12CuMgNi	1,6	317	NSF	ca. 4	[14]
replica technique	25,58	800 - 1000	AlSi12CuMgNi	1,44	294	NSF	ca. 4	[14]
gelcasting of foams	10	500	AlMg5	<1	320	NSF	0,09	[15]

NSF = Not specified

* Tensile, no compression values available

** lowest value for 34 ° angle to freeze direction, highest value in freezing direction tested

3 Experimental/ Materials and Methods

For the experiments, a macroscopic homogeneously and highly porous open-cell alumina ceramic foam, with an approximate relative density of 25 %, provided by Morgan Advanced Materials Haldenwanger GmbH, Waldkraiburg, Germany is used, who hold a patent on the low-cost manufacturing technique [16]. An interpenetrating metal ceramic composite is produced via gas pressure infiltration based on the ceramic foam and an AlSi10Mg aluminum alloy, as described by the authors [9]. The materials were cut into cubic samples of ca. 5 x 5 x 5 mm³ and the sample surface was grinded stepwise with silicon carbide paper up to grain size P800, with water as coolant. For in-situ microscopy one cube-surface also was polished with diamond suspensions (9, 3 and 1 μm) and OP-S-Suspension, each manufactured by Struers, Friedberg, Germany.

Compression tests were carried out with a universal testing machine of type 1464, with a load cell xforceK up to 50 kN, each of Zwick&Roell, Ulm, Germany. Interchangeable compression stamps with plane turned and then polished end faces (SiC grinding paper with grain size up to P4000 and water as coolant) were made of hardened machine screws of grade 12.9 with tensile strength of 1200 N/mm² and a yield strength of 1050 N/mm². Molybdenum sulfide (OKS Spezienschmierstoffe GmbH, Munich, Germany) was used as a solid lubricant between the sample and the stamps in accordance to DIN 50106 [17]. A preload of 20 N was applied onto the sample, before the data logging started. The strain rate during the compression tests was set to 10⁻³ 1/s. Abort criterions for the experiments were set for a minimum stamp distance of 3 mm and a drop in maximum force of 80 %. Three samples were tested with the in-situ testing. Therefore, load steps were integrated into the compression test procedure at stresses of 250, 300, 340, 360 and 380 MPa for the composite.

For optical elongation determination the ARAMIS Adjustable System with two 12 Megapixel cameras by GOM, Braunschweig, Germany was used. For the specific setup, lenses with a focal

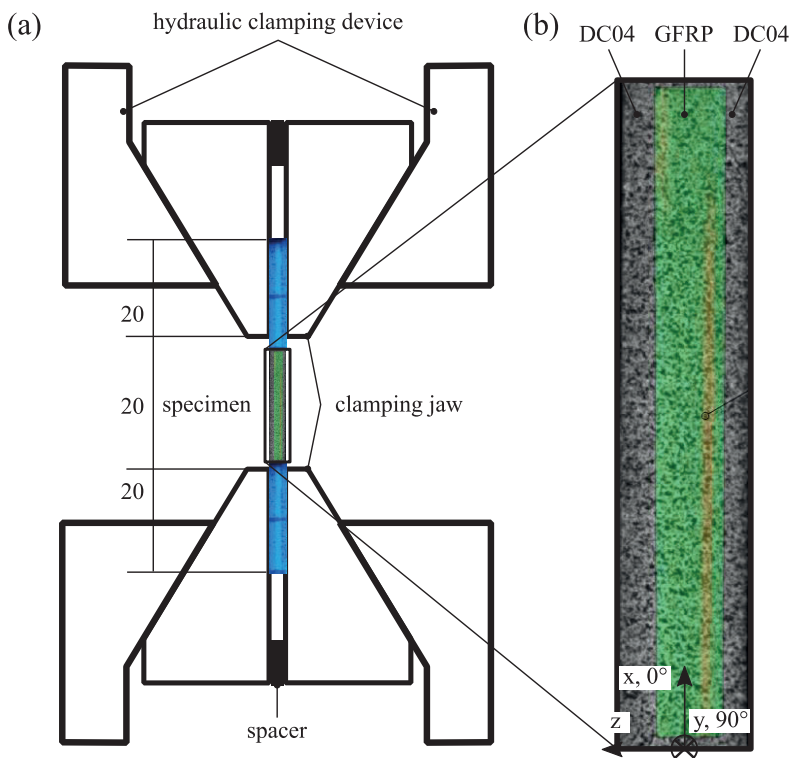


Figure 2: (a) Tensile test set-up with strain measuring in stacking direction. (b) Specimen with speckled pattern and measured strain field.

3 Results

The specimens with 0° and 90° orientation hardly differ in their deformation behavior. The 90° specimens have a slightly lower ultimate tensile strength. The deformation behavior of the $\pm 45^\circ$ oriented specimens show a significantly higher elongation at fracture (\sim factor 8). The Young's modulus E within a plate is independent of the fiber orientation. The modulus of elasticity increases with the FVC. The yield strength $R_{p0.05}$ shows no fiber orientation dependence within a plate. The yield strength increases with increasing FVC. The ultimate tensile strength R_m is strongly dependent on the FVC and the fiber orientation. The wet-compression plate with a FVC of 26 % shows a weak dependence on the fiber orientation.

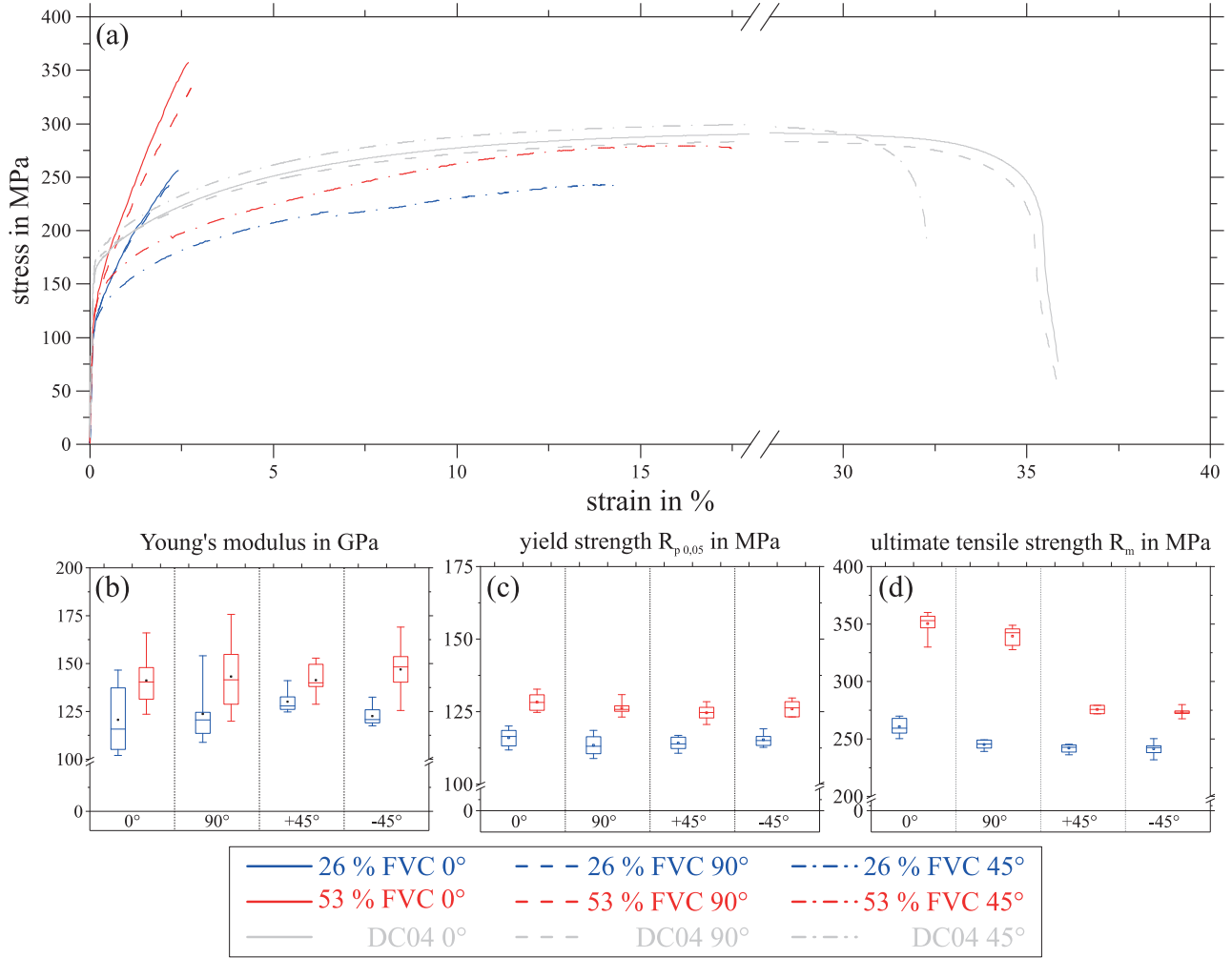


Figure 3: Tensile test results of FML and DC04 specimens with 0°, 90° and ±45° orientation. (a) Representative stress-strain diagram. (b) Box plot of Young's modulus. (c) Box plot of yield strength. (d) Box plot of ultimate tensile strength.

4 Discussion

The ultimate tensile strength decreases for 90° specimens compared to 0° specimens, because the fabric weight is 143 g/m² in the 0° direction and only 133 g/m² in the 90° orientation, which means that the fiber volume content (FVC) is slightly lower. The ratio between the fabric weight in 90° and 0° orientation is 133/143 = 0.93 and can also be found in Table 1, if one compares the ultimate tensile strength of 90° and 0° orientation. As stated before, the slight roving anisotropy has no influence on the Young's modulus and the yield strength. The Young's modulus of the FML is dominated by the metal sheet's high Young's modulus ($E_{DC04}/E_{GFRP} \approx 9$) and the higher volume content of the metal ($2t_{DC04}/t_{GFRP} = 2$). The effective layer stiffness can be expressed as spring stiffness c by

$$c = \frac{EA}{L} \rightarrow c_{FML} = 2c_{DC04} + c_{GFRP} \quad (1)$$

where E is the Young's modulus, A the cross-sectional area and L the length of the respective layer. For the FMLs stiffness, a parallel arrangement of springs can be assumed. The stiffness distribution between the layers determines the load distribution between the layers. Which can be calculated by

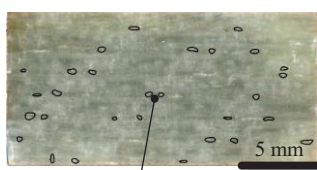
$$\frac{2C_{DC04}}{C_{GFRP}} = \frac{E_{DC04}t_{DC04}}{E_{GFRP}t_{GFRP}} \approx 18. \quad (2)$$

The stiffness distribution and thus, the load distribution determine the yield strength of the FML. In this study, all specimens show comparable yield strengths, because the local yield strength of the metal sheet is reached. The metal starts to flow and the effective stiffness of the FML decreases for which reason the load is transferred from the metal sheet to the GFRP by shear stresses. When the FVC of the GFRP layer increases, also the stiffness is increasing, which influences the load distribution between the layers and yields to higher FML yield strengths. While the total outer load is constant, the inner load on the metal sheets is decreasing and the flow stress of the metal sheets is not reached. After the load transition point (yield strength R_p), the GFRP layer dominates the deformation behavior and ultimate tensile strength. Specimens with a 0° and 90° orientation have higher Young's moduli and ultimate tensile strength due to more fibers in loading direction, which leads to lower elongations at fracture. The fibers in specimens with $\pm 45^\circ$ orientation drape under load and reach therefore higher elongations at fracture.

Table 1. Ratio of mechanical properties related to the 0° property of each plate calculated from the mean values.

	FVC	$90^\circ/0^\circ$	$+45^\circ/0^\circ$	$-45^\circ/0^\circ$
ratio of Young's modulus E	26 %	1.03	1.08	1.02
	53 %	1.01	1.00	1.04
ratio of yield strength $R_{p0.05}$	26 %	0.98	0.98	0.99
	53 %	0.98	0.97	0.98
ratio of ultimate tensile strength R_m	26 %	0.94	0.93	0.93
	53 %	0.97	0.79	0.78

The stated effect of stiffness and load distribution does not explain the differences between the mechanical properties of the wet-compression plate with 53 % FVC compared to the plate with 26 % FVC. In addition, it does not explicate the low orientation dependence of the wet-compression plate with 26 % FVC. One can see voids in the interface between the metal sheet and the GFRP of the wet-compression specimen in Figure 4.



voids in interface

Figure 4: Interface between metal sheet and GFRP.

The voids reduce the actual cross-section and lead to stress rearrangements due to notch effects. Infiltration of FML by the wet-compression molding process causes the voids. The polymer mixture flows first in-plane between the metal sheet and the upper fabric ply, when the upper mold gets into contact with the upper metal sheet. Interface in-plane flow resistance is low in contrast to the flow resistance in thickness direction of the fabric ply stack. When the pressure resulting from the closing mold is increasing, the fabric plies are infiltrated in thickness direction. The air gets trapped between the metal sheets, because the metal is not permeable to air. This results in many macroscopic voids in the interface between the metal sheet and the GFRP, as shown in Figure 4. The interface is of special interest for a hybrid material like a FML. The load transfer between the metal layers and the

GFRP is realized by shear stresses in the interface. The voids reduce thereby the load transferring capability of the FML and lead probably to earlier damage in the interface and delaminations.

5 Conclusion and outlook

In this paper, FMLs manufactured by the wet-compression molding process are tested in tensile tests. It could be shown, that the manufacturing process influences the mechanical properties mainly in the orientation dependence of the ultimate tensile strength by voids in the interface of metal and GFRP. The metal sheets and the metal volume content dominate the FMLs elastic properties. While the ultimate tensile strength is dominated by the FVC of the GFRP.

To further improve the mechanical properties of FML, several parameters of the wet-compression molding process can be optimized. For example with a slower closing profile of the press to give the air more time to escape from the mold. Instead of infiltrating from top to bottom, one could infiltrate from bottom to top by stacking the dry fabric plies on top of the polymer mixture. Therefore, a slow reacting matrix is needed, because the time in the heated mold increases before the mold is closed.

In general, to improve the mechanical properties of FML, a metal with a high yield strength should be chosen and the effective stiffness of the layers should be as close as possible to each other to get an even load distribution in the layers.

6 Acknowledgement

The German Research Foundation (DFG) kindly supports this research project (WE 4273/13-1, WE 4273/13-2). The Fraunhofer Institute for Chemical Technology kindly supports the manufacturing of the laminates. ARKEMA S.A. Colombes (France) kindly provided the polymer. United Initiators provided the peroxide and Evonik the coupling agent. The authors also thank their colleges for support.

7 References

- [1] A. Vlot, J.W. Gunnink, *Fibre Metal Laminates: An Introduction*. Dordrecht: Springer Netherlands; **2001**.
- [2] E.C. Botelho, R.A. Silva, L.C. Pardini, M.C. Rezende, A review on the development and properties of continuous fiber/epoxy/aluminum hybrid composites for aircraft structures. *Mat. Res.* **2006**, 9(3):247–56.
- [3] J. Sinke, Manufacturing of GLARE Parts and Structures. *Applied Composite Materials* **2003**, 10(4/5):293–305.
- [4] T. Mennecart, H. Werner, N. B. Khalifa, K. A. Weidenmann, in *Proceedings of the 13th Manufacturing Science and Engineering Conference (MSEC2018), June 18-22, 2018, College Station, Texas, USA*.
- [5] H. Werner, I. Sönmez, R. Wendel, F. Henning, K.A. Weidenmann, in *Proceedings of SAMPE Europe Conference 2017, Stuttgart, Germany, 2017*.

Influence of surface treatment on interfacial strength and tensile properties of thermoplastic based hybrid laminates

M. Trautmann¹, S. Mrzljak², F. Walther², G. Wagner¹,

¹ Chemnitz University of Technology, Institute of Material Science and Engineering (IWW), Group of Composites and Material Compounds, Chemnitz, Germany

² TU Dortmund University, Department of Materials Test Engineering (WPT), Dortmund, Germany

1 Introduction

A combination of thin metallic sheets and fibre-reinforced plastic layers called hybrid laminates (HL) can be used to design lightweight structures with an improved damage tolerance compared to pure polymer matrix composites and at the same time, these materials have a longer service life than the monolithic metal component. This advantageous combination has led to their increasing use in aircraft construction for GLARE, a layered compound of the aluminium alloy AA2024-T4 and continuous fibre-reinforced epoxy matrix [1].

In recent years, the focus of scientific studies has increasingly shifted to hybrid laminates based on fibre-reinforced composites with thermoplastic matrix such as polypropylene (PP) [2], polyamide 6 (PA 6) [3] or thermoplastic polyurethane (TPU) [4]. These compounds show advantages with regard to processability [5,6] and dynamic properties [7]. Hybrid laminates with thermoplastic matrix can be consolidated and formed in a hot pressing process [6,8]. In contrast to thermoset-based hybrid laminates produced in an autoclave process, thermoplastic-based hybrid laminates are suitable for a wide variety of continuous large-scale production and enable the large-scale use of hybrid laminates in the automotive and aviation industries.

An essential aspect of the material combination is the suitable adhesion between the fibre-reinforced plastic and the aluminium alloy. It can be assumed that the adhesion of the materials can be strongly influenced by the surface treatment of the aluminium component. One possibility to determine the shear strength is the examination of thermally joined single lap samples, which are easy to produce but do not reflect the real manufacturing process of hybrid laminates. A maximum shear strength of 18 MPa on the combination of AA6082 and glass fibre-reinforced PA 6 was determined with a plasma electrolytic anodic oxidation of the surface [9].

Another test method to measure the interlaminar properties of hybrid laminates with ductile components is by means of short bending tests according to DIN EN ISO 14130. This test configuration often leads to a plastic deformation of the ductile top layer or a shear failure that takes place in the FRP, which does not allow any statement about the interface. Therefore, in this study a double notched sample in accordance to the ASTM D3846-08 was utilised to measure the shear strength between a surface treated aluminium alloy and fibre-reinforced polyamide 6. In [10], the method was successfully applied to measure interlaminar shear properties between surface treated aluminium alloy sheets and the matrix of glass fibre reinforced epoxy. The authors display results between 20 and 70 MPa and found that a nanoscale sculpturing realised by an etching process increases the interlaminar properties significantly.

2 Experimental

2.1 Materials and manufacturing

The investigated hybrid laminate based on CAPAAL – a layered material compound that consists of surface treated aluminium alloy sheets AA6082-T4 with a thickness of 0.5 mm and layers of unidirectional fibre-reinforced plastics (FRP). The FRP-layer is build up of multiple layers of CePreg (Cetex Institut gGmbH, Germany) – a continuously produced unidirectional glass (GF-PA 6) and carbon (CF-PA 6) fibre-reinforced polyamide 6 with a calculated fibre volume fraction of 0.5. To compensate the mismatch in the coefficient of thermal expansion between the aluminium alloy and the CF-PA 6 an additional foil of PA 6 with a thickness of 40 μm and a layer of GF-PA 6 is added.

The surface of the aluminium alloy AA6082-T4 was modified using five different treatments:

I) Mechanical blasting: The sheets were blasted manually with a pressure of 1 bar on both sides by using high-grade Al_2O_3 with a grain size F24 (600-850 μm) in a working distance of 100 mm. The blasting material is applied at an angle of 90° to the surface.

II) Anodising: After a pre-treatment by etching the sheets in 10% sodium hydroxide and subsequent pickling, a 15 μm thick layer of Al_2O_3 is formed under direct current in sulphuric acid.

III) Phosphating: The phosphating was carried out using Bonderite[®] M-ZN process from Henkel. By dipping the sheets in a zinc phosphate solution, a conversion layer of small crystalline zinc-phosphatic mangan will be formed, which typically improves the adhesion of the lacquer.

IV) Adhesion promoter: After phosphating (see *III*) the co-polyamide VESTAMELT (Evonik Resource Efficiency GmbH, Germany) was applied evenly to the sheet as a powder by means of electrostatic spray coating and then melted in an oven at 200 $^\circ\text{C}$. This forms a uniform glassy adhesion film with an approx. thickness of 75 μm .

V) Etching: The alkaline chemical surface treatment is carried out by placing the sheets in 3% sodium hydroxide solution for 60 s.

The consolidation of the materials with a size of 260 x 260 mm^2 takes place in dip edged tool with a laboratory platen press Collin PM300. A maximum temperature of 295 $^\circ\text{C}$ is held for 24 minutes with a pressure of 1.5 MPa. As shown in Figure 1, a 2/1-configuration for tensile tests and a 1/2-configuration for measuring the interlaminar shear strength were pressed and cut in samples by water jet.

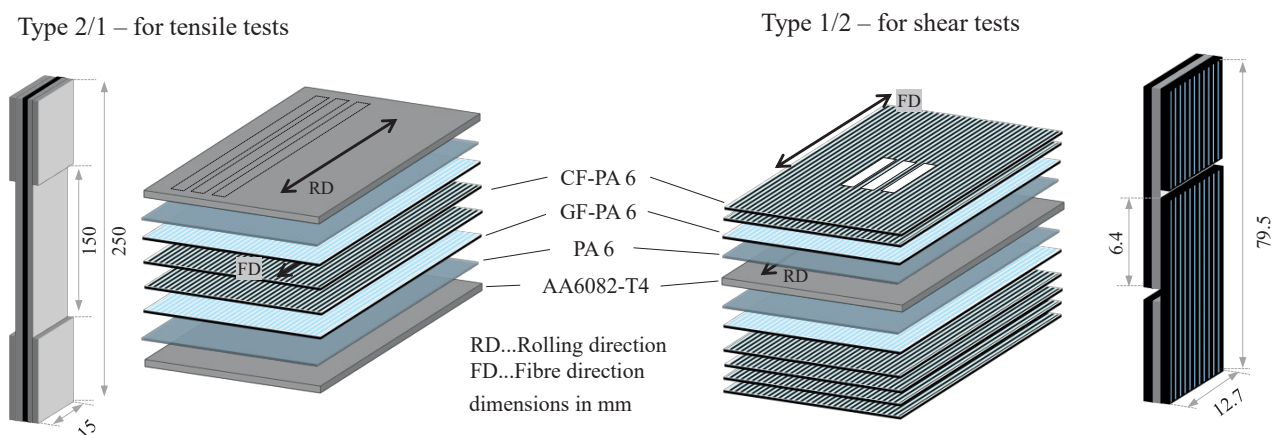


Figure 1: Hybrid laminates composed of aluminium alloy AA6082-T4 and a graded structure of glass- and carbon fibre-reinforced PA 6 in a 2/1-configuration for tensile tests and a 1/2-configuration to determine the interlaminar shear strength

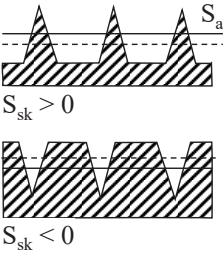
2.2 Methods

The surface roughness parameters like arithmetic mean deviation (S_a), root mean squared (S_q), and skewness (S_{sk}) of the treated aluminium sheets were carried out by Keyence VK X200 laser scanning microscope (LSM) in an area of $290 \times 200 \mu\text{m}^2$ with 10 analyzed lines of each sample. After the consolidation of the hybrid laminates, the thicknesses were examined on cross sections by light microscopy and scanning electron microscope Zeiss LEO 1455VP. The interlaminar shear strength was measured on the 1/2-configuration with double notched samples in geometrical accordance to ASTM D3846-08 as shown in Figure 1. In contrast to the standard, a tensile load was chosen instead of the proposed compression test, as otherwise the FRP will buckle. The mechanical properties were identified in tensile test on the 2/1-configuration in accordance to DIN EN 527-5 with water jet cut samples Type A (length: 250 mm, width: 15 mm). The gauge length is 150 mm. In the clamping area, on both sides an additional AA6082 sheet was added by epoxy glue. A minimum of three samples for each surface treatment were tested.

3 Results

The quantification of the surface roughness parameters by LSM shows that mechanical blasting and anodising process in particular can cause an increase of S_a and S_q compared to untreated aluminium sheet, whereas the other investigated processes do not cause any pronounced changes, Table 1. The increase in roughness is associated with an increase in the surface area and a formation of further bonding areas for the thermoplastic melt. The skewness describes the distribution of the height profile to the reference line. A positive value, as measured by phosphating, describes a profile determined by narrow peaks, which is caused by the grown crystals. In contrast the anodised surface is characterised by a slightly negative skewness.

Table 1. Roughness parameters of surface treated aluminium alloy AA6082-T4 measured by LSM transvers to the rolling direction

Surface treatment	Arithmetic mean S_a in μm	Root mean squared S_q in μm	Skewness S_{sk}	
Untreated	0.55 ± 0.12	0.66 ± 0.01	0.6 ± 0.1	
Mechanical blasting	5.74 ± 1.18	6.88 ± 1.13	-0.2 ± 0.4	
Anodising	2.13 ± 0.13	2.39 ± 0.10	-0.4 ± 0.1	
Phosphating	0.67 ± 0.15	0.95 ± 0.24	1.3 ± 0.8	
Adhesion promoter	0.49 ± 0.16	0.59 ± 0.18	0.5 ± 0.5	
Etching	0.70 ± 0.02	0.85 ± 0.02	0.9 ± 0.1	

The cross sections of hybrid laminates show a different material thickness by using identical pressing parameters, Figure 2 and Table 2. The rough surface of the blasted sheets leads to laminates with the highest thickness. In contrast the hybrid laminates with the anodised surfaces have a significant smaller thickness although the arithmetic mean roughness is higher than by phosphating, etching and adhesion promoter. In particular, the thickness of the CF-PA 6 layer is significantly less than that of the GF-PA 6 layer, which indicates that these layers are more strongly displaced from the laminate than the GF-PA 6 layers. The rheological behaviour of the thermoplastic melt during the consolidation process is influenced by the surface treatment, the fibres inside the FRP layer and the surface material. The results show that the alumina surface of the aluminium causes the strongest displacement of the thermoplastic material in the process. The material is pressed out through a gap between

dipping edge and tool cover plate. This also results in a strong change in the metal volume content, which in turn has an influence on the strength of the material compounds, see Table 2.

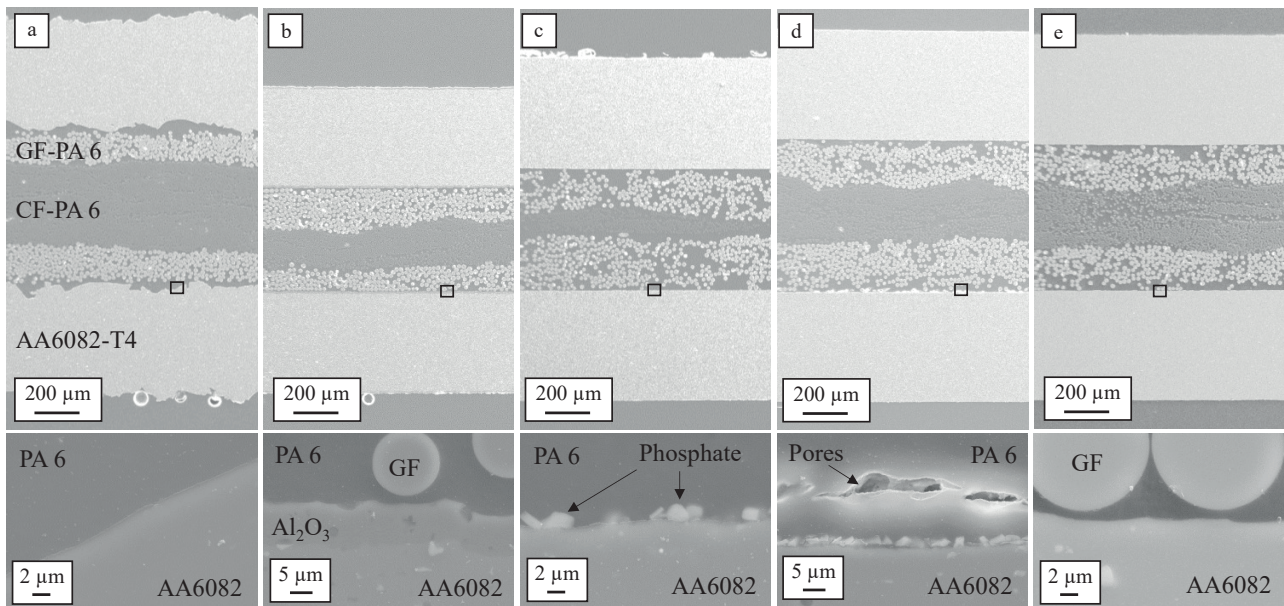


Figure 2: SEM cross sections of hybrid laminates with a mechanical blasted (a), anodised (b), phosphated (c), adhesion promoted (d) and etched (e) aluminium alloy AA6082-T4 and a graded structure of glass- and carbon fibre-reinforced PA 6 in a 2/1-configuration, below: detailed area of the interface

Detailed visual observations of the interface show a connection of the PA 6 without delamination for all variants, Figure 2 below. Especially with the mechanically blasted aluminium sheet a good mechanical interlocking can be achieved by undercut areas. Only in the interface with the adhesion promoter a pore seam between the GF-PA6 and the adhesion promoter is visible. Surfaces with a low surface roughness S_a , smaller $1 \mu\text{m}$ similar to the untreated rolling surface also show good adhesion to the PA 6. This implies that not only the microscopic form closure but also weak bonding forces between metal and FRP is responsible for the connection.

The cross sections show the unsteady position of the CF-PA 6 layer. By using the unidirectional orientation of all FRP tapes, small differences in the fibre distribution of the CePreg-material lead to displacement processes among each other in the viscous state during the pressing. A small change in the angle of the GF-PA 6 orientation leads to a significant improvement. The individual FRP layers form a uniform thickness, as fibres are restricted in their movement in the thickness direction.

Table 2. Geometrical results for cross-sections of hybrid laminates measured by ImageJ.

Surface treatment AA6082-T4	Thickness HL in mm	Thickness FRP mm	Metal volume ratio (MVR)
Mechanical blasting	1.67 ± 0.03	0.71 ± 0.03	0.57
Anodising	1.36 ± 0.01	0.46 ± 0.01	0.66
Phosphating	1.52 ± 0.01	0.54 ± 0.01	0.64
Adhesion promoter	1.64 ± 0.01	0.67 ± 0.01	0.59
Etching	1.68 ± 0.01	0.68 ± 0.01	0.60

The results of the interlaminar shear tests are displayed in Figure 3 in comparison to the measured arithmetic mean surface roughness. With maximum values of 31 MPa for etching and 28 MPa for blasting, significantly higher values can be determined than those measured on overlap joints of the

same material combinations in [9]. On blasted and etched specimens, residues of the FRP can be seen on the surface, which is due to an interlaminar failure of the composite material. The real interfacial strength of these surface treatments is even higher than the value determined. It is not possible to draw conclusions about the interfacial strength only from the roughness. The samples with etched surfaces have high shear strength values despite low roughness. It is assumed that different adhesion mechanisms are effective. Through mechanical blasting, the PA6 mechanically interlocks with the surface, whereas during etching, binding forces are responsible for cohesion.

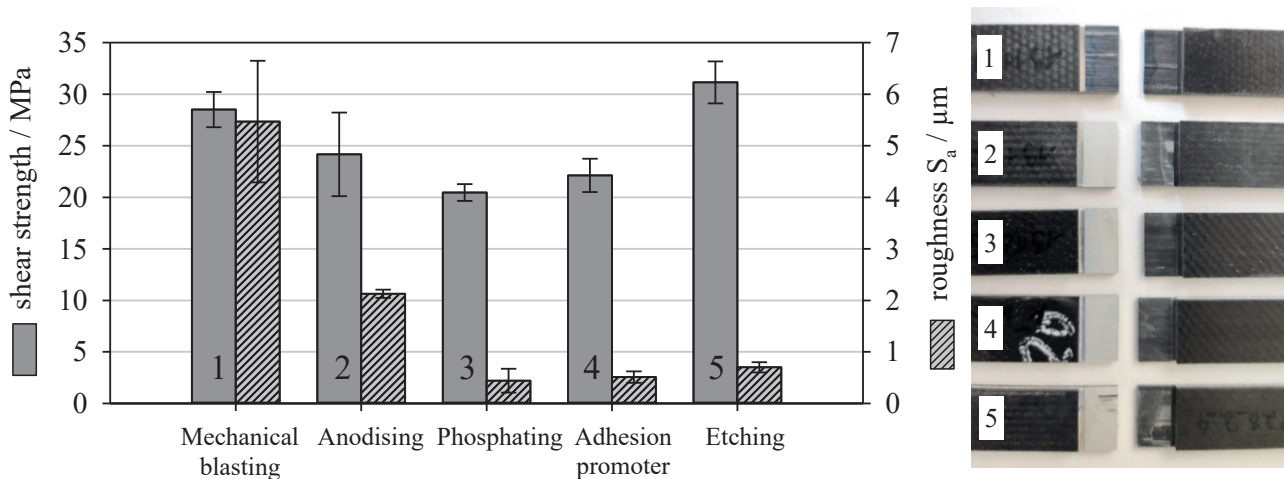


Figure 3: Results of interlaminar shear test of hybrid laminates with surface treated aluminium alloy AA6082-T4 and a graded structure of glass- and carbon fibre-reinforced PA 6 in a 1/2-configuration; fractography on the right

Measured tensile strengths of hybrid laminates with different surfaces is summarised in Figure 4. The qualitative results agree with the distribution observed by the interlaminar shear test. Etching leads the maximum average value of 480 MPa. The treatments with phosphating and adhesion promoter achieve significantly lower values between 200 and 300 MPa. A positive influence of the adhesion promoter can be recognised, although the effect is less than surface treatment by etching, blasting or anodising. It was found that the strengths depend strongly on the removal position from the hybrid laminate. Especially with anodised samples, the sample thickness was much smaller in the edge area than in the middle, which leads to a change in the metal volume ratio. This could explain the wider spread of results.

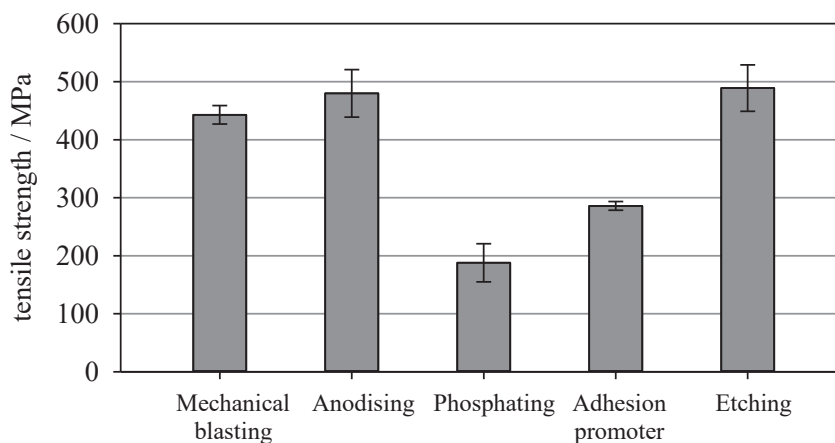


Figure 4: Tensile strength of hybrid laminates with surface treated aluminium alloy AA6082-T4 and a graded structure of glass- and carbon fibre-reinforced PA 6 in a 2/1-configuration

4 Conclusions

The following conclusions can be drawn from the investigations on the surface treated aluminium sheets AA6082-T4 in hybrid laminates based on fibre reinforced polyamide 6.

The surface of the aluminium alloy influences the rheological behaviour of the melt during consolidation process. The thickness of the laminates varies with different surface treatments in a pressure controlled process. Mechanically blasted and etched surfaces achieve similar interlaminar shear strength despite different roughness values. In further studies with a combination of these surface treatments a superposition of different adhesion mechanisms could be achieved. Besides the surface treatment, an influence of the metal volume ratio on the tensile strength values should be determined. This influence must be taken into account even more in future studies.

5 Acknowledgment

The research was carried within the project “Mechanism-correlated characterization of the deformation and damage behaviour of thermo-plastic-based fibre metal laminates for property-oriented process development”, which was funded by the German Research Foundation (Deutsche Forschungsgemeinschaft, DFG, funding no. 414332488). We would like to acknowledge Mr. Martin Risthaus from Evonic for providing surface treatment and Mr. Marco Fischer for supporting the experimental tests.

6 Literature

- [1] A. Vlot, J. W. Gunnink, *Fibre Metal Laminates: An Introduction*, Springer Netherlands, Dordrecht, 2001, ISBN 978-94-010-0995-9.
- [2] G. Reyes V., W. J. Cantwell, in *Composites Science and Technology*. **2000**, 60, p. 1085-1094
- [3] B. Wielage, D. Nestler, H. Steger, L. Kroll, J. Tröltzsch, S. Nendel, CAPAAL and CAPET - New Materials of High-Strength, High-Stiff Hybrid Laminates. In: Fathi, M., Holland, A., Ansari, F., Weber, C. (Hg.): *Integrated Systems, Design and Technology 2010*, Berlin, Heidelberg: Springer Berlin Heidelberg, 2011, p. 23-35
- [4] C. Zopp, D. Nestler, J. Tröltzsch, M. Trautmann, S. Nendel, G. Wagner, W. Nendel, L. Kroll, in *Key Engineering Materials*. **2017**, 742, p. 294-301
- [5] A. Sexton, W. Cantwell, S. Kalyanasundaram, in *Composite Structures*. **2012**, 94, p. 431-437
- [6] D. Nestler, M. Trautmann, C. Zopp, J. Tröltzsch, T. Osiecki, S. Nendel, G. Wagner, L. Kroll, in *Procedia CIRP*. **2017**, 66, p. 107-112
- [7] P. Compston, W. J. Cantwell, C. Jones, N. Jones, in *Journal of Materials Science Letters*. **2001**, 20, p. 597-599
- [8] L. Mosse, P. Compston, W. J. Cantwell, M. Cardew-Hall, S. Kalyanasundaram, in *Composites Part A: Applied Science and Manufacturing*. **2005**, 36, p. 1158-1166
- [9] D. Nestler, M. Trautmann, S. Nendel, G. Wagner, L. Kroll, in *Materialwissenschaft und Werkstofftechnik*. **2016**, 47, p. 1121-1131
- [10] B. Bosbach, M. Baytekin-Gerngross, E. Heyden, M.-D. Gerngross, J. Carstensen, R. Adelung, B. Fiedler, in *Composites Science and Technology*. **2018**, 167, p. 32-41

Influence of surface treatment on fatigue properties of thermoplastic based hybrid laminates

S. Mrzljak¹, M. Trautmann², G. Wagner², F. Walther¹

¹TU Dortmund University, Department of Materials Test Engineering (WPT), Dortmund, Germany

²Chemnitz University of Technology, Institute of Material Science and Engineering (IWW), Chemnitz, Germany

1 Introduction

The configuration variability of lightweight hybrid laminates made of metal sheets and fiber-reinforced polymer enables many possibilities regarding customizability at high specific strength. Combining aluminum sheets and carbon-fiber-reinforced thermoplastic layers can lead to high and durable mechanical performance (as shown for quasi-static and fatigue bending by [1]) while offering good formability and recyclability, making it suitable for e.g. automotive applications. But not just the material combination determines the performance of the hybrid laminate, also the interfacial bonding is an important factor to consider. Surface treatments to the metal sheets like mechanical treatment, chemical etching or electrochemical treatment can improve wettability and adhesion between metal and polymer, impacting on the mechanical properties of metal fiber laminates (e.g. in [2-4]). While much research regarding the influence of such metal surface treatments on the laminates mechanical quasi-static properties, such as interlaminar shear, tensile or flexural strength, is conducted, there is a lack of knowledge about the influence of metal surface treatments on the fatigue behavior.

In this study, the influence of aluminum surface treatment on the fatigue behavior of thermoplastic based hybrid laminates is investigated through the use of a short-time testing procedure (e.g., in [5]) and results are validated through S-N curve establishment. Different metrologies are used to enable detection of material response (microstructural changes, i.e. damage) and its progression until fatigue failure for interaction evaluation between fatigue load and material response (e.g. in [6]).

2 Specimen

The investigated thermoplastic based hybrid laminates CAPAAL are composed of a graded unidirectional 3B SE 4535 glass- and Panex 35 carbon-fiber-reinforced polyamide 6 layer (made by Cetex Institut gGmbH, Germany) with a fiber volume fraction of 0.5 placed between two 0.5 mm sheets of aluminum alloy AA6082-T4. The glass-fiber-reinforced polyamide 6 layers with additional 40 μm foils of polyamide 6 are implemented for compensation of the thermal expansion mismatch between the aluminum sheets and carbon-fiber-reinforced polyamide 6. The aluminum sheet rolling direction is aligned with the unidirectional fibers. Both glass- and carbon-fibers are equipped with a suitable sizing for impregnation and adhesion to polyamide 6. The melting point of the polyamide 6 is 219 °C.

2.1 Manufacturing process

Before hot-pressure consolidation of a laminate, four different aluminum surface treatments (initial arithmetic mean roughness $R_a = 0.55 \pm 0.12 \mu\text{m}$, measured with Keyence VK-X200) with regard to

adhesion properties were applied: *I) Mechanical blasting* where Al_2O_3 (aluminum oxide) was used at a blasting angle of 90° resulting in $R_a = 5.74 \pm 1.18 \mu m$. In order to minimize distortion of the aluminum sheet, both sides were blasted. *II) Anodizing* was carried out, after etching in 10% sodium hydroxide and subsequent pickling, under direct current in sulphuric acid, giving $R_a = 2.13 \pm 0.13 \mu m$. *III) Phosphating* was performed using the Bonderite[®] M-ZN process from Henkel, where roughness yielded in $R_a = 0.67 \pm 0.15 \mu m$. *IV) Adhesion promotion* was implemented through application of Vestamelt co-polyamide adhesion promoter from Evonik Resource Efficiency GmbH Germany to the aluminum sheets under $200^\circ C$ temperature, after preliminary phosphating (see *III*), resulting in $R_a = 0.49 \pm 0.16 \mu m$.

To achieve a successful lamination between the Fiber-Foil-Tape Unit (FFTU) [7] produced fiber-reinforced-polymer (FRP)-layers and the surface treated aluminum sheets, a Collin P300 PM laboratory press with dipping edge tool was used. Parameters for temperature and pressure were investigated separately in terms of full and homogeneous consolidation between matrix, fibers, and metal, resulting in $295^\circ C$ at 1.5 MPa for 24 min. Figure 1 shows cross-sections of all investigated hybrid laminate variants, showing different laminate thicknesses and proportions between aluminum and fiber-reinforced polymer, which are assumed to be due to the different flow conditions of the matrix on the treated aluminum surfaces during tempered pressure.

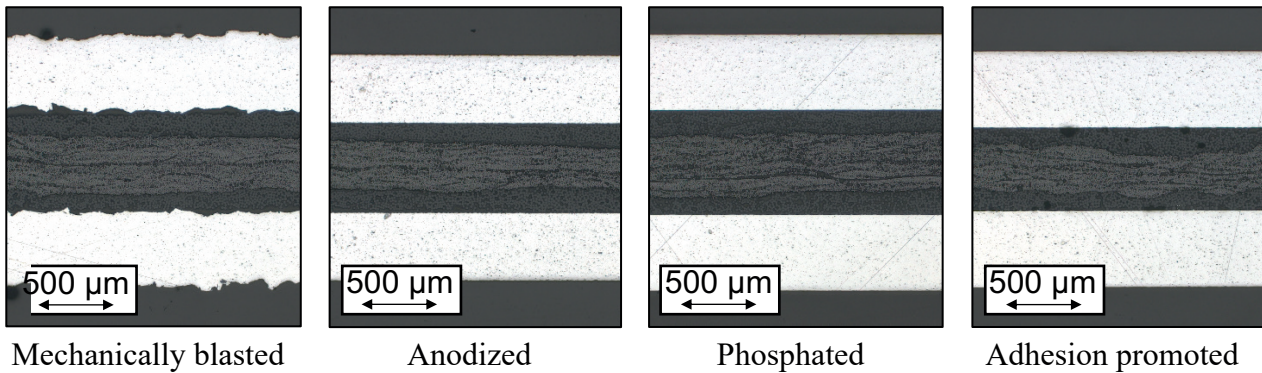


Fig. 1: Light microscope images of the hybrid laminates cross-sections (fiber direction out-of-plane) with different aluminum surface treatments

2.2 Specimen dimensions and preparation

For fatigue testing, specimen type A according to ISO 527-5 with a shorter distance between the protection tabs was selected in order to gather high resolution information about local material reactions by measurement instrumentation of a smaller area (Fig. 2 i). Specimens were cut by water jet and cutting edges grinded with SiC abrasive paper down to P4000 to reduce notches. To reduce stress concentrations at the transitional area of clamping and testing area, aluminum tabs with a thickness of 1.75 mm were adhesively bonded to the clamping area of the specimen with epoxy. For adhesion enhancement, the aluminum tab and clamping area of the specimen were mechanically blasted.

For digital image correlation (DIC) a speckle pattern was applied to the face and left side (laminated edge) of the specimens with spray paint to enable 2-sided local deformation measurement (Fig 2 ii).

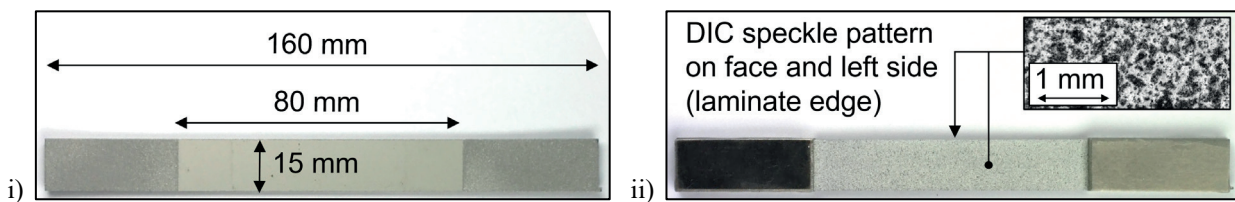


Fig. 2: i) Specimen dimensions and ii) specimen with end tabs and DIC pattern for deformation analysis

3 Experimental procedure

For the fatigue investigations a short-time procedure was used, combining multiple (*MAT*) and constant amplitude tests (*CAT*), which were carried out on a servo-hydraulic testing system (Shimadzu EHF-EV50, maximum force $F_{max} = \pm 50$ kN) with sinusoidal tension-tension load-time function at a stress ratio $R = 0.1$ and a testing frequency $f = 10$ Hz under ambient temperature with regard to ISO 13003. For the *MAT* the maximum starting stress $\sigma_{max,start}$ was 50 MPa followed by stepwise stress increase of $\Delta\sigma_{max} = 25$ MPa per $\Delta N = 10^3$ cycles up to specimen failure. The stress levels for the *CAT* were derived from the material reactions in the *MAT*, between the onset of first microstructural change (high cycle fatigue (*HCF*)) and specimen failure (low cycle fatigue (*LCF*)).

3.1 Fatigue testing measurement setup

The change in microstructure and properties of the specimen was measured by a combination of systems. Limes Q400 digital image correlation system (DIC) was used for surface deformation analysis of the front aluminum sheet (precision lens, 28 mm focal length) and laminate edge (macro lens, 70 mm focal length, with extension tubes) to observe interface reactions between the laminate partners (directions are shown in Figure 2 ii) and 3). DIC pictures were taken at maximum stress with the help of a Limes Maxtrigger box. MicroEpsilon TIM-160 thermocamera recorded the front aluminum surface temperature. For investigation of stress-strain hysteresis development a Shimadzu TCK-1-LH ($l_0 = 25$ mm, $\Delta l = \pm 1$ mm) extensometer, as well as the machine piston movement recorded by LVDT, and the engineering stress, derived from the load cell at initial specimen area, were used.

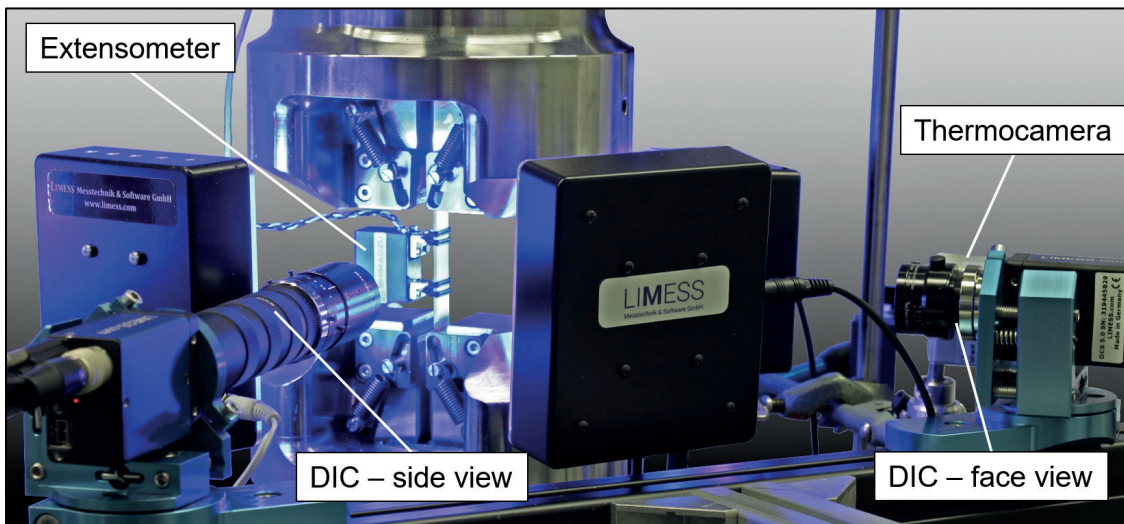


Fig. 3: Experimental setup containing Shimadzu EHF-EV50, Limes Q400 DIC cameras perpendicular to specimen (face and side view), MicroEpsilon TIM 160 thermocamera and tactile Shimadzu TCK-1-LH extensometer

4 Results

MAT were used for a first estimation of the aluminum surface treatment influence on fatigue behavior and revealed discernible differences with regard to fatigue life and damage development. Anodizing leads to the highest *MAT* fatigue life, while adhesion promotion treatment shows the lowest (Fig. 4 i). Looking at the DIC detected time of damage initiation during the *MAT*, a correlation between damage

initiation and MAT fatigue life is visible. The change in temperature ΔT reveals differences between the surface treatments, hinting at differing laminate properties and damage progressions (Fig. 4 ii). Mechanical blasting and anodizing show earlier a higher temperature increase before any visible damage, while adhesion promotion and phosphating only show significant temperature increase at damage initiation and propagation.

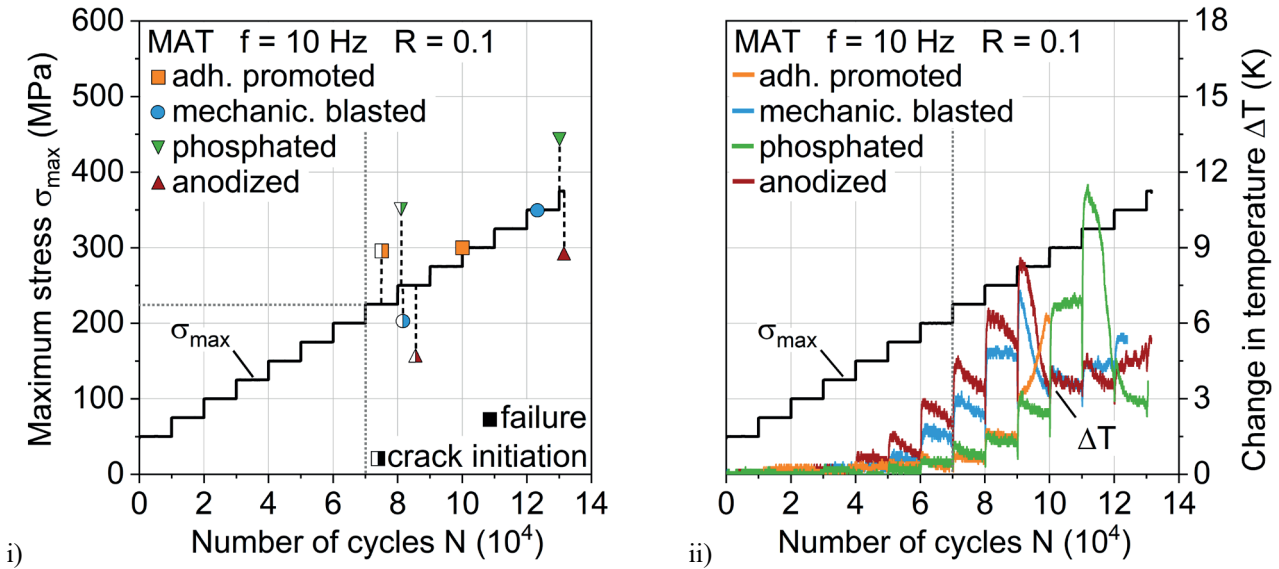


Fig. 4: Influence of aluminum surface treatment on i) MAT damage initiation and fatigue life and ii) change in temperature

The changes in dynamic stiffness C_{dyn} (change of force divided through change of piston movement: $(F_{max} - F_{min}) / (S_{max} - S_{min})$) (Fig. 5 i) illustrate, that the earlier temperature increases can be attributed to load-increased cyclic softening and hardening processes of the aluminum, which are particularly present in anodized surface treatment. Adhesion promoter and phosphating exhibit the same delayed cyclic hardening processes, which could be due to the phosphating of both. The plastic strain amplitude $\epsilon_{a,p}$ (Fig. 5 ii) correlates directly to the stiffness and temperature change, revealing the plastically deforming aluminum component as the main cause for the temperature increase. After the temperature maxima, stiffness decrease of fiber-reinforced polymers is visible.

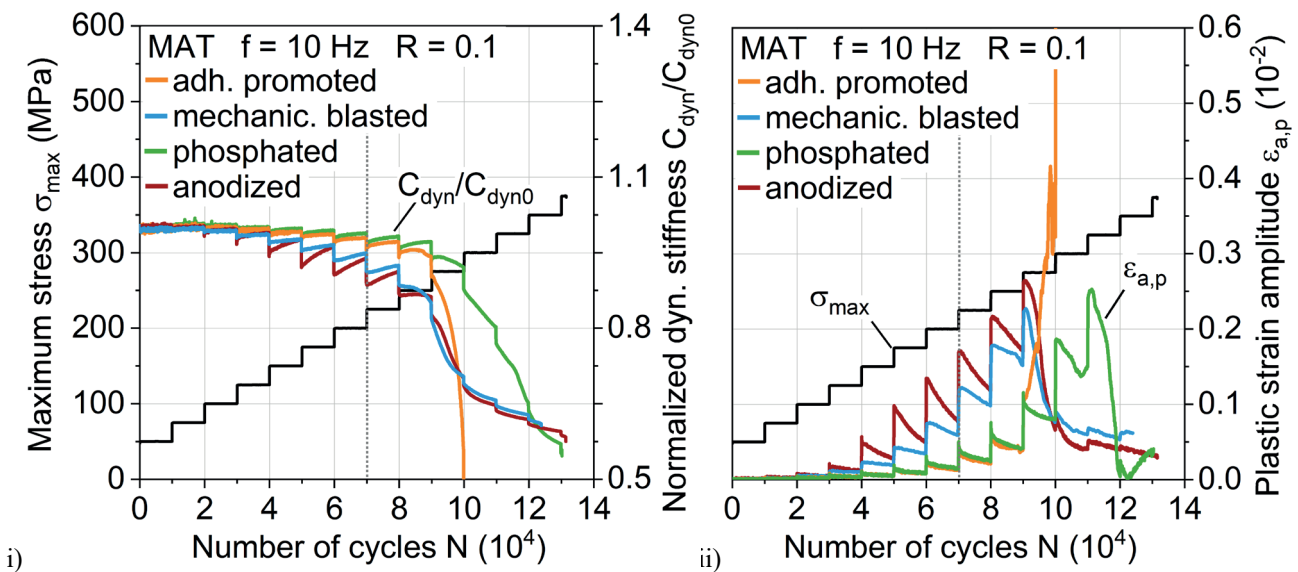


Fig. 5: Influence of aluminum surface treatment on i) dynamic stiffness and ii) plastic strain amplitude during MAT

Through front and in-plane observation of laminar damage propagation via DIC, differences depending on the surface treatment and related cyclic hardening progression were recognized. Figure 6 shows the specimen damage through strain analysis, representing the condition immediately before MAT failure. Visible aluminum cracks formed from the outer specimen edges to the inside, developing into interface cracks and delaminations. For the variants of later hardening (adhesion promotion and phosphating treatment), substantial amounts of delamination between the aluminum and FRP are present, while the variants inclined to earlier crack initiation (mechanical blasting and anodizing treatment) enable a reduction of stress concentrations and show locally restricted delaminations.

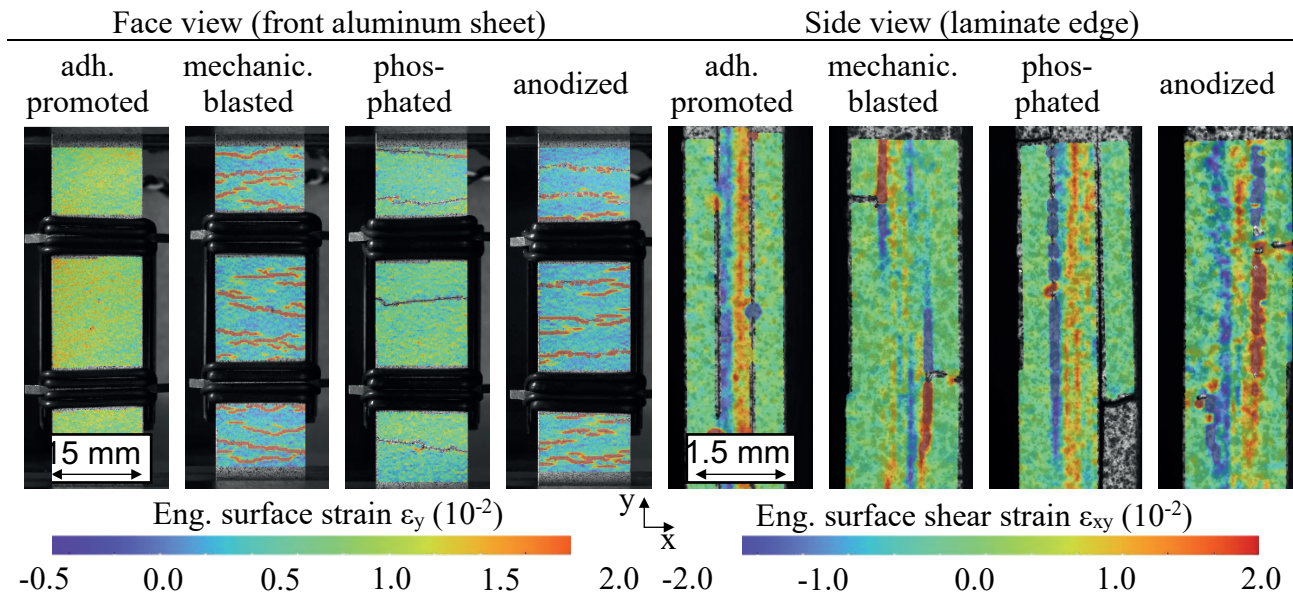


Fig. 6: DIC strain analysis images of front aluminum perspective and in-plane laminate perspective immediately before MAT failure for hybrid laminates with different aluminum surface treatments

The S-N relationship for each hybrid laminate with the individual treated aluminum surface confirms the MAT findings regarding fatigue lifetime, showing anodized and phosphated in general with the highest fatigue life. The extensive delaminations visible for adhesion promoter during MAT (Fig. 6) also take place in CAT, representing low interfacial load capacity between metal and FRP, reducing fatigue lifetime (Fig. 7). DIC analysis during MAT and CAT showed that the phosphated variant delaminates more gradually, leading to similar damage induced stress relieve and distribution as for anodized and mechanically blasted and therefore a higher fatigue life.

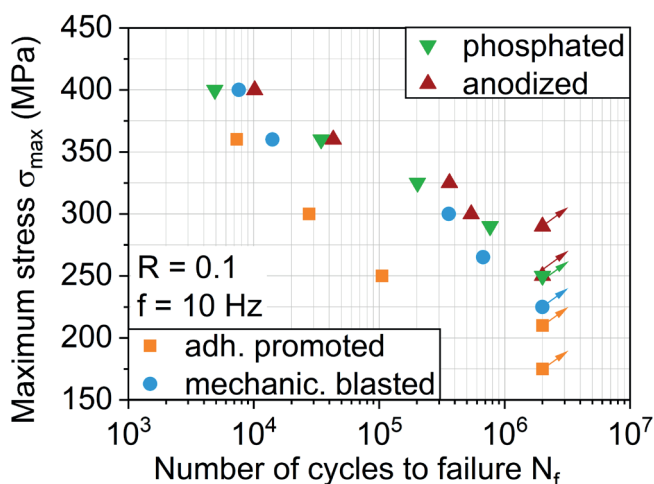


Fig. 7: S-N relationship for hybrid laminates with different aluminum surface treatments

5 Conclusions and outlook

The investigations regarding the influence of aluminum AA6082-T4 sheet surface treatment on the fatigue properties of the presented hybrid laminate led to the following conclusions:

By using multiple amplitude tests, DIC analysis, and hysteresis-stress-strain measurement an overview about the fatigue performance was established and validated successfully through constant amplitude tests. The fatigue damage development and fatigue life of hot-pressure consolidated thermoplastic-based hybrid laminates are highly influenced by the aluminum surface treatment. Anodizing and phosphating showed the highest fatigue life, while in comparison, the adhesion promoter led to significantly reduced fatigue life due to low interfacial load capacity. Damage induced stress relieve and distribution is highly affected by the surface treatments. Results show that graded crack initiation and propagation – which is influenced by the metal-FRP-interface, aluminum surface and the onset of aluminum cyclic hardening – tends to higher fatigue life, but needs further investigation.

In future studies, interfacial differences between the metal and FRP of the hybrid laminate need to be characterized in detail and should be analyzed during fatigue tests through e.g. accompanied microscopy. Since the investigated aluminum surface treatments lead to different laminate thicknesses, the related ratio of fiber-reinforced polymer and fiber density needs to be considered for each laminate variant with regard to a relative comparison of the individual and integral laminate partners fatigue performance.

6 Acknowledgment

The research was carried out within the project “Mechanism-correlated characterization of the deformation and damage behavior of thermo-plastic-based fiber metal laminates for property-oriented process development”, which was funded by the German Research Foundation DFG (Deutsche Forschungsgemeinschaft, DFG, funding no. 414332488). We would like to acknowledge Mr. Martin Risthaus from Evonic for providing surface treatment.

Literature

- [1] C. Zopp, A. Dittes, D. Nestler, I. Scharf, L. Kroll, T. Lampke, in *Composites Part B: Engineering*, **2019**, 174, 106260. DOI: 10.1016/j.compositesb.2019.107043
- [2] N.G. Gonzalez-Canche, E.A. Flores-Johnson, P. Cortes, J.G. Carillo, in *International Journal of Adhesion and Adhesives*, **2018**, 82, 90-99. DOI: 10.1016/j.ijadhadh.2018.01.003
- [3] W. Zhu, H. Xiao, J. Wang, C. Fu, in *Composites Part B: Engineering*, **2019**, 173, 111321. DOI: 10.1016/j.compstruct.2019.111321
- [4] V.S. Balakrishnan, A. Obrosof, F. Kuke, H. Seidlitz, S. Weiß, in *Composites Part B: Engineering*, **2019**, 173, 106883. DOI: 10.1016/j.compositesb.2019.05.094
- [5] F. Walther, in *Materials Testing* **56**, **2014**, 519-527. DOI: 10.3139/120.110592
- [6] S. Mrzljak, D. Huelsbusch, F. Walther, in *Proc. of the 7th International Conference on Fatigue of Composites*, Vicenza, Italy, **2018**, 1-9.
- [7] D. Nestler, M. Trautmann, C. Zopp, J. Trötzsch, T. Osiecki, S. Nendel, G. Wagner, L. Kroll, in *Procedia CIRP* **66**, Karlsruhe, Germany, **2017**, 107-112. DOI: 10.1016/j.procir.2017.03.221

Fatigue damage behavior of continuous-discontinuous fiber reinforced sheet molding compounds

M. Bartkowiak¹, W. Liebig¹, K.A. Weidenmann²,

¹Institute for Applied Materials (IAM-WK), Karlsruhe Institute of Technology (KIT), Karlsruhe,

²Institute of Materials Resource Management (MRM), University of Augsburg, Augsburg

Abstract

In this work, the fatigue behavior of continuous-discontinuous sheet molding compounds was investigated in a load-controlled tension-tension fatigue test under several loads. Carbon fibers function as continuous reinforcement whereas glass fibers are used for the discontinuous reinforcement. The matrix material is an unsaturated polyester polyurethane hybrid resin system without fillers in both cases. Digital image correlation was used for strain measurement. Damage evolution was analyzed visually and by means of volumetric images obtained in CT scans. Progressive damage of the continuous layers in form of interfiber fracture and fiber breakage begins with the first cycles at the edges of the specimen. Delamination and final failure of these layers preceded failure of the discontinuous phase. Damage in the discontinuous layer is delayed due to the constraining continuous layers. Compared to experimental data determined for the unreinforced discontinuous sheet molding compound specimens, considerably higher fatigue strength is achieved.

1 Introduction

Continuous fiber reinforced polymers are characterized by their high mechanical properties in terms of strength and stiffness. However, they are limited by their production costs and the low design freedom. In contrast, discontinuous fiber reinforced polymers, like sheet molding compounds (SMC), provide the possibility to manufacture parts with complex geometries at lower cycle times and lower production costs. The biggest disadvantage is a lower level of stiffness and strength. Hybrid composite materials combining discontinuous fiber-reinforced polymers with local continuous fiber reinforcements (CoDiCoFRP) aim to combine the advantages of both composite materials and therefore have significant potential for different engineering applications, as for example in the automotive industry. Different researchers have already shown the advantages of hybrid SMCs. Wulfsberg et al. [1] used pre-impregnated carbon fiber fabric to reinforce discontinuous carbon fiber SMC in a one-shot molding process resulting in an improvement of strength and stiffness. Gortner et al. [2] combined standard glass fiber SMC with continuous non-crimp glass fiber and carbon fiber fabrics and were able to produce complex component geometries with increased mechanical properties. The International Research and Training Group “Integrated engineering of continuous-discontinuous long fibre reinforced polymer structures” (DFG-GRK 2078) considers this new class of materials with the focus of further developing the manufacturing process, characterization and simulation methods and defining design guidelines for CoDiCoFRP structures [3]. Due to the materials complex microstructure, the prediction of the damage behavior and thus the mechanical properties is proving difficult. Trauth and Weidenmann have already investigated the mechanical material properties under quasi-static tension and compression load [4]. Trauth et al. [5]

considered the puncture properties of CoDiCoFRP under quasi-static and dynamic loads. Since automotive structural components are subjected to cyclic loads, profound knowledge of their fatigue behavior is necessary and thus considered in this study. A comparison of the fatigue behavior of the hybrid material and the discontinuous SMC serves the purpose of evaluating the effect of hybridization. Results of fatigue experiments on discontinuous SMC have already been presented by the authors [6].

2 Materials and Methods

2.1 Materials

2.1.1. Manufacturing of DiCo- and CoDiCoSMC panels

The adopted SMC process to manufacture continuous-discontinuous sheet molding compounds (CoDiCoSMC), that are considered in this study, was developed by Bücheler and Henning [7]. The SMC prepregs were manufactured on a conveyor belt (type HM-LB-800 by Schmidt & Heinzmann, Bruchsal, Germany). Both the continuous (CoSMC) and discontinuous glass fiber reinforced sheet molding compounds (DiCoSMC) are based on an unsaturated polyester polyurethane hybrid resin system provided by Aliancys, Schaffhausen, Switzerland with no fillers. The DiCoSMC prepregs are reinforced with 25.4 mm long glass fibers. Unidirectional carbon fiber non-crimp fabric is used for the CoSMC prepregs. The fiber weight fractions were determined by thermal gravity analysis and are approximately 45% and 65% respectively. DiCoSMC panels were manufactured by compression molding in a rectangular mold (800 mm x 250 mm). The discontinuous prepregs were cut into sheets with a size of approximately 400 mm x 250 mm and were placed in the center of the mold filling the mold in width direction completely. This leads to a material flow in length direction during compression molding. CoDiCoSMC panels were manufactured in a similar way in a one step compression molding process. The continuous prepregs were therefore cut into the size of the final plaque. The co-molding process and the architecture of the final laminate is shown in Figure 1(a) and (b). The red arrows in Figure 1(a) indicate the motion of the press and the flow direction of the DiCoSMC prepreg during molding respectively.

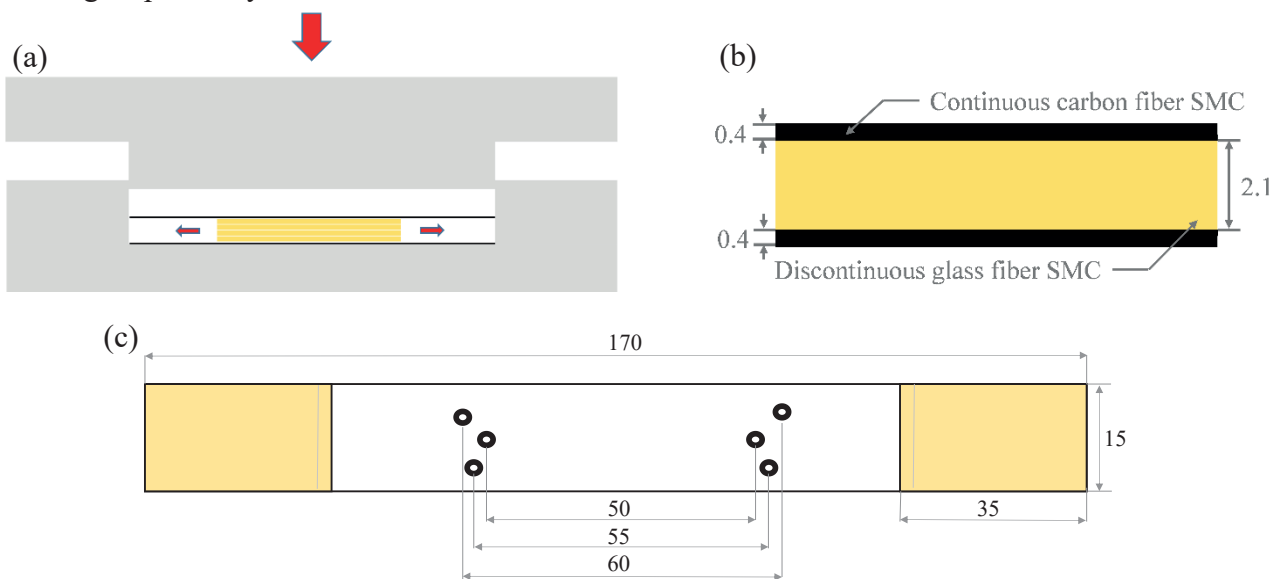


Figure 1: (a) Molding process, (b) laminate architecture of CoDiCoSMC panels and (c) dimensions of specimens.

2.1.2 Specimen preparation

Rectangle shaped specimens with a size of 175mm x 15 mm have been extracted in fiber direction via waterjet cutting by Genthner SchneidTechnik GmbH & Co. KG, Germany. End tabs made of a multiaxial glass fiber fabric and epoxy (1.3 mm PREGNIT GMBE by Krempel, Vaihingen an der Enz, Germany) were used for the CoDiCoSMC specimens to avoid damage of the outer carbon fiber layers due to clamping. No end tabs were needed for the DiCoSMC specimens.

2.2 Experimental studies

2.2.1 Mechanical testing

The experiments were carried out at room temperature ($T = 21 \text{ p/m } 1.5 \text{ }^\circ\text{C}$) on a servo-hydraulic testing machine from Zwick Roell (type 1478) with a load cell capacity of 100 kN according to DIN ISO 13003 [8]. Specimens were hydraulically clamped with a clamping distance of 100 mm. Tensile tests with a strain rate of $3 \cdot 10^{-4} /\text{s}$ as well as $0.12 /\text{s}$ were used to determine ultimate tensile strength at standard ($\text{UTS}^{\text{S,D}}$ for DiCoSMC and $\text{UTS}^{\text{S,C}}$ for CoDicoSMC) and fatigue rate ($\text{UTS}^{\text{F,D}}$ for DiCoSMC and $\text{UTS}^{\text{F,C}}$ for CoDicoSMC) respectively. Tension-tension fatigue tests were carried out under load control with a constant amplitude. Both material systems were tested at five different load stages that are listed in Table 2. The stress levels 100% $\text{UTS}^{\text{F,D}}$ and $\text{UTS}^{\text{F,C}}$ are listed only for the readers information. The stress ratio R was 0.1 and the frequency f was 5 Hz to minimize a temperature increase during loading. Due to the duration of the trials, specimens were only tested up to $3 \cdot 10^6$ cycles.

2.2.2 Strain measurement

The displacement of DiCoSMC specimens was measured by using a capacitive displacement sensor that measured the displacement of the moving jaw [6] considering the machine rigidity. This method cannot be used for the CoDiCoSMC specimens due to fatigue of the adhesive bond between the specimens and the end tabs. The displacement of the CoDiCoSMC specimens was therefore measured by using digital image correlation (DIC) with a ARAMIS 3D camera system by GOM GmbH, Braunschweig, Germany. For this purpose, reference point markers were applied to the specimens like shown in Figure 1(c) and the distance between different pairs of points was determined. The camera was triggered by the load signal of the testing machine. A picture was taken at the minimum and maximum load during each cycle and saved in a ring buffer to capture the final failure process. Additionally, 20 pictures per 10^x cycles were saved permanently.

Tabelle 2. Load stages for fatigue tests of CoDiCo- (left) and DicoSMC [6] (right).

load stage in % $\text{UTS}^{\text{F,C}}$	load stage in MPa	load stage in % $\text{UTS}^{\text{F,D}}$	load stage in MPa
100	456	100	237
79	360	79	187
74	337	69	163
69	315	58	137
64	292	51	120
59	270	42	100

3.2 Evolution of dynamic stiffness

The dynamic modulus equals the slope of a linear function through the maximum and minimum of the hysteresis loop and is a measure for damage evolution in the composite material [9]. The evolution of the normalized dynamic modulus is shown in Figure 3 for representative specimens of the tested load stages. Due to the transient response of the machine during the first cycles, the dynamic modulus was normalized to the fourth cycle. Reduction of stiffness is more pronounced for the DiCoSMC specimens. This is especially noticeable for specimens tested at a high load stage and in the region of low numbers of cycles. This trend can be observed even better in Figure 5, in which the damage variable defined by $1 - E_{\text{dyn}}/E_{\text{dyn},4}$ is plotted over the relative fatigue life. Up to 50% of fatigue life, stiffness degradation of the CoDiCoSMC specimens is small compared to the DiCoSMC specimens. A strong increase of the damage variable, that is observed for the specimens tested at 79% $UTS^{F,C}$ and 74% $UTS^{F,C}$, is due to partial failure of the reinforcing carbon fiber layer leading to interlaminar delamination in a considerably large area. Due to progressive damage of the continuous carbon fiber layers at high numbers of cycles, no reliable data could be collected by DIC.

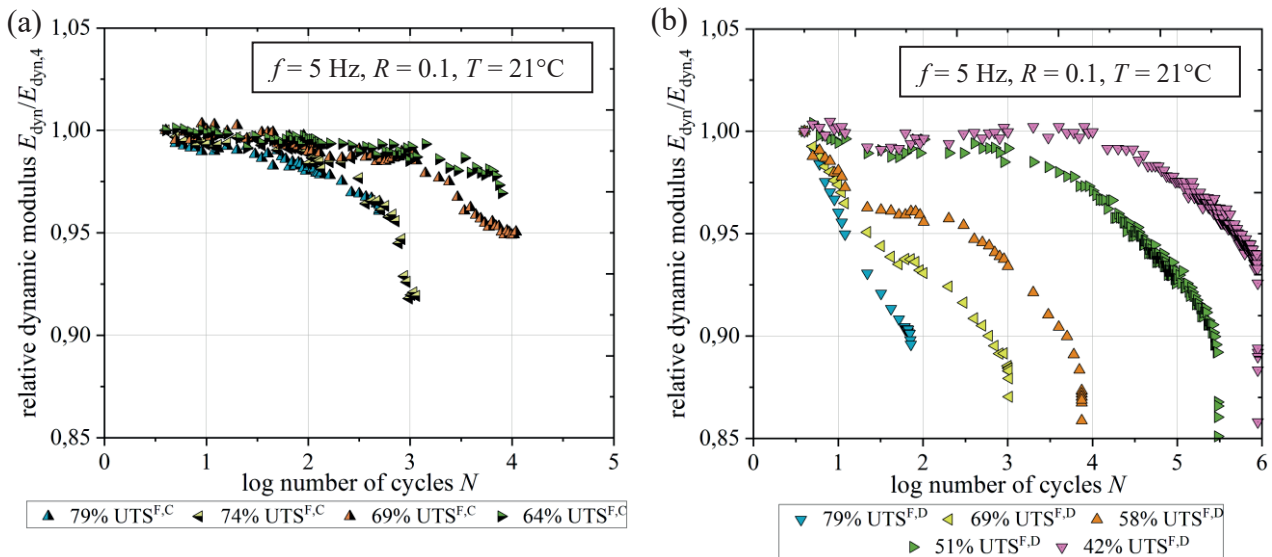


Figure 3: Evolution of relative dynamic modulus of (a) CoDiCo- and (b) DiCoSMC [6] specimens at different load

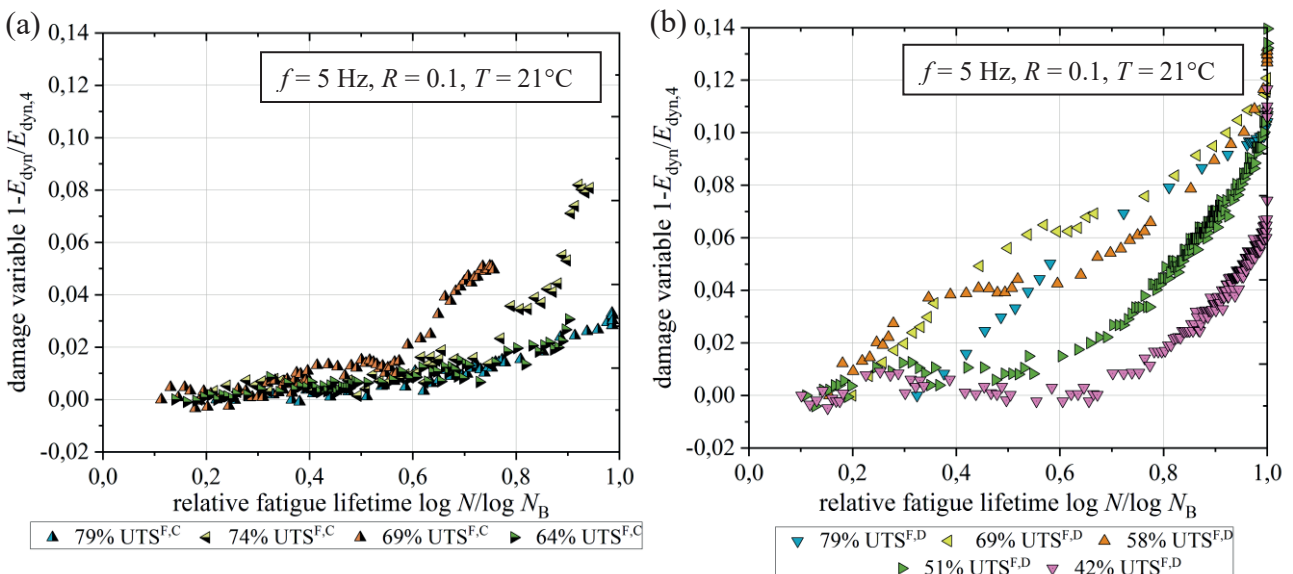


Figure 4: Damage variable $1 - E_{\text{dyn}}/E_{\text{dyn},4}$ of (a) CoDiCo- and (b) DiCoSMC [6] specimens at different load stages.

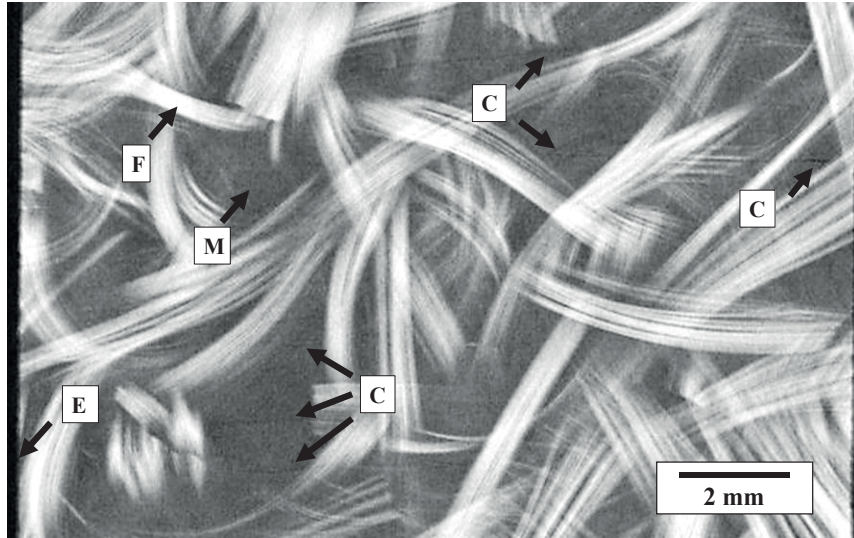


Figure 5: Volumetric image of a DiCoSMC specimen tested at 74% $UTS^{F,D}$ after 10 000 cycles; arrows indicate cracks (C), fiber bundles (F), matrix rich regions (M) and the specimen edge (E).

3.3 Damage analysis

Damage of the CoDiCoSMC specimens begins with fiber breakage in the outer carbon fiber layers at the edges of the specimens within the first cycles followed progressive damage of the carbon fiber layers. Final failure is characterized by large-scale delamination of the carbon fiber layers and local failure of the discontinuous layer. Damage in DiCoSMC and in the discontinuous layer of CoDiCoSMC was analyzed by means of volumetric images obtained in CT scans. Figure 5 shows a volumetric image of a DiCoSMC specimen tested at 74% $UTS^{F,D}$ after 10 000 load cycles. Thin cracks are visible in matrix rich regions. Volumetric images of CoDiCoSMC specimens tested at 74% $UTS^{F,C}$ (which corresponds to 142% $UTS^{F,D}$) showed no such cracks after the same number of cycles in the discontinuous layer.

4 Discussion

The decreasing slope of the S-N curve determined for CoDiCoSMC in Figure 2 caused by the reinforcement with the unidirectional carbon fiber layers is consistent with findings of Vassilopoulos [10], who showed that the slope for unidirectional carbon fiber composites is less steep compared to multidirectional glass fiber composites. It should be noted that the fatigue strength obtained for CoDiCoSMC is higher than the tensile strength of DiCoSMC (114% $UTS^{F,D}$). A comparison between the damage evolution in the hybrid CoDiCoSMC and the DiCoSMC demonstrates the constraining effect of the continuous carbon fiber layers. In [6] the authors examining the damage of the DiCoSMC specimens visually and saw a formation of small cracks beginning with the first cycles for all tested load stages. Crack density increased with the number load cycles until pseudo-delamination is observed locally before final failure of the specimens. The discontinuous layer in CoDiCoSMC cannot be observed visually. Figure 5 shows that these cracks can theoretically be identified in a CT scan. However they were not observed in CoDiCoSMC specimens that were tested under similar conditions. These findings match the results in Figure 3 and Figure 4. Since the crack density in the discontinuous layer increases considerably slower, stiffness degradation is not as pronounced as in the DiCoSMC specimens and occurs mainly due to progressive damage of the carbon fiber layers, which

can be observed visually during the experiments. Characterization methods for CoDiCoSMC need to be improved for further investigations. Optical strain measurement using DIC showed satisfying results until the carbon fiber layers failed extensively, which is why no reliable data was collected shortly before final failure. Since CT scans were performed on unloaded specimens, small cracks are difficult to detect. For a more detailed evaluation, in-situ experiments could be a promising method.

5 Summary and conclusions

In this work the tension-tension fatigue behavior of a CoDiCoSMC was investigated. Results were compared to those of DiCoSMC with regard to S-N data, stiffness degradation and damage evolution. A positive effect of hybridization was observed. The degradation of dynamic stiffness during loading was reduced and fatigue strength was increased considerably. The reinforcing continuous layers, restraining damage evolution in the discontinuous layer, experience progressive damage during fatigue loading. Observable damage in the discontinuous layer occurs locally, shortly before final failure of the specimens. The results obtained in this work underline the high potential of hybrid CoDiCoSMC.

6 Acknowledgement

The research documented in this manuscript has been funded by the German Research Foundation (DFG) within the International Research Training Group “Integrated engineering of continuous-discontinuous long fiber reinforced polymer structures“ (GRK 2078). The support by the DFG is gratefully acknowledged. Special thanks goes to Sergej Ilinzeer for manufacturing the SMC panels and to Ludwig Schöttl for CT scanning of the specimens and image processing.

7 Literature

- [1] Wulfsberg, J., et al., *Procedia Engineering* 81, **2014**, 1601-1607.
- [2] Gortner, F., et al, King Mongkut’s University of Technology North Bangkok *International Journal of Applied Science and Technology* 8.4, **2015**, 259-269.
- [3] Böhlke, T.; et al., *Continuous-Discontinuous Fiber-Reinforced Polymers – An Integrated Engineering Approach*, Hanser, Munich, **2019**.
- [4] Trauth, A., Weidenmann, K.A., *Composite Structures* 202, **2018**,1087-1098.
- [5] Trauth, A., et al., *Materials & Design* 143, **2018**, 224-237.
- [6] Bartkowiak, M., et al., *Proceedings of the American Society for Composites—Thirty-fourth Technical Conference*, **2019**.
- [7] Bücheler, D., Henning, F., *Proceedings of the 17th European Conference on Composite Materials*, **2016**.
- [8] ISO 13003:2003-12, *Fibre-reinforced plastics – Determination of fatigue properties under cyclic loading conditions*, **2003**.
- [9] O'Brien, T. K., Reifsnider, K.L, *Journal of composite materials* 15.1, **1981**, 55-70.
- [10] Vassilopoulos, A.P., Keller, T., *Fatigue of fiber-reinforced composites*, Springer Science & Business Media, **2011**.

Microstructural characterization of glass fiber reinforced SMC by nanoindentation and single-fiber push-out test

B. Rohrmüller^{1,2}, P. Gumbsch^{1,2}, J. Hohe¹,

¹Fraunhofer-Institute for Mechanics of Materials IWM, Wöhlerstraße 11, 79108 Freiburg, Germany,

²Karlsruhe Institute of Technology (KIT), Institute for Applied Materials, Kaiserstr. 12, 76131 Karlsruhe, Germany

1 Introduction

Fiber reinforced polymers (FRPs) are due to their high strength and low density an important material group in lightweight constructions. Due to their low density in comparison to metals they help to reduce weight and like this reduce fuel consumption in the mobility sector.

The investigated material is glass fiber reinforced Sheet-Molding-Compound (SMC), which has due to its production process a bundle microstructure [8]. The polymer is unsaturated polyether polyurethane hybrid (UPPH), a thermoset.

When we look on the microstructural level, FRPs are characterized by the behavior of fibers, matrix and the connecting fiber-matrix interface. That means that beneath the properties of fibers and matrix material, the interface also has a substantial contribution to the overall performance of a composite, as can be found for example in [3].

The aim of this contribution is to characterize numerically the fiber-matrix interface by FEM-simulations. This is done by experimental and numerical single-fiber push-out tests. In literature push-out tests are often simulated with an isotropic linear elastic matrix material model [1],[3]. In [6] push-out tests were simulated with an elasto-plastic matrix material model, which led to a better agreement instead of only using a linear elastic matrix material model.

Here we use a nonlinear elastic hyperelastic material model with a Prony series for viscoelasticity to describe the UPPH matrix. The UPPH matrix is characterized by nanoindentation tests on matrix rich regions of the composite, followed by FEM-simulations to calibrate the model. In a second step the calibrated matrix model, as well as from cyclic single-fiber push-out tests experimentally determined fracture toughness is used as input for a push-out simulation model. The interface strength is adapted to get an agreement between simulation and experimental push-out tests.

2 Methods

Nanoindentation tests are done on matrix rich regions of the composite to characterize the matrix behavior. Afterwards a simulation model of the indentation is built up to adjust the parameters of a hyperelastic material law with viscoelastic effects to describe the matrix. A Neo-Hooke model with a Prony series for viscoelasticity is used therefore.

Single-fiber push-out tests are conducted to characterize the debonding between fiber and matrix.

In a single-fiber push-out test a single fiber, laying vertically in a thin polished specimen, is loaded by a indenter tip to get a force displacement curve of the debonding. The single-fiber push-out tests are conducted quasi-statically and cyclic. The motivation for the cyclic single-fiber push-out tests is to determine experimentally the fracture toughness of the debonding between fiber and surrounding

matrix material. The method was proposed by [9] for ceramic composites and further developed for fiber reinforced polymers by [6],[7]. The experimentally determined fracture toughness is then used in the modelling of the interface for the push-out simulation.

2.1 Experiment

For the described nanoindentation and push-out experiments was used a TI-950 TriboIndenter from Hysitron.

2.1.1 Nanoindentation test

The nanoindentation tests in matrix rich regions from the composite were done with a diamond Berkovich modified tip, a three-sided pyramid with a half angle of 65.27° . The material specimens were cut out of the cross section of a material plate and polished on the surface. The polished specimens with a thickness of 1 mm were glued on a sample holder for testing. For the loading curve the loading rate divided by the load \dot{P}/P is held constant. The loading curve is followed by a hold time with constant force for 100 s during which the displacement is increasing due to viscoelasticity. An exemplary curve with $\dot{P}/P = 2/s$ can be seen in Figure 4 (left).

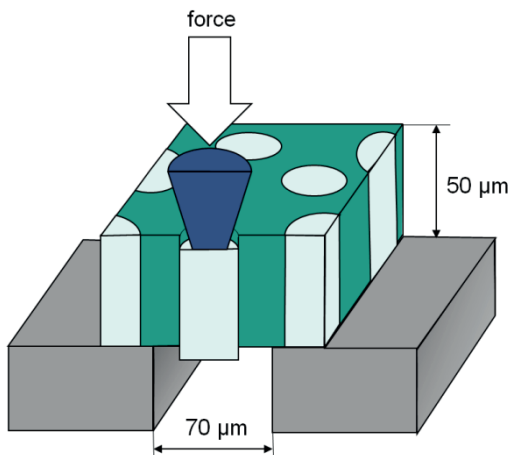


Figure 1: Sketch of single-fiber push-out test.

2.1.1 Single-fiber push-out test

For the specimen preparation of the push-out test slices with a thickness of 1 mm were cut from the cross section of a material plate. The slices of material were ground and polished on both sides. The thickness of the specimens at the end of the polishing process was at about $50 \mu\text{m}$. The tested fibers are perpendicular to the surface and lay during the testing over a groove with a thickness of $70 \mu\text{m}$ as can be seen in Figure 1. The specimen is glued on the sample holder during testing to reduce the compliance of the system. The indenter tip is a conical flat end indenter tip out of diamond with a diameter of $5 \mu\text{m}$ and an angle of 60° . As the diameter of the glass fibers is at about $13 \mu\text{m}$, the indenter tip only touches the fiber during the testing and not the surrounding matrix material. The tests are conducted displacement controlled with a displacement rate of 50 nm/s .

The tests are done quasi-static with increasing displacement until $5 \mu\text{m}$ and cyclic with loading and unloading cycles with increments of 200 nm per cycle, also until $5 \mu\text{m}$. An exemplary resulting force displacement curve for a cyclic push-out test can be seen in Figure 2. The middle and right picture shows the corresponding fiber after the test from front and backside.

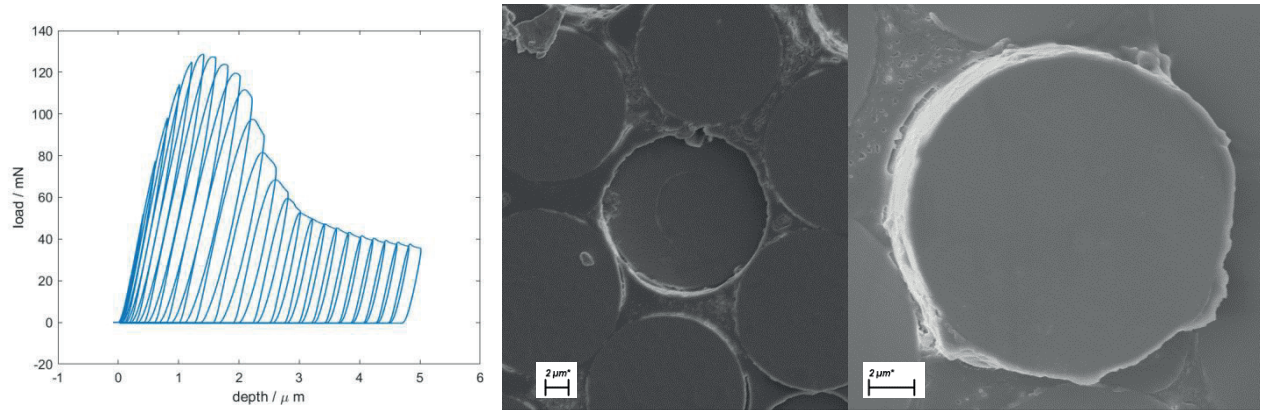


Figure 2: load-displacement curve of cyclic push-out test (left), pushed-in fiber on front surface (middle) and push-out fiber on the backside (right).

It can be observed a successive push-out behavior, as also observed in the literature in [7] for carbon fiber reinforced polyether ether ketone. That means we have a stable crack growth from the push-in of the fiber in the matrix on the front side until the push-out on the back side at a displacement of 3 μm . The nearly constant level of maximum force after a displacement of 3 μm is induced by friction between the debonded fiber from the surrounding matrix.

The cyclic push-out tests are evaluated energetically by separating each loading and unloading cycle in its elastic, friction and fracture energy contribution as proposed by [9],[6],[7].

2.2 Simulation

The matrix material and the fiber-matrix interface are characterized by FEM simulations.

2.2.1 Nanoindentation simulations

To determine more parameters than modulus and hardness, as classically done in nanoindentation testing, it is necessary to simulate the experiment in order to fit the simulation curve to the experiment by adapting the model parameters as for example done by [1].

The matrix material is simulated by the hyperelastic Neo-Hooke model with a Prony series for viscoelasticity. The strain energy potential for the Neo-Hooke model is given by

$$U = C_{10}(\bar{I}_1 - 3) + \frac{1}{D_1} (J - 1)^2 \quad (1)$$

with the deviatoric strain invariant \bar{I}_1 , the determinant of the deformation gradient J and the material parameters C_{10} and D_1 . The first part of the potential is incompressible and the second part compressible. More information on hyperelastic material models can for example be found in [5]. The parameters C_{10} and D_1 become time dependent to add viscoelastic behavior to the model. Therefore a Prony series is introduced for the dimensionless shear and compression modulus

$$\mathbf{g}_R(t) = 1 - \sum_{i=1}^N \bar{g}_i^P (1 - e^{-t/\tau_i}) \quad (2)$$

$$\mathbf{k}_R(t) = 1 - \sum_{i=1}^N \bar{k}_i^P (1 - e^{-t/\tau_i}) \quad (3)$$

with the material parameters \bar{g}_i^P , \bar{k}_i^P and τ_i and the number of series parameters N . The parameters of the Neo-Hooke model can then be written as

$$C_{10}(t) = \frac{C_{10}^\infty}{1 - \sum_{i=1}^N \bar{g}_i^P} \mathbf{g}_R(t), \quad (4)$$

$$D_1(t) = \frac{D_1^\infty}{k_R(t)} \left(1 - \sum_{i=1}^N \bar{k}_i^P\right). \quad (5)$$

The parameters C_{10}^∞ and D_1^∞ are describing the equilibrium curve after complete relaxation. For the simulation model a 60° 3D model of experiment is rebuilt as for example done in [4]. As for the simulation of the quasi-static push-out tests only loading and not unloading is considered, the simulation model of the nanoindentation is fitted only to the loading and holding part of the curve.

2.2.2 Single-fiber push-out test simulation

Simulations of the quasi-static push-out test are done to investigate the interface behavior and to determine interface model parameters. The simulation model can be seen in Figure 3. The indented fiber is surrounded by matrix material in which are embedded other fibers. The matrix is embedded in composite material. The diamond indenter tip is modelled as a rigid body, as diamond has a very high stiffness in comparison to glass fibers. The glass fibers are modelled as isotropic linear elastic with a Young's modulus of 73 GPa and a Poisson's ratio of 0.22. The matrix model and parameters are taken from the nanoindentation simulation. The fiber-matrix interface is modelled by cohesive

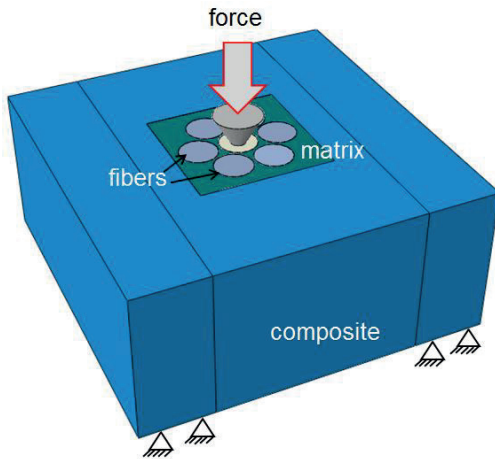


Figure 3: simulation model of single-fiber push-out test.

zone contacts with an uncoupled traction separation law. A quadratic stress criterion is used for damage initiation. The damage evolution is described by a power law form and linear softening. The parameters to adjust are the stiffness, the fracture toughness and the interface strength. The stiffness is a numerical value, the fracture toughness is determined from cyclic push-out tests and the strength is finally adapted on the quasi-static experimental push-out curves.

3 Results

The experimental nanoindentation force displacement curve with the fitted simulation curve for the loading and holding part is depicted in Figure 4 on the left. The resulting matrix model parameters are given in Table 1.

Table 1. Matrix material model parameters.

C_{10}^∞	D_1^∞	i	\bar{g}_i^P	\bar{k}_i^P	τ_i in s
724 MPa	0.01 1/MPa	1	0.13	0.11	2.9
		2	0.04	0.17	10
		3	0.009	0.22	720

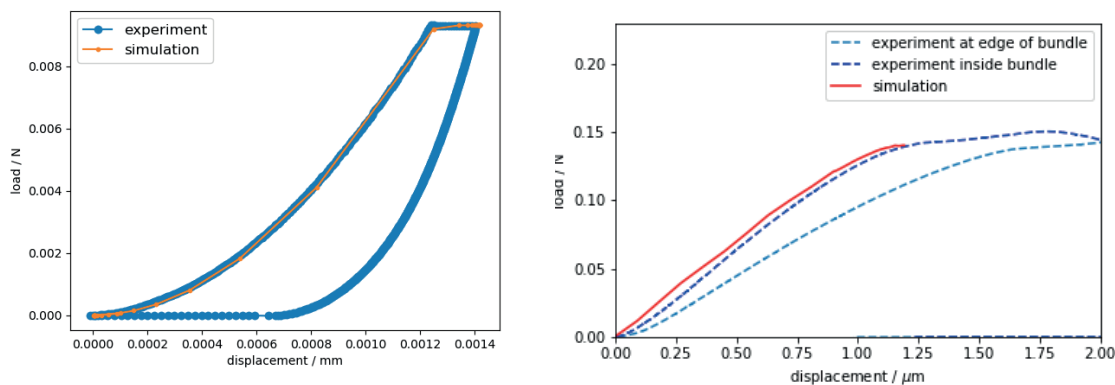


Figure 4: experimental and simulation results of nanoindentation (left) and push-out test (right).

The resulting fracture toughness from the cyclic push-out tests for 13 tested fibers is $107 \pm 20 \text{ J/m}^2$. For the push-out simulations a fracture toughness value for the interface of 107 J/m^2 is used. In Figure 4 (right) can be seen the experimental and simulation results for the push-out test. The simulation model, which models a fiber inside a bundle, can be adjusted with an interface strength of 70 MPa in normal and shear directions to the experimental curve of a fiber inside a bundle. The experimental curve of a fiber at the edge of a bundle shows a lower slope.

The slight shift between experiment and simulation can be explained by the fact that the surfaces in

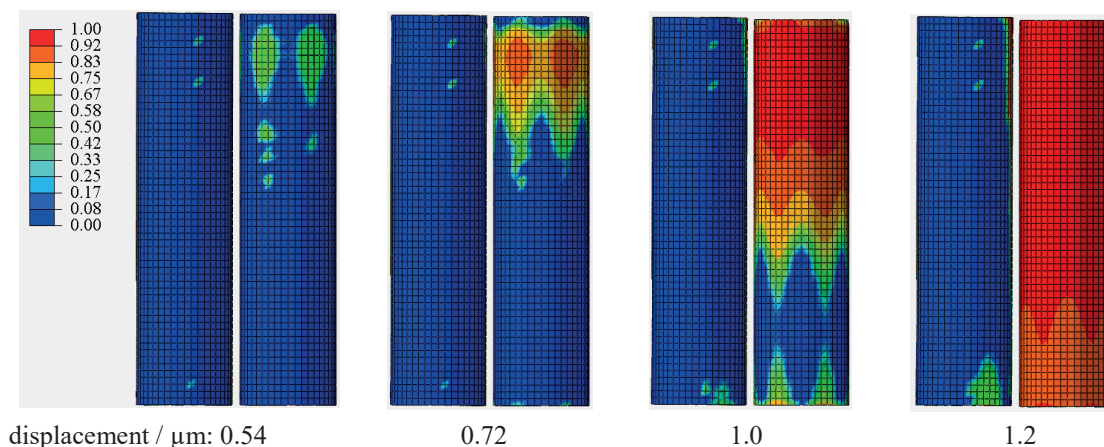


Figure 5: Interface damage evolution (0 undamaged, 1 completely damaged) for different displacements, indented fiber always on the right side, only one neighboring fiber is shown.

the simulation model between indenter tip and fiber are completely flat, while the fiber surface in experiment is slightly concave and there is no complete contact at the beginning of the test. The interface degradation for increasing displacements is shown in Figure 5. It can be seen a higher interface degradation where fibers are close together. The interface is not only damaged at the pushed-out fiber but also at the neighboring fibers.

4 Conclusion

The single-fiber push-out test could be investigated in experiment and simulation with an hyperelastic viscous matrix material model. The matrix model is calibrated on nanoindentation experiments with FEM-simulations. The push-out simulation model can be adapted to get a good agreement between experiment and simulation until the maximum force, even if there is a small shift in displacement because the concave fiber surface in experiment is not modelled. What cannot be modelled is the successive push-out behavior after the maximum force. In the simulation the interface is nearly destroyed at the maximum force. What might be added to simulation are production induced residual stresses due to temperature cooling and curing which are present in experiment.

5 Acknowledgement

The research documented in this manuscript has been funded by the German Research Foundation (DFG) within the International Research Training Group “Integrated engineering of continuous-discontinuous long fiber-reinforced polymer structures” (GRK 2078). The support by the German Research Foundation (DFG) is gratefully acknowledged. The support of David Bücheler and Sergej Ilinzeer (Fraunhofer Institute for Chemical Technology) for the UPPH SMC based composite production is appreciated.

6 References

- [1] B. Brylka, F. Fritzen, T. Böhlke, K.A. Weidenmann, *Proc. Appl. Math. Mech.* 11, 141 – 142 **2011**.
- [2] Z. Chen, S. Diebels, *Technische Mechanik*, 34, 3-4, **2014**, p. 166 – 189.
- [3] S. Fliegner, *Micromechanical finite element modeling of long fiber reinforced thermoplastics*, Fraunhofer Verlag, Stuttgart, **2016**.
- [4] M. Hardiman, *Nanoindentation characterisation of carbon fibre reinforced plastic microstructures*, University of Limerick, **2016**.
- [5] G. A. Holzapfel, *Nonlinear Solid Mechanics: a continuum approach for engineering*, John Wiley & Sons, Chichester, **2000**.
- [6] J. Jäger, M.G.R. Sause, F. Burkert, J. Moosburger-Will, M. Greisel, S. Horn, *Composites: Part A* 71, **2015**, p. 157–167.
- [7] J. Moosburger-Will, M. Greisel, M. Schulz, M. Löffler, W.M. Mueller, S. Horn, *Composite Interfaces*, **2019**.
- [8] P. Pinter, *Microstructure characterization of continuous-discontinuous fibre reinforced polymers based on volumetric images*, KIT Scientific Publishing, Karlsruhe, **2018**, p. 42.
- [9] W.M. Mueller, J. Moosburger-Will, M.G.R. Sause, S. Horn, *Journal of the European Ceramic Society* 33, **2013**, p. 441–451.

Surface hybridisation of semi-porous particle foams

W. Koshukow¹, M. Stegelmann¹, M. Krahl¹, M. Gude¹, L. Enneking², C. Buske²

¹Institute of Lightweight Engineering and Polymer Technology (ILK), Technische Universität Dresden, Dresden,

²Plasmatreat GmbH, Steinhagen

Abstract

Plasma treatment is a reliable technology for the activation of plastic surfaces. Surface modifications are evaluated with the aid of surface energy measurement, which in turn provides a basis for the derivation of adhesive potential. Sufficient adhesion is a prerequisite for the manufacturing of over-moulded structures.

The work presented in this paper investigates hybrid structures consisting of a semi-porous expanded polypropylene (EPP) particle foam core and an overmoulded layer of polyurethane (PU). Since the level of adhesion between EPP and PU is insufficient for an adequate level of bonding, it is necessary for the surface of the EPP to be modified with the aid of atmospheric plasma treatment (APT). APT and evaluation by means of contact angle measurement both reach their limits when applied to EPP due to the material's thin-walled foam structure and uneven surface. Specially adapted APT parameters are therefore required in order to ensure that adequate bonding between the EPP and the PU is achieved without compromising the physical integrity and visual appearance of the surface.

The new approach proposed in this paper uses surface energy determination on both homogenised and semi-porous EPP in order to analyse the transferability of plasma surface modification in EPP. Within the final step the relationship between surface activation, contact angle and adhesion was demonstrated using the floating roller peel test.

Keywords: *particle foam, expanded polypropylene (EPP), surface treatment, atmospheric plasma treatment (APT), polyurethane (PU), contact angle, surface energy, floating roller peel test*

1 Introduction

Particle foams are a well-established industrial material due to the potential offered by their hollow lightweight design and shaping versatility. The spread of the use of particle foams such as EPP is also attributable to their good insulation properties, high energy absorption rates and individually adjustable densities [1].

The manufacturing process for standard EPP generally results in a surface quality that is insufficient for Class-A surfaces (fig. 1a and 1b). Additional surface layers such as coating films are therefore typically required in order to seal and embellish the surface. In view of these developments, over-moulding of components with clear polyurethane systems represents an opportunity to protect the surface while also maintaining the desired appearance of the individualised structure. Pre-treatment of the low-energy surface of the EPP is nevertheless required in order to achieve sufficient chemical bonding between the particle foam and the polyurethane.

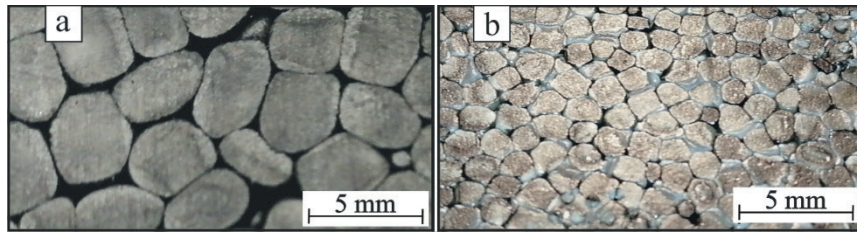


Figure 1: Surface of two particle foams: a) 50 kg/m³; b) 100 kg/m³

Plasma pre-treatment is a technologically and economically efficient means of increasing the strength of the bond between the surface and the coating [2]. A number of studies have already demonstrated the improvements in adhesion achievable by adjusting a variety of APT parameters. The evaluation of those improvements involves the use of surface energy measurements, mechanical pull-off tests and shear tests [3, 4]. Sufficient bonding with low-energy surfaces such as polypropylene (PP) or polyethylene (PE) – both of which are components of EPP – is dependent on a minimum surface energy of 38 mJ/m² [2]. Non-expanded PP and PE have surface energies of 31-32 mJ/m² [6], while the surface energy of EPP is approx. 23 mJ/m² [3]. The actual difference in surface energy depends on the composition of the particle foam in question, and in particular any additives used and their effect on the expansion process. It is assumed that thin-walled pore structures react to APT in a different way.

Plasma parameters characterised by high energy input, slow feeding rates and close nozzle position lead to visible and physical damage to the surface and are therefore unsuitable for the pre-treatment of EPP. Standard, non-material-specific parameter sets can also be disregarded as they do not exploit opportunities to use material-specific properties to achieve optimum bonding strength. As such, it is necessary to identify adapted plasma parameters that maximise adhesive quality without affecting the appearance of the foam. A qualitative means of using surface energy measurement to characterise the impact of APT is therefore required.

The measurement of the surface energy of EPP is difficult due to the pores and unevenness of its surface. Surface energy measurements therefore need to be carried out in sections where surface particles are large and closed. Despite being a technical possibility, this approach is prone to failure in the case of EPP with a low density of around 50 kg/m³ since surface conditions lead to an uneven formation of the test liquid droplets (fig. 2a) and amplify the amount of experimental effort required. An increase in density (to 100 kg/m³) nevertheless results in a decrease in particle size and an increase in the micro pore content of the surface, thus preventing reproducible measurements (fig. 2c).

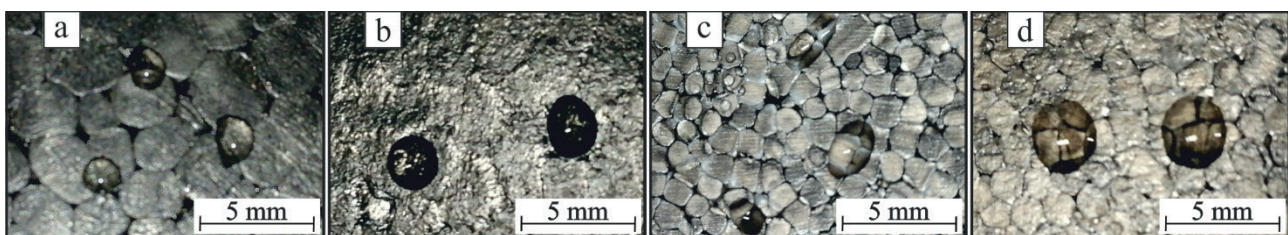


Figure 2: Drop shape on semi-porous surfaces a) and c) and homogenised surfaces b) and d)

A new approach to the determination of the surface energy of EPP was investigated with a view to ensuring reliable, efficient measurements. It was found that the surface of the particle foams could be homogenised by means of a gentle compression process without causing any significant change in density. The homogenised surfaces allowed the execution of the required measurements in accordance with DIN EN 828 (fig. 2b and 2d).

This paper describes a method for the indirect determination of the surface energies of particle foams and discusses associated possibilities and limitations.

2 Investigation

2.1 Materials and procedure

The low-density EPP “ARPRO A5635” (ARPRO) (fig. 1a) was selected for the experimental studies. The higher-density EPP “ASAHI KASEI Sunforce” (Sunforce) (fig. 1b) was also investigated in order to assess the transferability of the new method. Sunforce consists of a mixture of PP, PE and polyphenylene ether (PPE), whereas ARPRO only contains PP and PE. The two materials are referred to jointly as “EPP” in the following.

The surface of the EPP was homogenised (hEPP), pre-treated using APT and characterised with the aid of a contact angle measurement instrument (CAMI). The results were used to select the best APT parameters for the pre-treatment of the EPP. The subsequent overmoulding of the EPP with PU was followed by the determination of peel resistance using floating roller peel tests (fig. 3).

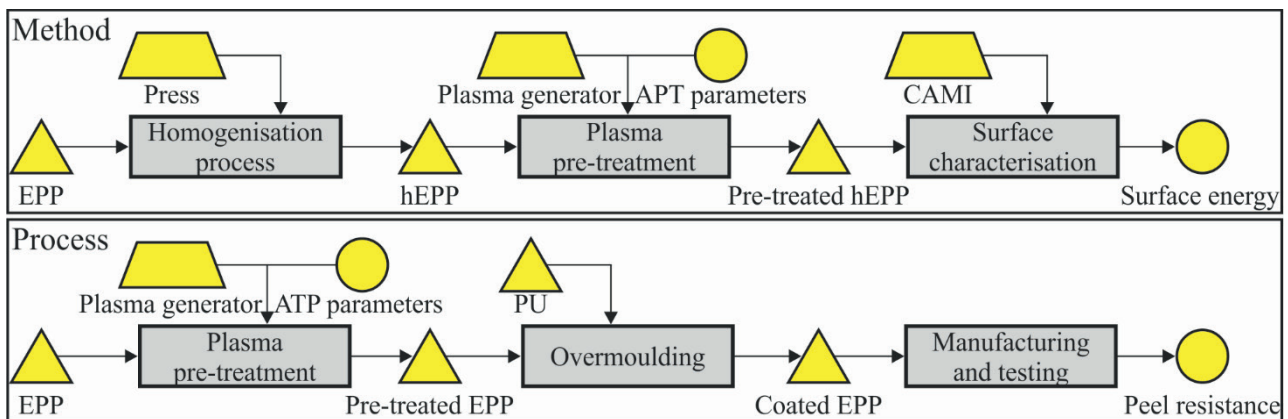


Figure 3: General methodological procedure and process diagram

2.2 Homogenisation process

A 4-stage compression process was used to achieve a plane EPP surface. The compression plates and the surface of the EPP were cleaned and degreased using isopropanol in order to avoid any contamination during the compression process. Each homogenisation process saw one pair of test specimens (dimensions: 120x80x16 mm) heated to 150 °C by the heated plates and compressed at a constant load of 2 kN for 1 minute. Homogenisation was carried out with the aid of a RUCKS laboratory press. The resultant surface was even and exhibited a significant 95 % reduction in bubbles and porous defects (fig. 2b and 2c).

One of the effects of surface homogenisation was a reduction in specimen thickness equivalent to the increase in local near surface density. The effect was greater in the case of ARPRO (final thickness: 8 mm) than in the case of Sunforce (final thickness: 13 mm).

2.3 Surface treatment

The selection of the APT parameters for the investigation was based on a literature review [7], previous experience gained at the ILK [8, 9], process window recommendations given by Plasmatreat GmbH, technical capabilities and economic factors. Reproducible results were achieved by setting up a robot-guided apparatus for the plasma treatment process. Generator FG5001 was used in combination with nozzle RD1004. Focus on a single influencing factor was ensured by only varying the distance between the nozzle and the surface. Frequency (21 kHz), plasma cycle time (100 %),

ionisation gas flow rate (45 l/min), nozzle rotation speed (2600 min⁻¹) and movement speed (10 m/min) remained constant. The various sets of APT parameters applied are listed in table 1. All parameters are subdivided into preselection parameters for the measurement of the surface energy of the homogenised substrate (Pre.) and final parameters for the floating roller peel tests (Fin.). The reference surface energy without APT was also determined (ARPRO: Ref. D1; Sunforce: Ref. D2).

Table 1: APT sets

	Pre. V1D1	Pre. V2D1	Pre. V1D2	Pre. V2D2	Fin. D1	Fin. D2
Distance [mm]	18	6	18	6	16	6
Density [kg/m ³]	50	50	100	100	50	100

2.4 Surface characterisation

The effect of APT was determined with the aid of contact angle measurements using the “Dataphysics OCA 15 EC” contact angle measuring instrument. Each test liquid contained different polar and dispersion components (water, diiodomethane and ethylene glycol). 10 drops of each liquid were applied to the APT-treated surface. The impact of drop settling on the measurement was minimised by measuring the contact angle 10 seconds after drop application. The polar and dispersion components of the hEPP surfaces were calculated using the Owens, Wendt [10], Rabel [11] and Kaelble [12] model and compared with the Young equation. The results are shown in figure 4.

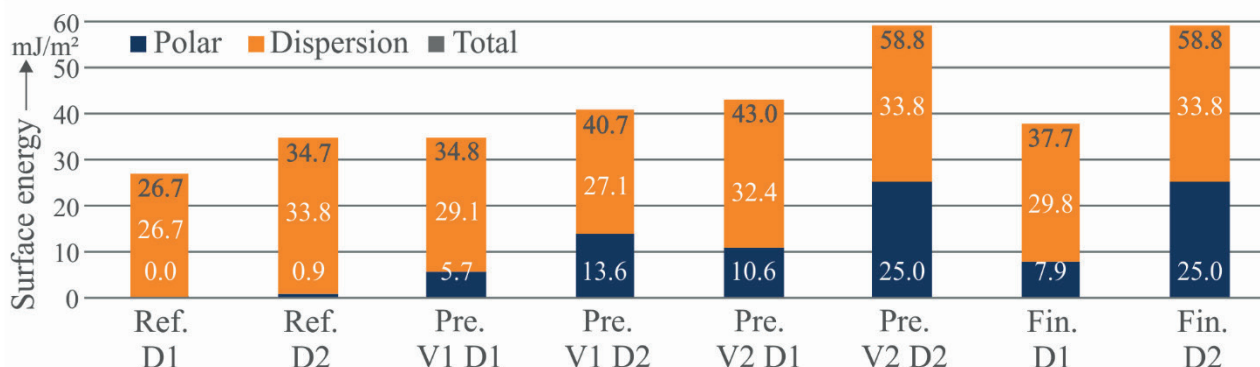


Figure 4: Surface energy and polar/dispersion components for different APT parameters

The results show the effect of APT as a function of the respective increase in surface energy. The increase in polar components shows that better results can be achieved by reducing the distance between the nozzle and the material.

The APT parameters for Sunforce can be transferred directly from hEPP to EPP. It is therefore assumed that surface energy measurements can also be transferred. This verifies the suitability of the method for high-density EPP.

ARPRO behaves differently, with the best set of parameters (Pre. V2D1) causing unacceptable damage to the surface of the EPP. It was for this reason that nozzle distance was increased until no surface damage occurred (Fin. D1). The resultant difference of 10 mm dictates that the transferability of results between hEPP and EPP is significantly lower in this case. This lack of transferability is attributable to the effect of compression during homogenisation. Higher material densities enable a reduction in the distance between the nozzle and the surface during APT, thus leading to a higher surface energy level.

2.5 Specimen manufacturing, floating roller peel tests

Floating roller peel tests were preceded by the overmoulding of a PU layer onto all specimens within an hour after APT. This approach ensures optimum bonding due to the dependence of plasma pre-treatment on ageing time [7]. The surface of the specimens was cleaned and degreased using isopropanol prior to overmoulding. The Rühl Puromer GmbH product “puopreg 185 LT IT” was selected as the overmoulding material. The coating was hand mixed before being applied to the surface.

For the subsequent curing process the specimens were stored at room temperature for 7 days. The PU layer was then sanded and bonded to a metal peel strip using a 2-component epoxy adhesive (Scotch-Welt DP490). A diagram of the bonding structure is provided in figure 5a. The width of the test specimen was set at 16 mm in order to reflect available manufacturing capabilities.

Uniform test conditions were ensured by storing all specimens in standard climatic conditions (23 °C, 50 % relative humidity) for a period of 24 hours prior to the test. The test itself was performed on a Zwick/Roell 1465 universal testing machine. Forces were measured over a distance of 200 mm at a travel speed of 100 mm/min and a preload of 5 N.

Examples of the results of the floating roller peel test are provided in figure 5b. It is noticeable that the materials tested performed differently depending on their chemical composition and mechanical surface structure. Sunforce failed at a peeling force of 17.62 N/mm ($\sigma = 6.01$), whereas the lower-density ARPRO failed at 6.19 N/mm ($\sigma = 3.03$). Monitoring of failure behaviour during the peeling process found adhesion delamination to occur between the PU and the EPP throughout the peel distance (fig. 5c and 5d). As the particle foams consist mainly of PP and PE, it can be assumed that surface texture was a significant factor in the difference between the peel forces observed. The higher number of smaller pores and greater unevenness that characterise the surface of the Sunforce material are conducive to mechanical undercutting and the strengthening of the bond between EPP and PU.

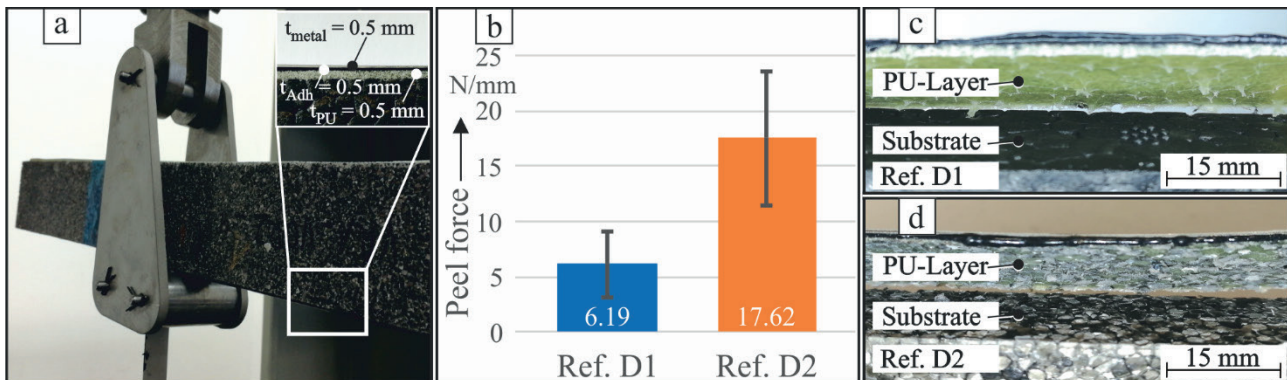


Figure 5: a) Test set up; b) Examples of the results of the floating roller peel test (carried out in accordance with DIN EN 1464); c), d) Failure pattern

Contrary to expectations, it was the consistent failure of the adhesive bond between the PU layer and the metal peel strip – and not the adhesive bond between the EPP and the PU – that caused all APT-treated specimens to fail the floating roller peel test. The increase in the strength of the bond between the PU and the APT-treated EPP indicates a shift in the fracture pattern. Although the accurate determination of the peel resistance of APT-treated EPP requires a specially adapted test setup, the variation of the adhesive used is not advisable due to the fact that the selected adhesive system possesses very good mechanical properties. It may be possible to improve the test setup by embedding the metal peel strip directly into the PU layer. Further investigation into the process flow and interaction mechanisms is nevertheless required.

3 Conclusion

The surface energy of semi-porous EPP is difficult to determine using contact angle measurements as described in DIN EN 828. A new approach was therefore investigated. In the case of high-density EPP in particular, the method under investigation proved to be a reliable and reproducible means of determining surface energy. It was possible to transfer the APT parameters for the Sunforce material directly from the homogeneous test surface to the EPP surface. The method therefore appears to be an adequate means of determining the surface energy of homogenised surfaces at this density.

In the case of the lower-density EPP, it was necessary to adjust the plasma parameters for the homogenised surface in order to prevent the surface from being burned by the plasma jet. It can be assumed that this issue is attributable to the compaction of the surface during the compression process. As a result, it may be possible to apply more intensive pre-treatment parameters without damaging the surface. This assumption is supported by the very large deviation from the parameters that can actually be applied.

Future work in this field needs to provide further evidence of the suitability of the method at hand by testing it in combination with particle foams of a variety of densities. The homogenisation process also needs to be improved in order to minimise the compression effect.

A significant difference in the peel resistance of the two material variants was observed. The fact that the base material was identical means that chemical bonding can be ruled out as a potential cause of the differences in their adhesive properties. It can be assumed that the cellular structure of an expanded plastic foam surface offers an advantage where bonding strength is concerned. An increase in density leads to a greater number of particle interspaces in the surface, which in turn results in an increase in peel resistance due to the higher degree of mechanical micro interlocking.

The pre-treatment of EPP using APT facilitates enhanced adhesion to PU systems. Despite the use of a variety of different adhesive systems, the consistent failure of the adhesive bond between the metal peel strip and the PU layer prevented the execution of any adhesion tests using the test setup described in this paper. It may be possible to eliminate this issue by embedding the metal peel strip directly into the PU layer.

4 Literature

- [1] M. Gude, H. Lieberwirth, G. Meschut, M.F. Zäh, E. Tekkaya, in *Plattform FOREL Bericht*, **2018**
- [2] S. Ebnesajjad, *Surface Treatment of Materials for Adhesive Bonding*, **2014**
- [3] P. Schreier, C. Tassl, V. Altstädt, in *AIP Conference Proceedings 1593 (378)*, **2014**
- [4] E. Moritzer, C. Leister, T. Nordmeyer, *J. Plast. Technol.*, **2015**, 11, 4
- [5] N. Encinas, J. Abenojar, M.A. Martinez, *Int. J. Adhes.*, 33, **2012**, 1–6
- [6] D.K. Owens, *Int. J. Polym. Sci.*, **1970**, 14, 1725
- [7] R. Wilken, H. Gleich, C. Buske, et. al., *Kunststoffe erfolgreich kleben*, **2018**, p. 84
- [8] A. Liebsch, R. Kupfer*, M. Krahl, D. R. Haider, W. Koshukow, M. Gude, in *Hybrid Materials and Structures*, **2018**
- [9] A. Liebsch, W. Koshukow, J. Gebauer, R. Kuper, M. Gude, in *2nd CIRP Conference on Composite Material Parts Manufacturing*, **2019**
- [10] W.K. Owens, R. C. Wendt, *J. Appl. Polym. Sci.*, 13, **1969**, 1741–1747
- [11] W. Rabel, *Farbe und Lack*, **1971**, 77 (10), 997–1005
- [12] D.H. Kaelble, *J. Adhes.*, 2, **1970**, 66–81

On fiber orientation statistics for woven fabrics in fiber metal laminates

P. Pinter¹, H.O. Werner², K.A. Weidenmann³, W. Liebig²

¹Volume Graphics GmbH, Heidelberg, ²KIT - IAM-WK, Karlsruhe, ³Augsburg University - MRM, Augsburg

1 Introduction

A common trend in material research and development is hybrid composites—for good reason. While bulk materials are limited to their bulk properties, a smart combination of bulk materials can exceed these limitations by far. This is the case if there are multiple unrelated functions the material must fulfill. In this contribution, the authors focus on fiber-metal-laminates (FML) manufactured by a combination of deep drawing and thermoplastic resin transfer molding (T-RTM) [1]. The reactive resin system is injected between the metal blanks and infiltrates the woven fabric while the deep drawing process. When the deep drawing process is completed, the matrix polymerizes to a thermoplastic and forms the interface to the metal sheets, as shown in Fig.1. Utilizing this process, hybrid laminates of woven glass fiber and steel blanks are manufactured. Expected benefits of the hybrid composite compared to its constituents are better impact and fatigue properties, which are well known and investigated for glass laminate aluminum reinforced epoxy (GLARE) [2], [3]. Moreover, the hybrid T-RTM process leads to a higher freedom of design, lower cycle times in production, and better subsequent forming behavior as well as recyclability compared to GLARE.

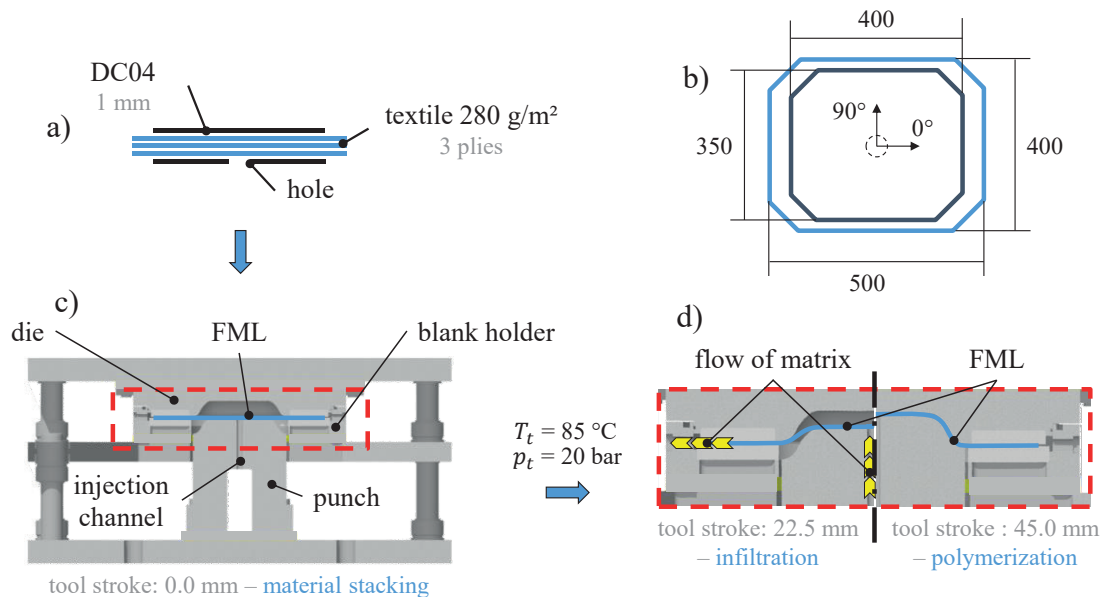


Figure 1: Process flow of combined deep drawing and injection process [5]. a+b) Principle of FML layup is a sandwich construction with metal blanks as face sheets and thermoplastic reinforced woven fabrics as intermediate layer. b+c) The tool holder clamps the structure and the composite is deep-drawn by the punch while the polymer is injected.

To simulate the deep drawing process, a draping simulation is implemented and applied [4], [5]. X-ray computed tomography is used to validate these results by acquiring volumetric images of a demonstrator part for the orientation analysis of draped fibers. Especially for woven fabrics, there are some challenges that have to be considered: First, samples must be sufficiently large to cover a region of interest that represents the surrounding woven fiber material. This requires a very robust orientation analysis, as the image resolution decreases with increasing sample size. Second, some orientation statistics (e.g., the orientation tensor of 2nd order) are not reasonable for this kind of structure. Thus, the main orientations of local orientation histograms are analyzed by using VGSTUDIO MAX 3.3 to compare them with forming simulations in a latter step. It is shown, that large samples with a length

of around 140 mm can be processed to evaluate local fiber orientation by means of computed tomography.

2 Fiber orientation analysis based on computed tomography

2.1 Basics

Whether short, long or continuous fiber reinforced polymers, micro computed tomography (μ CT) based microstructure characterization does usually start on the lowest scale possible – on the voxel level. Considering the local neighborhood of each voxel, it is possible to determine a local orientation, even though the full path of each fiber is not known. In VGSTUDIO MAX, the local neighborhood is defined by the “Integration Radius” parameter within the Fiber Composite Material Analysis (FCMA) settings. Depending on the available working memory, it can be reasonable to reduce the resolution of the FCMA analysis by the scale parameter. Values larger than one will run the analysis on a lower resolution and lead to a lower memory consumption. Setting the scale parameter lower than one will supersample the analysis results and hence increase the amount of memory needed.

2.2 Statistics

The in 2.1 mentioned parameters form the basis for orientation statistics since they give local discrete orientations at each point within the image. These local orientations can be depicted by a color overlay to verify the quality of an analysis. The color overlay enables to easily compare the evaluated orientation of a certain fiber with the visible orientation in the gray value image. Figure 2 shows the local fiber orientation coded by color on a woven glass fiber composite at a voxel resolution of 0.023 mm/voxel. Note that the resolution is lower than the fiber diameter of approximately 0.013 mm, what is true for all of the scanned samples within this contribution. The sample shown in Figure 2 a) is used for all statistics shown in section 2 of this contribution.

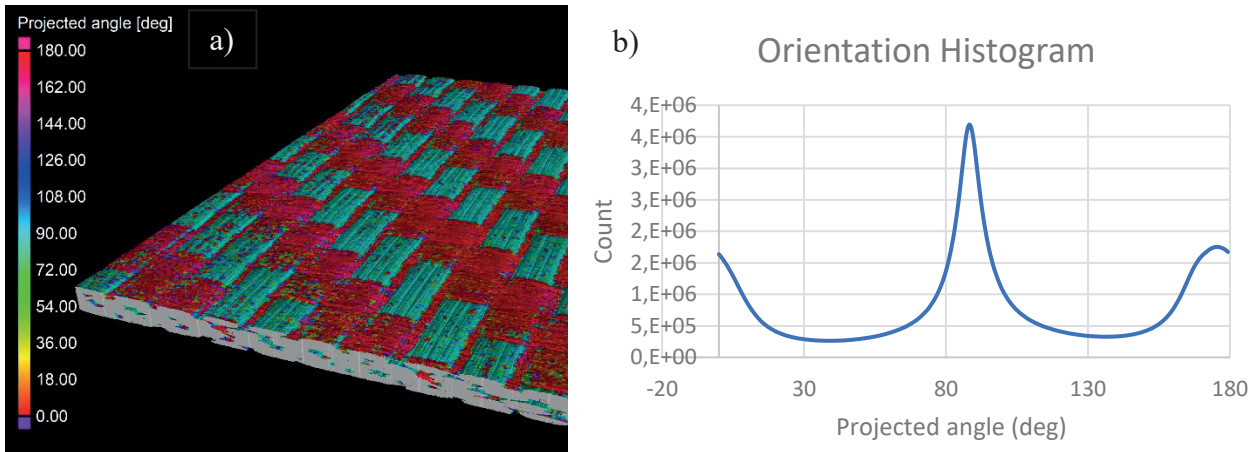


Figure 2: a) Evaluation of local fiber orientation coded by color. This is the basis for all following statistics. b) Orientation histogram of the data in a). The orientation distribution is bi-modal due to the woven structure.

2.2.1 Global or local statistics

Fiber orientation statistics can be evaluated either globally on the entire dataset or locally by various concepts. For local approaches, the dataset can be separated in multiple regions. A very simple method are regular integration meshes, which can be defined if samples have the shape of a cuboid. The integration mesh can be selected within the FCMA to calculate e.g. an orientation tensor and the fiber volume content within each mesh cell. Figure 3 shows an example of a regular integration mesh. If the geometry of the sample is more complex, it can be useful to import volume meshes to map the mentioned features on each cell. In VGSTUDIO MAX 3.3, it is even possible to import meshes consisting of shell elements and to define a thickness of the elements or even define multiple cells over

thickness. But local statistics can also be calculated without a mesh along a certain direction, if the orientation should be plotted over thickness of a plate. This is a common method for injection molded parts to validate flow simulations, but it can also be helpful for characterizing lay-ups.

2.2.2 Orientation Tensors

Orientation tensors have been introduced for describing fabrics statistically by Kanatani in 1984 [6]. A similar concept was applied for mechanical models by Advani and Tucker in 1987 [7]. The “empirical” orientation tensor of 2nd order is defined by

$$\mathbf{N} = \frac{1}{k} \sum_{i=1}^k \mathbf{n}_i \otimes \mathbf{n}_i = \frac{1}{k} \sum_{i=1}^k \mathbf{n}_i \cdot \mathbf{n}_i^T. \quad (1)$$

In the following, n is assumed to be a normalized vector pointing in fiber direction at an arbitrary position within the dataset. Depending on the type of input, k can e.g. represent the number of fibers by using microscopic images or in case of volumetric data, the number of voxels belonging to fiber material. As the information that can be stored by an orientation tensor of 2nd order is limited compared to a detailed statistic, it can only represent unimodal orientation distributions. The 2nd order tensor is usually illustrated by an ellipsoid in three dimensional (3D) (see orange ellipsoids in Figure 3 a)).

2.2.3 Orientation Histograms

As 2nd order orientation tensors are limited to unimodal distributions, orientation histograms describing the quantity of fiber voxels oriented in a certain orientation (Figure 2 b)) are the statistic of choice for woven fabrics. This is due to the fact that orientation distributions of woven fabrics are multimodal in most cases and will lead to a planar-isotropic configuration. To illustrate this problem, an orientation tensor can be calculated from two orientations of fibers that are perfectly aligned to the coordinate system. Assuming that both of the fibers have the same length and diameter, two normalized perpendicular vectors can be used:

$$\mathbf{n}_1 = \begin{pmatrix} 1 \\ 0 \\ 0 \end{pmatrix} \text{ and } \mathbf{n}_2 = \begin{pmatrix} 0 \\ 1 \\ 0 \end{pmatrix}. \quad (2)$$

The fiber orientation tensor of 2nd order is calculated based on the orientations \mathbf{n}_1 and \mathbf{n}_2 by using eq. 1 leading to a tensor representing a planar-isotropic orientation distribution:

$$\mathbf{N} = \frac{1}{2} * \begin{pmatrix} 1 & 0 & 0 \\ 0 & 0 & 0 \\ 0 & 0 & 0 \end{pmatrix} + \frac{1}{2} \begin{pmatrix} 0 & 0 & 0 \\ 0 & 1 & 0 \\ 0 & 0 & 0 \end{pmatrix} = \begin{pmatrix} 0.5 & 0 & 0 \\ 0 & 0.5 & 0 \\ 0 & 0 & 0 \end{pmatrix} \quad (3)$$

Thus, orientation histograms are used in the present contribution as a basis for determining the principal orientations of the woven fabric.

2.2.4 Principal Orientations

Orientation histograms provide much information because a quantity has to be stored for each bin over all orientations. This leads to huge amount of data if the orientation distribution is not carried out on the entire sample but on a FE-mesh. In this case it can be advantageous to process each local histogram and to store only principal orientations for each mesh cell. This option is available in the “layered integration mesh” mode of the FCMA. Moreover, the angular difference ϕ is calculated by the difference between the two highest peaks of the orientation histogram. If there is only one peak within the histogram, it is not possible to evaluate this feature resulting in a “not available (n/a)”

output. In order to validate drupe simulations of woven fabrics, the shear angle λ of the material is an important feature. It can be calculated from the angular difference ϕ by

$$\lambda = 90^\circ - \phi. \quad (4)$$

Figure 3 shows an analysis on a woven fabric including the local histograms in yellow while the angular difference is coded by color and the orientation tensors are depicted in orange. It can be seen that the orientation tensor does not provide information to calculate the angular difference.

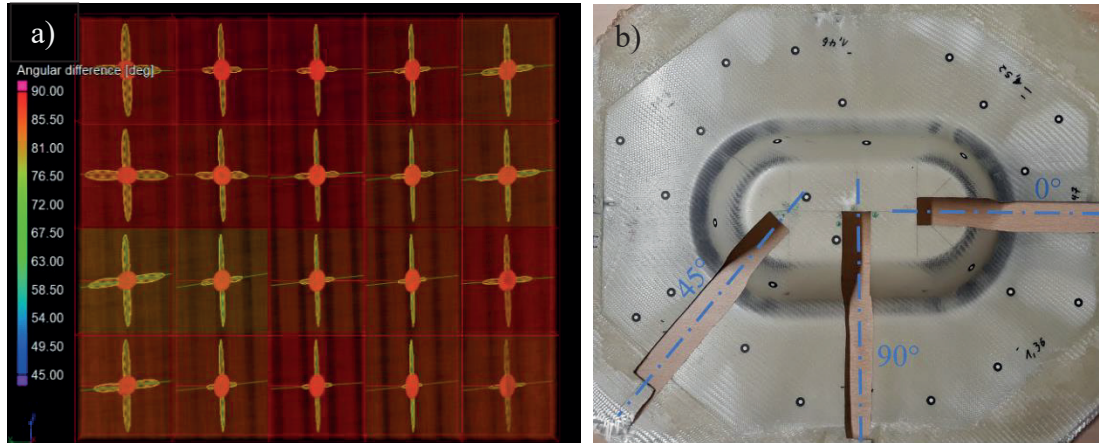


Figure 3: a) Orientation analysis shows the angular difference coded by color, the local orientation histograms in yellow and the orientation tensors in orange. Note that the local histograms show the bi-modal orientation distribution while the orientation tensors are unimodal. b) Entire double dome demonstrator part with cut out samples in 0° , 45° and 90° direction

3 Evaluation of the FML Double Dome Demonstrator

Orientation analyses are carried out on stripes of a deep-drawn part in order to determine the local shear angle. The laminates considered here consist of 1 mm DC04 steel sheets, three layers of 280 g/m² twill fabric 2/2 of E-glass fiber (Interglas 92125 FK800), which are orientated in either a (0/90) or (± 45) orientation and a 1:1 mixture of the acrylates Elium 130 and Elium 190 from Arkema S.A. with 2.5 % dibenzoyl peroxide from United Initiators is used as matrix. The plastic layers are removed from the metal blank to simplify the image acquisition, which can be quite challenging with materials of very different densities. Subsequently, stripes are cut from the part with a thickness of approximately 25 mm-30 mm to allow a sufficient resolution in the CT-scanner. For image acquisition, an YXLON Precision CT-scanner with a reflexion tube and tungsten target is used. The Perkin Elmer detector has a resolution of 2048 x 2048 at a pixel pitch of 0.2 mm. The sample at 45° is scanned with a voxel size of 0.023 mm in three steps along the rotational axis of the CT and stacked vertically. The other samples at 0° and 90° are stacked and scanned as a whole in three steps at the same voxel size. Figure 3 b) shows the sample extraction from the double dome demonstrator part. Note that the samples at 0° and 45° may overlap in the result because only a quarter of the sample was meshed and the samples are mapped on the same quadrant. This is valid due to the symmetry of the part.

Both samples at 0° and 90° have to be separated in a first step as they are included in the same volumetric dataset. Therefore, a coarse surface determination is carried out. This surface can be converted to a region of interest what enables to separate both samples easily. It is recommended to erode (shrink) these regions by one or two voxels to avoid edge effects in the further processing steps. The separated samples are aligned to the integration mesh, which is imported using the Nastran (*.bdf) file import. Since the mesh at hand uses shell elements, it is necessary to define a thickness of the mesh cells to include the entire data from the voxels. The samples are a little bit warped, so the thickness is set to 6 mm to include also the areas that would not be included using the exact geometry.

This has only minor influence on the result as there is only minor warpage. By using shell elements, it is also possible to create a certain number of cells over thickness and calculate the statistics separately. In the present case, the voxel size of the dataset is rather large and even larger than a fiber diameter. Also the part is relatively thin, so it does not make sense to apply the analysis on multiple mesh cells over thickness.

The fiber composite material analysis is carried out with a scale of 1.0 voxels, an integration radius of 1.0 voxels and a gradient threshold of 0. These parameters are used for all of the three samples. Within the FCMA properties, the imported mesh is selected and the angular difference is used as active column to use it as color coding in the resulting data. Finally, the features are exported in a .csv format.

4 Results and Discussion

With the above mentioned workflow, the angular difference is calculated and mapped to the FE-mesh using the three samples cut from the entire part. Figure 4 shows the final result. The 90° sample lead to angular differences between 90° and 80° so there is now significant shear deformation in this region. At the 0° sample, shear angles are also rather small, but the result is noisier – especially in the region of the surrounding rim of the part. The 45° sample shows a gradient in shear deformation over the sample, but there is a region where the angular difference is not calculated at all. Figure 5 illustrates the shear angle resulting from the process simulation that is performed in the multi-purpose finite element solver ABAQUS/EXPLICIT, based on an existing forming simulation framework developed at KIT-FAST [8], [9]. Results are in good correspondence to the CT analyses. But for the 45° sample, there are some areas where the angular difference is not calculated from the CT data (see Figure 4). Figure 5 b) gives detailed view into this region including the angular difference coded by color and the local histograms in yellow. Obviously, the angular difference was not evaluated as the orientation histogram is unimodal in this region and hence there is no second peak to calculate the angle. This problem stems from two different reasons: First, the image quality is less good at this position. This origins most likely from an inconvenient orientation of the region during the CT-scan. Unidirectional regions in fiber composites can cause minor image blur depending on the orientation and the trajectory of the CT-scanner relative to this region. Second, the shear angle is relatively small and peaks can easily overlap in the local histograms. Both effects led to the result in Figure 5 b). This problem can most likely be solved by doing the scan with another orientation of the sample.

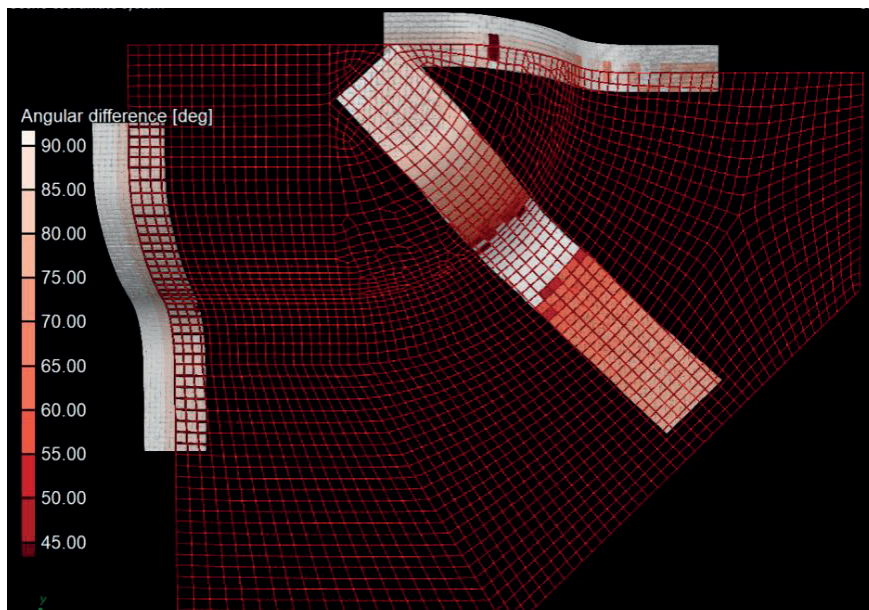


Figure 4: Angular difference of all investigated samples mapped on the FE-mesh.

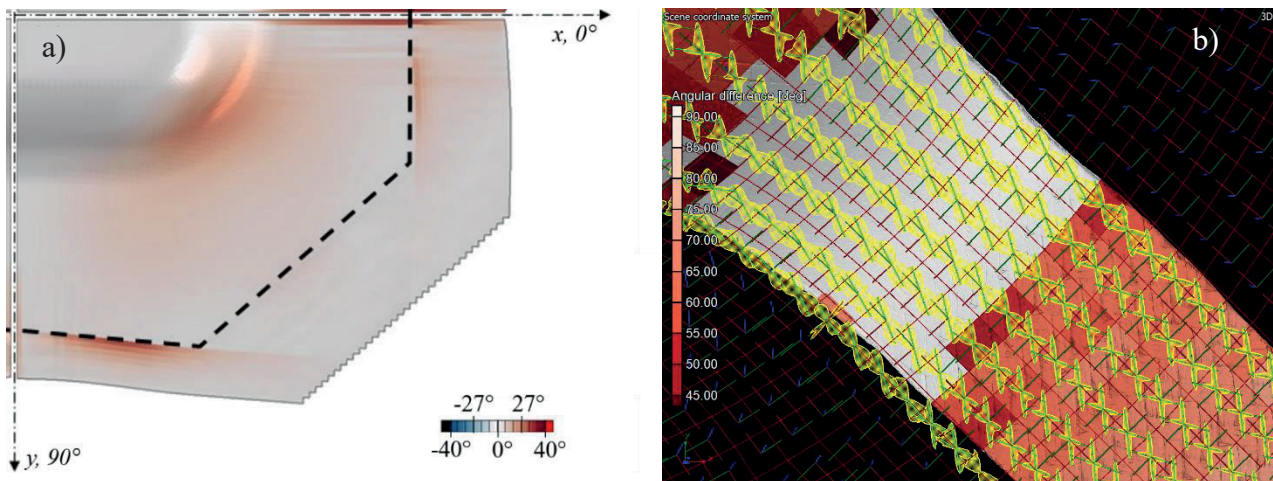


Figure 5: a) Simulation result of an ABAQUS simulation showing the shear angle coded by color. Note the definition of the shear angle in eq. 4. b) Local histograms and angular difference of the 45° sample. Local histograms became unimodal in the white areas and thus it is not possible to calculate an angular difference.

The angular differences in the 90° sample are very homogeneous and do not differ very much from the initial state of 90° . Whether the simulation nor the produced part indicates significant changes of the shear angle within this region. The sample at 0° leads a noisier result at the surrounding rim and a closer look to this region on the manufactured part shows that the woven fabric is kind of crumpled in this region. Thus, it is obvious that angular difference leads to noisy results when the angular differences are mapped in discrete regions of the mesh.

5 Summary and Conclusion

In summary it can be stated that computed tomography is a good tool to validate fiber orientation of drape simulations. The use of local orientation histograms and their principal orientations enables to derive shear angles of the fabric even from low resolution data with a voxel size larger than the fiber diameter. Nevertheless, depending on the quality of the scan and the architecture of the deformed woven fabric, there may occur some smaller regions where the shear angle of the simulation is not directly comparable to the results from CT-scans. These regions have to be identified and removed for the latter comparison.

Acknowledgements

The German Research Foundation (DFG) kindly supports this research project (WE 4273/13-1, WE 4273/13-2).

6 Literatur

- [1] T. Mennecart, H. Werner, N. B. Khalifa, K. A. Weidenmann, *Proceedings of the 13th Manufacturing Science and Engineering Conference (MSEC2018)*, Texas, USA, **2018**.
- [2] A. Vlot, J.W. Gunnink, *Fibre Metal Laminates: An Introduction*, Dordrecht, Springer Netherlands, **2001**.
- [3] E.C. Botelho, R.A. Silva, L.C. Pardini, M.C. Rezende, *Mat. Res.* **2006**, 9(3), 247–56.
- [4] H.O. Werner, D. Dörr, F. Henning, L. Kärger, *AIP Conference Proceedings*, **2019** 2113(1):20019.
- [5] H.O. Werner, C. Poppe, F. Henning, L. Kärger, *Pocedia Manufacturing* **2020**.
- [6] K. Kanatani, *International Journal of Engineering Science*, **1984**, 22.2, 149-164.
- [7] S.G. Advani, C.L. Tucker III, *Journal of rheology*, **1987**, 31.8, 751-784.

- [8] D. Dörr, W. Brymerski, S. Ropers, D. Leutz, T. Joppich, L. Kärger et al., *Procedia CIRP*, **2017**, 66, 101–6.
- [9] D. Dörr, F. Henning, L. Kärger, *Composites Part A: Applied Science and Manufacturing*, **2018**, 109, 585–96.

Microstructure characterization of discontinuous fiber-reinforced polymers based on volumetric images: Fiber bundle tracking and weld line investigation

L. Schöttl^{1,*}, W. V. Liebig^{1,4}, K. A. Weidenmann^{2,4}, K. Inal³, P. Elsner^{1,4}

¹Karlsruhe Institute of Technology, Institute for Applied Materials (IAM-WK), Karlsruhe, Germany

²University of Augsburg, Institute of Materials Resource Management, Augsburg, Germany

³University of Waterloo, Department of Mechanical and Mechatronics Engineering, Waterloo, Canada

⁴Fraunhofer Institute for Chemical Technology (ICT), Pfinztal, Germany

*corresponding author, Email address: ludwig.schoettl@kit.edu (Ludwig Schöttl)

Abstract

Discontinuous fiber-reinforced polymer hybrids (DicoFRP), such as sheet molding compounds (SMC) show many positive aspects like great process capability, low costs and good specific mechanical properties. As a result, the SMC material systems meets both, lightweight and mass production criteria. The microstructural architecture significantly affects the macroscopic mechanical properties of hybrid material systems. Consequently, methods for analyzing the microstructure in detail are essential for characterizing and predicting the DicoFRP behavior on the macroscopic scale. Volumetric images acquired by X-ray micro-computed tomography systems (μ CT) and image processing tools allow a three-dimensional characterization of composite microstructures in a non-destructive way. However, the limits of X-ray cone beam μ CT systems caused by the conflict between scanned volume and resulting image resolution have to be considered. In order to segment all individual fibers, volumetric images with sufficient high resolution are necessary and consequently, only small specimen volumes are analyzed. However, due to the SMC manufacturing process fibers are arranged as mesoscopic bundles within SMC components. To overcome the cone beam μ CT related conflict between the scanned volume and image resolution, this contribution applies a method to characterize the microstructure based on fiber bundles, instead of the individual fibers.

In cooperation with the research areas design and technology of the International Research Training Group "Integrated engineering of continuous-discontinuous long fiber reinforced polymer structures" (GRK 2078), the microstructure within a generic SMC component are characterized. In particular, the analysis of weld line microstructure is in the focus of interest.

Keywords: Sheet Molding Compounds, Fiber Bundle Characterization, Computed Tomography

1 Introduction

The microstructural fiber architecture of fiber-reinforced polymers (FRP), including fiber volume content and fiber orientation, significantly affects the macroscopic properties, such as stiffness (cf. [11]). Consequently, valid prediction models and characterizing methods of FRP microstructures are essential (cf. [1, 12]).

Micro-computed tomography systems (μ CT) obtain volumetric images of microstructures in a non-destructive way. There is a wide range of different image processing methods to characterize the microstructure of FRP based on volumetric images. A method for determining the local fiber orientation using volumetric images without identifying individual fibers by means of an anisotropic Gaussian filter is introduced by the authors Schladitz et al. [2]. The method is applied onto samples of polyester based sheet molding compounds (SMC). Another method for determining local fiber orientation without segmenting individual fibers is presented by the authors Pinter et al. [3]. The authors Pinter et al. determine the fiber orientation by means of the structure tensor, which is introduced by the authors Krause et al. [4].

In the field of medical science, there is a wide range of tracking algorithm to analyze brain structures based on magnetic resonance imaging (MRI). In particular, the second order probabilistic integration approach, developed by the authors Tournier et al. [5]. The authors Mori et al. [6] present a critical review of these approaches. Inspired by these tracking approaches, the SMC fiber bundles in this contribution are tracked by means of a probabilistic tracking algorithm, introduced by the authors Schöttl et al. [7].

Since the SMC microstructure changes across a weld line formation, this is a suitable application for the validation of SMC process simulation models. The authors Meyer et al. [8] and Silva-Nieto et al. [9] validated their introduced process simulation models for SMC, by means of weld line formations. In this contribution, the microstructure of a generic SMC geometry with a weld line is analyzed. As a result, the fiber bundle curvature across and within the weld line are determined.

2 Material

The tested SMC samples consist of an unsaturated polyester polyurethane hybrid (UPPH) resin matrix system without fillers from Aliancys, which is reinforced with glass fibers (GF Multistar 272) from Johns Manville. First, continuous fiber rovings are chopped into fiber bundles with a uniform length of typically 25.4 mm and a batch fiber mass content of 23 %. The chopped fiber bundles drop randomly oriented onto a resin coated carrier foil and are then covered by another resin coated carrier foil. Subsequently, the semi-finished SMC material is rolled up and matures. After maturation, the semi-finished SMC is formed into the final geometry by press molding, using two initial SMC charges. As a result, both flow fronts meet in the middle of the component and a weld line is formed (cf. [8]).

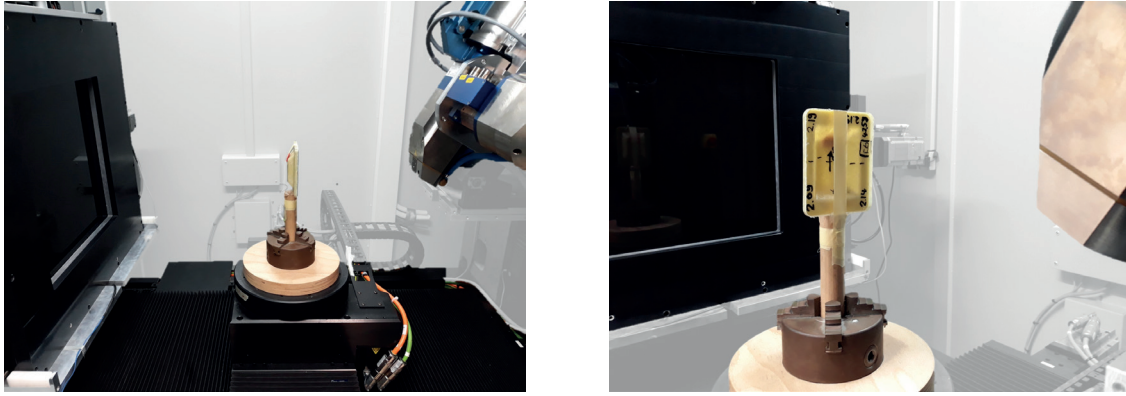


Figure 1: The scanned SMC geometry, detector and x-ray tube of the μ CT-system.

3 X-ray micro-computed tomography

The μ CT images in this contribution are generated using a X-Ray μ CT-system of YXLON with a reflection tube by Comet (see Figure 1). The Perkin Elmer flat-panel Y.XRD1620 detector resolution is 2048 times 2048 pixels and the pixel patch is 200 μ m.

The μ CT scans presented in this contribution are generated with an acceleration voltage, current, exposure time and frame binning of 150 kV, 0.05 mA, 1000 ms and 2, respectively. The μ CT scanning process takes 80 min to complete. The volumetric images are reconstructed through 2400 projections over 360° and the Feldkamp-Davis-Kress algorithm [10]. Resulting volumetric images are cropped, aligned and registered using the VG Studio Max software by Volume Graphics. The SMC geometry is scanned in two different ways. First, a volumetric image of the entire geometry is generated, with a reconstructed isotropic voxel edge length of 68.7 μ m (see Figure 2). Additionally, a second μ CT scan, where the SMC geometry is placed close to the x-ray focus spot is generated. As a result, a high-resolution volumetric image of the weld line with a isotropic voxel edge length of 17.2 μ m is acquired (see Figure 3).

4 Results and Discussion

Based on the volumetric images acquired by μ CT scanning and the fiber bundle tracking method (cf. [7]), the microstructure of a generic SMC geometry is analyzed. Figure 2 a) shows one of the 2400 projections and Figure 2 b) the reconstructed volumetric image of the entire SMC geometry. In Figure 2 a), changing fiber orientations around the weld line are observed. The images in Figure 3 show the weld line in a more detailed manner. The corresponding area is marked by a red box in Figure 2 a). The SMC fiber bundles within the volumetric image of Figure 3 c) are tracked. As a result, in Figure 4 a) the tracked fiber bundles, as well as the local fiber bundle curvature are illustrated. Figure 4 b) shows the distribution of the maximum and mean fiber bundle curvature across the weld line. Within the weld line, a maximum fiber bundle curvature of 1.65 mm^{-1} is reached. Within the analyzed area, the fiber bundle mean curvature is 0.28 mm^{-1} . As a result, the fiber bundle curvature increases significantly within the weld line.

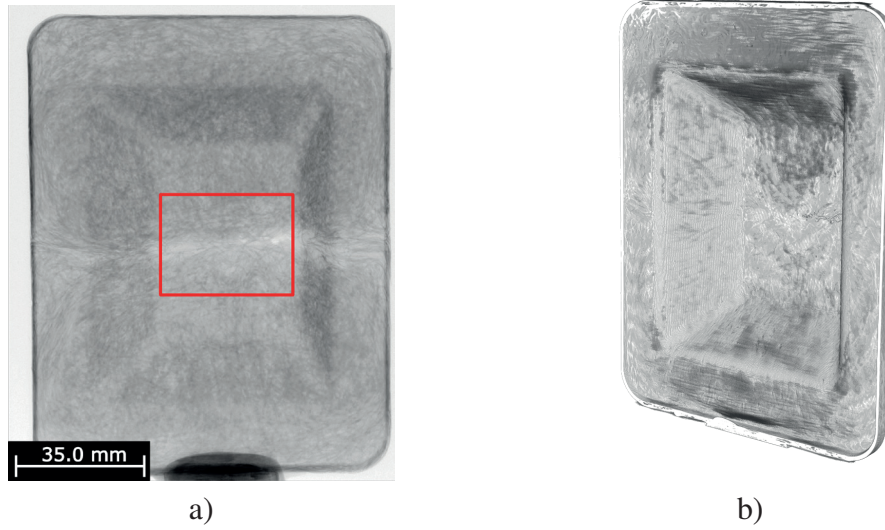


Figure 2: μ CT a) a projection and b) the reconstructed volumetric image of the entire SMC geometry.

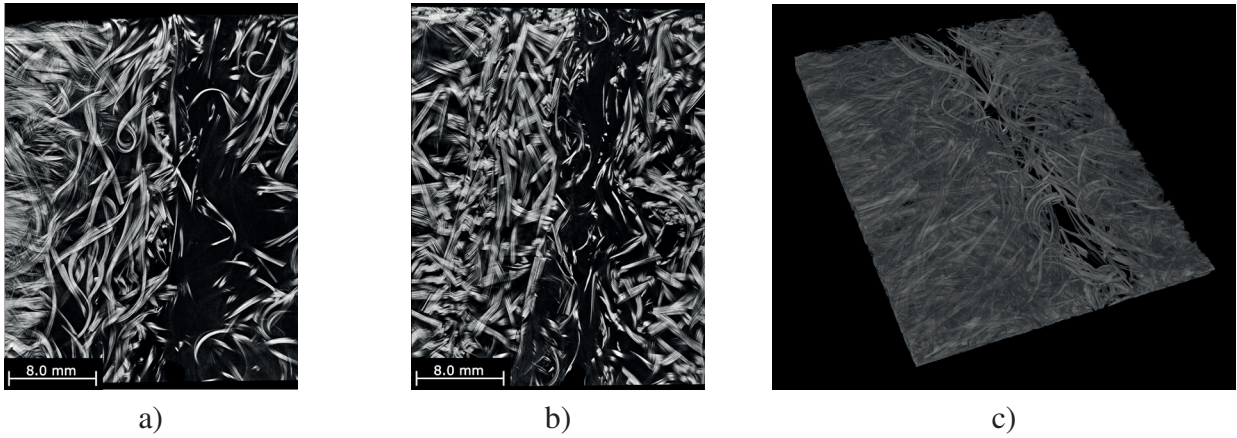


Figure 3: Two μ CT image slices at a) top ($z = 0.14$ mm) and b) core location ($z = 1.14$ mm), as well as c) a three-dimensional view.

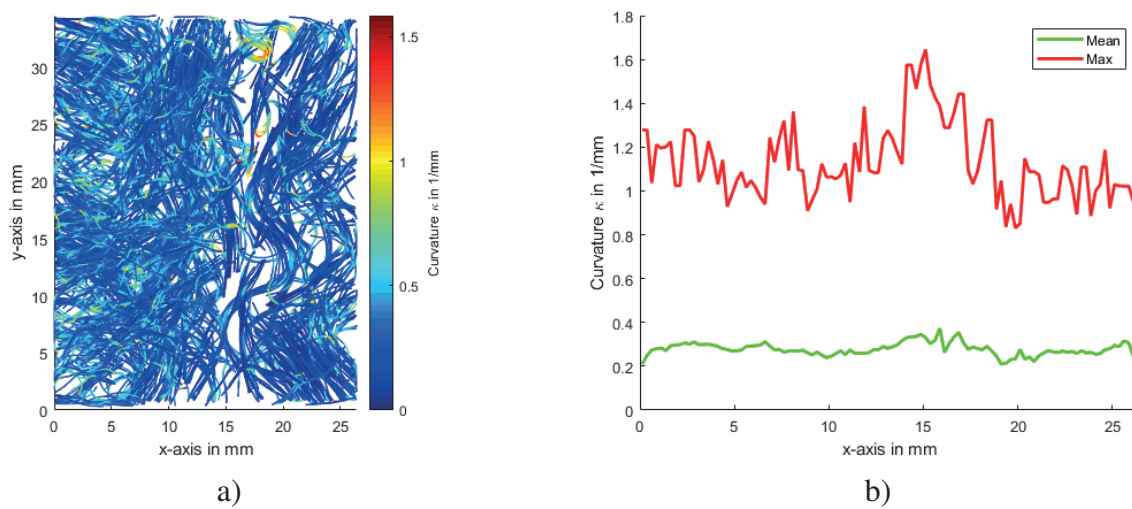


Figure 4: The determined a) local fiber bundle curvature and b) mean and maximum fiber bundle curvature across the weld line of the SMC geometry.

5 Conclusions

Microstructure characterization is essential for better understanding of fiber-reinforced polymers and enabling novel prediction models for process simulation. In this contribution, the microstructure of a generic SMC geometry is analyzed. Fiber bundles are tracked instead of individual fibers, increasing the necessary μ CT volumetric image resolution. As a result, a representative microstructure volume of the generic SMC geometry including a weld line is analyzed. The local, as well as the mean and maximum fiber bundle curvature across the weld line formation are determined.

Acknowledgments

The research documented in this manuscript has been funded by the German Research Foundation (DFG) within the International Research Training Group "Integrated engineering of continuous-discontinuous long fiber reinforced polymer structures" (GRK 2078). The support by the German Research Foundation (DFG) is gratefully acknowledged. As well the authors grateful appreciate the support of the Fraunhofer Institute for Chemical Technology (ICT) and the Institute of Production Science (wbk) by supplying the experimental forming results of the samples, which were finished under the project leadership of Sergej Ilinzeer and Lucas Bretz, respectively.

References

Journals

- [1] J. Görthofer, N. Meyer, T. D. Pallicity, L. Schöttl, A. Trauth, M. Schemmann, M. Hohberg, P. Pinter, P. Elsner, F. Henning, A. Hrymak, T. Seelig, K. A. Weidenmann, L. Kärger, and T. Böhlke. *Composites Part B: Engineering*. **2019**, 169, 133 – 147.
- [2] K. Schladitz, A. Bueter, M. Godehardt, O. Wirjadi, J. Fleckenstein, T. Gerster, U. Hassler, K. Jaschek, M. Maisl, U. Maisl, S. Mohr, U. Netzelmann, T. Potyra, and M. O. Steinhauser. *Composite Structures*. **2017**, 160, 195 – 203.
- [3] P. Pinter, S. Dietrich, B. Bertram, L. Kehrer, P. Elsner, and K. A. Weidenmann. *NDT & E International*. **2018**, 95, 26 – 35.
- [4] M. Krause, J. M. Hausherr, B. Burgeth, C. Herrmann, and W. Krenkel. *Journal of Materials Science*. **2009**, 45, 888 – 896.
- [5] J.-D. Tournier, F. Calamante, and A. Connelly. In *Proc. International Society for Magnetic Resonance in Medicine 18*, **2010**.
- [6] S. Mori and P. C. M. van Zijl. *NMR in Biomedicine*. **2002**, 15, 468 – 480.
- [7] L. Schöttl, K. A. Weidenmann, T. Sabiston, K. Inal., and P. Elsner. submitted to *NDT & E International*, **2020**.
- [8] N. Meyer, L. Schöttl, L. Bretz, A. N. Hrymak, and L. Kärger. *Composites Part A: Applied Science and Manufacturing*, **2020**, 132, 105809.
- [9] R. J. Silva-Nieto, B. C. Fisher, and A. W. Birley. *Polymer Composites*. **1980**, 1, 14 – 23.
- [10] L. A. Feldkamp, L. C. Davis, and J. W. Kress. *Journal of the Optical Society of America*. **1984**, 1, 612 – 619.

Books

- [11] P. Eyerer, T. Hirth, and P. Elsner. Springer, **2008**.
- [12] T. Böhlke, A. Hrymak F. Henning, L. Kärger, K. A. Weidenmann, and J. T. Wood. Hanser, **2019**.

Detection of damage in glass fibre-reinforced thermoplastics using active Lock-In thermography

Sonja Poleschke¹, Bernd Engel¹

¹Chair for forming technology, University Siegen
57076 Siegen, Germany

1 Introduction

Ensuring product quality is an integral part of industrial production. Either the component meets the requirements or the type, size and location of the defect leads to the selection of the part [1]. In the automotive sector, fibre-reinforced thermoplastics have established themselves as lightweight construction materials [2].

These can be examined by means of active Lock-In thermography [3]. It belongs to the non-contact and non-destructive testing methods. It is based on the fact that material defects influence the heat diffusion process in an object and can thus be analysed on the basis of the temporal course of the heat radiation at the object surface [1].

Active lock-In thermography is already used in testing and control procedures in materials research and development, for material characterization, for controlling processing and manufacturing and for production analysis [3]. In industrial production, the materials to be tested are examined in the near-surface area for homogeneity, compaction, defects, cracks, inclusions, moisture content and moisture distribution. The first industrial thermography applications are mainly found in the aerospace industry. These aircraft inspections are carried out, for example, on bondings of aircraft structures [1].

In this work, glass fibre-reinforced polypropylene is investigated by active Lock-In thermography. The material is prepared both without defects and with defined defects. Nine defect types are tested for their detectability.

The aim is to determine the correlation between defect type and size in glass fibre-reinforced polypropylene materials and the associated image information of the active Lock-In thermography.

2 Glass fibre-reinforced thermoplastics

In this work the material Tepex dynalite 104-RG600(x)/47% from the company Bond Laminates is investigated. It is a fibre composite material made of glass fibres in a matrix of polypropylene. The weight per unit area of the material is 600 g/m² according to DIN EN 12127. The material density is 1.68 g/cm³ according to ISO 1183-1. The melting temperature of the matrix is 165 °C according to ISO 11357-3. The material consists of three fabric layers, each 0.5 mm thick. As reinforcing structures 1200tex fibres of standard E-glass were used. Several parallel bundled fibres form a roving.

According to DIN EN 1049-2 the number of rovings is 2.5 per cm in longitudinal section and 2.5 per cm in cross section. The arrangement of the individual rovings in the fabric is orthogonal to each other [6]. The twill weave was chosen as the type of weave. The weft and warp threads do not alternate evenly. The weft thread passes under one warp thread and then over two or

more warp threads. Unmistakable for this weave are the diagonal lines in the pattern. The glass fibres have the property of a higher stiffness and strength than the matrix. The surrounding matrix gives the material ductility and protects the glass fibres from locally higher loads [6].

180 specimens were investigated using active Lock-In thermography. The number of specimens is due to further mechanical load capacity investigations, which are to be carried out following the investigations performed here. The dimensions of 90 samples are 250 mm x 25 mm, the remaining 90 samples are 80 mm x 25 mm. The thickness of the samples is 1.5 mm. Defect free samples and samples with defined defects were examined. 20 samples are free of defects.

Defined types of defects include fibre breakage, local and global fibre displacement, delamination and insufficient consolidation. These defects may occur during the production and forming of fibre composites. Each defect type was prepared in 20 samples. Fibre breakage and fibre displacement were introduced as one type of defect each in the top and middle fabric layer. The insertion of the defects was carried out by the company Bond Laminates.

Fibre breakage is a locally complete destruction of the glass fibre due to mechanical impact. It was created by manually cutting through a roving.

A local fibre displacement occurs when fibres are pushed out of their regular arrangement by external forces. This results in areas of high and low fibre density. Stiffness and strength are no longer continuously distributed over the fabric. It is introduced into the samples by local spiking of the fabric. The width of the displacement corresponds to about 1-2 rovings.

The global fibre displacement describes an overall distortion of the material. Here the fibres of one fabric are at an angle to the fibres of another fabric. A random distortion in warp and weft threads occurs. The global fibre displacement in the samples was caused by the fabric layers not being placed exactly on top of each other.

Insufficient consolidation causes air inclusions in the material. Consolidation means strengthening the bond between matrix and fibre. Thermoplastic filaments are melted under pressure and enclose the glass fibres [7]. If the two materials are not fully bonded, consolidation is insufficient. This defect was introduced on an area of 30 mm along the length of the specimen over the entire width of the specimen.

Delamination describes the separation of individual layers of tissue from each other. In this process, the individual layers can lose their adhesion to each other, but also the fibres can lose their adhesion to the matrix. The delamination was created with the help of a foil strip, which was inserted between two tissue layers on an area of 20 mm along the sample over the entire sample width before consolidation.

The tissue damage, such as fibre breakage and fibre displacement, was performed on the dry tissue before impregnation with the polymer matrix.

The flawless quality of the composite material is tested in in-process tests on the finished material, e.g. on the basis of the mechanics, thickness and appearance of the Bond Laminates material. In the following, each defect is presented as an example using a sample.

3 Lock-In thermography

The active Lock-In thermography belongs to the non-destructive and contactless testing methods. Using intensity-modulated halogen lamps, the component surface to be tested is homogeneously excited over a long period of time with a sinusoidal intensity curve [1]. The absorption of the sinusoidally modulated light produces a temperature modulation which is propagated as a thermal wave into the interior of the component. If this wave encounters an interface, i.e. a local change of the effusivity, a certain part of the wave reflects. The superposition of the surface temperature oscillation with reflected thermal waves forms the wave field which is measured by the infrared camera on the sample surface. The modulation of

the heat flux can be considered as a coding, which is decoded again by means of a Fourier analysis, whereby the uncoded interferences fall out, e.g. also the direct component of the temperature field. By utilizing the measurement information of the phase angle between the excitation and response sinusoidal curve, interference effects due to uneven heating can be reduced [1].

The phase describes the time delay of a thermal response in correlation to excitation at a specified frequency. This delay depends, among other things, on the thermal material properties and the geometry of the test object and can also be influenced by irregularities in the test object. The phase image contains information from component depths up to 6 mm [4]. The test method works without calibration.

4 Test setup

The test setup (see figure 1) includes the thermal imaging camera, two halogen lamps, the specimens and the thermography program. The equipment was purchased from the company edevis.

Thermal imaging camera Flir A655 sc, a LWIR precision camera. It has an uncooled vanadium oxide (VoX) microbolometer detector and a thermal resolution of <30 mK. It generates thermal images with up to 640 x 480 pixels at a frame rate of 50 Hz. The spectral range to be detected is 7.5 -14 μm . The temperature measuring range is -40 $^{\circ}\text{C}$ to 150 $^{\circ}\text{C}$.

The two halogen floodlights H25s from Hedler are operated with an electrical power consumption of 2.5 kW each. The light output of the four Osram light bulbs is a maximum of 4 kW. Throughout the entire investigation they emit electromagnetic waves in the range from ultraviolet to near infrared. The spectrum in the long-wave to far infrared range of halogen light falsifies the thermal image of the sample. Two glass filters, each 2 mm thick, reduce the proportion of the medium-wave and long-wave infrared of halogen light [5] and support the spectral separation of excitation and detection. They are made of borofloat 33 according to DIN ISO 3585 and EN 1748 T1 by Schott Technical Glass Solutions GmbH.

The setup corresponds to the reflection setup where camera and light are on the same side of the sample. Defects become visible during reflection measurement due to higher surface temperatures.

Each sample was fixed in a specially manufactured sample carrier. The camera was placed in front of the sample at a distance of 510 mm and at the same height as the defects (see figure 1). The two halogen spotlights were placed at the side of the camera. The distance from lamp 1 to the sample was 660 mm. Lamp 2 has a distance to the sample of 600 mm (see figure 2). If the centre of the objective and the sample are on the zero line, lamp 1 is at a distance of 240 mm horizontally and 120 mm vertically from it and lamp 2 is at a distance of 180 mm horizontally and 130 mm vertically from it.



Figure 1: Experimental setup

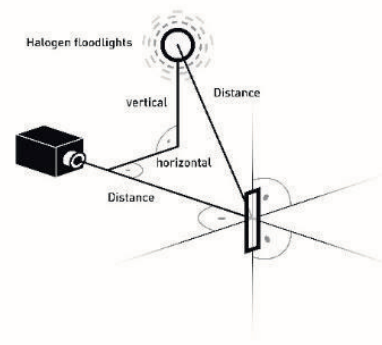


Figure 2: Test setup

The test specimens were excited in three measuring periods at a frequency of 0.05 Hz. The test duration is 60 s in total. The light intensity of 75 % corresponds to the light output of 3 kW. This is measured within a measuring period of 20 seconds once on the sample. Measurements are made at a room temperature of approx. 21 °C. The initial temperature of the material samples corresponds to approx. 21 °C. The thermal imaging camera has 100 frames per second generated in a window of 640 x 240 pixels.

5 Evaluation of test results

In this work the phase images of the samples are evaluated. On them the glass fibres are imaged darker than the polypropylene matrix. The absence of a fibre is visible on the image as bright as the matrix. Air inclusions appear on the phase image brighter than the fibres and darker than the matrix. Fibre breakage in the middle layer is not reliably detected (see figure 4). At one point two fibre ends with a brighter break can be seen. The entire structure of the sample appears blurred. The insufficient consolidation is visible as a bright area (see figure 5) over a length of 50 mm across the entire width of the sample. The pattern of fibres is ordered. The insufficient consolidation is clearly distinguishable from the defect-free area. It is clearly visible and can also be felt by a raised area of about 1 mm.

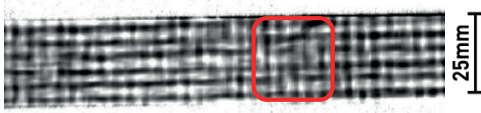


Figure 4: Sample 86, fibre breakage in central position

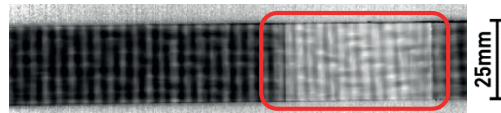


Figure 5: Sample 64, insufficient consolidation

Within a range of 10 mm², two ends of a dark fibre can be seen in sample 4 (see figure 6). They show the fibre breakage in the top layer. The delamination is shown on the phase image as a lighter area, not as sharply delineated as in the case of insufficient consolidation (see figure 7). It extends about 9 mm lengthwise over the entire width of the sample. This corresponds to the distance between four rovings. Matrix and fibres differ in this area.

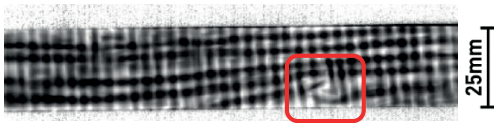


Figure 6: Sample 4, fibre breakage in top layer

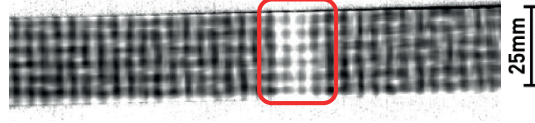


Figure 7: Sample 55, delamination

The fibre displacement globally in the top layer is visible by fibres not running parallel to the edge (see figure 8). Across the width of the sample, 3 mm wide bright lines can be seen between the rovings at a distance of 20 mm, which look like a pattern diagonally across the entire length of the sample. On the phase image, fibres and matrix appear blurred.

A light-coloured cross-strip with a width of approx. 3 mm between two rovings indicates a fibre shift locally in the top layer (see figure 9). An adjacent side to the defect shows shifted fibre lines that deviate from the parallelism to the edge of the sample.

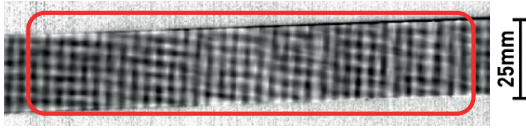


Figure 8: Sample 26, global fibre shift in top layer

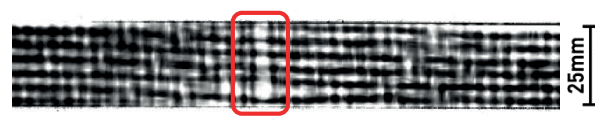


Figure 9: Sample 30, local fibre displacement in top layer

On sample 45 (see figure 10), the fibre displacement is visible locally in the central position as a bright spot of approx. 8 mm² in size. To the left of the conspicuity, the fibres no longer run parallel to the edge of the sample. No defects were introduced in sample 73 (see figure 11). On the phase image, the sample nevertheless appears blurred and shows irregularities in the grain structure.



Figure 10: Sample 45, local fibre displacement in central

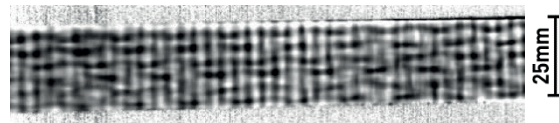


Figure 11: Sample 73, without errors introduced

On the phase image of sample 96, the global fibre shift in the central position is not visible (see figure 12).

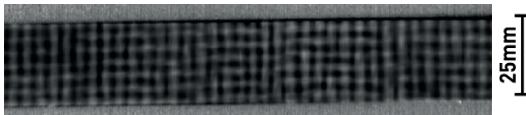


Figure 12: Sample 96, global fibre shift in central position

6 Conclusion and outlook

Fibre-reinforced thermoplastics are increasingly used as lightweight construction materials in the automotive industry. In this work samples of glass fibre-reinforced polypropylene in flawless condition and with introduced defined defects are investigated with active Lock-In thermography. The aim is to determine the correlation between defect type and size in glass fibre-reinforced polypropylene materials and the corresponding image information from active Lock-In thermography. Defects investigated include delamination, insufficient consolidation, fibre breakage and global and local fibre displacement in the upper and middle tissue layer. Using active Lock-In thermography, the sample material was optically excited with two halogen lamps with a light output of 3 kW in three measuring periods for 60 seconds at 0.05 Hz. An infrared camera in reflection arrangement measured the surface temperature of the sample. Information of the sample material becomes visible on the basis of the phase images output. Delamination and insufficient consolidation are clearly visible by bright areas on the phase image. Local fibre shifts are visible by the deviation of the linear arrangement of the fibres, which are displayed in dark areas. Fibre breaks are visible by black ends of the fibres. The global fibre shift is represented by the angular position of the structure to the sample edge on the phase image. Variations of excitation frequencies, changes in the number of measuring and settling periods and intensity modulation of the light could lead to more accurate and clearer error representations on the phase images. Defect detection in greater material depths could be possible by investigations with lower excitation frequencies.

7 References

- [1] M. Abuhamad, in *Spektrale Information in der Thermographie*. Universität des Saarlandes, Saarbrücken, **2011**, 11, 14, 44.
- [2] *AMITIE, Adaptive multimodale in-line Inspection Faserverstärkter Thermoplaste im Automobilen Leichtbau*,
<https://www.photonikforschung.de/service/nachrichten/detailansicht/industrie-40-potenzial-der-optischen-sensorik-erforschen.html>, abgerufen am **30.01.2020**.
- [3] C. Maierhofer, G. Busse, N. Holtmann, P. Myrach, M. Rahammer, M. Reischel, in *Standardisierung der Lockin-Thermografie: Vorstellung des TNS-Projektes und Auswahl der Probekörper*. Institut für Kunststofftechnik, Universität Stuttgart, **2013**, 2.
- [4] Norm *DIN EN 17119. Zerstörungsfreie Prüfung, Thermografische Prüfung, Aktive Thermografie*, Deutsche Fassung EN 17119:**2018**.
- [5] A. Gleiter, in *Mess- und Auswertemethoden für die dynamische Thermografie*. Universität Stuttgart, **2011**, 32.
- [6] J. Röster, H. Harders, M. Bäker, in *Mechanisches Verhalten der Werkstoffe*. **2008**, p. 295-296.
- [7] C. Hopmann, A. Böttcher, K. van der Straeten, R. Riedel, F. Schneider, C. Engelmann, K. Fischer, in *Neue Prozesskette für faserverstärkte Thermoplaste, InProLight: Automatisierte Fertigung verschnittoptimierter Leichtbauteile mit lokalen Eigenschaftsprofilen*. Springer-VDI-Verlag, Düsseldorf, **2014**, 577.

Comparison of anomaly detection capabilities of pulse phase thermography in transmission and reflection setup on Sheet Molding Compound

L. Bretz¹, M. Wilke¹, B. Häfner¹, G. Lanza¹

¹Karlsruhe Institute of Technology (KIT), wbk Institute of Production Science, Karlsruhe

Abstract – Pulse phase thermography (PPT) is widely used for non-destructive testing (NDT) of fiber reinforced polymers. Shades occur when inspecting three-dimensional (3D) specimens with a single flash lamp, but can be circumvented by using a transmission setup (TM). In this contribution, PPT is applied to a 3D specimen with reference defects in TM and compared to reflection mode (RM). The reference defects consist of PTFE and aluminum foil and are varied in position, size and depth. Reflector surfaces are constructed to enhance the thermal stimulus on the slants of the specimen in TM. The specimen-dependent construction method is presented. Using the reflectors leads to a higher contrast between defective and sound area in ampligrams. Ampligrams and phasegrams provide complementary information in TM, motivating a data fusion approach to improve defect information. Hit rates and detected defect sizes between RM and TM with and without reflector are compared. Overall, TM combined with reflector usage leads to the highest hit rate. Especially deeper defects and defects on slants are more reliably detected in TM. Detected defect size deviations are smaller in RM.

Keywords: Non-destructive testing, pulse phase thermography, transmission, fiber reinforced polymers

1 Introduction

Reducing overall CO₂ emissions can be accomplished by lightweight components [1]. Fiber-reinforced polymers (FRP) offer a high specific modulus. New hybrid material classes combine the advantages of different fiber types. An example of these hybrid fiber types are continuous-discontinuous fiber reinforced polymers. Sheet Molding compound (SMC), consisting of an unsaturated polyester polyurethane hybrid resin (UPPH) and discontinuous glass fibers (fiber length: 25 mm) offers a high design freedom. It serves as base material in the hybrid material class in combination with continuously reinforced carbon fiber patches. The patches contribute to the material combination with a higher stiffness. Defects still occur in the production of FRP, although they have been processed since multiple years [2]. The in-line quality assurance using active thermography for the detection of internal defects offers cost saving potentials, because material flaws are detected at their place of origin. This work focuses on the investigation and improvement of pulse phase thermography (PPT) in transmission mode (TM) for inspecting complex geometries. TM describes a measurement setup in which heat source and infrared camera are on opposite sides, in contrast to reflection mode (RM, same side). Inclined slopes on the specimen lead to shades and inhomogeneous heat input which is compensated in TM.

2 State of the Art

Thermography is subdivided into active and passive methods. An external stimulus is used in active mode to excite the part and investigate its thermal response. An infrared camera records the infrared emissions response. The usefulness of active thermography in non-destructive testing of composites has been shown [2, 3]. PPT combines the advantages of time efficiency (pulse thermography) and phase images (modulated thermography). The discrete Fourier transform (DFT) is applied to the time series of infrared images. This image time series represents the temperature evolution of the specimen induced by the thermal stimulus.

However, literature investigating the NDT applications of thermography in FRP mostly deals with planar geometries operating in reflection mode. 3D geometries can be investigated with additional heat sources compensating shades [3, 4]. More complex geometries have been investigated [5–7], but shadings did not occur for the investigated specimen. Transmission mode has been used to measure artificial defects (thickness: 1 and 2 mm) in planar composite specimens (thickness: 5 mm) [8, 9]. The temperature and phase contrast between sound and defect area increase with a smaller distance between heat source and defect [9]. Transmission transient thermography is suggested for impact studies and testing anisotropic materials [10]. Pan et al. used pulsed eddy current as a stimulus for the first time in transmission mode to detect impact damage and delamination in a planar specimen [11]. A detailed comparison of reflection and transmission comparison has been performed on planar composite specimens with artificial delaminations and impact damage [12]. The most relevant aspects are listed in **Table 1**. In contrast to Meola et al. [9], more defects are detected with a setup in which the distance between heat source and defect is larger, leading to a smaller camera distance to the defect. No study has so far investigated a PPT in transmission mode on a 3D part. Furthermore, no attempt has been made to adjust the heat radiation according to the geometry of the part in TM.

Table 1. Advantages and Disadvantages of reflection and transmission mode [12]

Reflection mode	Transmission mode
+ High sensitivity for defects close to the surface	+ Defect information in overall cross section is retrieved
+ Depth resolution can be estimated from PPT	+ Better correspondence with analytical calculations because no initial surface temperature needs to be estimated
– Investigation only possible on the upper surface	+ Defects with small aspect ratios can be detected in transmission mode
	– Depth information is nearly lost
	– Accessibility to the specimen from both sides necessary

3 Experimental Setup

3.1 Specimens

The specimen used for this work is a hat profile with different slants (dimensions: 120 mm x 94 mm). It consists of six planes: A bottom and a top horizontal plane, two planes angled with 40° and 60° with respect to the horizontal planes along the long edges, and two planes with 45° with respect to the horizontal plane along the short edges.

Specimens with different artificial defects have been produced for the examination. They consist of a structural SMC based on an unsaturated polyester polyurethane hybrid (UPPH) resin with 23 vol% (41 wt%) fiber volume content. A specimen is built out of 4 stacked layers of SMC in a highly viscous B-stage. Artificial defects, made out of PTFE (130 μm thickness) and aluminum (11 μm), are integrated between the individual layers. The specimens have an average wall thickness of approx. 3.6 mm, leading to an average layer thickness of approx. 0.9 mm. Three different geometric defect configurations have been produced: The first one consists of different defect sizes (25 mm², 49 mm², 100 mm²) between the second and third layer of SMC (blue, cf. **Figure 1** (b)). The second configuration alters the defect depth for a constant defect size of 100 mm² between the first and second layer (green, cf. **Figure 1** (c)) and between the third and fourth layer (red, cf. **Figure 1** (c)). The first layer describes the one closest to the camera. Both of these configurations are produced with PTFE and aluminum inserts.

The mold is heated to 145°C and closed with a hydraulic press with a maximum press force of 50 kN. Positional deviations occurred during the molding process.

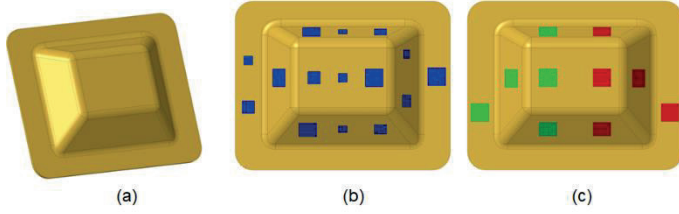


Figure 1. (a) Isometric view of the specimen (b) Specimen containing different defect sizes, named Alu_S and $PTFE_S$ (c) Specimen containing different defect depths (red defects are deeper), named Alu_D and $PTFE_D$

3.2 Construction of reflectors

The heat source (flash lamp) is considered as an ideal, fixed point for the construction of the reflectors for the 45° slants. The position of the specimen, the design area of the reflector and the first point of the reflector's plane R_1 closest to the specimen are initially set. A point of interest (POI) is set on the 45° slant of the specimen (point Z in **Figure 2**). The local orientation δ_i of the local reflector's surface is calculated based on the geometric properties given in **Figure 2**. Using the calculated angle and a chosen increment along the negative x-axis Δx (here: 5 mm to achieve a smooth surface considering accuracy of the 3D printer and small delta), the point R_2 ($x_2|y_2$) for the second reflector plane and its orientation δ_2 are calculated. The POI alternates between different positions on the slant to distribute the reflected energy.

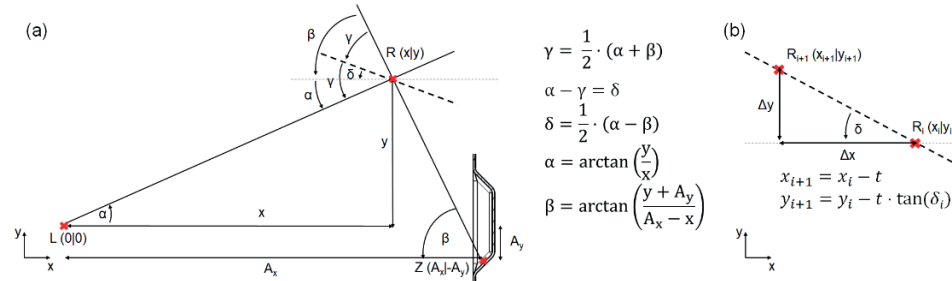


Figure 2. (a) Calculation for the orientation of the reflector (b) Calculation of the next point of the reflector

Another routine is used for the reflector construction for the 40° and 60° slants, because of the parabolic shape of the inner housing's reflection geometry of the flash lamp itself. This parabolic shape leads to a parallel alignment of the light bundles leaving the flash housing. Therefore, several tilted surfaces between the housing and the specimen build the surface of the reflector. The orientation and width of a partial surface is calculated using the condition that a reflected light bundle shall hit the full width of a slant mostly perpendicularly.

3.3 Apparatus and methods

A photographic flash stimulates the specimen (model VH3-6000 by HENSEL-VISIT, power: 6000 J). Images are generated by the thermal imaging camera ImageIR 5300 (InfraTec, camera resolution: 320 x 256 px). The objective has a focal length of 25 mm. The object distance to the midplane of the specimen is 320 mm. The IR camera and the heat source are carried by a CNC portal (cf. **Figure 3**). The temperature evaluation of the specimen is observed for 60s after the flash, leading to a minimal frequency of 0.017 Hz after the DFT. Experiments are conducted in TM and RM. In TM, the flash lamp is placed in a housing with the reflectors and the specimen for operator safety. In RM, the flash

lamp is oriented to illuminate the 40° slope of the demonstrator perpendicularly. DFT and image selection is performed with the software DisplayIMG 6 by edevis. MATLAB is used for the image analysis.

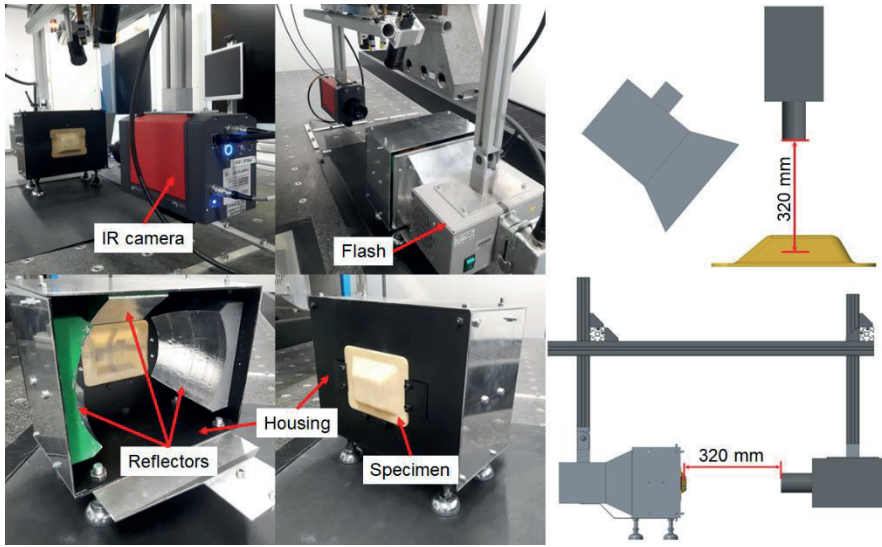


Figure 3. Experimental apparatus, housing and setup sketches for RM and TM

4 Defect evaluation routine

The infrared camera is calibrated with the MATLAB calibration toolbox, using a checkerboard pattern in the midplane of the specimen. Two laser-printed circles (nominal diameter: 10 mm), placed on the top and bottom plane, serve as a reference measurement. The measured reference diameter is 10.34 mm (top) and 10.05 mm (bottom), respectively. Amplitograms, phasegrams and thermograms are simultaneously considered in the evaluation. The images are exported as color images using the colormap representation ‘Rain’ for contrast enhancement [13]. Additionally, the contrast of the individual color channels is enhanced using MATLAB. Individual color channel values as well as their complements are binarized using a threshold of 0.75. Environmental influences on the borders are not considered. Morphological closing is performed on the resulting BLOBs (Binary Large Object) to smoothen them. Image features are only stored if they show an area between 10 and 300 mm². Features are assessed by their eccentricity and deleted if it surpasses 0.95. BLOBs with an extent (BLOB area divided by the area of the bounding box) less than 0.5 are deleted as well. Color channel information are merged by logical disjunction.

5 Results

5.1 Assessment of the reflector’s geometry in transmission mode

Initially, the temperature distribution using four different reflector configurations is evaluated on a specimen without any defects in the slants. Using the 60° and 45° reflectors rises the average temperature distribution in the specimen by 77.7% (cf. **Figure 4** and **Table 2**). The 45° reflectors prove to be useful regarding the increased energy input into the 45° slant. Because the 40° slant and the whole part show a similar temperature rise when using 60° and 45° reflectors, the 40° reflector is

not further used. 94.9% more energy is concentrated on the 45° slants in the third reflector setup. The energy input into the 60° slant is increased by 81.4%. The overall surface of a single 45° reflector is 159% larger than the surface of a 60° reflector, which explains the higher energy input. The temperature distribution is evaluated on a horizontal and a vertical line in TM for specimen Al_Us with and without the chosen reflector setup (45° and 60° reflectors, cf. **Figure 5**). The temperature increase in defect regions is minimal along the vertical and horizontal line. However, a comparison of Michelson contrasts of the maximum normalized signals in the defect regions on the 40° and 60° slants shows no improvement with reflector usage.

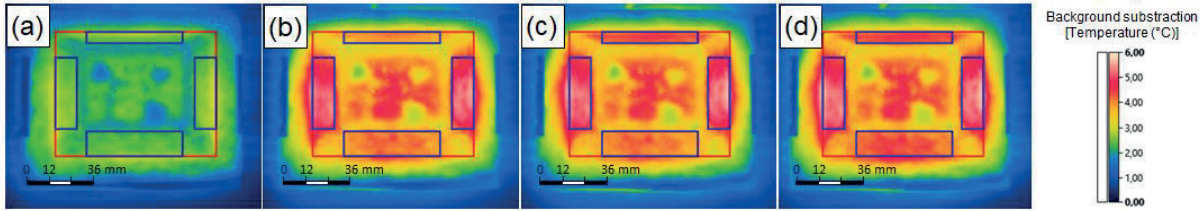


Figure 4. Thermograms and evaluated areas using (a) no reflectors (b) 45° reflectors (c) 45° and 60° reflectors (d) all reflectors

Table 2. Average temperature rise and standard deviation (SD) in parenthesis (°C) using different reflector setups

Area	Without reflectors	45° reflectors	60° and 45° reflectors	All reflectors
Whole part (red area)	2.29 (0.255)	4.01 (0.571)	4.07 (0.561)	4.13 (0.567)
45° slants	2.57 (0.182)	4.96 (0.344)	5.01 (0.332)	5.06 (0.342)
60° slant	2.37 (0.186)	3.86 (0.149)	4.30 (0.174)	4.36 (0.175)
40° slant	2.45 (0.147)	4.06 (0.153)	4.03 (0.163)	4.25 (0.185)

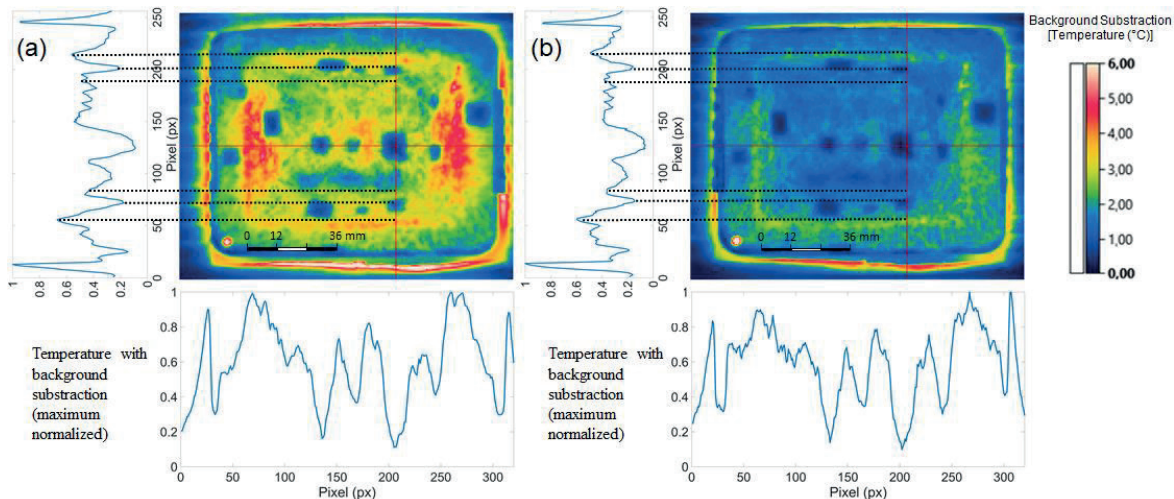


Figure 5. Normalized temperature distribution of specimen Al_Us along the vertical and horizontal axis with (a) and without (b) reflectors

The use of the reflector is further assessed by comparing hit rates and deviations in detected defect size with and without reflectors in TM (cf. **Figure 6**). The hit rate increases using the reflectors due to more detected smaller or deeper PTFE defects. The specimen PTFE_S contains many surface defects, making it difficult to detect defects in general and leading to a bad hit rate. However, deeper aluminum defects are already detected without reflectors, because of the higher difference in heat conductivity between inserts and SMC. Despite the higher probability of detection, the quantitative

measurement of defects worsens. Using reflectors improves hit rates especially in deeper layers and for smaller differences in heat conductivity of inserted materials.

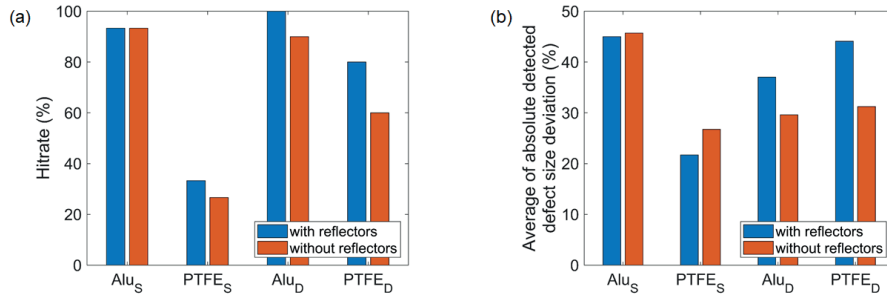


Figure 6. Assessment of reflectors' benefits in TM by (a) hit rates and (b) average absolute deviations in detected defect size

Detected defects for specimen PTFE_D in TM using reflectors and a comparison to no reflector usage is given in **Figure 7**. Two deeper defects on the slants are detected with reflectors (gray in **Figure 7** (c)). An increase in Michelson contrast can be observed in the ampligrams when using the reflectors. The data fusion of phasegrams and ampligrams is beneficial in TM as they complement each other in defect detection (cf. **Figure 7** (a) and (b)). The phasegram provides information closer to the surface (further away from the thermal stimulus), the ampligrams contrariwise.

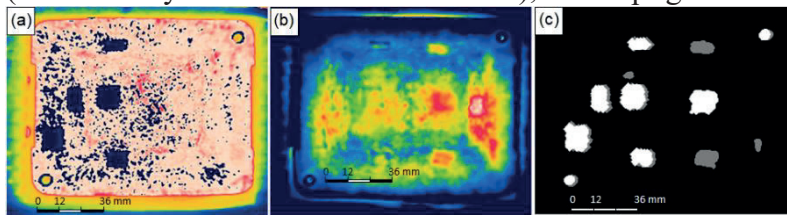


Figure 7. (a) Phasegram (0.251 Hz) and (b) ampligram (0.084 Hz) of specimen PTFE_D in TM using reflectors (c) Additionally detected defects (gray) compared to no reflector usage

5.2 Comparison of reflection and transmission mode

All defects in specimen Alu_S, except the small sized in the 60° slant, can be detected in TM (cf. **Figure 8** (a) and (e)). False positives are colored in black. The non-detected defects of Alu_S in RM are located on opposed slants with respect to the flash leading to strong background phase shifts (cf. **Figure 8** (b)). In TM, all defects of Alu_D are detected. Only the shallow defects in specimen Alu_D are detected in RM compared to TM, shown in **Figure 8** (c) and (d). Additionally, shades are circumvented in opposed slants with respect to the flash. Thus, TM leads to an overall higher hit rate, evading shades and detecting deeper defects. In TM mode, ampligrams contribute mostly to defect detection. Phasegrams contain more robust defect information in RM, in accordance with [14]. Nevertheless, absolute detected defect size variations are in average smaller in RM (cf. **Figure 8** (f)).

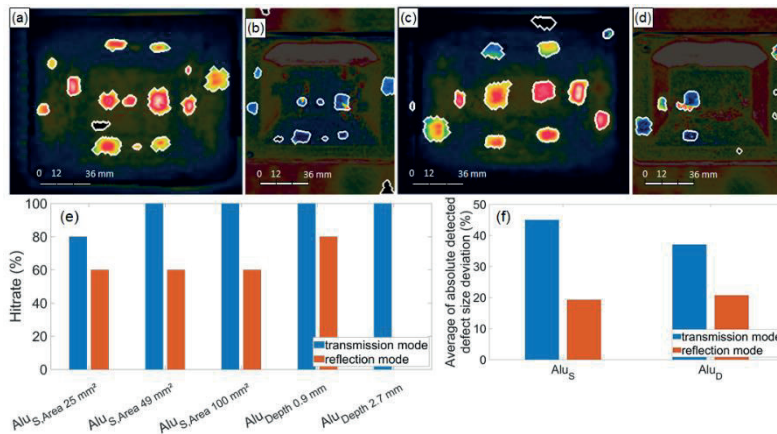


Figure 8: Detected and mapped defects in specimen (a) Alu_S in TM, ampligram (0.067 Hz) compared to (b) RM, phasegram (0.1 Hz) and (c) Alu_D in TM, ampligrams (0.050 Hz) compared to (d) RM, phasegram (0.15 Hz) (e) hit rates and (f) average absolute deviations in defect size

6 Conclusion and Outlook

An advantage of TM is the possibility to investigate 3D geometries with a single flash lamp while preventing shades. Additionally, TM allows the detection of deeper defects. Defect areas of 25 mm² in a depth of 1.8 mm can be detected on a 45° slant. RM has the advantage of smaller errors in geometric measurements. Additionally, it provides depth information, which is lost in TM. Further improvements of defect detection can be achieved by the usage of reflectors in TM, leading to a contrast increase in ampligrams. Data fusion of ampligrams and phasegrams are proven to be useful in TM. Further developments of reflectors should focus on a homogeneous temperature distribution in the overall part.

Acknowledgement – The research documented in this manuscript has been funded by the German Research Foundation (DFG) within the International Research Training Group ‘Integrated engineering of continuous-discontinuous long fiber reinforced polymer structures’ (GRK 2078). The support by the German Research Foundation (DFG) is gratefully acknowledged.

7 Literature

- [1] European Parliament. Setting emission performance standards for new passenger cars and for new light commercial vehicles as part of the Union's integrated approach to reduce CO₂ emissions from light-duty vehicles, Regulation (EG) No. 715/2007 (recast), Brussels, **2018**
- [2] M. Zaiß, M.-H.Jank, U. Netzelmann, T. Waschkie T, U. Rabe,H.-G. Herrmann, M. Thompson M,G. Lanza, in *Procedia CIRP* **2017**, p. 33–38.
- [3] C. Ibarra-Castanedo, X. Maldague, in *SPIE Sensing Technology + Applications*, Maryland, United States, **2015**.
- [4] C. Ibarra-Castanedo, X. Maldague, *Quantitative InfraRed Thermography Journal* **2004**, 1, p. 47–70.
- [5] G. Mayr, G. Hendorfer, *Quantitative InfraRed Thermography Journal* **2010**, 7(1), p. 3–16.

- [6] C. Ibarra-Castanedo, N.P. Avdelidis, E.G. Grinzato, P.G. Bison, S. Marinetti, L. Chen, M. Genest, X. Maldague, *Quantitative InfraRed Thermography Journal* **2006**, 3(1), p. 25–40.
- [7] P.D. Pastuszak, in *Procedia Engineering* **2016**, 157, p. 325–332.
- [8] G. Giorleo, C. Meola, *Journal of Materials Engineering and Performance* **2008**, 7(3), p. 367–374.
- [9] C. Meola, G.M. Carlomagno, L. Giorleo L, *Journal of Nondestructive Evaluation* **2004**, 23(4), p. 125–132.
- [10] C. Santulli, *Nondestructive Testing and Evaluation* **2003**, 19(3), p. 79–90.
- [11] M. Pan, Y. He, G. Tian, D. Chen, F. Luo, *NDT & E International* **2012**, 52, p. 28–36.
- [12] C. Maierhofer, P. Myrach, M. Reischel, H. Steinfurth, M. Röllig, M. Kunert, *Composites Part B: Engineering* **2015**, 57, p.35–46.
- [13] L. Bretz, T. Hinze, B. Häfner, G. Lanza, in *Procedia CIRP* **2019**, 85, p. 308–313
- [14] G. Busse, D. Wu, W. Karpen, *Journal of Applied Physics* **1992**, 71(8), p. 3962–3965.

ALTE FORMATIERUNG LITERATUR

- [1] European Parliament. Setting emission performance standards for new passenger cars and for new light commercial vehicles as part of the Union's integrated approach to reduce CO₂ emissions from light-duty vehicles. Regulation (EG) No. 715/2007 (recast). Brussels; **2018**
- [2] Zaiß M, Jank M-H, Netzelmann U, Waschkes T, Rabe U, Herrmann H-G, Thompson M, Lanza G. Use of Thermography and Ultrasound for the Quality Control of SMC Lightweight Material Reinforced by Carbon Fiber Tapes. *Procedia CIRP* **2017**; 62:33-38.
- [3] Ibarra-Castanedo C, Maldague X. Review of pulse phase thermography *Quantitative InfraRed Thermography Journal* **2015**; 1:47–70.
- [4] Ibarra-Castanedo C, Maldague X. Pulsed phase thermography reviewed. *Quantitative Infra-Red Thermography Journal* **2004**; 1:47–70.
- [5] Mayr G, Hendorfer G. Characterization of defects in curved carbon fiber reinforced plastics using pulsed thermography. *Quantitative InfraRed Thermography Journal* **2010**; 7(1):3–16.
- [6] Ibarra-Castanedo C, Avdelidis NP, Grinzato EG, Bison PG, Marinetti S, Chen L, Genest M, Maldague X. Quantitative inspection of non-planar composite specimens by pulsed phase thermography. *Quantitative InfraRed Thermography Journal* **2006**; 3(1):25–40.
- [7] Pastuszak PD. Characterization of Defects in Curved Composite Structures Using Active Infrared Thermography. *Procedia Engineering* **2016**; 157:325–332.
- [8] Giorleo G, Meola C. Location and geometry of defects in composite laminates from infrared images. *Journal of Materials Engineering and Performance* **2008**; 7(3):367–374.
- [9] Meola C, Carlomagno GM, Giorleo L. Geometrical Limitations to Detection of Defects in Composites by Means of Infrared Thermography. *Journal of Nondestructive Evaluation* **2004**; 23(4):125–132.
- [10] Santulli C. Impact damage characterisation of thermoplastic matrix composites using transmission transient thermography. *Nondestructive Testing and Evaluation* **2003**; 19(3):79–90.
- [11] Pan M, He Y, Tian G, Chen D, Luo F. Defect characterisation using pulsed eddy current thermography under transmission mode and NDT applications. *NDT & E International* **2012**; 52:28–36.
- [12] Maierhofer C, Myrach P, Reischel M, Steinfurth H, Röllig M, Kunert M. Characterizing damage in CFRP structures using flash thermography in reflection and transmission configurations. *Composites Part B: Engineering* **2015**; 57:35–46.
- [13] Bretz L, Hinze T, Häfner B, Lanza G. Evaluation of anomaly detection capabilities using a non-orthogonal camera angle in pulse-phase thermography. *Procedia CIRP* **2019**; 85:308–313
- [14] Busse G, Wu D, Karpen W. Thermal wave imaging with phase sensitive modulated thermography. *Journal of Applied Physics* **1992**; 71(8):3962–3965.

TOPIC

Design and Layout



@DGM_eV

#Hybrid2020

Surrogate modeling of hybrid material pairings including organic sheets

M. Richter^{1,2,*}, H. Gese¹, H. Dell¹, G. Oberhofer¹, F. Duddeck^{2,3}

¹ MATFEM Partnerschaft Dr. Gese & Oberhofer, Munich, Germany

² Department of Civil, Geo and Environmental Engineering, Technical University of Munich, Germany

³ School of Engineering and Materials Science, Queen Mary University of London, UK

Abstract: Organic sheets bear a huge lightweight potential to replace conventional steel sheets due to their high specific material parameters, promising deep-drawing properties, as well as capability of energy absorption. To establish organic sheets in a material mix, adequate joining technologies are required which allow to produce reliable, load-bearing joints in a reproducible manner for a hybrid material pairing between steel sheets and organic sheets. With the help of a remote laser, hybrid material joints are manufactured with a thermomechanical formed form-closure and characterized using a modified set-up specimen. Based on the experimental results, surrogate models are developed to represent the deformation and failure behavior of the joints in a simulation complying with industrial discretization. Prerequisite for this development is a phenomenological material model for the organic sheet covering its elasto-plastic hardening as well as fracture initiation ranging from a brittle mode in fiber direction to a ductile one in off-axis orientations. A workflow using quantifiable criteria is introduced which allows the objective calibration of the model parameters for multiple load-cases taking the locally induced damage by the joining process into account. This workflow is demonstrated here for the hybrid material pairing of an organic sheet 102RG600 Tepex® dynalite and ENAW6082-T6 and S355J2H. The results presented in this paper are based on the joint research project “LaserLeichter”.

Keywords: phenomenological material model, organic sheet, characterization of hybrid joints

1 Introduction

The application of multi-material design is offering new approaches for weight reduction of vehicles ensuring future transportation regardless of their powertrain. The hybrid construction allows the combination of material specific advantages by employing materials for their locally defined properties. As a chain can only be as strong as its weakest link, efficient joining technologies to create reliable, load-bearing joints are a key enabler for the multi-material design. The current state of the art of conventional joining technologies, like gluing or riveting, allows to do so but it suffers from the drawback of adding additional material to the joints and hence further increasing the weight and limiting flexibility. The use of a laser-beam for joining dissimilar material pairings of metals and reinforced thermoplastics, either directly by welding or indirectly via thermomechanical forming, is a promising approach. The use of the laser shows a high potential in terms of flexibility and industrial automation for the construction of structural parts.

Regardless of the type of propulsion technique, weight reduction of structural parts is a key-enabler for primary and secondary weight savings in the automotive sector. Organic sheets have a high potential for weight savings because of their superior mechanical properties as stiffness and strength per weight. An organic sheet is a semi-finished product consisting of an equally balanced weaving structure embedded in a thermoplastic matrix. Further, it can be deep-drawn as conventional steel sheets

and ribs and other functional parts can be added afterwards in a subsequent mold-injection process using the same thermoplastic matrix with short fiber reinforcement. Joining of two sheets can be achieved without additionally adding weight such as in the gluing or riveting using the bridge-deck-panel concept from the Fraunhofer Institute for Material and Beam Technology (IWS) in Dresden/Germany.

In order to establish not only the organic sheets but also possible hybrid joints with other metallic materials in a virtual development process, not only adequate material models are needed but also surrogate models for the joints [1]. They are described in the following.

2 Hybrid bridge-deck panel joints

Joints with a hybrid material pairing of SJ355J2H 1.50 mm and Tepex® dynalite 102RG600 2.0 mm are manufactured at the Fraunhofer IWS Dresden using the concept of bridge-deck panel joints. In this process, two sheets can be joined using a remote laser. The metallic sheet serving as the deck panel is cut open and a bridge is cut into the end of the organic sheet using a laser. The bridge is then inserted in the metallic deck panel so that it overlaps. In the last step, the material is heated by a laser and rolled over creating a bulk (see Figure 1). This bulk of material creates an undercut on the back-side of the deck panel resulting in a form-closure of the thermo-mechanically formed joint. Because of its shape this bulk of material is referred to as “rivet-head”.



Figure 1: Cross-section (left) and joined bridge-deck-panel joint (right) of a hybrid material pairing

Different symmetrical and unsymmetrical setups of geometrical rolls and process parameters are analyzed at the Fraunhofer IWS. In a subsequent step, the most promising concept resulting in the highest strength values is further investigated. Hybrid bridge-deck panel joints are tested under multi-axial loading with a quasi-static, monotonously increasing load – head tension, transversal and longitudinal shearing (see Figure 2). Different lengths of bridges are analyzed as well as adhesion promoters; in addition, adding a micro-structure to the back of the deck panel with the use of the laser to enhance the ultimate strength of the pairings is investigated.

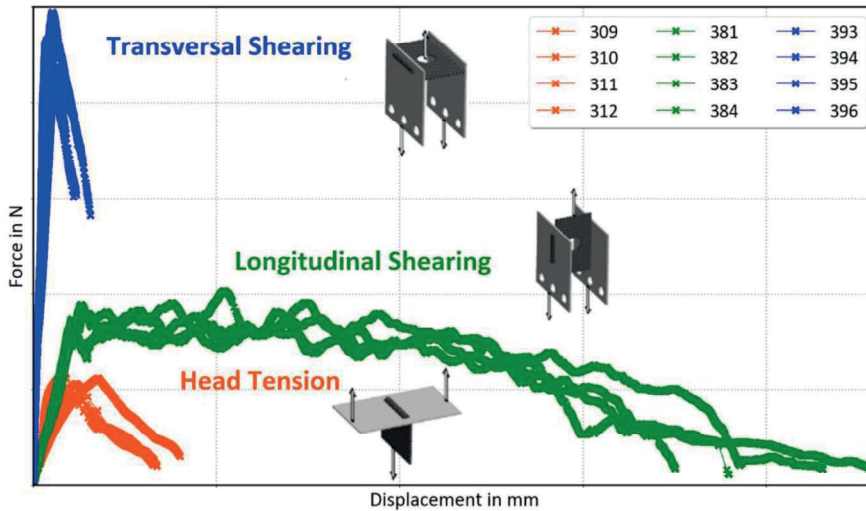


Figure 2: Force-displacement curves of the bridge-deck-panel joints with three different loading types

3 Phenomenological material modeling of organic sheets

Prerequisite for the simulation of the mechanical joints is a comprehensive description of the base material. For the complex material behavior of the organic sheet this remains until now a challenge [2] [3]. The complex material behavior derives from a combination of a relatively soft matrix and brittle endless fibers which are woven with the twill weave binding in a textile fabric which is equally balanced in weft- and warp-direction (see Figure 4).

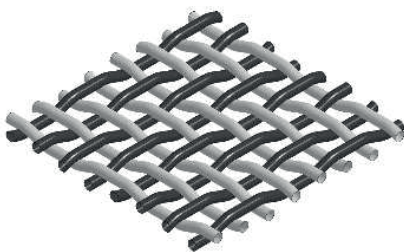


Figure 3: Weaving structure of the twill weave binding of the organic sheet 102RG600

Organic sheets are an example of endless fiber-reinforced plastics (EFRP) and are semi-finished products which may consist of multiple layers. A loading in-plane in fiber direction shows a very stiff behavior until brittle fracture occurs, whereas an in-plane loading in off-axis orientations shows a softer elasto-plastic behavior and a ductile fracture mode. Therefore the anisotropy in the elastic and plastic regimes as well as in fracture needs to be covered by the material model. With the user-defined material model MF GenYld+CrachFEM this is achieved by combining orthotropic elasticity with an orthotropic yield locus for plasticity [4]. After trespassing the elastic regime, the non-linearity of the material behavior is modeled with a stress-state- and strain-rate-dependent plastic hardening law accounting for the permanent deformations. This approach allows to model the effective material behavior - also referred to as the diffuse damage by [5] - measured in the experiments accumulating the damage on a micro- and meso-scale.

To meet the needs of the two different constituents of the organic sheet, fracture is covered with two separate models. First, an orthotropic, strain-based model to describe the failure initiation of the ductile orientation mainly dominated by the behavior of the thermoplastic matrix is proposed [6] [7]. Additionally, an orthotropic stress-based fracture model is used to account for the brittle behavior of the endless fibers. This combination allows to use the more sensitive measure for the fracture assessment – a threshold value in the stress- and in the strain-space for the fracture of the fibers and the matrix respectively. Lastly, the strain rate dependencies of plastic hardening behavior and fracture

need to be calibrated carefully to cover the opposing trends of the strain rate dependency from matrix and endless glass fibers in a single model.

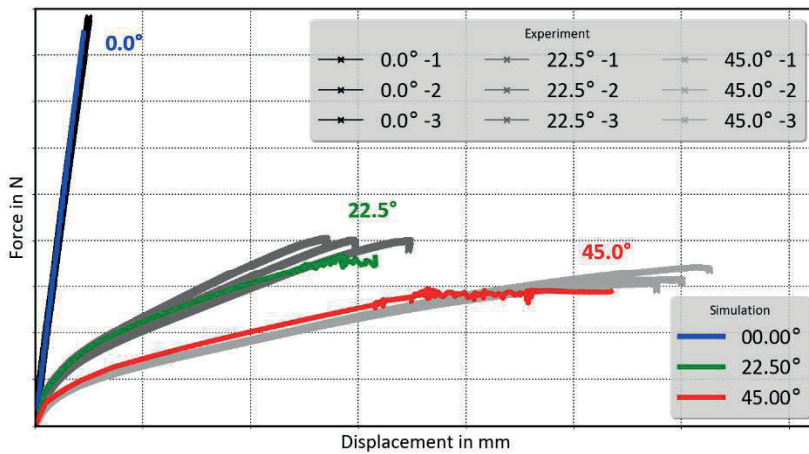


Figure 4: Comparison of force-displacement curves from experiment and simulation of the uniaxial tension for three different orientations

In this study, the user-defined material model MF GenYld+CrachFEM 4.3.0 in combination with *Abaqus explicit* 2016 are used for modeling the base material for the metallic sheet as well as the organic sheet [8] [9]. In Figure 4, the experimental results are compared to the simulation results for an in-plane, uniaxial loading under three different orientations. For the experiments the specimens in accordance DIN EN ISO 527-4 are used. The simulation results show a good agreement to the experimental results including an almost exact depiction of fracture under different orientations. Prior to the experiments for the material characterization, the coupons are conditioned in accordance with [10] to account for the moisture-dependent material properties of the PA6 matrix. The combination of different phenomenological modules in the material model MF GenYld+CrachFEM enables to depict the above discussed mechanisms on a macro-scopic scale covering also the its nonlinearities which originate predominantly from the matrix [11]. This allows engineers to keep the computational costs for a component level or for a full-vehicle crash level within a reasonable range.

4 Mechanical surrogate model

Basis for the development of surrogate models is a comprehensive material characterization of the base materials with the material model MFGenYld+CrachFEM, in order to correctly depict not only the elasto-plastic but also the fracture behavior phenomenologically. The objective for the development of the surrogate model is to substitute them into a component covering fully the deformation and failure behavior of dissimilar material pairings. As the time step size of an explicit crash simulation is determined by the smallest element length in the complete component, a very detailed model would dramatically increase the overall computational cost on a component level.

This development can be done via two steps as depicted in Figure 5. Based on the geometrical dimension from a cross-sectional cut, a fine-discretized and therefore detailed FE model is created. On the basis of metallographic analysis, micro-hardness measurements, and μ CT-scans of the joint, a detail model can be created. This model enables with a fine resolution a thorough look at the behavior of the joint and can serve as a “virtual laboratory”.

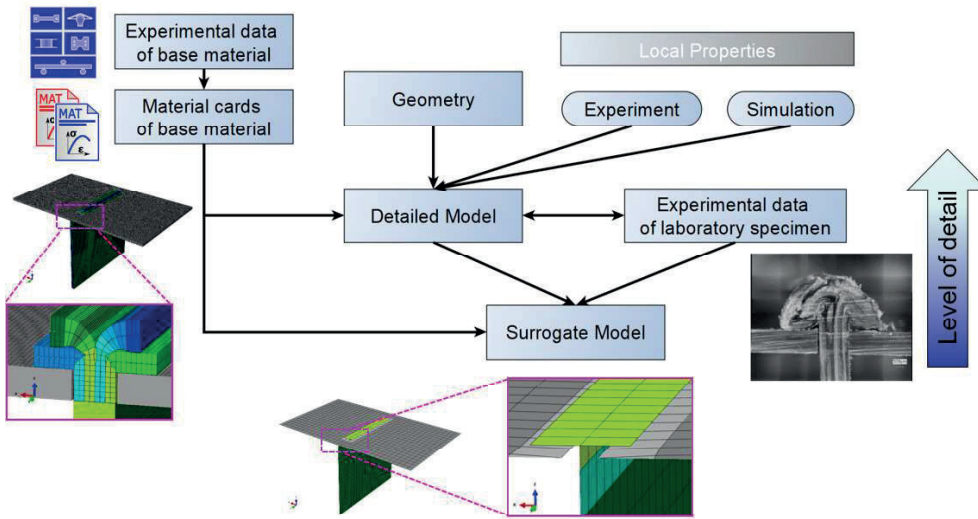


Figure 5: Scheme for the development of detailed and surrogate models for hybrid material pairings

This behavior needs to be abstracted in a consecutive step for the development of the surrogate model, so that with the use of a deliberate modeling, an industrial discretization can be deduced, for which the material parameters can be calibrated. Coarse shell discretization with an average shell length of 2.50 mm is used. The development of the surrogate models is hence a trade-off in computational cost and level of detail and resembles the best compromise of modeling the hybrid joints using solely shell elements.

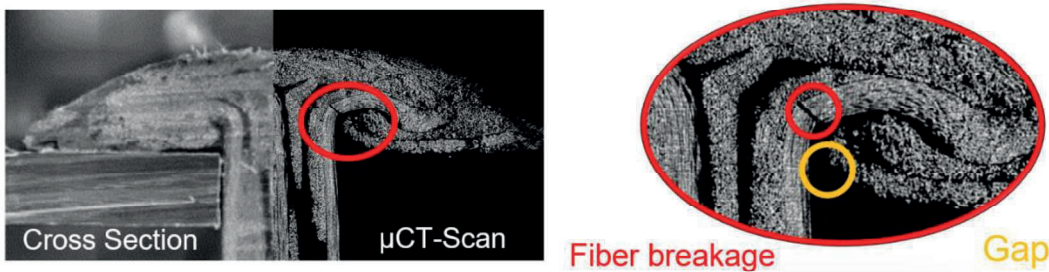


Figure 6: Cross-section cut and μ CT-Scan of the thermo-mechanically formed rivet head of organic sheet material

Figure 6 shows a cross-section of the bulk material shaped like a “rivet-head” creating the form-closure on the backside of the deck panel. With a closer look to the microstructure of the bulk material in the μ CT-Scan imperfections in the so-called “rivet-head” such as fiber breakage or spots with missing material can be found. This is a damage induced by the joining process with heat introduced by the laser and the subsequent mechanically forming step, which locally altered the properties of the base material. Therefore, this damage needs to be accounted for in the structural simulation. With the use of the user-defined material model it is further possible to initialize the locally induced damage by the joining process at the beginning of the simulation. The user-routine MF Init allows the initialization of Solution Dependent Variables (SDVs) in Abaqus individually per integration point (see Figure 7). With its use, gradients of material properties can be modeled in a single shell element.

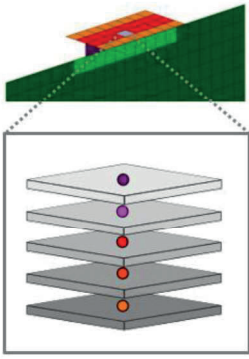


Figure 7: Initialization of History Variables in an inhomogeneous manner across the thickness of a shell element

Because simplifications need to be made for the calibration of the surrogate models in comparison with the detail model, not all joints can be modeled with the same precision across all loading scenarios. This is why quantifiable criteria for the evaluation of the model accuracy are introduced and weighted in accordance to the requirements of the model. With this procedure, an objective measure and target-oriented calibration of the surrogate model is feasible for the considered loading types head tension, transversal and longitudinal shearing. The simulation results using the optimal parameters of the surrogate model using purely shell elements are depicted in Figure 8 for a varying bridge length of 10.0, 20.0 and 40.0 mm. The deformation and failure behavior is well captured across multiple loading types. The biggest difference can be seen for the length of 10.0 mm, where very little bulk material can serve in the form-closure. Furthermore, the load-case of longitudinal shearing is difficult to capture. In this load-case the bridge of organic sheet is sheared off over the metallic deck panel. This is modeled using an edge-to-edge contact, which allows to capture the maximal strength well, but the element deletion after the onset of fracture will cause the oscillation of the force. This continuous shearing process of the organic sheet can hardly be captured using purely shell elements.

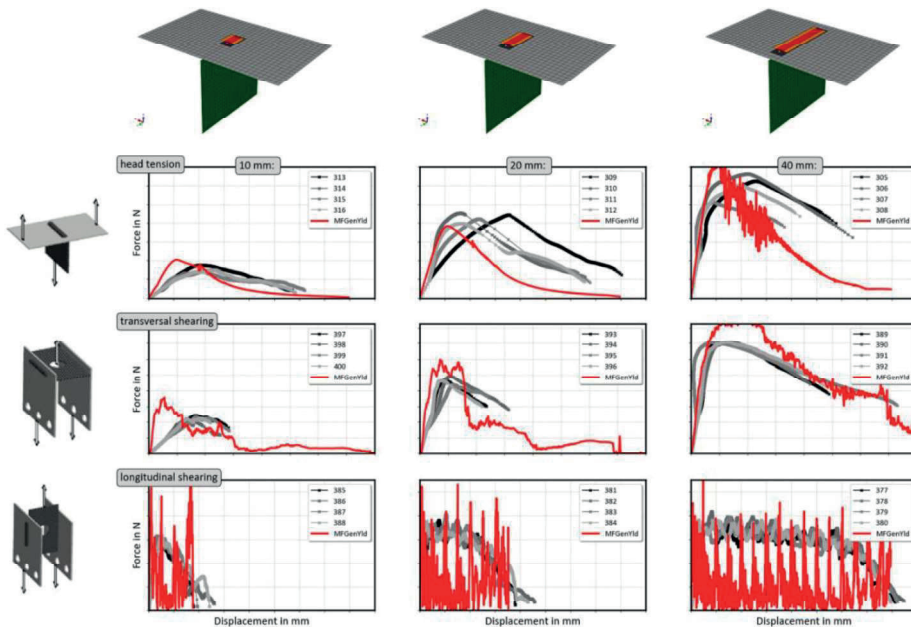


Figure 8: Force-displacement curves for a surrogate model for three loading types and varying bridge length

The developed method allows a systematic development of surrogate models with a special focus on the issues of dissimilar material pairings. The simulation results resemble a good approximation of the deformation and failure behavior, without strong increase of the computational cost.

5 Conclusion and Outlook

The organic sheets can be well modeled with a combination of different phenomenological modules in *MF GenYld+CrachFEM*. Further, a systematic approach for the development of surrogate models with a special focus on hybrid material pairings is established. Key enabler is the use of the subroutine *MF Init* which allows to integrate the locally altered material properties as e.g. the damage induced by the joining process in shell elements.

Until now, only a simple isotropic, post-critical module for metallic materials in *MF GenYld+CrachFEM* is established to model the organic sheets after the onset of fracture. An extension of the two-folded fracture evaluation with strain- and a stress-based fracture models will allow in the future to treat the two constituents of the composite separately.

However, the insertion of these surrogate models into the discretization of hybrid structures currently represents an additional effort, whose insertion in form of a submodel could be automatized in future projects.

6 Acknowledgement

The presented work above has been part of the research project "Development of laser-based joining technologies for dissimilar lightweight structures" which is funded by the German Federal Ministry of Education and Research (BMBF) under grant no. 13N12877. The authors are grateful for the contribution of the other research partners whose work and effort have been a valuable input for the basis of this work.

Further, this work would not have been possible without the help and support of our colleague Matthias Vogler, whose insight and understanding of both material characterization and material modeling were an essential contribution and valuable input. Sadly he passed away in the beginning of 2017.

7 References

- [1] M. Gude, H. Lieberwirth, G. Meschut, E. Tekkaya and M. Zäh, Forel-Studie 2018, Ressourceneffizienter Leichtbau für die Mobilität, **2018**.
- [2] M. Brandt, „Berechnungsmöglichkeiten für gewebeverstärkte thermoplastische Composites,“ in *Kunststoffe + Simulation*, München, **2016**.
- [3] J. Coulton, „CAE of Organo-Sheet Material,“ in *11th LS-Dyna Forum*, Ulm, Germany, **2012**.
- [4] M. Vogler, H. Dell, G. Oberhofer, and H. Gese, „Beschreibung von unverstärkten, kurzfaserverstärkten und endlosfaserverstärkten Kunststoffen in der Crashsimulation,“ in *Kunststoffe + Simulation*, München, **2016**.
- [5] R. Böhm, M. Gude, and W. Hufenbach, „A phenomenologically based damage model for textile composites with crimped reinforcement,“ *Composites Science and Technology* Vol. 70 No. 1, pp. 81-87, **2010**.
- [6] H. Hooputra, H. Gese, H. Dell and H. Werner, „A comprehensive failure model for crashworthiness simulation of aluminium extrusions,“ *International Journal of Crashworthiness* Vol. 9 No. 5, pp. 449-463, **2004**.
- [7] F. Brenner, H. Gese, H. Dell, G. Oberhofer, and G. Metzmacher, „Use of specific models for creep, plasticity and fracture in forming and crashworthiness simulation via UCREEP and VUMAT,“ Deutsche SIMULIA-Konferenz, 12.-13. November 2015, Aachen **2015**.
- [8] H. Gese, G. Oberhofer, F. Brenner, and M. Richter, „Comprehensive modeling of lightweight materials in crashworthiness simulation enables more reliable virtual development,“ *Enginesoft Newsletter* 4, pp. 54-58, **2018**.
- [9] H. Dell, M. Vogler, H. Gese, and G. Oberhofer, „Current solutions and open challenges in modeling organic sheets,“ in *CAE Grand Challenge*, Hanau, Germany, **2016**.
- [10] N.N. „Wasseraufnahme und Konditionieren von Formteilen aus Durethan,“ Lanxess, Deutschland, **2010**.
- [11] V. Ulbricht, M. Kästner, T. Lichtneckert, J. Brumund, K.-H. Modler, W. Hufenbach, R. Böhm, C. Ebert, B. Grüber, A. Langkamp, and M. Lepper, „Modelling of the effective material behavior of textile reinforced composites,“ *Journal of Plastics Technology*, **2007**.

Numerical investigation of the hole-drilling method applied to intrinsic manufactured metal-cfrp hybrids

S. Tinkloh¹, T. Wu², T. Tröster¹, T. Niendorf²

¹Paderborn University, Paderborn, Germany, ²University of Kassel, Kassel, Germany

Abstract: Automotive lightweight design is a considerable measure to meet the worldwide need for reducing CO₂ emissions. However, the lightweight potential of common lightweight materials like high strength steels or aluminium is limited. Even carbon fibre reinforced plastics (CFRP) components, which have superior lightweight characteristics, show limitations for the car body design, as catastrophic failure or high production costs. Hybrid allow to combine metals and CFRP in a manner to offset the drawbacks of every single material and reach an optimum of mechanical properties and costs. Nonetheless, an essential shortcoming of hybrid materials are thermally induced residual stresses after cooling down from the molding temperature to ambient temperature, driven by contrary coefficients of thermal expansion and chemically induced shrinkage of the CFRP.

Conventional methods for determining residual stresses in thickness direction are not reliably applicable for CFRP-metal hybrids. Several specific hybrid characteristics pose a challenge for conventional methods. A reliable experimental approach to accurately determine the residual stresses is the hole-drilling method. In order to comprehend the experimentally measured residual stresses, finite element simulations are carried out.

For a reliable prediction of the residual stresses on the macroscopic level during the curing process, a numerical homogenization technique of a representative unit cell is used to calculate effective cure-dependent properties. The simulation of the incremental hole drilling method is simulated by an implicit element remove technique. Furthermore, a fibre waviness is introduced with the goal of obtaining information about the sensitivity of the hole drilling method with regard to varying parameters.

1 Introduction

Time- and cost-efficient production of metal-CFRP hybrids can be achieved if the bonding between the components and the actual component production are integrated into a single process step [1], [2], [3], [4]. An essential shortcoming of intrinsic hybrid materials are thermally induced residual stresses after cooling down from the molding temperature to ambient temperature, driven by varying coefficients of thermal expansion and chemically induced shrinkage of the CFRP. The induced residual stresses are shown by structural deformations, which are reflected, for example, in a spring-in effect of closed angles. With regard to manufacturing technology, springback has a significant influence on the production of three-dimensional components and ultimately on the geometric design of the forming tools. The aim is to be able to predict the resulting deformations exactly. Since the springback results from the residual stresses present, knowledge of the residual stress state is essential.

For the systematic analysis of residual stress states in metal-plastic hybrids, the incremental hole drilling method (HDM) is used on the plastic side. The applicability for fibre-plastic composites poses a special challenge due to the specific properties of the FRP. The anisotropy, the microscopic heterogeneity, the viscoelasticity of the matrix, as well as the high stress gradient near the boundary layer, pores and delaminations have to be considered. The aim of this work is to precisely predict the residual stress state using numerical simulation methods. To this regard, a micromechanical approach for

the determination of effective cure-dependent elastic and expansion coefficients is presented. The effective material parameters are used to calculate residual stress states in intrinsic manufactured metal-CFRP hybrids. This model serves as a basis for further investigation of the incremental HDM. In detail, the production-related fiber waviness on the quality of the incremental HDM for metal-CFRP hybrids will be investigated.

2 Simulation of intrinsic manufacturing process

2.1 Effective cure-dependent properties

A micromechanical-based approach is chosen for the prediction of the residual stress state across multiple length scales. The approach is based on the numerical homogenization of a hexagonally packed three-dimensional unit cell. A thermo-chemo-mechanical material model for the matrix phase is defined in the microscopic unit cell to simulate the curing of the CFRP. First, the simulation of the microscopic unit cells was carried out using a prescribed time-temperature profile (see fig. 7). This was used to predict microscopic residual stresses in the fiber-matrix composite [6]. For homogenization of elastic properties, the degree of cure was varied in the interval $[0, 1]$ with a step size of 0.1. A degree of cure of 0 corresponds to the uncured state, 1 corresponds to the fully cured state. The effective stiffness of the representative unit cell is determined by numerical homogenization at the eleven discrete degrees of cure. The entries of the effective transversal isotropic elasticity tensor are shown in the figures Fig. 1 as a function of degree of cure.

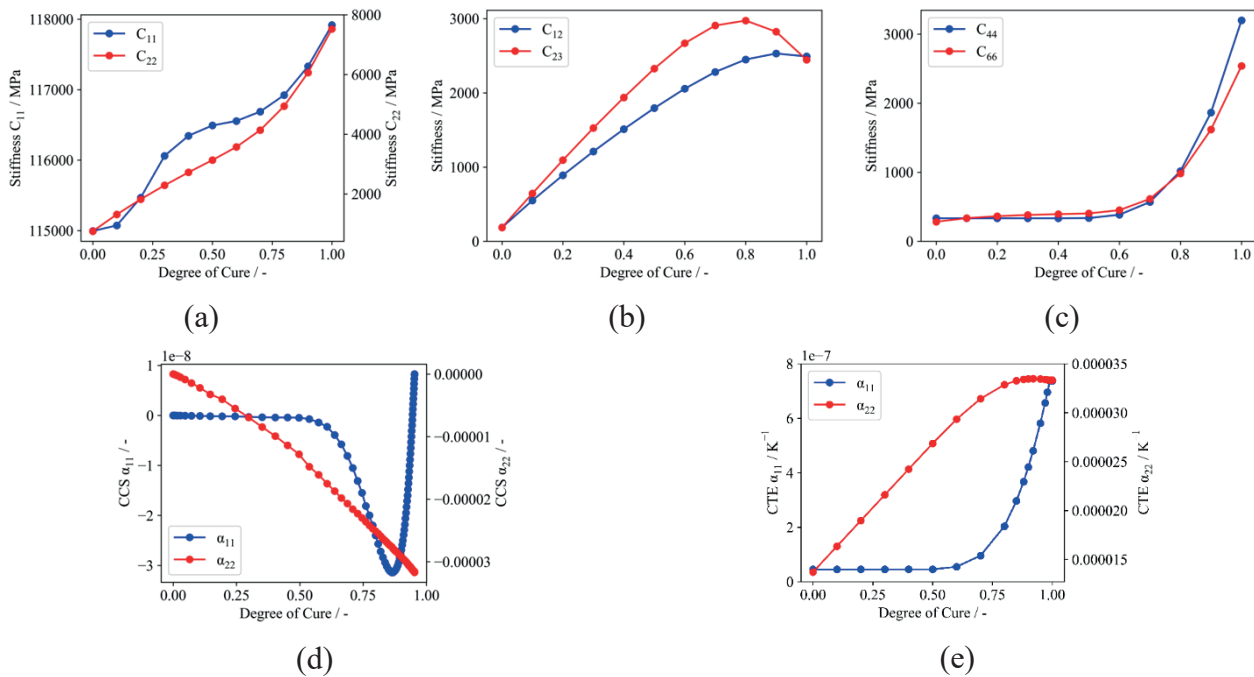


Figure 1: Evolution of the direct elastic coefficients as a function of the degree of cure (a), (b), (c). Due to the assumption of the transversal isotropy, the terms C_{22} and C_{33} are equal and C_{12} and C_{13} are equal. (d) and (e) show evolution of the effective transversal isotropic chemical shrinkage coefficient and thermal expansion coefficient as a function of degree of cure.

In addition to homogenized stiffness, an effective thermal and chemical coefficient of expansion was also calculated. For this reason a defined temperature difference ΔT was applied to the unit cell and the volume-averaged strains were then determined. The predicted effective transversal isotropic expansion coefficients are shown in figure 2 (d) and (e).

2.2 Residual stress prediction

Plane metal-CFRP hybrids were used for the residual stress measurements using the incremental HDM (fig. 2). Along the 2-axis the degrees of freedom in 1-direction are frozen at the slice plane. The interface is perfectly bonded starting at $t_0 = 0$. For the analysis, an uncoupled thermo-mechanical analysis was carried out by specifying the temperature field $T(\mathbf{x}, t)$ over the entire domain. The simulations were done with the finite element software Abaqus/Standard.

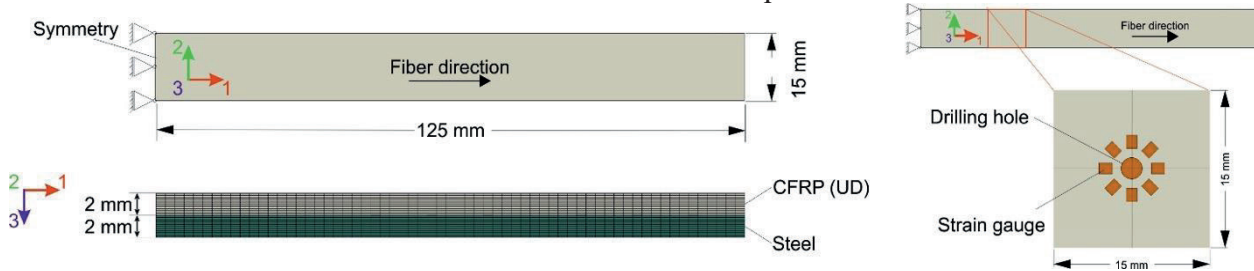


Figure 2: Schematic description of the boundary conditions, which were applied due to the symmetry (mirror symmetry about 1-3 plane and 2-3 plane) of the analyzed metal-CFRP specimen.

The degree of cure is calculated using the USDFLD user subroutine. The transversal effective thermal expansion coefficients and the effective chemical shrinkage coefficients are specified for the CFRP laminate using the UEXPAN user subroutine. The elasticity parameters are stored as tabulated data depending on the degree of curing. Further information on the homogenization method used here and the associated thermo-chemo-mechanical constitutive model are available in [6].

Figure 3 (a) shows the corresponding time-temperature profile, a constant curing temperature ($T=160\text{ }^{\circ}\text{C}$) is assumed. After curing is completed, the temperature is linearly ramped down to the ambient temperature of ($T=20\text{ }^{\circ}\text{C}$). The corresponding residual stress states after complete curing at curing temperature (red) and after cooling from the curing temperature (blue) are also shown in Figure 7 (b). Due to the chemical shrinkage and the cure-dependent thermal expansion of CFRP, residual stresses are already induced during curing. On the metal side, these are approx. 40 MPa at the interface to the CFRP.

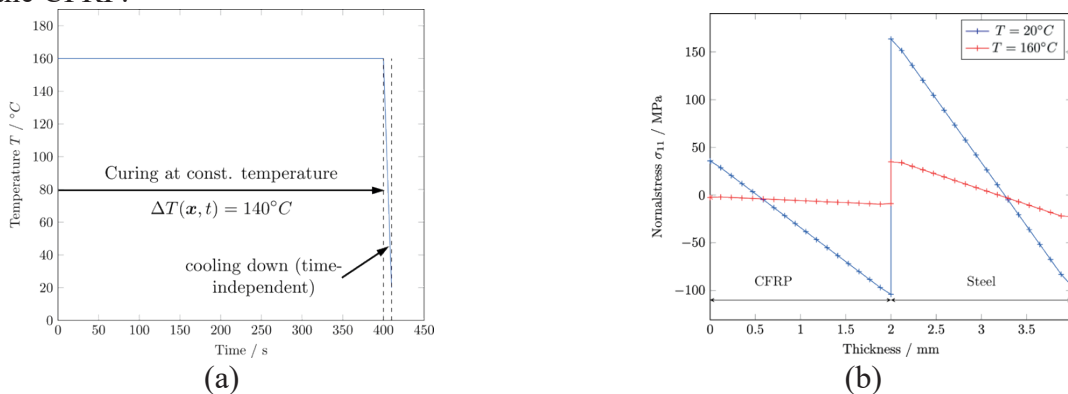


Figure 3: Prescribed time-temperature profile $T(\mathbf{x}, t)$ for the whole domain (left) and the corresponding residual stress state in thickness direction after curing completed (right, $T=160\text{ }^{\circ}\text{C}$) and after cooling down to ambient temperature (right, $T=20\text{ }^{\circ}\text{C}$).

3. Simulation of the incremental hole-drilling method

Finally, in this section the simulation of the incremental HDM is presented. In this context, the modelling technique, which is based on a submodel approach, is presented first. Following the verification of the approach with experimental results of the incremental HDM is discussed. In order to get a knowledge of influencing parameters, a fiber-imperfection is introduced and analyzed.

3.1 Modelling approach

The dimensions of the plate are large compared to the drilled hole diameter (2 mm). For a sufficiently accurate strain resolution around the borehole an element length of approx. 50 μm is required. A complete meshing of the geometry (see Fig. 2) with this element dimension is not possible. Furthermore, this would only require unnecessary computing capacity, as it can be stated that the borehole does not influence the global residual stress state in the plate, i.e. no coupling takes place. This means that the use of a submodel technique is appropriate. The model shown in Figure 6 is used to calculate the underlying global residual stress. In the next step, a submodel is defined that covers the borehole and the area of the applied strain gauges. The last step includes the simulation of the hole-drilling process using the functionality "model change" available in Abaqus/Standard. Defined layers are removed incrementally.

3.2 Validation

To validate the modeling approach, the results for the ideal compound are compared with the experimental results of the incremental HDM. In the experimental measurement 8 strain gauges were applied. For the calculation of the residual stress state in thickness direction 3 strain gauges are needed. Figure 5 shows the calculated residual stress in thickness direction for the CFRP and steel components. In addition, the measured residual stress curves are shown and the inversely calculated residual stress state with the simulated released strains is shown. It can be noted that the numerically predicted and the experimentally determined results are in good agreement. The state of residual stress determined by the simulated incremental HDM also agrees very well with the experimental results.

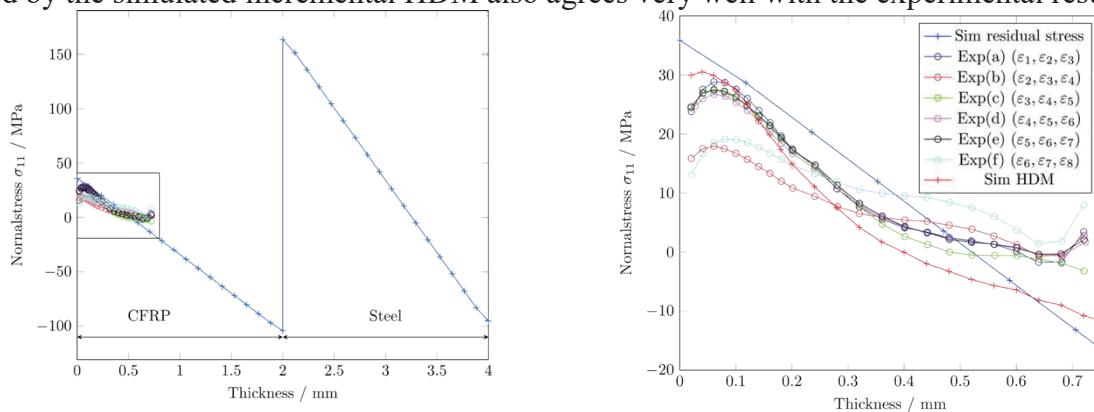


Figure 5: Validation of the predicted residual stress state in thickness direction by results obtained by the incremental hole drilling method. In addition, the simulated hole drilling method is (“Sim HDM”) also compared with experimental results.

3.3 Analysis of fibre waviness

The application of the incremental HDM represents a challenge on the CFRP side due to the heterogeneous microstructure. The influence of process-related defects, such as fiber waviness, which are induced during the manufacturing process, is unknown. In this section the influence will be investigated. In this context a sinusoidal fiber waviness is assumed

$$a \cdot \sin\left(\frac{2\pi \cdot x}{L}\right), \quad (1)$$

The angle of slope can be written as

$$\alpha = \arctan\left(\frac{2\pi}{L} \cdot \cos\left(\frac{2\pi \cdot x}{L}\right)\right). \quad (2)$$

Using the user subroutine ORIENT the slope angle varying along the x-axis was given up as a rotation angle around the z-axis.

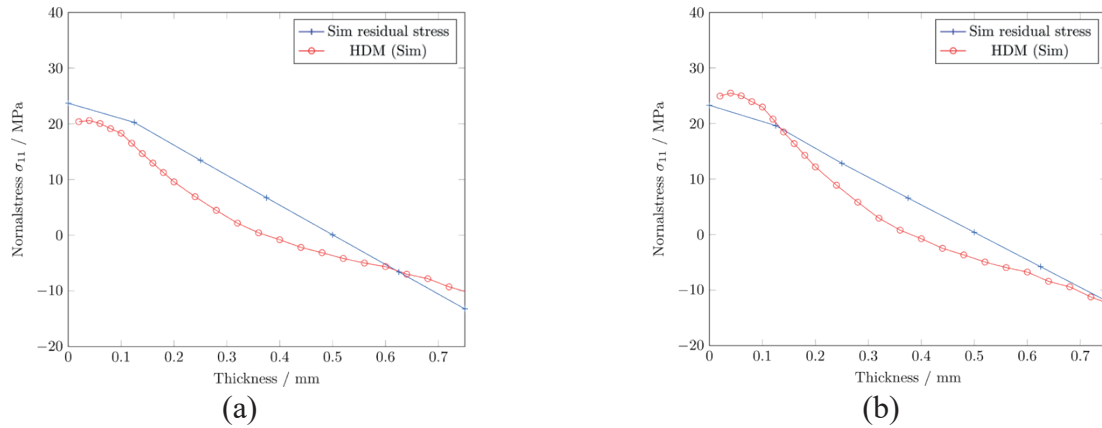


Figure 6: Comparison of the residual stress state determined with the simulated hole drilling method and with the actually existing residual stress state (a) $L = 2.29 \text{ mm}$; $a = 0.0526$ (b) $L = 27.9 \text{ mm}$; $a = 1.19$

In Fig. 6, a comparison between the actually residual stress state and the predicted residual stress state by means of simulated hole drilling method shown. It can be observed that due to the sinusoidal waviness of the fibers, the maximum residual stresses at the top of the surface is decreased by approximately 10 MPa (see fig. 5 and 6). The residual stress state is correctly measured for both fiber waviness values using the incremental hole drilling method. However, the influence of the waviness is slightly overestimated for the maximum residual stress σ_{11} at the top surface (see fig. 6 (b)).

If the released strains around the borehole are considered, it can be seen that an asymmetry of the strain distribution is induced by the fiber waviness. However, the asymmetry has already vanished in the region where the strain gauges are applied.

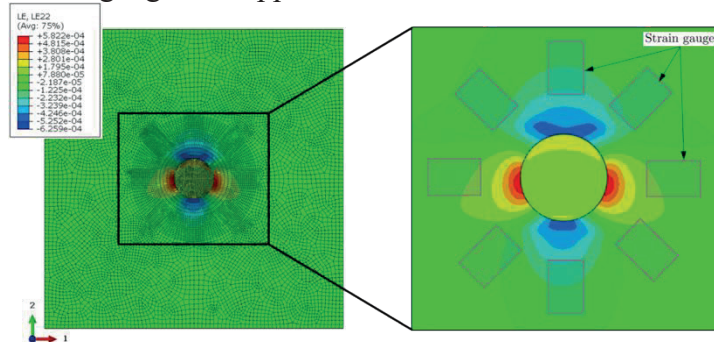


Figure 7: Contour plot of the strain distribution (ϵ_{22}) around the borehole (drilling depth: 0.8 mm). The right figure shows the arrangement of the strain gauges. Due to the fiber waviness, the strain distribution around the borehole is not symmetrical.

4 Conclusions & outlook

For a proper understanding and prediction of residual stresses in manufacturing processes of advanced hybrid structures, it is necessary to bridge the different length scales. For this purpose, effective cure-dependent properties were calculated. The advantage of the proposed approach is the numerical efficiency. Finally, the developed framework was validated by simulating an intrinsic hybridization of a 2D steel-CFRP plate. The predicted residual stresses in thickness direction were compared and validated by results obtained by the incremental hole drilling method. However, further investigations are necessary to validate the stress prediction across the whole thickness. In addition, the drilling process was modelled by an implicit element remove technique. The results are in good agreement with the experimental data. A further investigation of the influence of fiber waviness on the released strains and the subsequent predicted residual stresses were done. The residual stress state is influenced by the imperfection, however the hole drilling method can still adequately measure the residual stress state.

Nevertheless, it is not clear how inter- and intralaminar damage processes in the nearby drilling process zone influence the measurement of residual stresses. In this context, a multiscale technique is needed and taking the explicit simulation of the drilling process into account.

5 Acknowledgements

This research was supported by the Deutsche Forschungsgemeinschaft (DFG) (project number 399304816). The authors gratefully acknowledge for the financial support. The authors gratefully acknowledge the funding of this project by computing time provided by the Paderborn Center for Parallel Computing (PC2).

References

- [1] Z. Wang, C. Lauter, B. Sanitther, A. Camberg, *Manufacturing and investigation of steel-cfrp hybrid pillar structures for automotive applications by intrinsic resin transfer moulding technology 2* (2016) 229.
- [2] Z. Wang, M. Riemer, S.-F. Koch, D. Barfuss, R. Grutzner, F. Augenthaler, J. Schwennen, *Intrinsic hybrid composites for lightweight structures: Tooling technologies*.
- [3] R. Kießling, J. Ihlemann, M. Riemer, W.-G. Drossel, I. Scharf, T. Lampke, S. Sharafiev, M. Pouya, M. F.-X. Wagner, *On the development of an intrinsic hybrid composite*, Conference Series: Materials Science and Engineering 118 (2016) 012017.
- [4] R. Mahnken, C. Dammann, *A three-scale framework for fibre-reinforced polymer curing part I: Microscopic modeling and mesoscopic effective properties*, International Journal of Solids and Structures 100-101 (2016) 341 – 355.
- [5] C. Brauner, T. Frerich, A. S. Herrmann, *Cure-dependent thermomechanical modelling of the stress relaxation behaviour of composite materials during manufacturing*, Journal of Composite Materials 51 (7) (2017) 877–898.
- [6] S. Tinkloh, T. Wu, T. Tröster, T. Niendorf: *A micromechanical-based finite element simulation of process-induced residual stresses in metal-CFRP-hybrid structures*. Composite Structures (2020)

A holistic approach to optimization-based design of hybrid materials

M. Triebus¹, T. Tröster¹

¹Paderborn University, Paderborn

Abstract

Hybrid materials like fiber-metal laminates (FMLs) are able to lead to significant weight reduction with load adapted through-thickness and surface properties. In order to ensure that the full lightweight potential of hybrid components is exploited, a holistic top-down approach is considered. Starting with the final geometry and distributed stresses an optimal material distribution can be evaluated and transformed to a semi-finished blank. Nevertheless, the formability of this optimized FML is unknown, subsequently, the formability needs to be investigated and the thickness and surface properties need to be adapted to avoid forming failures. From a mathematical point of view, this is a classical multi-objective optimization problem with conflicting objective functions such as formability and lightweight factor for a given structural component. Therefore, the aim of the research project HyOpt is to obtain a purpose-built CAE method for tailor-made hybrid materials by using numerical optimization algorithms. By selecting material proportions, thicknesses and orientation angles, optima can be achieved in terms of lightweight, mechanical properties and forming characteristics. This holistic optimization routine demands basic investigations especially for suitable optimization algorithms.

1 Introduction

Lightweight body-in-white (BIW) structures play a significant role for automotive manufacturers to reduce the overall CO₂ fleet emissions, which are demanded by different governments around the world. The consequent need for automotive lightweight design has forced the automotive manufacturers to use a wide variety of materials. Recent BIW concepts as the BMW 7 G11 (2015) show a broad range of different materials such as aluminum, magnesium, steel and carbon-fiber-reinforced-polymers (CFRP) [1]. In addition, there is a significant increase of advanced production processes to use components with tailored properties. The idea of tailored-rolled-blanks, tailored-welded blanks or tailored-properties processes allow to design components with inhomogeneous material properties in one component [2]. Therefore, parts with load-adapted properties are possible, e.g. a b-pillar with maximum stiffness in the upper part and increased ductility in the lower part. Another approach for advanced lightweight components are through-thickness varying material properties. Classical sandwich material usually consists of a stiff face and a flexible core. The core carries the acting shear forces while the face material ensures bending stiffness. FMLs are able to increase the failure properties for dynamical loads e.g. crash and allow the FRP components to be orientated in predominant load directions. A widely used material in modern aircraft construction is the glass laminate aluminum reinforced epoxy (GLARE) [3]. However, the production of these components consisting of GLARE is still quite extensive and automation processes are the main research activities. In the research project LHybs it could be proven that a significant weight reduction could be achieved with

optimal through-thickness properties of FMLs for given objectives such as crash or stiffness properties [4]. Nevertheless, the formability of these FMLs is still challenging [5]. To summarize, the optimal material distribution for a given arbitrary (multi-) objective is optimal in all three spatial directions. Nowadays manufacturing processes and numerical tools provide engineers to reach maximum design freedom and rethink conventional objectives as a lightweight design [6].

2 HyOpt – A holistic approach

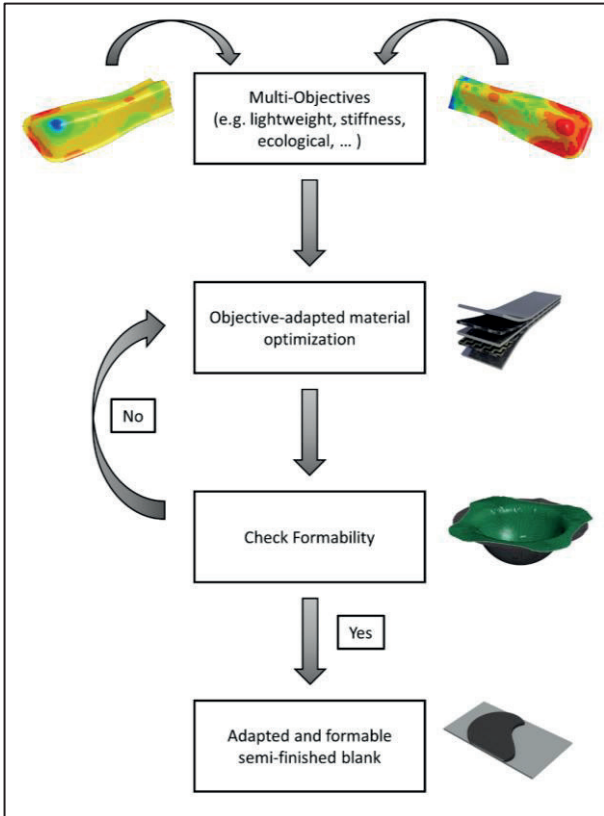


Figure 1: HyOpt – a holistic approach for optimization based design of hybrid materials

To ensure the full potential for the development of components a new holistic approach is going to be considered in the research project HyOpt, see figure 1. Starting with the final geometry of a component and the acting structural loads, objectives for the optimization routine will be defined, e.g. lightweight design w.r.t. constant stiffness and strength. These structural simulations are the input for the objective-adapted material optimization. A material database provides possible properties, which are considered during material optimization. In this way an optimal material distribution can be evaluated. In the next step, this resulting FML can be transformed to a semi-finished blank. A forming simulation is going to evaluate the formability of this FML. Critical forming limits are going to be avoided through locally adapted material orientation, which has been shown in [5]. By this adaption process the first draft for the resulting semi-finished blank has changed and needs to be reinvestigated if the defined objectives are still fulfilled. If this is not the case, the FML will be reevaluated until it fulfills the defined requirements. This is an iterative optimization process. The critical forming criteria need to be evaluated during the research project, as classical methods like forming limit curves (FLC) do fail to estimate the formability of hybrid laminates.

The resulting semi-finished blank with its material distribution and orientation tensors can be transformed into CAD-Data and be used in a fiber placement process [7]. Thus, the full process chain for the production of advanced lightweight structures is covered. One of the main goals of the research project HyOpt is the development of a stand-alone tool to design purpose-built hybrid materials – the HyOpt App. All aforementioned process steps will be integrated into one easy to use tool, which does not need expert knowledge of all involved stages. Through this easy workflow, the aim is to ensure broad distribution and acceptance of hybrid materials.

3 Evaluation of suitable optimization algorithms

During the the HyOpt process different kind of nonlinear optimization problems are considered. The field of nonlinear optimization is a broad field. The algorithms can be divided in gradient-free and gradient-based algorithms. Gradient-free methods like genetic algorithms are stochastic methods, which work on a random basis. Under the same start conditions they can lead to different results. Due to this stochastic characteristic, they are able to find global optima [8]. Gradient-based methods like the method of the steepest descent need gradient information of the underlying function. In this way, gradient-based optimization algorithms only work for differentiable functions. Moreover, they are usually restricted to find local optima, but have a high speed of convergence [9]. Both kind of algorithms are able to be constrained or unconstrained and therefore consider boundary conditions. Figure 2 shows an arbitrary simple material optimization problem.

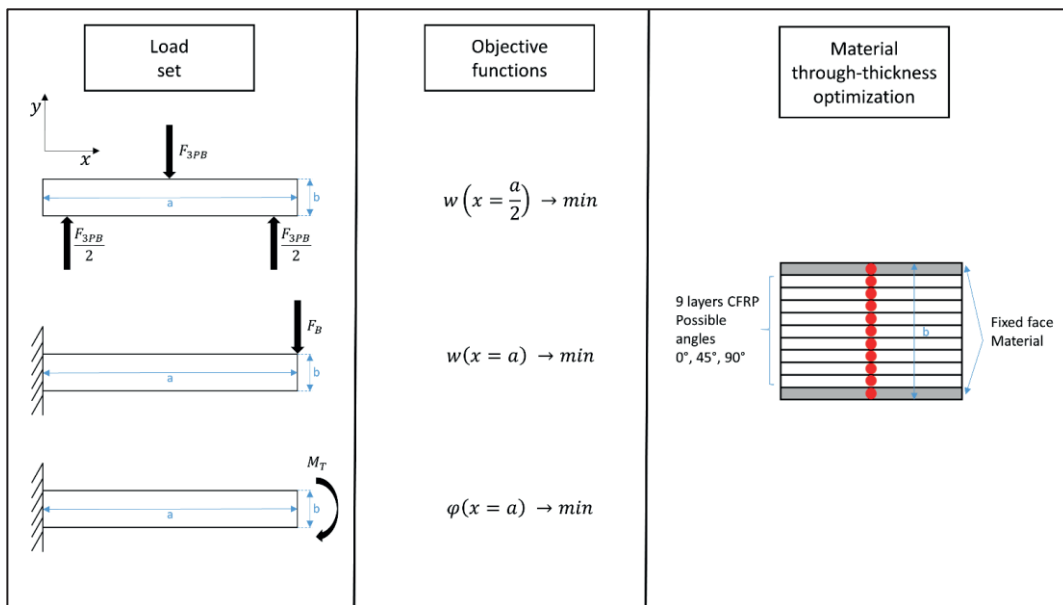


Figure 2: Example for a simple multi-objective optimization problem

For this problem there are already 19.683 (3^9) possible designs for the layer stack-up of the CFRP laminate. As we have three different load cases, this would lead to about 60.000 structural calculations, which – in this case – could be solved analytical or numerical. Nevertheless, this emphasizes that it is too expensive to evaluate all possible designs and it is inevitable to use methods of design of experiments [10]. Moreover as we are considering a holistic top-down approach in the HyOpt project the load set, which e.g. stem from full-vehicle BIW simulations, cannot be solved analytical anymore. In this way for the material optimization approach, it is useful to use as less simulations as possible

to decrease computational time. Moreover, the results from finite element simulations (FEA) are dependent of the solving strategy (explicit/implicit) and the discretization in time and space. Therefore, it is useful to use meta-model based optimization routines, which do create surrogate models from the response values of the simulations performed. There are different approaches for the functions of these meta-models. The easiest is a linear polynomial. A quadratic polynomial shows more flexibility, but does need more sampling points. The highest flexibility show neural networks as radials basis functions (RBF) or feed forward neural networks (FFNN) [11]. For these meta-model functions then gradient-free or gradient-based optimization algorithms can be used to find optima. Figure 3 shows a flowchart for a routine in the optimization program LS-Opt for the material distribution problem defined in figure 2 [12].

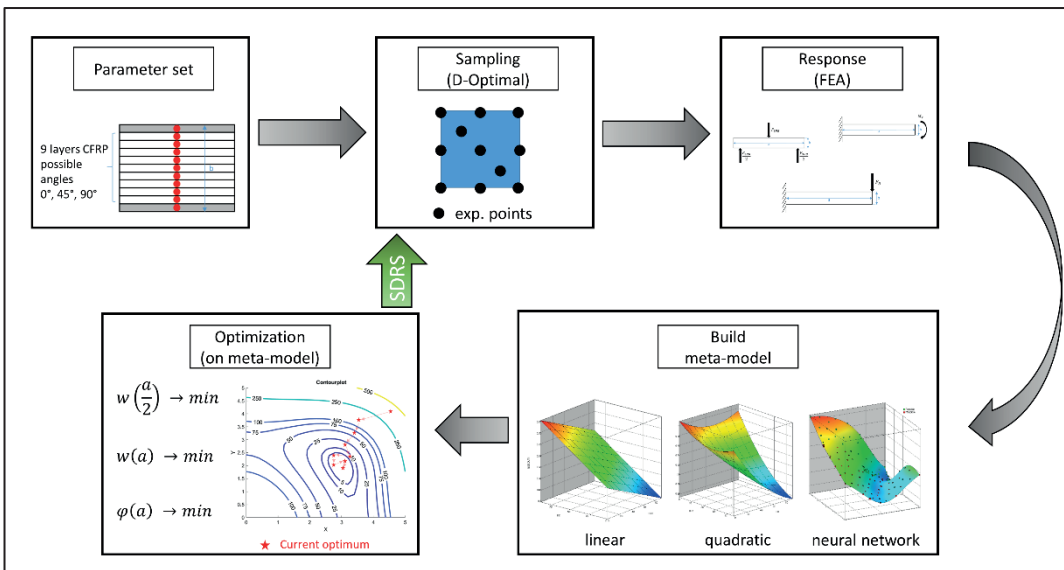


Figure 3: Flowchart for a meta-model based material optimization in LS-Opt

Due to their lack of accuracy, linear and quadratic meta-models are normally used with sequential domain reduction strategies (SDRS). After the optimization step the design space is reduced and a new set of experimental points around the current optimum is created. Therefore, the domain is iteratively reduced, see figure 3. The flowchart is the basis for the workflow of the material optimization in the HyOpt project.

4 Conclusion and outlook

Nowadays manufacturing processes and materials allow us to produce advanced lightweight design structures. The HyOpt approach is a holistic optimization-based routine, where selected components are optimized through-thickness and surface properties. Different algorithms and strategies for the optimization-based material design have been investigated. It has been shown that – as the number of design variables increases – only meta-model based optimization algorithms are suitable in terms of computational effort. The workflow for the material optimization routine has been shown and will be extended to more complex components and objectives in a next step. Furthermore, a material database will be created from which the optimization is evaluating the properties of the FML. In addition

the formability evaluation will be considered, these forming criteria for the FML need to be investigated experimentally.

5 Literature

- [1] J. Starke, *Carbon Composites in automotive structural applications* **2016**, Proceedings EuCIA: Composites and Sustainability, Brussels.
- [2] K. Mori et al., *Hot stamping of ultra-high strength steel parts* **2017**, CIRP Annals, Volume 66, p. 755-777.
- [3] A. Vlot, *Glare: history of the development of a new aircraft material* **2001**, Springer Netherlands, Dordrecht.
- [4] A. A. Camberg, T. Tröster, *Optimization-based material design of tailored stacked hybrids for further improvement in lightweight car body structures* **2018**, Proceedings of 3rd Int. Conf. on Hybrid Materials and Structures, Bremen.
- [5] T. Heggemann, W. Homberg, *Deep drawing of fiber metal laminates for automotive lightweight structures* **2019**, Composite Structures, Volume 216, p. 53-57.
- [6] M. Hahn, S. Gies, A. Erman Tekkaya, *Light enough or go lighter?* **2019**, Materials & Design, Volume 163, Article 107545.
- [7] J. Ufer, *Entwicklung und Validierung einer Technologie zur wirtschaftlichen Herstellung geometrisch komplexer Langfaser-Preforms unter Großserienrandbedingungen* **2017**, Dissertation, TU München.
- [8] V. Nissen, *Einführung in Evolutionäre Algorithmen: Optimierung nach dem Vorbild der Evolution* **1997**, Vieweg, Braunschweig.
- [9] J. Nocedal, S. J. Wright, *Numerical optimization* **2006**, Springer, New York.
- [10] H. Bandemer, A. Bellmann, *Statistische Versuchsplanung* **1994**, Teubner, Stuttgart.
- [11] C. M. Bishop, *Neural Networks for Pattern Recognition* **1995**, Oxford University Press, Oxford.

TOPIC

Intrinsic Hybrid Components



@DGM_eV

#Hybrid2020

Hybrid Fibre Reinforced Thermoplastic Hollow Structures with a Multi-Scale Structured Metal Load Introduction Element

V. Würfel¹, R. Grützner², F. Hirsch³, D. Barfuß¹, M. Gude¹, R. Müller², M. Kästner³

¹Technische Universität Dresden, Institute of Lightweight Engineering and Polymer Technology, Holbeinstraße 3, 01307 Dresden, Germany

²Fraunhofer-Institute for Machine Tools and Forming Technology IWU, Reichenhainer Straße 88, 09126 Chemnitz, Germany

³Technische Universität Dresden, Institute of Solid Mechanics, George-Bähr-Str. 3c, 01602 Dresden, Germany

1 Introduction

Carbon fibre reinforced polymers (CFRP) offer a considerable potential to save resources in lightweight constructions, due to their high specific mechanical material properties. However, joining operations are necessary in widely used monolithic or hybrid differential designs. In commonly used joining techniques for fibre reinforced materials, like bonding, bolting, riveting, welding or screwing, the join connection is formed after the manufacture of each single component in a subsequent process step [1]. This is often related to labour intensive operations like surface preparation and machining, which may add extra costs and or process-induced damage to the laminate. Metallic load introduction (LI) elements like inserts or onserts often reduce local stresses because of a material friendly enlarged load introduction area. Additionally, they offer the potential for an intrinsic manufacturing process, where consolidation of the CFRP part and joining are combined into one process step to reduce cycle times. For tubular structures, contour joints with metallic functional elements offer high load bearing capabilities. In intrinsic manufacture approaches for these structures, like the integral bladder assisted moulding process (IBM) [2] or the centrifugal process [3], the tubular CFRP component is consolidated and simultaneously moulded into a functional load introduction metallic element.

The aim of the presented approach is to utilize the benefits of intrinsic hybrid tubular structures with LI elements manufactured in the IBM process, enhance the performance and reduce cycle times by the use of braided carbon fibre reinforced thermoplastic tapes and hydroformed aluminium LI elements with a multi-scale structured contour design. This paper provides an overview of the intrinsic processing technology, the design of the contour joint and the development process assisted by simulation on all scales as well as the validation of the manufacturing quality and performance of the joint.

2 Intrinsic manufacturing process

The intrinsic manufacture-joining process for a tension-compression strut with a multi-scale structured LI element is presented in Fig. 1. In two separate process paths semi-finished parts are manufactured and the intrinsic hybrid is joined afterwards in an IBM process. The multi-layer tape-preform is produced in an innovative tape-braiding process. The metallic LI element is hydroformed in two

steps to sequentially form the necessary meso and macro structures for a form-fit connection. Subsequently, both semi-finished parts are joined in an integral bladder assisted moulding process, where the CFRP part is simultaneously consolidated and formed into the metallic LI element.

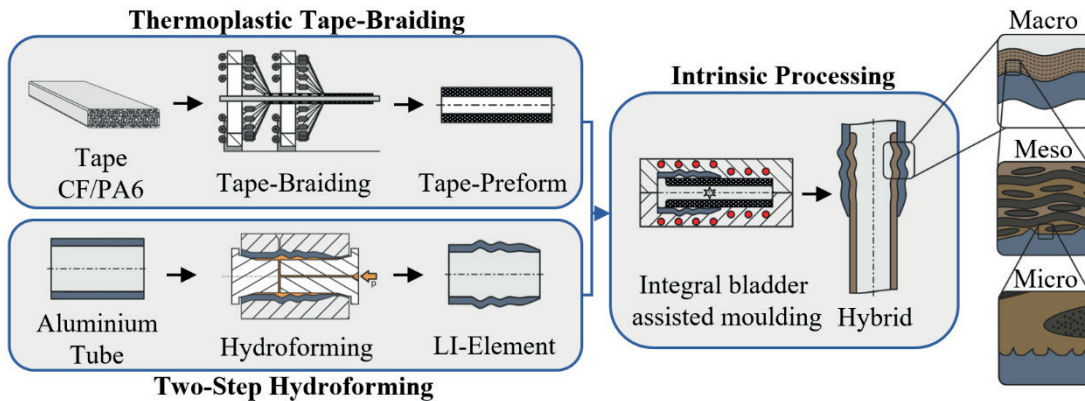


Fig. 1: Intrinsic manufacturing process with a multi-scale structured load introduction element

The utilisation of hydroformed metal tubes and braided thermoplastic tapes in combination with the bladder assisted moulding process enables a large-scale production of hybrid composite-metal structures without the need for any further trimming or joining operations.

2.1 Thermoplastic tape braiding

To achieve the aforementioned development targets of high performance and low cycle times, pre-impregnated unidirectional fibre reinforced thermoplastic tapes are used. Without the time-consuming impregnation step, only the individual layers of the tapes need to be fused together during consolidation, while closing of undulation gaps and forming into the LI element needs to be realised. Fibre damage is significantly reduced during the braiding operation, because the fibres are embedded into the matrix. Additionally, the tape braiding process offers high material output rates when multiple tapes are deposited simultaneously, complex contours and a high automation [4]. For a generic investigation, unidirectional carbon fibre reinforced Polyamide (PA) 6 tapes - Celanese, CF/PA6 Celstran® CFR-TP PA6 CF60-01- are used in this work.

2.2 Two-step hydroforming of load introduction element

A novel two-phase hydroforming process has been developed for a highly productive manufacture of metallic LI elements with multiscale structuring [5]. A tubular aluminium Al6060 T4 semi-finished part is inserted into a macrostructured outer tool together with the mesostructured inner tool (Fig. 2 left).

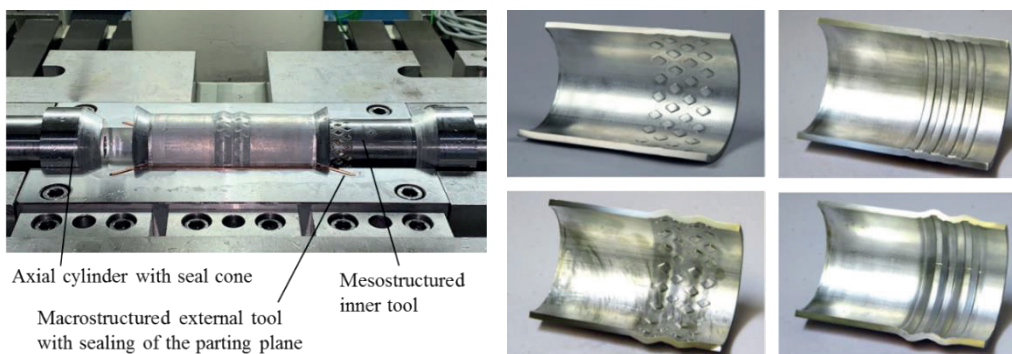


Fig. 2: Hydroforming tool (left), manufactured structures on meso- and combined meso-macro level (right)

In a first step, an external pressure is applied to achieve a diameter reduction in the joining zone of the metal tube by plastic deformation. The form elements of the mesostructure are moulded by forming the inner contour of the tube on the inner tool. In the second phase, a plastic diameter expansion of the metal tube is achieved by internal pressure application, whereby the macrostructure is formed on the outer tool. This combined process reduces resources, shortens handling times and allows the load introduction element to be manufactured in a single press cycle without the need for additional tools. Various types of undercut mesostructures have been designed, which either interact with individual fibres or create an interlocking joint with the tape braid. A diamond structure adapted to the braided fibre architecture and a structure with circumferential undercuts were realised (Fig. 2 right). Structuring depths of up to 0.8 mm could be achieved. A low-cost manufacturing alternative to the fibre interlocking patterns is a knurled inner meso contour which is an additional upstream process step.

2.3 Intrinsic processing by integral bladder assisted moulding

The two semi-finished parts are intrinsically joined in the IBM process. By pressure application to an internal bladder the thermoplastic preform is moulded and consolidated against a moulding tool in the tubular section and into the contours of the LI element, which thereby serves as the tool itself. Because of the use of fully impregnated thermoplastic tapes, two separate processing routes have been investigated: Variothermal heating of the moulding tool and external heating of the preform and subsequent consolidation and cooling in an isothermally heated moulding tool. To achieve very high heating rates in the variothermal consolidation route, thin aluminium tooling combined with inductive heating by an induction coil has been chosen to maximise efficiency and minimise cycle times. With internal pressure application during heating and air cooling cycle times of less than 10 minutes have been achieved [6]. Consolidation with isothermally heated tooling is also investigated. Hereby the braided tape preform is externally heated by infrared heating or by forced convection and then transferred into the moulding tool in which rapid cooling and consolidation takes place. With optimised heating and debulk of the preform, cycle times of one to two minutes are achievable with good laminate quality. Additionally, the process efficiency is increased because only the preform needs to be heated above the melting temperature while the moulding tool temperature just has to be maintained below the crystallisation temperature of the polymer.

3 Design of the contour joint and the development process assisted by simulation

During the development and design process several open questions must be answered, which are often hard or expensive to investigate experimentally. Thus, numerical investigations are suitable means. In Fig. 3 different finite element (FE) models are presented, which were developed to investigate different length scales. It can be distinguished between process simulations of the hydroforming and bladder assisted moulding steps and structural failure and strength simulations on the micro- and macroscale.

3.1 Structural simulation

Thorough investigations regarding the failure behaviour of the single parts, the material interaction and the effects of the structuring geometry are necessary to design contour joints. On the microscale in Fig. 3, a numerical model was developed, to study the influence of the interface roughness on the

overall strength and failure behaviour of the metal-composite interface, based on the modelling strategy presented by Hirsch and Kästner [7]. Therefore, a finite element model of a representative boundary layer between a metal component and CFRP is used to study the complex failure and damage mechanisms under mechanical loading. A distinction is made between adhesive failure of the metal-polymer and the fibre-polymer interfaces and cohesive failure of the polymer material. The numerical studies show, that rough or structured metal-polymer interfaces shift the dominant damage mechanism from pure adhesive to cohesive failure of the polymer and therefore lead to an increased effective strength of the boundary layer.

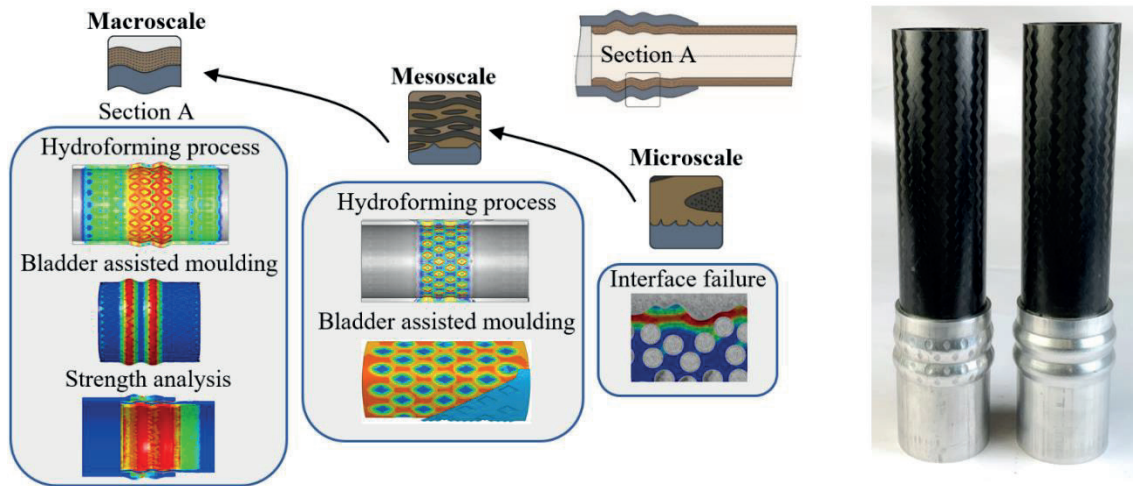


Fig. 3: Overview of the developed finite element models to investigate problems on different length scales - process influences are investigated with hydroforming and bladder assisted moulding simulations, whereas structural and failure behaviour are investigated on the micro- and macroscale (left), manufactured hybrid contour joints (right)

The simulations on the microscale give insight into the dominant failure phenomena and improve the accuracy of the cohesive zone approach in order to optimise the design and shape of the macro contour. Due to the high amount of design parameters of a contour joint, Barfuss et al. presented a design of experiment (DoE) approach to optimise the macro contour. Multiple FE simulations with linear elastic material behaviour and the CUNTZE failure mode criterion were used in the pareto optimisation to find the best design with the highest load bearing capability, which was assessed by inter-fibre failure, fibre failure and interface debonding. With an increasing number of undercuts and by grading of the macro contour, higher forces can be transmitted. A design guideline which considers the interface and manufacturing restrictions has been developed [8].

3.2 Process simulation

In order to understand process boundaries, numerical investigations of the manufacturing processes have been performed. The draping behaviour of the braided preform into the structured LI element during the bladder assisted moulding process was analysed to understand the reliance between process parameters and moulding quality. The textile architecture on the meso scale was modelled with the FE method of the embedded elements and the yarn moulding depth into the meso and macro structures of the LI element was investigated. Bridging effects due to a restricted inter-ply slipping behaviour of the tapes at tight corners can be predicted in good agreement to experimental measurements [9]. Hence, changes in the design of the structured LI element to improve moulding quality and joint strength can be made early in the development process. The detailed knowledge of forming design limitations of hydroformed metallic load introduction elements is the prerequisite for a fibre-adapted design of structures on meso and macro level. To consider these relationships in the design of the structures, the influence of geometrical parameters of the form elements on the meso level -

size, edge ratio, angle, position in the joining area - and macro level - number of undercuts, radial geometry amplitudes - as well as the process parameters - maximum pressure for the phases - on the forming of the multi-scale structuring were investigated and quantified by numerical sensitivity analyses. Robust process parameters for the reproducible production of the metallic load introduction elements with multi-scale structuring, taking into account the material-specific and load-dependent forming limit of the material as well as processing limitations were developed.

4 Validation of the joint

The performance of the presented hybrid composite structure is mainly influenced by the moulding quality of the undercut contours as well as the laminate quality of the composite. Because of the use of fully impregnated thermoplastic tapes, photomicrographic analyses show a very high laminate quality with almost no voids and a low amount of fibre undulation. Additionally, computer tomographic scans indicate good moulding quality of the meso structures which is necessary to achieve a high load bearing capability of the contour joint [6]. For the validation of the simulation results and the experimental verification of the calculated joint strength for different structuring types, the quasi-static pull-out strength of the hybrid joints was determined.

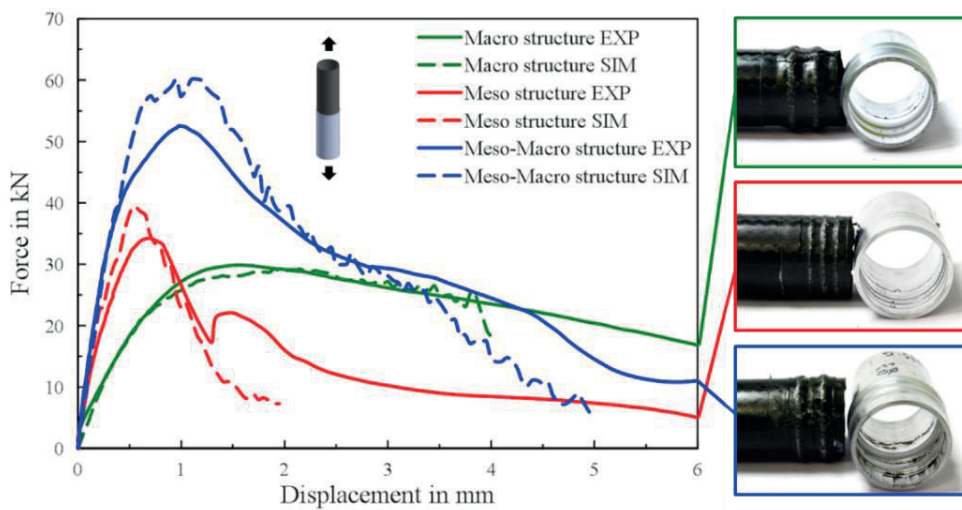


Fig. 4: Force - displacement curves from simulation / experiment for the meso-, macro- and combined structure with circumferential undercuts and failure images of the joints

The tests indicate that the combination of meso and macro form closure increased the maximum force as well as the joint stiffness and the energy absorption for all investigated structures. The structuring length optimised in [10] for joint failure was 30 mm for all hybrid joints tested. Fig. 4 shows an example of the structure with circumferential undercuts and a comparison of measured and simulated force-displacement behaviour of the hybrid structure. A good agreement between experiment and simulation can be found and thus the high prediction quality of the friction-based modelling approach can be confirmed. Joint strength values in the range of adhesive bonds are achievable [8].

Due to the potential for galvanic corrosion of the partnered materials and the tendency of crevice corrosion of the design cyclic corrosion tests according to VDA 233 – 102 recommendation have been conducted and the effects of corrosion damage as well as six anti-corrosion concepts have been studied. It was found, that crevice corrosion as well as galvanic corrosion are both present in the contour joint and a combination of edge sealing and anodising or sol-gel coating is recommended as a protective measure [11].

5 Conclusion

An overview into the design and intrinsic manufacture approach for hybrid tubular composite structures with multi-scale form-fit LI elements is presented. Targeting efficient production and high performance, the developed intrinsic manufacturing process shows a high potential for series production. With hydroforming of multi-structured aluminium load introduction elements as well as the use of tape-braided preforms in combination with the integral bladder assisted moulding process, hybrid hollow composite structures can be manufactured within a few minutes. Further investigations have to be made in order to optimise the heating and consolidation of the preform in isothermally heated tooling. Finite element simulations supported the whole development process. Structural simulations on the microscale are used to identify parameters of the cohesive zone model of the macro model, which is used to find the optimised geometry of the joint. Additionally, process simulations gave insight into the moulding behaviour of the composite and the aluminium tube and decreased experimental development effort. The simulative and experimental results show that the combination of multi structuring as well as a graded macro contour design improve the load bearing capability and should be utilised. Further tests with cyclic loading will be addressed for industrial application.

Acknowledgements

The authors gratefully acknowledge the funding of this work by the German Research Foundation, DFG, within the priority programme 1712: Intrinsic hybrid composites for lightweight structures - basics of manufacturing, characterization and design.

5 References

- [1] J. Töpker, J. Schulz, E. Haberstroh et al.: *Krafteinleitungselemente und Verbindungstechniken bei endlosfaserverstärkten thermoplastischen Hohlprofilen*, 3. AVK-TV Tagung Baden-Baden, **2000**
- [2] O. Helms: *Konstruktion und technologische Umsetzung von hochbeanspruchten Lasteinleitungssystemen für neuartige Leichtbaustrukturen in Faserverbundbauweise*. Dissertation, TU Dresden, **2006**
- [3] J. Nieschlag, P. Ruhland, S. Daubner et al.: *Finite element optimisation for rotational moulding with a core to manufacture intrinsic hybrid FRP metal pipes*. Prod. Eng. Res. Devel. **(2018)** 12: 239.
- [4] C. Garthaus, D. Barfuss, B. Witschel et al.: *Tape braiding: high-performance fibre-reinforced thermoplastic profile structures*. JEC Composites Magazine, No 96, 62-64, **2015**
- [5] M. Gude, R. Grützner, W. Hufenbach et al.: *Verfahren und Vorrichtung zur Herstellung mehrskalig oberflächenstrukturierter Hohlprofil mittels mediengestützten Umformens*. Patent DE 10 2014 000 944 B3. 02.04.2015
- [6] D. Barfuss, V. Würfel, R. Grützner. et al.: *Integral blow moulding for cycle time reduction of CFR-TP aluminium contour joint processing*. In proceedings 21st International ESAFORM Conference on Material Forming, Palermo, **2018**
- [7] F. Hirsch, M. Kästner: *Microscale simulation of adhesive and cohesive failure in rough interfaces*. Engineering Fracture Mechanics 178, 416-432, **2017**
- [8] D. Barfuss, C. Garthaus, M. Gude et al.: *Design of multi-scale structured Al-CF/PA6 contour joints*. International Journal of Automotive Composites, Vol. 2, No. 3/4, **2016**
- [9] D. Barfuss, R. Grützner, C. Garthaus et al.: *Design and intrinsic manufacturing of positive locking fibre thermoplastic-metal hollow structures*. In proceedings ECCM17, Munich 26-30th June, **2016**
- [10] D. Barfuß, R. Grützner, F. Hirsch, et al.: *Multi-scale structuring for thermoplastic-metal contour joints of hollow profiles*. Production Engineering, 12(2), 229-238, **2018**
- [11] V. Würfel, D. Barfuss, R. Grützner et al.: *Design and intrinsic processing of a hybrid CFR-TP contour joint with a multi-scale structured load introduction element*. In proceedings Hybrid Materials and Structures, Bremen, **2018**

Design and quality assurance of intrinsic hybrid metal-CFRP lightweight structures

Lucas Bretz¹, Fabian Günther², Hendrik Jost³, Michael Schwarz³, Vanessa Kretzschmar^{2,4}, Markus Pohl², Lukas Weiser¹, Benjamin Häfner¹, Jannik Summa³, Hans-Georg Herrmann³, Markus Stommel², Gisela Lanza¹

¹Karlsruhe Institute of Technology (KIT), Karlsruhe

²TU Dortmund University, Dortmund

³Saarland University, Saarbrücken

⁴Leipzig University, Leipzig

Abstract – The intrinsic production of metal-CFRP (carbon fiber reinforced polymers) hybrid structures allows a load-path-optimal design of connecting components. The interface of the hybrid part is of particular importance in design, production, and testing due to its force-transferring function. The special feature of the intrinsic connection is a thermoplastic jacket around the metal insert. It dampens vibrations, inhibits corrosions, and smoothens the stiffness gradient at the interface of metal and CFRP. A punched metal insert guarantees the suitability for mass production in the automotive industry, while the plastic jacket maintains a fiber adjusted geometry as well as a structured surface to maximize the joint strength. Load paths, stress distribution, and good drapability are taken into account. Finite element (FE) simulations and experiments are used to design and dimension the insert. Novel FE visualization methods for constructive design are developed and applied. The investigation of design elements on the mesoscale (mm) and microscale (μm) surface roughness shows improvements of the load transfer and reduces the damage propagation.

The intrinsic manufacturing is carried out by means of the resin transfer molding (RTM) process. In-line quality assurance starts with the inspection of the preform geometry. The data from two laser light section sensors are used for in-line measurements of complex 3D geometries. Ultrasonic sensors are used to check the curing degree of the resin during the infiltration. Afterwards, in-line quality assurance of the finished hybrid component is carried out by data fusion of laser light section sensors and active thermography. The data fusion enables a three-dimensional representation of the thermographic image and, thus, also a three-dimensional defect localization.

Active and passive thermography are suitable for characterizing the component under various load conditions. Damages can be reliably detected using active thermography, while passive thermography allows the in-situ observation of the damage propagation. This allows a detailed insight into the damage mechanisms under quasi-static and cyclic load. It is possible to predict the remaining service life of the component by observing the delamination growth under cyclic mechanical load.

The input of the in-line quality information in combination with the damage characteristics into a FE simulation enables the prediction of the individual component performance.

Keywords: Effects of Defects, Hybrid Metal-CFRP Structure, Intrinsic Manufacturing, In-line Quality Assurance, Load Path, Thermography

1 Introduction

The increasing demand for tailor-made lightweight materials by the automotive industry is leading to hybrid components, consisting of metal-plastic composites. Thin-walled structures of sheet steel with suitable plastic reinforcement are often used in the stressed areas. Due to the complex manufacturing technology, the production of such components is still very cost- and labor-intensive. The optimization of the manufacturing processes can make a significant contribution to the increased economic efficiency.

2 State of the Art

For the connection of CFRP and metals, conventional connection concepts are predominantly used, mainly bolt connections or adhesive joints [1]. However, form-fit connections such as loop connections are also common for high unidirectional load introduction. Adhesive connections are often used, but the production effort as well as the testing procedures are complex and critical to failure. Bolt connections are frequently used for flat, thick-walled components (also from the historical context of aluminum riveting in aircraft construction). However, drilling holes leads to a destruction of continuous fibers. Alternative connection concepts, such as laminar inserts or connections based on Integral Micro-Mechanical-Interlocking (IMMI) [2, 3], are being developed and investigated. Connections based on form-fit with small metallic pins are already in industrial use [4].

Visualization methods extend the Finite Element Analysis (FEA), which is used to design the hybrid composite structure. Kratz et al. [5] summarize advanced simulation methods existing in the field of structural mechanics and gave an introduction to the analysis of given various tensors, such as stress tensors. A technique called Hyperstreamlines [6] was introduced to display whole tensor information, while tracing principle (stress) directions. It is based on tensor lines [7], which are called stress trajectories in structural mechanics in the context of stress tensors. Such lines can be used as guides to improve the stiffness of a component [8].

In-line quality assurance techniques of carbon fiber preforms focused primarily on the usage of 2D camera systems. Dome lights are often used [9–12], because of the challenging reflective properties of carbon fibers. The combination of an image series allows the detection of gaps as well as an analysis of the fiber orientation. The investigations focused on planar geometries. Large 3D geometries were investigated in the aircraft industry [11, 13].

Damage mechanism in intrinsic hybrids are highly dependent of the used materials and the geometry. A successful investigation of damage mechanisms in a polymer composite with a combination of in-situ non-destructive testing methods (digital image correlation (DIC), infrared thermography and acoustic methods) is described in [14]. Further, Waugh et al. [15] and Genest et al. [16] showed how artificial and mechanical induced delaminations can be detected with thermography. The precise damage development of CFRP specimens under various quasi-static and dynamic load conditions is described by Gamstedt et al. and Jollivet et al. [17, 18]

3 Novel structural Concept for the Specimen Design

The investigated structural concept consists of a flat metal insert embedded in a CFRP laminate. In contrast to existing insert technologies, the interfacing layer between the insert and the CFRP is examined in detail. A plastic is introduced by overmolding the metal insert. This allows the boundary layer, which is decisive for the strength of the joint, to be extensively customized to the load situation. This approach allows for a cost-effective surface design of the insert, suitable for mass production, through the usage of the injection molding process. Form fit is used as dominant connection mechanism. The metal insert provides a macroscopic geometry in the scale of the insert. The plastic component is then used to create further undercuts to improve the form fit at various scale levels. In addition, the plastic component is used to adjust the force transfer between CFRP and metal in a manner avoiding local excessive stress at edges and keeping the force transfer as steady as possible.

3.1 Design Guideline

The development of the insert concept is based on the derivation of a basic insert geometry (metal component) which is designed on the basis of the available design space. Then, a global plastic geometry is derived and stiffness adjustments of the generated undercuts are carried out. In a fourth step, local changes of the geometry due to the load situations are introduced. These steps are described in the following section. Subsequently, the two-dimensional geometry is transferred to (multiple) curved CFRP laminates.

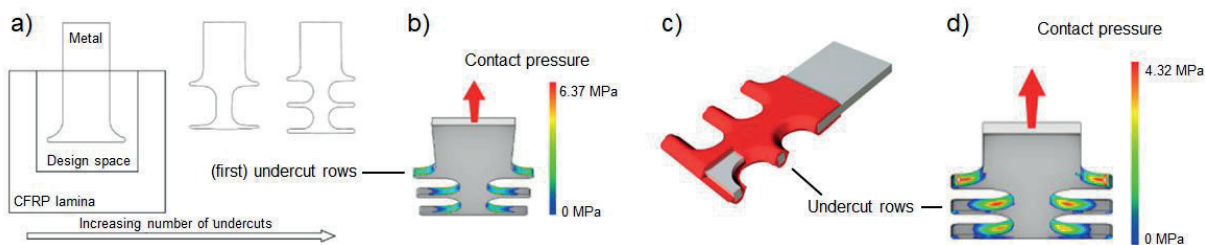


Figure 1: a) Insert design; b) Contact pressure under tensile loading; c) Polymer component on the metal insert (cut view); d) Contact pressure under tensile loading with polymer component

3.1.1 2D Inserts

Step 1, insert design: The available design space and the load cases that act on the metal insert affect the insert design. If loads in the laminate plane (tension, compression, shear) and loads transverse to it (torsion and bending) are considered simultaneously, several undercut rows on the insert are advantageous in order to minimize the maximum contact pressure at the insert boundary (cf. **Figure 1 a**)). **Figure 1 b**) illustrates the case of a tensile load. The force transmission is distributed over all undercuts. It is maximal at the edges of the insert.

Step 2, design of the polymer layer: The design of the polymer layer is based on the shape of the metal insert. It is a center-symmetrical overlay with beveled edges. Thus, a continuous surface profile is created (cf. **Figure 1 c**)). This results in an adjusted load distribution (cf. **Figure 1 d**)). The maxima are lower compared to the specimen without polymer layer and are located in the middle of the surfaces instead at the edges of the metal. This significantly reduces the notch effect on the material surrounding the metal.

Step 3, localized stiffness adjustment: The local adaptation of the stiffness takes into account the uniformity of the force transfer over the length of the insert. Similar to adhesive joints, the highest shear forces in the adhesive occur at the outer edges of the adhesive layer. The first undercut rows (cf. **Figure 1 b**) transmit more force than those behind them. Thus, the first undercut rows located close to the CFRP are designed with a lower stiffness to produce a uniform force transmission. The increased elasticity is achieved by replacing the metal undercut with plastic.

Step 4, stress adjusted modification of the polymer layer: Investigations of the deformation and the damage progress during dynamic high cycle fatigue tests with a swelling tensile amplitude show that the laminate detaches below the undercuts. The damage is initiated as delamination. Over the course of the tests, the delamination increases until the damage is so severe that component failure occurs. Adaptation of the plastic component enables significantly improved component performance due to a later start of damage and slower damage growth. The adaptation consists of locally shallower flank profiles in the plastic component at the points with a greater tendency to delaminate. **Figure 2** shows the original structure and one with adjusted flank design at locations with a high tendency to delaminate.

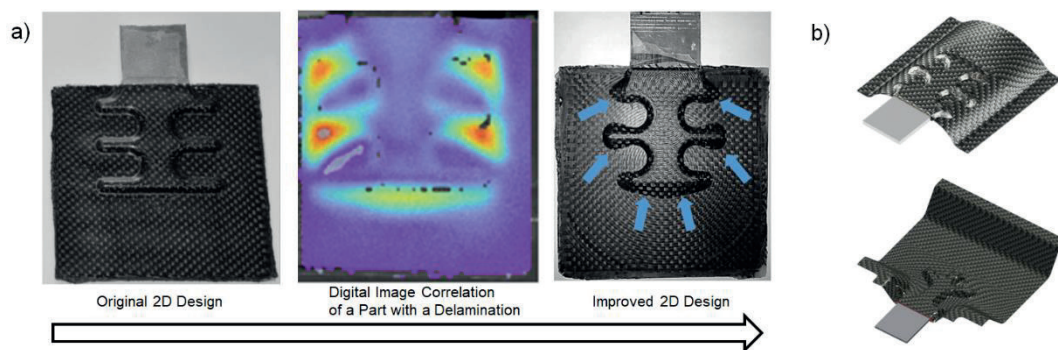


Figure 2: a) 2D specimen with initial and improved insert geometry; b) curved and 3D specimen

3.1.2 3D Inserts

The development of 3D inserts in more complex specimen designs shows that uniaxial, plane loads lead to significant 3D stresses and deformation. For this purpose, a curved component with insert was examined first before a complex specimen with 3D insert was designed. An even stress distribution under contact pressure and bending deformations shall be achieved in the design process. A general conclusion for valid design criteria is not possible due to the different deformation behavior depending on the specimen design [19].

3.2 Surface Design on Mesoscale

The mesoscale is considered as geometric surface structures in the size of millimeters, which are distinguished from the macroscale part structure (cm) and the microscale roughness (μm). The development and investigation of mesoscale surface structures were preceded by an experimental investigation using Single Lap Joint (SLJ) tensile shear tests. A polished reference specimen was compared with specimens with straight walls, round walls, holes, and pins. It was found that the structures have a great influence on the connection strength. The test specimens with pin structures showed the highest tensile shear strength [20]. The objective for further investigation was to determine the influence of the geometrical shape and orientation as well as the arrangement of the pins on the surface to increase the overall hybrid bonding strength by surface design.

The investigations were carried out both simulatively and experimentally. In the first step, simulative pin geometries were determined for the experimental investigation depending on the material pairing of thermoplastic Polyphthalamide (PPA) and CFRP [20]. On this basis, SLJ investigations were carried out to investigate the influence of individual pins as a function of geometry. The individual test sequences showed large scattering in the results, which makes it difficult to derive individual geometric correlations. However, the potential of the pins as possible crack stoppers in case of adhesion failure could be derived from several load displacement curves. In the experiments, it was clearly shown that adhesion variations due to production have a very large influence on the overall bond strength. From the comparison of the tests, it could also be concluded that the pin geometries used as individual elements represent defects in the adhesive bond. In order to counteract this in further simulative investigations, the influence of the adhesive strength was particularly considered. This led to an extensive parameter variation, which results in pin geometries, intended to strengthen the bond even with high adhesive joints [21].

An averaged tendency for increasing load transfers was shown in experimental SLJ tests with two to six pins. Due to the large number of possible pin combinations in a connection area, a Monte Carlo simulation approach was used to determine the interaction of several pins and possible dependencies [22]. Both the number of pins and the positioning were varied randomly on the surface of an SLJ sample. It could be determined that the maximum transmittable load cannot be further increased for a certain number of pins on the bonding surface under given boundary conditions. Furthermore, it could be concluded that certain pin arrangements are advantageous for the connection if damage propagation is considered. According to this, a pin density of about 15 % (pin area/total area), an even, wide distribution and an alternating arrangement of the pins is recommended [22].

Currently available visualization methods [5] were applied to investigate the influence of pin arrangements along load paths in the connection surface. From a range of methods, the Hyperstreamlines method was chosen [6] which allows the tracking of principle stresses while including whole tensor information as ellipsoidal shape along the paths. In a recent work, drawbacks of this method were found, especially for the application domain of indefinite symmetric second order tensors like stress tensors. A variant of Hyperstreamlines called Tensor Spines were presented [23]. Tensor Spines encode a tracked principle stress with a tube, which color and radius is proportional to the intensity of stress in its direction. The other two principle stresses are presented by planes perpendicular to the tube due to their direction-relation. The size of the planes is determined by a fraction between the tracked stress and the other principle stress. Furthermore, the planes are color-coded (red for tensile stress and blue for compressive stress). In addition, user-driven guides marking interesting breakpoints improve the reading of perpendicular stress values. Tensor Spines can visualize occurring in-plane stresses as well as the transferred forces normal to the surface at the material interface, as shown in **Figure 3 c)**. Using the visualization enables the user to identify areas of high and low stresses, to depict possible placement positions of pins on the insert jacket. The areas in light blue in **Figure 3 c)** indicate negative stresses perpendicular to major principle stresses. A user can chose a tolerated limit which is highlighted with a black line on the perpendicular surface when

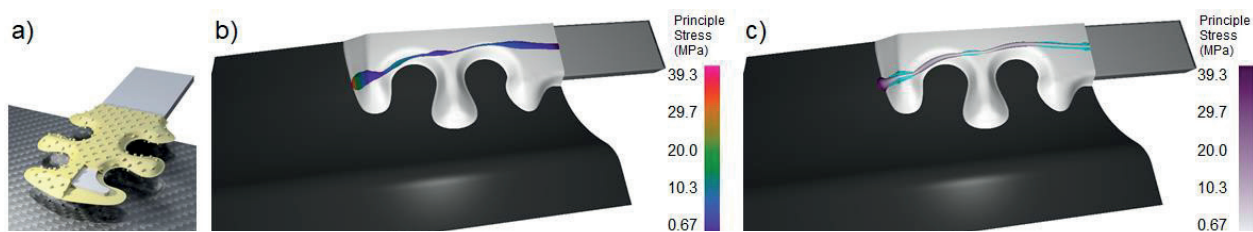


Figure 3: a) Insert with pins; b) Hyperstreamlines method; c) Tensor Spines method

exceeded. Thus, more information about the stress state is available through the Tensor Spines method.

A hybrid specimen was developed for experimental component testing. It has the same bonding characteristics as the specimen from section 3.1. Load bearings are larger through the combined use of friction-fit and form-fit by pins (cf. **Figure 3 a**)). Experimental results are still pending.

3.3 Surface Design on Microscale

The aim of microscale surface design is to determine the influence of different surface roughness to the bonding strength of thermoplastic-composite material joint by an intrinsic RTM process and to optimize the overall hybrid bonding. The investigation is carried out through experiments with SLJ specimens in quasi-static tensile tests and dynamic fatigue tests. The unstructured surface roughness is gained through the surface roughness in the mold cavity of injection molding from sand blasting with different sand grain sizes and varying the air pressure (cf. **Table 1**).

The quasi-static tensile test examined with 2 mm/min at a regular tensile testing machine shows the best performance with a roughness of 3.55 μm . Roughnesses of 5.5 μm and 6.7 μm show similar maxima, but have larger scattering. The dynamic fatigue tests were conducted with electric dynamic testing machine and a step loading method with a load ratio of $R = 0.1$ (200.000 cycles as default). If the run was successful, the upper load was increased by 100 N. Otherwise, it was lowered by 100N. In **Figure 4**, the average upper load for each roughness sample is shown. The fatigue tests show better results for higher roughness values. Samples with a roughness of 3.55 μm are comparably weak. The samples with higher roughness show better fatigue behavior. Overall, a roughness between 4 and 6 μm can be recommended for quasi-static and dynamic loading conditions in thermoplastic-composite parts.

Table 1: Table of correlation of thermoplastic surface roughness to cavity roughness

Cavity material	Steel	Steel	Steel	Steel	Aluminum	Aluminum
Sand grain size	polished	EK 24	EK 24	EK 24	EK 14	EK 14
Air pressure (bar)		1.8	3	7	4	6
Cavity roughness R_a (μm)	0.044	2.152	3.442	5.166	6.341	7.973
Specimen roughness R_a (μm)	0.25	2.25	3.55	5.59	6.71	9.34
Tensile strength (MPa)	3.07	6.55	8.92	7.87	7.1	5.9
Standard deviation of Tensile strength (MPa)	1.92	2.42	1.16	2.24	3.01	2.51

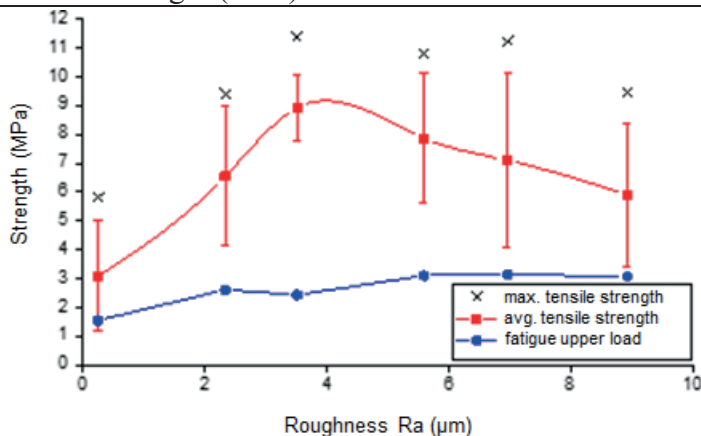


Figure 4: Influence of surface roughness on tensile strength and fatigue upper load

4 In-line Quality Assurance

The performance of intrinsic hybrid composites is determined by their load transfer capability between the intrinsically connected components. Therefore, particular attention needs to be paid to the transition zone and defects need to be avoided. For this purpose, a process-integrated quality assurance is required, which allows an in-line detection of critical defects in hybrid composite components. Different in-line measurement technologies taking into account the two states of the hybrid part before (CF preform) and after filtration (finished part) are presented. The focus is on measurement technologies which offer the potential for series production. [24]

4.1 2D Camera

The integration of inserts leads to a local influence of the fiber orientation. Therefore, the insert position relative to the fiber orientation should be measured [25]. The local fiber orientation of the top CF layer can be detected by means of a 2D camera system. In addition, diffuse dome illumination was used to compensate for the anisotropic reflection properties of the carbon fibers. The illumination color and the illumination height acted as setting parameters. The fiber orientation of different samples could be detected with a measurement uncertainty of approx. 0.1° . Existing algorithms [11, 12] were used, with optimal adjustment of the factors light intensity, relative position of camera, and light source with respect to the specimen as well as filter parameters [26].

4.2 Laser Light Section System

Preforms with high deviations from the specified geometry are to be identified before the cost-intensive infiltration process [27]. Therefore, the whole preform is to be detected as a 3D cloud of points (CoP). Limitations for a measurement system are the size of the part, the requirement of a contactless measurement for speed, and avoiding damage as well as highly reflective properties of CF. Laser light section sensors, based on the triangulation principle, fulfil the mentioned requirements. However, complex 3D parts, featuring steep slants and strong curvatures, need a measurement system which prevents shadowing effects. Therefore, a combination of two tilted laser light section sensors was used [28]. Both laser lines have width of 100 mm and provide a resolution of approx. $50\ \mu\text{m}$. The system needs to be moved in a path with a constant offset over the surface of the part to compensate the limited depth of sharpness (a few mm). If a part wider than 100 mm is measured, the part will be scanned in more than one path. Data processing is essential for the described system. The G-code of the measurement path was derived from the CAD file of the preform geometry. The two laser stripe sensors initially recorded independent CoPs. The z-values of the CoPs needed to be corrected because of the equidistant movement of the sensor system. The correction could be performed because of the known position of the tool center point (TCP). Additionally, the scan results of the different sensors and paths was fused into one global CoP by correcting the x-value shift. Afterwards, the deviations from the intended geometry were assessed by a disparity map. [28] The developed multi-sensor-system (cf. **Figure 5**) provided a measurement volume of $1000 \times 1000 \times 400\ \text{mm}$ (x,y,z) and was suitable for usage outside of a measuring room due to its robust kinematic and temperature in-sensitive base material (granite). [29]

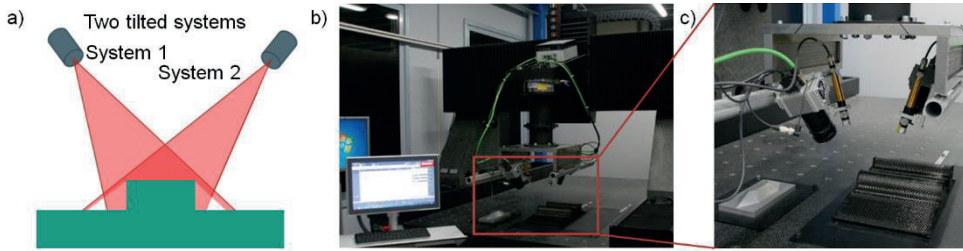


Figure 5: Principle and realization of combined laser stripe sensor system

4.3 Thermography

Active thermography offers the possibility to detect internal defects in a specimen, such as defects or pleats [30–32]. A data fusion system for thermographic data and CoPs [33] was developed (cf. **Figure 6 a**)). 3D thermographic evaluation offers the 3D defect localization based on frequency-dependent depth information while considering the measured outer geometry of the component which might differ from specified properties. Optimal settings could be identified to generate reliable CoPs for finished hybrid metal-CFRP components. A compromise was needed for generating scanning paths along the component due to the non-zero gradient perpendicular to the main axis of the metal insert. Additionally, a filter for outliers in the CoP compared to the CAD file was integrated to increase the robustness of the 3D mapping process of the thermographic image. A thermogram can further be used to detect fiber bundles in the top layer due to anisotropic heat conductivity. The 3D thermogram allows the evaluation of the 3D fiber alignment, which is of particular interest in the region of the metal insert (cf. **Figure 6 b**) and **c**)).

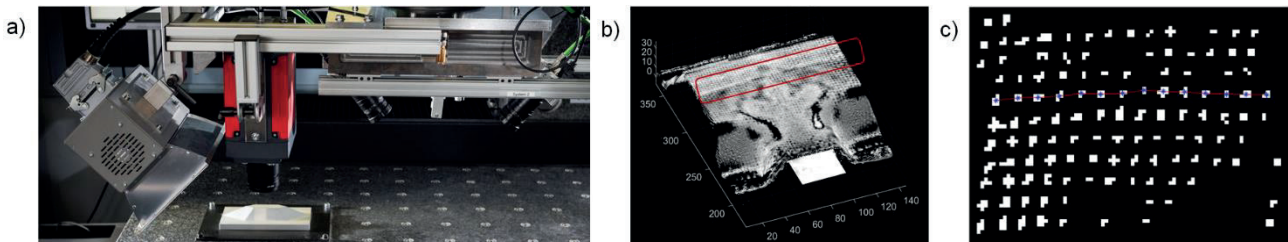


Figure 6: a) Multi-sensor system consisting of active thermography and laser stripe sensors; b) 3D thermogram of a part with detected delamination; c) Adaptive thresholding and fiber detection

4.4 In-process Eddy-Current Testing

A tool-integrated eddy-current system was developed in order to measure fiber misorientations of preforms during the preforming process (cf. **Figure 7 a**) and **c**)). The fixed sensor-integration into a tool could be justified by the known regions of interest for potential fiber misorientations. A time variable magnetic field was generated in emitting coils which produces eddy currents in the carbon fibers according to Maxwell's equation. Deviations from a specified configuration could be assessed due to the anisotropic electric conductivity of carbon fibers (cf. **Figure 7 b**)). The optimal sensor design was identified through an extensive Design of Experiments (DoE) [34]. A printed circuit board (PCB) design is more favorable compared to a cylindrical combination due to its flatness. Either a rigid (planar areas) or flexible (edges) PCB design is possible. A suitable sensor housing was designed for in-process integration of the sensor array. A multiplexer was used for signal distribution amongst the coils and a controller unit. The bottom of the sensor housing, where the sensor array was attached, was designed according to the geometry under investigation. Due to individual characteristics of each

one of the integrated coils, a zero-referencing of the individual coils needed to be performed initially. Afterwards, the fiber orientation was calculated based on four voltage peaks in a polar diagram. A cubic Bézier spline interpolation was used to calculate the peak angles. The expanded measurement uncertainty is calculated according to the Guide to the Expression of Uncertainty in Measurement (GUM) and VDA (German Automotive Industry Association) Volume 5.1. The expanded uncertainty with a coverage factor of $k = 2$ is $U_\alpha = 2.88^\circ$. Furthermore, the industry relevant preform defects (pleats, missing rovings and gaps) were detected by means of the machine learning technique of Support Vector Machines (SVM, cf. **Figure 7 d**). Three different defect sizes were exemplarily created per defect category and investigated. The correct defect type could be identified for 100 % of the validation data. Defect sizes were assigned correctly for 87 % of the pleats, 98 % of the missing

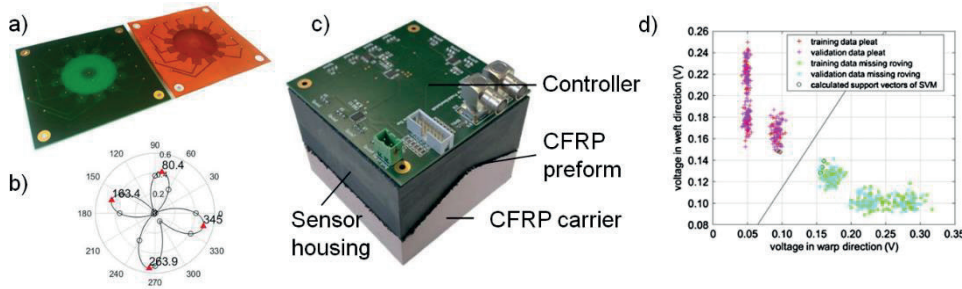


Figure 7: a) Eddy-current sensor arrays (rigid and flexible PCB) [34]; b) Measurement results given in a polar diagram [35]; c) Realization of eddy-current sensor [35]; d) Exemplary classification results with SVM [35]

rovings and 93 % of the gaps. [35]

5 Characterization of Interfaces

As interfaces in hybrid structures are of particular importance [36], they have to be characterized by non-destructive testing methods. The increasing complexity of the specimen geometry (from 2D to 3D) increases the difficulty of non-destructive testing as well.

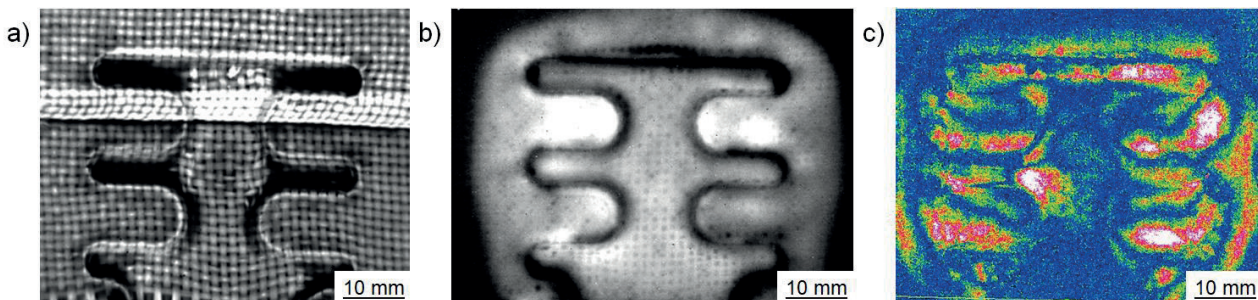


Figure 8: Active thermography diagrams of a) artificial induced defects in CFRP; b) mechanically induced defects at the interface CFRP and thermoplastic; c) passive thermography diagram of mechanically induced defects at the interface CFRP and thermoplastic

Active thermography was used for the detection of defects at the interface and in the CFRP component. **Figure 8** shows flash thermography diagrams of a hybrid sample with defects in CFRP and at the interface after mechanical experiments. Representative defects like pleats, gappings or fiber misalignment as well as mechanically induced defects at the interface could be detected in 2D geometries [30]. The mechanically induced delamination can be seen as bright areas around the insert. In-situ passive thermography can be executed during mechanical testing [37]. **Figure 8 c**) shows the

damage development at the interface CFRP/thermoplastic. The delamination (red and white areas) grows along the arms of the metal insert. Different factors can influence the lifetime of the hybrid structure [37]. Variations of different thermoplastic components and different defects in the CFRP-component lead to different load bearing capabilities of the structure. **Figure 9 a)** shows a comparison of different thermoplastic components. The hybrid structure with PPA GF30 (PPA with 30 vol% glass fiber content) reaches the best load bearing capability, whereas using a softer thermoplastic polyurethane (TPU) leads to the worst mechanical properties. **Figure 9 b)** gives a comparison between samples with delamination, pleat or fiber misalignment and defect-free samples. Samples with a pleat defect reach the worst load bearing capability.

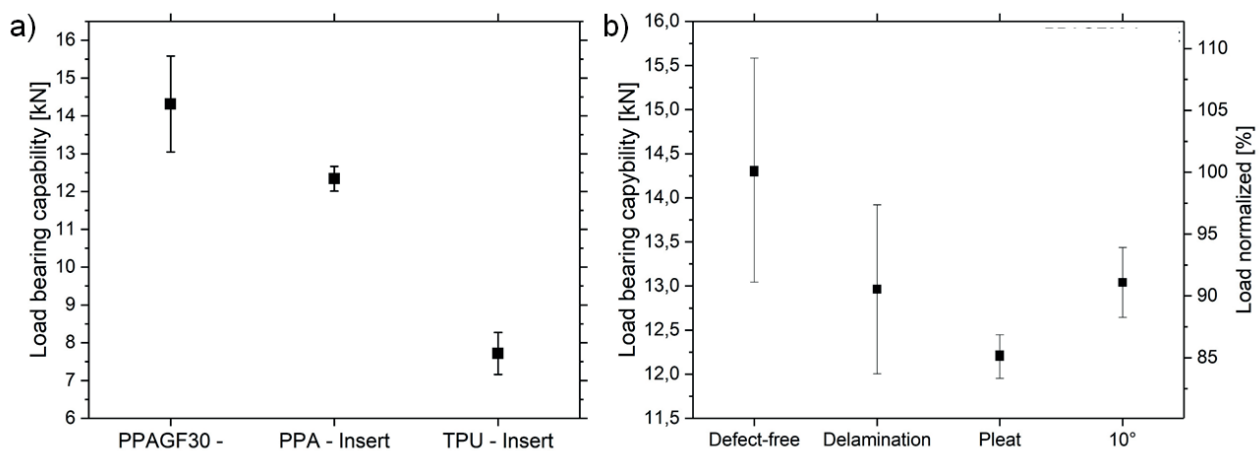


Figure 9: Maximum load bearing capability of the hybrid structure for a) different thermoplastics jackets and b) different defects in the composite in combination with a PPAGF30-Insert

Several difficulties occurred independent of the excitation mode because of the curved area of the 3D geometry. The energy could not be induced perpendicularly, which led to a less efficient heat input. Furthermore, the experimental setup does not allow the infrared camera to inspect the whole surface using the same camera angle. Potential defects at the interface were detected at the flat region of interest around the metal inlay. **Figure 10 a)** shows the force-displacement diagram of a 3D sample. The inspected sample reaches a maximum force of 7 kN at a displacement of 8 mm. The damage occurs gradually, identifiable through the sharp reduction of force. Additionally, the diagram shows a large energy dissipation of the sample because of the reached displacement. The passive thermography picture in **Figure 10 b)** shows a defect around the metal inlay in the 3D specimen, comparable to the 2D samples. These defects appear as yellow and red areas and represent mechanically induced delaminations. **Figure 10 c)** shows the infrared picture of flash thermography. The defect is located around the metal inlay, like in the picture of passive thermography, and can be seen as bright areas. Inductive thermography was used for the characterization of the 3D samples besides flash thermography. The fiber orientation was detected besides the delaminations (cf. **Figure 10 d)**).

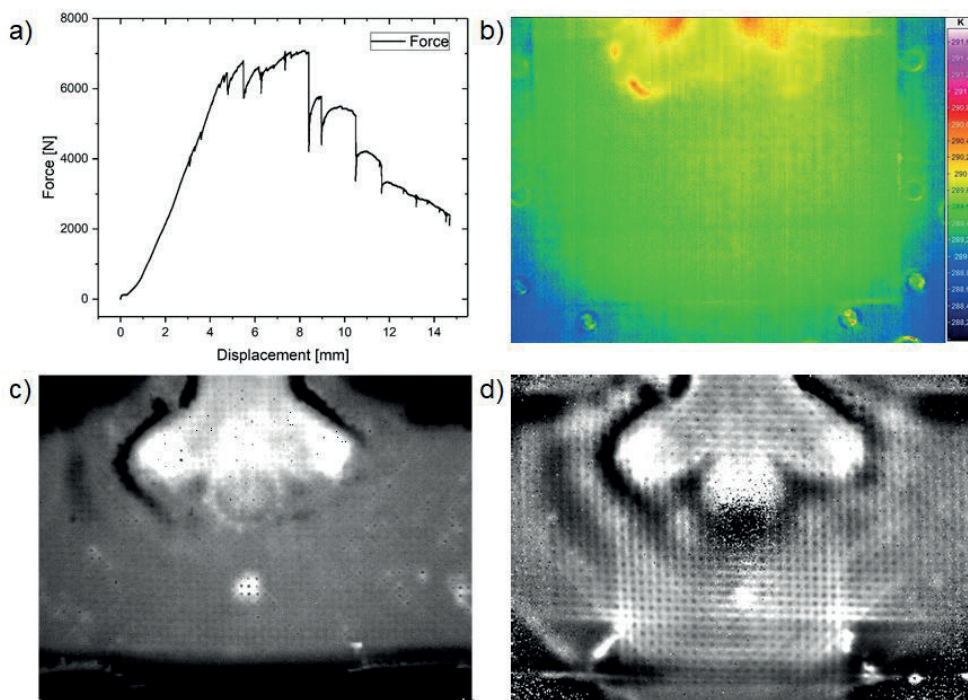


Figure 10: Characterization of 3D sample: a) force-displacement-curve; b) passive thermography at a displacement of 10mm; c) flash thermography of sample with delaminations; d) inductive thermography of sample with delaminations

6 Effects of Defects

The effects of various defects in the component was examined by means of a data fusion approach over the process cycle [21, 28]. Data fusion combines simulative predictions and information from quality assurance as well as experimental characterization. It allows statements about the effect of production errors on the product life cycle and prevents costs and production waste. Typical production errors for hybrid components, such as delamination, pleat and fiber misalignment, were taken into account. **Figure 9** shows the load bearing capacity, determined in experimental tests. Further investigated errors were (macro) pores and insufficient cross-linking of the resin. A detailed simulation model, incorporating a multi-continuum theory and a damage model, could successfully display different damage mechanisms for quasi-static and dynamic load cases. The observations agreed well with the experimental results. It could be concluded that the investigated defects led to different stress distributions, resulting in a faster progressive damage growth. Thus, the proposed model was suitable for the prediction of the effect of production-related defects. Further information were published in [32, 33].

7 Conclusion and Outlook

In this work, an undercut optimized design for connecting metal to CFRP is introduced. This is achieved by using a functional intermediate layer of a less stiff material, such as a thermoplastic. This significantly improves the load carrying capacity, especially in high cycle fatigue tests. Furthermore, the plastic layer offers many possibilities to improve the connection to the CFRP. The microscale

roughness influences as well as the influence of mesoscale structures on the surface of the thermoplastic has been investigated. A specific range of 4 to 6 μm for microscale roughness has proven to be favorable for both static and dynamic loads. Optimized pin geometries as well as guidelines for pin arrangements from simulated investigations are presented. Deviations from the preform design specification can be in-line-measured by 2D cameras (fiber orientation), laser light section (geometrical specifications), pulsed phase thermography (delaminations, pleats, fiber misorientations). Co-operative data fusion of thermography and laser light section combines the benefits of both measurement technologies. Eddy-current testing (fiber orientation, pleats, missing rovings and gaps) allows for an in-process integration in the preforming process. The combination of passive and active thermography before, during and after mechanical testing is beneficially for the interface characterization of hybrid metal-CFRP structures. The influence of various representative defects and of the thermoplastic interlayer on the mechanical behavior of the hybrid structures is evaluated. The techniques developed for 2D specimens was adjusted and improved for 3D structures.

Future efforts shall focus on the integrated component design based on the information gained through the in-line measurements during the production process and the in-situ measurements of the loaded component. The information gained in non-destructive testing could be used to design a damage model for the hybrid structure. The pending experimental investigations of the mesoscale structures will show potentials to improve the connection due to the large number of possible other surface structures, geometries and arrangements. The influence of an optimized microstructure can also be investigated in addition to the unstructured roughness on the mesoscale.

Acknowledgement – The authors thank the German Research Foundation (DFG) for funding the collaborative research program “Priority program 1712”.

8 Literature

- [1] H. Schürmann, *VDI-Buch. Springer-Verlag Berlin Heidelberg, 2. Ed., 2007*
- [2] S. Ucsnik, M. Scheerer, S. Zaremba, D.H. Pahr, *Composites Part A: Applied Science and Manufacturing*, **2010**, 41(3), p. 369 – 374.
- [3] R.W. Messler, *Journal of Thermoplastic Composite Materials*, **2004**, 17, p. 51–75.
- [4] P. Becker, A. Büter, *Lightweight Design*, **2017**, 10, p. 44–47.
- [5] A. Kratz, C. Auer, M. Stommel, I. Hotz, *Computer Graphics Forum*, **2013**, 32(1) , p.49–74.
- [6] T. Delmarcelle, L. Hesselink, *IEEE Computer Graphics and Applications*, **1993**, 13, p. 25–33.
- [7] R. Dickinson, *Proceeding Three-dimensional visualization and display technologies*, Los Angeles, CA, United States, **1989**, 1083.
- [8] A. Kratz, M. Schöneich, V. Zobel, B. Burgeth, G. Scheuermann, I. Hotz, M. Stommel, *Proceeding of IEEE Pasific Visualization Symposium*, Yokohama, Japan, **2014**.
- [9] W. Palfinger, C. Eitzinger, S. Thumfahrt, *Symposium on Automation of Advanced Composites and its Technology*, Munich, Germany, **2012**.
- [10] A. Miene, *5th meeting of working group "Werkstoff- und Bauteilprüfung", topic: "ZFP in der Produktion"*, **2010**.
- [11] A. Orth, *Entwicklung eines Bildverarbeitungssystems zur automatisierten Herstellung faserverstärkter Kunststoffstrukturen (Dissertation)*, Shaker Verlag, Aachen, Germany, **2008**.

- [12] C. Mersmann, Industrialisierende Machine-Vision-Integration im Faserverbundleichtbau (Dissertation), Apprimus Wissenschaftsverlag, Aachen, Germany, **2012**.
- [13] M. Göttinger, C. Weimer, A. Miene, *Deutscher Luft-und Raumfahrtkongress*, Aachen, Germany, **2009**, 8.
- [14] J. Cuadra, P.A. Vanniamparambil, K. Hazeli, I. Bartoli, A. Kontsos, *Composites Science and Technology*, **2013**, 83, p. 11–21.
- [15] R.C. Waugh, J.M. Dulieu-Barton, S. Quinn, *NDT & E International*, **2014**, 66, p. 52–66.
- [16] M.Genest, M. Martinez, N. Mrad, G. Renaud, A.Fahr, *Composite Structures*, **2008**, 88, p. 112–120.
- [17] E.K. Gamstedt, R. Talreja, *Journal of Materials Science*, **1999**, 34, p. 2535–2546.
- [18] T. Jollivet, C. Peyrac, F. Lefebvre, *Procedia Engineering*, **2013**, 66, p. 746–758.
- [19] F. Günther, L. Bretz, H. Jost, M. Schwarz, M. Stommel, G. Lanza, H.-G. Herrmann, *23rd International Dresden Lightweight Engineering Symposium*, Dresden, Germany, **2019**.
- [20] F. Günther, M. Pohl, V. Kretzschmar, G. Scheuermann, M. Stommel, *Proceedings of Hybrid – Materials and Structures*, **2018**, 3, p. 254–260.
- [21] F. Günther, M. Stommel, V. Kretzschmar, *Advances in Polymer Processing*, **2020**.
- [22] F. Günther, V. Kretzschmar, G. Scheuermann, M. Stommel, *22nd International Conference on Composite Materials*, Melbourne, Australia, **2019**.
- [23] V. Kretzschmar, F. Günther, M. Stommel, G. Scheuermann, *IEEE Pacific Visualization Symposium (PacificVis)*, Tianjin, China, **2020**.
- [24] G. Lanza, H.-G. Herrmann, M. Stommel, *Lightweight Design*, **2015**, 2, p. 48–53.
- [25] D. Berger, D. Brabandt, C. Bakir, T. Hornung, G. Lanza, J. Summa, M. Schwarz, H.-G. Herrmann, M. Pohl, M. Stommel, *Measurement*, **2017**, 95, p. 389–394.
- [26] D. Berger, G. Lanza, *Zeitschrift für wirtschaftlichen Fabrikbetrieb*, **2016**, 4, p. 178–182.
- [27] G. Lanza, D. Brabandt, *10th Global Conference on Sustainable Manufacturing*, Istanbul, Turkey, **2012**, p. 123–127.
- [28] D. Brabandt, G. Lanza, *Procedia CIRP*, **2015**, 33, p. 269–274.
- [29] D. Brabandt, S. Hettich, G. Lanza, *Lightweight Design*, **2015**, 8, p. 20–25.
- [30] M. Schwarz, M. Schwarz, S. Herter, H.-G. Herrmann, *Journal of Nondestructive Evaluation*, **2019**, 38(1):35.
- [31] M. Pohl, M. Stommel, F. Baumann, D. Berger, G. Lanza, J. Summa, M. Schwarz, H.-G. Herrmann, *wt-online*, **2017**, 7/8, p. 546–550.
- [32] D. Berger, M. Zaiß, G. Lanza, J. Summa, M. Schwarz, H.-G. Herrmann, M. Pohl, F. Günther, M. Stommel, *Production Engineering*, **2018**, 12, p. 161–172.
- [33] M. Schäferling, D. Berger, B. Haefner, G. Lanza, *International Symposium on Structural Health Monitoring and Nondestructive Testing*, Saarbrücken, Germany, **2018**.
- [34] D. Berger, G. Lanza, *Sensors*, **2017**, 18(1), 4.
- [35] B. Haefner, D. Berger, *Design, CIRP Annals*, **2019**, 68(1), p. 539–542.
- [36] J. Summa, M. Schwarz, H.-G. Herrmann, *Proceedings 5th International Conference on Integrity, Reliability & Failure*, **2016**, 5, p. 117–126.
- [37] J. Summa, M. Becker, F. Grossmann, M. Pohl, M. Stommel, H.-G. Herrmann, *Composite Structures*, **2018**, 193, p. 19–28.

Literatur

1. Schürmann H (2007) Konstruieren mit Faser-Kunststoff-Verbunden, 2. Aufl. VDI-Buch. Springer-Verlag Berlin Heidelberg, Berlin, Heidelberg
2. Ucsnik S, Scheerer M, Zaremba S, Pahr DH (2010) Experimental investigation of a novel hybrid metal–composite joining technology. *Composites Part A: Applied Science and Manufacturing* 41(3):369–374. doi:10.1016/j.compositesa.2009.11.003
3. Messler RW (2004) Joining Composite Materials and Structures: Some Thought-Provoking Possibilities. *Journal of Thermoplastic Composite Materials* 17(1):51–75. doi:10.1177/0892705704033336
4. Becker P, Büter A (2017) Hybride Leichtbauhinterachse für Elektrofahrzeuge. *Lightweight Des* 10(5):44–47. doi:10.1007/s35725-017-0049-9
5. Kratz A, Auer C, Stommel M, Hotz I (2013) Visualization and Analysis of Second-Order Tensors: Moving Beyond the Symmetric Positive-Definite Case. *Computer Graphics Forum* 32(1):49–74. doi:10.1111/j.1467-8659.2012.03231.x
6. Delmarcelle T, Hesselink L (1993) Visualizing second-order tensor fields with hyperstreamlines. *IEEE Comput. Grap. Appl.* 13(4):25–33. doi:10.1109/38.219447
7. Dickinson R (1989) A unified approach to the design of visualization software for the analysis of field problems. *Three-dimensional visualization and display technologies* (1083)
8. Kratz A, Schöneich M, Zobel V, Burgeth B, Scheuermann G, Hotz I, Stommel M (2014) Tensor Visualization Driven Mechanical Component Design. undefined
9. Palfinger W, Eitzinger C, Thumfahrt S (2012) Vision based sensor enabling automated production of composite materials. *Symposium on Automation of Advanced Composites and its Technology*
10. Miene A Bildanalytische Qualitätssicherung in der Preformfertigung. 5. Sitzung der Arbeitsgruppe "Werkstoff- und Bauteilprüfung", Thementag: "ZFP in der Produktion" 2010
11. Orth A (2008) Entwicklung eines Bildverarbeitungssystems zur automatisierten Herstellung faserverstärkter Kunststoffstrukturen. Zugl.: Aachen, Techn. Hochsch., Diss., 2008. *Berichte aus der Produktionstechnik*. Shaker, Aachen
12. Mersmann C (2013) Industrialisierende Machine-Vision-Integration im Faserverbundleichtbau. Zugl.: Aachen, Techn. Hochsch., Diss., 2012. *Berichte aus der Produktionstechnik*. Apprimus Wissenschaftsverlag
13. Göttinger M, Weimer C, Miene A (2009) Inline-Preformprozesskontrolle in der CFK-Fertigung. *Deutscher Luft- und Raumfahrtkongress*
14. Cuadra J, Vanniamparambil PA, Hazeli K, Bartoli I, Kontsos A (2013) Damage quantification in polymer composites using a hybrid NDT approach. *Composites Science and Technology* 83:11–21. doi:10.1016/j.compscitech.2013.04.013
15. Waugh RC, Dulieu-Barton JM, Quinn S (2014) Modelling and evaluation of pulsed and pulse phase thermography through application of composite and metallic case studies. *NDT & E International* 66:52–66. doi:10.1016/j.ndteint.2014.04.002
16. Genest M, Martinez M, Mrad N, Renaud G, Fahr A (2009) Pulsed thermography for non-destructive evaluation and damage growth monitoring of bonded repairs. *Composite Structures* 88(1):112–120. doi:10.1016/j.compstruct.2008.02.010
17. Gamstedt EK, Talreja R (1999) Fatigue damage mechanisms in unidirectional carbon-fibre-reinforced plastics. *Journal of Materials Science* 34(11):2535–2546. doi:10.1023/A:1004684228765
18. Jollivet T, Peyrac C, Lefebvre F (2013) Damage of Composite Materials. *Procedia Engineering* 66:746–758. doi:10.1016/j.proeng.2013.12.128

19. Günther F, Bretz L, Jost H, Schwarz M, Stommel M, Lanza G, Herrmann H-G Herausforderungen im Entwicklungszyklus von einfachen (2D) zu komplexen (3D-) CFK-Hybridbauteilen mit thermoplastumspritz-genen Metalleinleger 23. Internationales Dresdner Leichtbausymposium (2019)
20. Günther F, Pohl M, Kretzschmar V, Scheuermann G, Stommel M Optimising mechanical interlocking interface of CFRP-(Thermoplastic/Metal)-Hybrids Proceedings of the 3th International Conference - Hybrid – Materials and Structures (2018), S 254–260
21. Günther F, Stommel M, Kretzschmar V Potential of Mesoscale Structural Elements in the Interface of Hybrid CFRP-Metal-Parts on the Load Transfer Advances in Polymer Processing 2020
22. Günther F, Kretzschmar V, Scheuermann G, Stommel M Interlocking Interface Design in Metal-CFRP Joints using Monte-Carlo Simulation Approach 22nd International Conference on Composite Materials (2019)
23. Kretzschmar V, Günther F, Stommel M, Scheuermann G Tensor Spines - A Hyperstreamlines Variant Suitable for Indefinite Symmetric Second-Order Tensors IEEE Pacific Visualization Symposium (PacificVis) (2020)
24. Lanza G, Herrmann H-G, Stommel M (2015) Großserientaugliche Verbindungselemente für den hybriden Leichtbau. *Lightweight Design* (2):48–53
25. Berger D, Brabandt D, Bakir C, Hornung T, Lanza G, Summa J, Schwarz M, Herrmann H-G, Pohl M, Stommel M (2017) Effects of defects in series production of hybrid CFRP lightweight components – detection and evaluation of quality critical characteristics. *Measurement* (95):389–394. doi:10.1016/j.measurement.2016.10.003
26. Berger D, Lanza G (2016) Qualitätssicherung im Leichtbau. *ZWF* (4):178–182. doi:10.3139/104.111499
27. Lanza G, Brabandt D Sustainable automated production of fiber reinforced plastics (FRP) through inline quality assurance. 10th Global Conference on Sustainable Manufacturing 2012:123–127
28. Brabandt D, Lanza G (2015) Data Processing for an Inline Measurement of Preforms in the CFRP-Production. *Procedia CIRP* (33):269–274. doi:10.1016/j.procir.2015.06.048
29. Brabandt D, Hettich S, Lanza G (2015) Messtechnik für die Qualitätssicherung von Carbonfaser-Preforms. *Lightweight Design* (8):20–25. doi:10.1007/s35725-015-0049-6
30. Schwarz M, Schwarz M, Herter S, Herrmann H-G (2019) Nondestructive Testing of a Complex Aluminium-CFRP Hybrid Structure with EMAT and Thermography. *Journal of Nondestructive Evaluation* 38(1):35. doi:10.1007/s10921-019-0578-5
31. Pohl M, Stommel M, Baumann F, Berger D, Lanza G, Summa J, Schwarz M, Herrmann H-G (2017) Entwicklungsstrukturen intrinsischer Hybride. *wt-online* (7/8):546–550
32. Berger D, Zaiß M, Lanza G, Summa J, Schwarz M, Herrmann H-G, Pohl M, Günther F, Stommel M (2018) Predictive quality control of hybrid metal-CFRP components using information fusion. *Production Engineering* (12):161–172. doi:10.1007/s11740-018-0816-1
33. Schäferling M, Berger D, Haefner B, Lanza G (2018) Data Fusion for Quality Assurance of fibre-reinforced Plastics. *International Symposium on Structural Health Monitoring and Nondestructive Testing*
34. Berger D, Lanza G (2017) Development and Application of Eddy Current Sensor Arrays for Process Integrated Inspection of Carbon Fibre Preforms. *Sensors (Basel)* 18(1). doi:10.3390/s18010004
35. Haefner B, Berger D (2019) Design, data analysis and measurement uncertainty evaluation of an eddy-current sensor array for in-process metrology of carbon fiber reinforced plastics. *CIRP Annals* 68(1):539–542. doi:10.1016/j.cirp.2019.04.091

36. Summa J, Schwarz M, Herrmann H-G Evaluating the Severity of defects in a metal to CFRP hybrid-joint with in situ passive thermography damage monitoring Proceedings 5th International Conference on Integrity, Reliability & Failure (2016), Bd 5, S 117–126
37. Summa J, Becker M, Grossmann F, Pohl M, Stommel M, Herrmann H-G (2018) Fracture analysis of a metal to CFRP hybrid with thermoplastic interlayers for interfacial stress relaxation using in situ thermography. *Composite Structures* 193:19–28. doi:10.1016/j.compstruct.2018.03.013

Quantitative passive thermography for evaluation of fatigue damage in an intrinsic hybrid composite

J. Summa^{1,2}, F. Grossmann¹, H.-G. Herrmann^{1,2}

¹Universität des Saarlandes, Saarbrücken, ²Fraunhofer Institut für zerstörungsfreie Prüfverfahren IZFP, Saarbrücken

1 Abstract

In consequence of recent developments in lightweight design, structures composed of different materials have become of high interest for structural applications. Combining a variety of advantageous material properties, metal-carbon fiber reinforced polymer (CFRP) hybrid-composite are one particular class of those. However, the challenging production process and mechanical loading often result in imperfections and defects. Due to recent research and technological improvements, non-destructive testing methods are capable to detect such damages and imperfections with reasonable effort and therefore are often applied in industry. However, it is questionable how to evaluate the severity of detected defects in terms of the structural integrity or mechanical performance.

Within this work a new approach is proposed to evaluate fatigue damage using passive infrared thermography, which is applied during mechanical testing. This technique is well known to capture the dissipated heat due to damage. Best results for damage detection capabilities and values of dissipated heat can be obtained using the lock-in transformation, as it is less affected by camera calibration coefficients and experimental setup leading to the characterization of damage mechanisms and the measurement of defect size. The cross correlation of the measured defect size with mechanical values (e.g. dynamic stiffness, mechanical hysteresis) allows defining the residual bearable load and describing the dependency between the degradation of mechanical properties and the defect size.

2 Introduction

Multi-material design has drawn attention by automotive, aeronautical and applications in regenerative energy, since it seems most promising in weight reduction while compromising advantageous properties. However, the proneness of intrinsic interfaces to fatigue crack formation remains one of the major drawbacks. Presence of residual stresses and strong property gradients, hence stress concentrations [1], address the challenge of different joining techniques [2] to achieve an optimized force transition between the constituents and high resistance against fatigue.

Although many different criteria have been developed to evaluate the life-cycle performance and cracking of CFRPs, e.g. [3, 4], vast variety of influencing factors and the high scatter of material properties impair the subjects of condition monitoring and failure assessment of metal-CFRP hybrids. Thus, key to assess the damage state at intrinsic interfaces are nondestructive-testing techniques enabling to characterize the damage mechanisms and to understand the influencing factors. Such methods are eligible to develop tools for condition monitoring and a prognosis of rupture, as it can be seen for CFRP. Its inherent poor heat conductivity and low density are beneficial for thermography, which has been applied for quantitative damage characterization under quasi-static [5, 6] and fatigue loading [7, 8].

Following Palumbo et al. [9], the thermography signal is composed of the mean temperature and the reversible temperature variations that are modulated by externally applied stress waveforms. The latter incorporates the amplitude and phase information, as discussed by Palumbo, whereby the phase-information does not require a reference image for quantitative evaluation. In contrast, focusing on the increase in mean temperature and using the local heat-conduction equation [10], various studies aimed to predict upcoming failure by heat build-up measurements [7, 11, 12] and dissipative thermal energy [8], respectively. Furthermore, Summa et al. used passive in situ thermography to characterize the damage mechanisms of the hybrid-composite under investigation [13]. They found that a thermoplastic material at the interface leads to a redistribution of interfacial stresses, such that growth of delaminations between the middle CFRP-ply become the predominant damage mechanism. Based on these observations and following the approach of Naderi et al. [8], the correlation of thermography information, e.g. location and size of damage, with the mechanical properties is a promising tool to evaluate the damage severity.

3 Experimental Setup

3.1 Specimen Assembly

One constituent of the hybrid-composite under investigation is an aluminum plate that is inserted between the middle plies of the CFRP-laminate. A geometrical optimized thermoplastic layer is placed between those constituents resulting in a tight fit [14]. The geometrical optimization is conducted with the aim to reduce contact pressure and stress concentrations at the interfaces (figure 1).

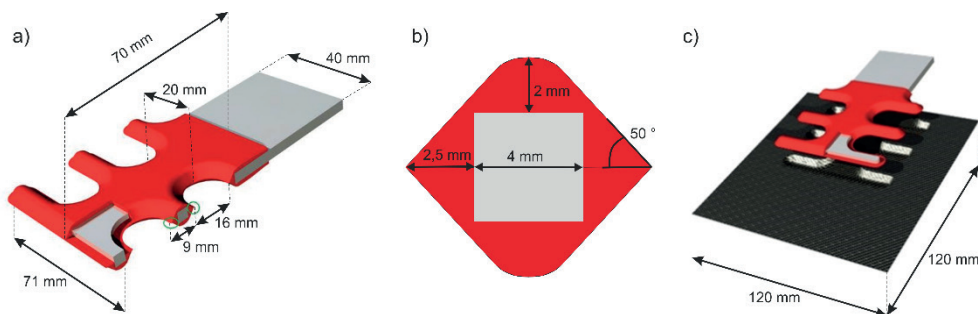


Figure 1: a) geometric shape of the Al-Thermoplastic insert, b) cross-section of polymer-coated arms, c) insert positioned between the CFRP-laminate [14]

The specimens were produced by direct injection-overmolding of a 4 mm thick metallic plate, Aluminum EN AW 6082 (AlMgSi1), with a 2 mm thick thermoplastic polymer. During the preforming the Al-Polymer-insert was placed between the middle plies of the CFRP-laminate (see figure 1 c), which was subsequently consolidated in resin transfer molding (RTM) process. The CFRP consists of four laminate plies $[0/90^\circ, \pm 45^\circ]_s$ with 30 vol-% 3K plain weave (Torayca FT300B) carbon fiber embedded in an epoxy matrix (Biresin CR170/CH150-3). Each ply has a thickness of 0.25 mm.

In this work two different thermoplastic materials are investigated: Vestamid® HT plus M1000, a high rigid Polyphthalamid (further called PPA, E-modulus: 3,5 GPa) and Vestamid® HT plus M1033, the same Polyphthalamid with 30 vol-% short glass-fiber reinforcement (hereafter named PPAGF30, E-modulus: 11.2 GPa). In addition, one reference insert is contemplated, which has the same contour as the others but is completely composed of aluminum (further named ‘full-al insert’).

3.2 Experimental Setup

For mechanical testing the specimens are mounted on an Instron 8500 with a 100 kN load cell. Therefore side-screw action grips are used with a clamping length of 25 mm at top and bottom and 10 mm on left and right side. The setup is complemented with *in situ* passive thermography. The used IR-camera is an InfraTec VarioCam® HD Head bolometer camera with a resolution of 1024 x 768 pixels, spectral sensitivity in the range of 7.5 to 14 μm and the noise equivalent temperature difference NETD being 50 mK (at $T = 303,15 \text{ K}$). The camera is 0,7 m orthogonal in front of the specimen and focused on the CFRP surface.

All tensile tests are driven displacement controlled with 2 mm/min cross-head speed, according to DIN EN ISO 527 [15]. The IR-camera is driven synchronously with 3 frames per second (fps).

All fatigue experiments are carried out load-controlled with a 5 Hz sinusoidal loading, R-ratio of 0.1 and the maximum applied force being $F_{max} = 7,5 \text{ kN}$. Note that the breaking criterion is complete rupture of the specimens. In fatigue experiments, the IR-camera is not driven continuously but triggered at certain number of cycles. At each trigger event, the camera captures 18 frames with 30 fps.

4 Results and discussion

The mechanical behavior and the damage mechanisms of the hybrid-composite strongly depend on the thermoplastic material, used as interlayer. Figure 2 summarizes the tensile tests of the hybrid-composite with aluminum-, PPAGF30- and PPA-inserts and the corresponding damage mechanisms observed using thermography.

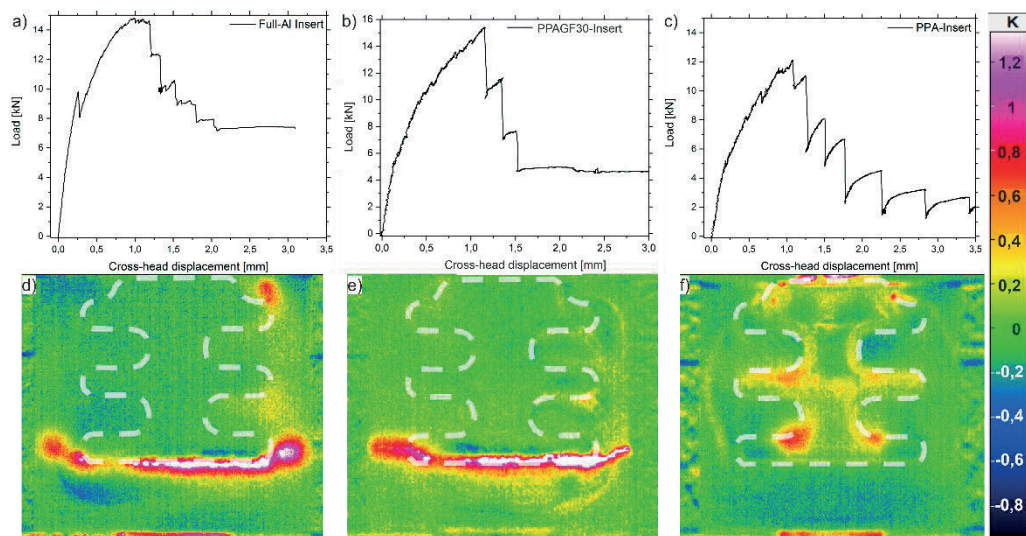


Figure 2: force-displacement diagrams of tensile tests with a) full-Al-insert, b) PPAGF30-insert and c) PPA-insert and corresponding characteristic thermography images (ΔT -contrast) at the incident of rupture of d) full-Al-insert, e) PPAGF30-insert and f) PPA-insert

Final failure of the hybrid-composites with the stiffer aluminum- and PPAGF30-inserts is accompanied by transversal cracking of the laminate, whereas successive growth of delaminations around the insert arms and below the insert are evident for the softer PPA-insert. Ellipsoidal shaped delaminations start below the insert and around the upper and middle arm and coalesce with increased loading. Note that warmer regions (red) indicate events of damage. Summa et al. [13] gives a detailed analysis

and interpretation of the damage mechanisms and influencing factors, e.g. the material at the interface.

Additional computer-tomography images validate (see figure 3) that passive thermography enables to measure the size of delaminations. Hence, assigning the delamination size of the PPA-hybrids (local minima, e.g. figure 2 c) with subsequent local maxima (residual strength) results in a plot of the residual strength against the delamination size (figure 4 b). From this figure, a linear relationship is found between the size of delamination and the residual strength.

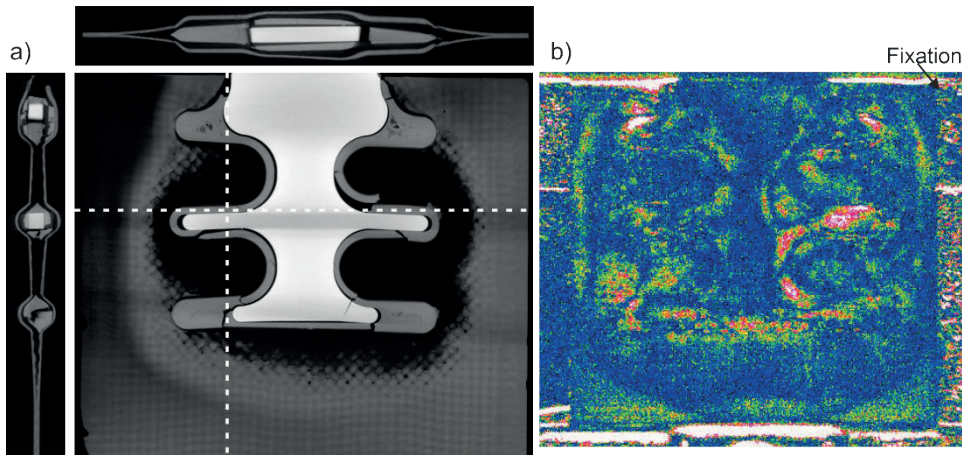


Figure 3: a) Computer-tomography scan of hybrid-composite: resolution of the image reconstruction is 130 μm Voxel-edge-length, b) corresponding thermography image (lock-in amplitude image)

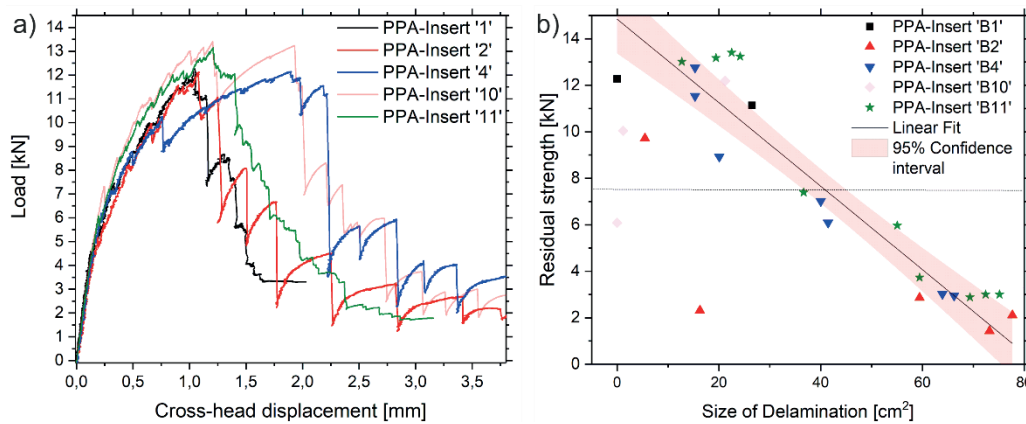


Figure 4: a) force-displacement diagrams of tensile tests with PPA-inserts, b) residual strength plotted against the size of delamination for hybrid composites with PPA-inserts, dashed line corresponds to maximum fatigue loading of 7,5 kN

The fatigue experiments are evaluated by means of the dynamic stiffness (secant modulus in force-displacement loop). Figure 5 a) depicts the decrease of the dynamic stiffness of the tested hybrid-composites with PPA-insert with respect to loading cycles. Although a relatively high scatter is evident amongst the specimens with PPA-inserts, the observed damage propagation is similar. Again, passive thermography is a viable method to characterize the damage, as it can be seen from the lock-in amplitude images for PPA-insert '32' in figure 5. Higher amplitude values (red and white) indicate the process zones of damage propagation. Thus, it is obvious from figure 5 b) that due to fatigue loading delaminations arise around the insert arms and below the insert. The subsequent growth of the delaminations (figure 5 c) accompanies the decrease in mechanical stiffness until the delaminations cause the residual strength to drop below 7,5 kN resulting in failure.

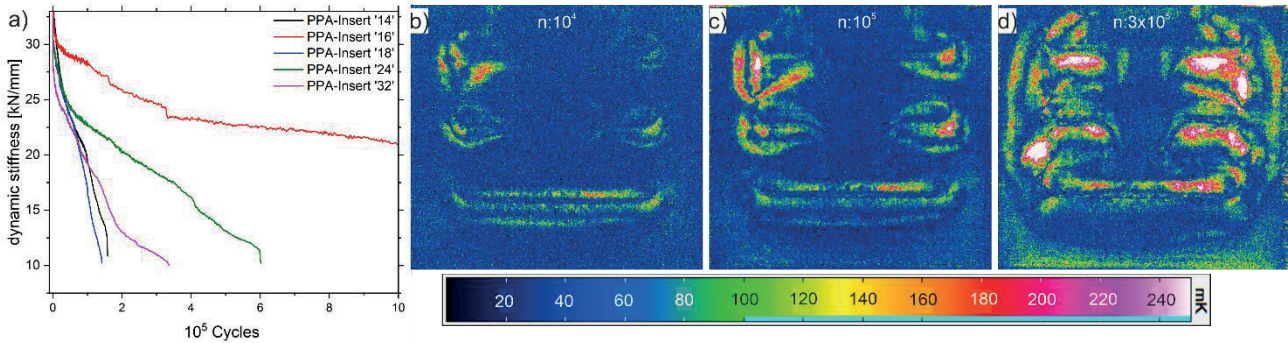


Figure 5: a) dynamic stiffness during fatigue experiments, lock-in amplitude images of specimen ‘PPA-Insert 32’ at b) 1000 cycles, c) 100 000 cycles and d) 300 000 cycles

Thereby, passive thermography enables measuring the size of delaminations, which shows a high scatter amongst the specimens with PPA-Insert with respect to time (figure 6 a). However, these results reveal that all specimens fail as the delaminations exceeds an area of approximately 42 to 50 cm², which agrees perfectly with the regime of the static residual strength (figure 4 b). In addition, a clear relationship between the dynamic stiffness and the size of delaminations can be found if plotted together (figure 6 b).

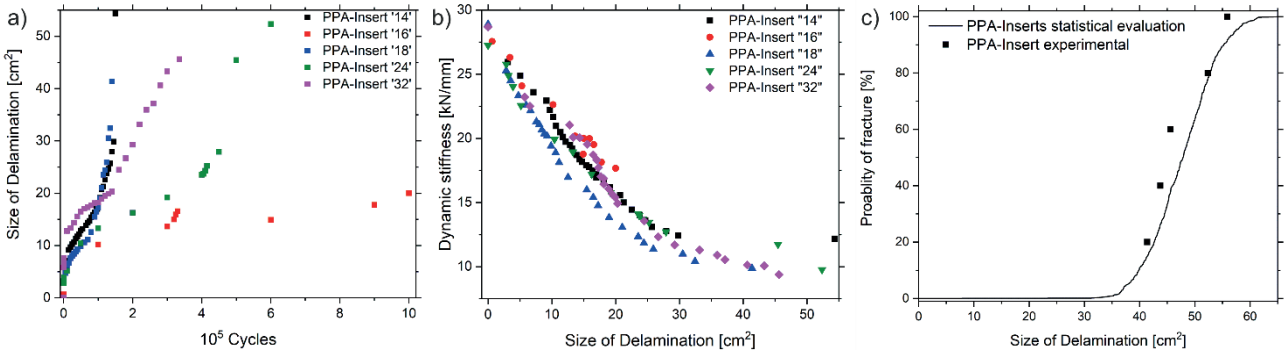


Figure 6: a) size of delaminations with respect to loading cycles, b) dynamic stiffness of specimens with PPA-Insert plotted against the size of delamination, c) relative probability of failure plotted against size of delamination for the hybrid-composite with PPA-Insert

In a similar way as Naderi et al [8] described the development of the thermally dissipated energy as a parameterized function of the number of cycles, the growth of the delaminations can be approximated using the dynamic stiffness J and mechanical hysteresis H (see [16]):

$$a(n) = J_0/J(a) \cdot (1 - \exp\{-H(n)\}) \quad (1)$$

Where a is the relative size of damage, J the dynamic stiffness as a function of damaged area, H the mechanical hysteresis. Using this approximation, a relative probability of failure is calculated as a function of the size of delamination (figure 6 c).

5 Conclusions

Combining quantities of mechanical testing and thermography assisted measurements of the damage size enabled to plot the (static) residual tensile strength as a function of the damaged area of a hybrid-

composites with a PPA-Insert. Under fatigue loading of 7,5 kN the hybrid-composites failed, as the delaminated area exceeded 42 to 50 cm². This agrees well with the estimated regime by static residual tensile strength.

During fatigue loading the dynamic stiffness decreased as a result of growing delaminations. However, the dynamic stiffness was found to be strongly dependent on the size of the delaminations. Both of the observed relationships, between the residual strength and the size of delaminations as well as between the dynamic stiffness and the size of delamination were suitable to estimate the relative failure probability over the measured size of delamination. Ultimately, combining passive thermography measurements and mechanical quantities enabled to evaluate the fatigue damage of the hybrid-composite, i.e. if certain mechanical loads result in unacceptable deformations or may cause failure.

Acknowledgements

The Authors kindly thank their research associates from LKT at TU Dortmund and wbk institute at KIT as well as German research committee for the project funding.

6 Literature

- [1] O. Al-Khudairi, H. Hadavinia, A. Waggott, E. Lewis, C. Little, , *Materials & Design* (1980-2015) 66 (2015) 93–102.
- [2] S.T. Amancio-Filho, J.F. dos Santos, *Polym. Eng. Sci.* 49 (2009) 1461–1476.
- [3] Davila, *Failure Criteria for FRP Laminates*, *Journal of Composite Materials* (2005) 323–345.
- [4] C. Hochard, Y. Thollon, *International Journal of Fatigue* 32 (2010) 158–165.
- [5] J.-M. Roche et al., in *QNDE 2012*, 15-20. Juli 2012, Denver, USA
- [6] C. Goidescu et al., *Composites Part B: Engineering* 48 (2013) 95–105.
- [7] J. Montesano, Z. Fawaz, H. Bougherara, *Composite Structures* 97 (2013) 76–83.
- [8] M. Naderi, A. Kahirdeh, M.M. Khonsari, *Composites Part B: Engineering* 43 (2012) 1613–1620.
- [9] D. Palumbo, R. Tamborrino, U. Galietti, P. Aversa, A. Tati, V.A.M. Luprano, *NDT & E International* 78 (2016) 1–9.
- [10] A. Chrysochoos, H. Louche, *International Journal of Engineering Science* 38 (2000) 1759–1788.
- [11] R. Steinberger, T. Valadasleitao, E. Ladstatter, G. Pinter, W. Billinger, R. Lang, *International Journal of Fatigue* 28 (2006) 1340–1347.
- [12] L. Jegou, Y. Marco, V. Le Saux, S. Calloch, *International Journal of Fatigue* 47 (2013) 259–267.
- [13] J. Summa, M. Becker, F. Grossmann, M. Pohl, M. Stommel, H.-G. Herrmann, *Composite Structures* 193 (2018) 19–28
- [14] M. Pohl, M. Stommel, in: *Proceedings of the 17th European Conference on Composite Materials 2016*, pp. 4025–4030.
- [15] DIN EN ISO 527, 1997, 2012
- [16] J. Summa et al., In: *Proceedings of the ICFC7*, Vicenza, Italy, 4-6 July 2018

TOPIC

Manufacturing



@DGM_eV

#Hybrid2020

MANUFACTURING OF HYBRID COMPONENTS BY VARTM-PROCESS USING NEW SEALING TECHNIQUE DEVELOPED

Deviprasad C J^{1*}, T. Stallmeister¹, Z. Wang¹ and T. Tröster¹

¹ Chair for Automotive Lightweight Design, University of Paderborn, Paderborn, Germany

* Corresponding author (deviprasad.jayasankar@Uni-Paderborn.de)

1 Introduction

Currently, resource efficiency and CO₂-reduction are getting more important in industrial production, especially in the automotive sector. To achieve this goal, automotive industries are exploring the methods to produce weight-reduced components (lightweight) without sacrificing its mechanical properties as it directly influences the safety of the occupant [1]. High strength steels are used to achieve in such a case, but it is limited to stability issues as the thickness reaches threshold value [2]. The other possibility is to use composites made out of FRP that are restricted to sports cars, aerospace etc. as they are expensive due to the high production cycle time and material cost [3]. However, a trade-off between low mass and acceptable cost can be achieved by hybrid lightweight design that uses the expensive FRP just in highly stressed areas. The hybrid components are light in weight compared to the metal components without sacrificing its mechanical properties along with being cheaper when compared to component made entirely out of FRP [4].

Resin transfer molding (RTM) manufacturing method is used in present research for producing hybrid components. In RTM Process, the dry fibre laminate is preformed and inserted into a cavity following the closure of cavity and injection of resin. The contours are sealed during the injection process until the resin has reached a certain degree of curing. The sealing of the mold influences the part quality. The sealings are used to prevent leakage as the matrix system has relatively low viscosity and is injected with high pressures. The seals undergo tremendous mechanical wear due to high clamping forces and thermal wear due to tool temperature and matrix reaction. This results in replacing of sealing after 10 to 30 production cycles that causes unproductive downtime of tool [5]. Figure 1 shows silicone polymer used as a sealing material for intrinsic manufacturing of metal-CFRP hybrid omega profiles by vacuum assisted RTM (VARTM) process [5].

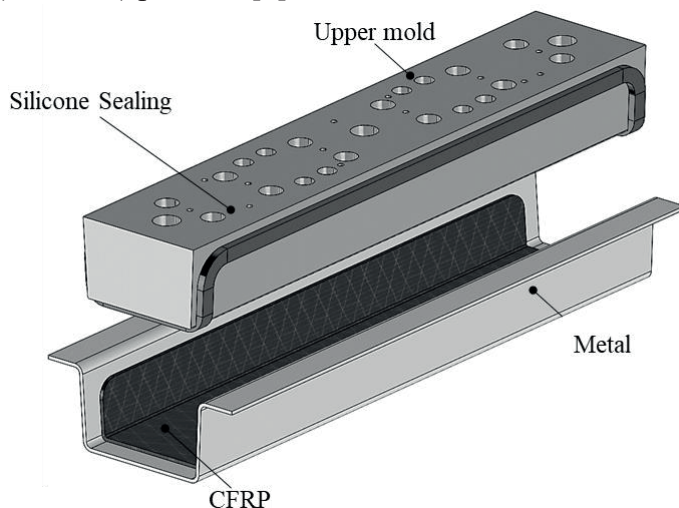


Figure 1: Tool with silicon sealing technique for intrinsic VARTM processes

New sealing material was introduced to replace silicone sealing made from high-performance thermoplastics by Murtfeldt kunststoffe, which is claimed to withstand several hundred production cycles up to 200 bars [6]. Fraunhofer ICT invented a process chain where the sealing is directly applied to the preform in order to decouple the maintenance-intensive components from the main tool [7]. In contrast, this research focusses an innovative sealing approach that works without any sealings and therefore contactless

1.1 Innovative sealing - working principle

The innovative sealing is based on accelerated curing of resin along with reduced cross-section (sealing tool) that provides increased flow resistance resulting in a self-sealing mechanism. As a result, the resin cures close to contour and therefore seals the cavity. Due to this self-sealing effect there is no need for further sealings. In case of vacuum assist, the conventional silicone sealing can be placed in areas with lower thermal and mechanical stress. The downtime for replacing the sealing material is eliminated resulting in a further optimized manufacturing method. Figure 2 shows the block diagram of innovative sealing's working principle. This concept is universally applicable to processes involving matrix injection and pressing sheet compounds, thus offers an enormous scaling potential.

The innovative sealing area consists of a rigid heating element and thermal insulation that are installed in the mold. The heating element locally delivers a significantly higher temperature than the rest of the mold and is thermally insulated. The thermal insulation prevents the main tool from heating up excessively.

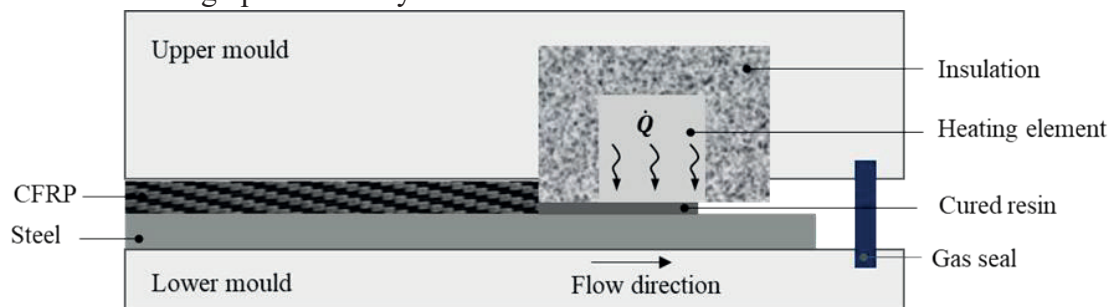


Figure 2: Sealing concept - working principle

2 Experimental investigation

2.1 Materials and methods

The preform used for the experimental research consists of unidirectional carbon fibre layers (HPT 320 CO 24K) with an area weight of 320 g/m². In order to process the layers into a preform, the fibres are coated with a thermoplastic epoxy binder that weighs 14 g/m² additionally. The injected resin is a medium viscous epoxy (EPIKOTE 05475) in combination with an amine curing agent (EPIKURE 05443). This matrix system is developed for serial production in automotive industry with low initial viscosity and a fast curing reaction. For the intrinsic manufacturing of hybrid components, a micro-alloyed steel plate (steel 1.0548) with a thickness of 2 mm is inserted. Its surface is sandblasted in order to increase the adhesive strength between the resin and steel.

The laminate structure consists of six layers of CFRP and 1 layer of glass fleece that are aligned in x-direction (0°) with a total thickness of 2 mm. The glass fleece (ForTex®Type SH35/1, area weight: 30 g/m²) prevents contact corrosion and causes a defined resin rich layer that is important for the adhesive strength of the hybrid laminate [8]. This layer design results in a fibre volume fraction of 55 %.

2.2 Manufacturing setup

Simplified 2D RTM tool that produces flat plate was used initially to validate the sealing concept as shown in Figure 3. Only one of four edges of the plate is sealed with the heating element and other three edges use a conventional silicone cord. A local higher temperature is achieved by a steel strip that is equipped by electric heating cartridges. This steel strip is mounted to the upper mold and allows the adjustment of its height respective to the distance between heating element and metal sheet that controls the gap height. Thermal insulation is obtained using special material made from glass fleeces (K-Therm®AS 600M) that has thermal conductivity of 0.26 W/(m K) when compared to steel that has higher value of 50 W/m K. The temperatures of the upper and lower mold can be measured with thermocouples at four different positions. Three electric heating cartridges each on upper and lower mold are used for thermal supply. The injection strategy can be adapted with different positions for sprue and riser. Firstly, the vacuum is obtained once the tool is closed. Preheating, mixing and injection into the mold is carried out with an RTM machine by Tartler. The mixed matrix (resin and curing agent) is injected under an initial temperature of 80 °C after the tool is closed, with preform and steel plate inserted with a controlled flow rate of 0.12 kg/min and a maximum pressure of 5 bar. The machine automatically reduces the volume flow rate when the maximum pressure is reached. The cavity temperature is 120°C while the temperature of the heating element is changed between different experiments ranging from 200 °C to 300 °C. The Gap height is also changed in order to achieve a complete sealing and good laminate quality. The size of the cavity is 150 x 150 x 4 mm and the preform is 125 x 150 x 2 mm.

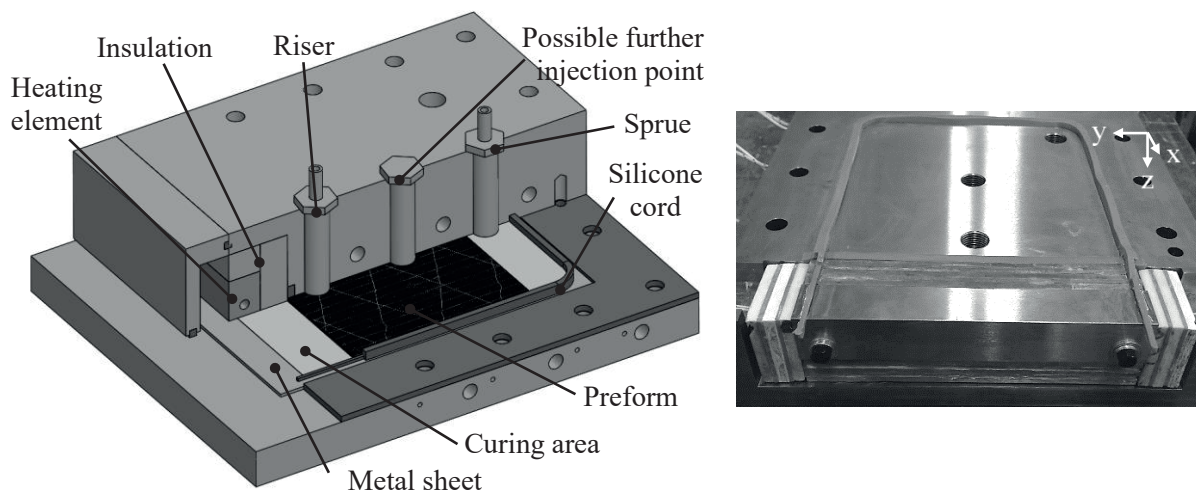


Figure 3: Sectional view (left) and upper mold (right) of RTM-tool with new sealing concept

First tests showed that the injection in the middle of the mold causes incomplete sealing. This is because the resin reaches the middle of the seal at first and then cures accordingly, the effective cross-section of the flow channel decreases and the flow velocity increases. This leads to uneven results over the length of the heating area and leakage at the sides of the innovative sealing. The remedy was to inject into an area of the cavity far away from the heating element without preform. In this way an even resin flow front distribution is achieved.

3 Results

The produced laminate quality is determined mechanically by interlaminar shear (ILS) tests and optically by microscope images. The ILS tests are carried out in accordance with DIN EN 14130. Specimens with a length of 20 mm and a width of 10 mm are placed in a three-point loading fixture, with the CFRP facing the two bearing points and the indenter hitting the steel side with a constant test speed of 1 mm/min. For microscope images, samples are taken from the plate, embedded, grinded and polished. Microscope images are made parallel to the fibre direction in order to see potentially irregularities like voids.

The technological feasibility of the concept could be proven on a two-dimensional level. The result of a preliminary test as well as the sampling positions from the manufactured hybrid plate are shown in figure 4. In this case, the steel strip was heated to 250 °C and the upper and lower mold to 120 °C. The gap between the heating element and the metal surface was adjusted to 0.1 mm. In fact, it was possible to stop the flow front within the gap. In addition, it was found that the cavity had a very homogeneous temperature distribution at all measuring points thanks to the thermal insulation, which leads to good laminate quality.

The effect of the heating element, which delivers a locally higher temperature can be seen on the right side of manufactured plate (figure 4). The surface of the metal sheet shows annealing colour on the area where the metal is not exposed to the resin. This effect enables a precise definition of the resin propagation due to the colour difference. The results of the ILS tests show the failure of the CFRP, which occurs in stages. Therefore, the failure force is evaluated at the first local force maximum in order to characterise the strength of the laminate before any damage appears. Figure 5 shows the results of the ILS tests with respect to the sampling positions of the heating element.

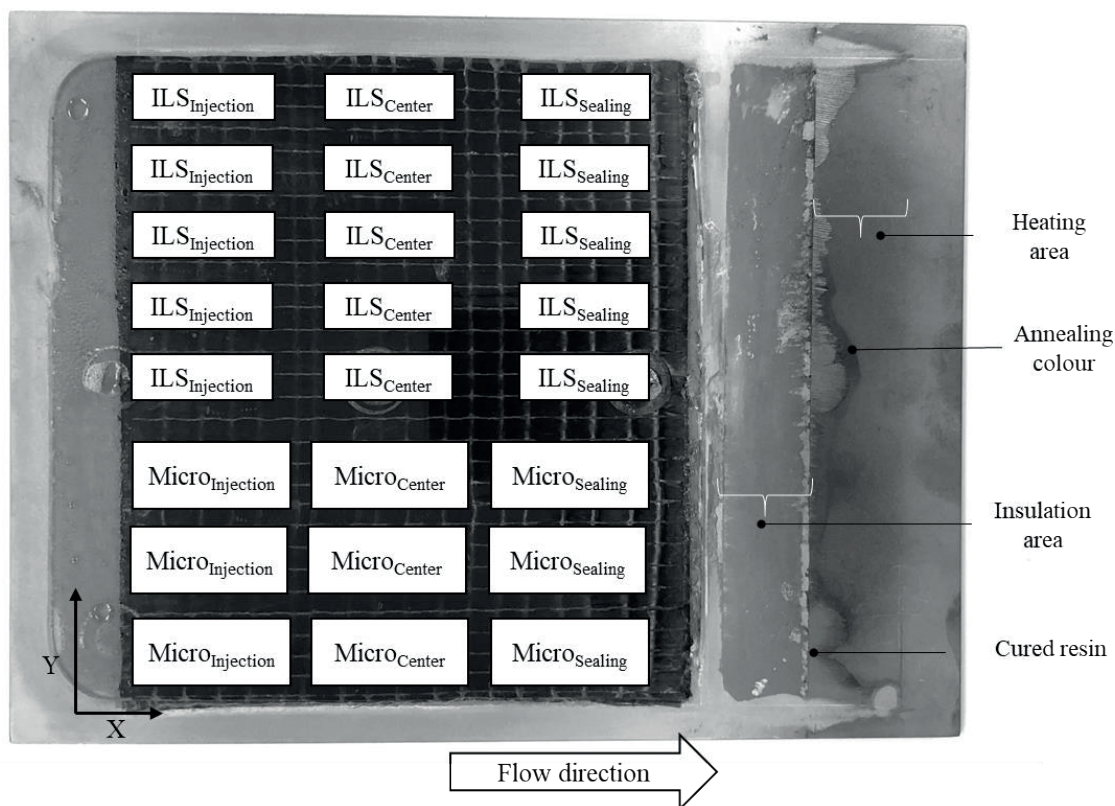


Figure 4: Result of a test with new sealing technology (gap height 0.1 mm, heating element temperature 250 °C)

The bar chart in figure 5 summarises the strength of specimens produced by conventional sealing and innovating sealing. The position of the sampling does not affect in both conventional and innovative sealing. At 250 °C a constant laminate quality can be achieved.

Further decrease in temperature results in incomplete sealing, but this may be prevented by an optimised heating element shape or other measures.

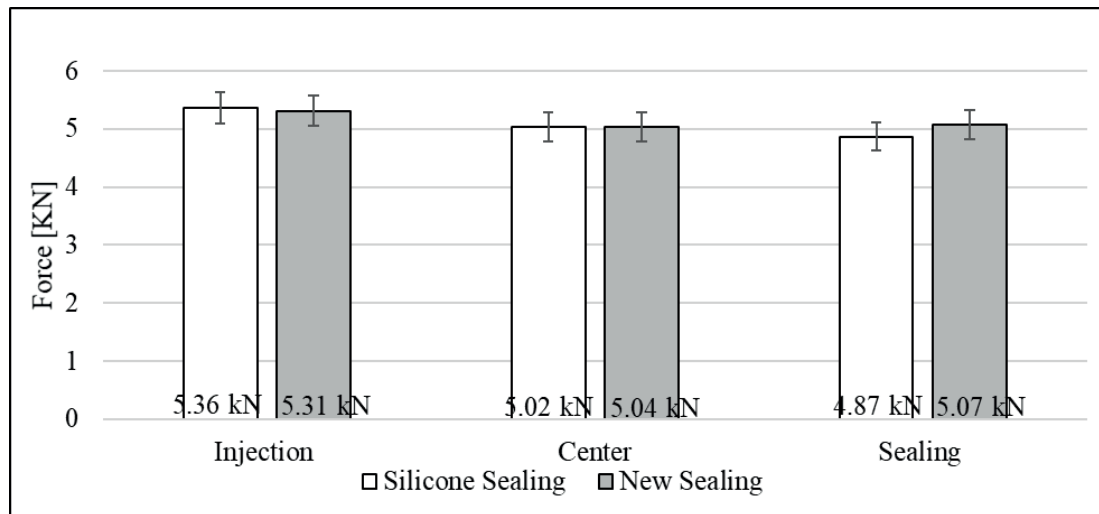


Figure 5: Results of average maximum forces with respect to sampling positions

From microscopic investigations it was observed that the sealing element has no negative effect on laminate quality. Figure 6 shows the alignment of the fibres as they are taken parallel to them. The fibres are aligned homogenous near the sealing are without any major porosity or voids due to uncontrolled curing.

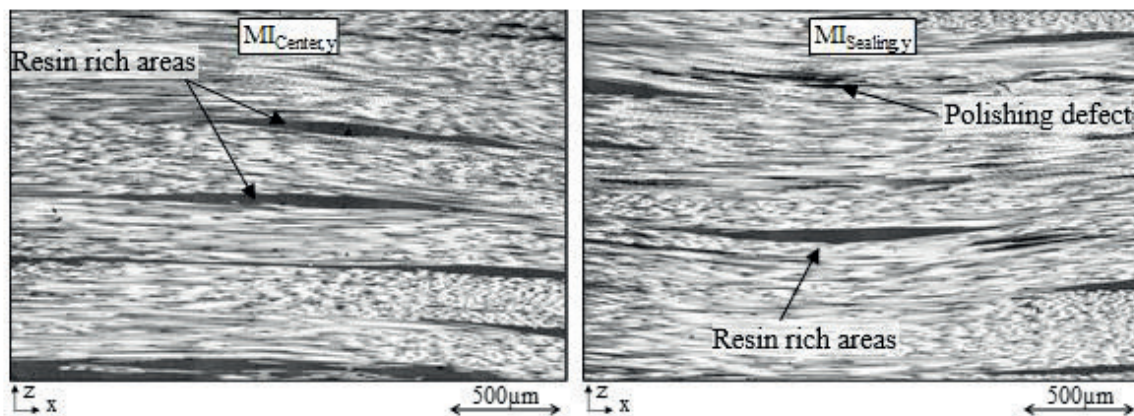


Figure 6: Microscope images parallel to the fibres at different positions of sampling - (gap height 0.1 mm, heating element temperature 250 °C)

4 Conclusion and Outlook

The functionality of the innovative sealing concept was validated successfully. The temperature of the heating element as well as the gap height have been evaluated in order to analyse the functionality of the innovative sealing concept. Results from ILS tests and microscope images showed that the locally higher temperature (250 °C) of the heating element does not negatively influence the laminate quality. With a gap height of 0.1 mm, a complete sealing could be achieved.

Thus, the use of locally accelerated resin curing for tool sealing represents too much technological advantage compared to conventional methods. This can be a promising approach

for reducing the downtime for maintenance occurred due to changing the sealing materials and complex lightweight structures can be manufactured in large series with significantly shortened process times.

Future investigations will focus on other parameters like surface roughness and contour of the sealing area in order to optimise the sealing and exploit the development potential that is still open. For this, the sealing technology needs to be transferred to three-dimensional tools in order to investigate the geometrical effect of production parts. In order to show the applicability for serial production, researches will focus on complex parts like a hybrid drive shaft. The reinforcement of an automotive drive shaft not only offers many property improvements and thus high economic potential but also particularly suitable for testing the new sealing technology due to the high production requirements.

5 Literature

- [1] M. Frantz, C. Lauter and T. Tröster, "Advanced manufacturing technologies for automotive structures in multi-material design consisting of high-strength steels and CFRP," in *56TH INTERNATIONAL SCIENTIFIC COLLOQUIUM*.
- [2] M. Kleiner, S. Chatti and A. Klaus, "Metal forming techniques for lightweight construction," *Journal of Materials Processing Technology*, vol. 177, no. 1-3, pp. 2-7, 2006.
- [3] P. Feraboli, A. Masini and A. Bonfatti, "Advanced composites for the body and chassis of a production high performance car," *Int. J. Vehicle Design*, vol. 44, 2007.
- [4] Z. Wang, C. Laute, B. S. and T. Tröster, "Intrinsic Manufacturing of Metal-FRP-Hybrid Structural Automotive Components by Resin Transfer Molding," in *18th International Conference on Composite Structures*, Lissabon, 2015.
- [5] Z. Wang, P. Sorge and T. Troester, "Intrinsic manufacturing of metal-CFRP hybrid omega profiles by resin transfer molding process," in *Z. Wang, P. Sorge and T. Troester, Intrinsic manufacturing of metal-CFRP Conference on Composite Materials Parts Manufacturing CIRP CCMPM 2017*, Karlsruhe, Germany, 2017.
- [6] G.-M.-. Kunststoffe, Branchen and Dichtungsmaterial-für-viele, "<https://www.murtefeldt.de/presse/anwenderberichte/dichtungsmaterial-fuer-viele-branchen/>," 2019.
- [7] T. Fürst, T. Huber, J. Kuppinger and F. Henning, "Molding Tools without Sealing Gaskets," in *Kunststoffe international, Carl Hanser Verlag*, Munich, 2015.
- [8] Z. Wang, T. Tröster, "Influences of interface on the mechanical and corrosion properties of steel-CFRP hybrid structures manufactured by vacuum assisted resin transfer molding," in *21st International Conference on Composite Structures 2018*, Bologna, Italy, 2018.
- [9] M. Cavazzuti, A. Baldini, E. Bertocchi, D. Costi, E. Torricelli and P. Moruzzi, "High performance automotive chassis design: a topology optimization based approach," *Struct Multidisc Optim*, pp. 44-56, 2011.

Screening tests of an one-shot forming process of fibre-reinforced thermoplastics and steel sheets to determine the geometrical accuracy

P. Kabala¹, M. Demes¹, T. Ossowski¹, J. Beuscher¹, K. Dröder¹

¹ Technische Universität Braunschweig, Institute for Machine Tools and Production Technology, Langer Kamp 19B, 38106 Braunschweig

1 Introduction

The increase in environmental awareness of customers as well as strict governmental regulations to reduce the emission greenhouse gases are current trends [1], which have to be considered in the automotive development by the manufacturers. In contrast, heavy passenger cars are becoming increasingly popular [2, 3]. Fuel and energy consumption rise with an increasing vehicle mass. A variety of approaches are available to the automotive industry to fulfill the contrary trends. Lightweight design is one approach to reduce the moving mass of cars and thus the emission of greenhouse gases. Fibre-reinforced thermoplastics (FRTP) are of great importance due to their good specific mechanical properties [4]. The pure substitution of steels by FRTP is associated with high material costs. Furthermore, there are no established joining processes for FRTPs, yet [5]. The intelligent combination of metals and FRTPs in a so-called hybrid lightweight design, allows a compromise between rising component costs and mass reduction. According to the state of the art, hybrid components are often manufactured in two subsequent process steps [6]. First, a metal sheet is formed. A typical forming process in metal processing is the deep drawing process. Then, a flat FRTP, such as organo sheets or tapes, is applied onto the already formed metal sheet in a thermoforming process. The production of a hybrid component on the basis of subsequent process steps leads to additional handling processes, logistical and plant costs, resulting in an increase in manufacturing costs. In order to reduce the complexity of the process chain, a one-shot manufacturing process is developed, which consists of an integrated deep-drawing of sheet metal and thermoforming process of FRTP. For this purpose, a forming tool is developed in order to obtain knowledge about the formability of sheet metal and FRTP tape as a hybrid semi-finished product. In the subsequent forming tests, the tool temperature and dwell time is varied to obtain a trend of the influence of both parameters on the spring back behaviour.

2 Hybrid forming process

2.1 Concept of an one-shot forming process

The deep-drawing process is a widely used forming process for sheet metals. A deep-drawing tool consists mainly of a die, a punch and a blank-holder. The semi-finished sheet metal product is first placed on the die and fixed by a blank-holder. Then, the sheet is formed by the punch. The blank-holder clamps the sheet and thus prevents the formation of wrinkles, which especially occur during forming of three-dimensional geometries. In order to avoid wrinkles, high blank-holder forces are often required. This results in high frictional forces between the steel sheet and the tool during forming. The frictional force also acts as resistance, which inhibits the sliding of the sheet metal into the tool cavity. The combination of the forming force of the punch and the frictional force of the blank-holder leads to an enlargement of the surface and a thinning of the material thickness on the flank. Therefore, high degrees of deformation can be reached during the deep drawing process [7].

The thermoforming process is a forming process of fibre unreinforced or reinforced thermoplastics. In the following, the focus is on fibre-reinforced semi-finished products. For this process, the FRTP material has to be heated up above the melting temperature of the matrix material to reach a low-viscous state. This allows a sliding of the fibres in the low-viscosity matrix to form the FRTP. After forming, the material must be cooled down in the tool. This ensures that the component can be removed dimensionally stable and is not damaged during removal [8].

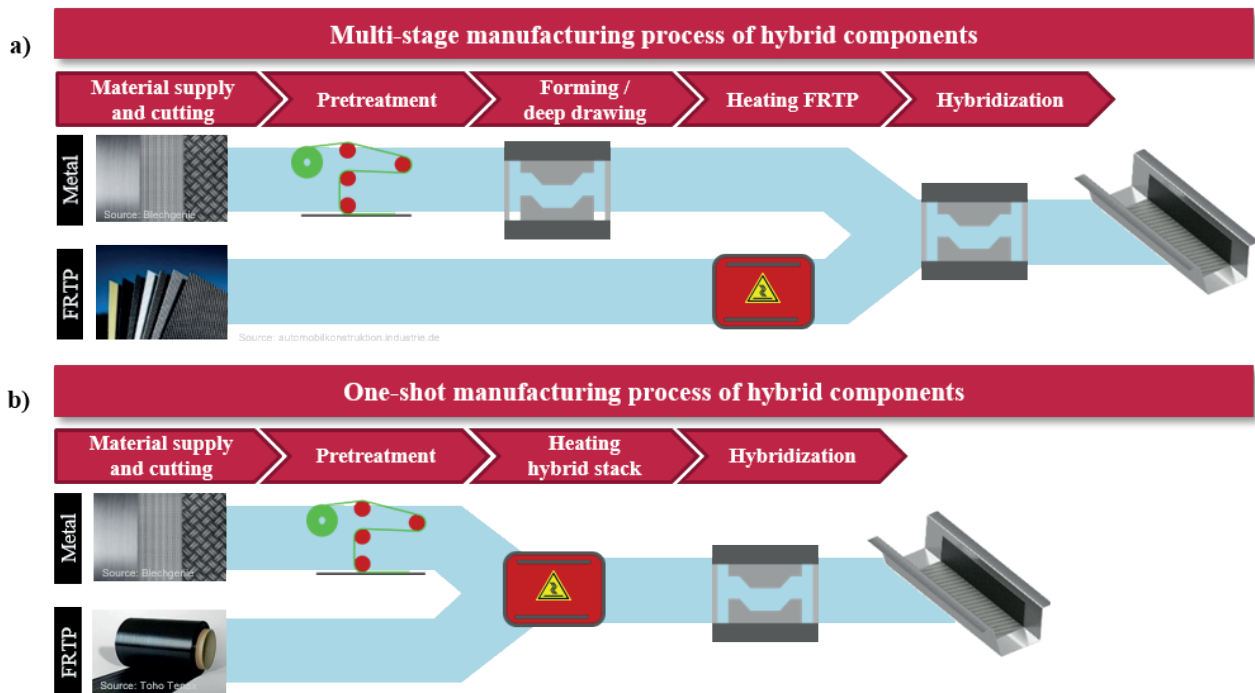


Figure 1: a) Multi-stage manufacturing process of hybrid components, b) One-shot manufacturing process of hybrid components.

In the course of lightweight design, FRTP are increasingly used. However, significantly lower degrees of deformation can be achieved during the forming of FRTPs along the fibre direction than with steels. This is due to the lack of ductility of the fibres. [9]. Consequently, in the thermoforming process FRTPs can only be draped. Therefore, the forming behaviour between steels and FRTPs is one of the biggest differences in terms of process techniques.

Due to the different forming properties, hybrid components are manufactured in a multi-stage process according to the current state of the art. Figure 1a shows this multi-stage process. First, the sheet metal is pre-treated (cleaning, cutting to size, applying adhesive, etc.) before it is formed. Afterwards, the FRTP is heated and draped into the formed sheet metal. By integrating both forming methods, one forming step can be reduced (see Figure 1b). The pre-produced hybrid semi-finished product, consisting of steel sheet and FRTP, is heated. Subsequently, both materials are formed in one step. During forming both materials can slide against each other. If a sliding is prohibited by geometrical restrictions, the FRTP can be applied to the steel sheet with an elongation reserve [10]. Thus, the widely differing maximum degrees of deformation can be compensated.

The high relevance for the development of a one-shot forming processes is shown by numerous publications to this topic. *Behrens et al.* developed a single-stage forming process for metal-FRTP-metal sandwich components [11, 12]. *Gresham et al.* demonstrated the influence of various process parameters on the forming behaviour of such sandwich structures [13]. The complex spring back behaviour of hybrid sandwich structures during bending was investigated by *Hahn et al.*

[14]. The publications mentioned here deal with a symmetrical layer structure (sandwich structure) consisting of metallic cover layers and a core of FRTP. An asymmetrical layer structure has the advantage that the hybrid component can be injection moulded afterwards to create stiffening elements or attachment points. However, it is not clear whether the properties, such as spring back or formability, can be transferred to an asymmetrical layer structure. Especially in the case of warpage, significant differences due to the delta-alpha problem can be assumed, which would otherwise mainly be compensated by the symmetrical layer structure.

2.2 Tool design

The forming tool for the integrated deep-drawing and thermoforming process is shown in Figure 2a. For the forming tests, a u-profile is investigated (see Figure 2b). Through the simple geometry fundamental knowledge about the limits of the forming process and warpage can be obtained.

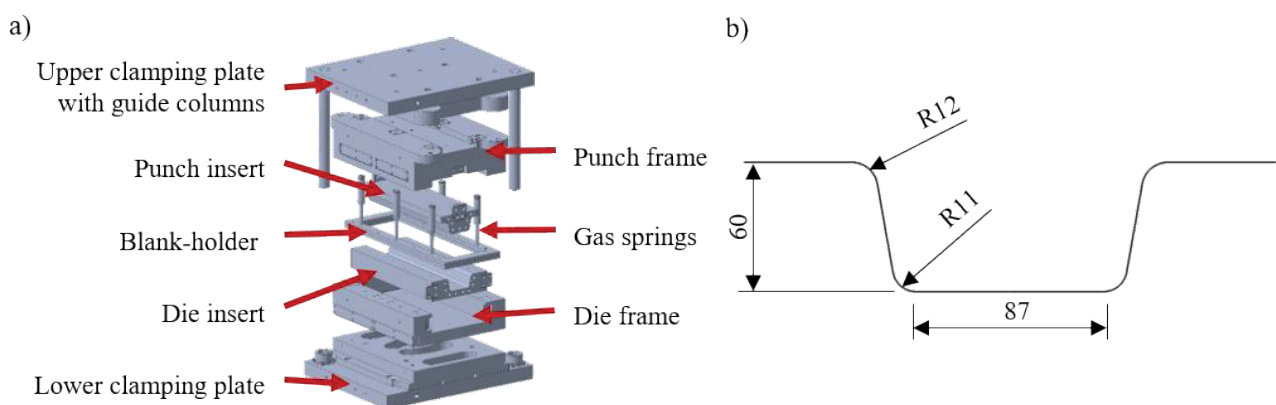


Figure 2: a) Exploded view of the forming tool, b) Cross sectional view of the u-profile geometry

A tool temperature control for the processing of semi-finished plastic products is essential to prevent premature cooling and solidification. Therefore, heating cartridges are located inside the punch and die insert in order to heat the tool surface. In this way, the cooling rate in the plastic can be specifically affected during the forming process. Thermocouples integrated close to the surface of the tool serve to control the tool temperature. This allows forming tests with reproducible temperature settings.

By integrating the deep-drawing process, a blank holder is implemented in the forming tool. To introduce the blank-holder force to the sheet, gas springs are used. The spring force can be adjusted variably via the gas pressure. In addition, gas springs offer a flat spring characteristic compared to disc springs or coil springs, so that the spring force is constant during the forming process [15].

3 Forming tests

The forming tests are carried out to record the effects of process parameters on the dimensional accuracy of the components. The dimensions of the hybrid semi-finished products are 361 x 80 mm²

before forming. The total thickness is 1 mm. The layer structure and the materials used are shown in Figure 3.

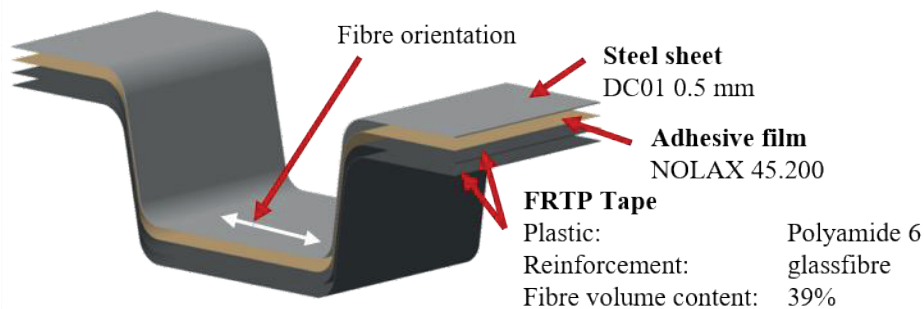


Figure 3: Layer structure of the hat profile.

The tape layers are placed on the laminated sheet and then heated to 240 °C in the oven. Afterwards, the heated hybrid semi-finished product is placed manually from the oven in the tool. During the tests, the tool temperature and the dwell time are varied in order to determine the effects of these process parameters on the spring back of the asymmetrical layer structure.

To determine the dimensional accuracy, the formed test specimen are digitized by an optical measuring system from GOM. The digital test specimen is then compared with a reference model that represents an optimum component without spring back effects. In detail, the angular deviation on the flank of the component is examined.

4 Results and discussion

During initial forming tests, the tool temperature and dwell time are varied. For this, setups of the tool temperature and three setups of the dwell time are investigated. This allows to made statements about coarse trends in the influence of both parameters on the spring back effect. Self-explanatory, further points has to be set up in order to obtain a higher significance of the influence of the parameters.

4.1 Specimen temperature during forming

Thermocouples are placed between the steel sheet and the FRTP to measure the temperature of the specimen during forming. The positions of the thermocouples and the temperature curves at a tool temperature of 80 °C and 120 °C are shown in Figure 4. The zero point of the time axis has been set at the point in time when the punch touches the semi-finished product. From the curve progressions it can be seen that at T2 there is a drop in temperature even before the actual forming process. In this area the semi-finished product is in direct contact with the colder tool, which causes the temperature loss. Approximately 2 s before the punch touches the semi-finished product, a sudden drop in temperature is recorded at T2. This corresponds to the time at which the unheated blank-holder presses on the semi-finished product. Initially, T1 has no contact to the tool surface. After the punch initiates the forming process, the temperature drops abruptly. Up to a time of 20 to 30 s after the tool has closed, no significant temperature drop can be detected in the test specimen.

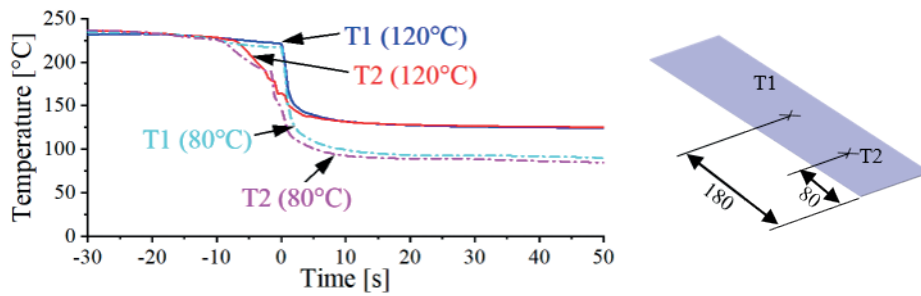


Figure 4: Temperature curves of the specimen during forming

4.2 Influence of the dwell time

Figure 5 shows that the spring back decreases with increasing dwell time, first. After a critical dwell time, the spring back increases. Consequently, a dwell time can be detected at which the spring back is minimum.

The decrease in the spring back effect between the first and the second point can be explained by the different coefficients of thermal expansion between PA6 and steel. During the cooling in a closed tool, steel and FRTP shrink to different degrees due to the different coefficients of thermal expansion. A thermal distortion in the specimen cannot occur as long as the tool is closed, since the tool wall acts as a geometric restriction. This leads to residual stresses in the boundary surface of the FRTP and the steel sheet. However these stresses can be partially relieved by the adhesive, since at short dwell times and high tool temperatures the specimen temperature is still in the range of the melting temperature of the adhesive film. Due to the viscous material behaviour, both materials can slide against each other. If the dwell time is short and the tool temperature high the adhesive film is still in a viscous state after the tool opens. Since the tool does not act as a geometrical restriction anymore, thermal distortion due to different coefficients of thermal expansion can occur. The viscous adhesive can still compensate these distortions through sliding effects. At longer dwell times, the adhesive solidifies completely in the closed tool. Sliding effects can no longer occur in the open tool, as this is prevented by the solid adhesive film. The spring back is less.

Between the second and the third point an increase in the spring back can be observed. In this case, the dwell time is sufficiently long so that the specimen cools down in the closed tool until it reaches the tool temperature. Over a longer period of time heat is transferred from the tool into the specimen. The longer the heat input is, the higher is the proportion of densely packed crystalline structures in the matrix material. This results in shrinkage effects in the FRTP and thus leads to an increase in spring back.

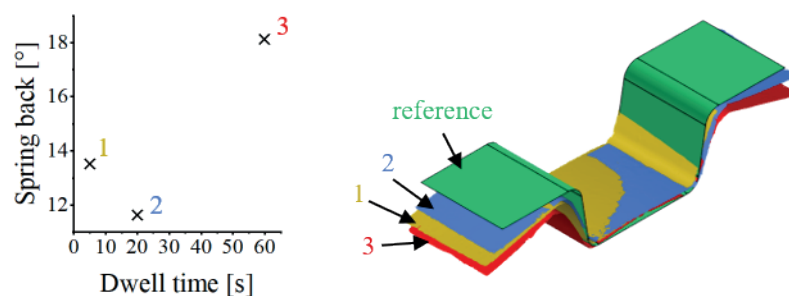


Figure 5: Influence of the dwell time on the spring back effect.

4.3 Influence of the tool temperature

Figure 6 shows that an increase in the tool temperature reduces the spring back. As shown in Figure 4 the specimen does not cool down evenly during forming. Before forming, the semi-finished product has direct contact with the die at both ends. In this area, the semi-finished product cools down faster. Subsequently, the punch touches the semi-finished product and initiates the forming process. This results in temperature gradients along the specimen and it starts to cool during the forming process. With a colder tool the temperature difference to the warm hybrid semi-finished product is higher. This leads to a high heat flow and the semi-finished product cools down faster. If the tool temperature is too low, the PA6 solidifies before the forming process is completed, which results in a higher spring back.

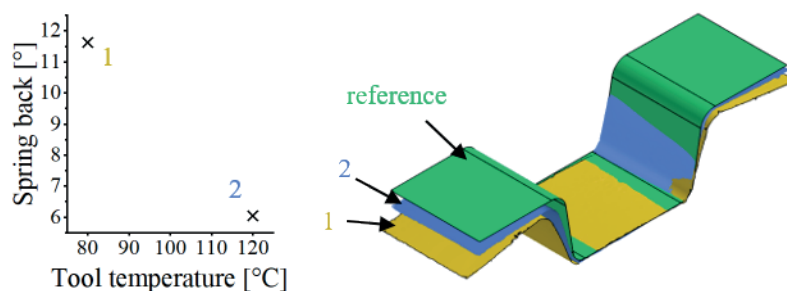


Figure 6: Influence of the tool temperature on the spring back effect.

5 Conclusion

In this paper a tool for the integrated deep drawing and thermoforming process is presented, with which first forming tests are performed. With the help of thermocouples between FRTP and steel sheet, conclusions can be drawn about the cooling behaviour during forming. The temperature curves can be used to justify the influence of the dwell time and tool temperature on the spring back behaviour. An examination of the dwell time shows that the spring back decreases up to a critical point. If this dwell time threshold is exceeded, the spring back increases. An increase in the tool temperature leads to a lower spring back effect. In order to obtain more information about the effects of both parameters, further dwell times and tool temperatures must be investigated. Furthermore, the influence of other process parameters, such as the press force and blank holder force, on spring back is to be examined. This is intended to collect information in order to adjust the process with regard to the optimization of the dimensional accuracy.

6 Acknowledgement

The authors thank for the financial support of the ZIM cooperation project ZF4096706 LP8, which is supported by the AiF within the program Zentrales Innovationsprogramm Mittelstand (ZIM) of the Federal Ministry of Economics and Technology.

7 Literature

- [1] P. Nieuwenhuis, P. Wells: The automotive industry and the environment. *Woodhead Publishing*, **2003**.
- [2] Neuzulassungen von Pkw in den Jahren 2008 bis 2017 nach technischen Merkmalen. Deutsches-Kraftfahrtbundesamt, https://www.kba.de/DE/Statistik/Fahrzeuge/Neuzulassungen/Motorisierung/n_motorisierung_pkw_zeitreihe_techn_merkmale.html?nn=652392. (accessed 06 January 2020), **2018**.
- [3] Neuzulassungsbarometer, https://www.kba.de/DE/Statistik/Fahrzeuge/Neuzulassungen/MonatlicheNeuzulassungen/2018/201812_GV1monatlich/201812_nzbarometer/201812_n_barometer.html?nn=653844. (accessed 06 January 2020), **2018**.
- [4] P. K. Mallick: Materials, Design and Manufacturing for Lightweight Vehicles. *Woodhead Publishing*, **2010**.
- [5] J. Yanagimoto, K. Ikeuchi: Sheet forming process of carbon fiber reinforced plastics for lightweight parts. In *CIRP Annals, Volume 61, Issue 1*, **2012**, p. 247-250.
- [6] M. Fahrig: Continuous-fiber-reinforced thermoplastic composites für lightweight car design. *Lanxess*, Cologne, Germany, **2019**.
- [7] E. Doege, B.-A. Behrens: Handbuch Umformtechnik. *Springer-Verlag Berlin Heidelberg*, Berlin Heidelberg, Germany, **2010**.
- [8] S. Engelmann: Advanced Thermoforming: Methods, Machines and Materials, Application and Automation. *John Wiley & Sons Inc.*, New Jersey, USA, **2012**.
- [9] R. M. Stack, F. Lai: Development in thermoforming thermoplastic components. In *Thermoforming Quarterly* 32, **2013**, p. 48-53.
- [10] P. Kabala, M. Demes, S. Bienia, A. Hürkamp, J. Beuscher, K. Dröder: Numerical model of an integrated deep-drawing and thermoforming process. In *4th International MERGE Technologies Conference (IMTC)*, **2019**.
- [11] B.-A. Behrens, S. Hübner, A. Neumann: Forming Sheets of Metal and Fibre-reinforced Plastics to Hybrid Parts in One Deep Drawing Process. In *Procedia Engineering, Volume 81*, **2014**, p. 1608-1613.
- [12] B.-A. Behrens, S. Hübner, N. Grbic, M. Micke-Camuz, T. Wehrhane, A. Neumann: Forming and Joining of Carbon-Fiber-Reinforced Thermoplastics and Sheet Metal in One Step. In *Procedia Engineering, Volume 183*, **2017**, p. 227-232.
- [13] J. Gresham, W. Cantwell, M. J. Cardew-Hall, P. Compston, S. Kalyanasundaram: Drawing behaviour of metal-composite sandwich structures. In *Composite Structures, Volume 75, Issues 1-4*, **2006**, p. 305-312.
- [14] M. Hahn, C. Weddeling, N. Ben Khalifa, A. Shabaninejad: Springback Behavior of Carbon-Fiber-Reinforced Plastic Laminates With Metal Cover Layers in V-Die Bending. In *ASME 2016 11th International Manufacturing Science and Engineering Conference*, **2016**.
- [15] H. Wittel, D. Muhs, D. Jannasch, J. Voßiek: Roloff/Matek Maschinenelemente. Normung, Berechnung, Gestaltung. *Springer Fachmedien Wiesbaden*, Wiesbaden, Germany, **2013**.

Combined Curing and Deep Drawing of Fiber Metal Laminates to Spherical Hybrid Components

H. Sapli¹, T. Heggemann¹, W. Homberg¹

¹ Chair of Forming and Machining Technology (LUF), Paderborn University, Warburger Str. 100, 33100 Paderborn

1 Introduction

One of the automotive industry's key priorities is to reduce fuel consumption and hence the CO₂-emissions of future car generations. This is a reaction to rising energy costs and to the increased environmental awareness in society. As a result, the automotive industry is increasingly focusing on lightweight construction [1]. The use of composite materials for car body parts enables considerable weight reductions. One approach is to replace high-density materials such as steel with lighter, low-density, high-strength materials, such as CFRP [2,3]. However, the high material and manufacturing costs make the use of composites in the automotive industry difficult. One promising approach is the combination of CFRP prepregs and high-strength steel alloys, such as Fiber Metal Laminates (FML), which consist of sheet metal cover layers with a CFRP core. FML can be processed by forming processes such as deep drawing and can thus be used to achieve the cost-efficient and automated production of lightweight structures with a high stiffness-to-weight ratio. A further advantage of hybrid components produced in FML is that their mechanical properties can be adjusted via the number and arrangement of the CFRP patches. [4,5]

CFRPs consist of fiber and matrix material and exhibit highly divergent forming behavior. When it comes to the fiber itself, the mechanical properties in the fiber direction are very different from those in the transverse direction [6]. Thermosetting matrix materials have to be cured until they have reached their final strength. The curing process is a function of the prevailing pressure, temperature and time.

Car body parts often have complex shapes, which are usually produced by deep drawing processes. During the deep drawing process, combined tension-tension and tension-pressure stresses are induced in the main forming zone of the component, the flange. Wrinkling of the flange can be observed, which is a consequence of tangential compressive stresses. To avoid this, the blank holder induces normal stresses on the surface of the flange. However, too high a blank holder force FBH can lead to material thinning and thus to fracture. [4,5] Deep drawing of FML sheets can lead to several characteristic defects: if the matrix material is not cured under pressure, the epoxy resin can flow into adjacent zones. This has a negative effect on the form and dimensional accuracy of the deep drawn FML parts. The main deformation mechanisms in terms of the forming behavior of CFRP patches are interlaminar layer slip, displacements in individual layers and cross flow and resin percolation inside the prepreg. [7,8,9] Buckled and torn rovings and also delaminations can thus be observed in the flange area. The drawing depth during the deep drawing of hybrid components has a significant influence on these deformation mechanisms and thus on the form and dimensional accuracy of deep-drawn hybrid components. A greater drawing depth leads to greater fiber displacement and hence to more pronounced wrinkle formation.

Because of this, current research at the LUF is investigating the deep drawability of FML sheets as a function of drawing depth during the deep drawing of spherical hybrid components. Measures are then being developed to improve the form and dimensional accuracy of such hybrid components.

2 Experimental Setup

At the LUF, experiments were designed to examine the forming behavior of FML sheets during the deep drawing process and an approach was then developed for improving the deep drawability of these sheets. The influence of the combined tension-tension and tension-pressure stresses was investigated on spherical specimens with different drawing depths, and the patch geometries of the specimens with an insufficient form and dimensional accuracy were modified. Patch modification enabled the loads acting on the different areas of the semi-finished products to be counteracted more effectively. During the deep-drawing process, the FML sheets are subject to bending stresses by the punch and to normal stresses at the blank holder. Combined tension-pressure stresses also occur in the flange area. These loads result in tangential compressive stresses acting on the semi-finished products.

2.1 Combined Deep Drawing and Curing Process

The experimental investigations were carried out with semi-finished products consisting of two circular metal sheets and three layers of CFRP. The sheet metal blanks in material HCT 490X had a thickness of $s_0 = 0.55$ mm and the CFRP layers of the thermosetting prepreg a thickness of $s_0 = 0.30$ mm, made by SGL Carbon. This prepreg was a unidirectional non-woven composite, pre-impregnated with epoxy resin in a weight proportion of 39 %. According to the manufacturer, the special feature of this thermosetting prepreg is the tough-modified epoxy resin system with highly variable curing conditions (curing temperature $T_C = 90 - 170$ °C, glass transition temperature $T_G = 120$ °C). To prepare the FML sheets, three CFRP layers were chambered with the sheet metal blanks in the form of upper and lower layers. The initial diameters D_0 of the blanks were determined as a function of the required drawing depth. In order to investigate the influence of the drawing depth on the deep drawability of FML sheets, five different drawing depths z were defined and, from these, the required initial diameters D_0 were determined, which are shown in **Table 1**:

Table 1: Defined drawing depth z and determined initial diameter D_0

Drawing Depth z	Initial Diameter D_0
$z_1 = 10$ mm	$D_{0,1} = 100$ mm
$z_2 = 20$ mm	$D_{0,2} = 125$ mm
$z_3 = 30$ mm	$D_{0,3} = 145$ mm
$z_4 = 40$ mm	$D_{0,4} = 160$ mm
$z_5 = 50$ mm	$D_{0,5} = 175$ mm

As shown in **Figure 1**, the active tool elements for the combined forming and curing process consisted of a die, a blank holder and a punch, in which heating cartridges were inserted. In addition, temperature-stable fluoropolymer foils ($s_0 = 12$ μ m) were used, which were placed between the tool elements and the specimen. This film was used to prevent any contamination of the tool elements by escaping resin and to minimize the friction between the tool surface and the specimen.

To avoid differences between the test boundary conditions, active tool elements were adapted for each spherical hybrid component with different drawing depths, which were designed on the basis of two specifications: the drawing depth z and the punch radius $r_P = 50$ mm. The blank holders and the dies were thus dimensioned to fit the punches. The specimens had a thickness of $s_0 = 2$ mm and hence the inner contour of the dies required a radius of $r_D = 52$ mm. The tool elements were inserted in a high-precision pillar guide rack. Finally, the test setup was mounted in a hydraulic press. After the active tool elements had been tempered to the curing temperature of $T_C = 170$ °C, the FML sheets were positioned centrally within the tool setup and the deep drawing process was started. The blank holder applies normal stresses to the specimen, thus suppressing any wrinkling of the flange area due to tangential compressive stresses. After finishing the forming process, the deep-drawn FML sheet remains in the closed tool for the curing time of $t_C = 8$ min. From previous investigations, these curing

conditions ($T_C = 170\text{ }^\circ\text{C}$; $t_C = 8\text{ min}$) had been determined for the CFRP prepreg used as giving optimum curing of the epoxy resin in the matrix material and thus maximum strength of the prepreg.

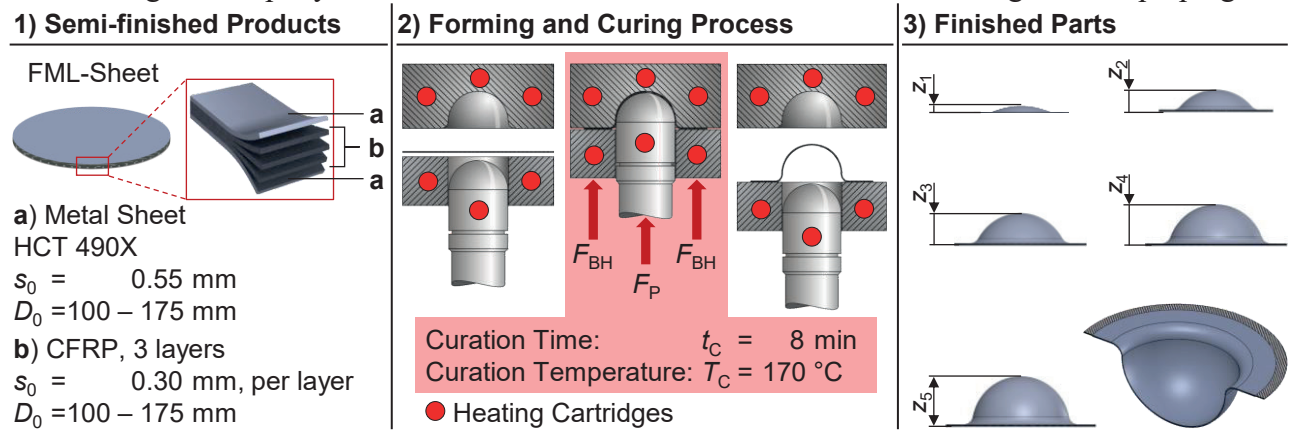


Figure 1: Schematic image of the semi-finished product (1), the combined forming and curing process (2) and the finished parts with different deep depths (3)

2.2 Investigated FML Sheet Designs

To improve the deep drawability of FML sheets, the prepreg geometries and composition were adapted to the load situation that develops due to the tangential compressive stresses which lead to material displacement in the semi-finished products during the deep drawing process. The CFRP core of the investigated FML sheets is thus composed of 3 layers with a $0^\circ/45^\circ/90^\circ$ fiber direction. This design leads to an asymmetrical layer structure and results from given boundary conditions. In order to better counteract the tensions that develop between the cover sheets, CFRP patches of different geometries (length, width and contour) were placed in different positions, as shown in **Figure 2**. The modification was carried out consistently for the differently sized specimens with the aid of four factors so as to permit a comparison of the results. The factors are dependent on the initial diameter D_0 .

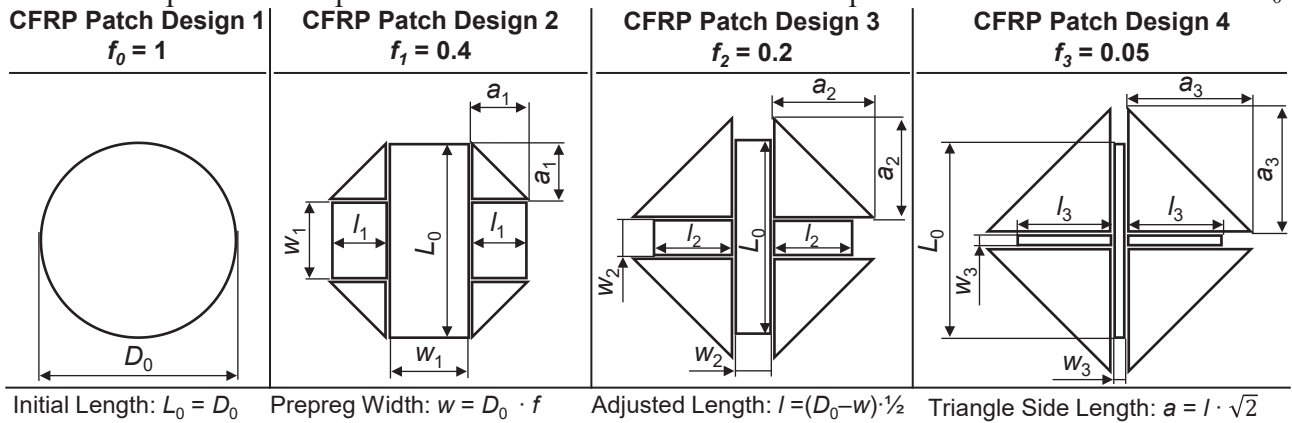


Figure 2: Schematic image of the geometry of the patch designs

Four different FML sheet designs with different patch modifications were investigated. While Design 1 has a unidirectional fiber orientation, the other Designs are assembled with rectangular and triangular patches so that the fibers of these patches are oriented to the “feed direction” of the FML sheet. The result is a radial arrangement and hence improved mobility of the fibers. The rectangular patches have the same width w , but differ in length by the initial length L_0 and the adjusted length l . The reason for this is that the use of the continuous initial length L_0 to all rectangular patches would lead to an overlap and thus to an irregularity in the thickness of the patches. On the contrary, using the adjusted length l to all rectangular patches would result in a further square patch in the middle of the structure, so that a total of five cuts would be used instead of three. However, this would lead to further gaps between the patches, so a combination of continuous and discontinuous rectangular

patches was used. The selected fiber orientation in combination with the radial fiber arrangement, it proved possible to achieve optimal absorption of the tangential compressive stresses acting during the deep drawing process. The structure of the FML Sheet Designs is illustrated in **Figure 3**. The bonding of the individual sheets was realized by the pre-impregnated epoxy resin of the prepregs.

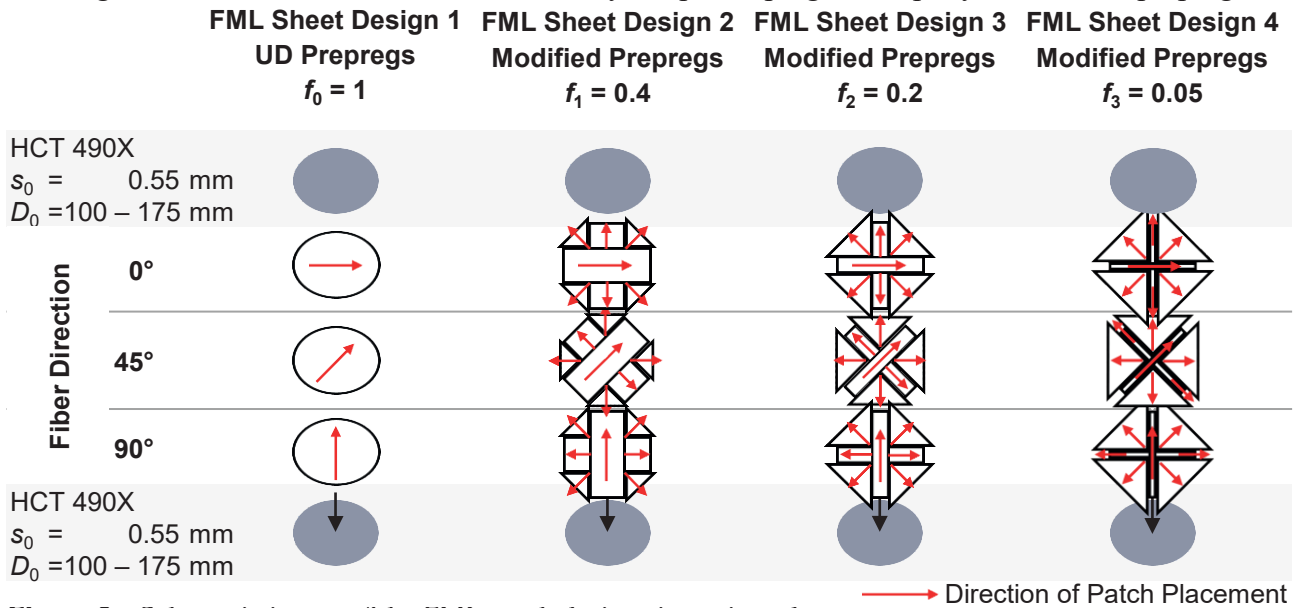


Figure 3: Schematic image of the FML patch designs investigated

This approach was used to investigate both the influence of the drawing depth z and the effects of the designs on the forming behavior of FML sheets. The analysis of the form and dimensional accuracy of the spherical hybrid components resulting from these test series was performed in two steps. On the one hand, the roundness of the inner contour of the hybrid components was measured with a coordinate measuring machine over defined height distances, thus revealing the roundness deviation. On the other hand, the samples were then CNC-milled step by step over the height distances, and the pleat thicknesses were scanned over the CFRP wall thickness curve using a light microscope.

3 Results

To investigate the influence of drawing depth and prepreg geometry on the form and dimensional accuracy of spherical hybrid components, FML sheets of different sizes for four different prepreg designs were deep drawn. For this purpose, the roundness of the inner contour and the CFRP wall thickness distribution of the specimens was measured over defined measuring depths z_{md} . The specimens with a roundness deviation below the tolerance of $R_{dev} < 0.2$ mm and without failure characteristics were defined as components without improvement potential in respect of their form and dimensional accuracy. The measurements were carried out over defined measuring depths, the number of which was dependent on the size of the drawing depth z . The starting measuring depth $z_{md} = 0$ mm was located in the feed zone from the top of the flange.

Figure 4 shows the roundness deviations at the measuring depth $z_{md} = 0$ mm of deep-drawn FML sheets with Design 1 (UD prepregs) and illustrates the influence of the drawing depth on the form accuracy of spherical components. A significant increase is seen in the roundness deviation R_{dev} analogous to the drawing depth z . The specimens with the drawing depths $z_1 = 10$ mm or $z_2 = 20$ mm have approximately the same roundness deviation $R_{dev} = 0.18$ mm. The roundness deviations of these specimens are thus below the tolerance line. These results show a very high form accuracy in the specimens and correspond to the optical inspection. A further increase in the drawing depth leads to significant growth in the roundness deviation and thus to decreasing form accuracy. The roundness

deviation increases with a drawing depth of $z_3 = 30$ mm to $R_{dev} = 0.91$ mm, with $z_4 = 40$ mm to $R_{dev} = 1.05$ mm and with a drawing depth of $z_5 = 50$ mm to a roundness deviation of $R_{dev} = 2$ mm.

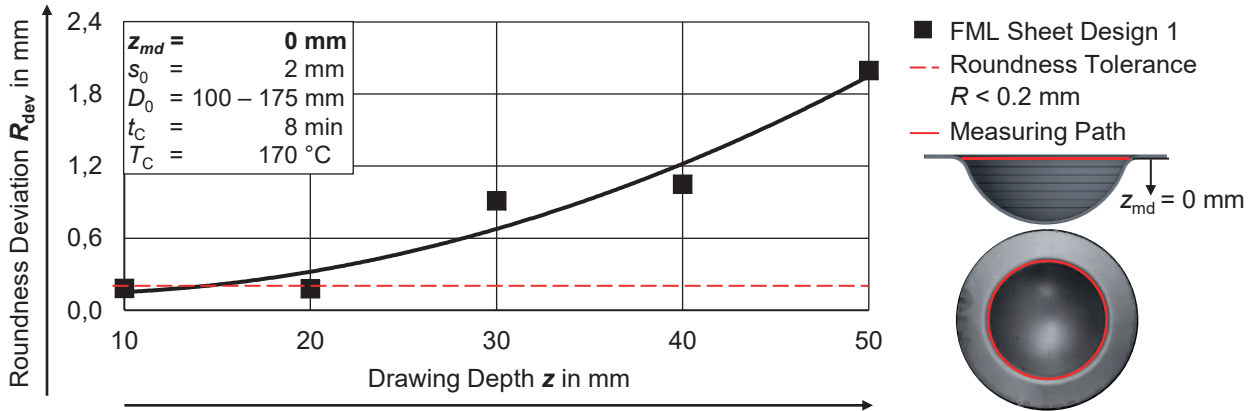


Figure 4: Roundness Deviation R_{dev} of the spherical specimens as a function of the drawing depth z

These results show too high a roundness deviation and hence too low a form accuracy for the specimens with drawing depths of between $z = 30 - 50$ mm. For this reason, the FML sheets of these spherical specimens were modified in order to improve their form and dimensional accuracy. To illustrate the influence of the patch modification on the formation of wrinkles, section views of the spherical specimens were taken over defined heights. These section views were used to determine the CFRP wall thickness distribution curve. A test of the metal blank wall thickness showed only a marginal change and can therefore be neglected. Due to the rotational symmetry, only a quarter of the wall thickness curve was recorded and analyzed. The CFRP thicknesses are given as average values, which represent the mean value of the total CFRP wall thickness distribution per measuring depth z_{md} .

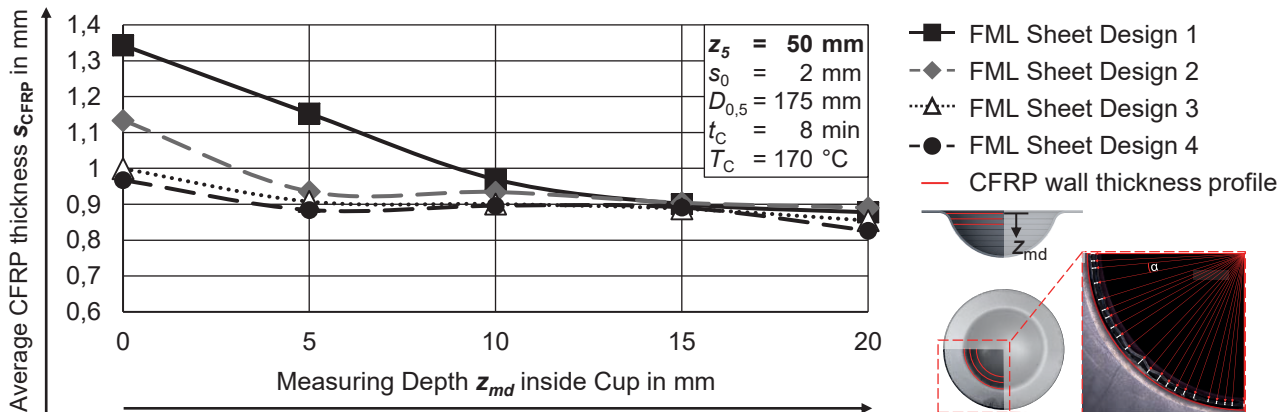


Figure 5: Average CFRP thickness of spherical specimens as a function of the FML sheet designs

Figure 5 illustrates the effects of the scrim modification of the preregs on the average CFRP thickness of the specimens as a function of the drawing depth $z_5 = 50$ mm. It can be clearly seen from the measuring depth $z_{md} = 0$ mm that the modification has led to a reduction of the average CFRP thickness from $s_{CFRP} = 1.34$ mm (FML Sheet Design 1 with UD layers) to $s_{CFRP} = 1.13$ mm (Design 2), $s_{CFRP} = 1$ mm (Design 3) and $s_{CFRP} = 0.96$ mm (Design 4). This also shows that increasingly large triangular cuttings (largest: Design 4) lead to a decrease in wrinkling. In the further course of the measuring depth, a decrease in the average CFRP thickness s_{CFRP} can be observed until the curves at the measuring depth $z_{md} = 15$ mm with an average CFRP thickness of $s_{CFRP} = 0.9$ mm almost bundle up. In addition, the effect of prepreg modification can be determined in the total reduction in CFRP thickness for all the FML Sheet Designs. On the one hand, the average CFRP thickness of Design 1 is reduced from $s_{CFRP} = 1.34$ mm to $s_{CFRP} = 0.87$ mm over the entire process. On the other hand, the progression of Design 4 is more constant, by comparison, as the CFRP thickness is reduced from only $s_{CFRP} = 0.96$ mm to $s_{CFRP} = 0.82$ mm, thus achieving a more stabilized deep drawing process.

4 Conclusion

In this study, experimental research was conducted into the development of a process and material design for the production of spherical hybrid components made of FML sheets. The main focus of these investigations was to determine the influence of the drawing depth and the modification of the patch geometry on the roundness of the inner contour and the wall thickness distribution of the deep-drawn spherical hybrid components. The aim of this investigation was to improve the form and dimensional accuracy of FML components produced by a combined forming and curing process.

Spherical hybrid components with drawing depths of $z_1 = 10$ mm and $z_2 = 20$ mm were produced without wrinkles. However, the hybrid components with drawing depths between $z_3 = 30$ mm and $z_5 = 50$ mm showed an increased formation of wrinkles in the inner contour. Wrinkle formation is the result of material displacement due to tangential compressive stresses during the forming process. The influence of the patch modifications performed correlates directly with the radial arrangement of the fibers. An increasingly small factor, as in FML Sheet Design 4 with $f_4 = 0.05$, leads to narrower laminate widths and larger triangular cuts. This significantly extends the radial fiber arrangement of the prepregs compared to FML Sheet Design 2 with the factor $f_1 = 0.4$. As a result, the semi-finished products are much better able to counteract the tangential compressive stresses that act during the deep-drawing process, resulting in a significant reduction in wrinkling and thus a significant improvement in the form and dimensional accuracy of spherical hybrid components.

5 Acknowledgements

The authors gratefully acknowledge the financial support from the European Regional Development Fund (ERDF) and the state of North Rhine-Westphalia (NRW).

6 References

- [1] Klein, B.: *Leichtbau-Konstruktion. Berechnungsgrundlagen & Gestaltung*. Vieweg-Verlag, **2007**.
- [2] W. Eversheim, K. Erkes, K. Kirberg, "Bewertung alternativer Fertigungslinien für Kfz-Pleuel – CFK-Verbund als Stahlsubstitution bietet Vorteile" in *Industrie-Anzeiger / Spezial, product report*, **1986**, Vol. 108.
- [3] D. Lutz, "Chassis lightweight design exemplified on a suspension strut – State of the art and potential" in *11. Aachen Colloquium Automobile and Engine Technology*, **2002**.
- [4] Johnsin, W., Mellor, P. B.: *Engineering Plasticity*, Vand Nostrand Reinhold, **1973**.
- [5] Doege, E., Behrens, B.-A.: *Handbuch Umformtechnik*, Springer-Verlag **2007**.
- [6] Spickenheuer, A: *Zur fertigungsgerechten Auslegung von Faser-Kunststoff-Verbundbauteilen für den extremen Leichtbau auf Basis des variabelaxialen Fadenablageverfahrens Tailored Fiber Placement*. Dissertation, TU Dresden, **2013**.
- [7] McEntee S.P.: Large Deformation finite element modelling of single-curvature composite sheet forming with tool contact. In *Composites Part A: Applied Science and Manufacturing*, **1998**.
- [8] Wang P., Hamila N., Boisse P.: Thermoforming simulation of multilayer composites with continuous fibres and thermoplastic matrix. In *Composites: Part B* **52**, **2013**.
- [9] Böhler P., Härtel F.: Identification of forming limits for unidirectional carbon textiles in reality and mesoscopic simulation, *Key Engineering Materials*, **2013**, Vol. 554-557, p. 423-432.

Hybridization for series production - continuous profile production by pultrusion

D. Löpitz¹, M. Knobloch¹, D. Wagner¹, W.-G. Drossel¹, M. Gedan-Smolka², K. Schubert², A. Marschner²

¹ Fraunhofer Institute for Machine Tools and Forming Technology IWU, Chemnitz

² Leibniz-Institut für Polymerforschung Dresden e.V. (IPF), Dresden

0 Abstract

An important factor for the success of electromobility is lightweight design - the lower the mass of a vehicle, the less energy is required for acceleration and movement, and the smaller, lighter and cheaper battery and drive technology can be designed. In close cooperation with partners from science and industry, the Fraunhofer Institute for Machine Tools and Forming Technology (IWU) develops solutions suitable for series production for a sustainable German automotive industry. Lightweight design in economical hybrid design is the focus of numerous development projects. In the research project "Hybrid Pultrusion", the research partners Fraunhofer IWU and the Leibniz-Institut für Polymerforschung Dresden e.V. (IPF) develop new methods for the reliable and reproducible production of hybrid components made of metal and fiber-reinforced plastics (FRP) by using the pultrusion process. A central focus in this project is the bonding mechanism between metal and FRP at the molecular level and the transfer of these phenomena to the pultrusion process.

1 Introduction

Hybrid materials are able to increase the potential of lightweight design of countless applications and thus make an essential contribution to energy-efficient, resource-saving and CO₂-minimized mobility [1]. However, the combination of two classes of materials (e.g. metal and FRP) to create a hybrid material is a major challenge for engineers, especially for the use of hybrid materials in large-scale production like automotive industry and transportation. The main disadvantages for series production are insufficient joining qualities, time- and cost-intensive pre- or post-treatment processes, long cycle times or the insufficient fatigue strength at changing climate conditions. Due to the different thermo-mechanical properties of metal and FRP, an excellent adhesion strength at the interface is necessary [2]. Gluing is one of the few processes that has been established on a large-scale production for joining FRP with metals in such a way that high safety standards can be maintained with regard to the fatigue strength in automotive applications [3, 4]. Gluing is a process of applying a nonmetallic material between two parts to create a material bonded through adhesion and internal strength [5]. As needed pre-treatment, application and curing of the glue are usually associated with additional time and costs, current research has a significant claim to reduce or even to avoid the use of glue by appropriate methods. The difficulties in joining metals and FRP without using glue are mainly caused by large differences in the thermal expansion coefficients and a poor molecular adhesion of both materials. In order to achieve a high molecular adhesion between metal and FRP, current research shows promising concepts and results. For example, adhesion promoter layers can be used, which take over the role of the glue in the hybrid composite and allow significantly faster cycle times [6].

The surface functionalization of the metallic joining partner, for example, offers a further innovative solution for completely dispensing with an adhesion promoter. By applying a microstructure with a laser, the surface is enlarged in such a way that the liquid thermoplastic matrix enters the undercut microstructure during the joining process and becomes firmly attached to it [7]. Other recently studied pretreatment methods deal with plasma pretreatment on the bonding surface [8, 9]. For the production of metal-FRP-hybrid components with thermoset matrix, approaches with functional powder coatings are particularly promising. As thermosetting reaction resins are initially in liquid form, the chemical processes taking place during curing can be used for the joining process without the need of further processing steps [2]. For the use of polyurethanes, it has already been demonstrated that reactive groups of the polymer forms a solid covalent bond with the powder coating [10, 11].

The objective of the research project "Hybrid Pultrusion" is to modify the powder coating for a covalent bonding to epoxy resins, which are used as standard thermoset for the pultrusion process. Those powder-precoated metals are added to the pultrusion process and their adhesion is tested.

2 Materials and methods

In the following, the examined materials are described, which are used in this project. Furthermore, the methods and processes used to manufacture hybrid specimen are presented.

2.1 Materials and Pretreatments

2.1.1 Components of the fiber-reinforced plastics

For the trials, materials are used as they are usually applied in the pultrusion process. The fiber material is a glass fiber roving of the type PulStrand4100 with 4,800 tex from the manufacturer Owens Corning. Table 1 shows the components of the anhydride epoxy resin system.

Tab. 1: Resin system

Component	Component name	Supplier
Resin	Araldite LY 3585 CH	Huntsman
Curing agent	Aradur 917-1 CH	Huntsman
Catalyst	Accelerator DY080	Huntsman
Internal Mold Release	IC25	ChemTrend
Filler	ASP 600 (0,6 μm)	BASF

2.1.2 Metallic component and powder coating

As the basic metallic component a cold rolled unalloyed steel sheet of the quality DC01/S235JR has been selected. The steel sheet is sandblasted with aluminum oxide (high class corundum) and pretreated with zinc phosphate leading to a fine crystalline layer. The metal gets a good corrosion protection. As previous investigations have shown this treatment is also necessary in order to achieve the highest possible adhesion in the later hybrid structure [11]. The powder coating materials consist of a two-step curable powder coating based on commercially available uretdione (internally blocked isocyanates) cross linkers, OH-functionalized polyester resins and a specific catalyst system which was developed at the IPF in the past. The curing mechanism is shown in figure 1. The primary focus

of the coating formulation is the variation of the OH-group number of the polymer resins to investigate their influence on the adhesive strength to the epoxy-matrix of the joint. Additionally, the post formability of the coating system, as well as the surface appearance should be maintained at a high level.

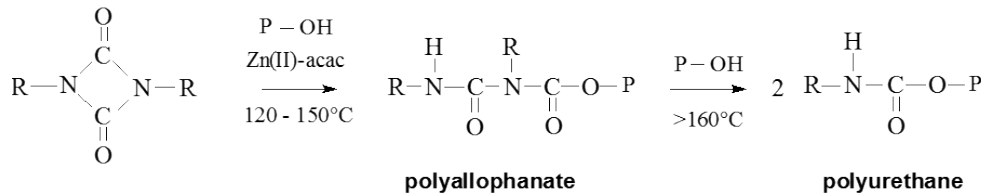


Fig. 1: Two step curing mechanism of the used uretdione powder-coating

The powder coating is applied to the metal sheets in the form of dry powder by using corona discharge. This technology uses a spray gun with an integrated high voltage cascade which charges an electrode and the powder and also generate an electric field between the gun and the grounded steel sheet. The powder particles moves along this field lines to the metal sheet. At last the powder coated sheets are cured at temperatures of 150 °C. This process step completes the first reaction step of the powder coating material resulting in a polyallophanate network and simultaneously creates a strong bonding to the metal.

2.2 Manufacturing processes

For the basic tests in the laboratory, the manufacturing process Resin Transfer Molding (RTM) was used which is a process for the manufacturing of long or continuous fiber reinforced components. It is particularly suitable for the fabrication of small series with manageable equipment. A RTM tool usually consists of an upper and a lower tool, between which dry, pre-assembled glass fiber layers are placed. After closing the tool, the cavity is pre-heated, evacuated and then the thermosetting resin is injected. Afterwards, the resin cures in the completely filled cavity to a FRP component [12].

The pultrusion process, which is focused for the later application, is one of the few manufacturing processes for continuous fiber-reinforced plastic profiles that is suitable for large-scale production. Figure 1 shows the basic features of the process: Semi-finished fiber products (1) are pulled from bobbins by alternately moving pulling devices (4) and pass through a resin bath (2). Afterwards, the impregnated fibers are pulled through a heated die (3), in which the liquid thermoset plastic cures completely within seconds. A saw (5) cuts the profiles to the desired length [13].

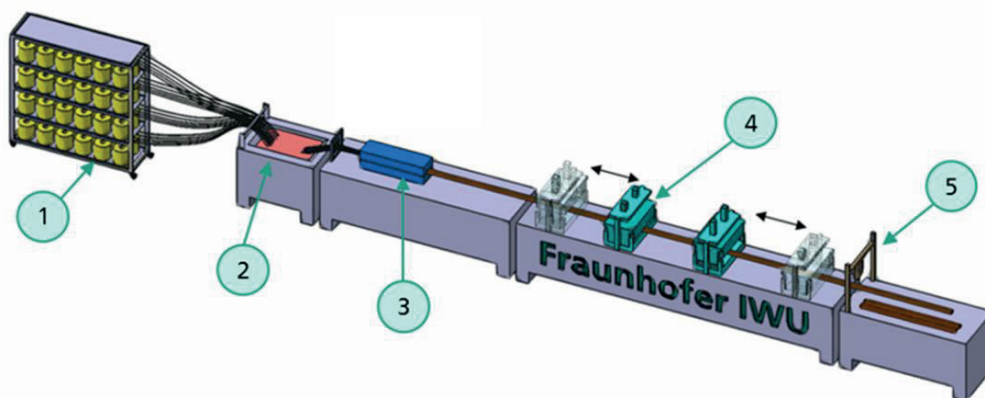


Fig 2: Pultrusion line

3 Specimen manufacturing

The test specimens were first manufactured under laboratory conditions at the Leibniz IPF in order to identify general process and material parameters. Subsequently, the results of the laboratory tests were adapted to the pultrusion process at the Fraunhofer IWU.

3.1 Manufacturing of laboratory specimen by RTM

For the variation of materials and process conditions, test plates with a total thickness of 4 mm were produced in extensive laboratory tests. For this, the pre-treated, powder coated metal and the glass fiber fabrics are placed in a RTM tool. Afterwards the tool is closed, evacuated and the resin system is injected. A pressure pot was used for this purpose by filling in the previously mixed resin system. Deviating from the recipe in table 1, the ASP600 filling material was not used due to the incompatibility with the used RTM technology. After consulting the manufacturer, however, this should not have any influence on the process behavior. Only in the pultrusion process it is not recommended to run the process without ASP600 due to the process control. After a curing cycle for 90 minutes at 90 °C, the hybrid structure was demolded and the specimens were cut out of the hybrid plate. For some specimens a subsequent thermal treatment was carried out at 160 °C for 2 hours with the aim of a further enhancement of the interlayer bonding between the powder coating layer and the epoxy matrix.

3.2 Manufacturing of specimen by pultrusion

In order to be able to produce hybrid test specimens by pultrusion, researchers of the Fraunhofer IWU have developed suitable delivery solutions for the metallic component. For manufacturing representative test specimens, it is necessary that the powder coated metallic sheets can be supplied into the process exactly in the direction of the fibers and that slippage of these is avoided. As the metallic semi-finished products coated by Leibniz IPF have a maximum length of 475 mm, a supply system was developed as shown in figure 3. Metal sheets with an optimized powder coating were used for the trials on the pultrusion line. As reference, some sheet metals without coating were also pultruded to hybrid specimens.

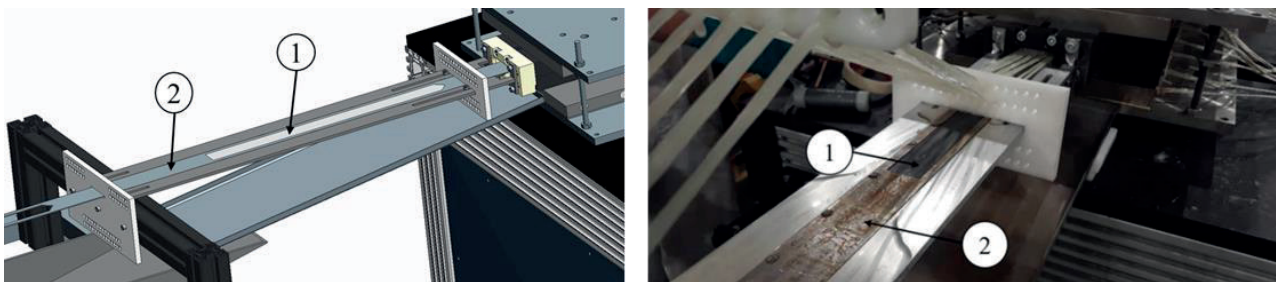


Fig. 3: Supply system for the metallic component (① – coated metal sheet; ② – delivery sheet)

In order to avoid skips in fiber volume content (FVC) during the pultrusion process, the metallic component must be supplied continuously, as every change of the FVC results in differences in the curing behavior of the resin system and associates problems such as cracks or material deposits. This is ensured by means of a metal sheet (see figure 3, ②) which is fed into the die during the entire process. The metal sheet has cut-outs at defined intervals into which the coated sheets (see figure 3, ①) are inserted. Due to the high thermal capacity of the added metallic sheet, it is necessary to

adjust the process parameters to ensure the curing of the epoxy resin as well as to make sure that the reactive groups of the resin can react with the powder coated metal to form a strong bond.

Table 2 shows the adjusted process parameters of the standard FRP-pultrusion and the hybrid pultrusion with FRP and metal. Best results for hybrid pultrusion could be achieved by increasing the temperature in heating zone 2 and reducing the process speed to one third.

Tab. 2: Process parameters

Parameter	Value standard pultrusion	Value hybrid pultrusion
Length of die [mm]	1000	1000
Number of heating zones [-]	5	5
Process speed [mm/min]	600	200
Temperatures in heating zone 1-5 [°C]	150-150-190-190-190	150-190-190-190-190

4 Tests, results and discussion

4.1 Optical and non-destructive analysis of the complete composite system

Figure 4 shows microscopic images of grinding patterns of the hybrid specimens manufactured by pultrusion. The left picture shows a direct bonding of metal to powder coating and powder coating to FRP. The right picture shows a hybrid specimen without powder coating. It can be clearly seen that there is no connection between metal and FRP as embedding material has deposited in the space between the two materials.

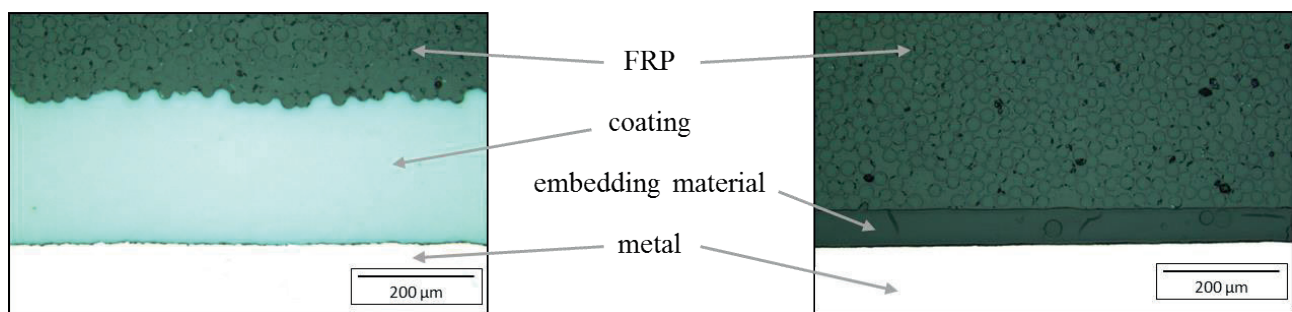


Fig. 4: Microscopic images of boundary layers (left: hybrids with powder coating; right: hybrids without powder coating)

4.2 Specimen preparation and lap shear test

To determine the bond strength, a lap shear test was carried out in accordance to DIN 65148 [14]. For this purpose, the hybrid parts manufactured by RTM and pultrusion were cut to standardized tensile test specimen (dimension 250 mm x 25 mm x 4 mm) on a water-cooled separating device. Then, two notches are put into the test specimen, resulting in the shearing area of 25 mm x 12.5 mm recommended in DIN 65148. The standard prescribes the use of a supporting device to prevent deformation in the shear zone. Figure 5 shows the final specimen for the lap shear test.

The standard prescribes a path-regulated test in which failure occurs within one minute after start. In a preliminary test with a test specimen, in which average adhesion values are expected, the test speed is set at 0.2 mm/min.

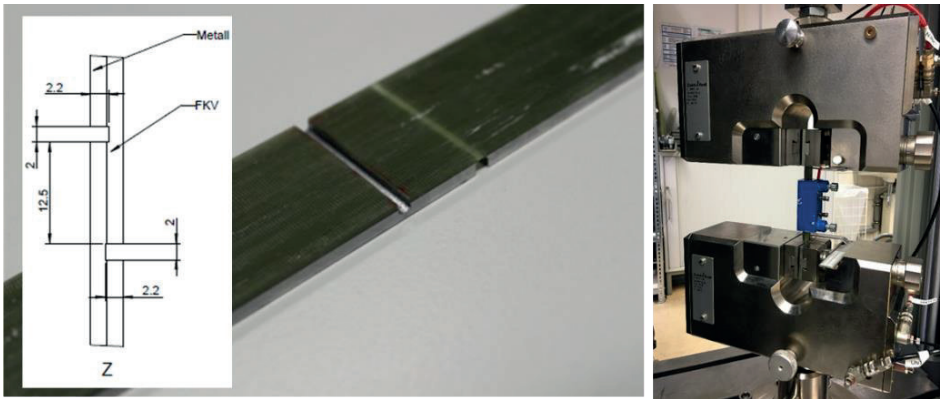


Fig. 5: Specimen preparation and geometry (left); lap shear test with supporting device (right)

4.3 Results of the lap shear test and discussion

Figure 6 shows the results of the lap shear tests of the RTM and pultruded specimens with the optimized powder coating before and after tempering. In each test series at least 6 specimens were tested.

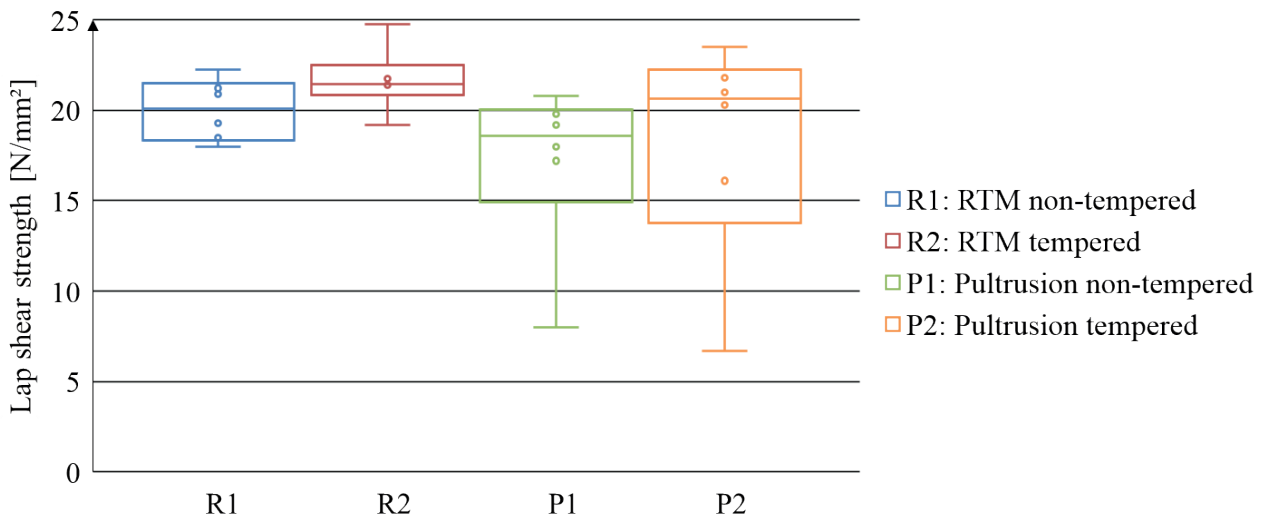


Fig. 6: Results of the lap shear test

As expected, the tempered specimens R2 and P2 show a slightly higher trend for the average lap shear strength than the non-tempered ones (R1 and P1). It is assumed that additional covalent bonds are formed by diffusion during the thermal treatment together with the relaxation of internal stress which resulted from the uneven cooling down after the fabrication in the RTM tool. The trend for the average lap shear strength of the specimens R1 and R2, which were manufactured under laboratory conditions by RTM, is slightly higher than those (P1 and P2) manufactured by pultrusion. The reason for this could be the much faster production speed of the pultrusion process. Due to the rapid heating, curing and cooling, there is a different shrinkage behavior of metal and FRP, resulting in stresses in the boundary layer. These stresses, together with a constant tensile stress on the glass fibers, prevent an optimum bond between metal and FRP. The residual stresses that form in the boundary layer of specimens P1 and P2 result in significantly higher standard deviations of the lap shear strength compared to specimens R1 and R2.

Due to the large standard deviation of the pultruded specimens, no clear statement can be made at this time about the comparison of laboratory and pultrusion specimens. Further investigations with a larger number of samples are planned in order to prove the trend shown in figure 6 with statistical certainty.

5 Conclusions and Outlook

The results of the tests indicate that powder coating has a high potential for the manufacturing of hybrid components made of metal and FRP. It has also been shown that the laboratory results can be transferred to the pultrusion process without any significant deterioration of the lap shear strength.

The current limit of the hybrid pultrusion process is, that only strips with a maximum length of 475 mm could be coated. For a series process, the coating technology must be upscaled so that metallic, coated components can be supplied endlessly from a coil to the pultrusion process. Depending on profile cross section the pultrusion process is only economical at production speeds of more than 500 mm/min. The project aims to significantly increase the pultrusion speed of currently 200 mm/min by optimizing process parameters without reducing the bond strength.

The next objective of the project is to prove that the results of simple strip specimens can be transferred to more complex components. It is planned to pultrude a side sill for an automobile, which is reinforced at certain points by powder coated metallic inserts. This hybrid sill is then to demonstrate its improved energy absorption capacity in crash tests.

6 Acknowledgement

This work was conducted within the project “Hybrid Pultrusion“, which was funded by the Sächsisches Staatsministerium für Wissenschaft, Kultur und Tourismus (SMWK).



Diese Maßnahme wird mitfinanziert durch Steuermittel auf Grundlage des von den Abgeordneten des Sächsischen Landtags beschlossenen Haushaltes.

7 Literature

- [1] Vogt, M., Malanoski, N., Glitz, R. u. Stahl-Rolf, S.: Bestandsaufnahme Leichtbau in Deutschland. Projekt IC 4 (2015), S. 10–15
- [2] Scheik, S., Schleser, M. u. Reisingen, U.: Thermisches Direktfügen von Metall und Kunststoff– Eine Alternative zur Klebtechnik? In: Leichtbau-Technologien im Automobilbau. Springer 2014, S. 89–94
- [3] Habenicht, G.: Kleben. Grundlagen, Technologien, Anwendungen. VDI-Buch. 2006
- [4] Brockmann, W., Dorn, L. u. Käufer, H.: Kleben von Kunststoff mit Metall. Berlin, Heidelberg, New York, London, Paris, Tokyo, Hong Kong: Springer 1989
- [5] DIN EN 923:2016-03, Klebstoffe_ - Benennungen und Definitionen; Deutsche Fassung EN_923:2015
- [6] Haider, D., Krahl, M., Koshukow, W., Wolf, M., Liebsch, A., Kupfer, R. u. Gude, M.: Adhesion Studies of Thermoplastic Fibre-plastic Composite Hybrid Components Part 2: Thermoplastic-metal-composites (2018)

- [7] Gebauer, J., Fischer, M., Lasagni, A. F., Kühnert, I. u. Klotzbach, A.: Laser structured surfaces for metal-plastic hybrid joined by injection molding. *Journal of Laser Applications* 30 (2018) 3, S. 32021
- [8] Gallant, D. u. Savard, V.: New Adhesive Bonding Surface Treatment Technologies for Lightweight Aluminum-Polypropylene Hybrid Joints in Semi-Structural Applications. *SAE International Journal of Materials and Manufacturing* 4 (2011) 1, S. 314–327
- [9] Hopmann, C., Wunderle, J., Neuß, A., Ochotta, P., Bobzin, K. u. Schulz, C.: Influence of surface treatment on the bond strength of plastics/metal hybrids. *Zeitschrift Kunststofftechnik* 1 (2015), S. 227–255
- [10] Kühnert, I., Gedan-Smolka, M., Fischer, M., Scholz, P., Landgrebe, D. u. Garray, D.: Prefinished metal polymer hybrid parts. *Technol Lightweight Struct* 1 (2017) 2, S. 89–97
- [11] Gedan-Smolka, M., Lehmann, F. u. Lehmann, D. (Hrsg.): *Catalysis in uretdione powder coatings enables innovative processing lines*. AMER CHEMICAL SOC 1155 16TH ST, NW, WASHINGTON, DC 20036 USA 2003
- [12] Hopmann, C. u. Michaeli, W.: *Einführung in die Kunststoffverarbeitung*. München: Hanser 2017
- [13] Starr, T. F. (H.): *Pultrusion for engineers*. Woodhead Publishing Series in Composites Science and Engineering. Boca Raton, FL: CRC Press 2000
- [14] DIN 65148:1986-11, Luft- und Raumfahrt; Prüfung von faserverstärkten Kunststoffen; Bestimmung der interlaminaren Scherfestigkeit im Zugversuch

Process analysis of thermoplastic-metal composite structures in 3D-Hybrid technology - A combined approach to quality assurance for robust manufacturing processes

D. R. Haider¹, M. v. Unold¹, M. Krahl¹, M. Gude¹

¹Technische Universität Dresden, Institute of Lightweight Engineering and Polymer Technology, Dresden

1 Introduction

Thermoplastic composites with metallic structures in a combined thermoforming and injection moulding process offers new possibilities for lightweight structures. Especially intrinsic joining in a one-shot manufacturing process opens up new possibilities using purposefully the specific properties of the different materials in an integral lightweight design (fig. 1). The potential of the 3D-Hybrid technology is demonstrated in several preliminary projects [1, 2]. One result is a significant reduction in mass with the same performance of the structural components.

For an industrial application, an intrinsic process brings a lot of challenges regarding the quality assurance of the parts. One important aspect is that the combination of several process steps in a one-shot process increases the complexity through the multitude of adjustable and interacting process parameters. The interactions of the process and disturbance parameters on the component properties are partly unknown for complex hybrid structures. Novel methods that allow early analysis and determination of significant process and quality parameters are therefore an essential basis for the efficient development of economical manufacturing processes [1, 3]. For the injection moulding process itself, 125 quality-relevant parameters for injection moulding have been identified by a VDI consortium [4]. For the complete intrinsic process of the 3D-Hybrid technology, the parameters from sheet metal forming, thermoforming and the joining process must also be added, but some of these have not yet been identified. This leads to time-consuming inter-operation loops in running-in processes and to incomplete quality assurance of the key parameters for new products.

In this study, a generic structure made of thermoplastic fibre composites sheets (TPC) combined with injection moulding compound (IMC) ribs is investigated (fig. 1). In a first step, a pre-analysis describes the robustness of the entire process chain related to the target parameters. To identify the process, disturbance and target parameters a combination of standard methods from data mining as well as from process and product optimization were applied. The data collection is based on a design of experiments. In a second step a parallel analysis with classical methods from statistical design of experiments and approaches of machine learning was compared.

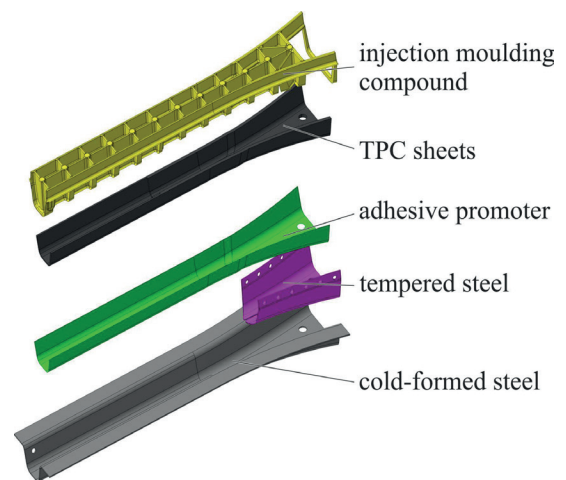


Fig. 1: Generic structure in 3D-Hybrid design.

2 Methodological approach

Several tools for quality assurance have become established as standard in the industry. The Six Sigma method defines, among other things, a procedure for process analysis and optimization using statistical methods such as statistical process control (SPC). In [5] common methods such as online process monitoring, online quality monitoring, quality control, quality optimization and expert systems for quality assurance are presented for plastic injection moulding. In this case, empirical models are usually developed to describe the correlation between process data and part properties. Generally, classical statistics and various methods of artificial intelligence are used for modelling. In the past years, different process models were investigated for injection moulding and implemented to an adaptive process control in the injection moulding machines to counteract disturbing influences in the process [6]. Such systems are not yet established in the field of hybrid composite parts.

The use of data mining methods in the field of fibre-reinforced plastics is mainly known in the application areas of mechanical and optical testing methods and simulation [7]. In the following, the potential of data mining methods in quality assurance is shown. First of all, the methodological approach is discussed and these are set in relation to established methods such as the Six Sigma strategy (fig. 2). Data mining describes a collection of techniques, methods and algorithms for the analysis of data. Data mining can refer both to the entire process of obtaining knowledge from data and specifically to the sub-step of pattern recognition or model building [8]. The KDD model (Knowledge Discovery in Databases) represents the basic procedure of a data mining process. The model begins on the basis of the raw data containing the knowledge to be gained and ends with the evaluation of the correlations [9]. But there is a lack of systematic consideration of the process, the selection of measured variables and data acquisition. Additionally, there is no evaluation of the analysis process. The CRISP-DM model (Cross-industry standard process for data mining) represents a procedure with the aim of standardizing the process and its integration into industrial process structures [8]. The model also assumes that the raw data are taken for granted. The data collection step is not taken into account.

Both the KDD model and the CRISP-DM model assume that the raw data are given. At the beginning of many analysis and optimization tasks, data sets are not yet available. Therefore, this procedure is extended with the methods from the Six Sigma strategy. The Six Sigma strategy structures the procedure for process and production optimization and is state of the art for analysis of manufacturing processes. Furthermore, data collection using statistical methods and experimental designs is a sub-step of the Six Sigma strategy.

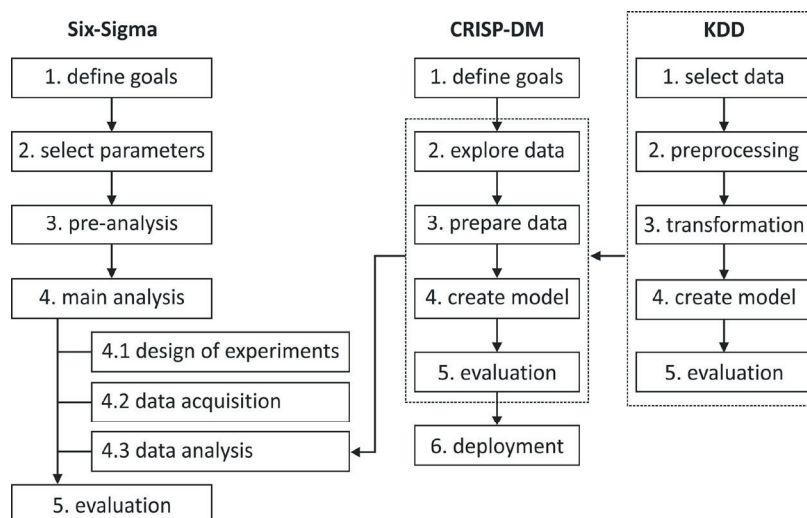


Fig. 2: Integration of the workflow models.

3 Experimental investigation

3.1 Material, process and data setup

The thermoplastic fibre composites sheet material Bond Laminates Tepex dynalite 102 RGUD600 (fabric, 80 % of glass fibres in 0 °-direction, 20 % in 90 °-direction) and the short glass fibre reinforced injection moulding compound from LANXESS PA66 GF30 (Durethan AKV30) were selected for the material combination. Both materials have a polyamide 66 matrix system. Further investigations were carried out without the combination with steel and adhesion promoter, since a preliminary analysis showed that the scattering from the maximum bond strength is higher due to unknown disturbance parameters [10]. The semi-finished TPC sheets are cut by waterjet cutting. The materials are dried at 80 °C for at least six hours before processing. The experimental setup of the process chain with the several selected process steps is illustrated in fig. 3. The main process steps are heating, transfer and thermoforming of the TPC sheet. The process steps thermoforming and injection moulding take place immediately after each other with mould closed. The tests were carried out with the following setting parameters: heating temperature TPC sheet of 310 °C, injection molding-melt temperature of 285 °C, holding pressure of 500 bar (10 s), injection velocity of 23 mm/s, mould temperature of 130 °C, temperature support tooling hot runner (between nozzle and mould) of 295 °C and cooling time of 40 s.

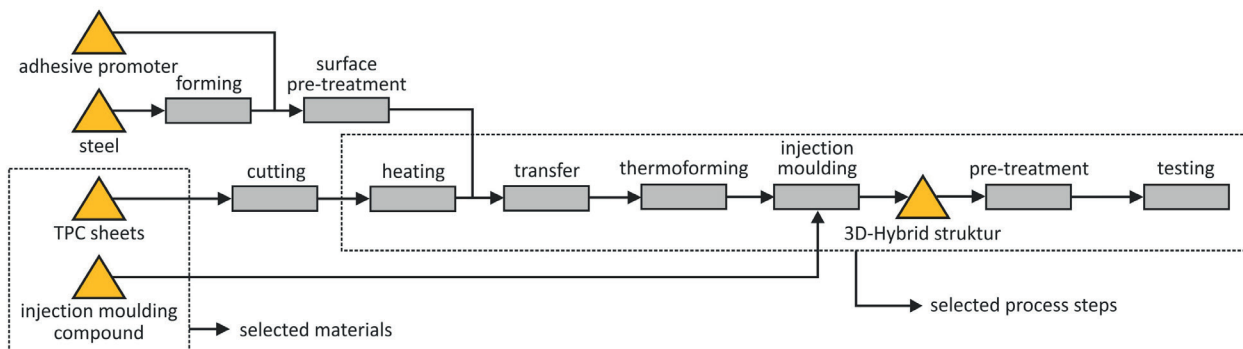


Fig. 3: Process chain model for the intrinsic joining (relevant steps for this investigation is marked with dashed boxes).

A large number of sensors were integrated in the process chain and an automated data handling system was set up to record the process parameters [3]. The data are handled in a fixed, tabular structure. Known disturbance parameters from the steps of component production, conditioning and testing were identified to further investigate or exclude their influence on the target parameters. The disturbance parameters are: deposit position of the semi-finished product in the tool, ambient temperature and humidity during test specimen production, water absorption/time/position during storage in climate chamber and water absorption/time in standard climate. The mechanical parameters are determined from the force-displacement diagram of the 2-point bending test (fig. 4). The test itself was performed on a Zwick/Roell Z250 universal testing machine. Forces were measured over a distance of 50 mm at a test speed of 20 mm/min and a preload of 5 N. Uniform test conditions were ensured by storing all specimen according to DIN EN ISO 1110. Before testing, the specimens are stored for between 1 h and 2 h under standard climatic conditions (23 °C, 50 % relative humidity). The calculation of the gradient is done via the secant at the force 50 N and 150 N. The deformation work was defined as the integral of the force over displacement with the limits of 5 mm and 30 mm. The largest measured force is defined as the maximum force.

3.2 Results of the pre-analysis

In a preliminary analysis (n=15) the scatter of the mechanical target parameters of the manufactured components is determined (fig. 4). Characteristic values in the linear-elastic (stiffness) and in the plastic range (maximum force, deformation work) are determined. A mean value of 75.93 N/mm and a standard deviation of 1.13 N/mm (1.48% rel.) are determined for the target parameter stiffness. In the plastic range of the properties, the relative standard deviation increases to 4.36 % (deformation work) and 2.08 % (maximum force). The preliminary analysis shows a stable process with a low dispersion of the target parameter in a normal distribution.

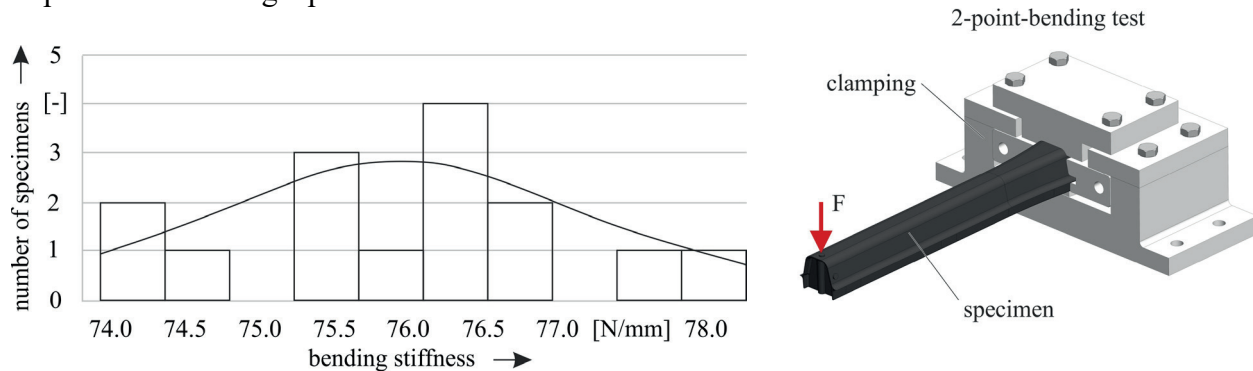


Fig. 4: Distribution of the bending stiffness in the pre-analysis; testing setup of the 2-point-bending test.

Table 1. Standard deviation of the target parameters of the test series.

target parameters	mean value	standard deviation abs.	standard deviation rel.
bending stiffness [N/mm]	75.93	1.13	1.48 %
deformation work [kJmm]	149.38	6.51	4.36 %
maximum force [kN]	2.14	0.04	2.08 %

3.3 Results of the DoE

Four factors were examined within a partial factorial experimental design with a total of eight factor levels (m) (table 2). The evaluation of the results was carried out on the one hand by determining the effects and associated confidence intervals using statistical descriptive parameters and on the other hand by machine learning methods. In addition, the influence of the disturbance parameters was also evaluated.

Table 2. Factor level combinations in partial factorial 2^{4+1} -DoE.

factor level (m)	holding pressure injection mould- ing [bar], (A)	heating temperature thermoplastic com- posite sheet [°C], (B)	mould temper- ature [°C], (C)	temperature sup- port tooling hot runner [°C], (D)	quantity (n)
1	350	300	80	285	12
2	600	300	80	305	12
3	350	325	80	305	12
4	600	325	80	285	12
5	350	300	130	305	12
6	600	300	130	285	12
7	350	325	130	285	12
8	600	325	130	305	12

According to fig. 5 left, the heating temperature (B) shows a statistically highly significant effect on the stiffness of the component. The effects of holding pressure (A), mould temperature (C) and temperature of the support tooling hot runner (D) and their twofold interactions are not statistically significant. An increase in the heating temperature from 300 °C to 325 °C leads to an increase in bending stiffness by 1.74 %, the deformation work by 1.69 % and the maximum force by 2.67 %.

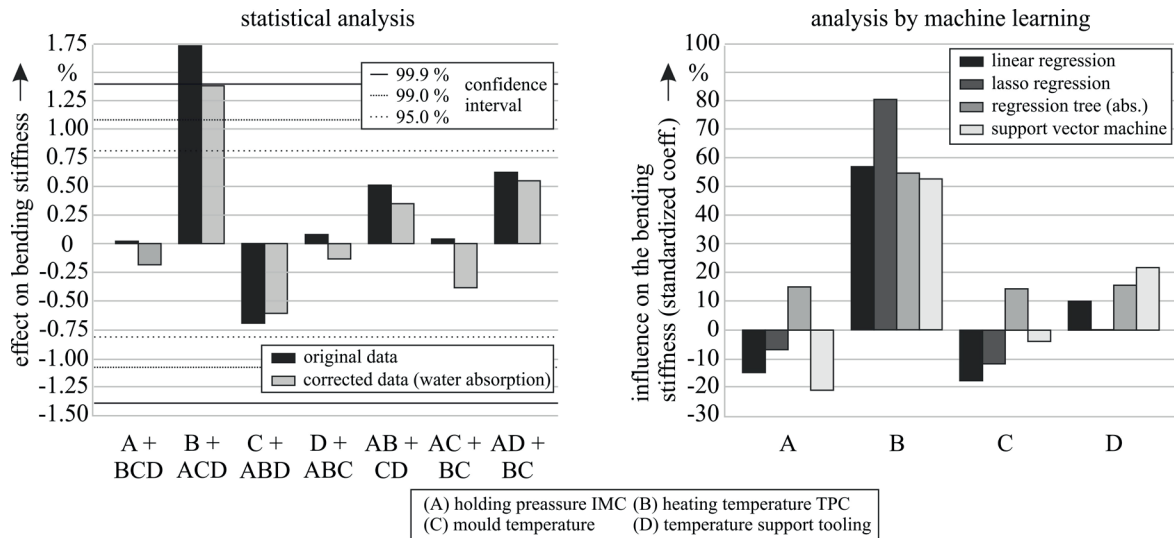


Fig. 5: Effects on the bending stiffness in the statistical analysis (left); standardized linear coefficients of the regression models on the bending stiffness in the analysis by machine learning (right).

An influence of the disturbance parameter water absorption on the mechanical target parameters could be shown. This is due to the scatter of water absorption caused by the temperature and humidity gradient in the height direction of the climate chamber. This systematic error in component conditioning distorts the mechanical properties of the components due to their different humidity content. By recording the disturbance parameter, its influence on the mechanical properties of a component can be corrected and shown as comparison in fig. 5 left. The heating temperature showed a highly significant effect even after correction of the largest recorded disturbance parameter in the process.

3.4 Results of the data mining

Two assumptions were made for the evaluation of the DoE. All process and disturbance parameters excluding the factors are constant and the values of the factor levels do not deviate from the target values defined in the test plan. The hybrid process contains disturbance parameters and as a result, the target value also scatters within a factor stage at constant process parameters. Moreover, the process values of the factors deviate from the values specified in the experimental design. This information is not taken into account in the evaluation of the DoE, so an additional evaluation is carried out using data mining methods. This enables the integration of process and disturbance parameters into regression models. The data preparation as well as the creation, training, testing and interpretation of the models is based on the KDD model. Linear regression models, lasso regression models, regression trees and support vector regressors were trained, tested and interpreted for evaluation. The pre-factors of each linear model are normalized for the evaluation, that their absolute sum is 100 %. Their results confirm with the evaluation of the DoE with regard to the influence of the heating temperature of the TPC sheet (fig. 5 right). The accuracy of the models was assessed by the mean-absolute-error (MAE). A low accuracy of the models and the resulting low significance of the interpretation of the models is due to a combination of a small number of data points, relatively small effects and large influences of the disturbance parameters. In addition, the dichotomous distribution of the

values in the two-step DoE can have negative effects. A too small deviation between the nominal values of the factor levels and the actual values did not lead to additional knowledge from the database of the DoE.

4 Conclusions

In this paper, a methodical approach to the analysis of the intrinsic process with a generic structure made of TPC sheets combined with injection moulding compound is investigated. Thereby methods from statistical design of experiments are used and extended with those of data mining. The analysis showed the heating temperature of the TPC sheet as the main influencing factor. An increase from 300 °C to 325 °C increases the mechanical properties in bending stiffness, deformation work and the maximum force. The identified disturbance parameter of water absorption during specimen conditioning showed the greatest influence on the target parameters. An evaluation of the data on the basis of a DoE with methods from data mining did not lead to any additional results. To achieve a higher model accuracy for future analyses, the influence of disturbance parameters should be investigated and reduced. Moreover, if the effects are not significantly above the 99.9 % confidence interval, the variance is too large in comparison and makes modelling difficult.

5 Acknowledgement

This research has received funding under the grant number 100339955 (“robust EVP 4.0” project) by the European Regional Development Fund (EFRE) and the German Federal State of Saxony.

6 Literature

- [1] D. R. Haider, M. Krahl, M. Gude, P. Kellner, D. Knötschke, in *Plastics in Automotive Engineering*, **2018**.
- [2] M. Gude at al., in *Plattform FOREL Abschlussbericht Q-Pro*, **2018**.
- [3] D. R. Haider, M. Krahl, M. Gude, R. Hengstmann, S. Titze, M. Haupt, in *SAMPE Europe Conference*, **2017**.
- [4] A. Jaeger et al., in *VDI-Statusreport Februar - Spritzgießen*, **2019**.
- [5] O. Schnerr-Häselbarth, *Automatisierung der Online-Qualitätsüberwachung beim Kunststoff-spritzgießen*, **2000**.
- [6] S. Haman, *Prozessnahes Qualitätsmanagement beim Spritzgießen*, **2003**.
- [7] C. Sorg, *Data Mining als Methode zur Industrialisierung und Qualifizierung neuer Fertigungsprozesse für CFK-Bauteile in automobiler Großserienproduktion*, **2014**.
- [8] J. Cleve, U. Lämmel, *Data Mining*, Oldenbourg, München, **2014**.
- [9] U. Fayyad, G. Piatetsky-Shapiro und P. Smyth, in *Artificial Intelligence Magazin*, **1996**, p. 37-54.
- [10] D. R. Haider, M. Krahl, W. Koshukow, M. Wolf, A. Liebsch, R. Kupfer, M. Gude, in *Hybrid Materials and Structures*, **2018**.

Influence of the morphology of nanoporous silicon dioxide based surface coatings on the interfacial strength of injection-moulded polymer-metal hybrids

M. Laux¹, Y. Löhr¹, R. Dreher¹, R. Emmerich¹, F. Henning^{1,2},

¹Department of Polymer Engineering, Fraunhofer Institute for Chemical Technology ICT, Pfinztal

²Institute of Vehicle System Technology at the Karlsruhe Institute of Technology KIT, Karlsruhe

1 Abstract

Plastic-metal hybrids already belong to the state of the art, as components can be designed to meet high demands thanks to the material combination. Especially injection moulded thermoplastic metal hybrids enable functional integration and economical manufacturing. One possibility to produce hybrids is the in-mould assembly using injection moulding. Due to short contact time, pre-treatment of the metal surface is necessary to ensure sufficient bonding to the overmoulded plastic component. Toxic pre-treatment methods such as pickling or priming are hardly used anymore because of ever stricter environmental conditions. It was found that nanoporous silicon dioxide based surface structures can offer an alternative to generate high bonding strengths [1]. The structures are coated on the metal surface in a microwave induced PECVD process. During injection moulding, the surface structure is infiltrated by the polymer, so that the solidification of the melt produces a form closure. Within these investigations the influence of different coating morphologies on the interfacial tensile strength was investigated using injection molded polyphenylene sulfide (PPS)-metal hybrids. Average adhesive tensile strength of up to 28 MPa and low scattering have been achieved. It was shown that the morphology of the nanoporous structure has a significant influence on the interfacial strength of the injection moulded hybrids.

2 Introduction

In general, the Plasma Enhanced Chemical Vapor Deposition (PECVD) process is used to create dense surface coatings such as protection layers. In a process developed at the Fraunhofer ICT, the PECVD is used to deposit nanoporous silicon dioxide based surface structures which can be used as a bonding agent for polymer-metal hybrids [2]. These kind of coatings are created thru the reaction of hexamethyldisiloxane (HMDSO) and oxygen to SiO₂, water and carbon dioxide using the plasma energy. The SiO₂ is deposited on the substrate surface where it forms different layer morphologies depending on the setting parameters. It is to be expected that different layer morphologies lead to different adhesive tensile strengths, which has already been observed on other adhesive layers such as pickled and corundum-blasted surfaces [1]. However, it is not proved yet which layer characteristics of the nanoporous structure significantly influence the achievable adhesion strength. Furthermore, it was necessary to analyze the adhesive strengths independently of the coating parameters since the coating system used has a considerable influence on the forming layers. In order to identify layer characteristics within

this research scanning electron microscope (SEM) images of the nanoscale silica layers were analyzed using image processing methods.

3 Methods

A 1000 x 560 x 337 mm vacuum chamber was used to apply the coating. The chamber is equipped with 144 gas feed tubes which supply the precursor molecule hexamethyldisiloxane (HMDSO) and oxygen. The flow rate of these gases were set to a value between 225 and 675 sccm depending on the experiment. The distance between the gas supply tubes and the mounting plate where the substrates were attached varies from 51 to 119 mm. Pressures between 0.5 and 0.8 mbar were chosen for the formation of layers. The coating time was chosen to be between 5 and 15 s. The temperature of the substrate was also adjusted, in a range from 30 to 110 °C. The applied power in the form of a plasma was controlled by the pulse duration of 4 to 20 ms and the pulse-pause ratio in the microwave cable.

To evaluate the morphology, layers were applied to polished pin stubs (alloy: AlMg3) and imaged with the aid of a scanning electron microscope (SEM). The images were evaluated regarding the morphology with the image processing program ImageJ.

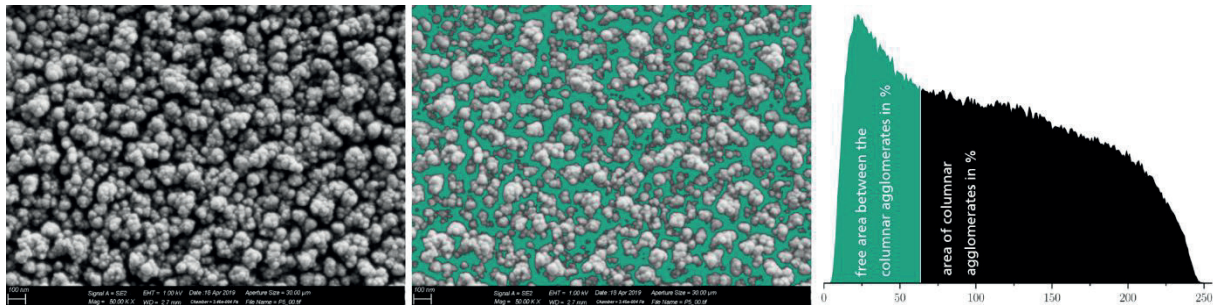


Figure 1: SEM image of a layer (left), SEM image of a layer with all pixels darker than the threshold colored green (middle), histogram (right)

As shown in Figure 1, the image is divided into free area between the agglomerates which represents the free capillaries and the area of the agglomerates based on brightness. The area of the individual agglomerates is averaged and the diameter that a circle with this area would have is calculated to obtain a comparison value. Figure 1 shows the analysis of the free area using a global threshold. In order to evaluate the data in a reproducible and more accurate way, the algorithm according to Sauvola [3] was chosen for this work. This algorithm uses a local threshold value method and is therefore robust against global differences in brightness that can be caused by the SEM itself.



Figure 2: Tensile test of a hybrid

In order to determine the adhesive tensile strengths when using the different layer morphologies, halved tensile bars out of Aluminum (AlMg3) were manufactured. To minimize the effect of surface enlargement due to micro-roughness the abutting face of the halved tensile bars was wet sanded with 2400 grit sandpaper. After cleaning with isopropyl the wet sanded end face was coated in the PECVD process. The coated specimens were joined in an injection moulding process using a 30 % glass fiber reinforced polyphenylene sulfide (Xytron G3010E). All test specimens were produced with the same injection molding parameters. The melt temperature was set to be 340 °C, the mould was tempered to 156 °C and the injection speed was chosen to be 57 cm³/s. To avoid mechanical stress during the ejection-process a tension rod tool with an ejector bar was used. For each morphology 6 hybrid tensile bars were produced and tested on a tensile testing machine (H&P Inspekt table 50) according to DIN EN ISO 527-1 [4] using a traversing speed of 1 mm/min as shown in figure 2.

4 Results

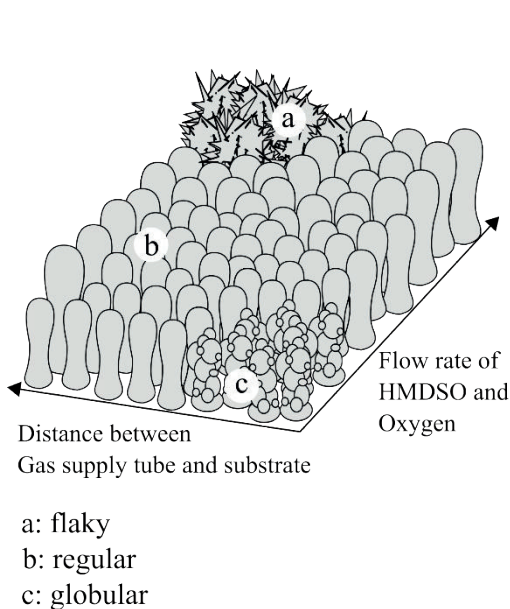
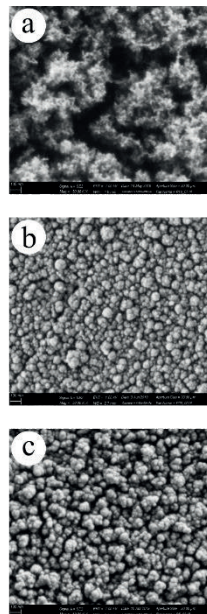


Figure 3: Schematic representation of the column structure as a function of the distance and the flow rate at 0.8 bar pressure in the coating chamber (left) and representative illustrations of the three types of coating occurring (right)



Different adjustment parameters result in different morphologies. The forming structure can be compared to columns which differ in distance, height and diameter. These range from flaky at high pressure, high flow rate and large distance between substrate and gas supply tubes to very globular structures that are formed at high pressure, low flow rate and small distance between substrate and gas supply. The deduced layer growing behavior shown in Figure 3 only applies to substrate temperatures less than 10 % of the melting point of silicon dioxide. Higher substrate temperatures are not part of this investigation as it is known that they lead to denser structures [5].

These dense structures do not show any undercuts and are not suitable to serve as an adhesion layer. Therefore, the main focus of this work is on the regular layers with an additional view on edge areas such as flaky and globular layers.

Figure 4 shows the adhesive tensile strength in dependence of the free area between the columnar agglomerates. The regular layers differ between 28 and 39 % of free area with a peak in adhesive tensile strength in the range of 33-38 % with average values up to 28 MPa. Globular layers are located around 37 % of free area but only show low adhesive tensile strengths. It is suspected that there is insufficient reaction time to form stable structures due to the small distance and flow rate.

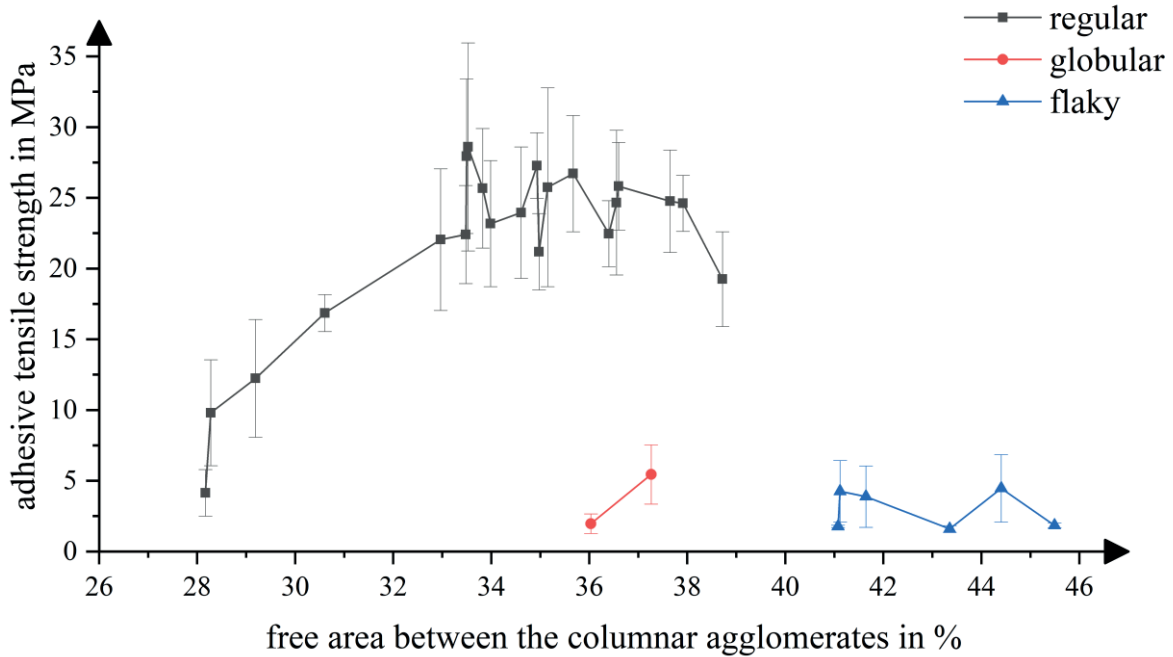


Figure 4: Schematic representation of the column structure as a function of the distance and the flow rate at 0.8 bar pressure in the coating chamber (left) and representative illustrations of the three types of coating occurring (right)

All investigated layers with a free area greater than 40 % have a flaky structure. Despite the numerous undercuts flaky structures perform poorly. It is assumed that the thin-walled flakes are unstable and therefore cannot transmit high forces.

A closer look at the regular layers reveals a strong increase in adhesive tensile strength up to a free area between the columnar agglomerates of 33 %. In the range of 33-38 % a plateau of the adhesive tensile strength can be observed which start to decrease at free areas higher than 38 %. A sweet spot can also be seen when the adhesive tensile strength is plotted over the column diameter as shown in Figure 5. Here the course is represented by layers with the same free area but different column diameters. The increase of the adhesive tensile strength with increasing column diameter can be explained by the capillary growing at the same time. With particularly small column diameters, the surface structure becomes very fine and thus the capillary to be infiltrated becomes small. The influence of the capillary size is still to be determined, but based on the Lucas-Washburn equation [6] it can be assumed that small capillary diameters are infiltrated slowly and therefore poorly by a molten thermoplastic such as the used PPS. This is counteracted by the column height, which increases with increasing column diameter, and thus the capillary depth. The deeper the capillary the more time is required for it to be completely infiltrated. Therefore, the adhesive tensile strength decreases again with high column diameters. It remains to be examined whether this effect is actually influenced by the infiltration or a

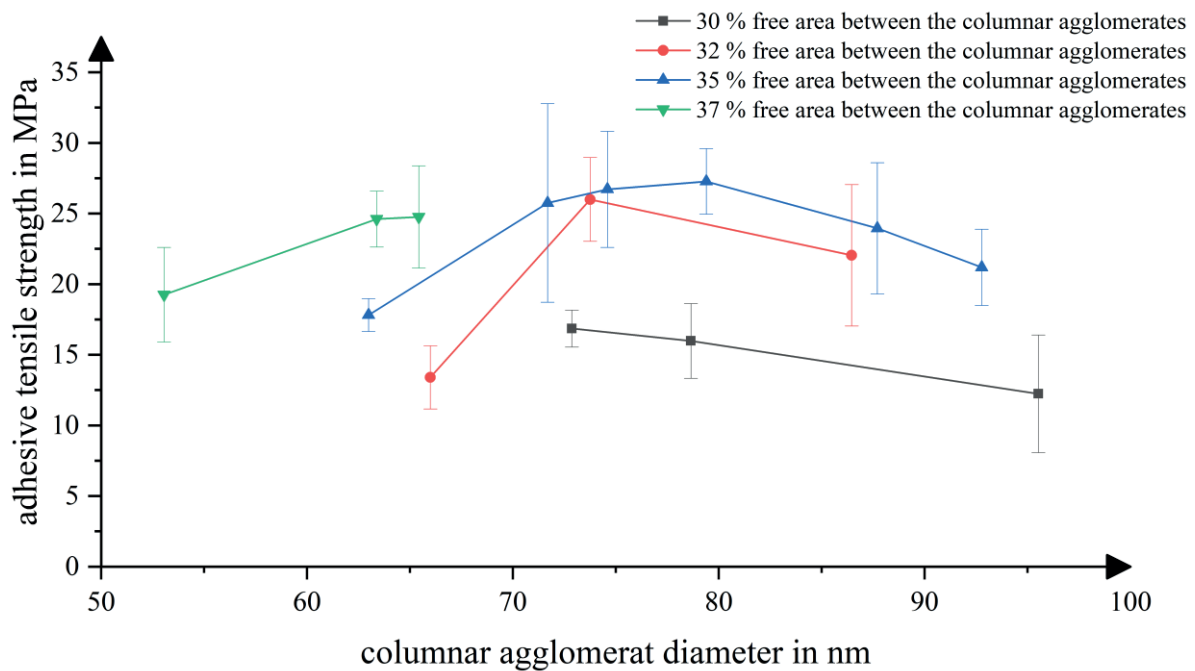


Figure 5: adhesive tensile strength over columnar agglomerate diameter

mechanical interaction. Therefore, and the fact that the layer height was not taken into account in these investigations, further research is necessary.

5 Conclusion

It could be shown that both the free area between the columnar agglomerates and the average agglomerate diameter have an influence on the adhesive tensile strength of the polyphenylene sulfide-silica interface. Highest bonding strengths occur when the free area between the agglomerates is in the range of 33-38 percent. Average adhesive tensile strengths of 28 MPa can be achieved. Both below and above, the adhesive tensile strengths drop significantly. Furthermore, it could be shown that also the average size of the agglomerates has an influence on the overall strength of the interface. Depending of the percentage of free capillaries highest adhesive tensile strength are achieved between 65-80 nm of average columnar agglomerate diameter.

6 Acknowledgment

The present research was created within the framework of the LeiMot – Leichtbaumotor (Lightweight Engine) project which is funded by the Federal Ministry of Economics and Technology (BMWi, funding number 19 18002G). Aim of the project is a weight reduction of a combustion engine through targeted structural optimization and the use of hybrid metal and plastic components.

7 Literature

- [1] M. Laux, B. Beck, R. Emmerich, R. Dreher, F. Henning, The effect of nanoscale surface structures on the interfacial strength of injection-molded PPS-Metal hybrids, *SAMPE Europe Conference 2017 Stuttgart – Germany*, **2017**
- [2] R. Emmerich, R. Dreher, H. Urban, M. Graf, *Nanoskalige Oberflächenstruktur zur Verbesserung der Adhäsion*. "Patent", **2015**
- [3] J. Sauvola, T. Seppanen, S. Haapakoski, M. Pietikainen, Adaptive document binarization, in *Proceedings of the Fourth International Conference on Document Analysis and Recognition Bd. 1*. **1997**, p. 147–152.
- [4] DIN, ENISO. 527-1: 2012-06, Kunststoffe–Bestimmung der Zugeigenschaften–Teil 1: Allgemeine Grundsätze (ISO 527-1: 2012). *Deutsche Fassung EN ISO 527*, **2012**
- [5] J. A. Thornton, *Journal of Vacuum Science and Technology* **11**, 666 (1974); Influence of apparatus geometry and deposition conditions on the structure and topography of thick sputtered coatings, **1974**
- [6] E. W. Washburn, The Dynamics of Capillary Flow, in *Physical Review* 17 (1921), S.374 **1921**

A highly economical inductive joining technology for fibre composite connections

Alexander Fröhlich¹, Martin Kroll¹, Patrick Rochala¹, Verena Kräusel¹,

¹ Institute for Machine Tools and Production Processes (IWP), Chemnitz University of Technology, Chemnitz, Germany

Lightweight materials such as carbon fibre reinforced thermoplastics (CFRP) and glass fibre reinforced plastics (GFRP) have become a key factor for success in industrial sectors such as transportation, automotive production and aerospace [1]. To enable a broad application of advanced lightweight materials, cost-efficient, reliable and automatable production processes are required. Currently, different mechanical, chemical and thermal technologies are used to join CFRP with each other or with GFRP [2]. Induction heating offers the advantage of direct heat generation in the workpiece. Therefore, the workpiece needs to be electrically conductive. Additionally, induction heating allows for very high heating rates and as a result, heating times can be reduced significantly. However, the introduced heat must be dissipated to finish the joining process and to facilitate the required curing. The hybrid technology of inductive contact joining (ICJ) was developed to join GFRP with CFRP by using an induction tool that allows for single-sided heating and rapid cooling by direct heat dissipation in the water-cooled induction coil. The direct contact of the induction tool cooling shifts the maximum temperature below the surface into the component volume. Shear tensile tests were performed to characterize the bond strength at heating times of $t_h = 2.0$ s and a process time of only $t_p = 4.0$ s without a prior surface pretreatment. The achieved tensile shear strength was $\tau_e \approx 32.5$ MPa.

1 Introduction

The successful industrial application of fiber-reinforced polymer composites (FRP) depends not only on material costs and consistent automation, but also largely on flexible and efficient joining technologies [1]. In addition to the possibility of integration into existing manufacturing processes, the required capital expenditure, the cost of the joining elements or consumables, compact tool dimensions, short joining times and component pretreatment are decisive factors for an industrial application [3]. For profiles in structural components, joining methods with one-sided accessibility to the joining area are desired [4]. The novel joining method of ICJ presented in this paper combines the process steps heating, joining, force application and cooling in a single induction tool and mounting.

2 Inductive contact joining

The Inductive Contact Joining method is a result of further development of published inductive joining approaches [5],[6],[7]. Figure 1 presents the schematic representation of the joining setup and the process flow, including the three major process variables of temperature T , joining force F and induction power P_i .

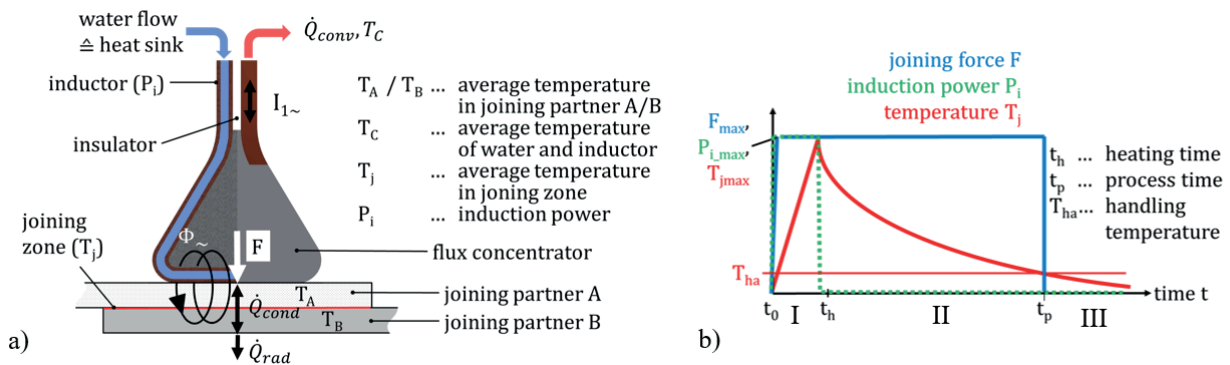


Figure 1: The hybrid ICJ tool and main parameters (a) [8], schematic diagram of joining force, temperature and induction power in the joining zone during the ICJ process (b) [9].

In order to create hybrid GRP or FRP joints with the new ICJ technology, the parts to be joined are arranged overlapping and the induction tool is positioned on top (phase I in Fig. 1b). When the generator is activated, the electrically conductive area below the inductor heats up and melts. The electrically insulating joining partner is heated in the area of the joining zone by heat transfer from the electrically conductive component (phase II in Fig. 1b). In this process, the molten portion of both joining partners are mixed with each other. This process is supported by the joining force F , which is applied simultaneously by the induction tool. When the electric energy supply by the generator is stopped, the melt cools down rapidly and solidifies (phase III in Fig. 1b). The water-cooled induction coil in direct contact and the fact that the locally limited induction heating allows to spread heat into the cooler areas of the components supports the high cooling-rate of the joining area.

3 Physical background

An alternating electromagnetic field induces a voltage in an electrically conductive material. The resulting eddy current causes a heat flow mainly by the Joule effect, depending on the electric resistance R over time in a cross section A . Ferromagnetic metals are additionally heated by magnetic hysteresis [10]. The heat flow depends on the current density J in the workpiece, and the current density decreases exponentially with the distance from the surface due to the skin effect. The current density is also determined by the penetration depth δ that represents the distance from the surface at which the current density has dropped to $1/e \approx 37\%$. This area represents about 63 % of the current density and approximately 86 % of the electrical energy that is transformed into heat (Figure 2). The penetration depth depends on the material parameters permeability μ , electrical conductivity σ and the frequency f of the electromagnetic field.

In carbon fiber reinforced materials, the electromagnetic field is induced in the electrically conductive fibers. When fibers are crosswise in contact, the current is transferred from fiber to fiber and horizontal eddy currents are generated. Resistance heating results in an increase in temperature so the matrix of the thermoplastic material heats up to the melting temperature and melts. If the fibers in the composite material are unidirectionally oriented, no horizontal eddy currents are generated due to missing crossing points. In this case, electromagnetic fields with higher frequencies are required to generate circumferential eddy currents in the carbon fiber.

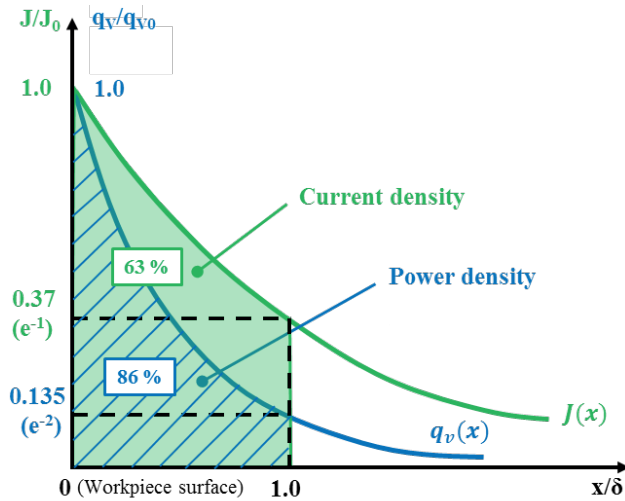


Figure 2: Exponential characteristic curves of the current density J and the generated power density q_v as a function of the distance x from the workpiece surface. q_{v0} is the generated power density on the surface of the workpiece [11].

4 Experimental setup and procedure

The aim of this study is to demonstrate the performance of the ICJ process. The focus is on the joining time and the achievable shear tensile strength of lap joints without prior surface pre-treatment.

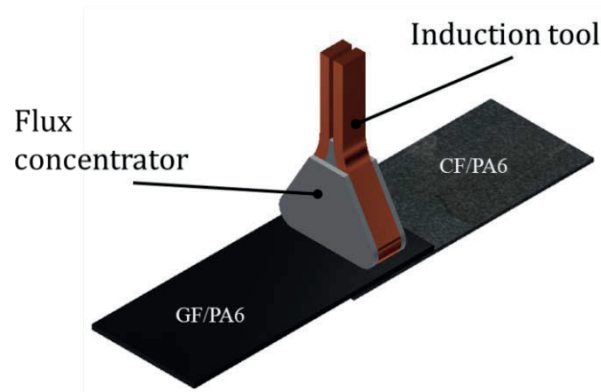


Figure 3: experimental setup of the inductive contact joining.

Tensile shear tests were carried out according to DIN EN ISO 14273 with a Hegewald & Peschke Inspekt 150 universal testing machine. The specimens, joined under the same condition were tested. Thereby, force F and displacement s were recorded during testing. The selected joining partners comprised a laminate of Tepex® dyalite 102-RG600(x) / 47 % roving glass polyamide (PA) 6 with a thickness of $s = 1.0$ mm, hereafter referred to as GF/PA6, and a laminate of Tepex® dyalite 201-C200(x) / 50 % roving carbon fiber polyamide CF/PA6 with a thickness of $s = 1.0$ mm. The PA6 matrix determines the composite melting temperature of $T = 220.0$ °C. The decomposition of polyamide starts above $T_{dec} \geq 300.0$ °C [12]. The geometry of specimens was in accordance with DIN EN ISO 14273. Dimensions of the sheets were specified with 100.0 mm \times 50.0 mm \times 1.0 mm for each joining partner. The components were cleaned with ethanol before joining. A further pre-

treatment was not carried out. After the joining process, the samples were cut, embedded in epoxy resin and cross sections of the joining area were prepared for optical microscopy. The sample was subsequently ground with a grain size of 220 to 1200.

The ICJ-tool is a press inductor, developed at Chemnitz University of Technology, with a contact surface $A_C = 12.0 \text{ mm} \times 6.0 \text{ mm} = 72 \text{ mm}^2$. The front side of the press inductor was manufactured by means of 3D casting and brazed to the inductor base body. The generator used was an EMAG eldec HFG50 with a maximum electric power of $P = 50.0 \text{ kW}$, which operates in the high frequency range of $250.0 < f < 350.0 \text{ kHz}$.

In the jig, the specimens were arranged in an overlapping structure as shown in Fig. 3. Therefore, the CF/PA6 sheet was placed at the bottom. The GF/PA6 sheet was positioned at the top of CF/PA6 sheet. The overlap area had a dimension of $A = 35.0 \text{ mm} \times 50.0 \text{ mm}$. The induction tool was then placed in the middle of the overlap area with its front side perpendicular to the longitudinal axis of the specimen (Figure 3). A joining force of $F = 320.0 \text{ N}$ was applied to the joining surface by the induction tool. The inductance, electrical resistance and coil length of the inductor the of the electrical properties of the specimen determined the resulting resonance frequency of $f = 324.0 \text{ kHz}$. The flux concentrator material Ferrotron 559 from Fluxtrol, Inc. was used to concentrate the electromagnetic field in the joining zone and for shielding.

5 Results

After extensive preliminary investigations on relevant joining parameters, with a heating time of $t_h = 2.0 \text{ s}$ and an induction power of $P_i = 3.5 \text{ kW}$ the best results were obtained. In this reference process, the process time (phase 1 to 3) was $t_p = 4.0 \text{ s}$.

Figure 4 shows the force-displacement curves of the examined samples. Until a tensile force of $F = 3,500.0 \text{ N}$ is reached, all samples show a linear relationship between elastic deformation and applied force. Due to the plain surface of the composite materials, irregularities often occurred due to specimens slipping in the jaws of the tensile testing machine. For this reason, only two tensile specimens were available for evaluation in these tests. Overall, however, the quality of the compounds produced by the ICJ method appears to be consistent.

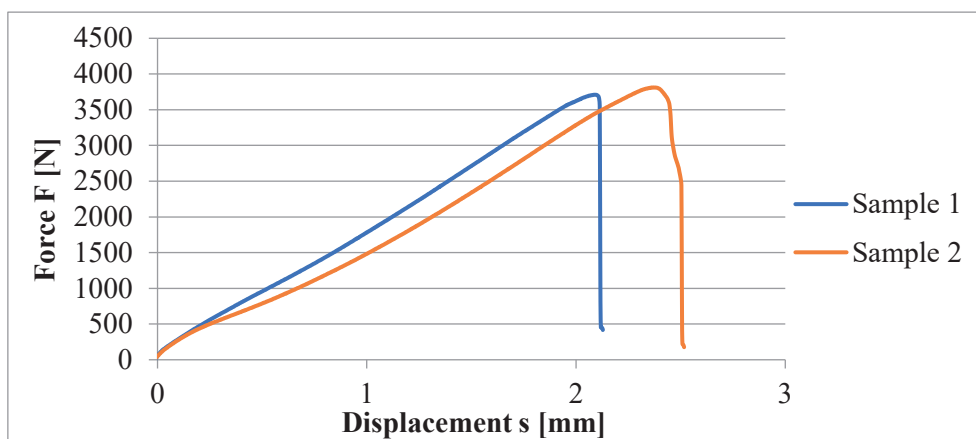


Figure 4: Force-displacement curve of the two tested samples.

The induction coil was designed to heat only a fraction of the available overlapping area to represent a mechanical joint with FRP or a spot-weld with metallic sheets. Therefore, the contact surfaces that transfer the load had to be defined to derive the effective shear tensile strength τ_e (Figure 5). The

relevant area was marked with white paint. An inspection with optical microscopy was used to determine the effective load bearing area (red area in micrographs of Figure 5). Since the entire fracture surface could not be captured by an objective, the image was divided into two areas.

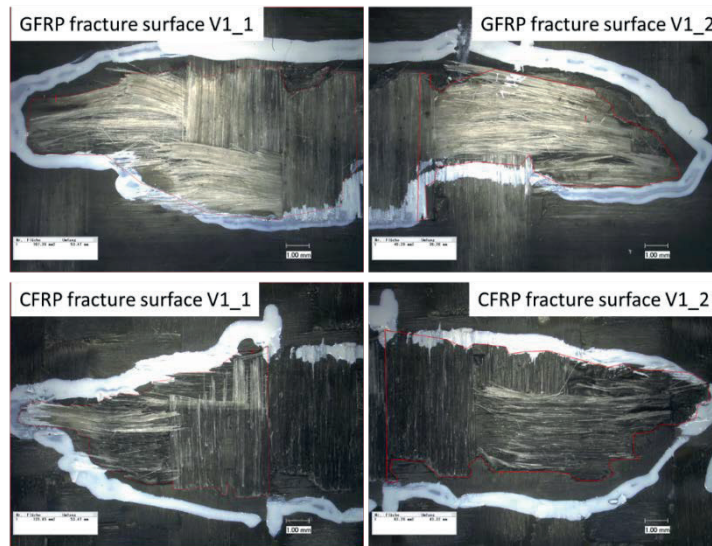


Figure 5: Determination of the load bearing area A_e between V1_CFRP with GFRP with section 1 (left) and section 2 (right)

In Table 1 the assumed effective load bearing area A_e for determining the effective shear tensile strength was calculated from the average of the measured CFRP and GFRP surfaces. The melted area in the joining zone is larger than the contact area A_C of the inductor.

Table 1: Determination of the shear tensile strength.

sample	surface section 1 [mm ²]	surface section 2 [mm ²]	total average load bearing area A_e [mm ²]	tensile force [N]	effective tensile shear strength τ_e [MPa]	inductor contact surface A_C [mm ²]
V1_GFRP	58.45	40.2	107.1	3711	34.6	72.0
V1_CFRP	52.27	63.2				
V2_GFRP	60.2	50.38	124.8	3812	30.5	
V2_CFRP	75.88	63.1				

The high strength can be explained by the substance-to-substance bond between the two components in the area of the joining position. As can be seen from Figure 5, fibre pull-out occurred during the lap shear tests. The fracture pattern indicates a cohesive failure in the base material. This is the reason for the high strength of the joint produced by ICJ.

The induction of eddy currents into the carbon fibers causes the polyamide matrix to heat up and form a material bond in the area under the contact surface of the inductor. The microscopic picture (figure 6) shows the joining zone of the samples.

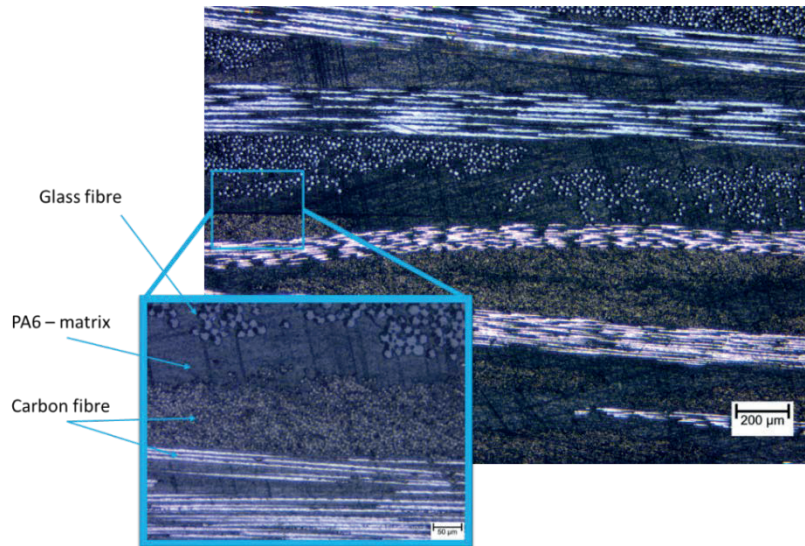


Figure 6: Micrograph of a cross section of the joining area between CFRP and GFRP components.

It can be observed that the thermoplastic matrices of the samples have mixed and fiber parts were introduced from one component into the other. This explains the high shear tensile strength of $\tau_e \approx 32.5$ MPa.

6 Summary and outlook

In the investigations presented, for overlapping joints of CFRP and GFRP, a shear tensile strength of about $\tau_e \approx 32.5$ MPa could be achieved with a heating time of $t_p = 2.0$ s and a process time of only $t_h = 4.0$ s without a prior surface pretreatment. Therefore, the investigations show that the technology of inductive contact joining is excellently suited for the economical production of high-strength connections between modern fiber composites. With this joining approach, only one of the two partners must contain electrically conductive components. In further investigations, the heating in the CFRP component is to be analyzed in more detail. For this purpose, a theoretical model of the composite material is to be elaborated, which will then be facilitated by FE simulation to determine electromagnetic field and current distribution analytically.

References

- [1] L. Ickert et al., *FAT-Schriftenreihe*, **2012**.
- [2] M. Mülle, M. Stegelmann, M. Gude, *Kunststoffe international*, **2016**, 01-02.
- [3] G. Meschut et al., *EFB-Forschungsbericht*, **2014**, Nr. 391
- [4] L. Dorn, K. Koppe, H. Rudolf, *Schweißen und Schneiden*, **2005**.
- [5] P. Mitschang, R. Velthuis, M. Didi, *Adv. Eng. Mater.*, **2013**, vol. 15, no. 9.
- [6] S. Scheik, *Aachener Berichte Fügechnik*, **2016**.
- [7] M. Hümbert, *Induktiver Schweißprozess für glasfaserverstärkte Thermoplaste und Stahl*, Dissertation, Technische Universität Kaiserslautern, **2018**.
- [8] V. Kräusel et al., *CIRP Ann.*, **2018**, vol. 67, issue 1, 5-8.
- [9] A. Fröhlich et al., *Procedia Manufacturing*, **2019**, vol. 35, 143-148.
- [10] G. Benkowsky, *VEB Verlag Technik*, Berlin, **1990**.
- [11] Hofmann C. et al., *20th International Conference on Solid-State Sensors, Actuators and Microsystems & Eurosensors XXXIII*, **2019**, 277-280.
- [12] RCT Reichelt Chemietechnik GmbH + Co., Datasheet Polyamid 6, **2018**, <https://www.rct-online.de/de/HmswGlossar/detail/id/8>.

Influence of Continuous Wave Surface Structuring and Zinc Coating on Bond Strength of Hybrid Joints Made of Steel and TP-FRPC

S. Weidmann¹, P. Mitschang¹,

¹Institut für Verbundwerkstoffe GmbH, Erwin Schrödinger Straße 58, Kaiserslautern

1 Introduction

The EU regulations regarding vehicle emissions stipulate a reduction in CO₂ emissions [1]. This requires a rethinking of car manufacturer e. g. to use consequent lightweight design. In order to reduce the energy consumption of vehicles, the weight of vehicle components must be reduced to lower the total weight. The most promising approach so far is to replace metal components with lightweight fiber-reinforced polymer composites (FRPC). Especially thermoplastic FRPC (TP-FRPC) are suitable as lightweight construction materials [2]. In contrast to thermoset FRPC, they can be processed cost-efficient within short cycle times in large scale production by established manufacturing processes as thermoforming or injection molding [2]. A further advantage of TP-FRPC is their weldability, which allow a joining of hybrid structures using surface-pretreated metals and TP-FRPC [3, 4]. Since the hybrid joining mechanism is primarily generated by a positive fit between the two different materials, it is not necessary to use additives such as adhesives, resulting in a weight neutral joint [5, 6]. By validating induction welding as a reliable hybrid joining method, this technology provides new manufacturing possibilities [3]. So, induction welding of hybrid structures is a key technology of tomorrow's hybrid lightweight design [7].

2 Hybrid Joining Techniques and Surface Pretreatment

A large number of researchers and industrial companies report on possibilities to join metals with FRPC. In addition to mechanical joining methods using joining elements such as screws or rivets, adhesive and thermal joining methods are used [6, 8, 9]. Adhesives are usually used to join metals with thermoset FRPC [6, 8]. Therefore, the joining zone usually has to be cleaned or pretreated before applying the adhesive [6]. In both, mechanical and adhesive joining, additional weight is added to the hybrid structure by glue or the joining elements. In hybrid thermal joining processes, which include induction welding, the thermoplastic matrix of the FRPC acts as an adhesive, so no additional weight is added. Furthermore, thermal joining processes are fast compared to adhesive or mechanical joining due to the lower number of process steps.

Eckstaedt et al. [10] present different approaches to achieve a surface pretreatment on metals. Two mechanical and two laser-based structuring processes were investigated. The mechanical processes are GripMetal™ and Coniperf™. In GripMetal™, hooks are shaped out of the metal surface by micro-punching. The Coniperf™ structuring process forms pockets in the metal surface.

The two laser based structuring processes differ in the type of laser irradiation. The first type of laser structuring produce “Cone-Like-Protrusions” (CLP by Pulsar Photonics GmbH). In this structuring process, a laser achieves a self-organized surface on the metal. The high structuring density and thus high relative surface area benefits physical bonding mechanisms between polymer and metal. Micro

positive fits between TP-FRPC and metal can be achieved by this type of surface pretreatment. The CLPs are only achieved in small process windows of structuring with almost no adjustment possibilities. In the second laser structuring process, a continuous wave (cw) spot laser moves continuously in line pattern over the joining zone of the metal. The metal is heated locally in a small area causing a sublimation of the metal which leads to a cavity. The depth of the cavity can be increased by several runs of the laser over the target positions of the cavities. The vapor pressure, generated by the sublimation of the metal, ejects molten metal out of the cavity. This melt deposits at the edge of the cavity, leading to a drop shape. In this process, it is possible to achieve cavities in the metal at a defined angle by means of an angled laser beam. The CLP structuring process is, in contrast to cw laser structuring, much more difficult to control. In cw laser structuring, the surface structuring can be adapted by varying parameters such as laser power, scanning speed, number of passes, distance between the cavities, irradiation angle, etc. to optimize the bonding mechanisms of the metal to the polymer. [10] Stress peaks in the joining area can be avoided by an adaptation of the orientation and number of cavities on the metal surface [11].

The metal specimens were joined by laser welding to the TP-FRPC in [10]. Steel with the material number 1.441 and a thickness of 3 mm was used for the GripMetal™ surface pretreatment and 1.4301 steel with a thickness of 2 mm for the remaining surface pretreatments. The FRPC used were glass fiber reinforced polyamide 66 with a thickness of 4 mm and a fiber volume content of 35 % (GF-PA66-4 mm), carbon fiber reinforced polyamide with a thickness of 4 mm and continuous fiber reinforcement with a fiber volume content of 52-55 % (CF-PA6-4 mm) and glass fiber reinforced PA66 with a thickness of 10 mm and a fiber volume content of 30 % (GF-PA66-10 mm). The highest tensile-shear strength with 27.5 MPa and peel load of 4 MPa was achieved with the GripMetal™ joined with CF-PA6-4 mm. The self-organized surfaces joined to GF-PA66-10 mm achieved the second highest strength with a tensile-shear strength of 27 MPa and peel load of 3 MPa. The cw laser structuring takes a few seconds per square centimeter, the CLPs a few minutes [11]. So, CLP structuring requires long cycle times and is therefore from a process engineering point of view from minor interest for high-volume production. [10]

Engelmann C. et al. [12] describe the cw laser structuring process in more detail. In their study, they investigated the influence of a variation of structuring parameters on bond strength of hybrid joints made of P260 steel and TP-FRPC as well as XSG steel and TP-FRPC. The TP-FRPC was a glass fiber fabric reinforced PA6.6 with a thickness of 1.5 mm (GF-PA66-1.5 mm). The best cavity shape was achieved by using a scan speed of the laser of 10 m/s, 4 repetitions and a structuring distance of 0.3 mm. The tensile shear strength of GF-PA66-1.5mm joined to P260 is 20.47 MPa and 17.8 MPa for XSG joined to GF-PA66-1.5 mm.

Arai S. et al. [13] show that a surface pretreatment of stainless steel (SUS304) by oxygen-plasma surface pretreatment in combination with UV-ozone-, oxygen plasma- or nitrogen plasma surface-treated cyclic olefin polymers (COP) lead to significant higher bond strengths compared to untreated COP in hybrid laser welding. When joining untreated COP with untreated or plasma treated SUS304, no hybrid joint was achieved. With the surface pretreatments of the COP, joint strengths between approx. 8 and 9 MPa were achieved. Ari S. et al. assume that oxygen functional groups are generated by the surface pretreatment of COP, allowing a bond between SUS304 and COP.

Rodriguez-Vidal E. et al. [14] investigated the influence on bond strength of different laser structure geometries in steel (HC420LA) joined with glass fiber reinforced polyamide 6 (GF30-PA6). The joining method used was laser conduction joining by heating the steel with a cw fiber laser. By testing the welded t-joints, it was found that the highest bond strength was achieved with the shortest distance between the cavities of the laser structure. Different alignment angles of the structuring show different types of failure. A significant influence of the structuring angles on bond strength was not determined. Lambiase F. et al. [15] investigated the influence of process parameters of friction assisted joining on bond strength of a hybrid structures made of laser-cross-structured aluminum (AA5053) and polyvinyl chloride (PVC). It was shown that the laser structuring lead to higher bond strengths than hybrid

joints of untreated aluminum and PVC. With optimized process parameters of the joining process (plunging force $F_z = 320$ N and Dwell time $Dt = 20$ s), a bond strength of 16.1 MPa was achieved, which is approx. 75 % of the bond strength of the PVC-PVC joints.

Heckert A. et al. [16] investigated the influence of laser-induced nanoscopic (structure height < 100 nm), microscopic (structure height 100 nm – 200 μ m) and macroscopic (structure height > 200 μ m) surface structures in aluminum (EN AW 6082) on bond strength of welded hybrid joints. The glass fiber reinforced TP-FRPC were short fiber reinforced polyamide 6 (GF15-PA6; fiber mass content 15 %), long fiber reinforced polyamide 66 (GF50-PA66; fiber mass content 50 %) and endless fiber reinforced PBT (GF60UD-PBT; fiber mass content 60 %). The joining process was heat-conduction joining (HCJ) using a diode laser in the wavelength of 808 nm. The microstructuring achieved the highest bond strength for GF15-PA6 with approx. 24 MPa and for GF-50-PA66 with approx. 35.5 MPa. For GF60UD-PBT the highest bond strength of approx. 37 MPa was achieved with a nanoscopic structure.

The studies presented provide an overview of used surface pretreatments. It was shown that nanoscopic surface pretreatments (structure height < 100 nm) in particular lead to high bond strengths. However, nanostructuring has the disadvantage that the structuring time is very long or the process design is very complex [11]. Cw laser induced surface structuring has the advantage that high structuring speeds can be realized. This advantage is of high interest for industrial large scale production and was therefore chosen for the study presented here.

2.1 Induction Heating and Welding

In induction heating, electro conductive materials (ECM) are heated as a result of induced electromagnetic alternating fields (EMF), as shown in Figure 1. The high-frequency EMF is generated around the induction coil when an alternating current flow through it, generated by a high-frequency inverter. The alternating EMF is induced without physical contact into the ECM. The EMF leads to a heating by resistance losses and, in the case of ferromagnetic ECM, additionally due to hysteresis losses. When welding TP-FRPC with TP-FRPC, the ECM are either the reinforcement structure (e.g. carbon fibers) or a welding filler, which is an ECM and placed in the joining zone.

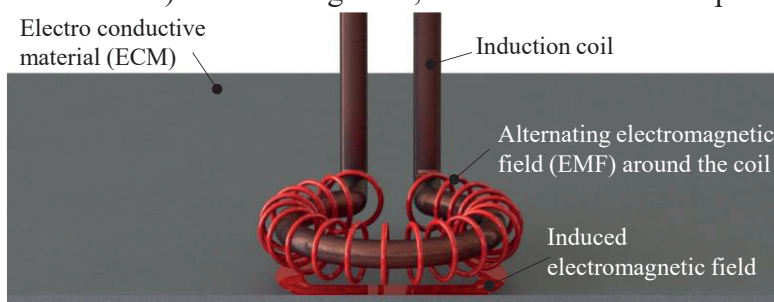


Figure 1: Physics of induction heating

In hybrid induction welding, the metallic joining partner acts as a heating element. When the melting temperature of the TP-FRPC at the interface to the metal is exceeded, the molten polymer is pressed into the cavities of the metal due to the simultaneously applied consolidation pressure. After cooling and thus a solidification of the polymer, the polymer in the cavities act as a link between TP-FRPC and metal. An adapted surface pretreatment of the metals enhances the bond between the different materials. The surface pretreatment can take place by laser, resulting in nano-, micro- or macroscopic structuring or mechanical by grinding or milling. Discontinuous induction welding is a quasi-static pressure welding process. A consolidation force is applied on the joining partners during heating and cooling. The force ensures an intimate contact, which benefit a bond between the materials.

3 Materials and Surface Pretreatments

Zinc coated 1.0338 steel, which is a common steel for deep-drawing in the automotive industry, was used as metallic joining partner. The steel sheets were surface pretreated by laser, as described in [12], resulting in different cavity shapes. The laser structuring in line pattern perpendicular to the load direction of 1.0338 was generated by a water cooled IPG 1000 W single-mode cw fiber laser. The focusing optic has a focal length of 330 mm, the resulting spot diameter was 40 μm . In order to investigate the influence of the zinc coating on joint strength, the laser surface pretreated 1.0338 specimen were dezincing (DZ) in 30 % sodium hydroxide solution for 72 h. Table 1 shows a summary of the materials and surface pretreatments used.

Table 1: Used steel sheets and surface pretreatments

Steel joining partner				Sketch of specimen
Acronym	Material	Surface pretreatment	Distance	
		Angle		
LS0.3 -45°	1.0338 Zinc coated	$\alpha = -45^\circ$	0.3 mm	<p>The sketch shows a side view and a lower view of a 1.0338 Lap-shear specimen. The side view shows a laser-structured surface with a structuring distance of 0.3 mm and a height of 1 mm. The angles are labeled as -45°, -30°, 0°, +30°, and +45°. The lower view shows a joining zone with a width of 25 mm and a length of 100 mm, with a distance of > 12.5 mm from the end to the start of the joining zone. The load direction is indicated by an arrow pointing left.</p>
LS0.3 -30°		$\alpha = -30^\circ$	0.3 mm	
LS0.3 0°		$\alpha = 0^\circ$	0.3 mm	
LS0.3 30°		$\alpha = +30^\circ$	0.3 mm	
LS0.3 45°		$\alpha = +45^\circ$	0.3 mm	
LS0.3 0°	1.0338	$\alpha = 0^\circ$	0.3 mm	<p>The sketch shows a side view and a lower view of a 1.0338 Lap-shear specimen. The side view shows a laser-structured surface with a structuring distance of 0.3 mm & 0.6 mm and a height of 1 mm. The angle is labeled as 0°. The lower view shows a joining zone with a width of 25 mm and a length of 100 mm, with a distance of > 12.5 mm from the end to the start of the joining zone. The load direction is indicated by an arrow pointing left.</p>
LS0.6 0°	Zinc coated	$\alpha = 0^\circ$	0.6 mm	
LS0.3 0°DZ	1.0338	$\alpha = 0^\circ$	0.3 mm	
LS0.6 0°DZ	Dezincing	$\alpha = 0^\circ$	0.6 mm	

Glass fiber reinforced polyamide 6 (GF-PA6) from BondLaminates, trade name Tepex ® dyalite 102-RG600(4) with a thickness of 2 mm, was used as TP-FRPC. The melting temperature of the Matrix is 220 °C, the reinforcement was glass fiber fabric, area weight: 600 g/m² and the fiber volume content 47 %.

4 Experimental Set-Up and Test Execution

In order to investigate the influence of surface structuring on bond strength, lap shear test specimens were manufactured according to DIN EN 1465. A test rig for discontinuous induction welding was used to weld the specimen. The main components of the test rig are a high-frequency inverter (True-Heat HF 5010 by TRUMPF) which is connected to the induction coil, a pneumatic press, an air nozzle for specimen cooling, a positioning tool on which the lap shear specimens are joined and a consolidation stamp in which the induction coil is located. The experimental set up is shown in Figure 2.

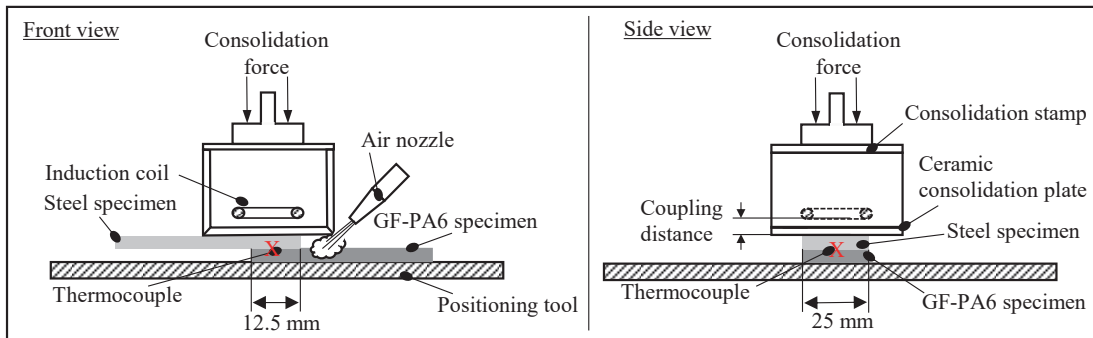


Figure 2: Experimental set-up discontinuous induction welding

The specimens were cleaned before welding in order to avoid influences such as contamination of the test specimens by oil or particle residues on the pretreated surface. For this, the surface pretreated metal specimens were first put in an ultrasonic bath for 15 minutes. In order to remove grease, the cleaning agent Ticopur TR7 was added to the ultrasonic bath. The TP-FRPC were not cleaned in an ultrasonic bath due to their hydrophilic matrix properties. They were dried in an oven at 80 °C overnight according to the data sheet. Both, the surface-pretreated metal sheets and the TP-FRPC were wiped with isopropanol right before welding. After cleaning, the specimens were fixed to each other with an overlap length of 12.5 mm using polyimide adhesive tape to avoid any slipping during joining. In the overlap, i.e. the joining zone, a thermocouple (Type E) was placed, which measures the temperature during the joining process. The thermocouple remains in the joining zone after welding. The thermocouple has almost no influence on the bond strength, due to the very small wire diameter in relation to the height and width of the structuring. After preparing the test specimens, they are placed on the positioning tool underneath the consolidation stamp. When the welding process starts, the consolidation stamp with inductor moves onto the test specimens and applies the consolidation force during the entire process time. The process diagram of induction welding is shown in Figure 3.

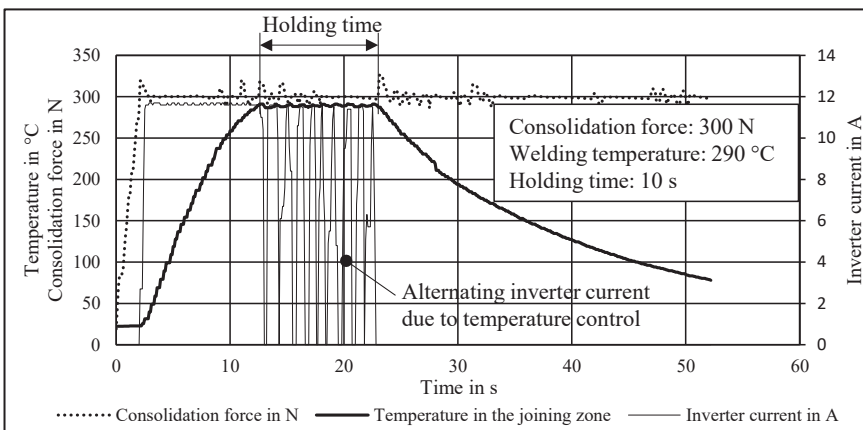


Figure 3: Process diagram induction welding

When the consolidation force is applied, the HF inverter switches on and an alternating field heats up the steel specimen. The metal sheets were heated until the welding temperature was reached, then the welding temperature was kept constant for 10 s. Thus, a homogeneous temperature distribution is achieved due to the heat conduction properties of the metal. After 10 s, the specimens were cooled by compressed air via an air nozzle. All hybrid specimens, investigated in this study, were joined according to the process flow shown in Figure 3.

In the first part of the study, the influence of the structuring angle on bond strength of the hybrid joints was investigated. Structuring angle means the angle between the surface and the structuring depth. An angle of 0° shows a groove perpendicular to the surface. Positive angles are oriented in direction of the later load direction. For this, lap shear test specimens were manufactured on the discontinuous induction welding test rig. Six lap shear test specimens were welded of each surface structure, five specimens for a statistically verified determination of the lap shear strength and one specimen for a micrograph.

In the second part of the study the influence of the optional zinc coating on the joint strength was investigated. After dezincing, the test specimens were cleaned in the same way as the specimens to examine the structuring angle. This ensures that residues of the sodium hydroxide solution do not affect the test results.

5 Results

The results of the lap-shear tests to examine the influence of the structuring angles are shown in Figure 4. The welding temperature, consolidation force, holding time, inverter power and specimen position were identical in each test.

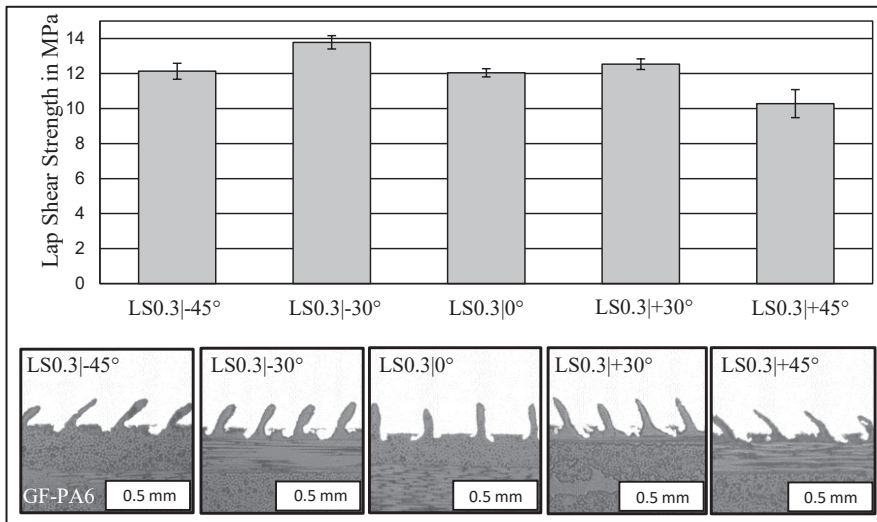


Figure 4: Influence of structuring angle on bond strength

The highest bond strength of 13.78 MPa was achieved using LS0.3|-30° and the lowest of 10.28 MPa using LS0.3|+45°. One reason for this may be that the polymer in the cavities of the laser structuring is more easily pulled out of the cavities during mechanical testing. Positive structuring angles may increase the pull-out effect of the polymer out of the cavities. The decrease in lap shear strength at a structuring angle of -45° can be explained by the peak angle, causing the polymer to be sheared off at the cavity edge. Furthermore, the cavities of the -45° structuring and +45° structuring are not as

wide, resulting in less polymer being able to carry the load during mechanical testing. As a result, a structuring angle of 0° seems to be a good compromise and works in all load directions equally.

In addition to the influence of the structuring angle, the influence of the structuring distance of 0.3 (LS0.3| 0°) and 0.6 mm (LS0.6| 0°), with and without a zinc coating on the bond strength was investigated. The results are shown in Figure 5.

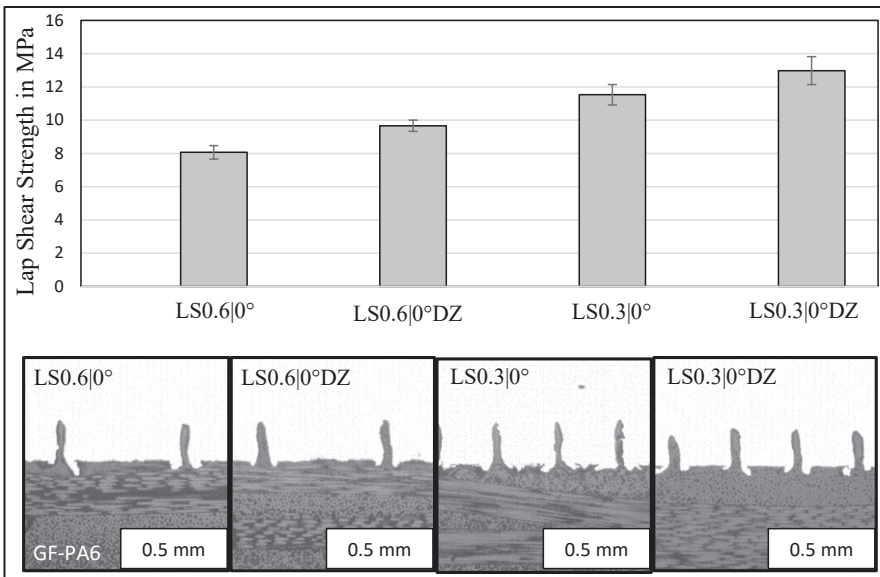


Figure 5: Influence of structuring angle and zinc-coating on bond strength

In both investigated structuring distances, the zinc coating reduces the lap shear strength of the hybrid joint. Furthermore, a structuring distance of 0.3 mm leads to a higher bond strength due to the higher number of cavities, which is the result of more positive fits between steel and polymer. The bigger steel surface of the LS0.3| 0° compared to LS0.6| 0° lead to more physical bonds at the molecular level, resulting in higher bond strength. The micrographs in Figure 5 show no difference between zinc coated and dezincd 1.0338. The higher bond strength of the dezincd hybrid joints indicates that better physical bonds are formed at the molecular level, resulting in higher bond strengths.

6 Summary

During the state of the art screening it became evident that the type of surface pretreatment in this study was also used for several studies. This is mainly due to the advantages of the velocity of the surface structuring process, the repeatability of the structuring results and the reliability of the structuring process.

It could be shown, that the structuring angle has an influence on the bond strength of hybrid joints. There is a difference of 12.6 % between the highest bond strength of 13.78 MPa using LS0.3| 30° and the bond strength of 12.04 MPa using LS0.3| 0° . However, a load dependent orientation of the structuring angle of the cavities is of minor meaning in the design of the hybrid joint. Particularly since load cases acting only from one direction are almost never encountered in practice. Similar to the results shown by Rodriguez-Vidal E. et al. [14] using laser conduction joining, it could be determined that a structuring angle has only a minor influence on the bond strength using induction welding, also.

A significant effect was found in the influence of the zinc coating on the hybrid joints. With a structuring distance of 0.3 mm in the steel sheets, the joint strength is 11.2 % higher with dezincing 1.0338. At a structuring distance of 0.6 mm the joint strength of the hybrid joints is 16.5 % higher with the dezincing 1.0338. The influence of the zinc coating on the bond strength in hybrid joining of steel with TP-FRPC has not been investigated previously, known to the authors.

7 Acknowledgements

This study has been conducted in the frame of the research project “FlexHyJoin”, funded by the Horizon 2020 Research and Innovation Programme of the EU, funding Code No. 677625.

8 References

- [1] Regulation (EU) 2019/631 of the European Parliament and of the Council setting CO₂ emission performance standards for new passenger cars and for new light commercial vehicles, and repealing Regulations (EC) No 443/2009 and (EU) No 510/2011, *Official Journal of the European Union*, 23 April **2019**.
- [2] H. Seidlitz, F. Kuke und N. Tsombanis, „Advanced joining technology for the production of highly stressable lightweight structures, with fiber-reinforced plastics and metal,“ *Technologies for Lightweight Structures - Special issue: 3rd International MERGE Technologies Conference (IMTC)*, pp. 54-67, 21-22 September **2017**.
- [3] S. Weidmann, M. Hümbert und P. Mitschang, „Suitability of thickness change as process control parameter for induction welding of steel/TP-FRPC joints,“ *Advanced Manufacturing: Polymer & Composites Science*, pp. 55-68, 2 April **2019**.
- [4] S. Weidmann und P. Mitschang, „Influence of Welding Temperature and Weathering on Inductive Welded Hybrid Joints Made of Steel and TP-FRPC,“ *22nd Symposium on Composites - Key Engineering Materials (Volume 809)*, pp. 217-224, June **2019**.
- [5] P. K. Bajpai und I. Singh, Reinforce Polymer Composites - Preprocessing, Characterization and Post Life Cycle Assessment, Weinheim: Wiley-VCH, **2019**.
- [6] A. Pramanik, A. K. Basak, Y. Dong, P. K. Sarker, M. Uddin, G. Littlefair und A. Dixit, „Joining of carbon fibre reinforced polymer (CFRP) composites and aluminium alloys – A review,“ *Composites: Part A*, pp. 1-29, 10 June **2017**.
- [7] S. Weidmann, V. Popow, J. Eckstaedt und C. Engelmann, „Production Cell for Fully Automated Joining of Hybrid Components,“ *Lightweight Design worldwide - 6/2018*, 01 12 **2018**.
- [8] G. Meschut und F. Augenthaler, „Hybridfügen von Mischbaustrukturen aus faserverstärkten Kunststoffen mit metallischen Halbzeugen,“ *Laboratorium für Werkstoff- und Füge-technik, Universität Paderborn*, **2015**.
- [9] T. Lindner, E. Saborowski, M. Scholze, B. Zillmann, Lampke und Thomas, „Thermal Spray Coatings as an Adhesion Promoter in Metal/FRP Joints,“ *MDPI Metals* **2018**, *8*, 769, pp. 1-10, 27 September **2018**.

- [10] J. Eckstädt und J. Rauschenberger, „Laser joining of textured metal and plastic components,“ *Lasers in Manufacturing Conference 2017*, **2017**.
- [11] C. Engelmann, A. Rösner, A. Olowinsky und V. Mamuschkin, „Mikrostrukturen zum lasergestützten Fügen von Kunststoff und Metall,“ *DVS Congress 2013 - Große Schweißtechnische Tagung*, p. 179, 16.-21. September **2013**.
- [12] C. Engelmann, D. Meier, A. Olowinsky und M. Kielwasser, „Metal meets Composite - Hybrid Joining for Automotive Applications,“ *Lasers in Manufacturing Conference 2015*, **2015**.
- [13] S. Arai, Y. Kawahito und S. Katayama, „Effect of surface modification on laser direct joining of cyclic olefin polymer and stainless steel,“ *Materials and Design*, pp. 448-453, 13 March **2014**.
- [14] E. Rodríguez-Vidal, C. Sanz, C. Soriano, J. Leunda und G. Verhaeghe, „Effect of metal micro-structuring on the mechanical behavior of polymer-metal laser T-joints,“ *Journal of Materials Processing Technology*, pp. 668-677, 28 October **2015**.
- [15] F. Lambiase, A. Paoletti, V. Grossi und A. Di Ilio, „Friction assisted joining of aluminum and PVC sheets,“ *Journal of Manufacturing Processes*, pp. 221-231, 12 August **2017**.
- [16] A. Heckert und M. F. Zaeha, „Laser Surface Pre-treatment of Aluminium for Hybrid Joints with Glass Fibre Reinforced Thermoplastics,“ *Physics Procedia 56 - 8th International Conference on Photonic Technologies LANE 2014*, pp. 1171-1181, **2014**.

Thermal joining of metal-polymer hybrid structures by using conventional welding processes

A. Haelsig¹, W. Georgi¹, E. Brueckner², P. Thieme¹, M. Gehde²

University of Technology Chemnitz, ¹Professorship of welding technologies, ²Professorship of Plastics Engineering

1 Introduction

Hybrid composites of metal and polymer enable adapted component requirements, such as an improved load transmission, an increased stiffness, an optimized corrosion behavior as well as an adapted damping capacity. However, these metal-polymer hybrid structures are also convincing due to their high material and operational demand efficiency.

Joining the individual components layer-by-layer (overlap joints) can be classified in adhesive bonding, welding-based techniques, mechanical fastening as well as hybrid joining technologies like over molding or combinations of the individual techniques above [1, 2]. In this regard, several welding processes were investigated or adapted for joining metal-polymer hybrid structures as well. Feasible strategies are laser welding [3, 4, 5, 6], friction stir welding [7], friction lap welding [8], friction spot welding [1], ultrasonic welding [9, 10] or induction welding [5, 11]. Another approach for joining the components layer-by-layer are mechanical fastening technologies like ultrasonic riveting [12], blind riveting [13], clinching [14] or screwing. However, in contrast to the layer-by-layer joining, the aim of the present paper was to investigate the joining of already existing hybrid structures. Regarding the manufacturing of such hybrid composites the current research shows some studies by using only one system and process. Examples for process combinations are hydroforming and injection molding as well as deep drawing and injection molding [15, 16]. The studies in [17] also give some information about the sheet metal forming by using the plastic melt as active fluid medium. In this context, the joining technologies are confronted with new challenges, as the individual components require material-specific and aligned thermal-rheological conditions for joining these hybrid parts simultaneously. The present paper gives an overview about the applicability of laser beam and TIG welding for joining these metal-polymer hybrid structures. The idea behind is to ensure a material-compatible joining of the inner polymer layer by using heat conduction effects during the joining of the metallic components.

Thermal joining methods such as laser beam welding, micro-plasma welding or TIG welding, as well as pressure welding methods such as friction welding or friction stir welding can be used for this purpose. For laser welding of hybrid components, a two-stage process is described in [18], in which in a first step the metal component is first structured by means of a laser beam and in a second step heated by means of a diode laser. The plastic, softened by heat conduction, then penetrates these structures and bonds with them. The same process principle is described in [19, 20]. Here, the structure is introduced into the metal surface by means of the "Remote Ablation Cutting (RAC)" process. In [21] results regarding laser welding of the aluminum alloy 7075 and the laser beam transparent plastic PET are presented. In all cases, however, it is a matter of an overlap joint, in which the cohesion is achieved by material bonding. In [22] the "Electro-Element Joining (EEF)" is presented, which uses resistance welding to weld an additional metallic joining element through the plastic joining partner onto the metal joining partner. The VDMA Guide to Technologies in Hybrid Lightweight Construction [23] lists various fusion welding processes for joining metal to metal. However, no processes are mentioned in which metal-plastic hybrid components are joined in butt joints.

The project starts at that level and will bring innovations to the topic of a targeted process regulation as well as an adjusted part design to join metal-polymer hybrids.

2 Scientific approach

The aim of the investigations was to analyze the applicability of conventional welding processes for the hybrid joining of metallic as well as polymeric partners within one process. For this purpose, the typical welding processes for the joining of thin metal components, i.e. laser beam welding and tungsten inert gas welding (TIG), were used. In order to be able to assess the applicability of the welding processes for hybrid structures, the process-dependent heat-affected zone was investigated as a function of the selected process parameters.

For this purpose, joint welds were carried out on $t = 2.00$ mm thick steel sheets of the material S235 (1.0038) with polypropylene (PP) plastic samples of the thickness $t = 4.00$ mm positioned directly below. The length of the two metal samples was 150 mm and the width 80 mm. The connection was made in the butt joint without a gap. The solid plastic specimen below also had a length of 150 mm and a width of 35 mm. The dimensions and material arrangements are shown in Figure 1.

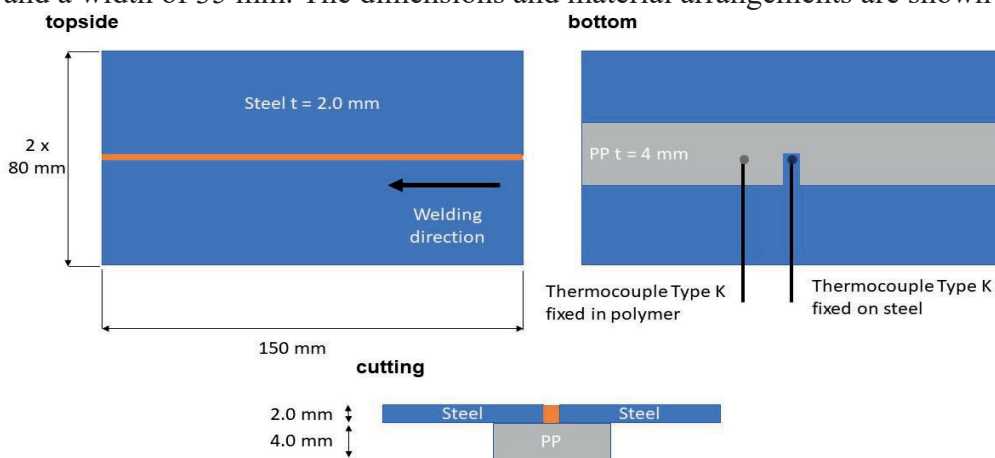


Figure 1. Dimension and system for joining analysis between metal and polymer

The specimens were clamped and fixed on a universal clamping table. On the steel side at the underside of the component thermocouples of the type K were attached 2 mm from the joint edge. On the plastic side, a type K thermocouple was also melted in directly below the weld seam 2 mm below the upper level of the plastic. The welding process handling was automated. In the case of TIG welding, a 6-axis robot was used and in the case of laser welding, a Cartesian CNC system was used. The welding parameters used are listed in Table 1.

Table 1. Parameter for welding process with laser beam and TIG

Laser beam	parameter	TIG-welding
TruDisc NdYAG	<i>type</i>	EWM Tetric 300
200 mm focal length	<i>distance</i>	1.5 mm to electrode
2000 W	<i>power</i>	240...1220 W
adapted to process	<i>welding speed</i>	30 cm/min
125 mm	<i>weld seam length</i>	125 mm
-	<i>electrode</i>	d = 3.2 mm, 40 °
-	<i>shielding gas</i>	10 l/min Argon

In laser beam welding, the laser beam power was kept constant and the focus position and welding speed were systematically varied. In TIG welding, the welding speed was kept constant and the welding current was adjusted. Both methods enabled the analysis of the influence of the energy per unit length on the weld seam quality as well as the thermal influence on the metal and polymer.

3 Results and Discussion

The test matrix (Table 1) described in the experimental description was systematically processed for both welding processes and the results were analyzed and evaluated. Depending on the system, the heat input as well as the heat-affected zones (HAZ) that are formed differ greatly between laser beam and TIG welding. Due to the different heating methods as well as the up to 1000 times higher power density per area of laser beam welding, the weld seam in the metal component is narrower and the heat input considerably lower. Figure 2 shows the temperature-time curve of the analyzed connection zone between metal and plastic (measured on the metal side). The peak temperature of TIG welding was 810 °C and 375 °C for laser beam welding. In relation to the melting temperature of the polypropylene used as the plastic partner, which melts at a temperature of 160 °C, this temperature threshold is exceeded for almost 49 s in TIG welding and approx. 10 s in laser beam welding. As a result, for laser welding the directly adjacent polymer is subjected to less thermal stress on the one hand, but on the other hand the melting zone that forms is smaller. While the melted area in the plastic is 6.2 mm² in TIG welding, this is 1.5 mm² in laser beam welding, when the energy by unit length is comparable with a level of 0.70 KJ/cm. This goes hand in hand with the reduction of the weld penetration of 0.61 mm (TIG) and only 0.26 mm for laser beam welding.

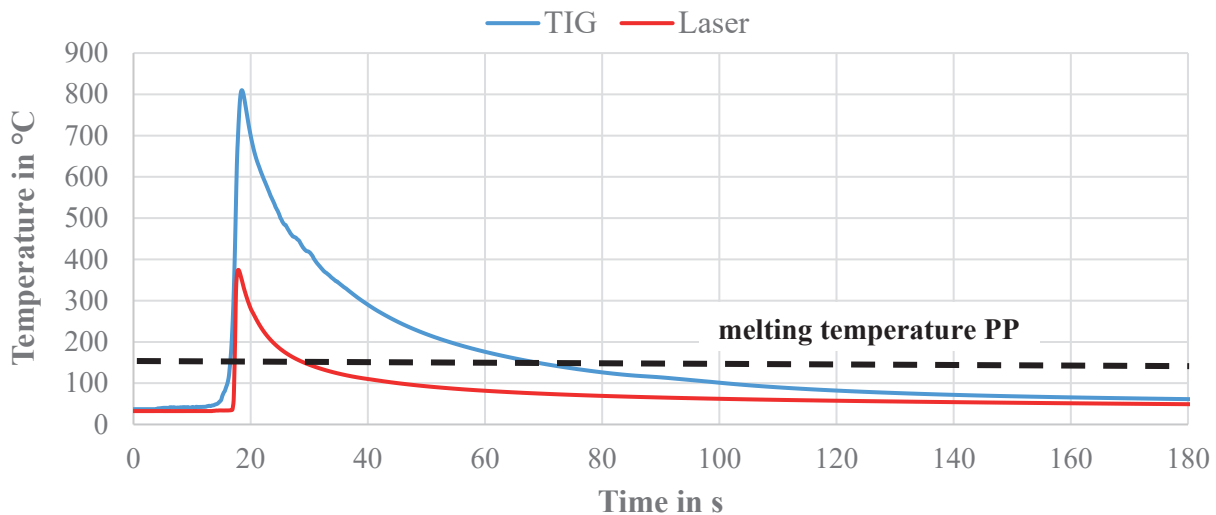


Figure 2. Temperature-time curve for full penetration of metal parts via TIG- and Laser welding

The severely limited thermal resistance of the plastic joining partner provides limiting conditions. The melting temperature of the PP used is $T_m = 160\text{ °C}$, while the steel joining partner melts at about $T_m = 1500\text{ °C}$. Additionally the polymer has a low specific thermal conductivity. This is $\lambda = 0.23\text{ W/(m}\cdot\text{K)}$ and that of the steel material $\lambda = 53\text{ W/(m}\cdot\text{K)}$.

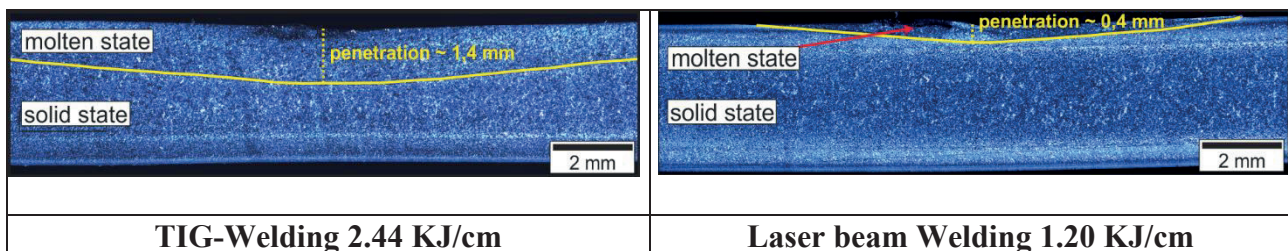


Figure 3. Microscopic analysis (polarized) of the plastic part shown by the cross section of the molten and solid state after TIG and Laser beam welding

As a result, the necessary high heat of the metal partner at the contact zone between metal and plastic is only slowly dissipated and transported into the interior of the plastic. In correlation to this, a maximum depth of melting of the plastic of 1.4 mm in TIG welding and 0.4 mm in laser beam welding was achieved and is shown in Figure 3 by analyzing the materials morphology. Due to the different cooling rate between injection molding and joining, the heat-affected zone (HAZ) shows a different morphological expression. A degradation of the polymer in the HAZ area could not be detected by OIT (oxidation induction time) measurements for both welding methods. However, these analyses with regard to the sample preparation proved to be difficult due to the small layer thicknesses and should be considered in more detail in further investigations.

The analysis of the metallic cross-sections shows that in TIG welding, both the welding depth and the heat-affected zone (HAZ) increase continuously with increasing energy per unit length. The through-welding of the $t = 2.00$ mm thick steel material was only carried out at an energy per unit length of almost 2.50 KJ/cm. In comparison, laser beam welding was able to achieve through-welding with an energy per unit length of 0.60 KJ/cm (Figure 4).

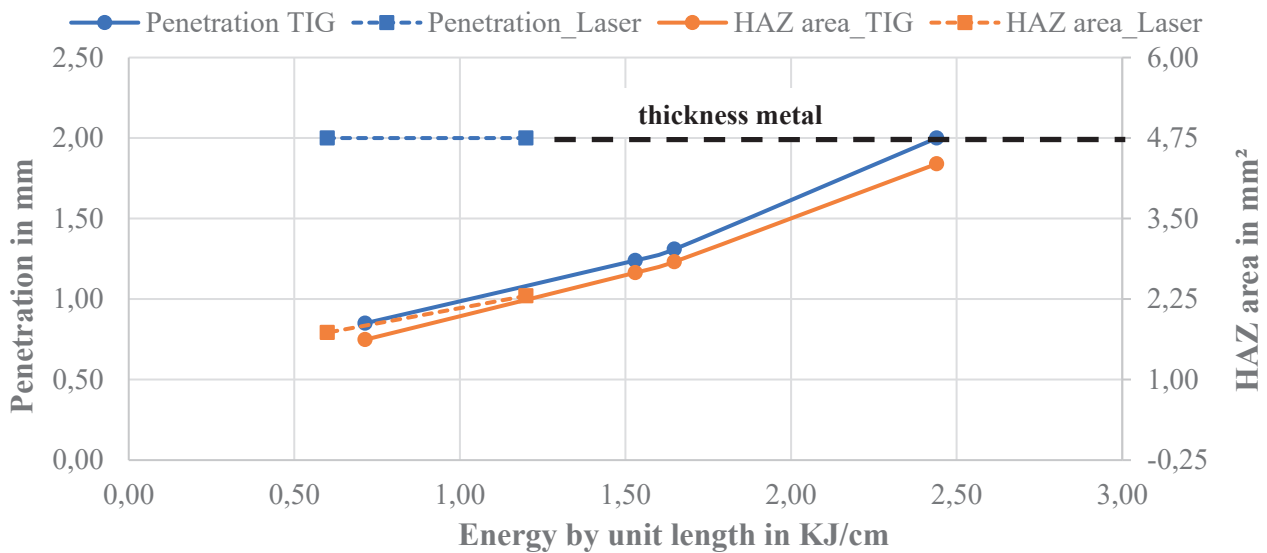


Figure 4. Analysis of the HAZ of the metal part for TIG- and Laser welding

In contrast, the molten area (HAZ area) remained at a similar level in the direct comparison of the two processes when the reference to the same energy per unit length is used (left area of Figure 5).

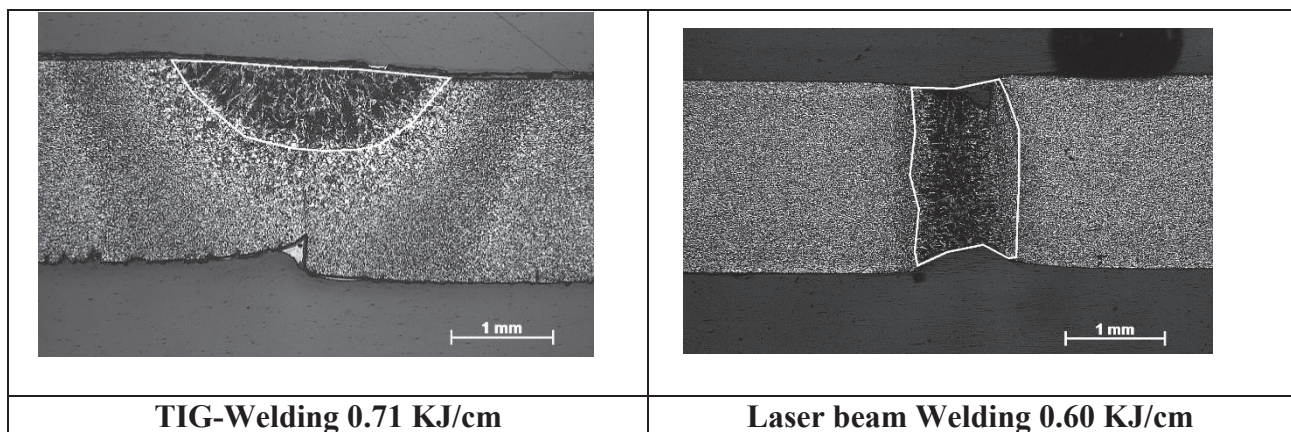


Figure 5. Cross section of the molten and solid state metal after TIG and Laser beam welding

Looking at the energy per unit length level of around 0.70 KJ/cm the molten area of the steel was around 1.60 mm for TIG and laser beam welding. However, the identical energy per unit length resulted in different weld seam geometries. In TIG welding the weld seam is rather wide and flat and in laser beam welding it is narrow and deep, see Figure 5. Analyzing the penetration and HAZ of the polymer (Figure 6) it was not possible to melt the whole polymer thickness with the joining heat of the connected metal sheets. With a comparable energy per unit length level of around 0.70 KJ/cm the HAZ was around 1.5 mm² (laser beam) and 6.2 mm² (TIG). So the width is wider and energy intensity is lower when using TIG welding for joining. To realize a good connection of metal and in parallel with the plastic sheets together it sounds to be better to prefer TIG-welding because the energy input in the polymer is more intensive.

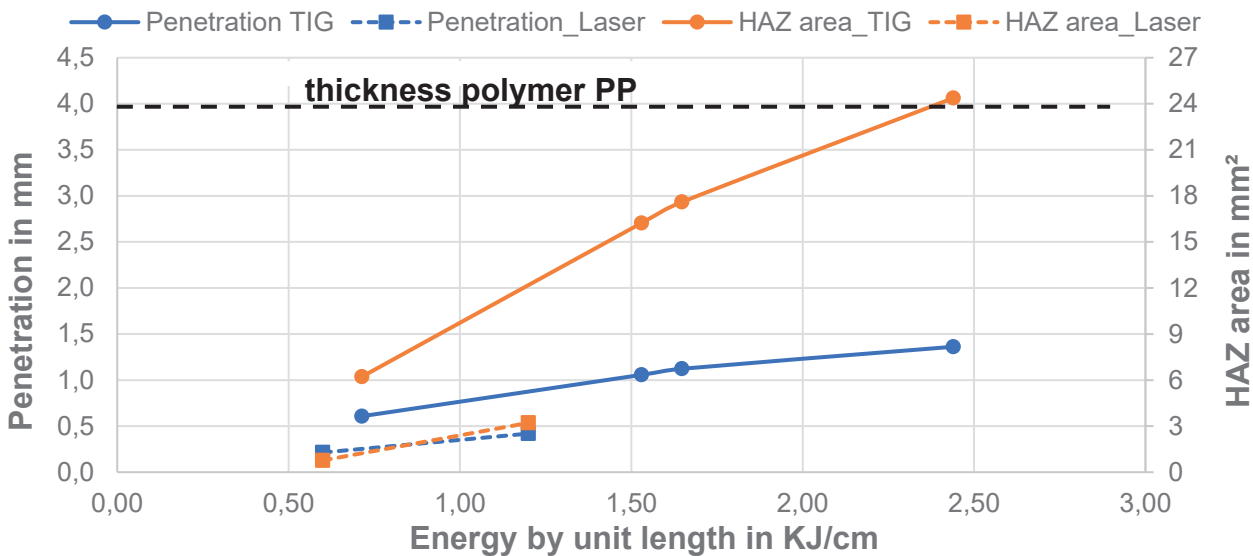


Figure 6. Analysis of the HAZ of the polymer part for TIG- and Laser welding

4 Conclusion

Direct joining of metal-polymer hybrids seems to be technologically feasible. The low heat conduction of the polymer and its low melting temperature are a relevant limiting condition. In parallel the metallic joining partner requires a temperature that is more than nine times higher in the case of steel for melting and subsequent joining. Summarizing the results of joining steel with polymer it is possible to join a 2,0 mm steel and a 1.5 mm polymer component (positioned below metal) completely via TIG welding in one run. Using laser beam welding the polymer component can only be about 0.5 mm thick. In the ongoing process it is worth to analyze the use of laser beam absorbing polymer to increase the penetration.

In order to solve this challenge innovative welding process adaptations, geometric applications in the area of the joining zone as well as investigations into suitable material pairings are required. For example, the difference between the melting temperatures of both material groups can be reduced to a difference factor of less than two by using aluminum ($T_m = 660\text{ °C}$) and PEEK ($T_m = 340\text{ °C}$). In addition, the mechanical and technological quality values of the hybrid joints and the influence of different joint preparations and local pressures have to be analyzed in the future.

5 Acknowledgments

This project is financed by the basic research fond of the University of Technology Chemnitz. This is a tax revenue on the basis of the budget adopted by the members of the parliament of Saxony.

6 References

- [1] Goushegir, S.M.: “Friction Spot Joining of Metal-Composites Hybrid Structures”; Ph.D. Thesis, TU Hamburg-Hamburg; 2015; ISSN: 2191-7833
- [2] Amancio-Filho, S.T.; dos Santos, J.F.: „Joining of Polymers and Polymer-Metal Hybrid Structures: Recent Developments and Trends”; *Polymer Engineering and Science*, p. 1461-1476; DOI: 10.1002/pen
- [3] Bergmann, J. P.; Stambke, M.: „Potential of laser-manufactured polymer-metal hybrid joints“, *Physics Procedia*; 39 (2012); p. 84-91
- [4] Cenigaonaindia, A.; Liébana, F.; Lamikiz, A.; Echegoyen, Z.: “Novel strategies for laser joining of polyamide and AISI 304”; *Physics Procedia*; 39 (2012); p. 92-99
- [5] Roesner, A.; Scheik, S.; Olowinsky, A.; Gillner, A.; Reisinger, U.; Schleser, M.: „Laser Assisted Joining of Plastic Metal Hybrids“, *Physics Procedia*; 12 (2011); p. 370-377
- [6] Rodriguez-Vidal, E.; Sanz, C.; Lambarri, J.; Renard, J.; Gantchenko, V.: „Laser joining of different polymer-metal configurations: analysis of mechanical performance and failure mechanisms“, *Physics Procedia*; 83 (2016); p. 1110-1117
- [7] Patel, A.R.; Dalwadi, C.G.: “A Review: Dissimilar Material Joining of Metal to Polymer using Friction Stir Welding (FSW)”; *IJSTE – International Journal of Science Technology & Engineering*, Volume 2, Issue 10, 04/2016
- [8] Liu, F.C.; Liao, J.; Nakata, K.: “Joining of metal to plastic using friction lap welding”; *Materials and Design*; 54 (2014), p. 236-244
- [9] Brueckner, E.; Georgi, W.; Gehde, M.; Mayr, P.: “Clinching and torsional ultrasonic welding – an innovative process combination for joining metal-polymer hybrid structures”, *AIP Conference Proceedings* 2055, 130003 (2019); <https://doi.org/10.1063/1.5084900>
- [10] Flock, D.; Haberstroh, E.; Bobzin, K.; Schläfer, T.; Warda, T.; Kutschmann, P.: „Ultrasonic welding of hybrid metal-plastic components with flame spraying of adhesion layer“, *Zeitschrift Kunststofftechnik – Journal of Plastics Technology*; Carl-Hanser-Verlag; 7 (2011)
- [11] Ramarathnam, G.; Libertucci, M.; Sadowski, M.M.; North, T.H.: “Joining of Polymers to Metal”; *Welding Research Supplement*; December 1992, p. 483-490
- [12] Brückner, E.; Friedrich, S.; Gehde, M.: „Ultrasonic upsetting – A new method of ultrasonic riveting to join hybrid material combinations“, *ANTEC 2015, Orlando, Florida, USA, March 2015*
- [13] F. Podlesak: „Entwicklung und Verifizierung eines vorlochfreien mechanischen Fügeverfahrens zum Verbinden von Leichtmetallen und Faser-Kunststoff-Verbunden“, *Dissertation 2017, ISBN 978-3-96100-016-6, Technische Universität Chemnitz*
- [14] W. Georgi: „Beitrag zum mechanischen Fügen von Metall-Kunststoff-Mischverbindungen“, *Dissertation 2014, ISBN 978-3-944640-15-0, Technische Universität Chemnitz*
- [15] Albert, A.; Drossel, W.-G.; Zorn, W.; Nendel, W.; Raithel, D.: “Process combination of hydroforming and injection moulding for the in-situ manufacturing of metal and plastic composite structures”, *Materials Science Forum*; 2015, Vol. 825-826, p. 522
- [16] Drossel W.-G., Lies C., Albert A., Haase R., Müller R., Scholz P.: “Process combinations for the manufacturing of metal-plastic hybrid parts”, *IOP Conference Series: Materials Science and Engineering*, Volume 118, Issue 1, 10 March 2016, Article number 012042, 18th Chemnitz Seminar on Materials Engineering, Chemnitz, doi:10.1088/1757-899X/118/1/012042
- [17] Tekkaya, A. E., Hussain, M. M., Witulski, J.: “The non-hydrostatic response of polymer melts as a pressure medium in sheet metal forming”, *Prod. Eng. Res. Devel.* 2012, p. 385-394
- [18] A. Munde: *Hybridbauteile: „Das Beste aus zwei Welten, Umformtechnik-Blech, Rohre“*, *Profile*, November 2012, Internet: https://www.umformtechnik.net/fachartikel/hybridbauteile-das-beste-aus-zwei-welten-%7C-b-r-p_21580_de/. Access: 13.01.2020
- [19] Wunderling, C., Meyer, S., M. FZäh, M. F.: „Thermisches Fügen von Metall-Kunststoff-Hybridverbindungen“, *Werkstattstechnik* Nr. 10, 2018, p. 708...715, Springer-VDI-Verlag GmbH & Co. KG, Düsseldorf
- [20] Rauschenberger, J., Cenigaonaindia, A., Keseberg, J., Vogler, D., Gubler, U., Liébana, F.: “Laser hybrid joining of plastic and metal components for lightweight components”, *Proceedings of SPIE - The International Society for Optical Engineering*, 2015, Conference Paper, ISBN 978-162841446-2, SPIE
- [21] Gisario, A., Mehrpouya, M., Pizzi, E.: “Dissimilar joining of transparent Poly(ethylene terephthalate) to aluminum 7075 sheets using a diode laser”, *Journal of Laser Applications*, No. 29, 2017, ISSN 1042346X, Laser Institute of America
- [22] Schwabe, F.: „Elektro-Element-Fügen: Leichtbaugerechtes & formschlüssiges Fügen von Hybrid-Bauteilen“, *Invention Store*, 2017, Internet: <https://www.inventionstore.de/angebot/4438/>. Access: 13.01.2020
- [23] VDMA-Arbeitsgemeinschaft Hybride Leichtbau Technologien (Hrsg.): *VDMA-Leitfaden Hybride Leichtbau Technologien – 31 Technologiesteckbriefe zu Fertigungs- und Fügeverfahren –2018*. Internet: https://lightweight.vdma.org/documents/266675/26503513/2018_07_04_Leitfaden_Erste_Aktualisierung_1530860642221.pdf/56a0360f-dd63-44ad-770d-249b624389a4/. Access: 13.01.2020

Determination of the mechanical properties of a sintered CFRP connection module joined by a thread forming screw

A. Marx¹, T. Hutsch², P. Schiebel¹, D. Feltin³, F. Hoffmeister⁴, A. Babbel⁴, A. Herrmann¹, T. Weißgärber²

¹Faserinstitut Bremen e.V., Bremen, ²Fraunhofer IFAM, Dresden, ³Hightex Verstärkungsstrukturen GmbH, Klipphausen, ⁴Schrauben Betzer GmbH & Co.KG, Lüdenscheid

Abstract

Multi-material designs of carbon fiber reinforced plastics (CFRP) and metals are used in a variety of applications. The joining between these two different materials is mostly done by conventional processes like adhesive bonding or mechanical joining elements (rivets and bolts). A new approach is the sintered connection module. It allows load introduction into the CFRP and joining between CFRP and metal. After a textile preforming process by the tailored fiber placement (TFP) technology a body of stainless steel is sintered locally on the textile using the powder metallurgical method of spark plasma sintering. Further processing with resin transfer molding (RTM) enables a CFRP part with a local steel body that assists joining by conventional metal techniques like screwing. This paper aims at the mechanical characterization of the sintered connection module. The specimens are tested under different quasi-static load conditions to evaluate load capacity and failure behavior. A M6 thread forming Pentaform screw is used as joining element. Additionally, CT images of the manufactured specimens are analyzed to identify the fiber structure inside the sintered metal. Metallography is used to examine the transition area between the carbon fibers and the sintered metal.

1. Introduction

The steadily increasing use of CFRP creates a need of new joining techniques. Adhesive bonding or mechanical joining, like riveting or bolts, are the most common techniques to join metal and CFRP. Mechanical joining especially leads to an increase of process steps in combination with weakening the composite due to drilling holes. This breaks the fiber continuity and increases the local stress.[1]

At the IGF project 17618 a combination of adhesive bonding and mechanical joining was investigated to join fiber reinforced plastics and metal.[2]

The KIT investigated the joining technology of embedded metal inserts in CFRP in the priority program 1712. The strength of this connection is influenced by the shape of the insert. Due to the design of the metal inserts only a connection on one side is possible.[3,4]

New joining techniques with less process time and steps and also less degradation of the composite material are needed. In the AiF ZIM Project “Sinterverbindung” (promotional reference number: ZF4139606EB7) a new approach in type of a sintered connection module was developed and investigated.

In 2015 a first approach for a sintered connection module was accomplished. Sintered bodies from aluminum and stainless steel were placed on textiles from carbon, glass and basalt fibers and integrated in CFRP laminates. In shear tests a strength of above 20 MPa was reached and the contact area between the upper and lower metal bodies was claimed to be responsible for the effective strength. Based on this work a European patent has been filed.[5,6]

In the current approach, the TFP technology is used to increase the strength of the notched CFRP specimens. By improving the fiber direction towards the load direction a notched composite reaches nearly the strength of an intact composite.[7,8]

A detailed process chain to manufacture the sintered connection module and an investigation of the strength between a sintered body of 4 mm height and a thread forming M6 Pentaform screw has already been investigated. An average load capacity of 11 kN could be reached. It was investigated that the sintered steel compacts during the thread forming process; this leads to an increase of hardness at the thread in the sintered body and shears off the flanks of the screw.[9]

2. Manufacturing

The TFP technology is used to produce a load optimized textile preform for the sintered connection. Teijin HTA40 E13 6K roving is fixed with the yarn Garment Dyeing 120, a Polyamide 6.0 yarn from Amann & Söhne GmbH & Co. KG. The TFP preform consists of 75 % fibers in tangential direction and 25 % fibers in radial direction. The center is left open with a diameter of 14 mm to ensure a continuous sintered body. The radial fibers form loops directed to center to align a form fitting connection with the sinter material, shown in Figure 1 a). In a textile preforming process the TFP preform is embedded between three lower and three upper carbon fiber layers of a non crimp fabric (NCF) with (0°/90° and 600 g/m²). The orientation of the layers is [0°/90°/45°/-45°/0°/90°]_s. To ensure a continuous sintered body, a hole with the diameter of 20 mm is in the NCF layers. For a better handling the NCF layers and the TFP preform are sewn together.

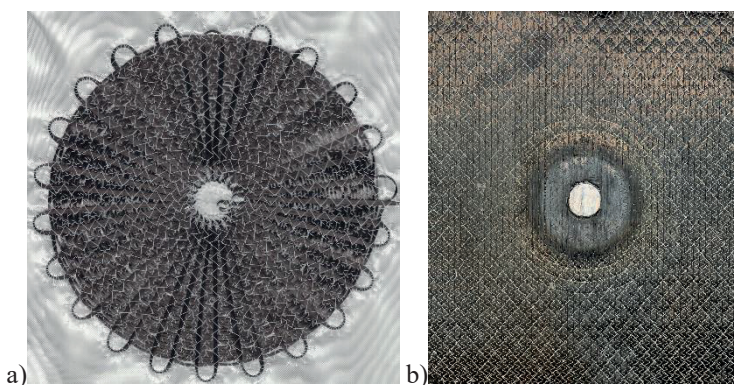


Figure 1: a) TFP preform; b) sintered hybrid preform

For the sintering process the used metal powder is ATMIX 316l PF 10F (mean particle diameter < 6.3 μm, EPSON ATMIX Corporation). The consolidation is done for each sample with Spark Plasma Sintering (SPS) technique (FCT-HP D 250/1, FCT Systeme GmbH). The metal powder and TFP preform are placed into the sintering tool setup according to Figure 2 a). The SPS setup is shown in Figure 2 b). After the consolidation process the sintered steel/CFRP connection module is removed from the sintering tools, shown in Figure 1 b).

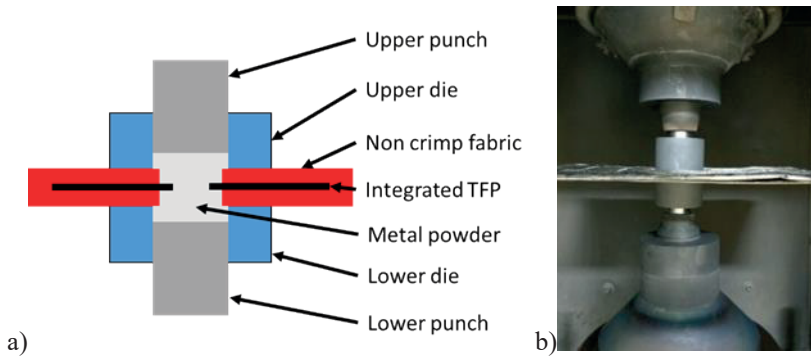


Figure 2: Consolidation of the steel/CFRP connection module; a) Schema of the tool setup; b) View in the sintering equipment

The specimens for the tests are plates with the dimensions of 240 x 240 mm and a height of 5 mm. The sintered body with a diameter of 30 mm is embedded in the center (Figure 3). The impregnation of the hybrid preform is done in the RTM process with the epoxy system Hexion RIMR 426 and the curing agent Hexion RIMH 435. The dry hybrid preform is placed in a RTM mold and heated in a Rucks KV 214 press. After the infiltration with resin, the specimens are cured at 80 °C for 120 minutes. Dependent on the test method a M6 thread forming screw of the type Pentaform is joint in the 5.5 mm diameter predrilled sintered body by a torque of 10 Nm.

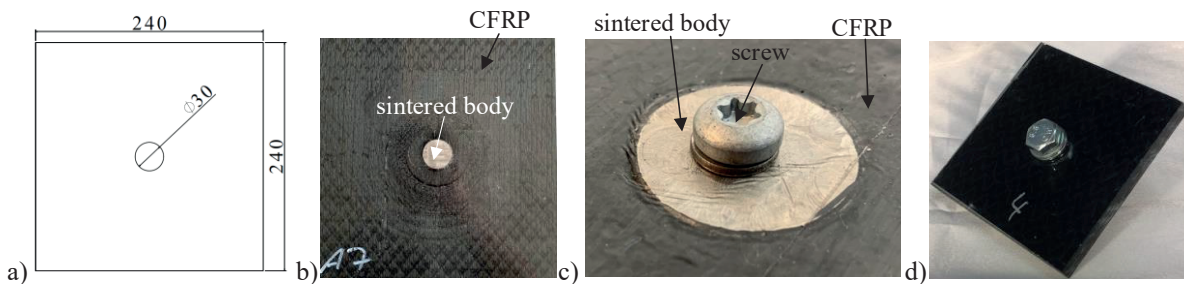


Figure 3: a) Dimensions of the specimen; b) exemplary picture of the used sintered CFRP specimen; c) sintered connection with joined M6 Pentaform screw; d) reference blind rivet nut with joint M6 screw

The fiber volume ratio (FVR) is determined by a wet chemical analysis. The TFP structure inside the laminate affects the local FVR. Within the TFP area, the FVR is 37 %. In the pure NCF area it is 34.7 %. As shown in the micrograph image (Figure 4), the sintered body is the highest position of laminate due to the integrated carbon fibers in the sintered body. In the closed chosen RTM mold no further compression of the textile is possible, which would lead to higher FVR. The transition area between the sintered body and the CRFP laminate indicates the compressed carbon fibers in the sintered body. This results in less sinter material and a change of the cross section for the sinter material.

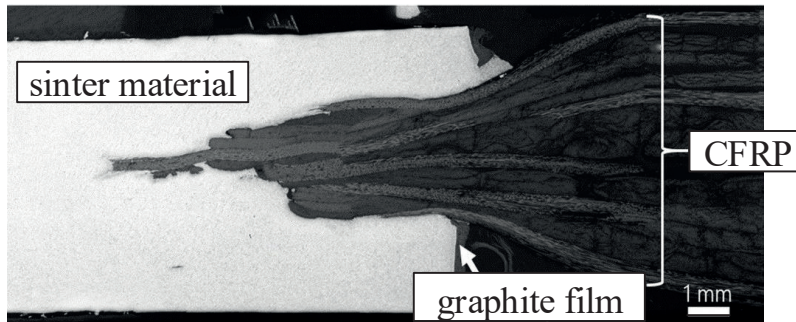


Figure 4: Micrograph image of the transition area between sintered steel and CFRP

Through computer tomography images (Figure 5) the position of the carbon fibers inside the sintered body can be considered. The fibers remain in the defined position and the center of the sintered body is fiber free for the joining with the screw. The top view demonstrates the loop shaped carbon fibers, filled with sinter material. The cross section shape of the sintered body is similar to a flat rivet with a continuous middle part and flat sides.

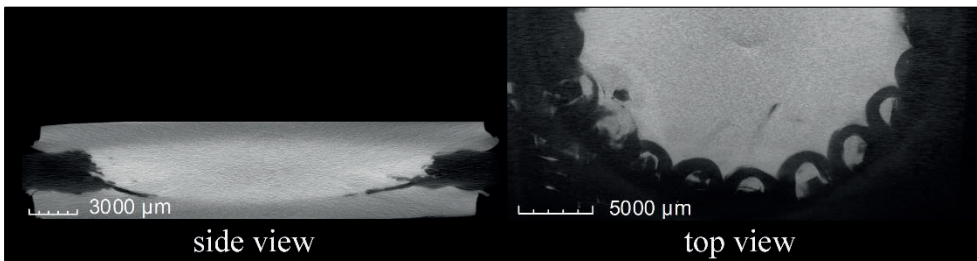


Figure 5: CT Image of the sintered connection module

3. Experiments

To determine the mechanical properties of the sintered connection module different quasi-static tests are conducted. The aim is to identify the load bearing capacity and the failure behavior of the sintered connection. The specimens are tested under shear and different push in loads. The tests are carried out on a universal testing machine Zwick Roell Z250 under the conditions of 23 °C and 50 % humidity. Due to the symmetry of the sintered connection module, only tests in one direction (push in) are carried out, to describe the mechanical behavior. To evaluate the results additionally reference tests of CFRP plates with the same composition of plies and blind rivet nuts with a joined M6 screw are performed.

3.1 Screw press out test

First screw press out test have already been conducted and described [9]. Due to an increase of the height of the specimens, the load capacity of the connection between the sintered steel and the M6 Pentaform screw could be increased to the same level as the blind rivet nut under tensile load. The average load capacity for the sintered body is 19,826 N at 0.8 mm displacement (Figure 6). The average load capacity for the reference blind rivet nuts depends on the load direction. Under tensile load it reaches 18,957 N at 2.8 mm displacement and under pressure the load drops down to 7,336 N between 2 and 4 mm displacement.

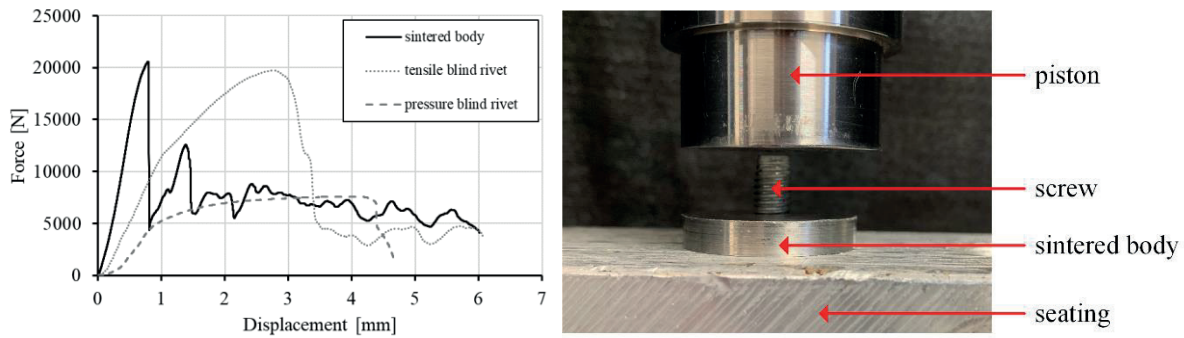


Figure 6: Typical load displacement diagram and picture of the test set up for the screw press out tests

The failure of the screw in the sintered body occurs by shearing of the flanks of the screw due to the hardening of the sinter material [9]. Therefore the skin surface of the pre-drilled hole is assumed as cross section area. This results in a surface of 86.4 mm² in a failure strength of 229 MPa for the connection between the sintered body and the M6 Pentaform screw.

3.2 Push in test sintered body

Push in tests of the sintered body in the CFRP plate are realized to investigate the strength of the connection between the sintered body and the CFRP. The specimens are clamped in a mounting frame between two steel plates with a hole of 35 mm diameter in the center. The test set up is intended to prevent bending. The force is raised by a piston with 20 mm diameter on the surface of the sintered body.

The test curves show a consolidation period until 1000 N followed by a rise to the peak and a slowly decreases. The reached average load capacity is at 37,559 N at 3.2 mm displacement (Figure 7). Since no screw is used in the test, no reference is needed.

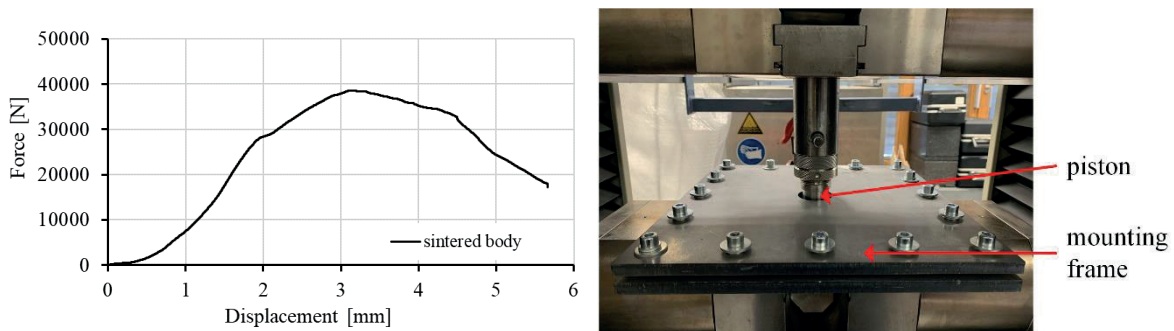


Figure 7: Typical load-displacement diagram and picture of the test set up for the push in tests of the sintered body

During tests the sintered body breaks under the load of the piston. Micrographics (Figure 8) show that the failure originates in the transition between the sintered body and the CFRP. Therefore, it is expected, that the thickness of the sintered metal above the integrated CFRP is responsible for the final resistance against the force in push or pull mode. Measurements of the micrographs indicate a thickness of the sintered metal above the CFRP of 1.4 mm by a diameter of 20 mm. No sudden failure occurs, after the maximum force is reached the sintered body is pressed out the CFRP laminate. Despite the failure, the carbon fibers stay attached to the sintered body.

As cross section area for the failure strength, the area of the side of a cylinder with the diameter of 20 mm and height of 1.4 mm is assumed. This results in an area of 87.9 mm² in a failure strength of 427 MPa.

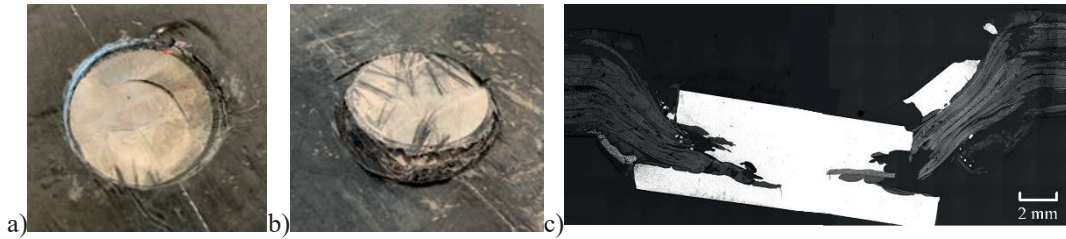


Figure 8: Pictures of the failed sintered body after push in test of the sintered body; a) bottom; b) top; c) a cross-sectional micrograph of the failure

3.3 Push in test sintered connection

For the push in tests of the joint sintered connection, specimens are clamped in a mounting steel frame with an open hole of the diameter 180 mm in the center. This allows a bending of the specimens during the test. The force is transmitted through a piston on the M6 Pentaform screw in the sintered body. The aim of this test is the investigation of the complex behavior of the sintered connection module under pressure with bending.

The documented curves start with a linear increase followed by a sudden decrease of force (Figure 9). This results in a failure of the sintered body. The average load capacity is at 8,390 N at 6 mm displacement. Reference tests with a blind rivet nut and a joined M6 screw reach at 6 mm displacement a force of 6,500 N and an average load capacity of 8,738 N at 8 mm displacement. The increase of the force is similar for the reference tests. The deformation of the blind rivet nut originates in a higher displacement until the failure occurs.

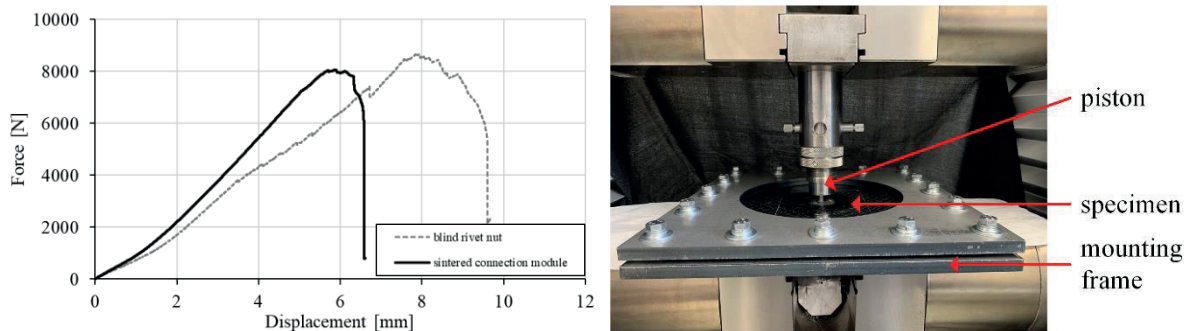


Figure 9: Typical load-displacement diagram and picture of the test set up for the push in tests of the sintered connection

The failure occurs in all specimens by a breaking of the sintered body. The screw joint remains unscathed. Micrographs (Figure 10) indicate the failure in the transition area between the sintered steel and the integrated carbon fibers, similar to the failure of the push in test of the sintered body. In this area the cross section of the sintered body changes and leads to stress concentration. The carbon fibers stay attached to the sintered body.

Due to the fact that the failure behavior is similar to the push in test of the sintered body, the same cross section area for the failure strength is assumed. An area of 87,9 mm² results in a failure strength of 95 MPa.

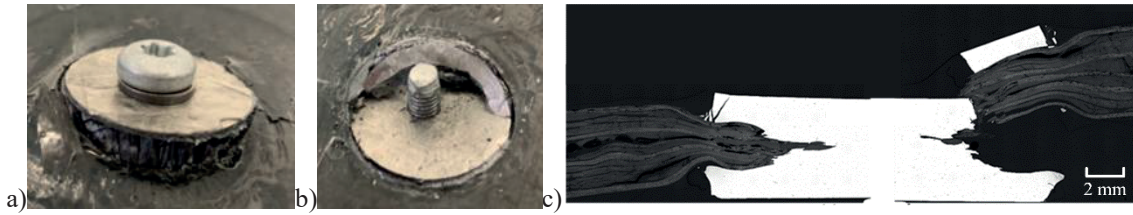


Figure 10: Pictures of the failed the sintered body after the push in of the sintered connection; a) bottom; b) top; c) a cross-sectional micrograph

3.4 Shear test

After a consolidation period until 2,000 N the force in the shear tests increases nearly linear. At the maximum, the force suddenly decreases due to the failure of the screw. The average load capacity is at 11,959 N at 1.8 mm displacement (Figure 11). The failure occurs in all test at the screw. The screw shaft is sheared off. With a cross section area of 20.1 mm² by a M6 screw this leads to a failure strength of 595 MPa. Reference shear tests with a blind rivet nut, joined by M6 screw reach an average load capacity of 12,985 N at 4.5 mm displacement. The reference tests show a similar behavior. Due to the fact of deformation of the blind rivet nut, the rise of the force occurs in flatter angle and the displacement in the reference tests is higher. The failure at the blind rivet nut arises also by shearing off the screw.

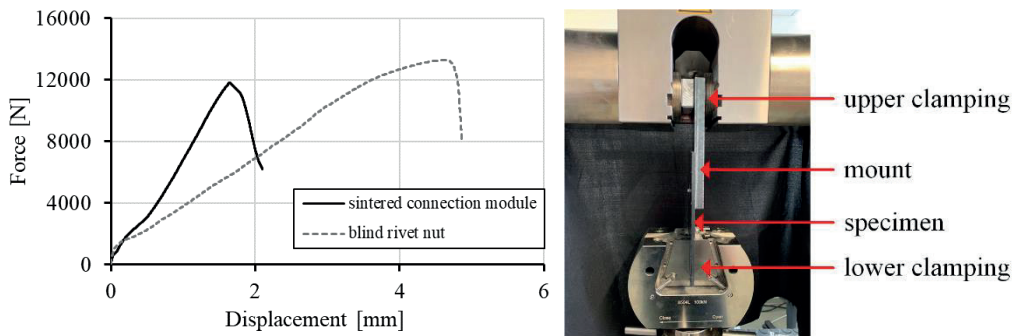


Figure 11: Typical load and displacement diagram and picture of the test set up for the shear test

4. Results and Discussion

Table 1 summarizes the load bearing capacity of the test sintered connection module and reference blind rivet nuts. At the push in and shear tests the reference blind rivet nut reaches slightly higher loads. The screw press out test illustrates the advantages of the sintered connection module. Due to its symmetry, the characteristics are the same for tensile and pressure. Compared to the blind rivets nuts, the properties for tensile load are almost similar (5 % higher) but the properties for pressure are 170 % higher.

Table 1: Comparison of the load bearing capacity of the sintered body in CFRP and reference blind rivet

	Sintered body		Reference blind rivet nut	
	Average load capacity	Standard deviation	Average load capacity	Standard Deviation
Push in sintered connection	8,390 N	1,806 N	8,738 N	1,241 N
Push in sintered body	37,559 N	3,429 N	-	-
Shear	11,959 N	314 N	13,094 N	367 N
Screw press out	19,826 N	2,878 N	Pressure 7,336 N	275 N
			Tensile 18,957 N	938 N

The conducted tests show either a failure of the sintered body or the screw. This fact creates the opportunity to adjust the strength of the sintered connection module. To increase the shear strength a larger screw is recommended. An increase of the strength of the sintered body is possible by a change of the transition area between carbon fibers and sintered steel. The different components of the sintered connection module allow an adjustment of the strength. The sintered connection module can be customized for different load cases and the failure can be predicted towards a fail-safe behavior.

Is the determined load capacity divided by the failure cross section area, the failure strength of the sintered connection is revealed, as shown in Table 2. Due to the tests, the highest strength occurs in the M6 Pentaform screw at the shear test. The connection between the sintered body and CFRP has the second highest strength. The lowest strength emerges at the push in test of the sintered connection.

Table 2: Failure strength related to cross section area

	Average load capacity	Cross section area	Failure strength
Push in sintered connection	8,390 N	87.9 mm ²	95 MPa
Push in sintered body	37,559 N	87.9 mm ²	427 MPa
Shear	11,959 N	20.1 mm ²	595 MPa
Screw Press Out	19,826 N	86.4 mm ²	229 MPa

5. Summary

Mechanical tests to investigate the load bearing capacity and failure behavior of the sintered connection module have been carried out and show that the present sintered connection module achieves load capacities in the range of blind rivet nuts. Due to the possibilities to modify the thickness, the diameter of the sintered connection and also realize different positions of the CFRP inside the sintered connection an adaption towards the needs of the final application is expected. The shear tests and push in tests indicate that either the sintered body or the joint screw fails. This shows the potential to adjust the failure of the sintered connection to a fail-

safe behavior with a rest strength remaining. For detailed mechanical specification more tests with different parameters are necessary. In order to reveal the full potential of the sintered connection module a more automated production process is necessary (Figure 12). An approach would be an automated sintering machine, which sinters the layers of carbon fibers in process of textile preforming. In this case the sintered bodies serve as handling points and as joining points. This approach will reduce process steps and production time. Also the final product can be mounted to constructions like conventional sheet metals.

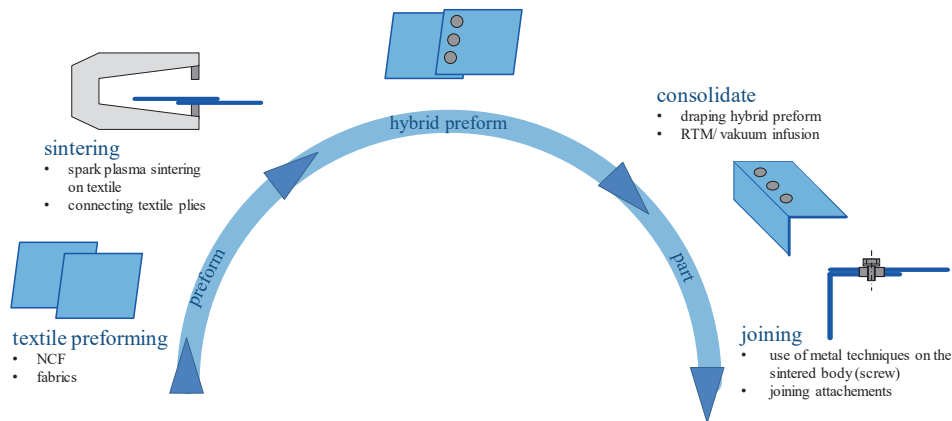


Figure 12: Automated process chain to manufacture the sintered connection module

Acknowledgement

The research project (promotional reference number: ZF4139606EB7) was funded by the Federal Ministry for Economic Affairs and Energy (BMWi). The BMWi is sincerely thanked for supporting this research project.

References

- [1] A. Pramanik, A. K. Basak, Y. Dong, P. K. Sarker, M. S. Uddin, G. Littlefair, A. R. Dixit, S. Chattopadhyaya, *Joining of carbon fibre reinforced polymer (CFRP) composites and aluminium alloys – A review*. Composites Part A: Applied Science and Manufacturing, vol. 101, **2017**, 1–29.
- [2] G. Meschut, F. Augenthale, *Hybridfügen von Mischbaustrukturen aus faserverstärkten Kunststoffen mit metallischen Halbzeugen*. Abschlussbericht IGF-Nr. 17618, **2015**.
- [3] J. Gebhardt, F. Pottmeyer, J. Fleischer, K. A. Weidenmann, *Characterization of Metal Inserts Embedded in Carbon Fiber Reinforced Plastics*. MSF, vol. 825-826, **2015**, 506–513.
- [4] J. Gebhardt, J. Schwennen, F. Lorenz, J. Fleischer, *Structure optimisation of metallic load introduction elements embedded in CFRP*. Prod. Eng. Res. Devel., vol. 12, **2018**, 131–140.
- [5] T. Hutsch, A. Lang, T. Schubert, P. Schiebel, M. Christ, T. Weißgärber, B. Kieback, A. S. Herrmann, *Metal/FRP Connection Module – A Powder Metallurgical Approach*. MSF, vol. 825-826, **2015**, 449–456.

- [6] T. Hutsch, A. Lang, B. Kieback, T. Weißgärber, A. S. Herrmann, Europäisches Patent 3102397, **2018**.
- [7] E. G. Koricho, A. Khomenko, T. Fristedt, M. Haq, *Innovative tailored fiber placement technique for enhanced damage resistance in notched composite laminate*. Composite Structures, vol. 120, **2015**, 378–385.
- [8] K. Gliesche, *Application of the tailored fibre placement (TFP) process for a local reinforcement on an “open-hole” tension plate from carbon/epoxy laminates*. Composites Science and Technology, vol. 63, **2003**, 81–88.
- [9] A. Marx, T. Hutsch, P. Schiebel, D. Feltin, F. Hoffmeister, A. Babbel, T. Weißgärber, A. Herrmann, *Sintered Connection - A Steel/CFRP Connection Module*. KEM, vol. 809, **2019**, 203–209.

Joining of Additively Manufactured Titanium with Different Surface Structures with Fiber-Reinforced PEEK for Lightweight Design Applications

J. Moritz¹, P. Götze², T. Schiefer¹, A. Klotzbach¹, J. Standfuß¹, E. López¹, F. Brückner^{1,3}, C. Leyens^{1,2}

¹ Fraunhofer Institute for Material and Beam Technology IWS, Dresden, Germany

² Technische Universität Dresden, Dresden, Germany

³ Luleå University of Technology, Luleå, Sweden

1 Introduction

Lightweight design applications, which are becoming increasingly important, e.g. in connection with fuel savings in transport, can be further promoted through the use of polymer composite-metal hybrid parts. These hybrid structures are particularly interesting for applications in the automotive and aerospace sector, because they take advantage of the high fracture toughness of the composite component on the one hand and the good impact resistance of the metal part on the other hand.[1,2]

Several publications have focused on the bonding of polyether-ether-ketone (PEEK) and titanium, mainly for the use in aviation or biomedical applications.[3–5] Titanium is often employed in technical high-performance applications on account of its high specific strength and excellent corrosion resistance. PEEK combines high toughness, fatigue resistance and good thermal stability [1,4] and can tolerate temperatures of up to 177 °C in long-term operation and is therefore applied in lightweight components that are intended for the use at increased temperatures.[6]

In order to enhance the bond strength of the joint, the metallic counterpart is often pretreated using a laser in order to generate defined surface structures and patterns and enlarge the surface area.[4,7–9] However, the surface pretreatment means an additional step in the process chain for manufacturing hybrid joints. Conversely, additive manufacturing allows specific surface features to be integrated directly during production of the component. Furthermore, additively manufactured parts are intrinsically rough, which may facilitate mechanical interlocking at the interface. Therefore, the aim of this study was to elucidate the potential of different surface features of additively manufactured titanium samples on the bond strength of hybrid joints.

Thermal joining processes, which e. g. rely on induction heating, are highly suitable for joining fiber-reinforced polymers and metals because of the fast heating and the short process times, which make the technology very economical.[10–13] The entire process is carried out under a constant joining pressure to improve the heat transfer and wetting in the joining zone. An alternating electromagnetic field is induced in the metal component by means of an alternating voltage, resulting in heat development due to eddy current losses.[11,14] As a consequence of the heat input, the polymer is softened or partially melted and wets the surface of the metal. A firm bond between metal and polymer is formed during solidification.[15] The bond strength is governed by both micro-mechanical interlocking and physical adhesion forces.[15]

In this study, different surface features of titanium samples were produced via electron beam melting (EBM). The effect of those surface structures on the bond strength between titanium and carbon fiber reinforced PEEK was investigated.

2 Experimental Procedure

Since the bond strength of the hybrid joint should be evaluated from tensile shear samples, all samples were designed according to DIN EN 1465 as cuboids with a side length of 105 mm x 25 mm x 2 mm using Autodesk Inventor 2016. In order to investigate the effect of different surface structures, pins and grooves with a trapezoidal cross-section were chosen as interlocking structures. These features were positioned on top of the cuboids in such a way that the patterns covered the entire area of the future overlapping length. Thus, three basic sample groups were defined: „as built“, „grooves“, and „pins“. The dimensions of those grooves and pins as specified in the CAD design are illustrated in Figure 1.

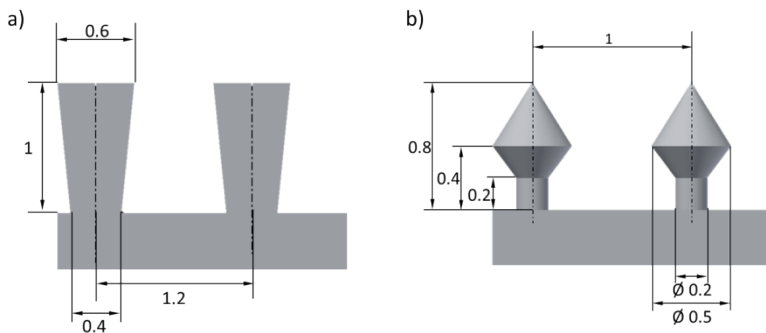


Figure 1: Design and dimensions of a) groove and b) pin surface structures

The titanium samples were manufactured additively by means of electron beam melting using an Arcam A2X EBM machine. In this powder bed based process, each layer of powder is first sintered with a defocussed electron beam to avoid smoke effects. Then, the powder is selectively melted according to the cross-section of the component in the respective layer using a focussed beam before the build platform is lowered and a new powder layer is applied. The sample orientation on the substrate plate is visualized in Figure 2.

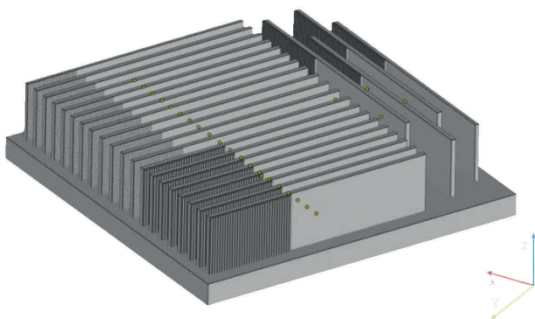


Figure 2: Position of tensile shear specimens on substrate plate

After sample manufacturing, a part of the specimens was milled at the future overlapping area. Approximately 200 μm of material were removed until a comparatively smooth surface was obtained. Five samples were left in the milled state as a control group with no surface structures, whereas the

rest of the milled specimens was then structured using a fiber laser (IR laser source, line distance 0.2 mm, scanning velocity 10 m/s) which was scanned over the surface twice. Thus, a control group with state-of-the-art surface structures (referred to as „laser structured“) was obtained as reference samples.[7]

The titanium specimens were then joined to the composite by means of thermal direct joining. Here, carbon fiber reinforced PEEK (CF-PEEK) with a multi-axial non-crimp fabric and a fiber content of 60 % as reinforcing material was utilized. Before joining, the CF-PEEK was cut into 105 mm x 25 mm x 2 mm pieces. A 0.4 mm thin PEEK foil was placed between the two joining partners to serve as a hotmelt, which should ensure a good bonding between metal and polymer. Samples were joint with an overlapping length of 12,5 mm with a press force of 300 N, which was applied locally at the joining zone using a joining gun (Figure 3). An EFD Minac 18/25 generator was used for induction heating at a power of 7.5 kW and a frequency of 20 kHz. Heating time was 30 s, followed by cooling with pressurized air. The experimental setup is illustrated in Figure 3.

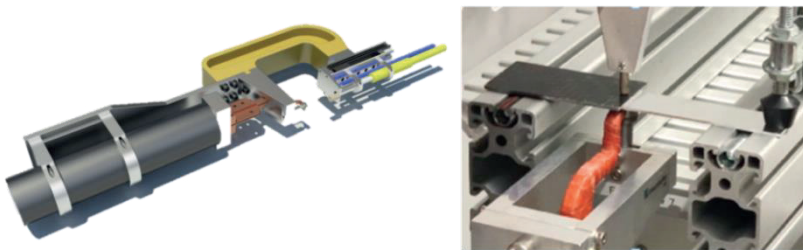


Figure 3: Joining gun (left) and experimental setup during thermal direct joining (right)

In order to evaluate the embedment of the groove- and pin-shaped structures in the CF-PEEK material, metallographic cross-sections of those joints were prepared and analyzed by means of an Olympus GX51 inverted metallurgical microscope.

Tensile shear testing was conducted according to DIN EN 1465, using a Zwick Z050 multiaxial material testing machine with a 5 N preload and a test speed of 10 mm/min. During testing, optical strain measurements by means of a GOM ARAMIS 5M system for non-contact 3D deformation measurements based on grayscale analysis were performed.

3 Results and Discussion

The obtained surface structures after additive manufacturing, laser surface structuring and milling are shown in Figure 4, respectively.

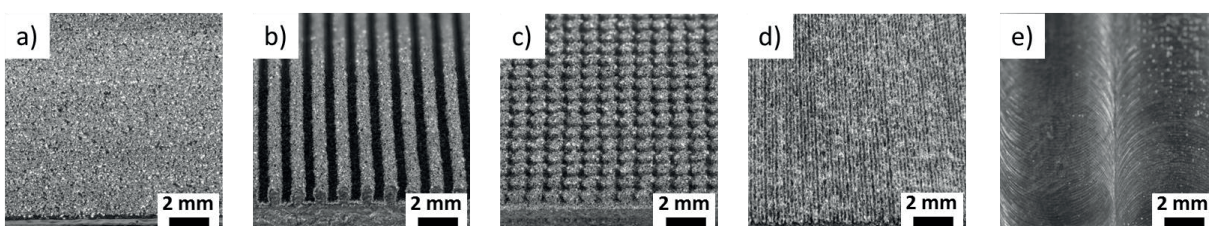


Figure 4: Close-up view of titanium samples with a) as-built surface, b) groove-shaped surface structures, c) pin-shaped surface structures, d) laser structured surface, e) milled surface

The as-built surface exhibits a rough surface with partly molten particles, which is typical for the EBM process. These irregular surface structures could potentially serve for micro-mechanical interlocking. Both the grooves and pins provide structures for macro-mechanical interlocking. However, comparing those images to the sample design presented in Figure 1, it is obvious that the resolution is limited by the EBM process, e. g. due to the melt pool size or adhering particles. Those partly molten particles might again have an influence on micro-mechanical interlocking. In the case of laser surface structuring, fine and comparatively well defined patterns are visible.

The metallographic cross-sections (Figure 5) provide evidence that the grooves and pins were embedded in the solidified PEEK from the hot melt. In order to achieve a complete embedment, it might be beneficial to have more material available for the hot melt, i.e. to use a thicker PEEK foil or a PEEK composite with a top layer with a lower fiber content.

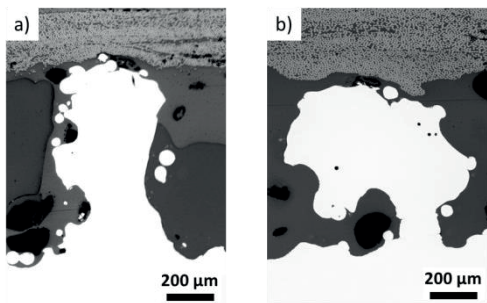


Figure 5: Metallographic cross-section of joint with a) grooves and b) pins on the titanium counter-part

Nevertheless, the surface structures did not penetrate the fiber reinforced composite due to the high fiber content. The rough surface and the adhered particles which are visible around the grooves and pins originate from the additive manufacturing process. The fact that they are also fully surrounded by PEEK supports the assumption that the inherent surface roughness contributes to bond strength.

Figure 6 visualizes the shear strength – shearing displacement diagram as well as the maximum shear strength values for the different surface structures.

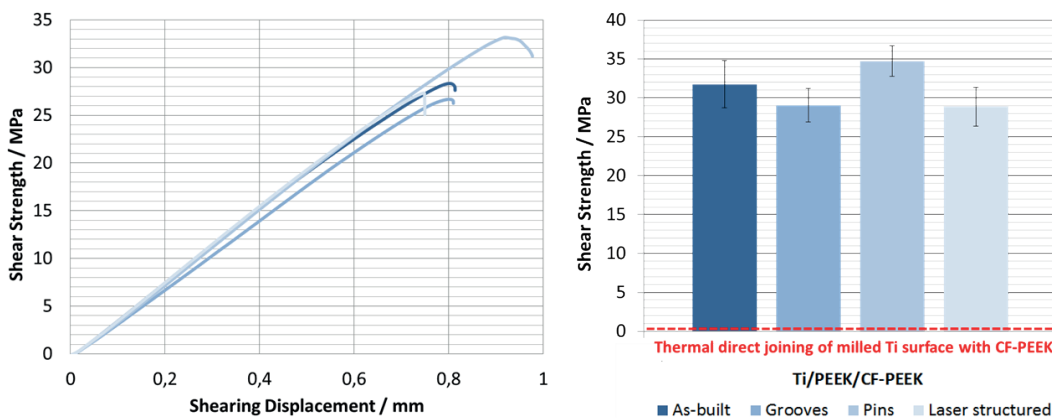


Figure 6: Shear strength - shearing displacement diagram and maximum shear strength values for different surface structures

All additively manufactured structures were competitive with the state-of-the-art laser surface structuring in terms of shear strength. The highest tensile shear strength was obtained with the pin structures. In contrast, the bond strength between the carbon fiber reinforced PEEK and the milled reference sample was so weak that it could not be measured properly because the specimens fell apart.

Woitun et al. reported that an increase in true surface area and a uniform distribution of stress, which can be achieved by evenly distributed surface structures, are among the most important factors for improving the bond strength of metal-polymer joints.[16] Even though the true surface area of the obtained structures still needs to be studied, it is plausible that the as-built surface roughness, especially in combination with the groove and pin structures, lead to a significant increase in surface area compared to the milled surface. These results strongly suggest that additive manufacturing can provide very effective interlocking structures for thermal direct joining. Since even the as-built titanium surface lead to shear strength above 30 MPa, additional surface pretreatment steps might no longer be needed for certain joining applications if one counterpart of the joint is produced by additive manufacturing.

Exemplary still frames from digital image correlation as well as representative images of the fractured surfaces after tensile shear testing of the additively manufactured samples are shown in Figure 7.

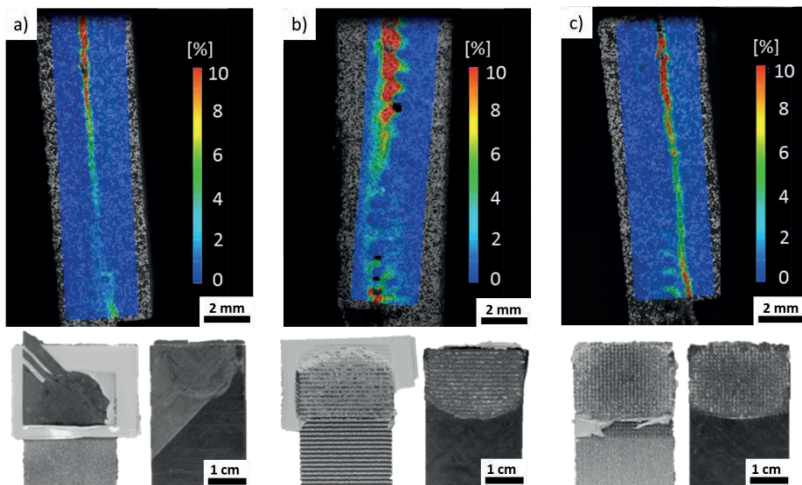


Figure 7: Digital image correlation during mechanical testing of additively manufactured specimens and fracture analysis after failure of a) titanium part with as-built surface, b) titanium part with groove-shaped structures, and c) titanium part with pin-shaped structures

It appears as if the crack is deflected at the additively manufactured macrostructures. Apart from that, there seems to be an additional bending moment due to the protruding structures, which might have had an influence on test results. The specimen with the as-built titanium part exhibits cohesive failure within the carbon fiber reinforced PEEK. On the other hand, cohesive failure within the PEEK film was observed for the groove and the pin structures. Fracture analysis suggests that the PEEK hotmelt formed a stable bond with both the metal and the composite counterpart of the joint.

4 Conclusions and Outlook

In the presented study, thermal direct joining was successfully applied for joining additively manufactured titanium with different surface structures and carbon fiber reinforced PEEK. The shear strength that could be achieved with the additively manufactured structures was competitive to laser surface structuring and significantly improved in comparison to a milled, unstructured surface. Among all sample groups, the best results were obtained with pin-shaped surface structures.

It was concluded that additive manufacturing can provide a viable way of fabricating interlocking structures for joining, even if only the inherent roughness of the as-built surface is used. Thus, it

might be possible for some applications to omit additional surface treatments such as laser structuring. Applications might be in the transport sector, due to the elimination of process steps and the possibility for lightweight design, or in biomedicine, as there is no need for adhesives, which could pose a potential health risk. Nevertheless, more detailed investigations are required in order to verify those results. First investigations show promising results for salt spray testing. Further studies should address the optimization and simulation of the interlocking structures, the applicability to other materials and joining methods and the long-term bond stability. After that, the findings could be transferred to more complex geometries.

5 Literature

- [1] P. Cortés, W.J. Cantwell, Structure–properties relations in titanium-based thermoplastic fiber–metal laminates, *Polym. Compos.* 27 (2006) 264–270.
- [2] R. Falck, S.M. Goushegir, J.F. dos Santos, S.T. Amancio-Filho, AddJoining, *Materials Letters* 217 (2018) 211–214.
- [3] K. Schulze, J. Hausmann, S. Heilmann, B. Wielage, Bruchmechanische Untersuchung der Titan-PEEK-Grenzfläche in thermoplastischen Titan-CF/PEEK-Laminaten durch Mixed-Mode-Bending-Versuche, *Mat.-wiss. u. Werkstofftech* 45 (2014) 537–545.
- [4] B. Henriques, M. Sampaio, M. Buciumeanu, J.C.M. Souza, J.R. Gomes, F. Silva, O. Carvalho, Laser surface structuring of Ti6Al4V substrates for adhesion enhancement in Ti6Al4V-PEEK joints, *Materials science & engineering. C, Materials for biological applications* 79 (2017) 177–184.
- [5] M. Harhash, A. Carradò, H. Palkowski, Lightweight titanium/polymer/titanium sandwich sheet for technical and biomedical application, *Mat.-wiss. u. Werkstofftech* 45 (2014) 1084–1091.
- [6] M. Ramulu, P. Stickler, N. McDevitt, I. Datar, D. Kim, M. Jenkins, Influence of processing methods on the tensile and flexure properties of high temperature composites, *Composites Science and Technology* 64 (2004) 1763–1772.
- [7] J. Gebauer, M. Fischer, A.F. Lasagni, I. Kühnert, A. Klotzbach, Laser structured surfaces for metal-plastic hybrid joined by injection molding, *Journal of Laser Applications* 30 (2018) 32021.
- [8] S. Zimmermann, U. Specht, L. Spieß, H. Romanus, S. Krischok, M. Himmerlich, J. Ihde, Improved adhesion at titanium surfaces via laser-induced surface oxidation and roughening, *Materials Science and Engineering: A* 558 (2012) 755–760.
- [9] K. Schulze, J. Hausmann, B. Wielage, The Stability of Different Titanium-PEEK Interfaces against Water, *Procedia Materials Science* 2 (2013) 92–102.
- [10] A. Klotzbach, M. Langer, R. Pautzsch, J. Standfuß, E. Beyer, Thermal direct joining of metal to fiber reinforced thermoplastic components, *Journal of Laser Applications* 29/2 (2017).
- [11] P. Mitschang, R. Velthuis, M. Didi, Induction Spot Welding of Metal/CFRPC Hybrid Joints, *Adv. Eng. Mater.* 15 (2013) 804–813.
- [12] S. Scheik, Untersuchungen des Verbundverhaltens von thermisch direkt gefügten Metall-Kunststoffverbindungen unter veränderlichen Umgebungsbedingungen, 2016.
- [13] A. Klotzbach, Laser joining process yields metal-thermoplastic hybrid parts, *Industrial Laser Solutions* (2019) 18–21.
- [14] Roesner, Scheik et al. 2011 - Innovative approach of joining hybrid.
- [15] D. Flock, Heat Conduction Bonding of Plastic-Metal Hybrid Parts, 2011.
- [16] D. Voitun, M. Roderus, T. Bein, E. Kroner, Precise Laser Structures as a Tool to Understand Metal-Polymer Joints, *International Congress on Applications of Lasers & Electro-Optics ICALEO*, Orlando (2019).

Multi-Component High Pressure Die Casting (M-HPDC): Influencing Factors on Bond Quality of Metal-Plastic Hybrids and its Necessity of Process Data Logging

P. Messer¹, U. Vroomen¹, A. Bührig-Polaczek¹

¹Foundry-Institute, RWTH Aachen University, Aachen, Germany

1 Introduction

In many fields, highly innovative lightweight construction concepts are required whose specifications can no longer be met by one material alone. In addition to lightweight constructions using fiber-reinforced plastics and aluminum-steel hybrids, plastic-aluminum hybrid constructions in particular have a high potential for weight reduction. For the manufacturing of hybrids, highly automatable processes are demanded in order to enable economic production.

2 State of the art

A distinction will be made between in-mold and post-mold process routes for the production of metal-plastic hybrid components. In the following, these two process routes which are used in established processes are briefly introduced. Furthermore, the state of the art with regard to process data logging is outlined below.

2.1 In-mold- and post-mold-assembly

There are already many applications for plastic-metal hybrids that can be divided into post-mold assembly (PMA) and in-mold assembly (IMA). With PMA, both joining partners are manufactured separately and joined in an additional process step, compared to IMA, where the primary shaping and joining of the second component are combined in one process step. In both cases, the bond is mostly achieved by a macroscopic form-fit, which requires appropriate preparation of the metallic semi-finished products. This is associated with the consequence of long process chains and the necessity of extensive plant engineering. [1, 2, 3]

2.2 Data logging

In many industries, the traceability of the value-added chain is already a central point when selecting suppliers. The requirements here can be very different. In some cases, it is sufficient if only the origin of the components can be traced, while in other cases 100% documentation of all manufacturing parameters is required. The last-mentioned case in particular requires a suitable infrastructure that can access the manufacturing parameters directly at the production line and store them in a database

for each component. In many cases, these parameters are already available in the machine control system and can be read out by a server via standardized interfaces such as OPC UA (Open Platform Communications Unified Architecture). However, in order to be able to store this data in a structured and meaningful way, a profound understanding is required, since although machine data can be accessed via OPC UA, this data is not available in a uniform or easily accessible format and needs to be extracted from the source code during a specific period of the cycle.

In research, this often leads to the situation that this data is often not accessible, so that process data must be documented manually, which means that a large number of parameters, which may have an unknown influence on the process, are not or not sufficiently documented.

3 M-HPDC and its process cycle

In Chapter 2.1, the difference between IMA and PMA has been shown. The M-HPDC process, developed at the Foundry Institute, offers the possibility to realize the primary shaping of both a metal and a plastic component in the same die and on only one production machine. The Foundry Institute is equipped with a Frech DAK 450-40 high pressure die casting (HPDC) machine, which has been extended by an Arburg Allrounder 570S injection molding (IM) unit, enabling both materials to be processed on a single system. The IM-unit is mounted onto the pillars of the HPDC-machine using a special bracket. In this way, a system design can be achieved which is consistent with the already well-established expansion from 1-component to 2-component IM-machines.

3.1 Process cycle of M-HPDC process

The M-HPDC process consists of a combination of conventional HPDC and IM processes. The sequence is illustrated in Figure 1.

The cycle begins by spraying in order to apply release agent and to cool down the die. Since this is a two-component process, the slider moves to the HPDC position before the die closes and the actual shot can take place. Once the aluminum casting is sufficiently solidified, the die opens to relieve the slider, allowing it to move to the IM position. As soon as the die is closed again, the injection of the plastic component takes place and another cooling time is required until the hybrid component has reached a sufficiently low demolding temperature. The die can now be opened and the component ejected. After the cycle, the overflow beans and the gating systems just need to be separated.

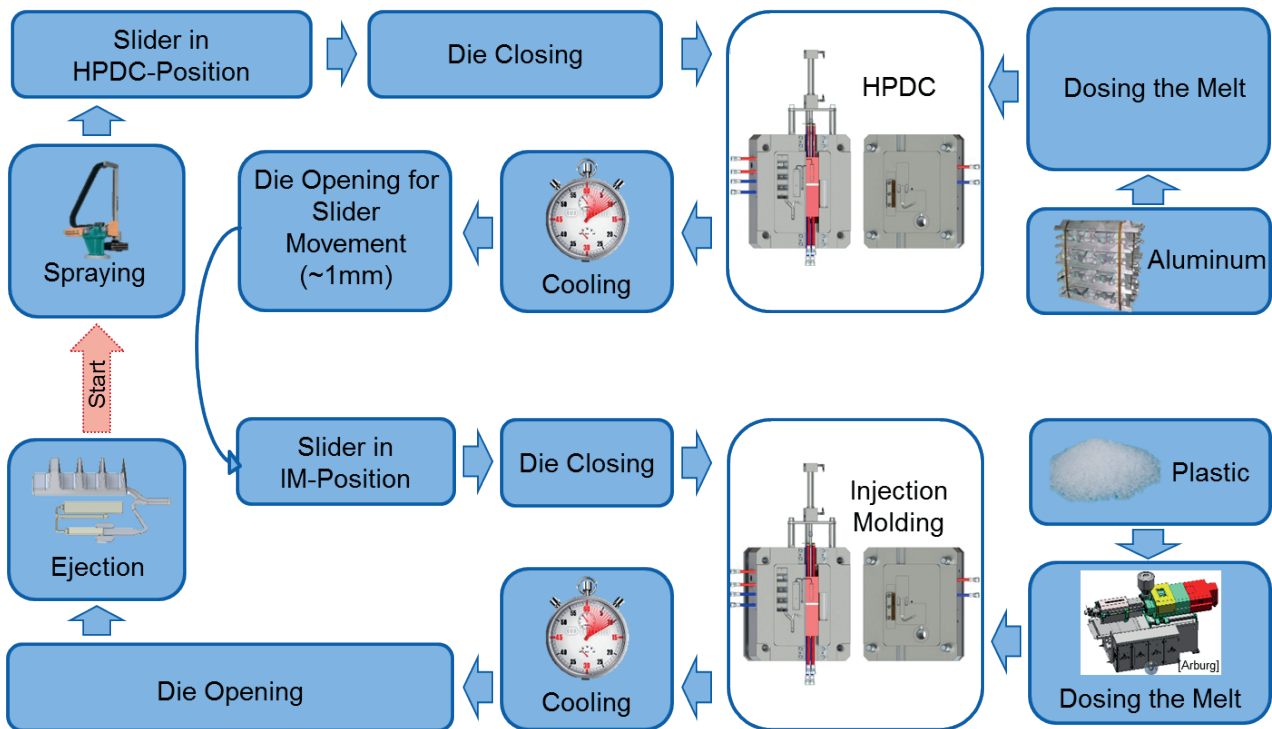


Figure 1: Cycle of M-HPDC Process

4 Temperature influence on bond quality

The hybrid die shown below allows the manufacturing of an overlap shear tensile specimen, which was designed according to the Standard DIN EN 1465 [4]. The aim of this geometry is the determination and quantification of influencing factors on the bond strength, which is based on micro-bracing of the plastic onto the surface roughness of the Al-component. In order to be able to map the surface topography of the Al-component by the plastic, a deep understanding of the process and in particular the targeted temperature control in the joining area is necessary, since HPDC and IM each have different temperature control requirements

4.1 Temperature setup within the die

The hybrid die has a variety of temperature control options based on liquid temperature control with oil or water. During the presentation of the hybrid die at the Euro Hybrid 2018 [5], a heating ceramic was also shown, which was intended to provide a further possibility for temperature control of the joining area. However, the usage of the heating ceramic has not proved to be practicable, as moisture gets into the die due to the spraying process and a hermetic sealing of the heating ceramic is extremely difficult due to the high die temperatures in die casting, as conventional seals are thermally overstrained. For this reason, the die configuration shown in Figure 2 is limited to an extensive liquid temperature control system, which will be discussed below.

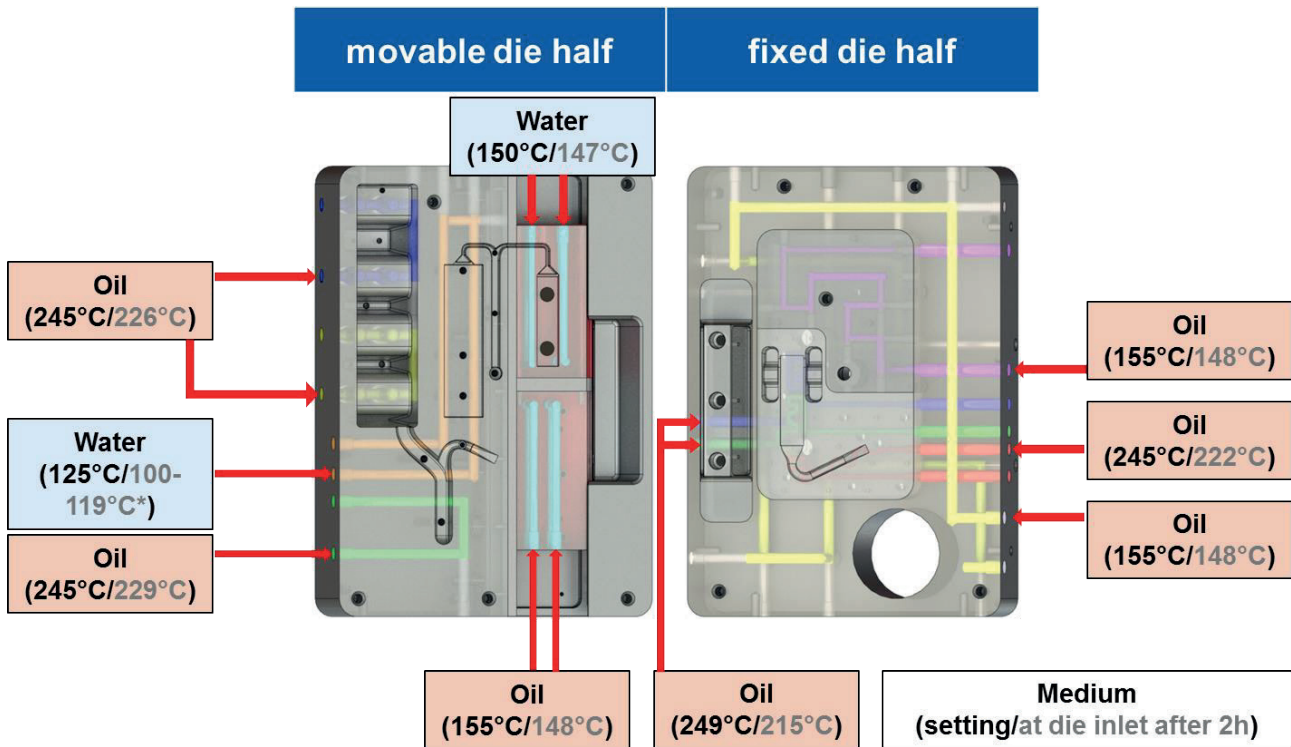


Figure 2: Tempering Possibilities of the die

In the configuration shown in Figure 2, three oil units with a total of five circuits and one water unit with two circuits are used, whereby the inputs are connected in parallel with a flow temperature set to 155°C and are controlled by a variothermal temperature control unit from SINGLE Temperiertechnik GmbH, Hochdorf.

Since, as already mentioned, the use of a heating ceramic has proven to be impractical, the focus of the investigations was placed on determining suitable temperature control windows by using liquid temperature control units only. Usually the die temperatures in HPDC are significantly higher than those in thermoplastic injection molding (here PA6GF30), so that a compromise has to be found. In particular, the question of the maximum possible die temperature at which the plastic can safely be demolded was addressed. It turned out that the die must not exceed 150°C in areas of the cavity that come into contact with the plastic, as otherwise it is no longer possible to safely demold the component.

4.2 Deviation between set and actual temperature

It is obvious that the temperature set on the temperature control unit does not match exactly the temperature that actually arrives in the corresponding die area. To understand the process, however, a precise knowledge of the actual temperatures in the die is essential. On the one hand, this is necessary to determine the maximum die temperatures, which enable reliable and reproducible demolding of the plastic, and on the other hand, to understand the temperature influence on the bond strength.

The measurements (**Figure 3**) show that there are considerable deviations between the set flow temperature, the temperature at the inlet of the die and the actual die temperature.

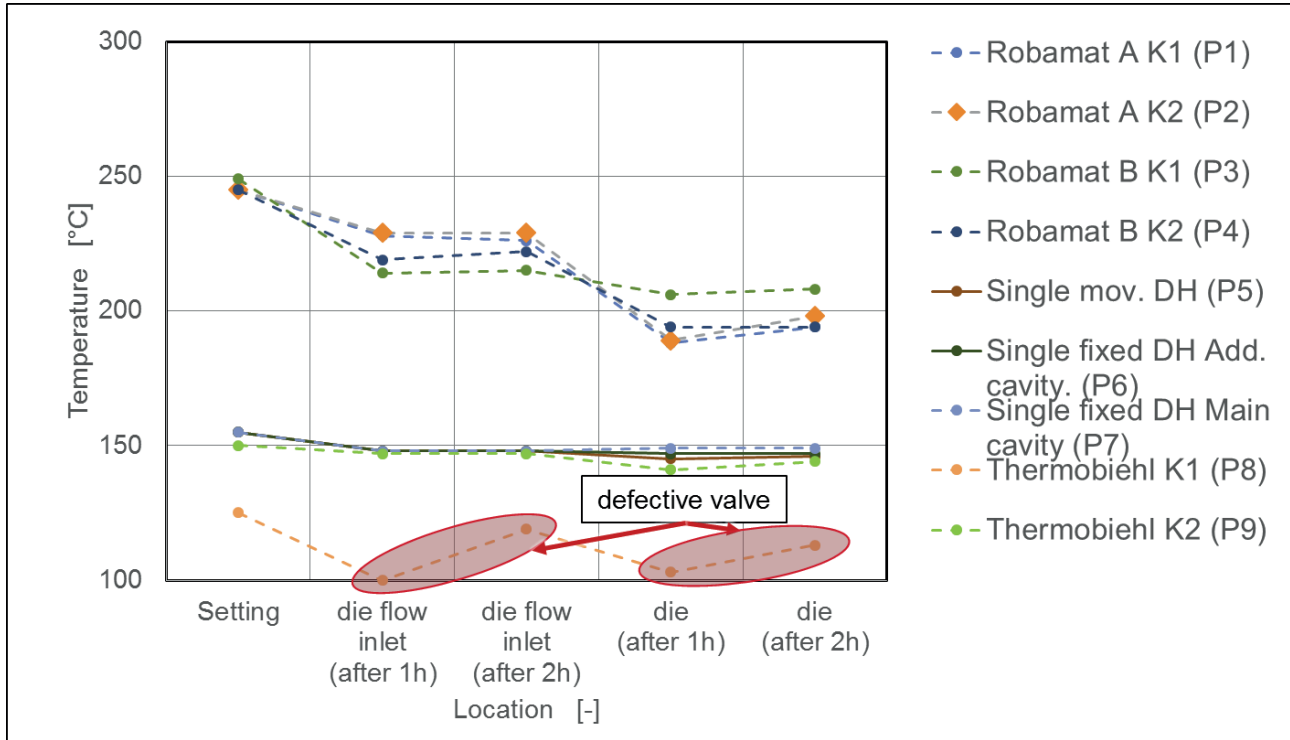


Figure 3: Deviation of flow- and die- temperatures

5 Data-logging during process development

As part of the test series, all recordable target values of the test setup were documented. However, the target values documented in this way have a much lower information content than a shot-precise recording of the actual values, measured during the process. The benefits of recording actual values are discussed below.

5.1 Benefits of machine data

In particular process developments where a large number of plants and control systems have to "harmonize" with each other, systematic data acquisition is a very valuable support to identify and eliminate error sources. Process windows are often not yet defined and the correlations between different control variables are not yet known, so that error analyses are very complex.

As a concrete example, the initially incomprehensible measured values (measured values Thermobiehl K1) from **Figure 3** should be mentioned here. In the end, after a long period of troubleshooting, it turned out that a defective valve was the cause of the fluctuations, which could have been found much earlier on the basis of a continuous recording of set and actual values of the temperature control circuit.

6 Summary and Outlook

As a result of the investigations, the understanding of the process has been significantly expanded. Unfortunately, the heating ceramics proved to be not practicable with the consequence that a revision of the die is necessary, since surface temperatures of 150°C are the maximum for demolding the used PA6GF30, but too low for reaching best bond qualities. The revision will enable dynamic tempering by means of two liquid tempered circuits, which will be placed right under the surface of the cavity in order to keep the die hot during joining and lowering the temperature afterwards for demolding. In the new die insert, thermocouples will be integrated as well, which enable continuous temperature measurement in the process. In order to be able to record machine and sensor data in a meaningful way, the manufacturing cell is currently being comprehensively networked by means of OPC UA within the framework of the Cluster of Excellence “Internet of Production” (IoP).

6 Acknowledgement

Funded by the Deutsche Forschungsgemeinschaft (DFG, German Research Foundation) under Germany's Excellence Strategy – EXC-2023 Internet of Production – 390621612.

7 Literature

- [1] Lao, B., Druckgegossene Metallhybridstrukturen für den Leichtbau- Prozess, Werkstoffe und Gefüge der Metallhybriden, in Fakultät für Georessourcen und Materialtechnik 2013, RWTH Aachen University.
- [2] Schenke, G., D. Joop, and A. Bührig-Polaczek, Hybride Fertigungsverfahren zur Umsetzung gussintensiver Leichtbaukonzepte - Grundlagenforschung und Prozessentwicklung am Gießerei-Institut der RWTH Aachen University, in Verbundwerkstoffe / Werkstoffverbunde 2013. 2013.
- [3] Brecher, C. and D. Özdemir, Integrative Production Technology. 2017: Springer.
- [4] DIN EN 1465, Klebstoffe –Bestimmung der Zugscherfestigkeit von Überlappungsklebungen; Deutsche Fassung EN 1465:2009.
- [5] J. M. Hausmann, M. Siebert, A. v. Hehl, Proceedings Euro Hybrid Materials and Structures 2018, 3. Internationale Konferenz, 222-226

Experimental investigation of the load bearing capacity of inserts embedded in thermoplastic composites

Juliane Troschitz¹, Robert Kupfer¹, Maik Gude¹

¹Technische Universität Dresden, Institute of Lightweight Engineering and Polymer Technology (ILK), Dresden

Abstract

Thermoplastic composites (TPC) are predestined for use in lightweight structures especially for high-volume applications. In many areas of lightweight construction, the use of metal inserts is established for load introduction into composite structures. The inserts can be integrated during composite fabrication or subsequently in separate process steps. The authors pursue the approach of embedding inserts in TPC during compression moulding without fibre damage. The technology is based on the concept of moulding holes by a pin and simultaneously placing an insert in the moulded hole. In this paper, the performance of such embedded inserts is compared to subsequently integrated commercial solutions like blind rivet nuts. To evaluate the joint strength, in-plane loading tests, torsion tests as well as out-of-plane loading tests are carried out.

Keywords: glass fiber reinforced polymers; joining; short-term strength test

1 Introduction

TPC have a high potential for large-scale production particularly for applications in the transportation industry. Reasons are high specific mechanical properties as well as established efficient manufacturing processes with short cycle times [1], such as compression moulding. For composites the embedding of metal inserts is established as a reliable and efficient joining technique [2]. Metal inserts can increase the joint strength of bolted joints by reducing stress concentrations in the composite around the hole [3], as observed numerically [4] and experimentally [5].

Joining elements can be integrated in composites in a separate downstream process step – in the following called fasteners – or during part manufacturing process – in the following called inserts. For downstream joining, a large number of commercially available fasteners (CAF) exists. Such fasteners are typically inserted and fixed into a previously cut hole, for example by screwing [3] or by bonding [6]. In addition, a joint can be realized by plastic deformation of the fastener, see blind rivet nuts [7].

In case of composites with thermoset matrix, metal inserts are often integrated before or during the part manufacturing, e.g. in the resin transfer moulding (RTM) process [8]. During the embedding of the insert, the reinforcing structure can be locally oriented around the insert without fibre damage as shown by Ferret et al. [9], Gebhardt and Fleischer [10], and Wilkening et al. [11].

TPC are characterised by weldability, meltability and warm formability, allowing alternative approaches for joining processes. In [12], a technology for process-integrated embedding (PIE) of inserts in TPC while compression moulding is described. The developed technology bases on the concept of moulding holes introduced by Kupfer et al. [13]. Thereby, the reinforcing fibres are not cut

by drilling but reoriented by a tapered pin in plasticised state of the TPC [14]. The integration of the embedding process of metal inserts into the composite component manufacturing process provides the opportunity of reducing the manufacturing costs and the number of process steps.

Fig. 1 illustrates the process steps of the PIE schematically. First, the TPC sheet is warmed above melting temperature of the polymer matrix (a). Subsequently, a handling device transfers the TPC sheet into the compression mould (b). Immediately after mould closing and shaping the warm TPC sheet (c), a two-parted pin tool (consisting of tapered pin and pin retainer) is shifted forward forming a hole by displacing the reinforcing fibres and the still molten thermoplastic matrix (d). The pin tool is equipped with a metal insert, which is precisely positioned flush with the composites surface. Afterwards, a ring shaped counterpunch recompresses the squeezed-out material (e). The embedding (steps d and e) requires less than one second. After the cooling and solidification the shaped TPC part with integrated metal insert is demoulded (f).

In this paper, the load bearing behaviour of such PIE inserts is compared to subsequently integrated CAF. TPC test specimens with different types of joining elements are manufactured and in-plane loading tests, torsion tests as well as out-of-plane loading tests are carried out.

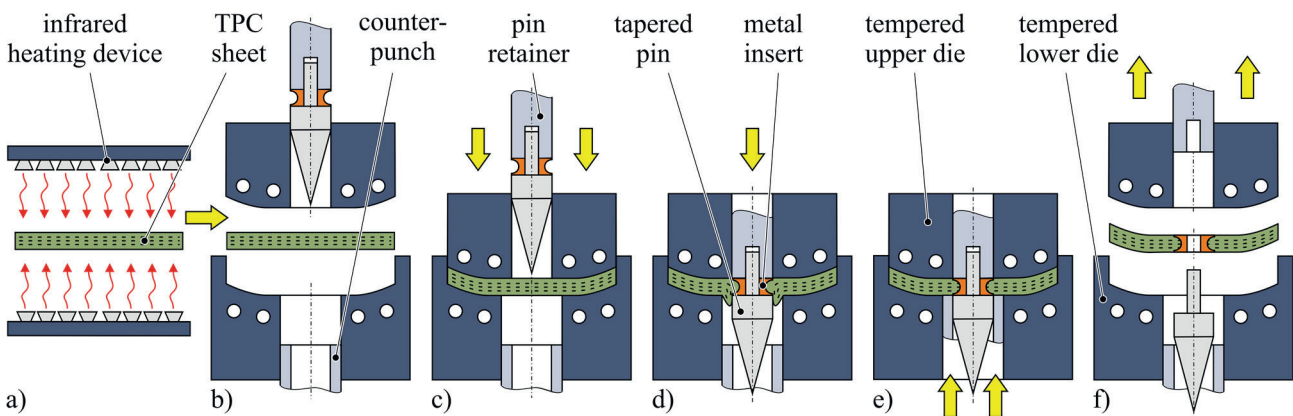


Figure 1: Schematic illustration of process-integrated embedding (PIE) of metal inserts in TPC.

2 Materials and specimen specification

The investigations are performed on TPC sheets made in an autoclave of glass fibre reinforced polypropylene (GF/PP) unidirectional tapes Celstran® CFR-TP PP-GF70 with 45 vol.-% fibre content. The laminate structure is $[(0^\circ/90^\circ)_4]_s$ resulting in a TPC sheet thickness of 4.3 mm.

A prototypical tempered steel mould (40 °C) on laboratory scale with vertical flash face is applied for the process-integrated embedding of inserts into plane TPC specimens. Therefore the TPC sheet is heated up to 210 °C before pressing process. Three different insert types, all made of steel 1.2210, are investigated (Fig. 2). The insert type PIE-1 is rotationally symmetric whereas PIE-2 and PIE-3 have an anti-rotation function due to the non-circular shape. The outer diameter of PIE-1 is equal to the diameter of the smallest circle enclosing the non-circular variants. All three insert variants have the same thickness (4.3 mm) as the laminate so that they are flush with the laminate surface after embedding. Consequently, there is no disturbing contour on the final part surface.

To compare the performance of PIE inserts to subsequently integrated commercial solutions three types of CAF are investigated: Anchor®, MICROBARB® and RIVKLE® SFC (Fig. 3). Table 1 summarises the specifications of the selected CAF. To install the fasteners to the TPC pre-holes are drilled with diameters recommended by the CAF manufacturer (cf. Table 1).

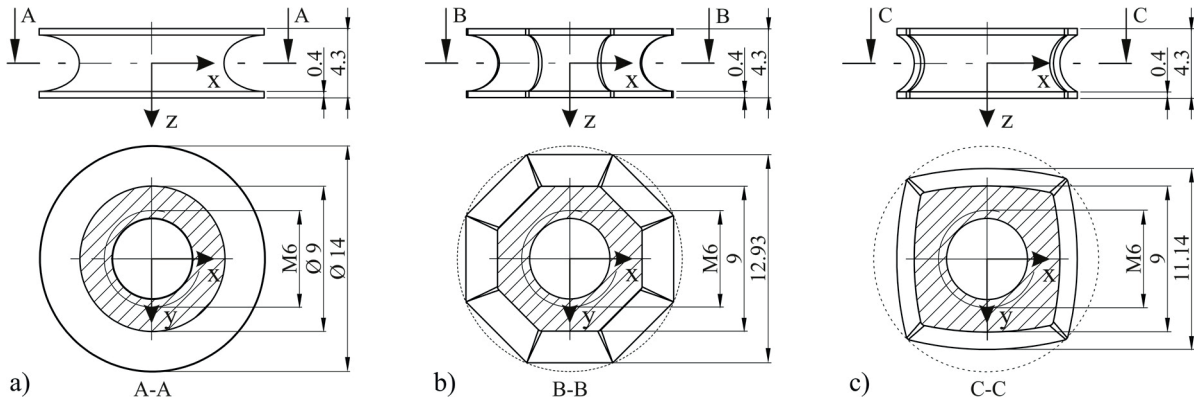


Figure 2: Prototypic inserts for process-integrated embedding: a) PIE-1 (2.3 g), b) PIE-2 (2.1 g), c) PIE-32 (2.1 g).

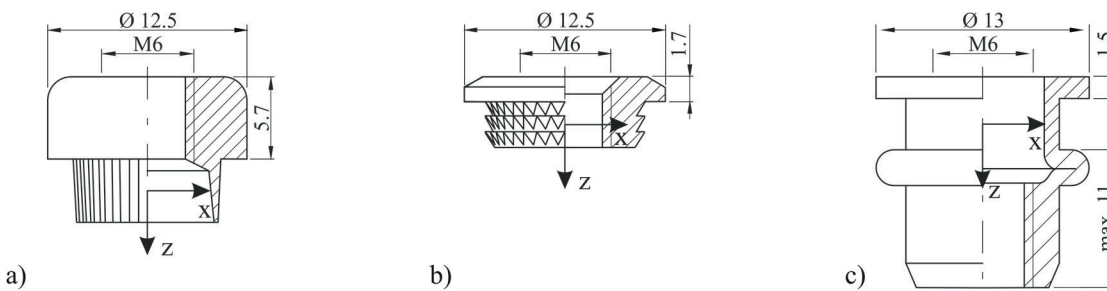


Figure 3: Schematic illustration of the investigated fasteners a) CAF-1, b) CAF-2, c) CAF-3.

Table 1: Specifications of the investigated fasteners.

	Anchor [®] (CAF-1)	MICROBARB [®] (CAF-2)	RIVKLE [®] SFC (CAF-3)
Type of fastener	Rivet bushing	Press-fitting insert with micro knurling	Blind rivet nut
Manufacturer	Kerb-Konus-Vertriebs-GmbH	KVT-Fastening GmbH	Wilhelm Böllhoff GmbH & Co. KG
Material	Stainless steel	Brass	Steel
Mounting thread	M6	M6	M6
Weight	5.5 g	2.3 g	5.1 g
Installation	Pressing with plastic deformation of the element	Heat insertion	Riveting process with manual setting tool
Pre-hole diameter	9.7 mm	9.55 mm	9.1 mm

3 Test setup

To compare the different types of joining elements, in-plane loading tests, torsion tests and out-of-plane loading tests are performed on a universal testing machine. The setup of the quasi-static in-plane loading test is illustrated schematically in Fig. 4a. The load is applied to the joining elements by a M6 threaded rod. The test specimen is clamped to the movable traverse that moves with a constant velocity of 2 mm/min. All test specimens have a length of 150 mm and they are cut after the integration of the joining elements. In tests on specimens with pin-loaded holes (hole diameter D) different failure modes arise due to the variation of the sample width w and edge distance of the hole e . In [13] GF/PP test specimens with $e/D = 2$ and $w/D \geq 3$ showed bearing failure. To ensure a fail-

safe behaviour of the joints, in this work the specimen dimensions are set to $e/D = 2$ and $w/D = 4$ with the diameters D assumed as follows: $D = 12$ mm for PIE-1, PIE-2 and PIE-3, $D = 9.5$ mm for CAF-1 as well as CAF-2 and $D = 9$ mm for CAF-3. In the quasi-static torsion tests a torsional moment is applied to the joining elements by a M6 socket head screw (Fig. 4b). The size of the TPC test specimens is 100×100 mm² and the joining elements are positioned in the centre. The test specimens are clamped between steel plates with a clearance hole of 18 mm diameter. For the quasi-static out-of-plane loading tests (pull-out) the same test set up and specimen geometry are used. However, the load is applied to the insert by a M6 threaded rod at a constant crosshead velocity of 1 mm/min (Fig. 4c). All types of joining elements are investigated in positive and negative z-direction (cf. Fig. 2).

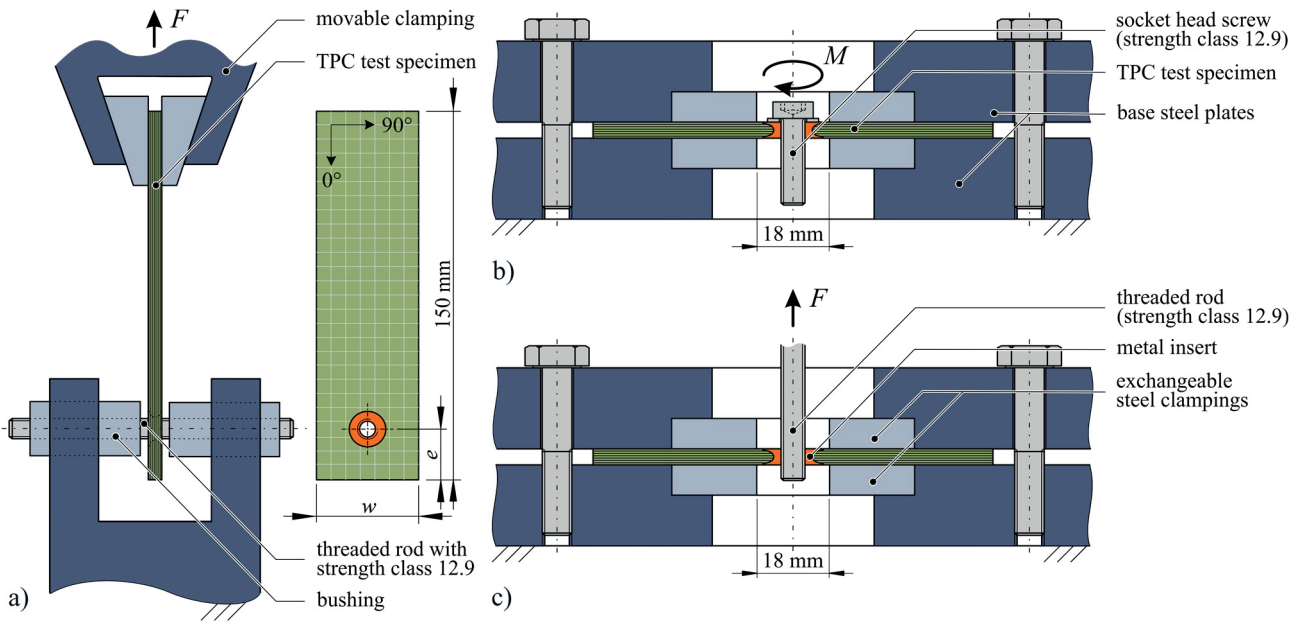


Figure 4: Schematic illustration of a) the in-plane loading test setup and specimen geometry, b) the torsion test setup and c) the out-of-plane loading test setup (pull-out).

4 Results

The results of the in-plane loading tests are summarised in Fig. 5. All joining elements show similar load-displacement curves. First there is a progressive initial range before reaching an almost linear section. Then the graphs show a slightly degressive increase up to the ultimate load. With PIE-1 and PIE-2 the highest ultimate loads of 9.8 kN and 8.6 kN are achieved (Fig. 6a). For these two types, a slight insert deformation on the outer edge can be detected in addition to laminate bearing (Fig. 5b). CAF-1 and CAF-2 show laminate shear out failure and not bearing failure as expected (Fig. 5b). To obtain bearing failure for all joining elements, an increased edge distance e could be used in future investigations.

In the torsion tests the highest ultimate torsional moment of 20.4 Nm is obtained with PIE-3 that has a non-circular contour adapted to the fibre orientation (Fig. 6b). Surprisingly, CAF-3 with 14.8 Nm reaches the second highest torsional moment without torsional form-fit, but only by force-fit. PIE-2 with a moderate form-fit for torsional loading, is with 13.1 Nm in the same range as CAF-3. CAF-1 and CAF-2 achieve the lowest ultimate torsional moments because of the small grooves and teeth, which only provide a slight form-fit. As PIE-1 has no anti-rotation function due to its circular shape it is not investigated in the torsion tests. The results show that due to the high design freedom of PIE

inserts, with a non-circular contour adapted to the fibre orientation high ultimate torsional moments can be achieved.

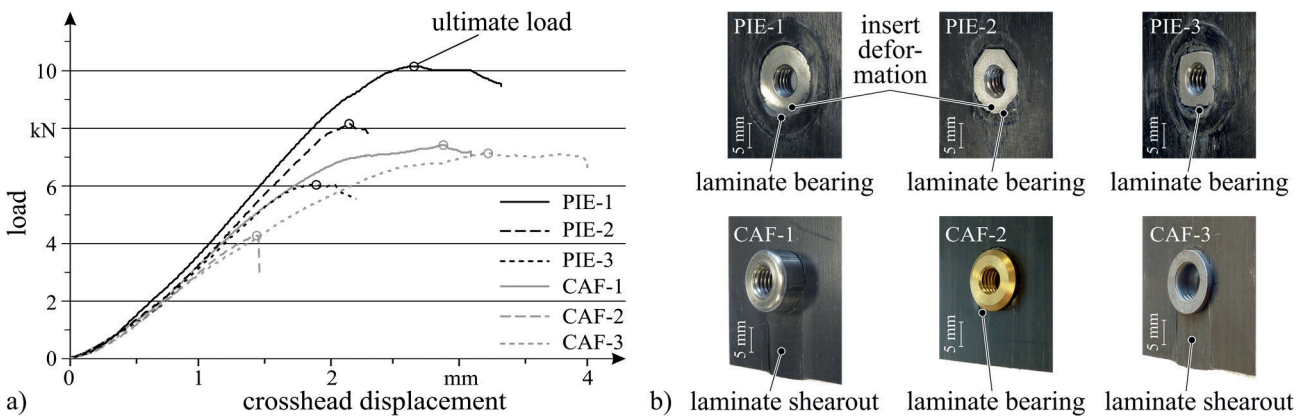


Figure 5: Results of the in-plane loading tests: a) representative force-displacement curves, b) typical failure behaviour.

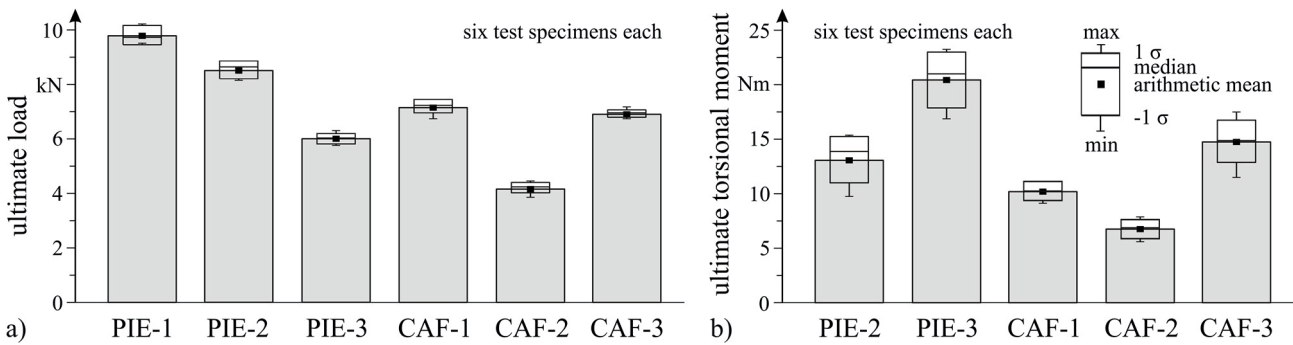


Figure 6: a) Ultimate loads of the in-plane loading tests, b) ultimate torsional moments of the torsion tests.

During pull-out testing it was observed, that for all investigated joining elements the pull-out behaviour is significantly different in both testing directions (Fig. 7). This even applies for PIE inserts, although both – the insert itself as well as the lay-up of the laminate – are symmetric to the laminate midplane. This indicates, that the local material structure of the TPC resulting from the embedding process has a significant influence on the pull-out behaviour and has to be taken into account when designing such joining zones (cf. [13]). However, the difference of the ultimate pull-out loads depending on the test direction is higher for all tested CAF than for PIE inserts.

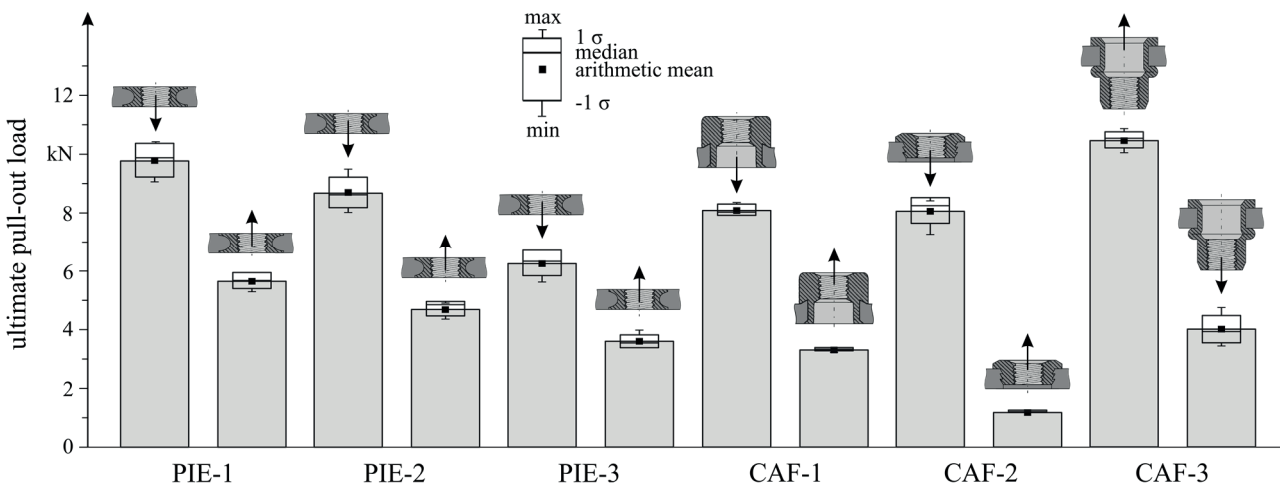


Figure 7: Results of the pull-out tests: ultimate loads for six test specimens each.

The ultimate pull-out loads of CAF-3 cannot be exceeded by the PIE inserts, but with 9.8 kN PIE-1 reaches the same range. In this context it is to be noted that the PIE inserts with 2.1 g to 2.3 g weight less than half of CAF-3 (cf. Table 1) and have no disturbing contour on the laminate surface like all three tested CAF do.

5 Conclusions

In this paper the capability of metal inserts embedded in TPC during part manufacturing is compared to subsequently integrated commercially available fasteners. The PIE inserts can achieve better capability in in-plane loading tests and with a non-circular design adapted to the fibre orientation even higher moments in torsion tests. In contrast to the investigated CAF, the PIE inserts have no disturbing contours on the final part surface and nevertheless achieve pull-out loads in the same range as the commercial solutions. The PIE process offers a high freedom in the design of the inserts, e.g. regarding the shape of the axial and rotational form-fit, so that they can be adapted and optimized for different applications and requirements. In addition, the integration of the embedding process into the main part manufacturing process provides great potential for reducing the number of process steps and manufacturing costs.

6 Acknowledgement

The authors gratefully acknowledge the financial support by the German Research Foundation (DFG) within the scope of research project “Simulation-assisted development of material-, load- and process-specific inserts for thermoplastic composites” (project number: 408132410).

7 References

- [1] B.-A. Behrens, A. Raatz, S. Hübner, C. Bonk, F. Bohne, C. Bruns, M. Micke-Camuz, *Procedia CIRP* **2017**, *66*, 113–118.
- [2] A. Herwig, P. Horst, C. Schmidt, F. Pottmeyer, K. A. Weidenmann, *Production Engineering, Vol. 12, no. 2*, **2018**, 121–130.
- [3] V. Mara, R. Haghani, M. Al-Emrani, *J. Compos. Mater., Vol. 60, no. 21*, **2016**, 3001–3018.
- [4] A.R. Rispler, G.P. Steven, L. Tong, *Compos. Sci. Technol., Vol. 50, no. 1*, **2000**, 95–106.
- [5] P.J. Herrera-Franco, G.L. Cloud, *J. Compos. Mater., Vol. 26, no. 5*, **1992**, 751–768.
- [6] P.P. Camanho, F.L. Matthews, *Proc. Instn. Mech. Engrs., Part L* **2000**, *214*, 33–40.
- [7] J. Sprovieri, *Assembly* *8, 5th August*, **2014**.
- [8] P.P. Camanho, C. Tavares, R. de Oliveira, A. Marques, A. Ferreira, *Compos. Part B* **2005**, *36*, 372–383.
- [9] B. Ferret, M. Anduze, C. Nardari, *Compos. Part A Appl. Sci. Manuf.* **1998**, *29*, 693–700.
- [10] J. Gebhardt, J. Fleischer, *Procedia CIRP* **2014**, *23*, 7-12.
- [11] J. Wilkening, F. Pottmeyer, K.A. Weidenmann, In: *Proc. ECCM17*, **2016**.
- [12] J. Troschitz, R. Kupfer, M. Gude, *Procedia CIRP* **2019**, *85C*, 83-88.
- [13] W. Hufenbach, F. Adam, R. Kupfer, In: *Proc. ECCM17, 6-7 June*, **2010**, Paper ID 461, 1–9.
- [14] R. Kupfer, *Dissertation*, Technische Universität Dresden, **2016**.

Investigations on possible joining processes for lightweight body structures for commercial vehicles in municipal service operations

T. Schiefer¹, A. Mahlme², D. Theis¹, B. Ganbaatar¹, M. Sauer¹, F Zimmermann¹, A. Klotzbach¹, J. Standfuß¹, M. Zimmermann^{1,3}

¹ Fraunhofer Institute for Material and Beam Technology IWS, Dresden, Germany

² PROFIL Verbindungstechnik GmbH & Co. KG, Friedrichsdorf, Germany

³ Technical University Dresden, Chair of Mechanics of Materials and Failure Analysis, Dresden, Germany

1 Introduction

Due to the efforts in the vehicle sector to meet the current requirements of the European Union, alternative drive technologies are not only being developed and tested by the well-known passenger vehicle manufacturers. For new registrations of light commercial vehicles, a limit value of 147g/km for CO₂ emissions has to be achieved until 2021 [1]. Especially in the area of municipal, inner-city light commercial transporting vehicles, the long service life and low average speed combined with low daily mileage, the use of alternative drives such as electric motors in combination with accumulator media presents an attractive option. This particular vehicle type consumes four to five times more fuel and therefore produces four to five times more emissions such as CO₂ than vehicles of this class used for other purposes [2].

In the manufacture of electrically powered urban commercial vehicles for municipal service operations, the weight of the vehicle must be reduced by using lightweight construction materials, to achieve a similar effective payload compared with conventional vehicles in steel construction. Material combinations such as fibre composites made of thermoplastic matrix and glass fibre reinforcement as well as light metals such as aluminium alloys offer the possibility for weight reduction. However, new material combinations also require the use of alternative joining technologies, since conventional welding is not applicable.

Since the 2000s, more and more investigations in the field of material-locking joining by means of adhesives have been carried out on material combinations of typical representatives of technical plastics such as polypropylene or polyamide with endless reinforced glass fibres, a low-cost consumer market high-performance composite material, [3-5]. Efficient and high-performance joining technologies are becoming increasingly important for the manufacture of complex products such as electric vehicles [6]. Modern multi-material mixed construction methods can only be used efficiently where appropriate joining technologies are available. Whereas in the 1980s steel bodies were joined cost-effectively by resistance spot welding [7], current composite bodies such as the AUDI TT (built in 2014) were not only produced with thermal joinings (e.g. resistance spot welding) but also with numerous mechanical processes (e.g. semi-tubular punch riveting), as well as in combination with bonding [8].

Within the publicly funded project "UTILITAS - Ultralight superstructures for commercial vehicles in municipal service operations", material-adapted joining techniques are being investigated: mechanical joining using insert technology, adhesive bonding and hybrid joining using both technologies as well as a new type of direct thermal joining using HPCI® technology [9] for consistent lightweight material construction in the field of municipal vehicle superstructures for light commercial vehicles. Within the framework of a study on resource-efficient lightweight construction for

electric mobility [8], an overview of the currently used joining processes for combinations of metals and polymers was compiled. It is clearly evident that, in addition to the classic joining processes of mechanical joining or bonding, more and more combinations of different joining processes are required.

2 Experimental Procedure

The joining experiments were carried out using fibre reinforced composites consisting of glass fibre Polyamide 6 matrix (GF/PA6) e.g. organic sheet, Tepex® dynalite 102 RG 600 from the manufacturer Bond Laminates GmbH. These are endless fibre reinforced fabrics with a fibre volume share of 47 %. The layer thickness is approx. 0.5 mm and the total thickness approx. 4.5 mm.

A typical aluminium wrought alloy, EN AW 6082 (3 mm thickness), in the condition T6 - solution annealed, artificially aged, which is also used in automotive engineering, was chosen as the metallic joining partner.

For the mechanical load cases tensile (90° to the joining plane) and tensile shear (in the direction of the joining plane) corresponding specimens were tested by four joining methods investigated: Bonding, direct thermal joining by means of inductive heating, mechanical joining by means of self-punching, cold-pressed thread inserts and hybrid connections made by mechanical joining and bonding.

For a better comparison of the achieved strengths/transferable forces of the composites, lap shear tests according to DIN EN ISO 14273 and tensile tests according to DIN EN ISO 16237 were carried out. The lap shear test specimens have the dimensions 107 mm x 45 mm, with an overlap of 22 mm (30 mm) and tensile test specimens 150 mm x 50 mm, resulting in a square joining area of 50 mm x 50 mm for the two-dimensional joining methods, respectively.

Prior to joining, the sample surfaces were pre-treated material-specifically and customized for each joining method. The aluminium samples were processed using continuous laser radiation with a wavelength of 1070 nm. The macroscopic laser structuring / ablation was carried out at a Multi Remote System (MuReA) developed at Fraunhofer IWS, which transmits the wavelength 10600 nm as well as 1070 nm via 3D large-field scanners in a fast deflecting manner to component surfaces for ablation or welding. The ablation tests were carried out with a 3 kW single mode fibre laser YLS-3000-SM, IPG using the scanner system Axialscan 50 with high speed and high power kit, Raylase GmbH. For the parameter study, the process parameters laser power, deflection speed of the laser beam, line distance between the laser tracks and the repetitions, were varied.



Figure 1: Multi-Remote-System

In addition, the fibre composite specimens were also pre-treated for the adhesive bonding tests. The thermoplastic fibre composite samples were treated with atmospheric pressure plasma. For this, the source Plasmatreater AS400 with the rotation unit RD 1004 of the company Plasmatrete GmbH was used. After a parameter screening, the plasma treatment was finally carried out on the samples to be bonded with the following parameter settings: distance between the lower edge of the nozzle and the upper side of the sample of 4 mm, a traversing speed of 10 mm/min and a flow rate of the process gas (compressed air) of 4000 l/min. The generator was operated with a frequency of 25 kHz at 400 V electrical voltages. Reactive chemical end groups are created on the thermoplastic sample surface which leads to a better wetting and bonding of the adhesive polymer. An evaluation of the optimum process parameters was carried out during plasma treatment screening with a comparative static contact angle measurement using deionized water and diiodomethane.

The joining was technology-specific, a tough-elastic two-component, epoxy-based construction adhesive, Scotch-Weld DP490 (3M) was used for the bonds. This adhesive is characterised by good cohesive strength and moderate elasticity and is suitable for use up to 80°C for metallic and plastic surfaces. During the tests, the samples were cured at an accelerated rate for three hours in a heating cabinet at 65°C. For larger structural components, crosslinking is also possible at room temperature.

For direct thermal joining a prototype of the Heat Press Cool Integrative - Joining Tool (HPCI®) developed at Fraunhofer IWS was used. The aluminium specimen is heated inductively with an induction generator (EFD Minac 18/25) at a frequency of 20 kHz with a power of 7.5 kW. At the same time, the joining partners are permanently pressed together with a punch realizing a force of approx. 290 N. In this case, heat conduction melts the thermoplastic matrix of the fibre composite material and flows into the surface structure of the aluminium sample created by laser radiation. After 50 s or 110 s, the heating process is completed, and the material is now rapidly cooled down with the use of compressed air.

For mechanical joining, a special thread insert was developed at Profil Verbindungstechnik GmbH and completely inserted into the fibre composite using approx. 40 kN. The experimental tests were based on an M5 stainless steel insert (Figure 2). They were screwed together with a torque of 5.9 Nm in accordance with DIN EN ISO 898. The aluminium samples have a pre-drilled hole with a diameter of 5.5 mm. For an additional increase of the pulling force, the specimen is placed during joining in such a way that the insert head is on the side facing away from the joining zone.

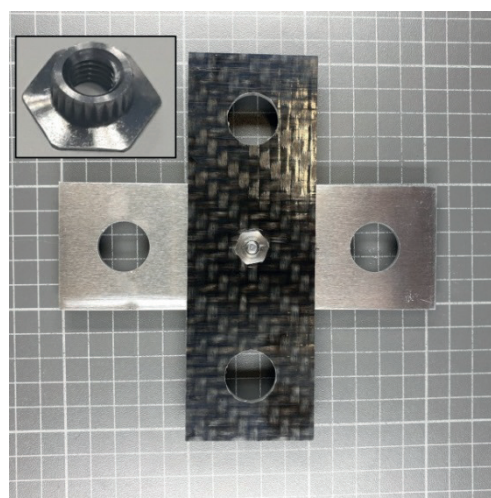


Figure 2: Mechanically joined cross tension test sample and the used M5 insert

Hybrid joining is a combination of bonding and mechanical joining and it is a suitable method for fixing the bond during the setting time.

The mechanical tests of the joined composites were performed on a multi-axial universal testing machine Z50, Zwick Roell. The test speeds were 5 mm/min for the lap shear test and 1 mm/min for the tensile test for all four different joining methods (Figure 3). The maximum breaking forces until failure were determined. The test was terminated when a force drop of 90 % of the maximum value was reached.

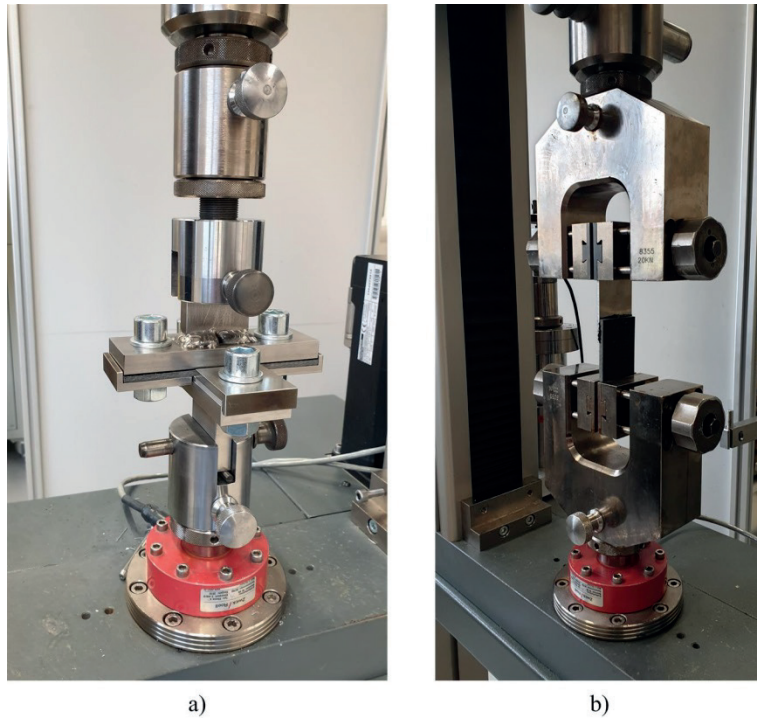


Figure 3: Mechanical test setup a) cross-tension, b) Single lap shear geometry

In order to determine the maximum breaking forces of aged joints, additional series of samples were prepared, which were subjected to a cyclical, alternating climate change test in a climatic chamber for 1000 hours (approx. six weeks) after joining and, if necessary, crosslinking the adhesive polymer. During this test (P-VW 1200), the temperature is changed alternately between -40°C and 80°C within a 12 hour cycle with a temperature gradient of 1 K/min and kept constant in the limit temperatures for four hours at the temperature extremes. During the holding time at 80°C , an additional humidity load of 80 % r. h. is superimposed. This provokes swelling of both the fibre composite and the adhesive and a potential influence of corrosion phenomena caused by the aluminium body becomes visible. The temperature differences also cause material-specific elongations.

3 Results and Discussion

The tensile shear test results, shown in Figure 4, demonstrate the potential of the two-dimensional joining processes of direct thermal joining and adhesive bonding. Hybrid joining also performs very well due to the insert geometry, the high material thickness of the fibre composite material as well as the surface area used. The lap shear tests of the mechanical and hybrid joints were repeated with an overlap of 30 mm, as it has caused the material failure of the fibre composite. There is still po-

tential to increase the strength by a geometric variation and the associated possibility of greater surface utilization. Besides the maximum shear forces, the force-displacement diagrams are very interesting, so mechanical joining and hybrid joining offer the possibility of higher deformations up to total failure of the joint.

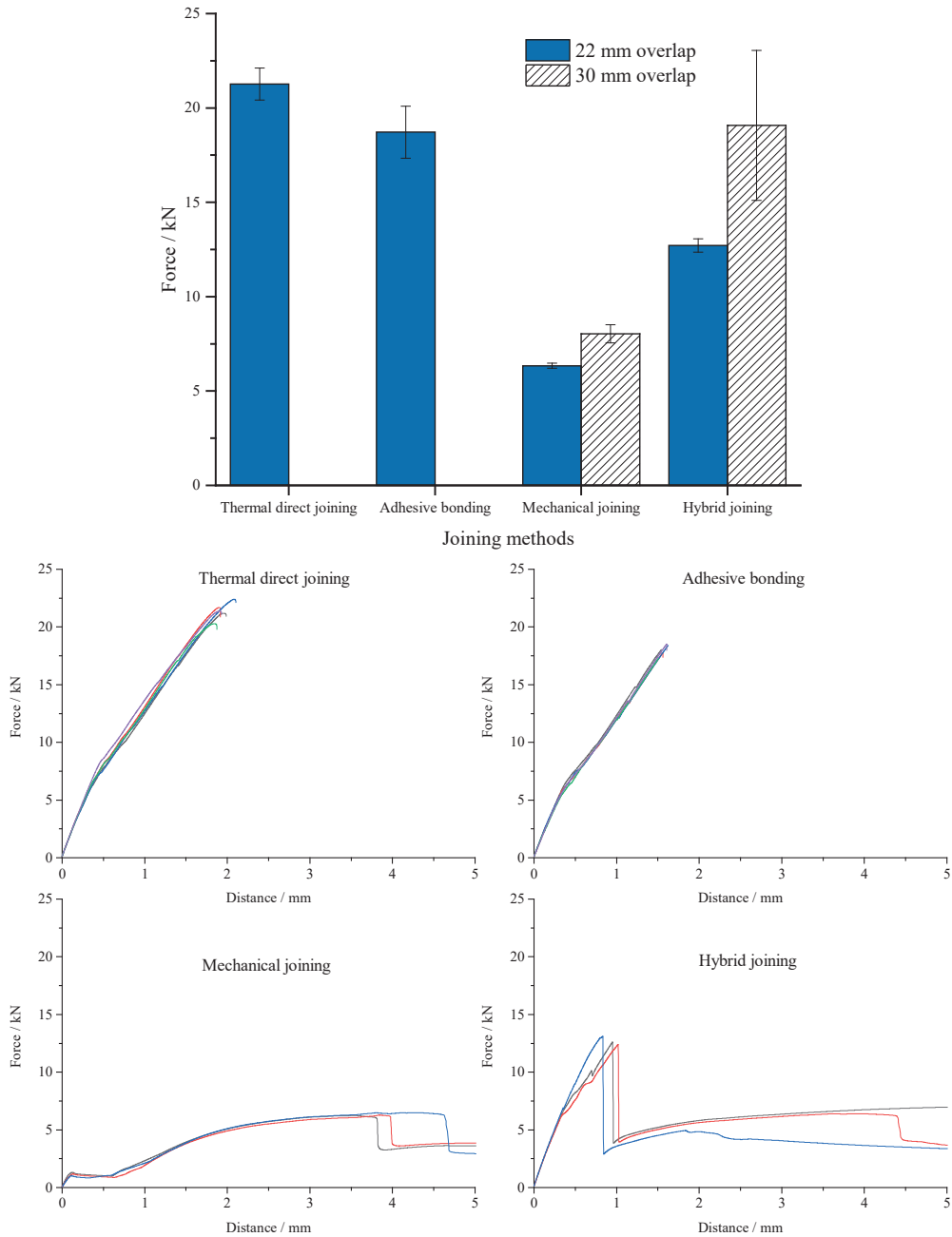


Figure 4: Tensile shear test results and force distance curves of the four joining processes

4 Conclusions and Outlook

By means of a material-specific and parameterized physical surface pre-treatment, the transmittable forces in mixed joints can be significantly increased not only in the case of pure material-locking

joints by means of adhesive bonding, also in the case of joints based on form and material locking (direct thermal joining).

The current results of the investigations show the great potential of the different joining methods in the field of lightweight construction using multi-material combinations. Detachable connections by mechanical joining of special inserts can be realized just as well as non-detachable surface joining technologies such as conventional structural bonding. In order to realize large structures without expensive and complex joining devices by means of bonding, hybrid joining as a combination of mechanical joining for the fixing process and adhesive bonding was also investigated. The torque of the screw tightening has a great influence on the effective bonding surface.

In addition, the aging resistance of the joints of the investigated material pair GF/PA6 and aluminium at standardised climate change tests from the automotive industry is currently being tested.

After finishing the cyclically alternating climate tests reliable data for the residual strength of the joints investigated will be available.

Acknowledgements

The research was funded by the Federal Ministry of Economics and Energy (BMWi) based on the decision of German Bundestag within the project “UTILITAS” (19I18005C) supported by TÜV Rheinland Consulting GmbH.

5 Literature

- [1] Ernst, C.-S.; Harter, C.; Olschewski, I.; Eckstein, L.: CO₂-Emissionsreduktion bei Pkw und leichten Nutzfahrzeugen nach 2020 (2015).
- [2] Stan, C.: Alternative Antriebe für Automobile, 4. Aufl. 2015. Berlin, Heidelberg 2015.
- [3] Köckritz, T.; Schiefer, T.; Jansen, I.; Beyer, E.: Improving the bond strength at hybrid-yarn textile thermoplastic composites for high-technology applications by laser radiation. *Int. J. Adhes. Adhes.*, 46, 85 (2013).
- [4] Pap, J.-S.; Jansen, I.; Beyer, E.: Strukturelles Kleben von textilverstärkten Thermoplasten mit zähelastischen Klebstoffen. *DVS-Berichte Band 303*, 2014.
- [5] Schiefer, T.; Jansen, I.; Bieda, M.; Pap, J.-S.; Lasagni, A.-F.: Large area surface structuring by Direct Laser Interference Patterning for adhesive bonding applications. *J. Adh. Soc. Japan* 51 (2015) S1.
- [6] Lässig, R. u.a.: Serienproduktion von hochfesten Faserverbundbauteilen – Perspektiven für den deutschen Maschinen- und Anlagenbau. Amsterdam, Berlin, Zürich: Roland Berger Strategy Consultants, 2012.
- [7] Eickenbusch, H.; Krauss, O.; Verein Deutscher Ingenieure e.V. (Hrsg.): Werkstoffinnovationen für nachhaltige Mobilität und Energieversorgung. Düsseldorf, 2014.
- [8] Stegelmann, M.; Gude, M.; Müller, M.; Lieberwirth, H.: FOREL-Studie – Chancen und Herausforderungen im ressourceneffizienten Leichtbau für die Elektromobilität. 2015.
- [9] Klotzbach, A.: Laser joining process yields metal-thermoplastic hybrid parts. *Industrial Laser Solutions* March/April 2019.

Investigation of automated nibbling as an alternative cutting technology for machining of fiber-reinforced polymers

Langer, J.^{1*}, Gerstenmeyer, M.¹, Schulze, V.¹

¹wbk Institute of Production Science, Karlsruhe Institute of Technology (KIT), Germany

*Corresponding author: Kaiserstr. 12, 76131 Karlsruhe, Germany, +49 (0) 721 608-42455, jannis.langer@kit.edu

Abstract: Today, milling is the most frequently used process for contour machining and trimming operations of fiber-reinforced polymers (FRP) on an industrial scale. Disadvantages of this process are dust generation as well as machining-related damage such as delamination. An alternative technology for the processing of FRP, with the potential of overcoming these disadvantages, is a punching process with feed called nibbling. This hand-guided process, known from sheet metal processing, has so far only marginally been mentioned for the processing of FRP materials. The aim of this study is to investigate the correlation of workpiece material and process parameters like feed rate with feed forces, tool wear, machining induced damage as well as workpiece cutting edge quality. In order to achieve these objectives, a hand-held nibbling tool was integrated into a machining center to ensure automated and reproducible machining of FRP. Slot nibbling tests were carried out on glass (GFRP) and carbon (CFRP) fiber-reinforced sheet molding compounds (SMC). Force measurements serve as characteristic values to assess the fundamental mechanisms. The evaluation of the workpiece quality as well as surface damage such as delamination, matrix spalling and fiber fraying are carried out by the use of microscopic imaging. The results show fundamental characteristics of nibbling FRP. The work provides a basis for highly productive, automated nibbling of FRP.

Keywords: nibbling, automation, machining induced damage, quality, dust, FRP, SMC

1 Introduction

Machining of fiber reinforced polymers (FRP) poses a great challenge due to the often insufficient cutting quality which is expressed in structural workpiece damage such as delamination [1] and fiber fraying [2]. Past investigations showed that there is a dependence of the tool geometry [3], layer structure, fiber orientation and feed rate [4] on resulting damage when milling FRP [5]. It is also important to ensure that the clamping is as rigid as possible when milling [6] and drilling [7] FRP, which makes machining more difficult. Since there is a broad variety of FRP materials on the market today, each characterized by different fiber orientations and layer structures, radically new processing strategies need to be considered to process these materials economically.

Nibbling is one possible technology that has hardly been considered as a separation process for industrial scales so far, although it seems very promising with regard to the challenges stated before. The process of nibbling can be described by punching sheet components with continuous feed. During machining, the tool moves continuously through the workpiece after each punch. Using this technique, holes that are bigger than the actual tool [8] as well as shapes in almost any geometric complexity can be produced using only one tool [9]. Due to constant feed rate, a fine ripple pattern, also referred to as nibbling marks, is created by the repositioning, as each punching process leaves its own imprint. These nibbling marks are comparable to feed marks known from milling operations. They depend largely on the feed of the tool and the punch radius [9]. Since the tool can be rotated,

form elements that are larger than the actual tool can be produced and the possibilities of conventional punching are significantly expanded by nibbling [8]. The technology was originally used to process workpieces made of sheet metal [10]. Present research approaches regarding nibbling are limited to studies from the 1990s on automated tool selection for CNC nibbling of sheet metal [11,12]. The possibility to use nibbling for the separation of FRP was first mentioned in 1985 by König et al. but has not been further scientifically investigated since that time [13]. However, the process of shear-cutting of FRP was assessed in many studies [14,15]. Compared to conventional machining processes, nibbling of FRP comes with the advantage of a kinematics-related reduction of dust generated during machining [16]. Only recently, the idea of a hand-held electronic power tool was realized by TRUMPF releasing a specialized FRP-Nibbler [17]. Until now there is no research published that has dealt with the particular mechanisms, primarily the influence of feed and tool wear, on the workpiece quality when nibbling FRP.

2 Materials and Methods

2.1 Materials

For the experimental investigation, glass (GFRP) and carbon (CFRP) fiber-reinforced thermoset sheet molding compound (SMC) with random fiber orientation were used. Both materials have a fiber mass content of 41 wt.-% and a thickness of 2.3 mm.

2.2 Methods and Equipment

The investigation of the specimens nibbling properties was performed by slot nibbling experiments with a TruTool FCN 250 Nibbler by TRUMPF on a machining center HELLER MC16. Only original TRUMPF tools were used for the investigation. The punch has a diameter of 8.5 mm. The cutting gap is 3.15 mm wide, although the device is only designed for material thicknesses up to 2.5 mm. The forces were measured using a three component force measuring platform type 9255SP by KISTLER. The resulting forces were recorded with DasyLab. A tactile coordinate measurement machine type Mahr Surf XCR20 by MAHR was used to measure tool wear of the punch and the die. The wear measurement was performed along the red line in Fig. 1b) and c). Additionally, a ZEISS microscope type Stemi SV11 was used to optically measure tool wear as well as evaluate the workpiece quality and the nibbling induced damage. As shown in Fig. 1 the wear measurement was performed in the center as well as on the right and the left flank of both tools.

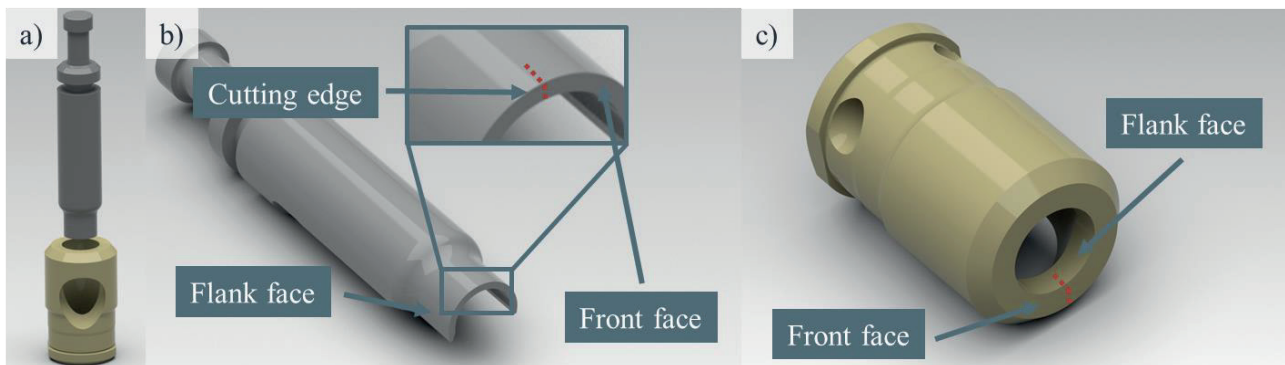


Fig. 1: a) Rendering of punch and die, detailed depiction of b) punch, c) die. Red line: path of tactile wear measurement.

3 Experimental Setup

A customized mount was designed and manufactured in order to integrate the hand-held power tool into the machining center. A single sided clamping system used to fix the specimens on the force measuring platform during the machining operation was also custom made and installed. The experimental setup is shown in Fig. 2a. Due to the closed construction of the nibbling tool (Fig. 2b), the cutting forces could not directly be measured with this setup. Therefore force measurements were conducted in feed direction (Y-direction). Aim of these measurements was to understand the influence of feed rate on the stress between the front face of the punch and the workpiece. The maximum feed rate of the nibbler in manual operation varies between 1300 and 1900 mm/min depending on the laminate to be processed and the materials thickness. Manual pre-tests resulted in a maximum speed of approx. 1600 mm/min for the material to be investigated. In order to gain an understanding of the influence of the feed rate, the experiments in this study were carried out with slower feed rates of 320, 640 and 1280 mm/min, representing 20, 40 and 80 % of the maximum possible feed rate.

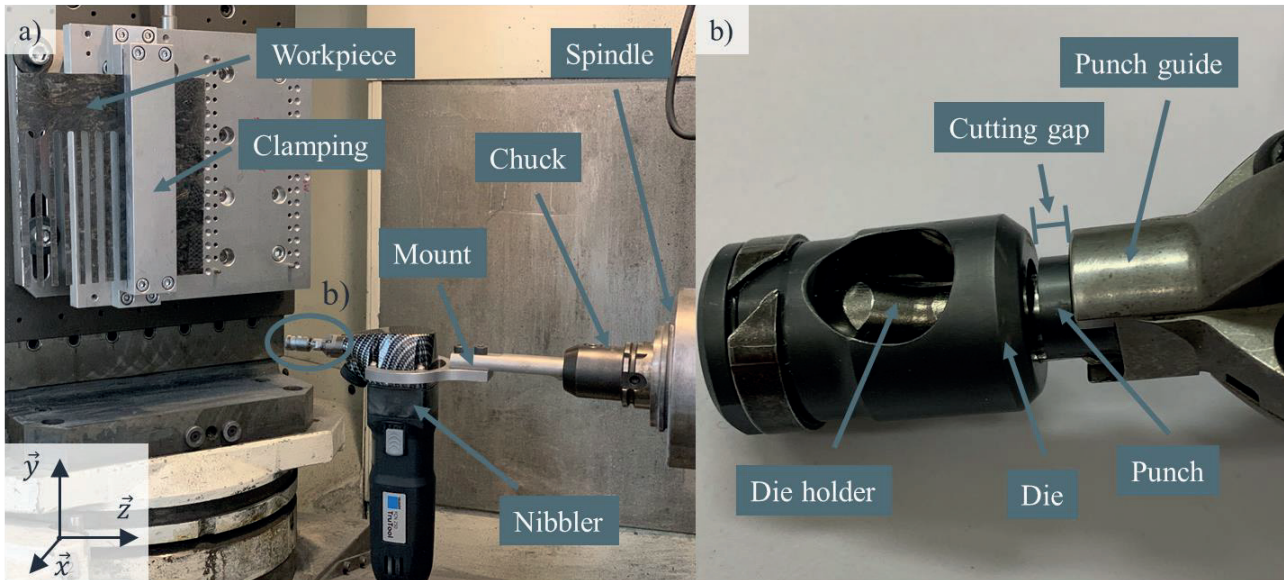


Fig. 2: a) Experimental setup and b) close up of the nibbling tool.

4 Results

4.1 Feed forces

The examination of the feed forces was performed with three different feed rates of 320, 640 and 1280 mm/min for GFRP as well as CFRP SMC. The length of the nibbled slot was 160 mm for all experiments. The mean values of the feed force (force in Y-direction) recorded by the force measuring platform are shown in Fig. 3. The observed trend of the maximum feed forces differs significantly for the nibbling of GFRP compared to CFRP. When doubling the feed from 320 to 640 mm/min, the resulting feed force increases by 59 % when nibbling GFRP. Another doubling of the feed to 1280 mm/min leads to a further increase of the force by 45 %. However, this effect cannot be observed for the CFRP specimens. Here an increase of the feed from 320 to 640 mm/min leads to a

raise of feed force by 30 %. A further increase of the feed from 640 to 1280 mm/min leads to a decrease of the resulting force by about 7 %. At the same time, it could be observed that the noise generated from the processing was reduced to a perceptible extent. Manual nibbling is a force-controlled process in which an even, constant feed is achieved. Due to the integration into the CNC machining center, the process is path-controlled. The process tends to chatter, making it unstable. It can be assumed that the selected feed rates are not ideal for achieving a stable, chatter-free process. Increasing the feed rates closer to the maximum value might lead to a smoother processing with reduced chatter.

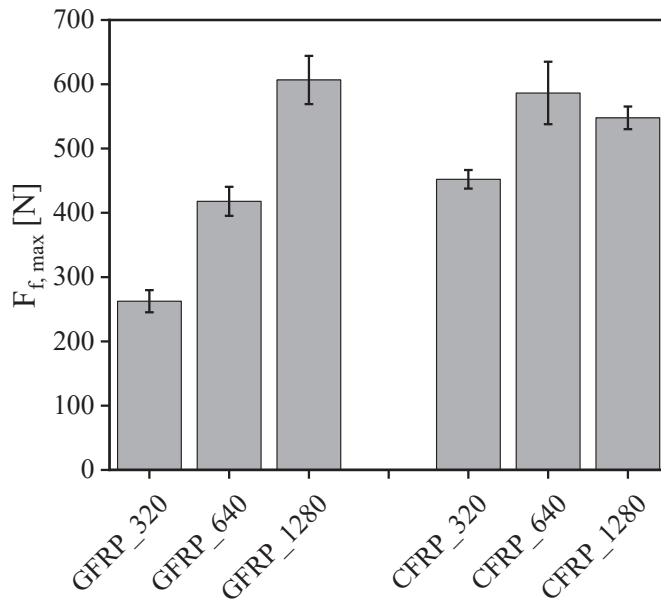


Fig. 3: Mean values of the maximum feed force $F_{f,max}$.

4.2 Tool wear

Wear of both, the punch and the die was analyzed by tactile as well as microscopic imaging. For comparing the initial cutting edge preparation with the occurring tool wear, both tools were measured before the experiments were conducted. During the experiments, the wear state was measured after every 480 mm of cutting distance. The location of the wear measurement is depicted in Fig. 1. An individual set of tools was used for each material. The results of the microscopic wear measurement for the punch in new condition as well as after a cutting distance of 7200 mm with variable feed rates between 320 and 1280 mm/min are shown in Fig. 4. The initial tool edge preparation of the punch revealed a cutting edge radius of about 11 μm . After processing a total of 7200 mm of GFRP and CFRP, the wear state of the punch showed a cutting edge radius of 17 μm and 97 μm respectively. The die showed a cutting edge radius of 15 μm after cutting the GFRP SMC and 164 μm after processing the CFRP material. There was no local difference in tool wear observable along the tools. The results from the microscopic imaging can also be seen in the tactile measurements shown in Fig. 5. Only very little tool wear was measured for the nibbled distance in GFRP. In contrast to this, there is significant tool wear observed during nibbling of the CFRP.

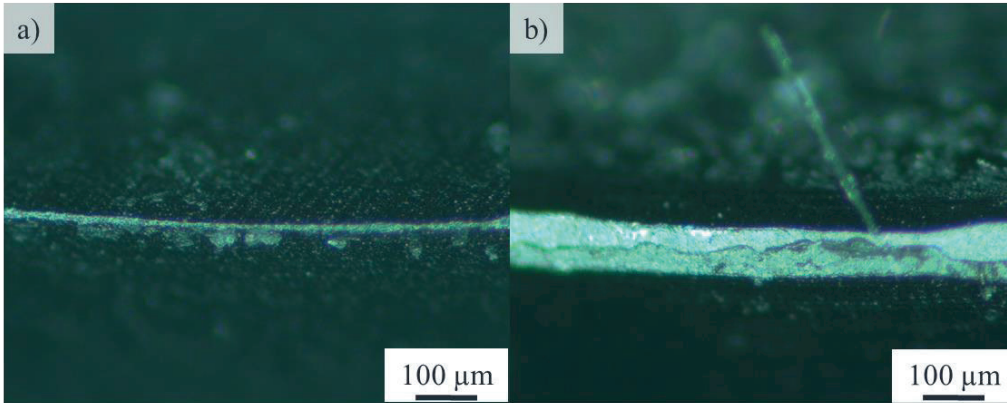


Fig. 4: Microscopic images of center of the cutting edge of the punch a) new, b) after 7200 mm cutting distance in CFRP.

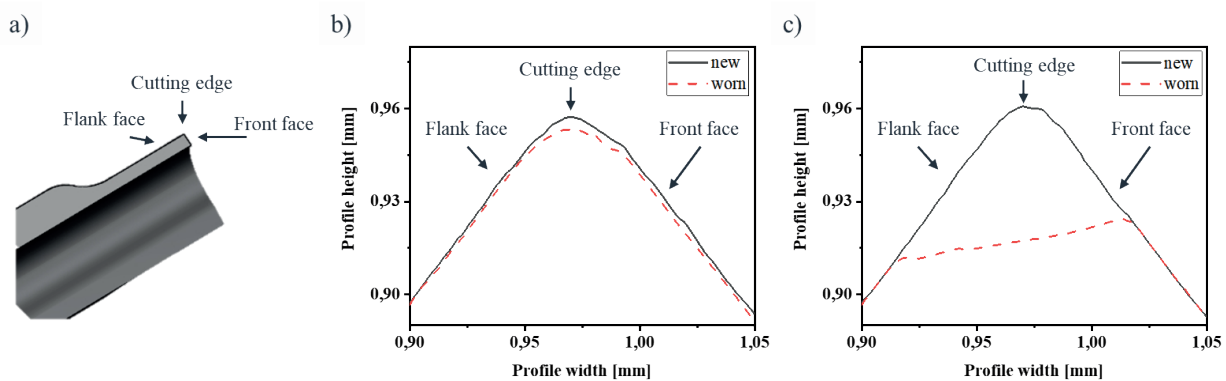


Fig. 5: a) Cross section of punch and tactile measured profiles along the plane of the cross section in new and worn condition after 7200 mm cutting distance in a) GFRP and b) CFRP.

4.3 Workpiece quality and nibbling induced damage

The achieved workpiece quality was satisfactory overall. As expected, nibbling marks could be observed on all specimens (Fig. 6). The distance between these marks depends on the feed rate. The lower the feed, the less feed marks are visible on the workpiece. An influence of the workpiece material or the tool wear state on the appearance of the nibbling marks could not be observed. As shown in Fig. 7, there was some nibbling induced damage observable. Fiber fraying (Fig. 7a) could only be detected on few specimens. In contrast to milling, a correlation between fiber fraying, feed rate and tool wear could not be observed. Delamination of fiber bundles (Fig. 7b) on the surface was observed for both materials. This effect was always more prominent on the clamped side of the workpiece compared to the unclamped side. This result is in direct contrast to the findings from milling and drilling of FRP. No influence of feed rate or tool wear on the delamination could be observed.



Fig. 6: Macroscopic Image of damage free contour of the workpiece cutting edge with feed marks, nibbled at 1280 mm/s.

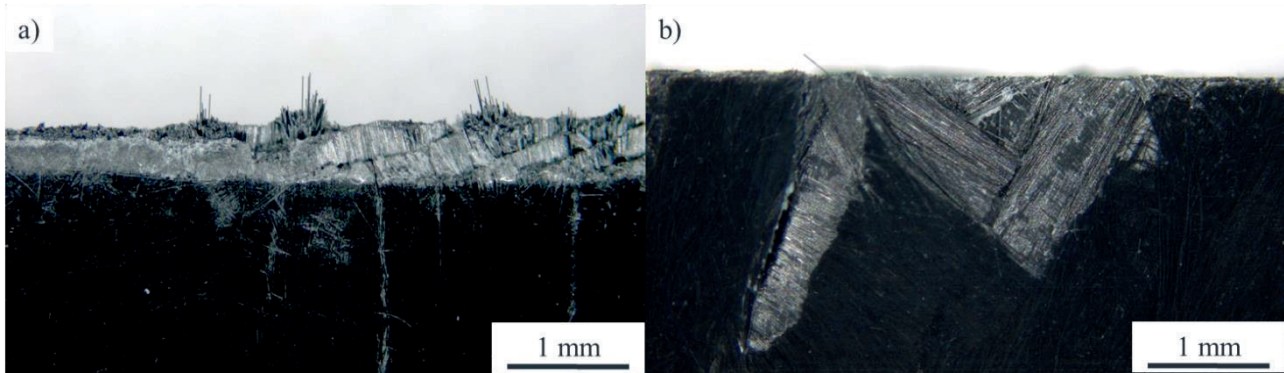


Fig. 7: Microscopic images of nibbling induced damage on the workpiece cutting edge a) fiber fraying and b) delamination of fiber bundles on the surface.

5 Conclusion

In this paper, an investigation of nibbling of glass and carbon fiber reinforced SMC is presented. The results lead to the following conclusions:

- The measurable feed forces, caused by the continuous feed of the closed tools front face against the workpiece, tend to increase for higher feed rates.
- Especially for lower feed rates, the feed forces are considerably higher when nibbling CFRP compared to GFRP. At higher feed rates, the influence of the material on the feed force decreases. It is assumed that unsuitable feed rates cause the process to chatter, making it unstable. This effect could only be perceived acoustically in the experiments. Further experiments have to be performed to investigate the chatter in detail.
- A special test setup is required to measure the cutting forces. This will be necessary in the future to investigate the separation mechanisms in more detail.
- Only slight tool wear has been observed during nibbling of GFRP while nibbling of CFRP caused significant tool wear to both the punch and the die.
- In contrast to the findings from drilling and milling of FRP, the effect of delamination is more prominent on the clamped side of the workpiece. A flexible clamping system might help to reduce nibbling induced damage and should be further investigated.
- A distinct separation of sheared and fractured areas in the shearing process could not be observed in the conducted experiment.

The results of these investigations are the basis to further research on automated nibbling of FRP and understanding the influence of the continuous feed on the shearing mechanism as well as the resulting workpiece quality. In conclusion, nibbling has proven to be a promising technology for processing FRP. In comparison to milling, the observed damages to the workpiece are significantly reduced. The tool wear seems to be especially high when nibbling CFRP, so that further research is necessary to assess this issue. In addition, the influence of the wear condition on the component quality should be assessed in the future.

Acknowledgements

The research documented in this paper has been funded by the German Research Foundation (DFG) within the International Research Training Group “Integrated engineering of continuous-

discontinuous long fiber reinforced polymer structures” (GRK 2078). The support by the German Research Foundation (DFG) is gratefully acknowledged. The authors also gratefully acknowledge Fraunhofer Institute of Chemical Technology for fabrication of the demonstrator by compression molding process as well as TRUMPF Schweiz AG for supplying the TruTool FCN 250 Fiber Composite Nibbler and all necessary tools and equipment for the conduction of the experiments.

5 References

- [1] H. Hocheng, C.K.H. Dharan, *J. of Engineering for Industry* **1990**, 112, p. 236-239.
- [2] Klocke et al., *Manufacturing Engineering and Materials Processing* **1999**, 53, p. 249-266.
- [3] A. Helfrich, F. Zanger, V. Schulze, *14th International Conference on High Speed Machining HSM 2018*, San Sebastian, Spain.
- [4] A. Helfrich, S. Klotz, F. Zanger, V. Schulze, in *Procedia CIRP* **2017**, 66, p. 193-198.
- [5] M.A. Karataş, H. Gökkaya, *Defence Technology* **2018**, 14, p. 318-326.
- [6] S. Klotz, F. Zanger, V. Schulze, in *Procedia CIRP* **2014**, 24, p. 38-43.
- [7] S. Klotz, M. Gerstenmeyer, F. Zanger, V. Schulze, in *Procedia CIRP* **2014**, 13, p. 208-213.
- [8] T.M. Hancock, *Computers in Industry* **1989**, 13, p. 245-251.
- [9] VDI 2906 Blatt 4: Quality of cut faces of (sheet) metal parts after cutting, blanking, trimming or piercing Nibbling **1994**.
- [10] M. Kolbe, W. Hellwig, in *Spanlose Fertigung Stanzen 2018*, 12, Springer Vieweg, Wiesbaden, Germany.
- [11] H.T. Loh, A.Y.C. Nee, N.F. Choong, *J. of Mater. Process. Tech.* **1990**, 23, p. 107-119.
- [12] N.F. Choong, A.Y.C. Nee, H.T. Loh, in *Computers in Industry* **1993**, 23, p. 205-222.
- [13] König et al., in *CIRP Annals – Manufacturing Technology* **1985**, 34:2, p. 537-548.
- [14] D. Tatsuno, T. Yoneyama, K. Kawamoto, M. Okamoto, in *Polym. Compos.* **2016**, 39, p. 2571-2586.
- [15] K. Ogi, S. Yashiro, *20th International Conference on Composite Materials ICCM 2015*, Copenhagen, Denmark.
- [16] P. Dubler, A. Gebhardt, *Experience Composites Symposium 2016*, Augsburg, Germany.
- [17] https://www.trumpf.com/en_INT/company/presse/global-press-releases/press-release-detail-page/release/first-of-its-kind-nibbler-for-fiber-composite-materials/ [accessed: 19.01.2020]

Study on Water Jet Cutting of Fibre-Reinforced-Plastics-Metal-Laminates

Vicky Reichel^{1,2}, Felix Rothe^{1,2}, Fridolin Franke¹, Daniel Lattek¹, Jan Beuscher^{1,2}, Klaus Dröder^{1,2}

¹ Technische Universität Braunschweig, Institute of Machine Tools and Production Technology, Braunschweig, Germany ²Open Hybrid LabFactory e.V., Wolfsburg, Germany

The use of hybrid components made from metal and fibre-reinforced-plastics (*FRP*) is growing but inhibited by cost and economic manufacturing processes. A typical process step needed to manufacture hybrid components is trimming before and after consolidation of the *FRP*. There are several cutting processes possible on hybrid *FRP*-metal-laminates but with a wide range of different process characteristics. A process used in several industries at small to medium scale production is water jet cutting (*WJM*). This paper investigates the water jet cutting process related dependences on the failure behaviour of two-dimensional specimens of different *FRP*-metal-laminates. With regards to vary the layer setup of steel and *FRP* the results are described by quality characteristics like surface roughness, geometrical trueness and precision of the cut.

1 Introduction

The advantage of hybrid *FRP*-metal structures (*FML*) is the possibility to achieve a weight reduction of a structure while the mechanical properties stay constant or even improve [1, 2]. The production of economic hybrid structures (compared to conventional steel parts) is possible by reducing the manufacturing steps, improve process quality or integration of additional functions, since the material costs of *FRP* are much higher than for metals. The lack of knowledge of efficient machining processes with high quality is one of the obstacles for the use of *FMLs* in large scale production. Cutting processes are used for different process steps: the preparation of semi-finished products, cutting operations for holes and drillings as well as post processing and finishing steps. Regarding this, the knowledge about cutting processes is crucial to achieve the aim of the economic production of *FML*. Furthermore, the effects of material damage after cutting processes are mostly unknown, but these areas are often initiation locations for overall failure of components, especially delamination in *FRP*. There is a wide variation of possible cutting processes for *FMLs*: milling, laser beam cutting and waterjet cutting are totally different processes with particular operation characteristics [3, 4]. The aim of this paper is the investigation of the effects detected on the cutting edge of single and multi-layered *FMLs*. The different material characteristics in *FMLs* lead to different cutting edge geometries depending on thickness and layer variation of the hybrid component. There are a lot of investigations targeting the optimization of *WJM* process parameters on *FML* [5–7]. This study works with different layering and cutting directions to investigate the *WJM* cutting process on *FMLs*. For evaluation the surface roughness and dimensional trueness were detected.

2 Water jet cutting on hybrid materials

The process of *WJM* cutting uses the kinetic energy of a highly pressurized water beam to cut materials via erosion and removes the material. The technique is suitable for a lot of materials which differ highly in their mechanical properties (e.g. ceramics, glass, plastics, metals) as well as for composite

structures [8–11]. Some advantages are: tool-free processing leading to no tool wear, low thermal impact [8] leads to possibility to cut materials with different thermal resistance, high flexibility on geometries with high accuracy at low cutting forces [5] and the absorption of cutting dust. A disadvantage using *WJM* cutting is the consumption of costly abrasive materials and water itself. Also the cutting quality depends on the traverse speed what limits the process speed in some cases to a low level.

A *WJM* cutting process can be performed without any abrasive but also with abrasive for materials with higher strength and density. Caused to the generated negative pressure of the fluid, the abrasive is merged into the beam (venturi-effect at the mixing chamber). Due to the ablative procedure the beam loses energy over the depth of the work piece. In combination with the transverse motion this leads to drag of the stream (*table 1*). High feed rates leads to less time for the beam to extend to the bottom side of the work piece. This leads to higher surface roughness and therefore lower quality cuts (*table 1(b)*) [8, 13]. Also the geometrical dimensions of the kerf depend highly on the cutting speed. Lowering the traverse rate leads to a fully extended vertical beam formation and reduces kerf angles α (*table 1(a)*) This also goes along with nozzle distance to the work piece: too high stand-off distance leads to wider kerf dimensions.

Water jet machining of *FML* is actively addressed in recent research investigations [5–7]. A specific type of *FML* made of aluminium sheets and glass-fibre-reinforced-plastics (*GFRP*) layers is comparable to the material combination used in this research due to the behaviour multi material design. In [3] some results on cutting edge geometry and surface quality were shown. Inappropriate use leads to cracks and delamination in the *FRP* material which reduces the performance of laminate. To avoid defects by manufacturing processes this research focusses on kerf surface quality parameters.

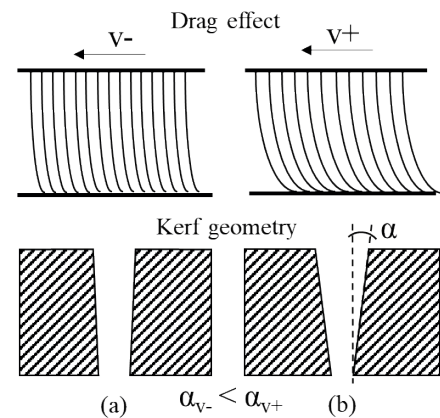


table 1 cutting characteristics

3 Experimental Setup

3.1 Materials

The single-layer *FML* are each made of one layer *FRP* and one layer steel. The study aims to figure out what influence the fibre setup has. Usually unidirectional fibre composites tend to be susceptible to damage induced by cutting forces. Varying the metal material it is intended to show the extent to which the different strengths of steel influence the overall performance of the laminate. The different strength classes of the bonding agents should provide a prediction to the workability of the *FML* types in *WJM* cutting. There were 18 different plate variations manufactured and tested in two cutting directions. With the investigation of multi-layer hybrid laminates [14, 15], a specimen dimension has to be selected that allows large step intervals in the Design of Experiments. With large step intervals, effects can be identified with higher reliability. There were 27 *FML* variations investigated according to the specimen design in [16]. The chosen manufacturing method is based on the investigations in [15] and the relevant manufacturing techniques of [17]. *Table 1* shows the specimen and processing parameters of both single and multi-layer plates.

Table 1. Specification of *FML* laminates

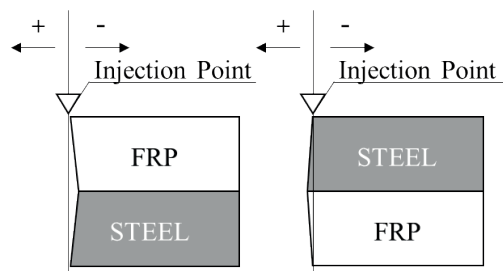
	Steel	Bonding agent	<i>FRP</i>		Manufacturing
Single-layer FML plate	HX340 LAD Z100 MB, d: 1 mm	Nolax A22.501 (DIN 1465: 12 MPa)	Tepex dynalite 102-RG600, d: 2 mm (GF Fabric-PA6)		Thermoforming specimen size: 250 mm x 250 mm press parameters: T = 220 °C p = 100 N/cm ² t = 360 s heat up, 120 s cool down
	22MnB5 AlSi, (HF) d: 1 mm	Betamate 1480v203 (DIN 1465: 27 MPa)	BASF Ultratape B3EG12, d: 2 mm, (GF Tape PA6)		
		Vestamelt Hylink (DIN 1465: 8 MPa)	BASF Ultratape B3EC12, d: 2 mm (CF Tape PA6)		
Multi-layer FML plate	1.4310; d: 1.5 mm	SuraLink® 021	Glass-Fibre	Epoxy	Vacuum infusion Fibre volume content: 42%
		Surface sandblasted	HP-U400E UD	RIM 935/ RIMH 937	

3.2 Schematic

To evaluate the influence of the stacking direction (*FRP*-steel or steel-*FRP*) the single-layer specimen are used to show dependences. The multi-layer specimens are used to show dependences on the cutting edge of layer variations in the hybrid laminates. The specimen plates used for the experiments are cut into specimen sizes of 25 mm x 100 mm (single-layer) and 30 mm x 300 mm (multi-layer). *Table 2* contains the cutting parameters used for this.

Table 2. Processing Parameters for WJM (l.) and measure procedure for dimensional deviation (r.)

Parameter	Unit	Value
Abrasive Material	-	corund
Cutting Speed	mm/min	325,05
Nozzle Diameter	mm	0,3048
Abrasive mass flow rate	Kg/min	0,3
Machine	-	Omax 5555
Selected Material	-	Mild Steel
Water Pressure	MPa	360
Abrasive index	-	0,96
Stand-off distance	mm	1



The material kind and thickness selection influences parameters like traverse speed and water pressure. Machine manufacturers do not offer material choices for hybrid materials. Therefore, the material with higher density is selected which is in that case the steel component.

3.2.1 Design of Experiments (DOE)

For the single-layer specimen every possible stacking combination for steel and *FRP* was realised. The used bonding agent depended on the type of *FRP* used due to the specific strength, for example the Vestamelt was only possible for Tepex GF woven fabric. For the multi-layer hybrid laminates it was more difficult to use a simple statistical design. Therefore the statistical design based on [18] was used for investigation. The procedure for identifying the relevant factors is based on a categorical factor allocation for the hybrid laminate [19, 20]. The resulting *DOE* allows regression analysis based on effect coding.

3.2.2 Evaluation methods

To investigate the kerfs surface roughness in dependency to layer position and quantity the size of for R_a and R_z [both in μm] are recorded. The R_a value shows the arithmetical mean deviation of the assessed profile while R_z detects the maximum height of the profile. The values were detected with an Hommel T1000 using the stylus method in accordance to DIN 25178-601 [21]. The goal is to evaluate the relation between roughness over depth and stacking variation. The deviation is measured, as shown in *Table 2 (r.)*. The maximum deviation of every single layer is measured. This optical measurement was made with Keyence VHX700F digital microscope and software.

4. Experimental Results and Discussion

4.1. Single-layer FML

At the single-layer specimen, the roughness was measured at steel and on *FRP* layers. In *Figure 2* the values for R_a on steel and *FRP* are shown for the different cutting directions. In the upper left chart, it can be determined that the steel values are lower than the *FRP* values. It was demonstrated that the values for the HX340 steel slightly show higher values than HF steel. The *FRP* values (see upper right chart) only show high spread of values and therefore a high deviation for the cutting direction steel-*FRP*. The type of bonding agent neither the type of used *FRP* influence the surface roughness of the different steel types.

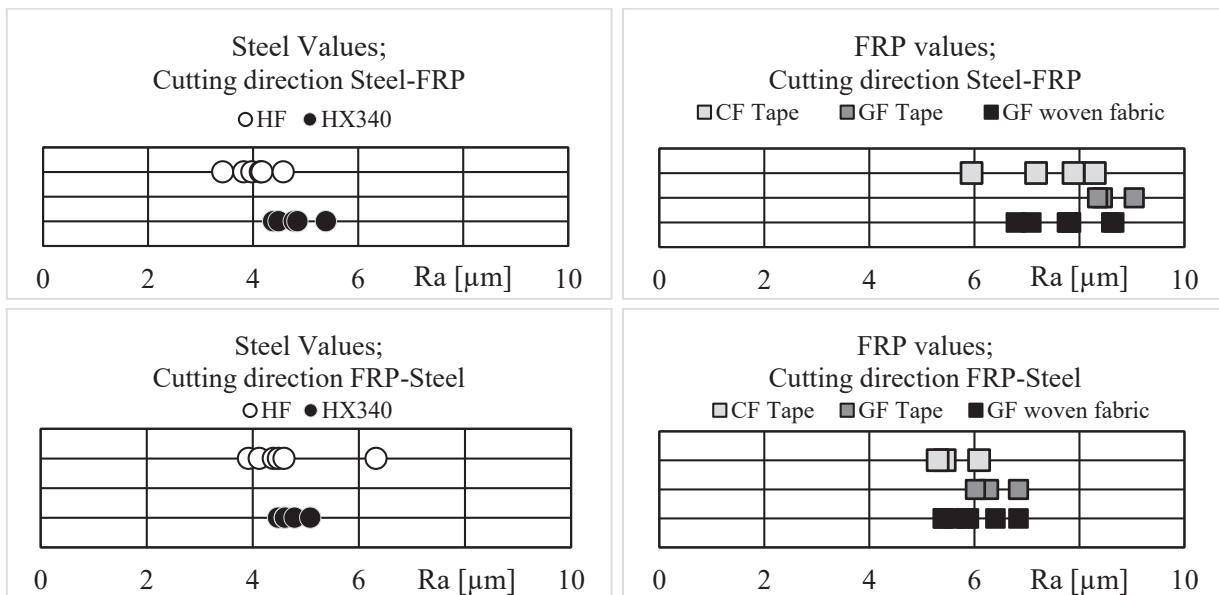
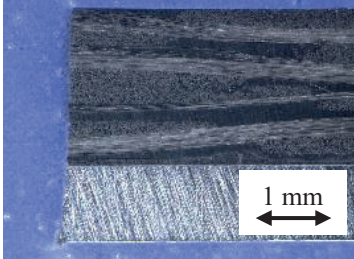
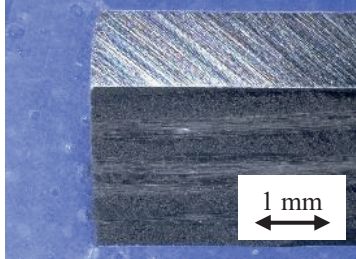


Figure 2: Steel and *FRP* roughness values for different cutting directions

When looking at the values of the other cutting direction *FRP*-steel it can be stated that the roughness values of *FRP* and steel are closer to each other. Also the deviation of the *FRP* for R_a and R_z values ascends. The values for the steel surface roughness are fairly close together so it can be said that they do not depend on the cutting direction. One of the reasons related to high values on *FRP* is the erosive principle of *WJM* cutting method. The reason for higher *FRP* values are caused to the removed steel particles. They are solved into the abrasive water jet beam. This solution seems to have a high influence on the surface of *FRP*. When the *FRP* layer is faced upwards in the cutting process the missing steel particles lead to lower roughness values. When looking at the fibre type it shows up that carbon fibres lead to the lowest roughness R_a : 5.305 μm while glass fibre tapes show the highest amount on

R_a : 9.042 μm . The test on significance (significance level 0.01) show that tapes have a higher influence on the roughness as woven *FRP* has. The *FRP* values show higher deviations at all time in comparison with steel values (see *Table 3*) This deviations can be explained by induced damage by *WJM* cut. The surface is not getting as homogenous as a steel surface gets.

Table 3: Deviations of R_a for steel and *FRP* values for different cutting directions and micro sections

	FRP-steel	Steel-FRP
FRP	$\varnothing 5.9 \mu\text{m} \pm 0.47 \mu\text{m}$	$\varnothing 7.8 \mu\text{m} \pm 0.62 \mu\text{m}$
Steel	$\varnothing 4.5 \mu\text{m} \pm 0.31 \mu\text{m}$	$\varnothing 4.4 \mu\text{m} \pm 0.27 \mu\text{m}$
Microsection		

It was detected that the deviation of the single-layers depends on the cutting direction. The steel layer always shows a reduction of the kerf size as a consequence of the attenuation of the waterjet. *FRP* has less density than steel. While processing steel a longer time period to cut the same thickness in *FRP*, more material is removed from the *FRP* layer. Due to the material selection the cutting parameters are not optimal for the *FRP*. When cutting the *FRP* layer it can be seen that the kerf is enlarged especially when cutting steel first. Within the data base no significant terms could be verified.

4.2. Multi-layer *FML*

The dependencies determined at the single-layer specimen also influence the characteristics of the cutting edge on the multi-layer specimen. For those the roughness was only measured at steel layers due to higher reliability of the values (as shown in 4.1). *Figure 3* shows the averaged roughness R_z of different stacking sequences on each individual layer and the minimum and maximum surface roughness values. The extrema (min. and max.) indicate the range of the roughness measurement and the spread of the roughness values as a result of the position of each layer. Both from the scattering and from the spreading two conclusions can be drawn from the measurement results of the roughness distribution: The deeper the cut the rougher the surface of the steel. Secondly, the more layers of steel are cut ahead, the rougher the total surface roughness. Also the surface roughness increase for each subsequent layer.

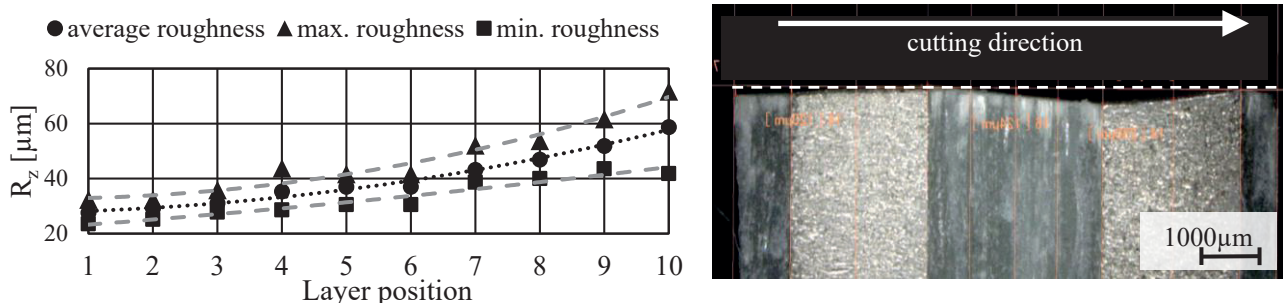


Figure 3: Surface roughness values in relation to the laminate layer for all stacking sequences (l.) and exemplary micro section of cutting edge

These effects are influenced by the decrease of the total energy of the cutting jet and by the changing mixing ratio of the abrasive (steel, fibres, matrix). As the energy of the water jet decreases, turbulence is formed and kerf of the steel is less parallel. The material erosion from the upper layers mixes with

the abrasive. The earlier the beam cuts a steel surface in stacking sequences, the higher is the energy loss of the beam and the higher are the total deviations in the layers. Each previous layer influences the deviations of the following layers. As seen in 4.1 a preceding steel layer tapers the kerf on steel, a GFRP layer expands it. This effect is higher, the less frequently the change with an upstream layer of different material takes place.

5 Conclusion

The aim of the paper was to detect the surface roughness and geometrical deviation on different materials in single and multi-layer hybrid laminates. The specimens have been investigated separately: in the single-layer specimen the materials for *FRP*, metal and bonding agents were varied while on the multi-layer specimen the overall thickness and design of layer variation were examined. All specimens were cut with the same cutting parameters.

The results are summarized as follows:

- A geometrical deviation of *FRP* and steel layer at the cutting edge is always present.
- The deviation gets significant with increasing thickness of the *FML*. The deviations of the cut and the deviations of the measurement method lead to a reduction of the statistical significance. This is compensated with a higher laminate thickness so that the identified effects become statistically significant.
- The effect is caused by the *WJM* method itself: erosive cut leads to dispersion of values. Also the measurement capability influences the effect of geometrical deviation. A microsection is a snapshot of a single perspective. Comparing another snapshot from the same cutting edge could show a minor but relevant deviation. The measurement was taken at pictures on a screen so that deviation from this cannot be excluded.
- Detection of general reliance of surface roughness on cutting depth. Increase depth show higher roughness values. This is caused by the related energy loss and therefore increasing turbulences of the water jet.
- Increasing number and proportion of metal layers lead to higher roughness of the overall *FML*. The abrasive mixture changes: the dissolved steel particles are leading to a higher roughness value at the following layers. The phenomenon could be detected for single and multi-layer specimen.
- *FRP* layers show higher surface roughness values and deviations than steel layers.

To improve a following study, the usage of a 3D measuring method with better capability of the cutting edge surface could solve the measurements critical points. The database should be extended to increase reliability of the values. This would lead to better detection of material relations on surface roughness and geometrical deviation. Also the experimental base on the multi-layer specimen should be enhanced by asymmetrical layer types to identify effects and interactions between parameters more clearly.

6 References

- [1] Fink, A.: *Lokale Metall-Hybridisierung zur Effizienzsteigerung von Hochlastfügestellen in Faserverbundstrukturen*, Dissertation. Braunschweig **2010**.
- [2] Fleischer, J.; Roth, S.; Sommer, C.; *Faser-Metall-Gummi-Hybridlaminat*. ZWF Zeitschrift für wirtschaftlichen Fabrikbetrieb, **2016**, 111, 483–486.

- [3] Sinke, J.; *Manufacturing of GLARE Parts and Structures*. Applied Composite Materials **2003**, 10, 293–305.
- [4] Tyczyński, P.; Lemańczyk, J.; Ostrowski, R.; Ewa S'liwa, R.; *Drilling of CFRP, GFRP, glare type composites*. Aircraft Engineering and Aerospace Technology, **2014**, 86, 312–322.
- [5] Reddy, V. N.; Venkatesh, B.; *Optimization of parameters in abrasive water jet machining of glass laminate aluminium reinforced epoxy (GLARE)*. Materials Today: Proceedings **2019**, 19, 890-894.
- [6] Paul, S.; Hoogstrate, A. M.; van Praag, R.; *Abrasive water jet machining of glass fibre metal laminates*. Proceedings of the Institution of Mechanical Engineers, Part B: Journal of Engineering Manufacture **2002**, 216, 1459–1469.
- [7] Ramulu, M. e. a.; *Abrasive Waterjet Machining Effects on Kerf Quality in Thin Fiber Metal Laminate*. WJTA-IMCA Conference and Expo; **2015**.
- [8] Alberdi, A.; Suárez, A.; Artaza, T.; Escobar-Palafox, G. A.; Ridgway, K.; *Composite Cutting with Abrasive Water Jet*. Procedia Engineering, **2013**, 63, 421–29.
- [9] El-Hofy, M.; Helmy, M. O.; Escobar-Palafox, G.; Kerrigan, K.; Scaife, R.; El-Hofy, H.; *Abrasive Water Jet Machining of Multidirectional CFRP Laminates*. Procedia CIRP; **2018**, 68, S. 535–540.
- [10] Phapale, K.; Singh, R.; Patil, S.; Singh, R.K.P.; *Delamination Characterization and Comparative Assessment of Delamination Control Techniques in Abrasive Water Jet Drilling of CFRP*. Procedia Manufacturing **2016**, 5, 521–535.
- [11] Schürmann, H.; *Konstruieren mit Faser-Kunststoff-Verbunden*. 2nd ed., Springer, Berlin, Heidelberg, **2007**.
- [12] Jagadish; Gupta, K.; et al.; *Introduction to Abrasive Water Jet Machining.; Abrasive water jet machining of engineering materials*. **2020**; 1-11.
- [13] Kumar, P.; *Surface Roughness in Abrasive Water Jet Cutting*. URL: <https://www.researchgate.net/publication/318339878>.; **2016**.
- [14] Rothe, F.; et al.; *Economic evaluation of alternative process chains for the large-scale manufacturing of metal-fiber laminates*. Procedia CIRP; **2019**; 13-19.
- [15] Rothe, F.; et al.; *Study on the Optimized Manufacturing of Hybrid Laminates for a Leaf Spring*. Congress of the German Academic Association for Production Technology; Springer; **2018**; 433-444.
- [16] Rothe, F.; et al.; *Potential hybrider FKV-Metall-Laminat zur Variation der Federrate von Blattfedern*. Tagungsband 9. Landshuter Leichtbau-Colloquium; **2019**; 9-19.
- [17] Mallick, P. K.; *Composites engineering handbook*. Dekker; New York; **1997**.
- [18] Arminger, G.; *Multivariate Analyse von qualitativen abhängigen Variablen mit verallgemeinerten linearen Modellen*. Zeitschrift für Soziologie; **1983**; 12; 49-64.
- [19] Wiczorek, D.; *Empirische Entwicklung von Prognosemodellen für die Auslegung von Rollenfördermodulen*. Dortmund, Techn. Univ., Diss., **2011**.
- [20] Gerig, T. M.; *Multivariate Analysis*. Techniques for Educational and Psychological Research.; Technometrics **1975**; 17, 141–142.
- [21] DIN EN ISO 25178-601: *Geometrische Produktspezifikation (GPS) - Merkmale von berührend messenden Geräten (mit Taster)*. Beuth Verlag, Berlin; **2010**.

TOPIC

Oral Poster Presentation



@DGM_eV

#Hybrid2020

Contribution to Structural Mechanics of Patch-Based Composites

A. Baumer¹, A. Baeten¹

¹Augsburg University of Applied Sciences, Augsburg, Germany

Abstract: Fiber Patch Placement (FPP) is a novel, fully automated and resource-efficient manufacturing technology for composite structures of complex geometry. A patch-based laminate layup offers curvilinear fiber orientations along load paths and provides high freedom of design with least waste and fiber distortion. Initial research on this new type of composites has shown that, due to the patch-based fiber architecture, the structural mechanics of FPP laminates is fundamentally different in comparison to classic laminates. While in classic laminates the load transmission is performed mainly via normal stresses in the continuous fibers, in patch-based composites there is a shear-dominated part of transmission of forces between the patches. In this paper that structural mechanical difference is investigated with regard to the tensile strength properties of unidirectional reinforced composites. Additionally, an analytical method is presented to determine the elasticity constants of a structural FPP lamina based on a meso-mechanical approach.

Keywords: fiber patch placement, composite materials, structural mechanics, patch-based laminates

1 Introduction

The technology of fiber patch placement sets a new milestone in manufacturing of high-performance composite structures, as it enables fully-automated processing of fiber-reinforced plastics with defined variable fiber orientation. This qualifies the FPP process for a wide range of applications in high-tech industries such as aerospace, automotive or medical technology. Being a young technology, a lot of research work has to be done for comprehensive characterization of FPP laminates to achieve certification for named industrial applications.

First, MEYER [2] developed the basic manufacturing process for fiber-patch-based preforms and created first design guidelines for patched laminates. The Cevotec GmbH (a spin-off of Technical University of Munich, founded in 2015) further developed the process, transferred it to a high technology maturity level, as shown in Figure 1, and started selling the system in different configurations. Various design parameters of FPP laminates (patch-length, patch-thickness, overlap pattern, etc.) have been investigated experimentally by HORN [3] and KUSSMAUL [4], validated by FEA (Finite Element Analyzes). The research to date focused on plane and unidirectional FPP laminates, but there are also first considerations for curved geometries and load paths. In this work, the structural mechanical considerations aim to deliver an analytical description for the elasticity parameters of a FPP lamina to explain the experimentally determined laminate stiffness. The strength estimation is done with the HASHIN criterion for tensile failure, as it includes the interaction between tensile stresses and shear stresses inside the lamina. [7]

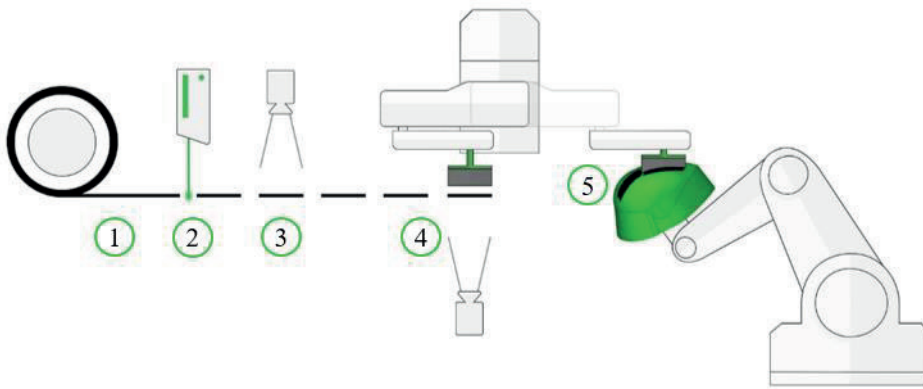


Figure 1: Schematic illustration of the FPP-Process: ① feeding of (unidirectional) fiber tape, ② (laser-) cutting of fiber tape in patches, ③ inspection of fiber patches, ④ picking up and position check of fiber patches, ⑤ placing the patches onto the forming tool. [1]

2 Engineering Constants of an FPP lamina

Patch-based laminates have a significantly different fiber architecture compared to classic laminates with continuous plies, as shown in Figure 2. As with classic laminates, a complete structural mechanical description of FPP laminates also requires knowledge of the elementary engineering constants.



Figure 2: Principal laminate lay-ups: classic laminate with continuous plies (left), classic FPP laminate (middle), FPP laminate with scaly overlap pattern.

For the determination of the moduli of elasticity one individual structural FPP lamina is considered (see Figure 3) and the following assumptions are made: [2]

- unidirectional fiber orientation along x-axis,
- constant patch thickness,
- patch length and overlap length \geq critical fiber length l_{critical} ($l_{\text{critical}} \approx 1,000 \times$ filament diameter; $l_{\text{critical, CFRP}} \approx 5 \text{ mm}$),
- patch pattern with negligible gaps (resin pockets) at butt joints,
- neglecting of bending moments or stress concentrations at fiber ends.

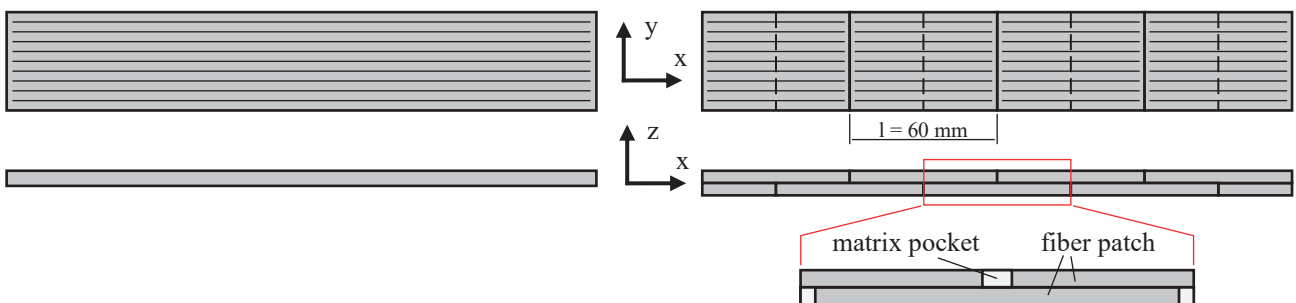


Figure 3: Conventional UD-FRP (unidirectional Fiber-Reinforced Plastic) lamina (left), structural FPP lamina with representative unit cell (right).

To derive the engineering constants of a structural FPP lamina, SCHÜRMANN's micro-mechanical elastic spring models are applied on a meso-mechanical scale. First, a representative meso-mechanical model is created. After that, an appropriate spring model has to be selected (parallel connection or series connection). Finally, the engineering constants are determined with an elasto-static approach: a system of equations of equilibrium of forces, kinematic relations and law of elasticity. [5]

2.1 Longitudinal Young's Modulus E_{\parallel}

Figure 4 shows the uniaxial loading of the FPP unit cell in fiber direction (x-axis). The material behavior will be investigated in sections (1) through (5).

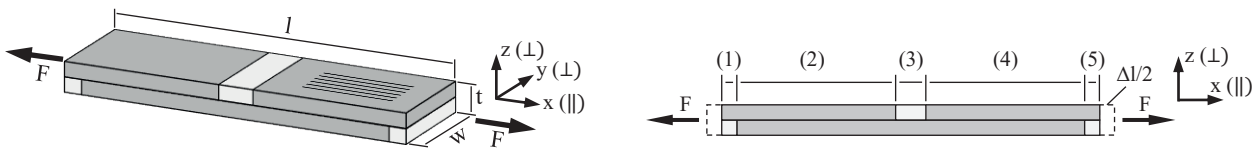


Figure 4: Representative unit cell of FPP lamina with uniaxial loading in fiber direction.

In section (2) and (4) the longitudinal Young's modulus corresponds to that of the patch material or the continuous reinforced composite material: $E_{(2)} = E_{(4)} = E_{\text{patch}}$.

The Young's modulus in the matrix gaps or butt joint sections (1), (3) and (5) is the arithmetic mean of the patch and matrix material: $E_{(1)} = E_{(3)} = E_{(5)} = (E_{\text{patch}} + E_{\text{matrix}})/2$.

To obtain the Young's modulus for the complete FPP unit cell it is necessary to connect the sections in series:

- Equilibrium of forces: $F_{\parallel} = F_i$ or $\sigma_{\parallel} = \sigma_i$; $i = (1), (2), (3), (4), (5)$
- Kinematic relations: $\Delta l_{\parallel} = \sum \Delta l_i$; $\Delta l_i = \varepsilon_i \cdot l_i \Rightarrow \varepsilon_{\parallel} \cdot l_{\parallel} = \sum \varepsilon_i \cdot l_i$
- Law of elasticity: $\varepsilon_i = \frac{\sigma_i}{E_i}$; $\frac{\sigma_{\parallel}}{E_{\parallel}} = \sum \frac{\sigma_i}{E_i} \cdot \frac{l_i}{l_{\parallel}} \Rightarrow \frac{1}{E_{\parallel}} = \sum \frac{1}{E_i} \cdot \frac{l_i}{l_{\parallel}}$

\Rightarrow Assumptions made: $\frac{l_{(2)}+l_{(4)}}{l_{\parallel}} \approx 1$ (patch sections) ; $\frac{l_{(1)}}{l_{\parallel}} = \frac{l_{(3)}}{l_{\parallel}} = \frac{l_{(5)}}{l_{\parallel}} \approx 0$ (butt joint sections)

Following this argumentation the conclusion is that the patch-based fiber architecture shows the same stiffness in fiber direction as endless-reinforced composite material. This was proven by experiments in the work of HORN. [3]

2.2 Transverse Young's Modulus E_{\perp}

The transverse Young's modulus is determined analogous to the longitudinal modulus of elasticity. Figure 5 shows the uniaxial loading of the FPP unit cell transverse to the fiber direction (y-axis). The section wise definition of the Young's modulus applies here the same way as in section 2.1, just for the transversal load case.

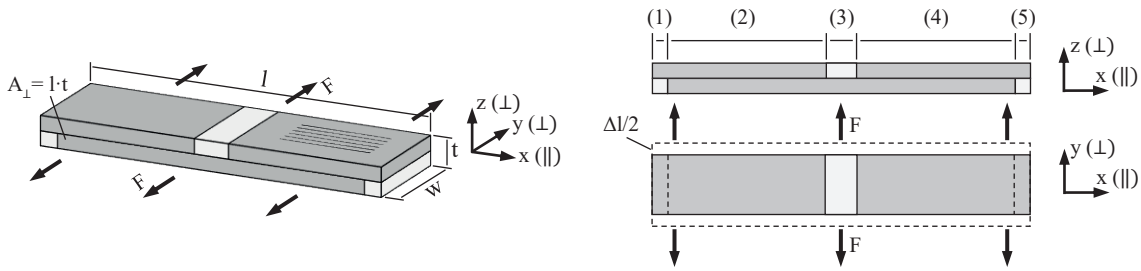


Figure 5: Representative unit cell of FPP lamina with uniaxial loading in transverse to fiber direction.

For determination of the transversal Young's modulus of the unit cell the sections (1) to (5) are considered as parallel connected.

- Equilibrium of forces: $F_{\perp} = \sum F_i$ or $\sigma_{\perp} \cdot A_{\perp} = \sum \sigma_i \cdot A_i$; $i = (1), (2), (3), (4), (5)$
- Kinematic relations: $\varepsilon_{\perp} = \varepsilon_i$
- Geometrical relations: $A_{\perp} = \sum A_i$; $A_{(2)} = A_{(4)} \Rightarrow A_{\text{patch}} = 2A_{(2)}$
 $A_{(3)} = A_{(1)} + A_{(5)} \Rightarrow A_{\text{gap}} = 2A_{(3)}$
- Law of elasticity: $\sigma_{(2)} = \sigma_{(4)} = E_{(2)} \cdot \varepsilon_{(2)}$ (patch sections)
 $\sigma_{(3)} = \sigma_{(1)} + \sigma_{(5)} = E_{(3)} \cdot \varepsilon_{(3)}$ (butt joint sections)
 $\Rightarrow E_{\perp} \varepsilon_{\perp} A_{\perp} = E_{(2)} \varepsilon_{(2)} 2A_{(2)} + E_{(3)} \varepsilon_{(3)} 2A_{(3)}$
 $\varepsilon_{\perp} = \varepsilon_i \Rightarrow E_{\perp} A_{\perp} = E_{(2)} 2A_{(2)} + E_{(3)} 2A_{(3)}$
 $\Rightarrow E_{\perp} = \frac{2A_{(2)}}{A_{\perp}} \cdot E_{(2)} + \frac{2A_{(3)}}{A_{\perp}} \cdot E_{(3)}$

\Rightarrow Assumptions made: $\frac{2A_{(2)}}{A_{\perp}} \approx 1$ (patch sections) ; $\frac{2A_{(3)}}{A_{\perp}} \approx 0$ (butt joint sections)

The analysis reveals that $E_{\perp} = E_{(2)} = E_{\text{patch}}$. Thus the transverse Young's modulus of the FPP lamina is equivalent to the continuous fiber-reinforced composite.

2.3 Conclusion about Engineering Constants of FPP lamina

The investigation has shown that the Young's moduli E_{\parallel} and E_{\perp} of a structural FPP lamina are identical to conventional continuous fiber-reinforced composites and can be determined with the same rules of mixture. This leads to the assumption that the residual elastic constants $G_{\parallel\perp}$, $\nu_{\parallel\perp}$, $\nu_{\perp\parallel}$ and their homogenization models for endless-reinforced composites can also be applied to FPP composites. As a next step, tensile tests along (DIN EN 2561) and transverse (DIN EN 2597) to the fiber direction are performed to verify the analytical considerations. The experimental data will also be used to validate the FE simulation model of the tensile specimen.

3 Tensile Strength and Failure of FPP laminae

Considering unidirectional fiber composite laminates under tension load longitudinal to the fibers, HORN [3] showed that continuous laminates and patch-based laminates have identical Young’s modulus. This has been elaborated theoretically in the previous chapter. In reality, however, for an unidirectional laminate lay-up and due to the discontinuous fiber architecture the tensile strength of FPP laminates has to be lower than for classic laminates. According to HORN’s work it is about 52 – 57 % of endless fiber-reinforced composites. To investigate this phenomenon, the critical spot of a FPP structure, the butt joint of two patches in the outer layer is considered in detail in Figure 6.

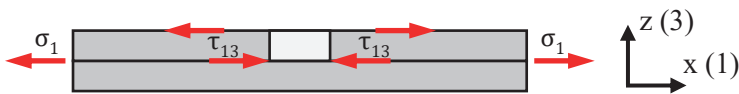


Figure 6: Stresses at butt joint of two fiber patches under uniaxial tensile load.

Under uniaxial tension load in fiber direction x (1) the butt joint of two fiber patches causes shear stresses τ_{13} at the patch ends beside the tensile stresses σ_1 . This is based on the assumption, that the contribution to load transfer of the matrix inside the gap is negligible. In the cross-section of the butt joint the tensile strength is estimated according to: $R_{FPP} = (R_{patch} + R_{matrix})/2$. This results in a strength of the FPP laminate of slightly more than 50 % of continuous fiber composite. Of course, in this load range the tensile strength of the patches is not yet exhausted. This implies that the shear strength limit S_{13} at the patch end is already reached at this load, causing the laminate to fail.

An analytical comparison of the tensile strength between a continuous unidirectional reinforced composite lamina and a structural FPP lamina depending on the fiber orientation is displayed in Figure 7. The material used for this investigation is a common carbon fiber / epoxy composite IM7 / 8552 (fiber volume content = 60 %) and the material data are taken from KADDOURS’ work for the *third world-wide failure exercise*. [6] The patches of the FPP lamina have a length of 60 mm and overlap each other by 50 % as illustrated in the previous Figures. Both laminates are exposed to uniaxial tensile load. To consider the influence of the shear stress, a linear correlation between the shear stress τ_{13} and the tensile stress σ_1 is assumed.

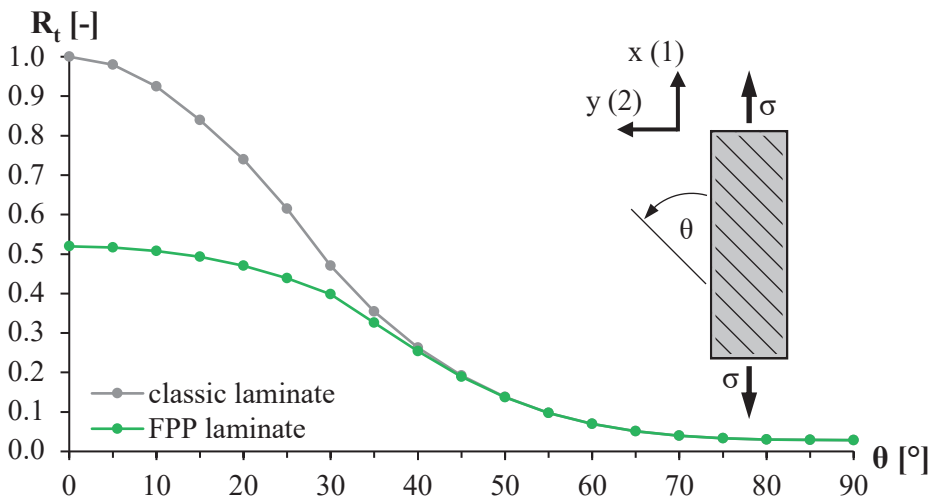


Figure 7: Tensile strength of an unidirectional CFRP laminate as a function of the fiber orientation / off-axis angle θ .

The stresses have been calculated with use of the Classical Laminate Theory (CLT) and the laminate strength was determined by HASHINS' failure criteria for tensile load. [7]

$$\left(\frac{\sigma_1}{R_1^+}\right)^2 + \left(\frac{\tau_{12}}{S_{12}}\right)^2 + \left(\frac{\tau_{13}}{S_{13}}\right)^2 = 1 \quad ; \quad \left(\frac{\sigma_2}{R_2^+}\right)^2 + \left(\frac{\tau_{12}}{S_{12}}\right)^2 + \left(\frac{\tau_{13}}{S_{13}}\right)^2 = 1$$

Longitudinal fiber tensile failure Transverse fiber tensile failure

Due to the varying off-axis angle both longitudinal (fiber-dominant) and transverse (matrix-dominant) failure mode have to be checked simultaneously. The results show that from an off-axis angle $\theta \geq 40^\circ$ the difference in tensile strength between classic and FPP composites vanish. This agrees well with the work of HORN in terms of tendency.

4 Conclusion and Outlook

Given the discontinuous fiber structure and high design freedom of fiber orientation, FPP laminates can only reach their full potential in geometrical complex structures with curved load paths. Nevertheless, a comprehensive development of the structural mechanics of patch-based composites on a reduced and simplified level sets the foundation for further investigations. This paper shall complement the existing research on FPP laminates with regard to analytical definition of fundamental elasticity parameters and strength estimation. The next step of this research work is to build a simulation model according to the test standard requirements in order to perform virtual tensile tests of FPP laminate specimen with defined patch lay-up and overlap pattern. Material parameters such as tensile strain and strength are obtained from experimental test series in order to calibrate the simulation and review the analytics for validity.

5 References

- [1] N. N., *CEVOTEC – FPP Technology*, www.cevotec.com/fpp-technologie, December 2019.
- [2] O. Meyer, *Kurzfaser-Preform-Technologie zur kraftflussgerechten Herstellung von Faserverbundbauteilen*, Dissertation, Universität Stuttgart, 2008.
- [3] B. Horn, *Beitrag zum Materialverständnis von langfaserpatch-verstärkten Bauteilen*, Dissertation, Technische Universität München, 2018.
- [4] R. Kussmaul, *Design and Optimization of Variable Stiffness Composite Structures from Patched Laminates*, Dissertation, Eidgenössische Technische Hochschule Zürich, 2019.
- [5] H. Schürmann, *Konstruieren mit Faser-Kunststoff-Verbunden*, Springer-Verlag, Berlin, 2007.
- [6] A. S. Kaddour, et al., *Mechanical properties and details of composite laminates for the test cases used in the third world-wide failure exercise*, Journal of Composite Materials, Volume 47, 2013.
- [7] M. Flemming, S. Roth, *Faserverbundbauweisen – Eigenschaften / mechanische, konstruktive, thermische, elektrische, ökologische, wirtschaftliche Aspekte*, Springer-Verlag Berlin-Heidelberg, 2003.

Part automated method for repairing composite parts

B. Manin¹, A. Raina¹, T. Quadflieg¹, T. Gries¹

¹Institut für Textiltechnik der RWTH Aachen University (DE)

1 Introduction

Fibre-Reinforced Plastics (FRP) have outstanding mechanical properties and low density. This group of materials is therefore well suited for lightweight constructions. Currently established FRP repair processes are mainly found in the aviation industry and are used for cost-intensive structural components.

In the publicly funded cooperation project *Automated Repair Patch Production - ARP2*, the Institute of Textile Technology in Aachen (ITA) is developing a process chain for the automated production of repair patches for FRP components in cooperation with Sabanci University.

Aim of repair is to restore the mechanical properties of a damaged component. Thereby the aspects: power flow, reliability and economy are in part clearly contradictory. [1] Various repair strategies have been established in the past. However, the basic repair procedure remains the same. Thus, each repair process starts with the damage detection. It is examined whether the damaged component can be repaired or whether a replacement is necessary, this often depends on the construction (integral or differential design method). If a repair takes place, the repair method is selected and carried out in the next step. However, the industrially established repair process is characterized by a high amount of manual work in all process steps. [2][3]

2 Repair process within the ARP2 project

The standard repair process begins with damage detection. Here the type and size of damage is recorded visually. In the next step, the damaged area is prepared. The process step includes the removal of individual laminate layers, wherein a so-called shank structure is introduced into the component and individual textile layers are exposed (see Figure 1, left). The shaft geometry is crucial for a high-quality repair, as it transmits the forces of the repair patch and the component. In the currently established repair processes, the shaft is manually inserted into the component. Therefore the quality often depends on the human expertise. In the next step, the contours of the exposed textile layers are recorded. Once the contours are known, the individual textile layers can be cut to size. The layer structure of the repair patch usually corresponds to that of the component. In the last step, the repair patch is placed on the damaged area. The patch can be cut from prepreg material or coated with resin in a subsequent infusion process.

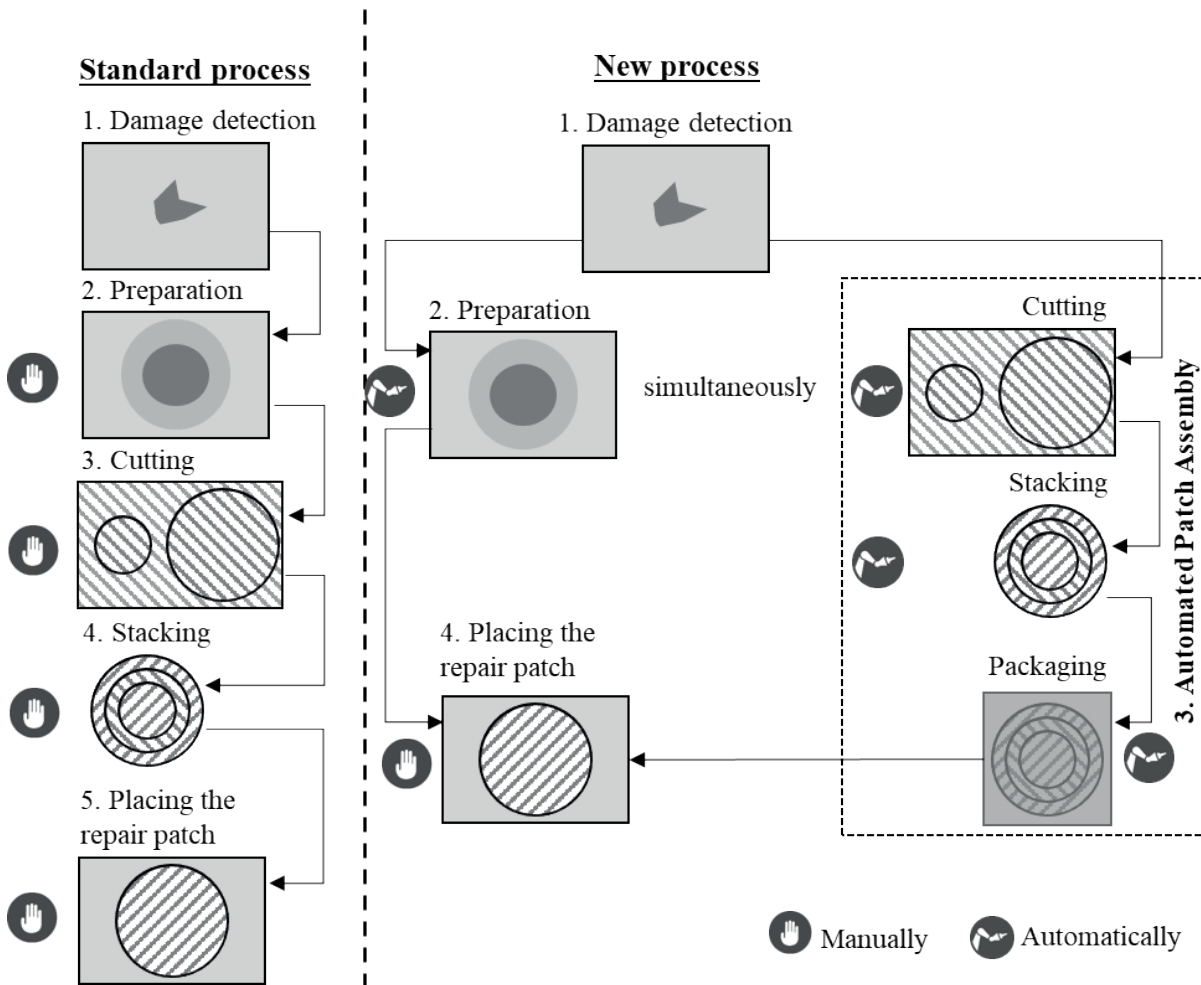


Figure 1: Classification of the Automated Repair Patch Production (ARP2) project in the new repair process and comparison with the established repair process

Individual process steps are automated in this newly developed repair process. The damaged area is recorded and digitized with a camera system. The matrix material and the reinforcing fibers are removed by a short-pulse laser system, whereby the shaft geometry is introduced into the damaged area. This allows the shaft geometry defined in the repair standard to be applied exactly to the component. Thus, the quality no longer relies on the human expertise. Current laser shank technologies offer a geometric accuracy of 20 μm . At the same time, the fiber orientation of the exposed textile layers can be measured inline in the laser-assisted ablation process. Thus, laminate irregularities caused by the damage or during component manufacture can be detected and taken into account in the shank geometry. In this way, an exact, layer-by-layer removal of the laminate layers is achieved, resulting in high repair quality.

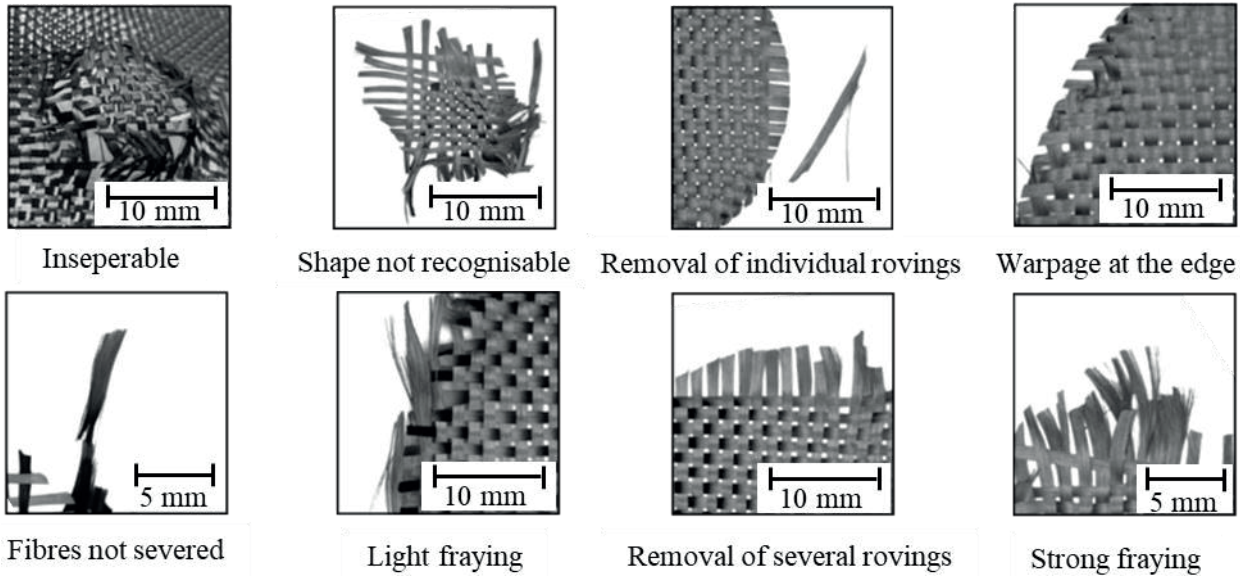
During the shanking process, the component surface is scanned with the laser. This generates a digital point cloud. This is transmitted to the process chain in the form of a matrix. The entries of the matrix describe the component height and have a defined, resolution-dependent distance to each other. The matrix is loaded into a commercial CAD software. From the individual points the shaft geometry can be virtually simulated and the patch size can be determined in the CAD software.

The production of the repair patch takes place in the developed robot cell at a different location to the component repair station.

A circular damage spot with a diameter of 25 mm serves as a demonstrator. The component consists of 8 laminate layers of carbon fabric.

2.1 Cutting the textile patch layers

The geometries of the individual textile layers of the repair patch are derived from the recorded damage data. During the analysis of the cutting process, the cutting qualities were examined as function of the cutting speed and the sample size for the cutting technologies: Oscillating Drawing Knife (ODK), Rotating Knife (RK) and Ultrasonic Knife (UK). The evaluation of the cutting quality is carried out according to created evaluation criteria (see Table 1). Figure 2 shows the error occurring in cutting tests with all cutting technologies. The cutting quality is measured over the fibre course.



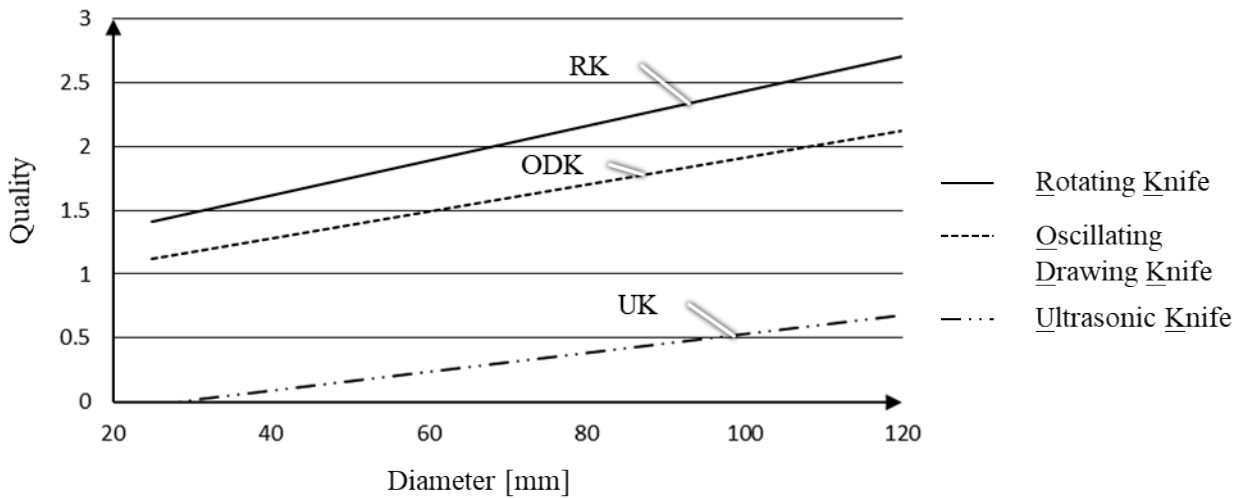
Picture 2: Occurred material defects with all cutting technologies

The evaluation of the cutting technology is between 0 and 3 points. Cuttings in which no rovings are detached and there are no undulations in the edge area are evaluated as fault-free. Consequently, these cuttings are evaluated with rating scale of 3. Blanks with slight undulations in the edge area are rated with 2 points. Samples with quality numbers 1 and 0 cannot be used for the repair of structural components, because individual rovings are detached or the cut geometry is deformed. The evaluation criteria for the cutting are summarized in table 1.

Table 1: Evaluation criteria in the cutting process

Category	Criteria
0	Blank cannot be removed Geometry warped Several rovings removed from the blank Strong fraying of the rovings
1	Complete severing Few rovings removed from the blank Slight distortion at the cutting edge
2	Complete severing No rovings removed from the blank No distortion of the cut edge Only selective fraying of the rovings
3	Complete severing No rovings removed from the blank No distortion of the cut edge No fraying of the rovings

Round blanks with diameters between 25 mm and 117.4 mm are required for the defined demonstrator geometry. Results of the test series carried out are shown in picture 3.

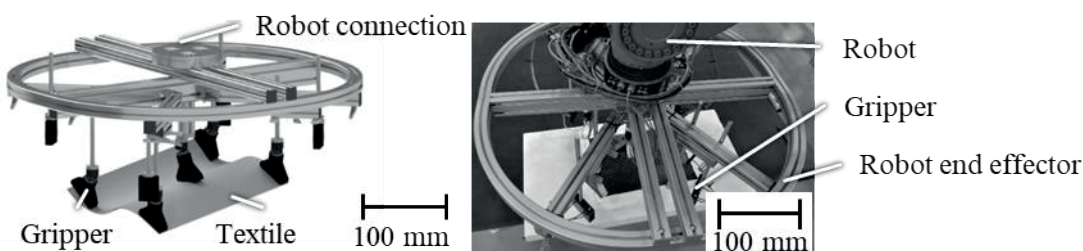


Picture 3: Achieved quality of the individual cutting technologies depending on the sample diameter

The results prove that the highest cutting qualities can be achieved with the RK technology. The achievable cutting quality increases with the sample diameter. Furthermore, the test results prove that without auxiliaries for small blanks of less than 64.6 mm, no sufficient quality can be achieved with any of the technologies investigated. The main reason for this is the fibre displacement in the edge area of the sample and the distortion of the sample geometry. If the textile material is fixed with vacuum pressure on a cutting mat, sufficient quality can be achieved with the rotating knife technology even for diameters of 25 mm. In addition, the cutting speeds for all technologies between 4 mm/s and 167 mm/s are examined. For UK cutting technology, the best cutting results are determined for slow speeds (4 mm/s). The RK technology showed the best, constant results between 67-133 mm/s and the ODK at 133 mm/s.

2.2 Stacking and Patch Preparation

Following the cutting process, the individual textile blanks are stacked to form a repair patch. The layer structure corresponds to the laminate layers of the component to be repaired. For this stacking process step, a gripping tool is developed at ITA. The procedure is based on VDI 2221. After a concept evaluation and elaboration, the gripper system shown in figure 3 is implemented. The system can be adapted to different geometries. By using different gripping techniques (Vacuum Gripper, Needle Gripper and Bernoulli Gripper) it is possible to grip various types of textiles between 5 mm and 1000 mm diameter. At the same time the end effector is used to handle the packaging material and interact with the packaging station. The adjustable gripper elements allow gripping of curved geometries.



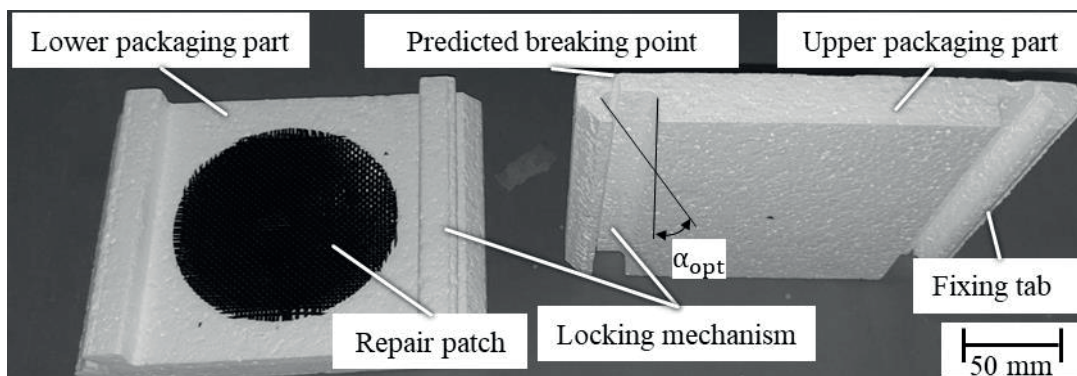
Picture 4: Robot end effector for gripping, positioning, depositing reinforcing textiles and foam materials

2.3 Packing and transporting the repair patch

The new repair process separates locally the production of the repair patch and the repair location. For this reason, the data collected from the damage are transferred digitally to a robot cell, where the repair patch is produced and packed ready for shipment. The goal is to have the repair patch available at the repair location within 24 hours after damage detection. Within the ARP2 project, possible packaging materials will be examined with regard to economic and technical aspects. In order to ensure a safe and cost effective transport, Expanded Polystyrene (EPS) has been chosen as packaging material. Besides the protection of the repair patch against environmental influences, further requirements for the packaging have been identified on the process side, these are:

- Automated closing of the package with the robot
- Easy removal of the repair patch from the packaging
- Two-part packaging (storage and fixation of the repair patch, sealing of the packaging)
- Packaging must be grippable with the developed robot tool
- The closing mechanism must be capable of being closed by a linear movement
- Protection of the repair patch against foreign particles (solids, liquids and gases)

In order to enable automated closing of the packaging, a locking mechanism is developed (see Picture 5), which can be used to connect the upper and lower parts of the package with each other in a form-fit manner. In doing so, the hook-shaped fixing tabs snap into the lower half of the package. In order to open the package again, the fixing tabs are broken off by the worker immediately before the repair patch is placed on the damaged area. The optimum angle α_{opt} is determined in a series of tests. This angle must be adjusted so that the packaging can be closed with a linear movement and at the same time both halves of the packaging do not separate from each other when lifting off.

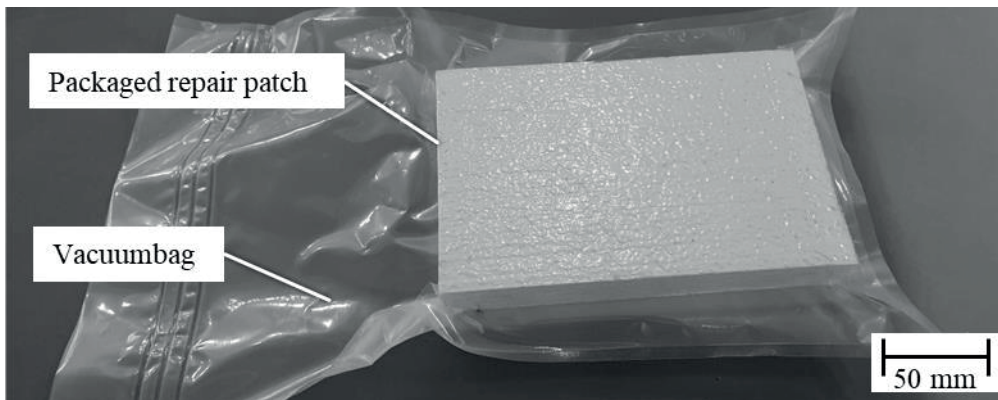


Picture 5: Two-part styrofoam package with inserted repair patch

Not all of these requirements can be met by the EPS material alone. For example, the Polystyrene packaging does not provide protection against foreign particles and humidity. For this reason the developed packaging is sealed in a vacuum bag in a downstream process step. In this way the repair patch is evacuated from the environment and at the same time protected from mechanical influences. To automate the packaging process it is necessary to handle the vacuum bag automatically. Coarse to fine structured vacuum bags are established in industry. Coarse structured materials are mainly characterized by the outstanding air flow when evacuating the packaged goods.

To handle the vacuum bag, it must be gripped. Vacuum grippers made of elastomers are most appropriate for this purpose. In a series of tests it is determined that the best gripping results can be achieved with finely structured vacuum bags. A finely structured vacuum bag provides the best compromise

between air flow and handling. In the Picture 6 is a ready to shipment packed repair patch shown.



Picture 6: Repair patch packed für shipment

3 Conclusion

The available results of the ARP2 project prove, that it is possible to partially automate the repair process of FRP components on a demonstrator geometry. The placement of the repair patch is still done manually even with the newly developed repair process. With the rotation knife technology, repair patches of sufficient quality can be produced from a diameter of 70 mm. The precision in stacking the individual textile layers is defined by the industrial robot used and the process dynamics. The developed packaging enables the transport of flat repair patches and protects them from foreign particles and mechanical influences. In further investigations an economic comparison of the newly developed process with an established process will be carried out. Furthermore, the individual process steps continue to be optimized.

We thank the BMBF and DLR for funding the project and our project partners from Sabanci University, Turkey for the cooperation.

4 Literature

- [1] P. Abel Hybride Fügeverfahren für Reparatur faserverstärkter Kunststoffe, Shaker Verlag 2016, p. 7
- [2] F. Ellert, Eine Instandhaltungssystematik für Bauteile aus Kohlenstofffaserverbundwerkstoff, Shaker Verlag, 2015
- [3] M. Kämpchen, H. Reimerdes, Abschlussbericht der Reparaturgruppe, in *Produktionstechnik für Bauteile aus nichtmetallischen Faserverbundwerkstoffe, Arbeits- und Ergebnisbericht 1999/2000*
- [4] M. Schlummer, A. Mäurer, S. Wagner, A. Berrang, T. Siebert, F. Knappach, Recycling of flame retarded waste polystyrene foams (EPS and XPS) to PS granules free of hexabromocyclododecane (HBCDD), Fraunhofer Institute IVV

Material selection for temperature sensitive actuators manufactured from shape memory alloy wires embedded in polymer structures

P. Eyer¹, A. Trauth¹, K.A. Weidenmann¹

¹Institute of Materials Resource Management (MRM), Augsburg University

1 Abstract

Additive manufacturing allows the integration of shape memory wires into polymer matrices. Actuators produced in this way offer a wide range of shapes and wire integration appropriate to external loads is realisable. Prestrained Nickel-Titanium (NiTi) wires and a polymer matrix are co-deposited simultaneously using an Arburg plastic freeformer. Actuation of the shape memory alloy is possible using conductive heating. Amorphous thermoplastics with high glass transition temperatures and high elastic strains are preferred matrix materials. Material selection based on Ashby maps implies that Polycarbonate (PC), Polypropylene (PP), Polyethylene (PE) and Polyamide (PA) are the most promising matrix materials processible with the Arburg freeformer. Mechanical characterisation reveals the best matrix material for this purpose. As a next step, adhesion between NiTi wire and the matrix material will be investigated.

2 Introduction

Shape memory alloys (SMA) have the ability to undergo large deformations, but can return to their undeformed shape by heating, which can result in a high actuation energy. Several applications for automotive [1], aerospace [2] and medical [3] industry can be found in the literature, mainly for NiTi as bulk material. Integration of SMA's in the shape of wires in polymer or metal matrix material offers a high design freedom and results in many benefits including actuation, vibration control, damping, sensing and self-healing [4, 5]. Especially utilisation of additive manufacturing allows almost any kind of shape. Actuators have recently been produced by additive manufacturing using shape memory polymers (SMP). These SMP can be easily linked to other thermoplastics, but have to be activated by heat from the outside which makes them react inert [6, 7]. Actuators made from SMA wires integrated in polymer matrices react much faster since actuation using conductive heating is possible. Furthermore, elasticity of metallic matrix materials is limited and the heat input from the composite extrusion process increases the transition temperature of the SMA [4]. In this regard, hybrid composites of SMA and polymer matrices have not been fully investigated yet. Most of the investigations focus on small-scale, primarily for research applications and the suitability for large-scale commercial production has not been addressed yet. The same applies for inelastic mechanisms in the matrix phase and their impact on the effective composite properties [8].

Furthermore, for actuators manufactured from SMA embedded in polymer matrices through additive manufacturing, no information about the optimum material combination can be found in the literature. In order to investigate the properties of the compound, first of all the properties of the single components are characterised.

3 Experimental

Manufacturing of the actuators intend to be performed by simultaneous co-deposition of NiTi wires and a polymer matrix using Arburg plastic freeformer (APF). The machine enables potentially to process every thermoplastic material available in pellet form without fillers directly into any desired shape using an integrated injection moulding set. First, the granulate is plasticised using a 15 mm heated cylinder. Afterwards, a high frequency nozzle closure is used to discharge up to 240 droplets per second. Each droplet is then placed at the previously calculated position by a moveable carrier. In this way a three-dimensional part is produced layer by layer [9]. For the manufacturing of actuators, the matrix material has to fulfil the following constraints:

- Usage of amorphous thermoplastics to limit the shrinkage and consequently problems resulting from residual stresses.
- Elastic elongation must be higher than 2,5 % to achieve deformation of the actuator without damaging the matrix material.
- The glass transition temperature must be above the usual operating temperatures of actuators (10°C-70°C) to prevent creeping. For this purpose, a glass transition temperature of at least 80°C is necessary.

Selection of possible matrix materials considering the constraints is performed using Ashby maps which are created using Granta Design CES EduPack [10]. Ashby maps illustrate the properties of different materials against another. Axes of the diagram are chosen according to the constraints and all materials in question are represented by bubbles in the diagram as the properties have a characteristic span of values [11]. Figure 1 illustrates the Ashby map for the glass transition temperature against the elongation at yield as these are the constraints for the aforementioned case. The constraints for this study, which are stated above, are represented by the red straight lines in the diagram. Therefore, blue pigmented materials in the diagram are unsuitable for this case and materials in the upper right corner of the diagram (indicated by the arrow) offer the best combination of properties. As a consequence, the following thermoplastics are particularly suitable: Polycarbonate (PC), Polypropylene (PP), Polyethylene (PE) and Polyamide (PA).

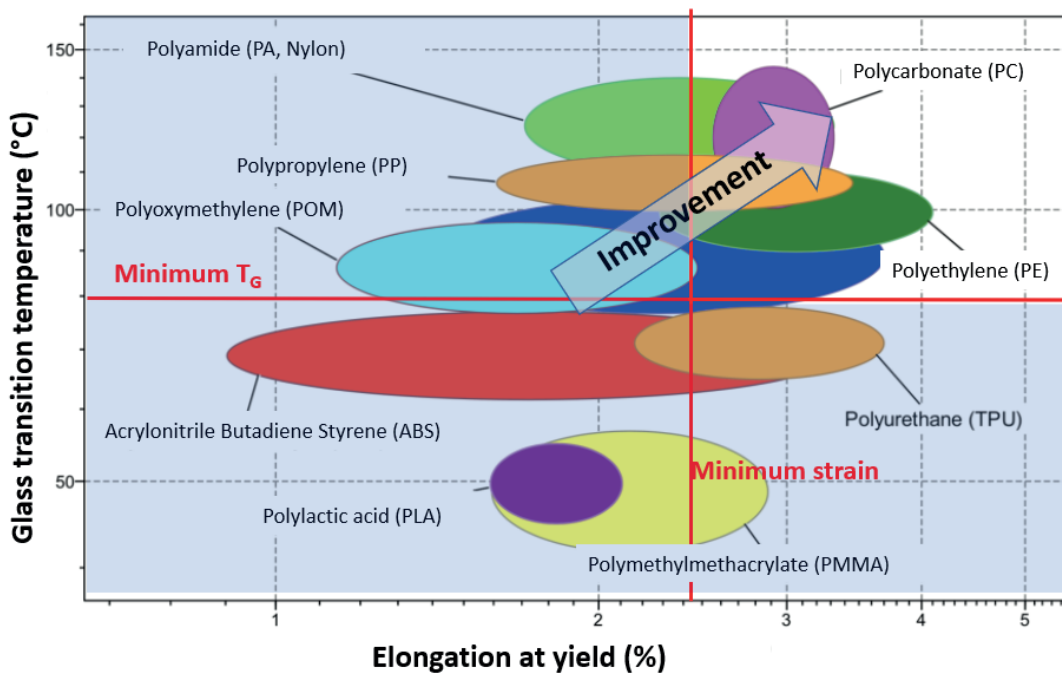


Figure 1 Ashby map of eligible matrix materials and the limiting constraints

For material manufactured in the Arburg freeformer it is unknown in which part of each bubble the exact values of the particular properties are, since the properties depend, inter alia, on the manufacturing process. That is the reason why the material properties are determined exemplarily for Acrylonitrile butadiene styrene (ABS) since this is the most common material manufactured on the Arburg freeformer. For the manufacturing of the ABS samples, Terluran GP35 granulate is used as recommended by Arburg. Properties of the granulate are listed in Table 1 as stated in the manufacturer information. Samples are manufactured on the Arburg freeformer using the parameters listed in Table 2. Static tensile tests are used to determine the maximum elastic elongation as well as the Young's modulus. Differential scanning calorimetry (DSC) tests are used to determine the glass transition temperature. For the purpose of comparison, the glass transition temperature (T_g) is also measured using dynamic mechanical analysis (DMA) tests according to DIN EN ISO 6721-1 [12].

Table 1 Properties of ABS as stated in the manufacturer information [13]

Material	Young's modulus	Elongation at yield	Glass transition temperature	Test standard
ABS (Terluran GP35)	2300 MPa	2,4 %	n.a.	DIN 527-1

Table 2 Manufacturing parameter for manufacturing of ABS samples in Arburg freeformer

Nozzle temperature	Installation space temperature	Layer thickness	Drop diameter
240°C	70°C	0,2 mm	0,268 mm

3.1. Tensile Tests

Tensile samples of ABS are manufactured on Arburg freeformer, shape of the samples are defined as described in DIN EN ISO 527-2 Typ 1A [14]. For the purpose of comparison three samples are tested initially. Tensile tests are performed on a Zwick Roell Zmart Pro 1474 with a load cell range up to 50 kN and strain is measured using GOM Aramis 8M video strain measurement system. Loading speed is 1 mm/min with a preload of 10 N. Young's modulus is calculated according to DIN 527-1 by the slope of the regression line in the area of 0,05 % to 0,25 % strain [14]. The elastic elongation is determined at the transition from linear to non-linear evolution of the stress strain response.

3.2 Differential Scanning Calorimetry (DSC)

For DSC measurements one cube with an edge length of 2,5x2,5x2,5 mm³, produced on the Arburg freeformer, is tested exemplarily. DSC test is performed on a Netzsch Polyma and starts from - 40°C up to 180°C with 10 K/min. Glass transition temperature is determined according to DIN EN ISO 11357-2 using the turning point procedure [15].

3.3 Dynamic Mechanical Analysis (DMA)

DMA is performed on a TA Instruments Q800 using dual cantilever test on rectangular samples produced by the Arburg freeformer with the dimensions of 70x10x4 mm³, frequency of 1 Hz, heating rate of 3 K/s and amplitude of 20 µm. As described in [16] there are several methods to determine the glass transition temperature. In this case the tangent method according to DIN 65583 is used [17] to specify T_g exemplarily for one sample as the 2 % method results in very small values for T_g.

4 Results and Discussion

4.1 Mechanical properties

An exemplarily stress-strain response resulting from uniaxial tensile loading of an ABS specimen is shown in Figure 2. Young's moduli of the three specimens are equal to 2230,3 ± 11,85 MPa, which is slightly below the value mentioned in the data sheet of the granulate producer. Since the additive manufacturing process leads to a less dense material compared to the injection moulding process, which was potentially used by the granulate producer to establish the data sheet, the Young's modulus is usually lower after processing. Elongation at break is 1,6 % ± 0,0025. Elastic elongation is about 0,6 % which is less than the elongation at yield stated in the manufacturer information. Furthermore, it is below the elastic elongation of 2,5 % stated for the SMA wire.

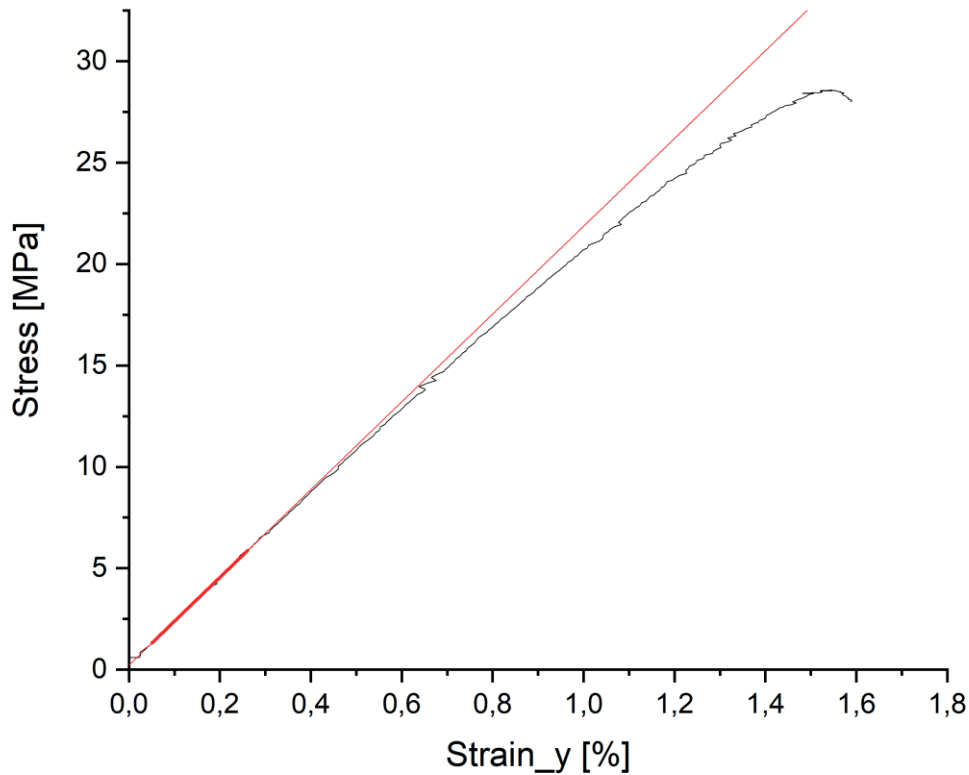


Figure 2 Stress strain diagram used for determination of the Young's modulus exemplarily determined for ABS. Considered strain region for the determination of the Young's modulus is indicated by the red line.

4.2 Thermal properties

Figure 3 illustrates the results of the DMA measurement of one representative ABS sample. The glass transition temperature of ABS is about 92°C. DMA test indicates a storage modulus of 1376 MPa which is much lower compared to the Young's modulus determined at the tensile tests. For a room temperature of 23°C the two moduli are comparable, but in this case the storage modulus is measured in a bending test whereas the Young's modulus is determined in a uniaxial tensile test. This could be the reason for the differences of the values.

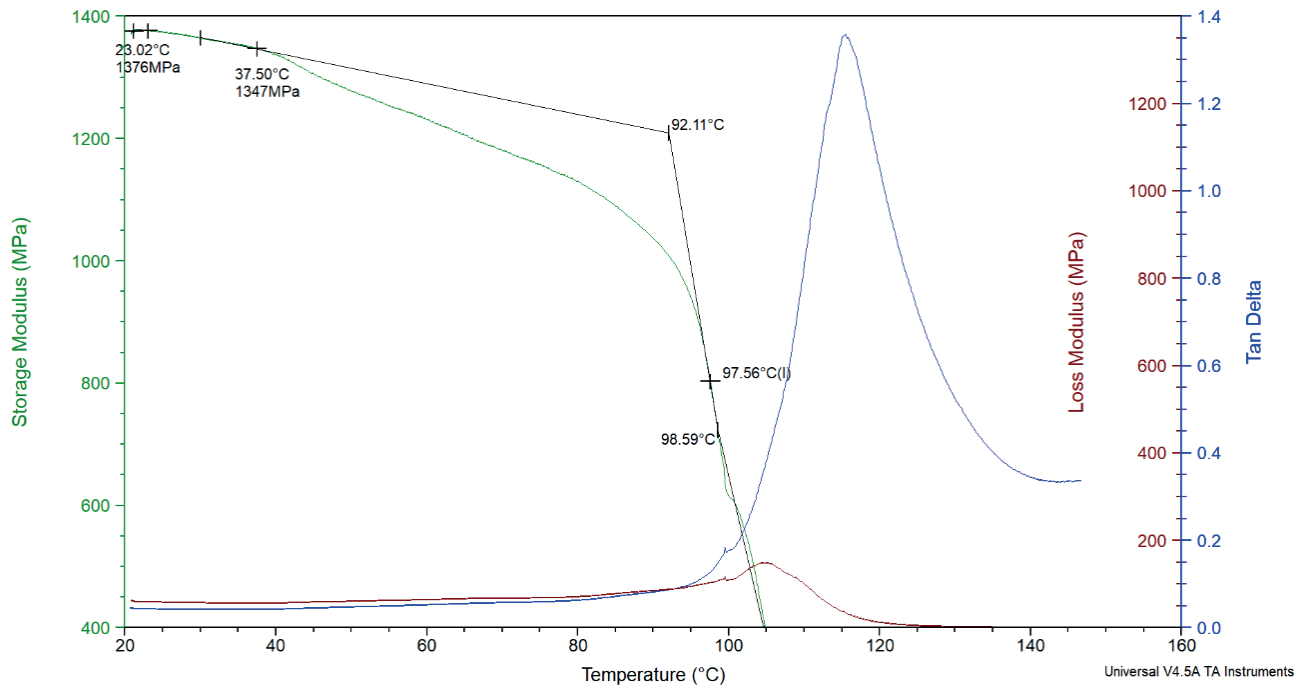


Figure 3 DMA measurement results for ABS sample. Tangent method according to DIN 65583 is used to determine the glass transition temperature

Results of the DSC measurement of a representative ABS specimen are shown in Figure 4. The glass transition temperature is calculated to 101°C which is above the result of the DMA test. But the drop of the specific heat capacity is comparatively small which makes it difficult to identify the exact glass transition temperature. The second endothermic peak at around 140°C is probably caused by the melting process of the specimen.

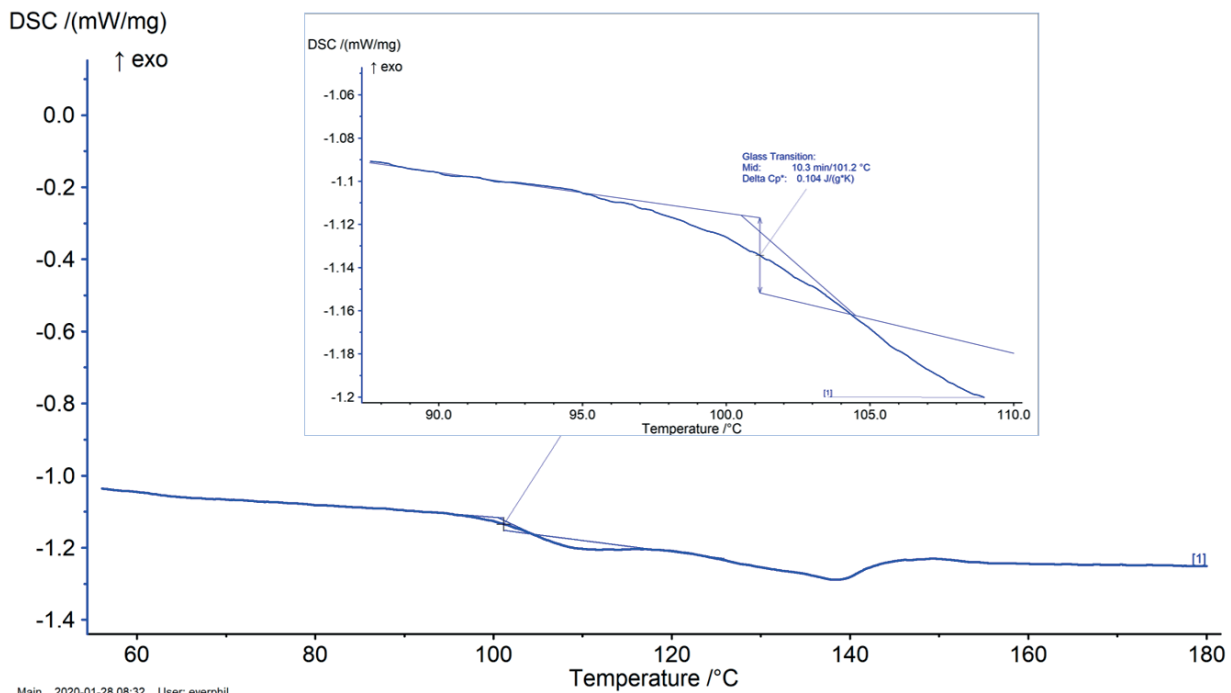


Figure 4 Results of the DSC testing of the ABS sample. Turning point procedure is used to determine the glass transition temperature

5 Summary and Outlook

Results of the tested ABS samples show that neither the Young' modulus nor the maximum elastic elongation are as good as the values in the manufacturer information. But attention must be paid to the fact that the manufacturer information was determined on samples produced by injection moulding. Therefore, the conducted experiments show that the manufacturing of samples on the Arburg freeformer results in worse mechanical properties compared to samples produced by injection moulding. As a consequence, the properties in the manufacturer information cannot be used for severe material selection. That is the reason why samples of the other materials in question need to be tested in DMA, DSC and tensile tests. Furthermore, the experiments show that the values for the properties of ABS are situated in the left corner of the bubble in the Ashby map in Figure 1. Therefore, the test results of the other materials planned to test, will be potentially situated in the left corner of the bubbles as well. Therefore, the properties of the other materials in question have to be determined and the material selection has to be conducted again as the most appropriate materials until now for this case could be unsuitable then. The most appropriate material will be determined then by establishing a new Ashby map based on the results of the tests.

Afterwards alloy composition of the SMA wire will be adjusted so that the transformation temperature is above the installation space temperature of the Arburg freeformer and below glass transition temperature of the matrix material used because thermoplastic polymers tend to creep above glass transition temperature. The average installation space temperatures for the manufacturing of ABS varies between 70°C and 80°C and the glass transition temperature of ABS is measured to be within the range of 92°C and 101°C in this study. Therefore, there is a gap of about 20°C where the transition temperature should be. But the transition temperature is influenced by stress and the alloy composition as investigated by [4]. Therefore, it will be difficult to adjust the transition temperature within the narrow gap of 20°C.

In the future Arburg freeformer will be used to produce polymer samples with embedded SMA wires. Young's modulus of the matrix material will determine the volume fraction of SMA wire in the matrix material as the restoring force of the SMA wire has to be sufficient to deform the matrix material elastically. Therefore, matrix materials with higher stiffnesses require higher volume fractions of SMA for sufficient deformations. Static tensile and bending tests will be conducted on composite samples to determine the properties. Furthermore, pull-out tests will be conducted to determine the strength of the interface between matrix and SMA wire.

6 Acknowledgement

The authors are especially grateful for the financial support from the DFG (WE 4273/20-1). In addition, we thank Jörg Dittus from wbk Institute of Production Science at Karlsruhe Institute of Technology for manufacturing samples of the different matrix materials on the Arburg freeformer.

7 References

- [1] M.-W. Han et al., *Composites Part B: Engineering* **2016**, 285–298.
- [2] S. D. Oehler, D. J. Hartl, R. Lopez, R. J. Malak und D. C. Lagoudas, *Smart Mater. Struct.* **2012**, 9, 1–16.
- [3] N.B. Morgan, *Materials Science and Engineering: A* **2004**, 1-2, 16–23.
- [4] P. Pinter, A. Reeb und K. A. Weidenmann, *Materials Science Forum* **2015**, 205–212.
- [5] C. Dahnke, A. Shapovalov und A. E. Tekkaya, *Procedia Engineering* **2017**, 1511–1516.
- [6] J. Raasch, M. Ivey, D. Aldrich, D. S. Nobes und C. Ayranci, *Additive Manufacturing* **2015**, 132–141.
- [7] A. Lendlein und S. Kelch, *Angewandte Chemie* **2002**, 12, 2138–2162.
- [8] B. T. Lester, T. Baxevanis, Y. Chemisky und D. C. Lagoudas, *Acta Mechanica* **2015**, 12, 3907–3960.
- [9] A. Kloke, *Kunststoffe International* **2018**, 11, 15–21.
- [10] *CES EduPack*, Granta Design, **2019**.
- [11] M. F. Ashby, *Materials Selection in Mechanical Design*, 3rd ed, Elsevier, Oxford, **2005**.
- [12] *Kunststoffe-Bestimmung dynamisch-mechanischer Eigenschaften* DIN EN ISO 6721-1, **2019**.
- [13] INEOS STYROLUTION *Teerluran GP-35-Technical Datasheet*, [Online] available at: https://www.ineos-styrolution.com/Product/Teerluran_Teerluran-GP-35_SKU300600120829_lang_de_DE.html. access on: 28. 01 2020.
- [14] *Kunststoffe-Bestimmung der Zugeigenschaften* DIN EN ISO 527-1, **2012**.
- [15] *Kunststoffe-Dynamische Differenz-Thermoanalyse (DSC)* DIN EN ISO 11357-2, **2019**.
- [16] J. Wolfrum, G. W. Ehrenstein und M. A. Avondet, *Journal of Composite Materials* **2000**, 21, 1788–1807.
- [17] *Faserverstärkte Kunststoffe* DIN 65583, **1999**.

Processing relationships of hybrid polymer-metal composites in the injection moulding process

A. Schwarz¹, W. Liebig^{1,2}, K. Weidenmann^{1,3}, P. Elsner^{1,2}

¹Fraunhofer Institute for Chemical Technology (ICT), Pfinztal, ²Institute for Applied Materials (IAM), Karlsruhe Institute of Technology, Karlsruhe, ³Institute for Materials Resource Management, University of Augsburg, Augsburg

1 Abstract

This paper describes the production of polymer-metal-hybrids with different manufacturing parameters during the injection moulding process and their influence on the shear strength. The joining between a polyamide 12 and an aluminium sheet is investigated with variable melting temperatures of the polymer, holding pressure or rather mould temperature of the injection mould. In spite of the variability of the parameters, all process employments established a connection between the parts. It was also shown, that the melting temperature correlates with the shear strength, but the shear strength values are significantly lower than stated in the literature. Finally, the successful joining of the materials to a hybrid demonstrate that such a connection method has the potential to insert in different application fields.

2 Introduction

Scientists have been researching for new engineering materials with high mechanical properties and low manufacturing effort for a long time [1]. For the manufacturing of a polymer-metal-hybrid (PMH) there are different technologies like injection over-moulding PMH, metal over-moulding PMH, adhesively-bonded polymer-metal hybrid structures and direct-adhesion polymer-metal-hybrid technology. All these production technologies have more than one production-step [2].

The advantage of combining metal and plastic parts is to reduce the total weight [3] and to generate desired properties which cannot be realised with a single bulk material. Manufacturing of a hybrid composite structure often is a two-stage process. The first step is the manufacturing of single parts and the second step is the in-mould or post-mould assembly of two or more parts. Correspondingly, a two-step process is labour-intensive and time-consuming in contrast to a one step process [4].

In this work, the realization of the connection between metal and polymer parts in a one step by using the injection moulding process is analysed. To define the technical process limits, different materials are produced in several test series, while varying the parameters melting temperature, holding pressure and mould temperature. To evaluate the influence of the manufacturing parameters, samples of the hybrid are analysed with optical methods and the shear edge test. Shear strength is determined from this test, which allows to draw conclusions on the quality of adhesion to be reached.

3 Experimentation

3.1 Materials

In the context of the investigations presented here, the polymer PA12 Grilamid TR60 was used. The material has an amorphous structure and is heat resistant. For the combination between polymer and metal in the injection moulding process, an aluminium EN AW-1050A was used and coated with adhesive technicoll 9110 which is activated by higher temperatures.

Table 1: Characteristics of the polymer PA12 Grilamid TR60

Polymer	Glass transition temperature /°C	Absorption of moisture /%	Density /kg/m ³	Young's modulus /MPa
PA 12 Grilamid TR60	300-320	2,0	1060	2200

3.2 Processing parameters

During the manufacturing of the hybrids, various process parameters were applied. The parameters melting temperature, holding pressure and mould temperature were modified gradually. The grades of the parameters were the maximum, minimum and the mean value of the processing area, summarized in Table 2.

Table 2: Processing parameters of the samples PA12 Grilamid TR60

Sample	Melting temperature /°C	Mould temperature /°C	Holding pressure /bar
A1	290	60	300
A2	290	100	300
A3	290	60	650
A4	290	100	650
A5	290	80	475
A6	350	60	475
A7	350	100	475
A8	350	80	300
A9	350	80	650
A10	350	80	475
A11	320	60	300
A12	320	100	300
A13	320	60	650
A14	320	100	650
A15	320	80	475

3.3 Test methods

Figure 1a) shows the tool that was used for the manufacturing of the hybrids. The cutting plate was placed on the aluminium and filled with polymer during the injection moulding process. Samples of

the hybrid were taken 60 mm (near) and 150 mm (distant) away from injection point to investigate changing adhesion. The samples were extracted with the measurement of 12,5 mm x 25 mm. The shear strength between the material parts is investigated by using the shear edge test [5]. The testing device and a test sample is demonstrated in Figure 1b). To hold the test sample in position it is inserted between two support plates and the upper and lower frame displace the different parts of the hybrid during the test. As a result, a force-displacement-curve can be recorded. The testing device is installed in the tension testing machine (Inspekt table blue), the force is measured by a load cell with 5 kN and the testing speed is set to 1 mm / min. With the geometry parameters of the test samples the shear strength can be determined [6]. For the optical analysis a macroscope (Leica Wild M 420), a light microscope (Leica DMRE) and a scanning electron microscope (Zeiss) were used. For the microscope analyses the samples were embedded in a cold cast resin, treated with 4000 μm grade sandpaper and polished with an OPS disc. The samples for the REM-analyses were coated with gold and an EDX-analysis was performed to take a closer look at the interface.

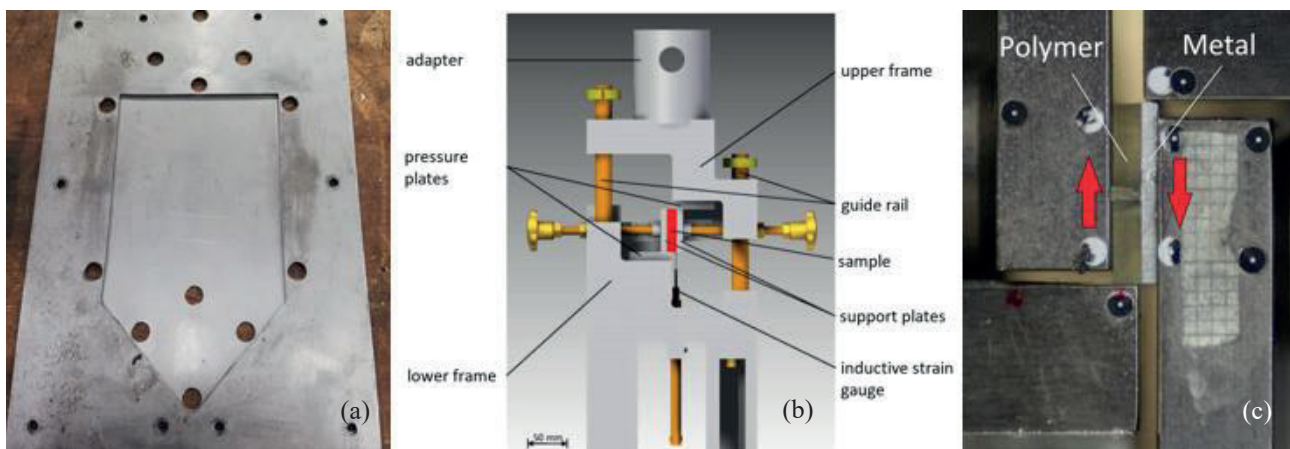


Figure 1: (a) Insertion tool [7], (b) testing advice of the shear strength test [5] and (c) a mounted test sample.

4 Results

4.1 Influence of manufacturing parameters on interface properties

After the shear edge test, the resulting shear strengths are dependent on the manufacturing parameters melting temperature, holding pressure and mould temperature. In Figure 2 shear strength values over the samples are indicated. Sample A14 has the highest shear strength and was manufacturing by applying the highest melting temperature, holding pressure and mould temperature. With increasing melting temperature above the other parameters, the shear strength of the last tested samples (A10-A15) increase. With the series of experiments, the shear strength along the flow path of the polymer melting was investigate and samples near and further away from the sprue were taken from the hybrid. The adhesion between polymer and metal changes between the area near and distant from the sprue. Figure 2 presents the average values of the hybrid samples. Figure 3 shows the force-displacement-curve of different samples with the same manufacturing parameters. During the shear edge test, the samples show two fracture forms, ductile and brittle, respectively.

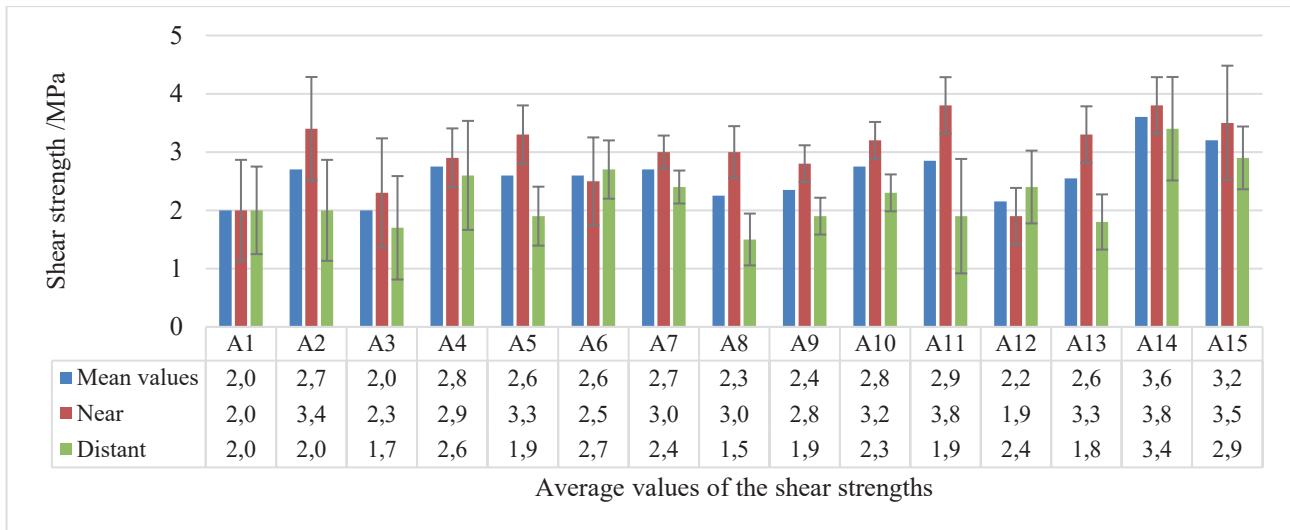


Figure 2: Shear strength of different Grilamid TR60 samples, about the hole part (mean values) and near according to further away from the sprue.

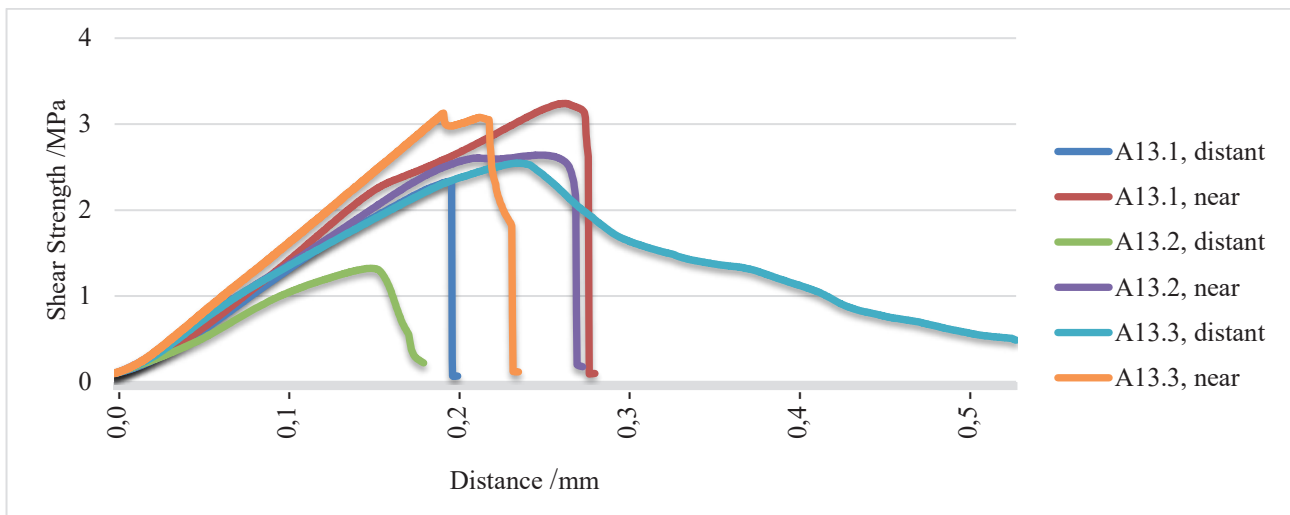


Figure 3: Force-displacement-curve after the shear edge test of three samples (Grilamid TR60) with following parameters, mould temperature 60 °C, holding pressure 650 bar and melting temperature 320 °C.

4.2 Optical analysis

After the shear edge test, the polymer part of most samples is completely removed from the aluminium, but some aluminium sheets have residues of polymer on their surface. Figure 4 a) presents a recording of a polarized, macroscopic analysis of such an aluminium sheet, the area of red polymer is marked. Near the interface, the polymer structure shows cracks like a drop-shaped structure. This can be a reason of the break out of the polymer and can reduce the complete bond strength of the hybrid, compare with Figure 4 b).

A detailed view of such a crack is shown in Figure 5 a). Inside the crack there are filamentary material structures, which remained on pulled apart adhesion promoter. The structure disappears if the electron beam of the scanning electron microscope is on this area for a long, because of the high energy input.

Figure 5 b) shows another border area with drop-shaped structure, adhesion promoter and metal. An EDX analysis cannot be performed because the adhesion promoter and the polymer consist of carbon chains and do not result in different deflections.

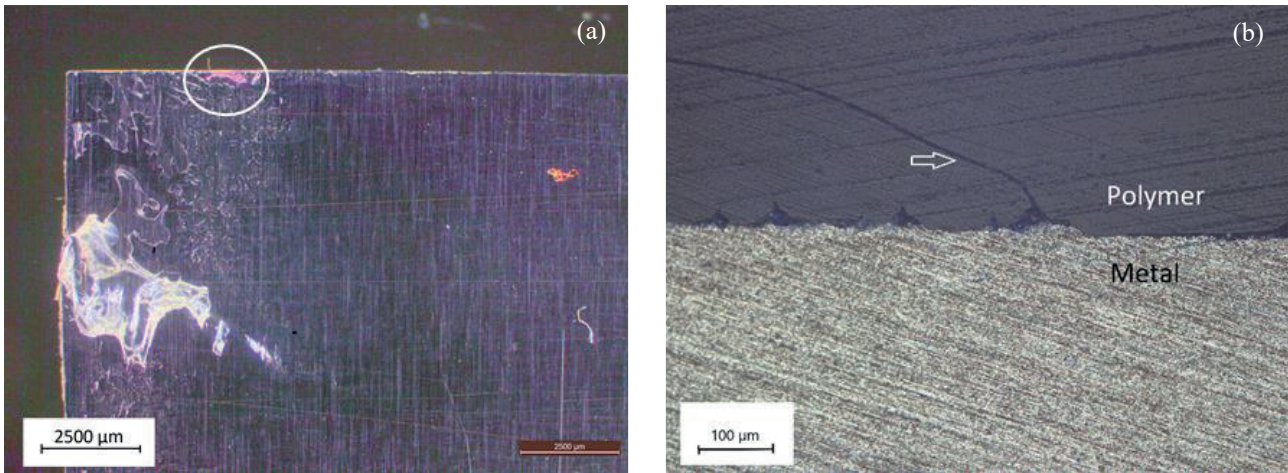


Figure 4: (a) Macroscopic analysis of a shear edge sample with polymer arrears in the white circle, (b) microscopic analysis of the interface with a crack structure inside the polymer like a drop-shaped structure [7].

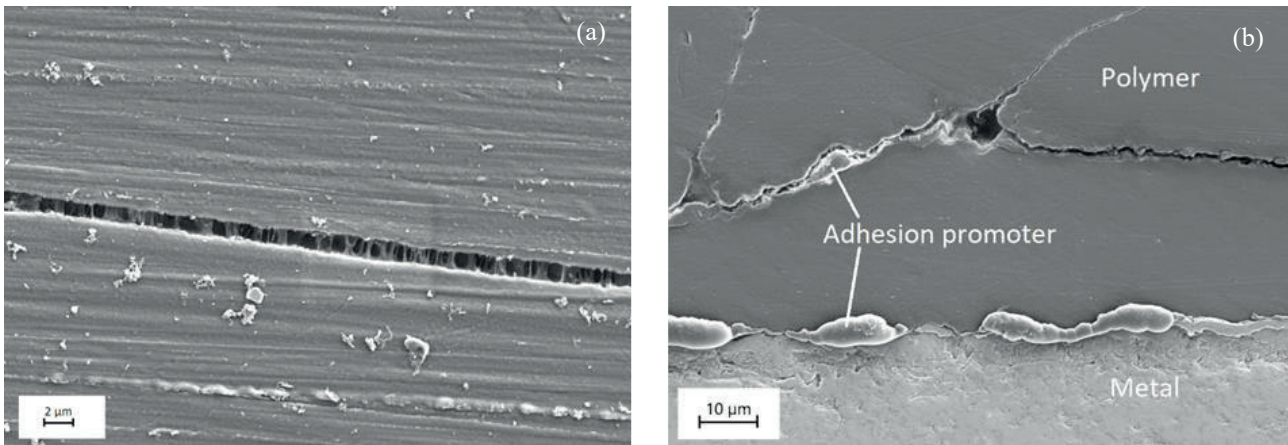


Figure 5: (a) Scanning electron microscope analysis of a fissure, (b) the material transition [7].

5 Discussion

The melting temperature, holding pressure and mould temperature have an influence on the shear strength of the hybrid. The series of experiments show that a higher manufacturing temperature of the whole tool results in higher shear strength. The final shear strength of 3,4 MPa is low in contrast to values of 17 MPa between an aluminium (EN AW-6082) and a polyamide 6 with a NiAl5 coating stated in literature [8]. The coating between the parts can significantly disturb the result of the adhesion between the parts. Other forms of surface treatments, like pin microstructures, realised better shear strengths because they achieved a self-locking between polymer and aluminium after the production [8].

The adhesion coating that was used is activated by a rise in temperature and the polymer cool down depends on the melt path after the mould injection. After investigation of the samples, lower shear strengths were established with increasing length of the melt path. Beside the manufacturing parameters, geometry and size of a component is also important for the final production of a hybrid. The analysis of the interface between polymer and aluminium shows another influence on the polymer promoter inside the polymer matrix, in form of a polymer drop-shaped structure. Because of the carbon compounds of polymer and promoter, a verification by an EDX could not be performed, but the probability that the drop-shaped structure is pure polymer and not a drop of promoter is high. The material quantity of the structures in Figure 4 b) is more than the applied adhesive amount and the analysis of the fissure in Figure 5 a) supports this assumption. By considering the interface, the different structure behaviours of the samples can be explained. If the interface of the shear edge sample has many drop-shaped structures, no ductile slipping occurs but the sample breaks brittle. Ductile slipping results from the parts sliding to each other without an interlock of the interface because of the drop-shaped structure.

6 Conclusion

The present work showed that the resulting process-structure-property relationships of hybrid polymer-metal composites in the injection moulding process can be modified by different manufacturing parameters. If the parameters are in the upper processing range, the properties of the hybrid can be improved, but the material properties and the adhesion promoter must be suitable for injection moulding. To characterize the final influence of the adhesion promoter on the interface, further investigations in form of activation and application possibilities are necessary. A supporting analysis of the temperature profile inside the injection tool during the injection is appropriate for understanding the adhesion promoter effect of the hybrid connection.

7 References

- [1] J.-K. Kim, T.-X. Yu, *Journal of Materials Processing Technology*, **63**, 33–42.
- [2] M. Gruzicic, *American Journal of Science and Technology* **2014**, *Vol. 1, No. 4*, 168–181.
- [3] S. Amancio-Filho, J. Santos, *Polymer Engineering & Science* **2009**, *8*, 1461–1476.
- [4] E. Haberstroh, M. Sickert, *International Journal of Applied Science and Technology* **2014**, *3*, 29–34.
- [5] K. Weidenmann, L. Baumgärtner, B. Haspel, *Materials Science Forum* **2015**, 825–826.
- [6] H. Werner, in *SAMPE Europe Conference*, Stuttgart, Germany, **2017**, p. 1–7.
- [7] A. Schwarz, *Masterarbeit Karlsruher Institut für Technologie (KIT)*, **2019**.
- [8] E. Saborowski, A. Dittes, P. Steinert, T. Lindner, I. Scharf, A. Schubert, T. Lampke, *Materials (Basel)* **2019**, *18*.

IMPRINT - IMPRESSUM HYBRID - MATERIALS AND STRUCTURES 2018 - PROCEEDINGS Editors Joachim M. Hausmann, Marc Siebert, Axel von Hehl Compilation Fraunhofer-Institut für Intelligente Analyse- und Informationssysteme IAIS © DGM - Deutsche Gesellschaft für Materialkunde e.V.
Besucheranschrift: Wallstraße 58/59 10179 Berlin
Postanschrift: DGM - Deutsche Gesellschaft für Materialkunde e.V. c/o INVENTUM GmbH Marie-Curie-
Straße 11-17 53757 Sankt Augustin
T +49-(0)69-75306 750 F +49-(0)69-75306 733 E-Mail: dgm@dgm.de Web: www.dgm.de
ISBN 978-3-88355-417-4 Das Werk einschließlich seiner Teile ist

IMPRINT - IMPRESSUM

HYBRID - MATERIALS AND STRUCTURES 2020 - PROCEEDINGS

Editors

Joachim M. Hausmann, Marc Siebert, Axel von Hehl, Kay A. Weidenmann

Compilation

DGM-Inventum GmbH

© DGM - Deutsche Gesellschaft für Materialkunde e.V.

Das Werk einschließlich seiner Teile ist urheberrechtlich geschützt. Jede Verwertung außerhalb der engen Grenzen des Urheberrechtsgesetzes ist ohne Zustimmung der DGM und der Herausgeber unzulässig und strafbar. Das gilt insbesondere für Vervielfältigungen, Übersetzungen, Mikroverfilmungen und die Einspeicherung und Verarbeitung in elektronischen Systemen.

This work including all its parts is protected by copyright. Any use outside the strict constraints of the German Copyright Law without the permission of the DGM and the editors is prohibited and liable to prosecution. This applies particularly for reproduction, translation, adaption on microfilm, and storage or processing in electronic systems.

Organizer

DGM | Experience · Competence · Knowledge
German Materials Society

Deutsche Gesellschaft für Materialkunde e.V.

c/o DGM-Inventum GmbH

Marie-Curie-Straße 11 - 17

53757 Sankt Augustin

GERMANY

T +49 (0) 69 75306 750

www.dgm.de

dgm@dgm.de

Eventmanagement

DGM-Inventum GmbH
Messe · Konferenz · Fortbildung

DGM-Inventum GmbH

Marie-Curie-Straße 11 - 17

53757 Sankt Augustin

GERMANY

T +49 (0) 69 75306 788

<https://hybrid2020.dgm.de>

hybrid@dgm.de